

# **TWO-PHASE HEAT TRANSFER IN MULTI- CHANNEL FLAT HEAT PIPES**

A thesis submitted for the degree of Doctor of Philosophy

By:

**Valentin Patrick Pascal Guichet**

Department of Mechanical and Aerospace Engineering,

Brunel University London

**September 2022**

---

# Abstract

---

Heat pipes have recently been introduced as thermal absorbers for photovoltaic panels, with the objective of increasing the performance of Photovoltaic/Thermal (PV/T) technologies, which simultaneously produce electrical and thermal energy. To best fit surface cooling applications, advances in the heat pipe designs have been witnessed with the recent introduction of multi-channel flat heat pipes as efficient heat transfer mediums between photovoltaic cells and heat sink. Despite the promising experimental results observed, the complex two-phase heat transfer mechanisms taking place in multi-channel flat heat pipes are poorly understood and remain to be investigated. In addition to the lack of theory and analytical models considering the flat shape and multi-channel internal geometry, numerical modelling of heat pipes using computational fluid dynamic (CFD) technics is still at an early stage. In this regard, this study investigates thoroughly the two-phase heat transfer in a novel multi-channel flat heat pipe using three approaches: theoretical, numerical, and experimental. The main objectives of this research are as follows: 1) Provide a better understanding of two-phase heat transfer in a multi-channel geometry, 2) Develop an analytical model to predict the performance of a multi-channel flat heat pipe which considers the two-phase heat transfer mechanisms taking place in this new geometry, 3) Simulate the working cycle of multi-channel heat pipes using Computational Fluid Dynamics (CFD) techniques, and 4) Compare the developed analytical model and numerical simulations with experimental data.

In this thesis, analytical, numerical, and experimental investigations of two-phase heat transfer in a novel multi-channel flat heat pipe are reported. Based on the two-phase heat transfer theory, a novel analytical model was proposed and used in an iterative tool to predict the performance of the multi-channel heat pipe. In addition, several in-house user-defined functions (UDFs) have been developed and tested to simulate the two-phase heat transfer in multi-channel heat pipes using the Lee model. To develop the analytical and numerical models, a unique three leg multi-channel heat pipe was built and tested. In a second phase, the developed models have been used to predict the thermal performance and simulate the two-phase heat transfer in a novel multi-channel flat heat pipe. The models have been compared to experimental findings from the multi-channel flat heat pipe apparatus for validation.

The research demonstrated that the analytical model proposed can predict and describe the two-phase heat transfer that allows the novel multi-channel flat heat pipe to be one of the most efficient Photovoltaic/Thermal systems reported up to date. New opportunities for surface cooling applications using the promising multi-channel flat heat pipes are emerging.

---

## Declaration

---

No part of this thesis has been submitted in support of an application for any degree or qualification of Brunel University London or any other University or Institute of Learning.

---

# Acknowledgements

---

First, I would like to express my sincere gratitude to my supervisor, Professor Hussam Jouhara, the Head of the Heat Pipe and Thermal Management Research Group, who gave me the opportunity of studying a PhD degree at Brunel University London. In addition to his constant guidance and support, he shared with me his profound interest and passion in this area of research throughout my PhD work. His high competence and expectations of me encouraged me to ensure the quality of my work is of the highest possible standards.

I want to thank Dr. Bertrand Delpech for his constant temperance, calm, and managing skills that have guided me since the first day of my PhD. Bertrand has also supported me personally to fit in the group and conduct my research in accordance with the Group's high standards.

Thank you to all my colleagues from the Heat Pipe and Thermal Management Research Group who made this adventure and challenge more enjoyable every day. It was a great honour for me to learn by your side.

I want to address special thanks to my colleagues and friends Dr. Navid Khordehgah and Dr. Daniel Brough who supported me during my PhD work. They gave me strength and motivation to overcome all the challenges faced during my research work.

I want to thank my friends who supported me throughout the past years. They are a true inspiration to me and help me become a better person. It is a real chance for me to grow older knowing that they will always be here if needed.

Finally, I can't thank enough my family, the people close to my heart, my sister, and my parents. They took care of me from the day I was sent on this planet and gave me unconditional love. You are everything to me, and I hope I can make you proud.

---

# Publications

---

## Published Journal paper

- [1] V. Guichet, S. Almahmoud, and H. Jouhara, "Nucleate pool boiling heat transfer in wickless heat pipes (two-phase closed thermosyphons): A critical review of correlations," *Therm. Sci. Eng. Prog.*, vol. 13, 2019, doi: 10.1016/j.tsep.2019.100384.
- [2] V. Guichet and H. Jouhara, "Condensation, evaporation and boiling of falling films in wickless heat pipes (two-phase closed thermosyphons): A critical review of correlations," *Int. J. Thermofluids*, vol. 1–2, 2020, doi: 10.1016/j.ijft.2019.100001.
- [3] V. Guichet, N. Khordehghah, and H. Jouhara, "Experimental investigation and analytical prediction of a multi-channel flat heat pipe thermal performance," *Int. J. Thermofluids*, p. 100038, Jul. 2020, doi: 10.1016/j.ijft.2020.100038.
- [4] V. Guichet, B. Delpech, N. Khordehghah, and H. Jouhara, "Experimental and theoretical investigation of the influence of heat transfer rate on the thermal performance of a multi-channel flat heat pipe," *Energy*, vol. 250, p. 123804, Jul. 2022, doi: 10.1016/J.ENERGY.2022.123804.
- [5] N. Khordehghah, V. Guichet, S. P. Lester, and H. Jouhara, "Computational study and experimental validation of a solar photovoltaics and thermal technology," *Renew. Energy*, vol. 143, pp. 1348–1356, Dec. 2019, doi: 10.1016/J.RENENE.2019.05.108.
- [6] H. Jouhara, S. Almahmoud, D. Brough, V. Guichet, B. Delpech, A. Chauhan, L. Ahmad, N. Serey, "Experimental and theoretical investigation of the performance of an air to water multi-pass heat pipe-based heat exchanger," *Energy*, vol. 219, 2021, doi: 10.1016/j.energy.2020.119624.
- [7] V. Guichet, B. Delpech, and H. Jouhara, "Experimental investigation, CFD and theoretical modelling of two-phase heat transfer in a three-leg multi-channel heat pipe," *Int. J. Heat Mass Transf.*, vol. 203, p. 123813, Apr. 2023.

## International conferences

- [1] S. Almahmoud, V. Guichet, and H. Jouhara, "Experimental and analytical investigation of a multi-pass air to water heat pipe heat exchanger performance based on the  $\epsilon$ -NTU method", in *International conference on Advances in Energy Systems and Environmental Engineering – ASEE 2019*, Wroclaw university of Science and Technology, Poland, 2019
- [2] V. Guichet, N. Khordehghah, and H. Jouhara, "Experimental investigation and analytical prediction of a multi-channel flat heat pipe thermal performance", in *Industry Sustainable Energy and Environmental Protection conference – ISEEP 2020*, Gloucestershire Science & Technology Park, United Kingdom, 2020
- [3] V. Guichet, N. Khordehghah, and H. Jouhara, "A multi-channel flat heat pipe as a smart cooling material", in *7<sup>th</sup> International Conference on Material Science and Smart Materials – MSSM 2021*, Brunel University London, United Kingdom, 2021.
- [4] V. Guichet, N. Khordehghah, and H. Jouhara, "Influence of the heat transfer rate on the thermal performances of a multi-channel flat heat pipe", in *International conference on water, energy, and climate change – WECC 2021*, University of Sharjah, United Arab Emirates, 2021.
- [5] V. Guichet, L. De Silva, B. Delpech, and H. Jouhara, "A low GWP refrigerant as a replacement of R134a for two-phase heat transfer in a multi-channel flat heat pipe", in *8<sup>th</sup> International Conference on Material Science and Smart Materials – MSSM 2022*, Brunel University London, United Kingdom, 2022.
- [6] V. Guichet, B. Delpech, and H. Jouhara, "Modelling of two-phase heat transfer in a three-leg multi-channel heat pipe", in *14<sup>th</sup> International conference on sustainable energy & environmental protection – SEEP 2022*, Brunel University London, United Kingdom, 2022.

---

# Table of Contents

---

<b>Abstract.....</b>	<b>2</b>
<b>Declaration.....</b>	<b>3</b>
<b>Acknowledgements.....</b>	<b>4</b>
<b>Publications.....</b>	<b>5</b>
<b>Table of Contents .....</b>	<b>7</b>
<b>List of Figures.....</b>	<b>11</b>
<b>List of Tables .....</b>	<b>17</b>
<b>Nomenclature .....</b>	<b>18</b>
<b>Chapter 1 - Introduction and motivation .....</b>	<b>24</b>
1.1 General Background .....	24
1.2 Research motivation.....	26
1.3 Thesis structure.....	27
<b>Chapter 2 - State of the Art .....</b>	<b>30</b>
2.1 Photovoltaic-thermal (PV/T) systems .....	30
2.1.1 Air type PV/T collectors .....	31
2.1.2 Liquid type PV/T collectors.....	32
2.1.3 Heat pipe-based PV/T collectors .....	35
2.1.4 Comparison of existing PV/T systems .....	44
2.2 Multi-channel heat pipes .....	46
2.3 Computational fluid dynamic (CFD) modelling of heat pipes.....	55
2.3.1 Phase change models and source terms.....	55
2.3.2 Simulation of thermosyphons .....	59
2.3.3 Comparison of thermosyphon simulations.....	73
2.4 Research gap identification .....	75
<b>Chapter 3 - Apparatus, experimental procedure, data reduction and error propagation</b>	<b>76</b>
3.1 Three-leg multi-channel heat pipe apparatus.....	76
3.1.1 Apparatus.....	76
3.1.2 Thermocouple locations .....	88
3.2 Multi-channel flat heat pipe apparatus .....	92
3.2.1 Apparatus.....	92
3.2.2 Thermocouple locations .....	97
3.3 Experimental test bench .....	99
3.4 Experimental procedure .....	102

3.4.1	Three-leg multi-channel heat pipe experimental procedure .....	102
3.4.2	Multi-channel flat heat pipe experimental procedure .....	105
3.5	Data reduction.....	109
3.5.1	Heat transfer rate .....	109
3.5.2	Flat heat pipe cooling manifold thermal resistance .....	110
3.5.3	Three-leg heat pipe top cylinder thermal resistance .....	110
3.5.4	Heat flux.....	110
3.5.5	Heat pipe thermal resistances and heat transfer coefficients.....	111
3.6	Error propagation and standard deviation.....	112
3.6.1	Uncertainties .....	112
3.6.2	Error propagation .....	113
3.6.3	Standard deviation .....	115
<b>Chapter 4 -</b>	<b>Theoretical modelling .....</b>	<b>119</b>
4.1	Two-phase heat transfer in single heat pipes .....	119
4.1.1	Two-phase working cycle in a single thermosyphon.....	119
4.1.2	Equivalent thermal resistance network .....	120
4.1.3	Pool boiling .....	122
4.1.4	Filmwise condensation .....	139
4.1.5	Falling film warmup, evaporation and boiling.....	150
4.2	Multi-channel heat pipe model.....	160
4.2.1	Geometry .....	160
4.2.2	Two-phase working cycle in a multi-channel geometry.....	161
4.2.3	Equivalent thermal resistance network .....	163
4.3	Theoretical modelling of the three-leg multi-channel heat pipe apparatus .....	167
4.3.1	Equivalent thermal resistance network of the overall apparatus .....	167
4.3.2	Heat source – Bottom cylinder .....	170
4.3.3	Three-leg multi-channel heat pipe model.....	171
4.3.4	Heat sink – Top cylinder.....	173
4.4	Theoretical modelling of the multi-channel flat heat pipe apparatus.....	176
4.4.1	Equivalent thermal resistance network of the assembly .....	176
4.4.2	Heat source.....	177
4.4.3	Multi-channel flat heat pipe model.....	177
4.4.4	Heat sink.....	182
4.5	Working fluid properties.....	184
4.6	Energy balance and iterative model .....	185
4.6.1	Energy balance .....	185
4.6.2	Simplified flowchart of the iterative model.....	186
4.6.3	Detailed flowchart of the iterative model.....	188



<b>Chapter 5 - Computational fluid dynamics (CFD) modelling .....</b>	<b>192</b>
5.1 Methods for CFD modelling of two-phase flow .....	192
5.1.1 Introduction to computational fluid dynamics (CFD) .....	192
5.1.2 Multi-phase flow modelling .....	193
5.1.3 Volume of Fluid (VOF) model and source terms .....	194
5.1.4 Lee model for two-phase heat transfer and source terms .....	196
5.1.5 User defined functions (UDF) .....	197
5.2 CFD simulation of the three-leg multi-channel heat pipe .....	199
5.2.1 Objectives .....	199
5.2.2 Geometry .....	199
5.2.3 UDF development for two-phase heat transfer .....	200
5.2.4 Mesh sensitivity analysis .....	205
5.2.5 Boundary condition comparison .....	211
5.2.6 Lee models comparison .....	212
5.2.7 Saturation temperature comparison .....	215
5.2.8 Condensation coefficient comparison .....	219
5.2.9 Conclusion and limitations of the Lee model for the three-leg heat pipe simulation .....	221
5.3 Single channel simulations .....	224
5.3.1 Objectives .....	224
5.3.2 Mesh sensitivity analysis .....	224
5.3.3 Conduction profile comparison .....	227
5.3.4 Velocity profile comparison .....	231
5.3.5 Boiling flow investigation .....	234
5.3.6 Conclusion on the single channel simulations .....	240
<b>Chapter 6 - Experimental results and discussion .....</b>	<b>241</b>
6.1 Three-leg multi-channel heat pipe apparatus .....	241
6.1.1 Impact of the heat transfer rate on the thermal performance of the three-leg multi-channel heat pipe .....	241
6.1.2 Three-leg heat pipe temperature profile for thermal resistance model validation 249	
6.1.3 Identification of the optimized two-phase correlations .....	258
6.1.4 Two-phase model validation – three-leg heat pipe .....	275
6.2 Multi-channel flat heat pipe apparatus .....	285
6.2.1 Impact of the heat transfer rate on the thermal performance of the multi- channel flat heat pipe .....	285
6.2.2 Identification of the optimized two-phase correlations .....	293
6.2.3 Two-phase model validation – multi-channel flat heat pipe .....	306

6.2.4	Impact of the tilt angle on the thermal resistance of the multi-channel flat heat pipe	315
6.2.5	Infrared imaging of the multi-channel flat heat pipe .....	323
6.2.6	Phasing out of R134a to a low GWP refrigerant .....	333
<b>Chapter 7 - Conclusions, impact, and suggestions for future work .....</b>		<b>338</b>
7.1	Conclusions from study .....	338
7.2	Impact on the research field .....	341
7.3	Recommendations for future work.....	343
<b>Annexes .....</b>		<b>346</b>
Annexe 1	.....	346
Annexe 2	.....	348
Annexe 3	.....	351
Annexe 4	.....	353
Annexe 5	.....	354
Annexe 6	.....	357
Annexe 7	.....	360
Annexe 8	.....	366
Annexe 9	.....	367
Annexe 10	.....	367
<b>References.....</b>		<b>368</b>

---

# List of Figures

---

Figure 1-1. Power generation capacity by source between 2000 and 2020 and scenario until 2040, adapted from the International Energy Agency [8] statistics.....	25
Figure 1-2. Research study approach.....	28
Figure 2-1. State of the art progression .....	30
Figure 2-2. Micro-heat pipe array (MHPA) and the MHPA based PV/T developed by <i>Deng et al.</i> [42], [43]. .....	36
Figure 2-3. Heat pipe based PV/T system developed by <i>Gang et al.</i> [44], [45] .....	37
Figure 2-4. Heat pipe based PV/T system developed by <i>Moradgholi et al.</i> [46] .....	38
Figure 2-5. Heat pipe based PV/T system developed by <i>Hu et al.</i> [47] .....	39
Figure 2-6. The multi-channel flat heat pipe (heat mat) based PV/T developed by <i>Jouhara et al.</i> [18], [48] and its large scale testing on a complete solar roof. ....	40
Figure 2-7. Micro-heat pipe array (MHPA) and the MHPA based PV/T presented by <i>Modjinou et al.</i> [49] .....	41
Figure 2-8. Wicked heat pipe based PV/T presented by <i>Wu et al.</i> [15] .....	42
Figure 2-9. Micro-channel loop heat pipe based PV/T presented by <i>Yu et al.</i> [50], [51] .....	43
Figure 2-10. Micro-heat pipe array used for latent heat thermal energy storage, by <i>Diao et al.</i> [55].....	46
Figure 2-11. Micro-channel flat heat pipe presented by <i>Zhao et al.</i> [56].....	47
Figure 2-12. Air-cooled multi-port flat heat pipe developed by <i>Zhao et al.</i> [57].....	48
Figure 2-13. Smaller heat mat used for battery management, by <i>Jouhara et al.</i> [58] .....	49
Figure 2-14. Flat plate heat pipe developed by <i>Chen and Chou</i> [59] .....	50
Figure 2-15. Heat pipe solar collectors presented by <i>Azad</i> [60] .....	51
Figure 2-16. Multi-channel heat pipe developed by <i>Sun et al.</i> [54].....	52
Figure 2-17. Radiative multi-channel heat pipe developed by <i>Almahmoud and Jouhara</i> [62], [63].....	53
Figure 2-18. Multi-channel heat pipe developed by <i>Delpech et al.</i> [64].....	53
Figure 2-19. Pressure boundaries considered in the model by <i>Wang et al.</i> [70].....	58
Figure 2-20. a) Vapour velocity contours and b) Filmwise condensation in the simulation by <i>Alizadehdakhel et al.</i> [80] .....	61
Figure 2-21: Volume fraction contours of vapour showing the modelling of pool boiling (a) and Filmwise condensation (b) in a thermosyphon, by <i>Fadhl et al.</i> [84] .....	62
Figure 2-22. Temperature contour of the thermosyphon, by <i>Fadhl et al.</i> [84].....	63
Figure 2-23. a) Volume of Fluid profile and b) Velocity vectors in the simulation of <i>Asmaie et al.</i> [87] .....	65
Figure 2-24. a) Temperature contour of the R134a thermosyphon, and b) Vapour phase contour of the R404a thermosyphon at a time $t=60s$ , by <i>Fadhl et al.</i> [89] .....	66
Figure 2-25. Temperature and Volume of fluid contour for a TPCT with and without fins at the condenser, from <i>Fertahi et al.</i> [93].....	68
Figure 2-26. Vapour volume fraction contours, from <i>Wang et al.</i> [96] .....	70
Figure 2-27. Vapour volume fraction contours, from <i>Hosseinzadeh et al.</i> [98] .....	71
Figure 3-1. Heat transfer schematic in the three-leg multi-channel heat pipe.....	77
Figure 3-2. Heat transfer schematic in the three-leg multi-channel heat pipe assembly .....	78
Figure 3-3. Design stages of the three-leg heat pipe .....	79
Figure 3-4. Manufacturing drawings of the three-leg heat pipe .....	80
Figure 3-5. Three-leg heat pipe thermal resistance network used for sizing calculation.....	81
Figure 3-6. Finite element analysis of the three-leg heat pipe elements .....	84
Figure 3-7. Manufacturing process of the three legs heat pipe prototype.....	86
Figure 3-8. Three-leg multi-channel heat pipe apparatus.....	87

Figure 3-9. Omega 2-Piece Mica Insulated Band Heater 800W used on the three-leg heat pipe apparatus .....	88
Figure 3-10. Thermocouple locations on the three-leg multi-channel heat pipe only .....	89
Figure 3-11. Thermocouple locations on the three-leg multi-channel heat pipe assembly .....	90
Figure 3-12. Heat transfer schematic of the multi-channel flat heat pipe assembly .....	92
Figure 3-13. (A) Multi-channel flat heat pipe investigated and (B) its cooling manifold .....	93
Figure 3-14. Cooling manifold internal structure .....	94
Figure 3-15. Multi-channel flat heat pipe assembly with silicon flat heaters as a heat source and a cooling manifold as a heat sink .....	94
Figure 3-16. Multi-channel flat heat pipe drawing .....	95
Figure 3-17. Channels of the multi-channel flat heat pipe .....	96
Figure 3-18. Open groove of the multi-channel flat heat pipe .....	97
Figure 3-19. Thermocouple locations on the multi-channel flat heat pipe .....	97
Figure 3-20. Installation of the thermocouples on the flat heat pipe .....	99
Figure 3-21. Experimental test bench while testing the multi-channel flat heat pipe .....	100
Figure 3-22. Experimental test bench while testing the three-leg multi-channel heat pipe ..	101
Figure 3-23. Piping and instrumentation diagram (P&ID) of the multi-channel flat heat pipe test rig .....	102
Figure 3-24. Usual heat pipe testing protocol – no steady state reached .....	104
Figure 3-25. Three-leg heat pipe final experimental protocol .....	105
Figure 3-26. Front and back heat pipe surface set up during infrared imaging experiments. ....	109
Figure 3-27. Theoretical and experimental errors of the heat transfer rate and equivalent top cylinder resistance during the multi-channel flat heat pipe experiments .....	115
Figure 3-28. Theoretical and experimental errors of the boiling, condensation, and total thermal resistances during the three-leg heat pipe experiments .....	116
Figure 3-29. Theoretical and experimental errors of the heat transfer rate and cooling manifold resistance during the multi-channel flat heat pipe experiments .....	117
Figure 3-30. Theoretical and experimental errors of the boiling, condensation, and total flat heat pipe thermal resistance during the multi-channel flat heat pipe experiments .....	118
Figure 4-1. Two-phase working fluid cycle in a wickless heat pipe (thermosyphon) .....	119
Figure 4-2. Single thermosyphon thermal resistance model .....	121
Figure 4-3. Cyclic model of bubble growth from a surface, adapted from <i>Carey</i> [24] .....	124
Figure 4-4. Bubble growth from a surface, stage $t = t_0$ .....	124
Figure 4-5. Bubble growth from a surface, stage $t = t_1$ .....	124
Figure 4-6. Bubble growth from a surface, stage $t = t_2$ .....	125
Figure 4-7. Bubble growth from a surface, stage $t = t_3$ .....	125
Figure 4-8. Bubble growth from a surface, stage $t = t_4$ .....	126
Figure 4-9. Bubble growth from a surface, stage $t = t_5$ .....	126
Figure 4-10. Bubble departure frequency, bubble growth period and waiting period, from <i>Collier and Thome</i> [78] .....	128
Figure 4-11. Pool boiling curve of water at 1 atm pressure, adapted from <i>Yunus A. Cengel</i> [20] .....	130
Figure 4-12. Bubble phenomena during nucleate boiling regime, from <i>Gaertner</i> [95] .....	131
Figure 4-13. Map of the condensation modes by <i>Tanasawa</i> [175] .....	140
Figure 4-14. <i>Nusselt</i> [18] theory, film condensation on a vertical plate .....	141
Figure 4-15. Falling film boiling, model by <i>Cerza and Sernas</i> [233] .....	157
Figure 4-16. Multi-channel geometry schematic .....	161
Figure 4-17. Two-phase working fluid cycle in a multi-channel geometry .....	162
Figure 4-18. Schematized development of the theoretical model of a multi-channel heat pipe .....	164

Figure 4-19. Multi-channel heat pipe thermal resistance model .....	166
Figure 4-20. Thermal resistance network of the multi-channel three-leg heat pipe assembly .....	168
Figure 4-21. Equivalent thermal resistance network of the multi-channel three-leg heat pipe assembly .....	169
Figure 4-22. Experimental equivalent heat sink thermal resistance of the three-leg heat pipe and respective approached function .....	175
Figure 4-23. Thermal resistance network of the multi-channel flat heat pipe assembly .....	176
Figure 4-24. Radial conduction geometry of the multi-channel flat heat pipe considered ....	178
Figure 4-25. Multi-channel flat heat pipe thermal resistance simplification .....	181
Figure 4-26. Experimental cooling manifold thermal resistance and respective correlated functions .....	183
Figure 4-27. Simplified flow chart of the theoretical model calculation procedure .....	187
Figure 4-28. Detailed flowchart of the theoretical model calculation procedure .....	189
Figure 5-1. Multi-phase flow data structure .....	193
Figure 5-2. User defined inputs to the ANSYS Fluent solver, adapted from [249] .....	198
Figure 5-3. Three-leg heat pipe geometry considered for CFD simulation .....	199
Figure 5-4. Vapour phase mass source term UDF for Lee model .....	200
Figure 5-5. Modified Lee model UDF with computational saturation temperature (part1) ....	202
Figure 5-6. Modified Lee model UDF with computational saturation temperature (part2) ....	203
Figure 5-7. Three-leg heat pipe – mesh comparison .....	206
Figure 5-8. Temperature evolution in the three-leg heat pipe during the mesh sensitivity analysis simulations .....	208
Figure 5-9. Mesh sensitivity analysis – heat pipe temperature after 20s .....	209
Figure 5-10. Mesh sensitivity analysis – Accuracy and calculation time for 20s simulated with different meshes .....	210
Figure 5-11. Boundary condition comparison .....	212
Figure 5-12. Lee model comparison .....	214
Figure 5-13. Saturation temperature comparison .....	216
Figure 5-14. Transient warmup of the three-leg heat pipe with $T_{sat}=290K$ .....	217
Figure 5-15. Transient warmup of the three-leg heat pipe with $T_{sat}=300K$ .....	218
Figure 5-16. Condenser temperature simulated at different condensation mass transfer coefficient $\beta_c$ , adapted from <i>Kim et al.</i> [71] .....	220
Figure 5-17. Difference of temperature between the simulations and experimental data at various condensation mass transfer coefficients .....	221
Figure 5-18. Lee model parameters adjustment to fit heat pipe simulation to experimental data .....	223
Figure 5-19. Single channel simulation geometry .....	224
Figure 5-20. Single channel – mesh comparison .....	225
Figure 5-21. Single channel - mesh sensitivity analysis .....	226
Figure 5-22. Temperature profile of the flat heat pipe channel cross-section and comparison with circular channels .....	227
Figure 5-23. Conduction parameters to determine the conduction resistance for one channel .....	229
Figure 5-24. Conduction thermal resistance of the flat heat pipe channel (from CFD) and corresponding correction factor .....	230
Figure 5-25. Velocity profile of the channels at similar inlet velocity .....	232
Figure 5-26. Velocity profiles of the channels at similar inlet mass flow rate .....	233
Figure 5-27. R134a boiling pattern in the multi-channel flat heat pipe channel – 3D view ...	235
Figure 5-28. R134a boiling pattern in the multi-channel flat heat pipe channel – Cross-section view .....	236

Figure 5-29. Solid and liquid temperature profile in the multi-channel flat heat pipe channel .....	237
Figure 5-30. Water boiling pattern in the multi-channel flat heat pipe channel – 3D view....	238
Figure 5-31. Water boiling pattern in the multi-channel flat heat pipe channel – Cross-section view.....	239
Figure 6-1. Impact of the heat flux on the local boiling heat transfer coefficients of the three-leg heat pipe.....	242
Figure 6-2. Impact of the heat flux on the local boiling thermal resistances of the three-leg heat pipe .....	243
Figure 6-3. Impact of the heat flux on the total boiling thermal resistance of the three-leg heat pipe .....	244
Figure 6-4. Impact of the heat flux on the local condensation heat transfer coefficients of the three-leg heat pipe .....	245
Figure 6-5. Impact of the heat flux on the local condensation thermal resistances of the three-leg heat pipe.....	246
Figure 6-6. Impact of the heat flux on the total condensation thermal resistance of the three-leg heat pipe.....	247
Figure 6-7. Share of the boiling and condensation thermal resistances in the total thermal resistance of the three-leg heat pipe.....	248
Figure 6-8. Impact of the heat transfer rate on the total thermal resistance of the three-leg heat pipe .....	249
Figure 6-9. Average temperature of the three-leg heat pipe at different level for various heat transfer rates – Vertical validation.....	250
Figure 6-10. Impact of the heat transfer rate on the temperature difference between different levels of the three-leg heat pipe – Vertical validation .....	251
Figure 6-11. Impact of the heat transfer rate on the temperature of the three parallel legs at the evaporator section – Horizontal validation .....	254
Figure 6-12. Impact of the heat transfer rate on the temperature of the three parallel legs at the adiabatic section – Horizontal validation .....	255
Figure 6-13. Impact of the heat transfer rate on the temperature of the three parallel legs at the condenser section – Horizontal validation.....	256
Figure 6-14. Temperature profile of the three-leg heat pipe during its transient warmup.....	257
Figure 6-15. Pool boiling heat transfer coefficient with the boiling heat flux – Bottom collector .....	259
Figure 6-16. Best pool boiling heat transfer coefficient correlation with the boiling heat flux – Bottom collector.....	260
Figure 6-17. Best pool boiling correlations with the experimental pool boiling heat transfer coefficient in the bottom collector .....	261
Figure 6-18. Error made on the predicted bottom collector pool boiling heat transfer coefficient by the most accurate correlations .....	262
Figure 6-19. Average error of the pool boiling correlations over the whole range of heat transfer rate – Bottom collector.....	263
Figure 6-20. Best pool boiling heat transfer coefficient correlation with the boiling heat flux – Single leg .....	264
Figure 6-21. Best pool boiling correlations with the experimental pool boiling heat transfer coefficient in a leg.....	265
Figure 6-22. Error made on the predicted pool boiling heat transfer coefficient in a leg by the most accurate correlations .....	266
Figure 6-23. Average error of the pool boiling correlations over the whole range of heat transfer rate – Single leg .....	267

Figure 6-24. Falling film boiling heat transfer coefficient with the boiling heat flux – Single leg	268
Figure 6-25. Condensation heat transfer coefficient with the condensation heat flux – top collector	269
Figure 6-26. Best condensation heat transfer coefficient correlation with the condensation heat flux – top collector	270
Figure 6-27. Best condensation correlations with the experimental condensation heat transfer coefficient in the top collector	271
Figure 6-28. Error made on the predicted top collector condensation heat transfer coefficient by the most accurate correlation	272
Figure 6-29. Average error of the condensation correlations over the whole range of heat transfer rate – Top collector	273
Figure 6-30. Pool boiling heat transfer coefficient prediction – Three-leg heat pipe	275
Figure 6-31. Local pool boiling thermal resistances prediction – Three-leg heat pipe	276
Figure 6-32. Prediction error on the local boiling thermal resistances – Three-leg heat pipe	277
Figure 6-33. Equivalent boiling thermal resistance prediction - Three-leg heat pipe	278
Figure 6-34. Condensation heat transfer coefficient prediction – Three-leg heat pipe	279
Figure 6-35. Local condensation thermal resistances prediction – Three-leg heat pipe	280
Figure 6-36. Prediction error on the local condensation thermal resistances – Three-leg heat pipe	281
Figure 6-37. Equivalent condensation thermal resistance prediction - Three-leg heat pipe	282
Figure 6-38. Total three-leg multi-channel heat pipe thermal resistance prediction	283
Figure 6-39. Prediction error on the total three-leg multi-channel heat pipe thermal resistance	284
Figure 6-40. Impact of the heat transfer rate and coolant flow rate on the boiling thermal resistance of the multi-channel flat heat pipe	285
Figure 6-41. Difference of temperature between the thermocouples RB and LB at the condenser	287
Figure 6-42. Condensation thermal resistances of the multi-channel flat heat pipe calculated with the left thermocouples LB, right thermocouples RB and temperature average of all the thermocouples	288
Figure 6-43. Impact of the heat transfer rate and coolant flow rate on the condensation thermal resistance of the multi-channel flat heat pipe	290
Figure 6-44. Share of the boiling and condensation thermal resistances in the total thermal resistance of the multi-channel flat heat pipe	291
Figure 6-45. Impact of the heat transfer rate and coolant flow rate on the total thermal resistance of the multi-channel flat heat pipe	292
Figure 6-46. Pool boiling heat transfer coefficient with the boiling heat flux and heat transfer rate	294
Figure 6-47. Predicted pool boiling heat transfer coefficient with the experimental pool boiling heat transfer coefficient	295
Figure 6-48. Best pool boiling correlations with the experimental pool boiling heat transfer coefficient	296
Figure 6-49. Error made on the predicted pool boiling heat transfer coefficient by the most accurate correlations	297
Figure 6-50. Average error of the pool boiling correlations over the whole range of heat transfer rate	299
Figure 6-51. Laminar condensation heat transfer coefficient with the condensation heat flux and heat transfer rate	300

Figure 6-52. Wavy condensation heat transfer coefficient with the condensation heat flux and heat transfer rate .....	301
Figure 6-53. Turbulent condensation heat transfer coefficient with the condensation heat flux and heat transfer rate .....	302
Figure 6-54. Predicted laminar condensation heat transfer coefficient with the experimental condensation heat transfer coefficient .....	303
Figure 6-55. Average error of the condensation correlations over the whole range of heat transfer rate .....	304
Figure 6-56. Pool boiling heat transfer coefficient prediction – Multi-channel flat heat pipe.	307
Figure 6-57. Pool boiling thermal resistance prediction – Multi-channel flat heat pipe.....	308
Figure 6-58. Prediction error on the boiling thermal resistance – Multi-channel flat heat pipe .....	309
Figure 6-59. Condensation heat transfer coefficient prediction – Multi-channel flat heat pipe .....	310
Figure 6-60. Condensation thermal resistance prediction – Multi-channel flat heat pipe .....	311
Figure 6-61. Prediction error on the condensation thermal resistance – Multi-channel flat heat pipe .....	312
Figure 6-62. Total multi-channel flat heat pipe thermal resistance prediction .....	313
Figure 6-63. Prediction error on the total multi-channel flat heat pipe thermal resistance ...	314
Figure 6-64. Impact of the tilt angle on the multi-channel flat heat pipe boiling thermal resistance.....	315
Figure 6-65. Impact of the tilt angle on the multi-channel flat heat pipe condensation thermal resistance.....	317
Figure 6-66. Impact of the tilt angle on the adiabatic and condenser temperature of the heat pipe at a heat transfer rate of 1500W. ....	319
Figure 6-67. Impact of the tilt angle on the multi-channel flat heat pipe total thermal resistance.....	320
Figure 6-68. Impact of the tilt angle on the multi-channel flat heat pipe total thermal resistance for low, medium, and high heat transfer rates.....	321
Figure 6-69. Infrared imaging of the front and back surfaces of the multi-channel flat heat pipe at a heat transfer rate of 1000W. ....	323
Figure 6-70. Detailed infrared imaging of the front heat pipe surface.....	324
Figure 6-71. Detailed infrared imaging of the cooling manifold .....	325
Figure 6-72. Detailed infrared imaging of the back heat pipe surface .....	326
Figure 6-73. Thermocouple's location on the infrared imaging of the condenser .....	327
Figure 6-74. Infrared imaging of the back heat pipe surface with a cooling manifold placed on the side .....	328
Figure 6-75. Comparison between the traces of thermal paste on the condenser and infrared imaging of the condenser. ....	329
Figure 6-76. Infrared imaging of the front heat pipe surface at various tilt angles .....	330
Figure 6-77. Infrared imaging of the back heat pipe surface at various heat transfer rates .....	331
Figure 6-78. Infrared imaging of the transient warmup of the multi-channel flat heat pipe... ..	332
Figure 6-79. Global warming potential (GWP) of refrigerants.....	334
Figure 6-80. Boiling thermal resistance comparison between R134a and Opteon .....	335
Figure 6-81. Condensation thermal resistance comparison between R134a and Opteon ...	336
Figure 6-82. Total thermal resistance comparison between R134a and Opteon .....	337
Figure 0-1. Three-leg heat pipe design calculation tool interface (1).....	346
Figure 0-2. Three-leg heat pipe design calculation tool interface (2).....	347
Figure 0-3. Variation of the factor $f_1$ [108].....	348
Figure 0-4. Multi-channel flat heat pipe model interface.....	353
Figure 0-5. Single channel mesh selected and equivalent cylindrical channel .....	367



---

## List of Tables

---

Table 2-1. State of the Art on PV/T systems.....	44
Table 2-2. <i>Schrage</i> [66] phase change model .....	55
Table 2-3. <i>Lee</i> [67] phase change model.....	56
Table 2-4. Investigation of the evaporation and condensation mass transfer coefficients values in the Lee model, from <i>Kim et al.</i> [71] .....	57
Table 2-5. <i>Wang et al.</i> [70] phase change model.....	58
Table 2-6. <i>Nichita and thome</i> [74] phase change model.....	59
Table 2-7. State of the art of available simulations of thermosyphons. ....	73
Table 3-1. Thermocouples labels and locations on the three-leg multi-channel heat pipe.....	91
Table 3-2. Thermocouples labels and location on the multi-channel flat heat pipe.....	98
Table 3-3. Estimated measurement uncertainties.....	112
Table 4-1. Nucleate pool boiling heat transfer coefficient <i>h<sub>nb</sub></i> correlations .....	133
Table 4-2. Filmwise condensation heat transfer coefficient <i>h<sub>c</sub></i> correlations.....	146
Table 4-3. Falling film warmup (sensible heating) heat transfer coefficient <i>h<sub>ff</sub></i> correlations .....	151
Table 4-4. Falling film evaporation heat transfer coefficient <i>h<sub>ff</sub></i> correlations.....	152
Table 4-5. Falling film boiling heat transfer coefficient <i>h<sub>ff</sub></i> correlations .....	158
Table 4-6. List of the thermal resistances included in the multi-channel thermal resistance model. ....	165
Table 4-7. Use of each thermal resistance by the iterative model.....	170
Table 4-8. Cooling manifold thermal resistance correlated functions .....	184
Table 4-9. Working fluid characteristics and corresponding functions' names. ....	185
Table 5-1. R134a liquid phase properties .....	204
Table 5-2. R134a vapour phase properties.....	204
Table 5-3. Temperature measurement in the conduction profile of simulated channels .....	228
Table 5-4. Conduction thermal resistances of the 3 investigated channels .....	229
Table 5-5. Boundary condition of the channels.....	231

# Nomenclature

$A$	Surface area	$m^2$
$c_p$	Specific heat	$J/kg.K$
$c_v$	Specific heat at constant volume	$J/kg.K$
$C$	Constant	dimensionless
$C_{sf}$	Constant in Rohsenow correlation depending on the surface-fluid combination	dimensionless
$D$	Diameter	$m$
$D_d$	Bubble departure diameter	$m$
$De$	Dean number	dimensionless
$D_{sm}$	Sauter mean diameter	$m$
$f_d$	Bubble departure frequency	$s^{-1}$
$\vec{F}_{CSF}$	Continuum surface force	$N$
$g$	Gravitational acceleration	$m/s^2$
$\vec{g}$	Volumetric force vector	$m/s^2$
$h$	Heat transfer coefficient	$W/m^2.K$
$h^*$	Dimensionless heat transfer coefficient,	dimensionless
$i_{lv}$	Latent heat of vaporization	$J/kg$
$J$	Solar irradiation	$W/m^2$
$Ja$	Jakob number, ( $Ja = \Delta T c_{p,l} \rho_l / \rho_v i_{lv}$ )	dimensionless
$k$	Thermal conductivity	$W/m.K$
$K_a$	Kapitza number, ( $K_a = g \mu^4 / \rho \sigma^3$ )	dimensionless
$L$	Length	$m$
$L_b$	Bubble length scale, ( $L_b = [\sigma / g(\rho_l - \rho_v)]^{1/2}$ )	$m$

$l_0$	Viscous length, ( $l_0 = [\mu_l^2/\rho_l^2g]^{1/3}$ )	m
$m$	Mass	kg
$\dot{m}$	Mass flow rate	kg/s
$\dot{m}_M$	Mass transfer rate	kg/m <sup>2</sup> .s
$M_{mol}$	Molecular weight	kg/kmol
$n$	Number of units	dimensionless
$Nu$	Nusselt number, ( $Nu = hL/k$ )	dimensionless
$p$	Perimeter	m
$P$	Pressure	N/m <sup>2</sup> or Pa
$Pe$	Film Peclet modulus, ( $Pe = Re_f Pr_l$ )	dimensionless
$P_{el}$	Electrical power	W
$Pr$	Prandtl number, ( $Pr = \mu c_p/k$ )	dimensionless
$\dot{Q}$	Heat transfer rate	W
$q''$	Heat flux per unit surface area	W/m <sup>2</sup>
$\vec{q}''$	Heat flux vector	W/m <sup>2</sup>
$q'''_g$	Volumetric heat source	W/m <sup>3</sup>
$r$	Radius	m
$R$	Thermal resistance	K/W
$Re$	Reynolds number	dimensionless
$Re_f$	Falling film Reynolds number, $Re_f = 4\Gamma_z/\mu_l$	dimensionless
$R_{gas}$	Universal gas constant	J/mole.K
$s$	Safety coefficient	dimensionless
$S$	Shape factor	m
$S_E$	Energy source term	J/m <sup>3</sup> s

$S_M$	Mass source term	kg/m <sup>3</sup> s
$S_w$	Yield tensile strength of the wall	MPa
$S_x$	Uncertainty related to the variable $x$	Unit of $x$
$t$	Time	s
$t_w$	Wall thickness	m
$T$	Temperature	K
$T_s$	Surface temperature	K
$T_{sat}$	Saturation temperature	K
$T_v$	Vapour temperature	K
$T_w$	Wall temperature	K
$u_z$	Velocity in the z direction	m/s
$U$	Internal energy	J/kg
$\vec{U}$	Internal energy vector	J/kg
$v$	Velocity	m/s
$v_y$	Velocity in the y direction	m/s
$V$	Volume	m <sup>3</sup>
$\vec{V}$	Velocity vector	m/s
$V_{water\ in\ 10s, manual, i}$	Volume of water manually recovered in 10s	ml
$w$	Pitch	m
$x$	Coordinate	m
$y$	Coordinate	m
$z$	Coordinate	m
<b>Greek Symbols</b>		
$\alpha_l$	Liquid phase volume fraction	dimensionless
$\alpha_v$	Vapour phase volume fraction	dimensionless

$\beta$	Constant	dimensionless
$\beta_{e/c}$	Mass transfer coefficient of evaporation/condensation	$s^{-1}$
$\Delta$	Difference	dimensionless
$\delta$	Falling film condensate thickness	m
$\delta_{tp}$	Thermal paste thickness	m
$\eta$	Efficiency	%
$\Gamma$	Mass flow rate of liquid per unit periphery	Kg/m.s
$\rho$	Density	$kg/m^3$
$\sigma$	Surface tension	N/m
$\sigma_w$	Wall stress	MPa
$\tau$	Shear stress	$N/m^2$
$\vec{\tau}$	Stress tensor	$N/m^2$
$\mu$	Dynamic viscosity	Pa.s
$\psi$	Mixing Coefficient in El-Genk [1] correlation	dimensionless
<b>Subscripts</b>		
$a$	Adiabatic	
$alum$	Aluminium	
$atm$	Atmospheric	
$avg$	Average	
$ax$	Axial	
$BC$	Bottom cylinder	
$boiling$	Boiling	
$c$	Condenser/Condensation	
$cav$	Cavity	

<i>condensation</i>	Condensation	
<i>conduction</i>	Conduction	
<i>cs</i>	Cross-section	
<i>E</i>	Energy	
<i>e</i>	Evaporator/Evaporation	
<i>el</i>	Electrical	
<i>ext</i>	External	
<i>ff</i>	Falling film	
<i>fc</i>	Forced convection	
<i>ffb</i>	Falling film boiling	
<i>heaters</i>	Heaters	
<i>hp</i>	Heat pipe	
<i>i</i>	Inner	
<i>in</i>	Inlet	
<i>int</i>	Internal	
<i>l</i>	Liquid	
<i>lv</i>	Liquid-vapour	
<i>M</i>	Mass	
<i>max</i>	Maximum	
<i>mix</i>	Mixture	
<i>mol</i>	Molar	
<i>nb</i>	Nucleate boiling	
<i>o</i>	Out, outer	
<i>out</i>	Outlet	

<i>pb</i>	Pool boiling	
<i>PV</i>	Photovoltaic	
<i>s</i>	Solid, surface	
<i>sat</i>	Saturation	
<i>TC</i>	Top cylinder	
<i>tot</i>	Total	
<i>tp</i>	Thermal paste	
<i>v</i>	Vapour	
<i>W</i>	Wall	
<i>water</i>	Water	
<i>3LHP</i>	Three-leg heat pipe	
<b>Superscripts</b>		
"	Per surface area	m <sup>-2</sup>
*	Dimensionless	dimensionless
·	Per unit of time	s <sup>-1</sup>
<b>Acronyms</b>		
CFD	Computational fluid dynamic	
UDF	User defined function	
VOF	Volume of Fluid	

---

# Chapter 1 - Introduction and motivation

---

## 1.1 General Background

In agreement with the current global warming concerns and rising price of energy, environmentally friendly technologies aiming at recovering renewable energy represent a main area of research and a major challenge for our future. Step by step, renewable energies are becoming more significant in our production strategies: in 2017, the electricity production from renewable resources (including biofuels, hydro, geothermal, solar, wind and tide) reached 25% of the global power generation [2]. The next year, in 2018, the electricity generation from renewables rose by 450 terawatt-hours (TWh) which was 7% more compared to the previous year [3]. Among the most promising renewable energies, solar energy is inexhaustible on a human scale, available worldwide, and presents an incredible potential to produce electrical and thermal energy. However, this potential remains largely under-exploited. Indeed, according to the International Energy Agency statistics, solar energies provided 303 TWh in 2016, 454 TWh in 2017, and 570 TWh in 2018, which represent 1.2%, 1.8%, and 2.1% of the global power generation for each year, respectively [2], [4]–[6]. Nevertheless, solar energy is a main component of renewable energies: in 2017, solar energy contributed to 7% of the renewable electricity produced in the world and ranked third after hydro energy (66%) and wind energy (18%) [7]. Due to its largely unexploited potential, solar is the technology that is progressing the fastest. This is mainly explained by the significant rise in the amount of electricity that solar generators can produce, also known as Power Generation Capacity. As shown in Figure 1-1 which presents the power generation capacity by source from 2000 to 2020 and the predicted scenario until 2040 [8], solar power generation capacity is increasing faster than any other source of energy.



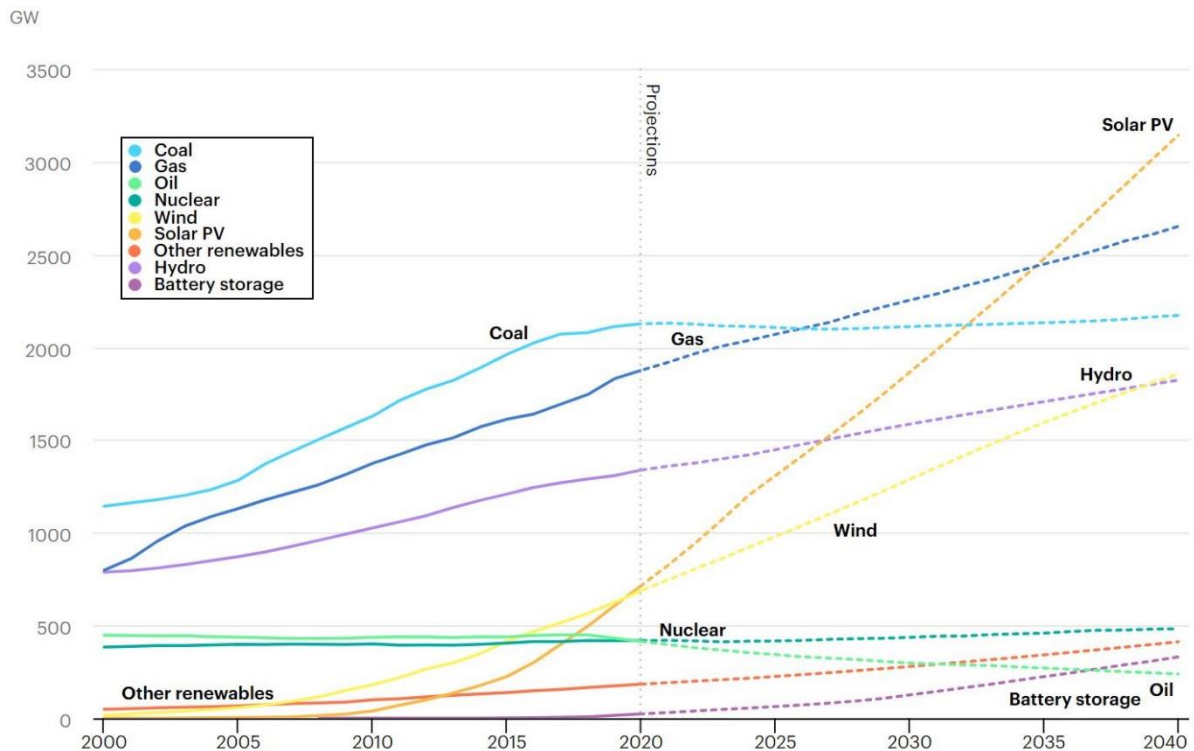


Figure 1-1. Power generation capacity by source between 2000 and 2020 and scenario until 2040, adapted from the International Energy Agency [8] statistics.

Indeed, each year, the share of electricity generation from solar photovoltaic (PV) increases more than any other renewable energy with a growth of 22% in 2019, compared to 12% of growth for wind and 8% for Bioenergy [7]. According to the predictions, solar is expected to become the energy source with the highest power generation capacity by 2035.

If solar irradiation is largely used to produce electricity with photovoltaic cells (Solar-PV), this energy can also be recovered as heat (Solar-Thermal). Depending on the end-user, Solar-Thermal can be preferred as heat is relatively easy to store and can be reused with very limited transformation needed. Furthermore, Solar-PV faces a main obstacle which is the drop of the photovoltaic module efficiency with rise in temperature by 0.5%/°C [9]. Indeed, according to several studies [10]–[13], an increase of the photovoltaic cell temperature has a direct negative impact on the solar panel performance. To tackle this issue, hybrid Photovoltaic/Thermal (PV/T) systems have appeared and have struck twice with one stone: if on the one hand PV/T systems permit simultaneous production of electrical and thermal energy, on the other hand, the cooling of the photovoltaic cell increases its electrical production.

To improve further the performance of PV/T systems, heat pipes have recently been introduced as efficient conducting materials between the photovoltaic cell and the heat sink. Based on a two-phase cycle of a working fluid, heat pipes can passively transmit large amounts of thermal energy from small temperature gradients. Inside the heat pipe, a working fluid is maintained under saturation condition, evaporates at the contact of the heat source (evaporator), and

releases its thermal energy by condensing at the contact of the heat sink (condenser). By doing so, the equivalent thermal conductivity of heat pipes can reach 100 kW/m.K which is 250 times higher than that of copper [14].

In addition to their high thermal conductivities, the advantages of using heat pipes in PV/T are multiple. While efficiently cooling the photovoltaic cell and optimizing the production of electricity, heat pipes also provide an isothermal distribution of temperature along the panel which reduces the internal stresses [15] and increases the lifespan of the system. Heat pipes also act as thermal diodes and prevent the heat sink fluid from freezing inside the panel under cold conditions. Finally, as the heat sink fluid does not need to go through the entire panels to cool the PV cells, the hydraulic resistance of the fluid is decreased, and the pump work required reduced. Despite the promising potential of using heat pipes in PV/T, this recent technology is yet to be adopted in large-scales [16]. This is mainly explained by technical limitations such as low module efficiencies and lack of heat pipes adaptability to cool the flat surface of the PV cells, which have conveyed economic limitations.

In this regard, multi-channel flat heat pipes have recently been developed to improve the heat recovery from flat surfaces such as photovoltaic cells. By using a novel internal multi-channel geometry, heat is efficiently recovered by two-phase heat transfer through the channels, which assure a uniform temperature distribution of the heat pipe surface. Moreover, the heat transfer surface area is significantly improved by the flat shape of the heat pipe which optimizes the contact between the heat pipe and the PV cells. During the past five years, the performance of multi-channel flat heat pipes has been experimentally investigated and has placed this innovative technology as one of the most efficient PV/T technologies reported up to date [17], [18].

## **1.2 Research motivation**

In this research, the motivation for investigating two-phase heat transfer in multi-channel flat heat pipes is to contribute to the development of innovative waste heat recovery technologies with the objective of producing and recovering energy in a more sustainable way. From a research point of view, the fundamental knowledge built throughout the study, together with the analytical and numerical modelling techniques of multi-channel flat heat pipes, provide a better understanding of the operation of multi-channel heat pipes. This will lead to the future development of new efficient heat pipe prototypes. Moreover, improved predictions of multi-channel heat pipe operation and performance is made possible. From an industrial point of view, better performance prediction is also valuable and allows a better estimation of the pay-back time of an installation. For industrialists, this study participates in attesting the potential of innovative multi-channel flat heat pipes as a cost-effective solution for improved heat

recovery in solar-thermal applications. The ultimate goal of this research is the widespread use of multi-channel flat heat pipes and the opening of new opportunities for other applications requiring surface cooling such as battery thermal management.

### **1.3 Thesis structure**

This study investigates two-phase heat transfer in a novel multi-channel flat heat pipe by using three approaches: Analytical, Numerical (CFD), and Experimental. The objectives of this research are as follows:

- Investigate the two-phase heat transfer in a multi-channel flat heat pipe.
- Develop an analytical model of a multi-channel flat heat pipe considering the two-phase mechanisms in a multi-channel geometry to predict its performance.
- By using computational fluid dynamic (CFD) methods, simulate the two-phase heat transfer taking place in multi-channel heat pipes and the operation of a novel multi-channel flat heat pipe.
- Validate the analytical model and numerical simulations developed with experimental results.
- Attest and disseminate the potential of multi-channel flat heat pipes for Photovoltaic/Thermal applications and surface cooling.

The investigation of two-phase heat transfer is significant in better explaining and understanding the promising potential of multi-channel flat heat pipes observed experimentally. This will also contribute in identifying limits and possible improvements for future prototypes of multi-channel flat heat pipes to push further the surface cooling performance. To address the objectives fixed in this study, the following approach is adopted:

- i. Based on the two-phase heat transfer theory, a novel analytical model of a multi-channel heat pipe is proposed.
- ii. A three leg multi-channel heat pipe is built and tested to develop the new multi-channel model proposed. The impact of the heat transfer rate on the multi-channel heat pipe thermal performance are investigated.
- iii. A numerical simulation of the three leg multi-channel heat pipe is made by using the computational fluid dynamics (CFD) software ANSYS FLUENT and including an in-house user-defined function (UDF) to describe the mass and heat transfer taking place during evaporation and condensation processes.
- iv. The analytical model is adapted to predict the performance of a multi-channel flat heat pipe used for PV/T application.
- v. The operation of the multi-channel flat heat pipe is simulated on ANSYS by using the previously validated techniques of two-phase flow modelling.

- vi. The analytical and numerical models developed are compared with the experimental investigation of a multi-channel flat heat pipe. In addition to the heat transfer rate and coolant flow rate, the impact of the tilt angle on the thermal performance of the multi-channel flat heat pipe is studied.
- vii. Infrared imaging of the multi-channel flat heat pipe surface in addition to the working fluid replacement for environmental purposes are also studied.

To visualize the approach adopted, Figure 1-2 schematizes the Analytical modelling, Numerical modelling (CFD) and Experimental validation of the two experimental rigs tested in this study, namely a three leg multi-channel heat pipe and a multi-channel flat heat pipe used for PV/T applications.

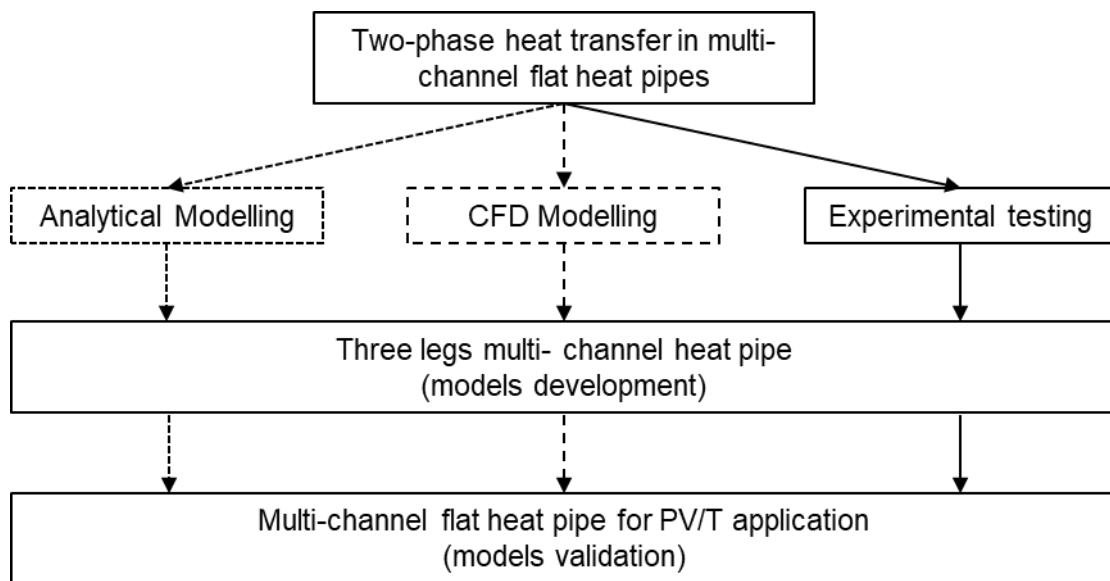


Figure 1-2. Research study approach

This thesis consists of seven chapters organized as follows:

**Chapter 1** describes the research background and current challenges faced, identifies the motivation at the origin of this work, and presents the objectives of this research and the scientific approach adopted to reach these objectives.

**Chapter 2** reviews the state of the art of works related to the current research and is articulated according to three axes. Starting from the application, up to date Photovoltaic/Thermal (PV/T) systems are first reviewed and compared to the novel multi-channel flat heat pipe Photovoltaic/Thermal (PV/T) system to highlight its potential. In a second stage, available investigations of multi-channel heat pipes are analysed. Finally, studies focusing on the numerical simulation (CFD) of heat pipes and thermosyphons (wickless heat pipes) are reported.

**Chapter 3** presents the two experimental rigs built and tested during this research, namely: 1) a three leg multi-channel heat pipe and 2) a multi-channel heat pipe for PV/T application. The experimental procedure, data reduction and error propagation are also detailed.

**Chapter 4** is the two-phase heat transfer theoretical section of this research work. After introducing the basics of two-phase heat transfer, a novel analytical model of a multi-channel heat pipe is developed. This model is then adapted to predict the thermal performance of the two experimental arrangements tested.

**Chapter 5** deals with the numerical modelling of heat pipes. After introducing the multi-phase flow modelling techniques commonly used, the three leg multi-channel heat pipe and multi-channel flat heat pipes for PV/T application are simulated using the computational fluid dynamic software ANSYS Fluent.

**Chapter 6** presents and discusses the experimental results for the two arrangements tested. The impact of factors such as heat transfer rate, coolant flow rate or tilt angle of the multi-channel flat heat pipe are investigated. In addition, the experimental results are compared with the theoretical and numerical models of multi-channel heat pipes developed to make conclusions on their capacity to describe the two-phase heat transfer mechanisms taking place. Infrared imaging of the multi-channel flat heat pipe and working fluid replacement are also presented.

**Chapter 7** concludes this research work by recalling the context and challenges of this study, describing how the objectives have been addressed, listing and discussing the main discoveries and results, and providing recommendations for further investigations of two-phase heat transfer in multi-channel flat heat pipes.

---

## Chapter 2 - State of the Art

---

The present State of the Art is articulated around three main axes: Photovoltaic/Thermal (PV/T) systems, multi-channel heat pipes, and computational fluid dynamic (CFD) simulations of heat pipes. The objective is to compare the performances of the multi-channel flat heat pipe studied with existing PV/T systems. The performances of reported air type PV/T, liquid type PV/T and heat pipe-based PV/T are analysed to identify the potential of multi-channel flat heat pipes for photovoltaic/thermal applications. Then, published studies in the field of multi-channel heat pipes are described and reviewed to state the progress of research achieved to date, and to highlight clearly the research gap that remains to be explored. Finally, the available computational fluid dynamic (CFD) studies of heat pipes, the modelling methods used, and the accuracy of simulations achieved by researchers are analysed. This aims at identifying the best performing methods and potential limits currently faced while simulating heat pipes and thermosyphons. The analysis of CFD simulations of heat pipes is relevant for the definition of the phase change model that will be used to simulate the multi-channel heat pipes.

The state of the art follows an upside-down triangle approach illustrated in Figure 2-1.

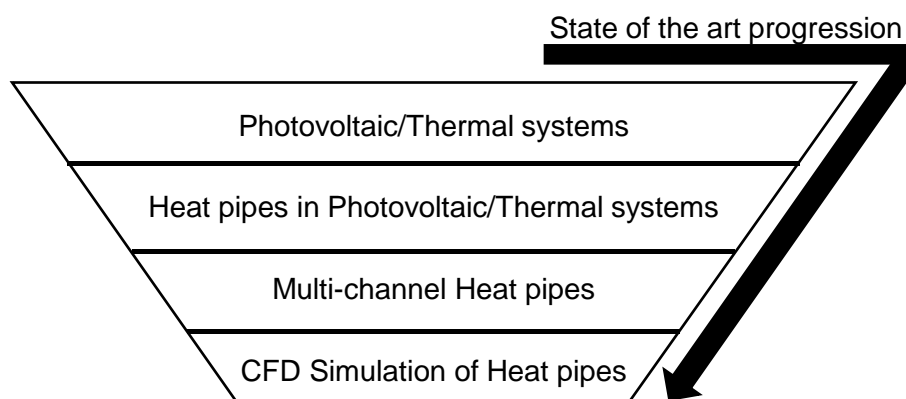


Figure 2-1. State of the art progression

### 2.1 Photovoltaic-thermal (PV/T) systems

Combined Photovoltaic/Thermal (PV/T) systems have been developed to tackle the loss of photovoltaic (PV) cell efficiency with an increase of temperature with a double objective: simultaneously to cool down the PV cell while also recovering thermal energy. The hybrid photovoltaic/thermal modules collect the thermal heat generated by the photovoltaic cell while generating electricity and convey this heat to a heat sink such as water that can be used for household purposes. There are different types of PV/T modules depending on the collector technology [19]. In the scope of this study, three types of PV/T systems have been reviewed: air type PV/T collectors, liquid type PV/T collectors, and heat pipe-based PV/T collectors. As

their names indicate, air type and liquid type PV/T collectors respectively use air and liquid as heat sinks to cool down the photovoltaic cells. On the other hand, heat pipe-based PV/T collectors use a heat pipe structure at the back of the PV cell to transmit energy to a heat sink.

In the following sections, the performances of developed PV/T systems are compared in terms of thermal efficiency, electrical efficiency, and total efficiency. The total, thermal and electrical efficiencies  $\eta_{tot}$ ,  $\eta_{th}$ ,  $\eta_{el}$  are calculated from:

$$\eta_{tot} = \eta_{th} + \gamma\eta_{el} \quad (2-1)$$

$$\gamma = \frac{A_{PV}}{A_{tot}} \quad (2-2)$$

$$\eta_{th} = \frac{\dot{Q}}{A_{tot}J} \times 100 \quad (2-3)$$

$$\eta_{el} = \frac{P_{el,max}}{A_{PV}J} \times 100 \quad (2-4)$$

with  $A_{PV}$  the photovoltaic cell area (m<sup>2</sup>),  $A_{tot}$  the total area of the PV/T system (m<sup>2</sup>),  $\dot{Q}$  the heat transfer rate (W),  $P$  the electrical power (W), and  $J$  the solar irradiation (W/m<sup>2</sup>).

### 2.1.1 Air type PV/T collectors

In air type PV/T collectors, air is used as a heat sink to cool down the photovoltaic cells. The air circulation near the cells is crucial to achieve an optimum cooling. Thus, through the years researchers have developed different shapes of air collectors for more efficient heat recovery. The simplest form of an air type PV/T collector consists of having an air passage under the photovoltaic cells. *Tiwari and Sodha* [20] used an air collector with such an air flow cooling down the PV cells and investigated the impact of glazing on the air type PV/T collector performances. A Tedlar film was also added on the module to bond the cells. It was observed that a glazed PV/T air collector without Tedlar reached the highest performance with an overall efficiency of 37%. Yet, the PV cell temperature could not be reduced below 70°C. To achieve a better cooling, instead of having only one pass of air, *Sopian et al.* [21] developed a double pass air PV/T system. In this configuration, the photovoltaic cells were situated in the middle of the panel. At the top and bottom of the cells, air channels allow a circulation of the coolant flow from top to bottom. By doing so, the double pass air PV/T achieved an electrical efficiency of 11%, a thermal efficiency of 50%, and a total efficiency of 61%. This is a major improvement when compared to a single pass air PV/T. *Othman et al.* [22] also developed a double pass air PV/T collector but added an absorber plate with fins at the back of the photovoltaic modules. The main objective of adding fins is to increase the heat transfer area between the hot PV cell and the air stream. An improvement of the heat recovery can also be expected due to an increase of air mixing which leads to a higher forced convective heat transfer coefficient. Even if photovoltaic cells of poor quality were used (electrical efficiency about 4.3%), the average

thermal efficiency under optimum conditions was 58.0%. The total efficiency of this PV/T system with a double pass air collector and fins was 62.3%. At the back of the photovoltaic cells, *Jin et al.* [23] developed a rectangle channel tunnel absorber. This absorber consisted of 27 rectangular, 1.2cm wide, parallel channels into which the air flow was divided. The developed absorber with parallel tunnels was compared to a simple single pass absorber. It was found that, at low coolant mass flow, the electrical efficiency of the PV/T system was improved by 1% by using the new absorber plate. Yet, with higher air mass flow rates, the difference of electrical efficiency between the rectangular channel absorber and the single pass absorber was no longer significant. Nonetheless, the thermal efficiency of the rectangle channel tunnel absorber was significantly higher than a single pass air flow absorber. The electrical, thermal, and total efficiency of the PV/T panel with a rectangle channel tunnel absorber were 10.0%, 54.7%, and 64.7%, respectively. *Bambrook and Sproul* [24] designed an unglazed, single pass, open loop PV/T air system. The influence of the air mass flow rate on the thermal and electrical efficiencies was investigated. Between an air flow rate of 0.05 kg/s.m<sup>2</sup> and 0.1 kg/s.m<sup>2</sup>, the relative electrical efficiency increase was 15% whilst the relative thermal improvement was 38%. Yet, to decrease the pressure drop, large ducts were used which is an important limit of air type PV/T collectors, which needs to be considered. Indeed, if on the one hand increasing the number of air passage and reducing the channels dimensions can lead to better heat transfer, on the other hand this causes a significant increase of the fan power required to achieve a given cooling air flow rate. Under optimum operating conditions, the average electrical and thermal efficiencies were 12% and 55% respectively. The average overall efficiency of the system was 67%. *Kumar and Rosen* [25] evaluated the performance of a double pass PV/T air collector with a special focus on the use of small fins to increase the heat transfer rate between the PV cell and the working fluid. By increasing the heat exchange surface with fins, the cell temperature was decreased from 82°C to 66°C which leads to a 15.5% and 10.5% gain of thermal and electrical efficiencies, respectively. Under optimum conditions, the average electrical efficiency was 15% whereas the average thermal efficiency reached 60%. The average equivalent efficiency for a maximum air flow rate of 0.15 kg/s was 75%. The review of air PV/T presented is not exhaustive but only aims at providing some guidance on the efficiency of air type PV/T collectors when compared to heat pipe-based PV/T.

### **2.1.2 Liquid type PV/T collectors**

In liquid type PV/T collectors, a liquid coolant flows in the panel and recovers thermal energy by forced convection. Due to its availability and widespread use in both industry and the private sector, water is usually chosen as a coolant. The heat recovered by a PV/T panel can reduce the need for electricity to produce hot water. In liquid type PV/T collectors, the water passage at the back of the photovoltaic cells is of importance to optimize the cooling of the cells and



improve the heat recovery. In their work, *Sun et al.* [26] used a water collector which comprised 10 vertical tubes linked at the top and bottom. The effects of panel tilt angle and connection mode of the PV modules was studied. It was shown that the series connection can result in a 5.4% increase of energy benefits whilst improving heat recovery by 11.4%. Under optimum conditions, the electrical efficiency was 10.1% and the thermal efficiency reached 34.9%. The maximum average overall efficiency that can be reached with this system is 45%. *Tripathi and Tiwari* [27] experimentally evaluated the performance of a fully covered concentrated PV/T water collector. They showed that a manual maximum power point tracking technique was more efficient than a fixed position. Reflectors were used on the side of the PV/T to concentrate the solar irradiation onto the photovoltaic modules. The PV/T water collector consisted of an absorber and four water tubes in parallel. It was found that, at midday, the solar cell temperature could not be cooled lower than 90°C. For this module with reflectors, the electrical and thermal efficiencies of the PV/T module were 8.9% and 37% respectively. The overall efficiency reached 46%. *Kostic et al.* [28] also added reflectors to improve the performance of a PV/T water collector performance. The cooling water was flowing through nine parallel copper tubes. Yet, by adding reflectors, it was observed that the maximum overall efficiency decreased from 60.1% to 46.7%. The photovoltaic modules used were of low quality as the electrical efficiency was only 5.1%. Nevertheless, having a higher number of parallel copper tubes in the water collector improved the heat recovery in comparison to the work by *Tripathi and Tiwari* [27]. Indeed, the thermal efficiency of the PV/T water collector developed by *Kostic et al.* [28] was 46.8%. Hence, the average total efficiency of the PV/T module without reflectors was 51.9%. After investigating the modelling of a PV/T system, *Dupeyrat et al.* [29] designed and tested a single glazed PV/T liquid collector in which water was used as a coolant. The water collector consisted of five parallel water tubes. The authors tested direct lamination of PV cells on a metal heat exchanger in order to improve the performance of the system. As a result, the average electrical, thermal, and overall efficiencies were 7.6%, 50.0%, and 57.6%, respectively. *Lalovic et al.* [30] developed a hybrid amorphous silicon PV/T water collector. At the back of the photovoltaic cells, aluminium fins transmitted heat to copper tubes in which water circulated. The copper tubes were inserted inside in the aluminium fins. In this study, *Lalovic et al.* [30] reported that the aim was to construct a simple and cheap PV/T system. At a temperature of 80°C, the PV cell efficiency decreased by 15%. Both single glazing and double glazing have been tested. The maximum thermal efficiency with single glazing reached 53% whereas it reached 64% in the case of double glazing. The average thermal efficiency of the collector with double glazing was 54%. Unfortunately, due to the low electrical efficiency of the amorphous PV cell, the average overall efficiency of the developed PV/T system was 58%. *Ji et al.* [31] designed a flat plate glazed PV/T collector in which they glued the PV modules onto the surface of a flat-box aluminium absorber with silicon gel. The aluminium collector

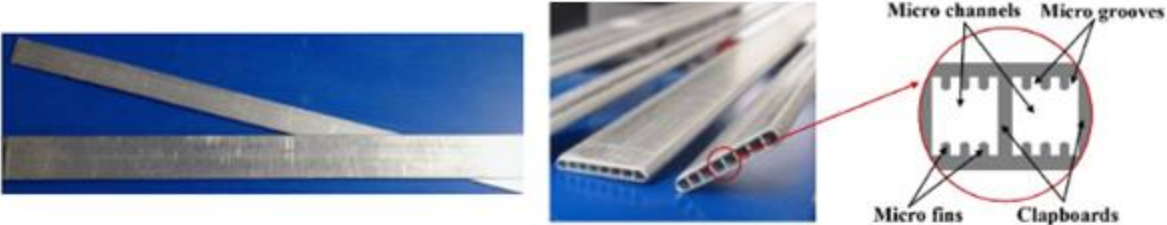
consisted of Al-alloy battens with a 20 x 10mm rectangular cross section placed in parallel and linked at the top and bottom of the channels. The PV module was made of a transparent front layer, EVA (Ethylene–Vinyl Acetate) layers, interconnected crystalline PV cells and a back opaque TPT (Tedlar–Polyester– Tedlar) layer. The thermal efficiency of the developed PV/T system was 48.7%, and the electrical efficiency was 10.1%. Hence, the total efficiency of the PV/T collector developed by *Ji et al.* [31] is estimated to be 58.8%. *Sandnes and Rekstad* [32] based their liquid type PV/T on a black plastic absorber made of polyphenylenoxid. The polymer collector consisted of a flat plate containing parallel channels in which ceramic granulates have been placed. The heat sink liquid (water) was flowing through the parallel channels. To tackle the issue of differential thermal expansion between the PV cell and the polymer collector, a silicon adhesive was used at the interface. The maximum photovoltaic cell temperature recorded in this study was 45°C. The electrical and thermal efficiency for this system was 11.8% and 55%, which gives a total efficiency estimated at 66.8%. *Coventry* [33] developed a parabolic trough photovoltaic/thermal collector that was named CHAPS by the authors in reference to “combined heat and power solar” collector. The CHAPS prototype consisted of glass-on-metal mirrors that reflected and concentrated the solar radiation on the PV cell. The PV cell was placed upside down on top of the mirrors. One drawback of this system is that the PV cell surface is quite small compared to the mirror surface. At the back of the PV cells, a conduit in which water with anti-freeze and anti-corrosion additives flows was used to cool down the cells and recover thermal energy. For this PV/T collector, the thermal efficiency was 58%, the electrical efficiency was 11%, and the total efficiency was observed to be 69%. With the objective of comparing simple and complex designs, *Zondag et al.* [34] tested several designs of PV/T water collectors. In total, nine designs of PV/T were investigated which can be categorized in four groups: sheet-and-tube PV/T collectors, channel PV/T collectors, free flow PV/T collectors, two-absorber PV/T collectors. Some factors such as the number of covers for the sheet-and-tube PV/T collectors, the location of the channel in channel PV/T collectors, and the presence of insulation or not in two-absorber type PV/T collector were also investigated. The best overall efficiency was obtained by the insulated two-absorber PV/T collector, which showed a 66% thermal efficiency, 8% electrical efficiency, and 74% overall PV/T efficiency. Similarly, *Fadhel et al.* [35] proposed another innovative design of the absorber plate. In their system, the authors opted for a spiral shape absorber made of a single water pipe. This absorber was placed at the rear of the photovoltaic cells, which were isolated from the ambient by an air gap and a layer of glass. The maximum thermal efficiency observed rose to 64.4% on sunny days and the electrical efficiency was up to 12.1%. The highest combined efficiency was 76.5% for this prototype. In terms of average efficiencies, the proposed prototype presents electrical, thermal, and total efficiencies of 12%, 63% and 75%. *Nahar et al.* [36] introduced a novel thermal collector design excluding the absorber plate to

improve the heat transfer. The encapsulated photovoltaic module was directly attached to a parallel plate thermal collector by removing the absorber plate. However, when the absorber plate was removed, the overall efficiency of the liquid type PV/T decreased by 4.4%. With the parallel plate thermal collector, the difference of temperature within the panel can be as high as 30°C. This fact can be a source of stress inside the PV module which can decrease the life span of the PV/T system. The global efficiency of this water PV/T system could reach 80% at high coolant flow rates. The electrical and thermal efficiencies were 11% and 69% respectively. A complex water type PV/T system was proposed by *Nasrin et al.* [37]. At the top of solar cells, Fresnel lenses have been placed to converge the solar irradiation onto a localized photovoltaic area. At the back of the cells, the water collector consisted of passes made using sixteen baffles with the objective of increasing the flow Reynolds number and thus improving the forced convective heat transfer coefficient. The electrical efficiency of the solar panel used was 10.6%. The water multi-channel collector achieved a thermal efficiency of 71.0%. To date, the overall efficiency of this water type PV/T system is one of the highest reported in the literature and is reported to be 81.6%. Similar to air PV/T modules, other liquid type PV/T modules may be found in the literature.

### **2.1.3 Heat pipe-based PV/T collectors**

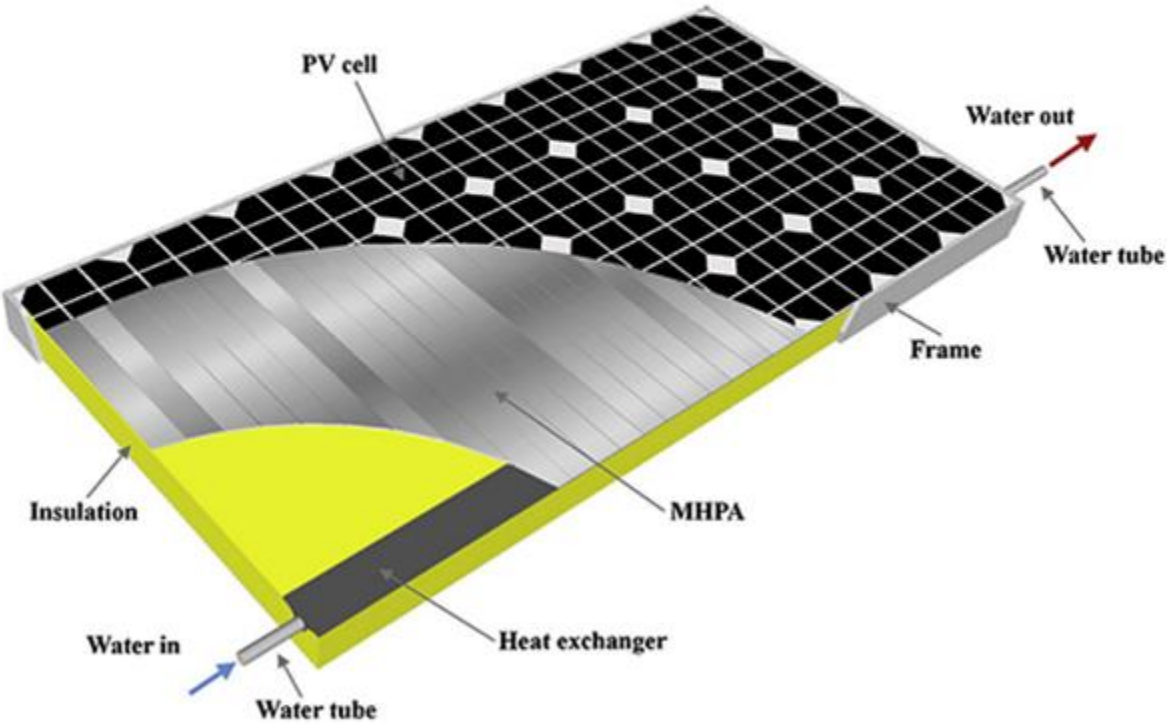
Heat pipes have been proposed as a promising solution to photovoltaic/thermal systems to overcome the working fluid freezing issues of liquid type PV/T when exposed to cold climates. In addition to uniformly cooling the photovoltaic modules, heat pipe collectors have increased the lifespan of PV/T whilst significantly decreasing the coolant circuit resistance [38]. One of the first reported uses of thermosyphons (wickless heat pipes) in PV/T is attributed to *Akbarzadeh and Wadowski* [39] who, in 1996, used a single cylindrical thermosyphon to cool a photovoltaic cell. Reflectors were used to concentrate the solar radiation on the cell. At the top of the heat pipe (condenser section), the heat was dissipated in the ambient air. Hence, in this system, thermal energy was not recovered. To increase the heat dissipation, fins were placed on the condenser section of the heat pipe. This system maintained the cell temperature below 46°C, the authors report. Similarly, *Anderson et al.* [40] used a copper/water cylindrical heat pipe with aluminium fins for the cooling of a concentrated photovoltaic system. The cooling was operated by natural convection only. Nevertheless, the maximum rise of the PV cell temperature was 40°C whereas it could reach 210°C without cooling [40]. *Tang and Zhao* [41] designed a micro heat pipe array and investigated the cooling of photovoltaic cells using both air and water cooling. The best performance was obtained while using water as a working fluid. In the case where air was used as a coolant, the photovoltaic cell temperature was reduced by 4.7°C which led to an increase of the electrical efficiency of 2.6%. When water was selected to cool the photovoltaic cells, the cell temperature decreased by 8°C and the electrical

efficiency was improved by 3%. For this system, the maximum electrical efficiency recorded was 13.5%. However, the thermal energy released was not collected. One of the first truly heat pipe based PV/T systems in which combined electrical and thermal production was achieved has been reported by *Deng et al.* [42], [43]. These researchers developed a micro-heat pipe array (MHPA) to guarantee a uniform temperature of the photovoltaic cell, high reliability of the panel, low coolant pressure drop, and a resistance to freezing. The designed and manufactured aluminium micro-heat pipe array consisted of parallel micro channels in which micro fins increased the forced convective heat transfer between the wall and the coolant. All the micro channels were independent heat pipes and not connected to each other. The micro-heat pipe array (MHPA) developed and a schematic of the MHPA based PV/T system is presented in Figure 2-2.



a) Photo of the MHPA

b) Cross section of the MHPA



c) Schematic of the MHPA-PV/T module

Figure 2-2. Micro-heat pipe array (MHPA) and the MHPA based PV/T developed by *Deng et al.* [42], [43].

The main advantage of the MHPA proposed is its flat shape which allows an optimum contact with the photovoltaic cells. A year of experiments have been conducted during which the PV/T panel was installed on a roof in China. For typical days of spring, summer, autumn and winter, the electrical efficiency was 11.8%, 11.9%, 13.7%, and 14.7%; the thermal efficiency was 31.6%, 33.0%, 24.9%, and 17.2%; which gave an overall efficiency of the MHPA PV/T of 45.4%, 45.0%, 38.7%, and 31.9%. *Gang et al.* [44], [45] developed a heat pipe based PV/T with the objective of having a PV/T that can be used in cold regions. At the back of the PV modules, the thermal collector consisted of a large aluminium plate on which water-copper heat pipes had been placed. The PV modules were directly in contact with the aluminium plate and, at the back of the plate, the copper heat pipes were evenly spread across the length of the system. As for the photovoltaic modules, the PV cells were resting on a layer of Tedlar polyester (TPT) which is an electric insulator. This layer was black to enhance radiation heat transfer. At the top of the PV/T system, the condenser section of the heat pipe was placed inside a water channel where the water flow recovered heat by forced convection. The cross section and the total heat pipe based PV/T system developed by *Gang et al.* [44], [45] is presented in Figure 2-3.

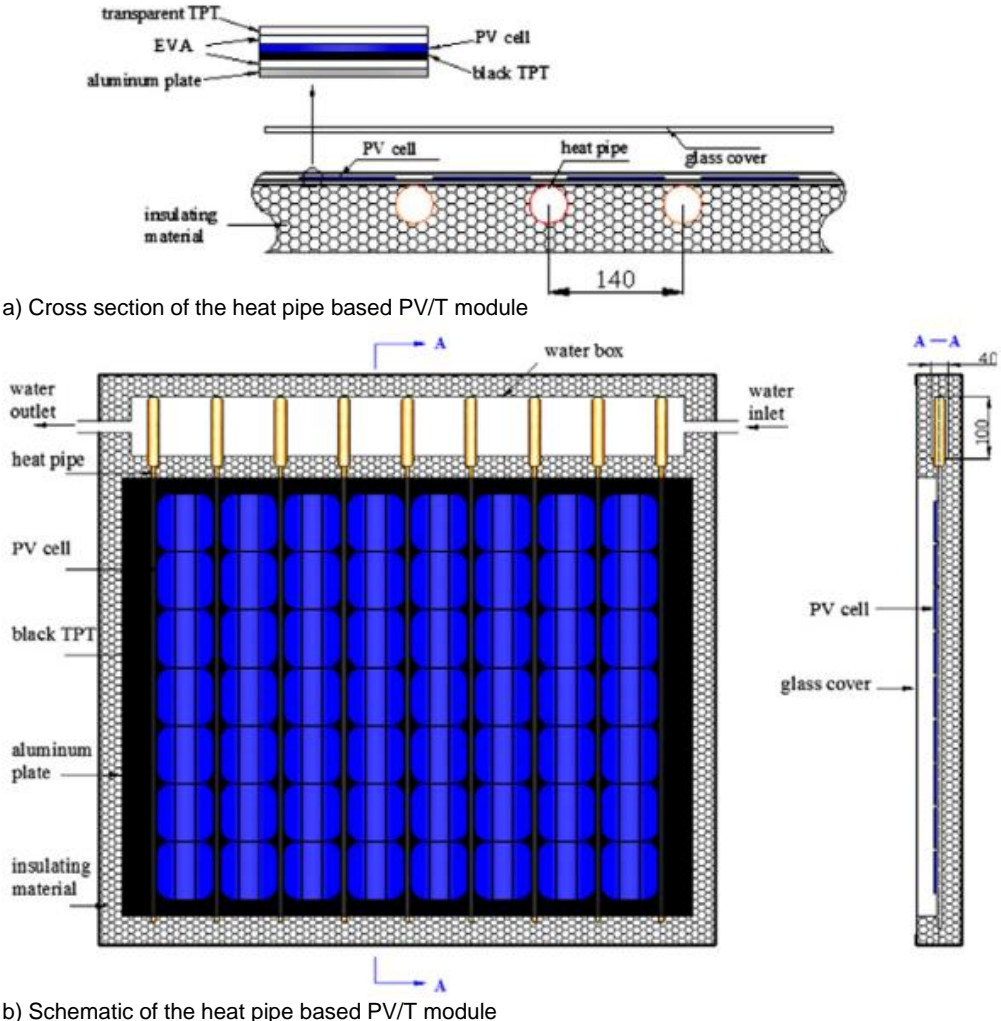


Figure 2-3. Heat pipe based PV/T system developed by *Gang et al.* [44], [45]

In comparison to the MHPA-PV/T developed by *Deng et al.* [42], [43], the heat pipe based PV/T module by *Gang et al.* [44], [45] introduced a significant limit which is the cylindrical shape of the heat pipe. Indeed, having cylindrical heat pipes reduces the contact area with the flat shape of the photovoltaic cells. Moreover, the authors had to use an aluminium plate between the cells and the heat pipes, which increases the thermal resistance and limits the heat recovery. It is also worth noticing that each heat pipe was working independently, meaning that the heat pipe working temperatures can be different for two heat pipes as the cooling water temperature increases. This means that the heat pipe temperature is lower near the water inlet whereas it is hotter close to the outlet. Eventually, this may have induced a non-uniform cooling of the PV cells on the horizontal axis. As a result, the authors observed that a maximum temperature of 53°C was reached on the photovoltaic cells at midday. The daily electrical and thermal efficiency of this heat pipe-based PV/T system was 9.4% and 41.9% respectively. The overall efficiency of this module was estimated at 51.3%. *Moradgholi et al.* [46] used parallel cylindrical tubes linked at the top and bottom for cooling the cells. This apparatus consisted of a multi-channel heat pipe as the top and bottom section of each parallel channel is linked. This layout allows a circulation of the working fluid inside the legs of the thermosyphon and thus, provides a uniform temperature on the horizontal axis across the PV/T module. The working fluid selected was Methanol. At the top of the parallel tubes, a cooling jacket was placed for heat recovery. The heat pipe based PV/T developed by *Moradgholi et al.* [46] is presented in Figure 2-4.

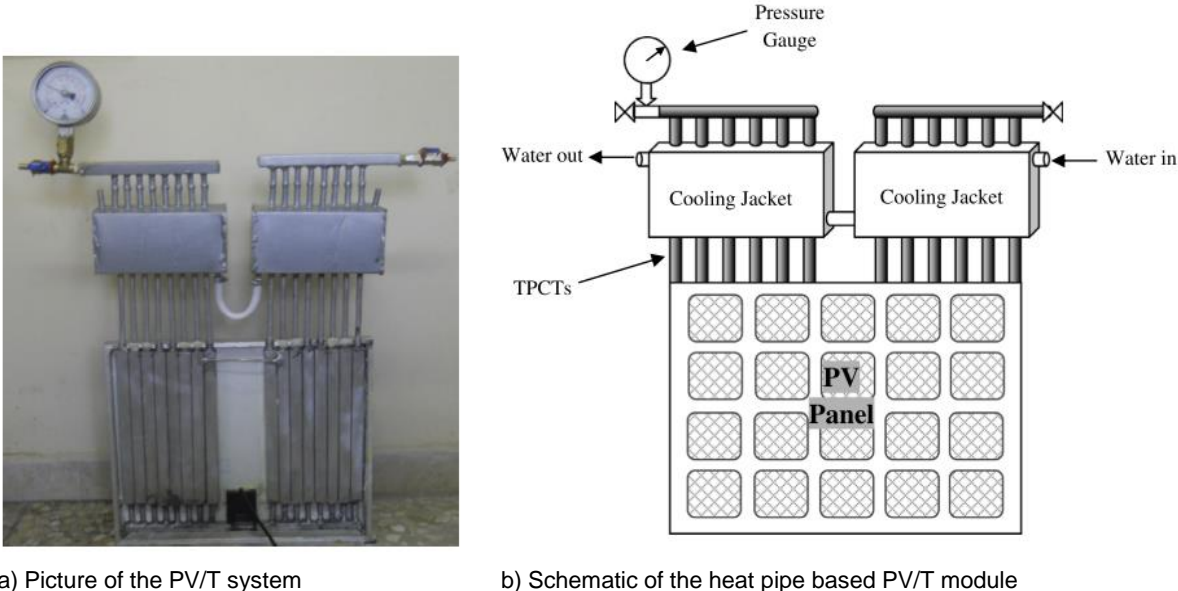


Figure 2-4. Heat pipe based PV/T system developed by *Moradgholi et al.* [46]

It can be observed that a major disadvantage with this multi-channel heat pipe-based PV/T is the limited contact between the cylindrical channels and the flat photovoltaic modules. By using

this multi-channel heat pipe, a temperature drop of the PV cell of 15°C was achieved (from 50°C to 35°C). This resulted in an increase in the electrical efficiency of 5.7%. Both spring and summer conditions were tested. The electrical efficiency of this PV/T was 12.4% on average. The total efficiency of the PV/T module was 30% in spring and 56% in summer. A system similar to the one presented by *Gang et al.* [44] was tested by the same group of researchers in the study presented by *Hu et al.* [47]. The PV/T module consisted of 9 cylindrical copper heat pipes which worked independently. Again, to make the connection between the heat pipes and the photovoltaic modules, an aluminium plate was used. The heat pipe-based PV/T presented by *Hu et al.* [47] is shown in Figure 2-5.

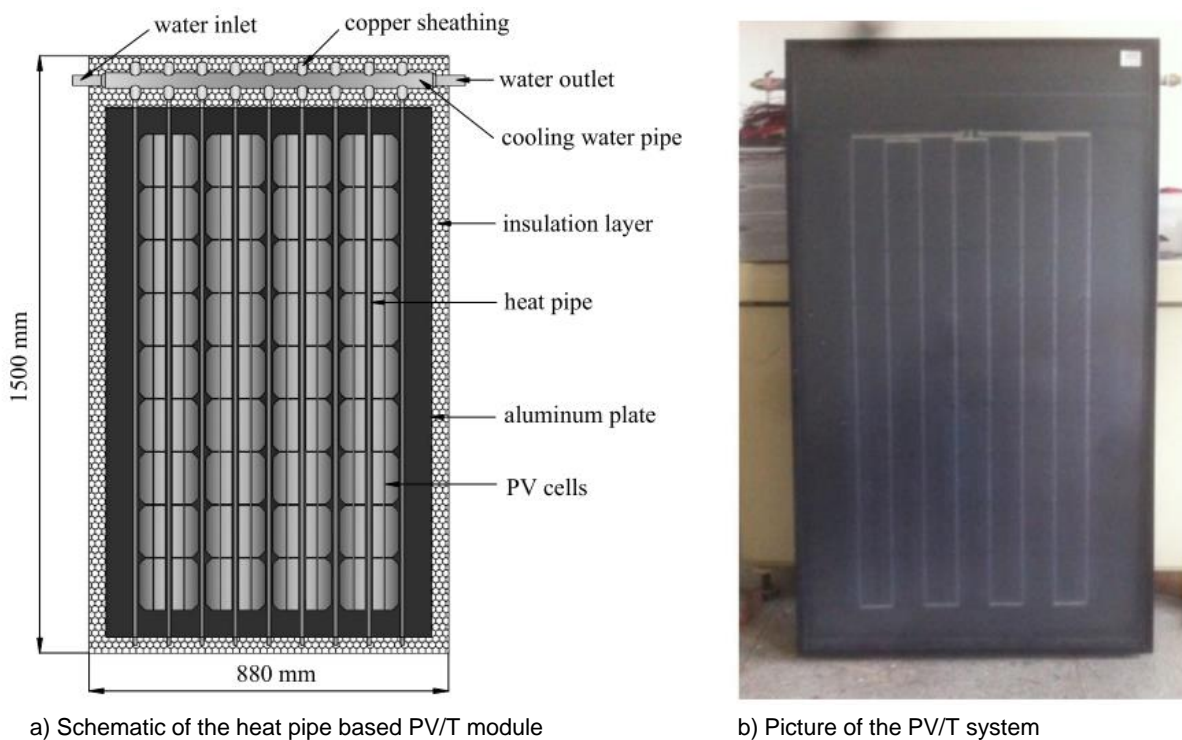


Figure 2-5. Heat pipe based PV/T system developed by *Hu et al.* [47]

In their study, the authors tested wickless heat pipes and wire-meshed heat pipes made in copper. The effect of the tilt angle of the PV/T was also investigated. It was found that, at a tilt angle lower than 20° with the horizontal axis, the wire-meshed heat pipe was advised. However, at higher tilt angles, the two types of heat pipes showed a similar performance. Indeed, the average thermal efficiency of the wickless heat pipe-based PV/T was 50% whereas the wire-meshed heat pipe-based PV/T was 47%. The electrical efficiency of this system was about 6% which gave an overall efficiency of the wickless heat pipe-based PV/T system of 56%. With the objective of providing a uniform temperature distribution in both vertical and horizontal directions, and considering the need of a flat shape thermal collector to improve the contact with the photovoltaic cells, *Jouhara et al.* [18], [48] developed a novel multi-channel flat heat pipe called a “heat mat”. The heat mat is made of aluminium in which parallel channels are connected at the top and bottom. The channel has a special internal shape which aims at

improving the conduction heat transfer from the PV cell to the heat pipe working fluid. The top surface of the heat mat is perfectly flat which allowed an optimum contact with the photovoltaic modules and was painted in black. To recover the thermal energy collected, a cooling manifold was placed at the back of the heat mat. The cooling manifold had a shape similar to the heat mat in which the coolant (water) flows through the multi-channels. It was reported by the authors that this PV/T can also be used as an energy-active building envelope material (also known as building-integrated photovoltaic/thermal (BIPV/T) collector). As shown in Figure 2-6, this technology was investigated at a large scale with the construction of a complete solar roof.

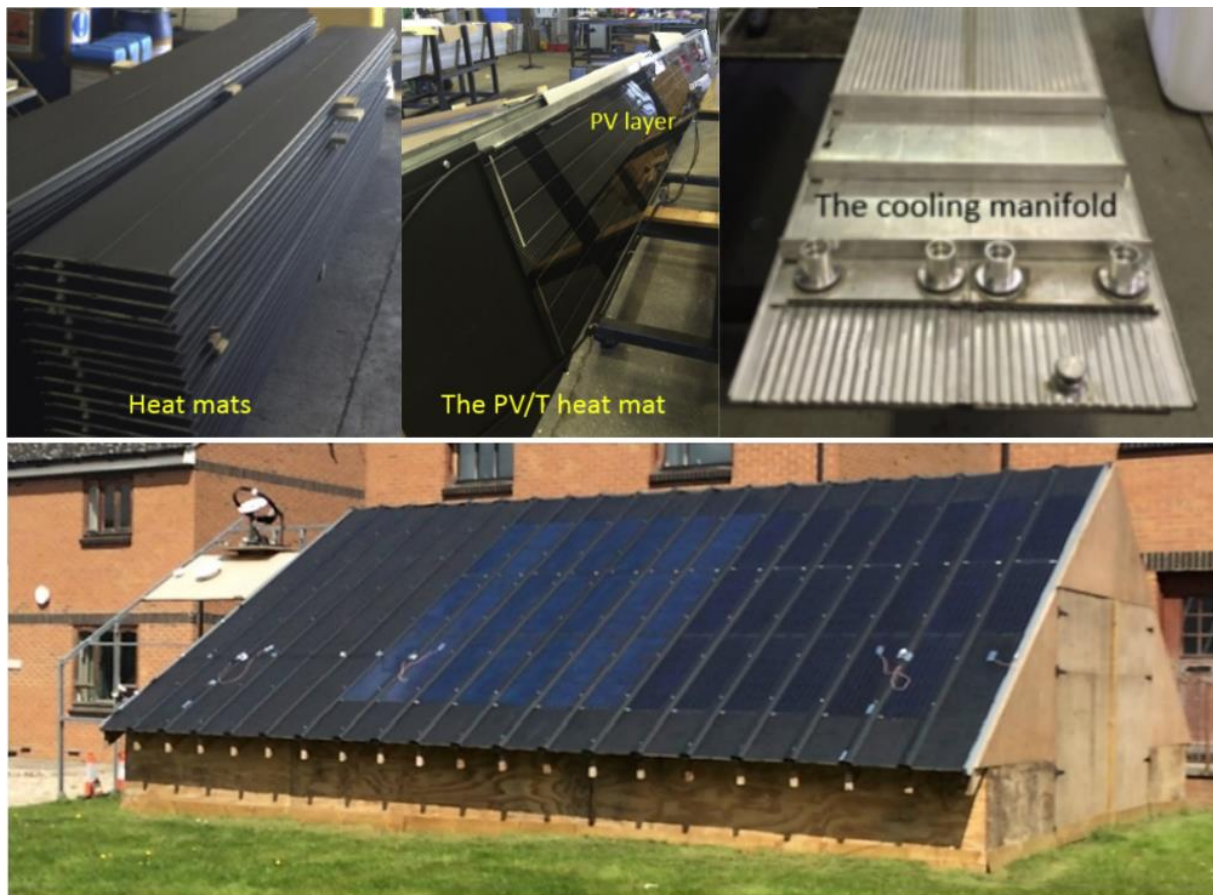


Figure 2-6. The multi-channel flat heat pipe (heat mat) based PV/T developed by *Jouhara et al.* [18], [48] and its large scale testing on a complete solar roof.

In addition, the heat mat PV/T module was also tested in a laboratory environment. By using the heat mat as thermal collector, the photovoltaic cell temperature was decreased from a range of 40-58°C to a range of 28-33°C, which led to an electrical efficiency enhancement of 15%. The heat mat was tested with and without PV modules. When no PV module was placed at the top of the heat mat, thermal energy was directly recovered by radiation. It was found that the thermal efficiency of the heat mat without photovoltaic cells was 64% whereas it was reduced to 49% with photovoltaic cells placed on its surface. Overall, the electrical and thermal efficiency of the heat mat-based PV/T system was 7.0% and 49.4%. Hence, the total efficiency of this PV/T using a multi-channel flat heat pipe was 56.4%. Similarly to *Deng et al.* [42], [43],



*Modjinou et al.* [49] also used a micro channel heat pipe array (MHPA) for their PV/T system. The micro channel heat pipe array used was exactly the same as the MHPA presented earlier by *Deng et al.* [42], [43]. The micro channel heat pipe was made of aluminium with fins inside the channels. In each micro channel heat pipe array, each channel worked independently. In their system, *Modjinou et al.* [49] used six micro heat pipe arrays in parallel. Surprisingly, the MHPA surface was too small to cover the complete PV cell surface. This can be observed in Figure 2-7.

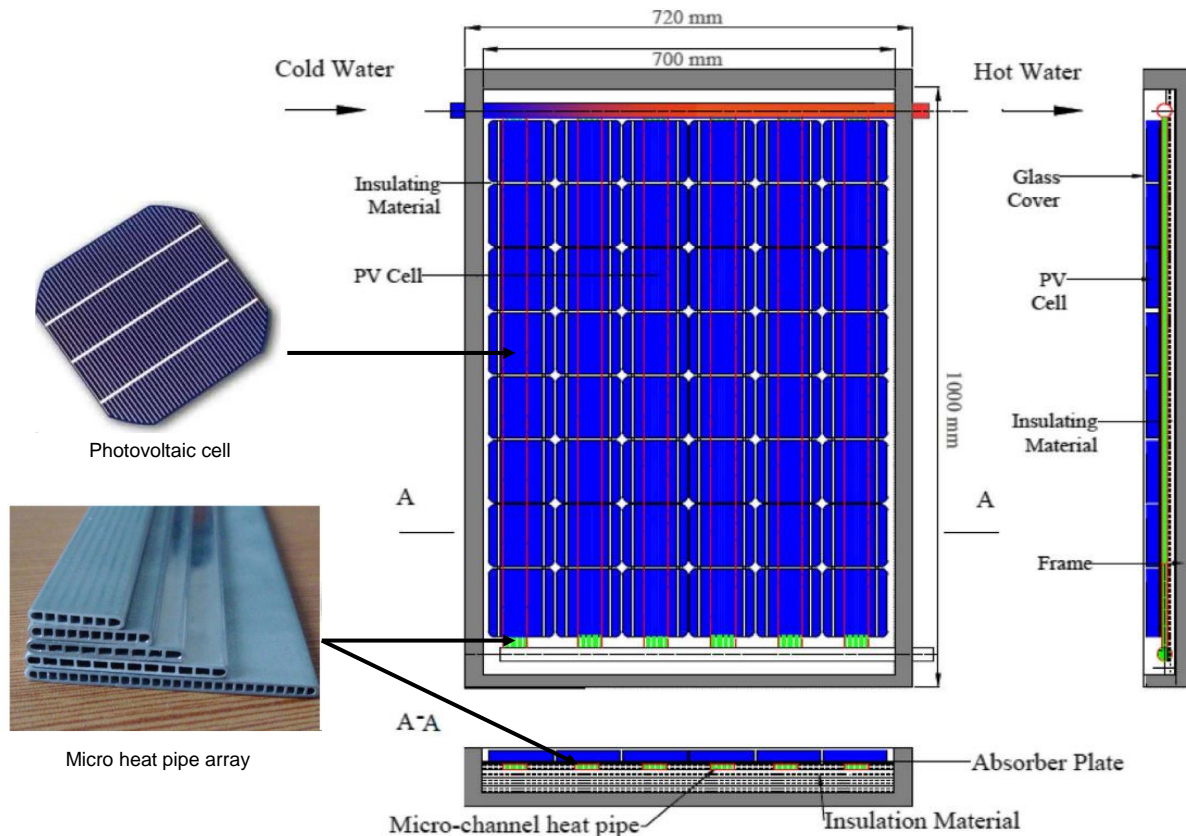


Figure 2-7. Micro-heat pipe array (MHPA) and the MHPA based PV/T presented by *Modjinou et al.* [49]

The PV/T system developed was tested under real conditions in China. On the day of the investigation, there was a maximum irradiation of  $900 \text{ W/m}^2$  and an ambient temperature of  $33^\circ\text{C}$  was reached. It was found that the daily thermal efficiency of the PV/T was 50.7% whereas the electrical efficiency of the cells was 7.6%. The overall efficiency of this micro channel heat pipe array (MHPA) based PV/T was 58.3%. Despite the cylindrical shape of their heat pipes, *Wu et al.* [15] proposed a heat pipe photovoltaic/thermal (PV/T) collector using wicked heat pipes for the cooling of the PV cells. In this system, 14 parallel, independent, and circular heat pipes have been used. A thermal contact material was used at the cylinder-flat plate interface to make the connection between the heat pipe and the solar PV panel. At the condenser section of the wicked heat pipes, fins were attached to the heat pipe surface to

increase the heat transfer area and to improve the heat transfer with the cooling water. A schematic of the PV/T proposed by *Wu et al.* [15] is presented in Figure 2-8.

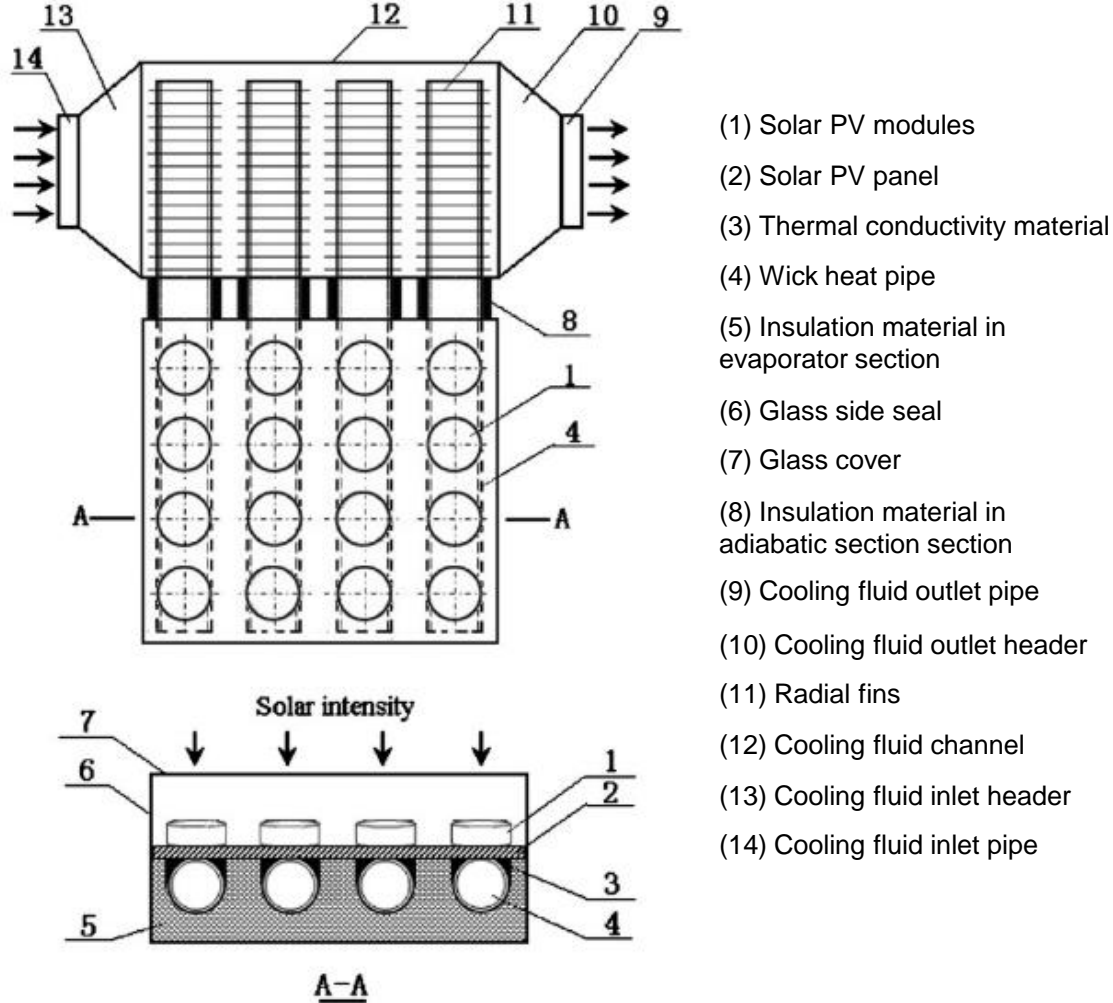


Figure 2-8. Wick heat pipe based PV/T presented by *Wu et al.* [15]

Again, due to the independence of each parallel heat pipe, a disadvantage of this system is the only partially isothermal temperature distribution of the photovoltaic cells. As the cooling water temperature increases in the condenser section, it is to be expected that the working temperature of the wick heat pipes increases closer to the water outlet temperature. In addition, due to the circular shape of the heat pipe used, the contact is not optimum, and some space between each heat pipe remains uncooled. Nevertheless, the performance of the system reported was surprisingly high, as authors reported an electrical efficiency of 8.2% and a thermal efficiency of 57.4%. The overall efficiency of this wick heat pipe-based PV/T system was estimated at 65.6%. The heat pipe based PV/T system with the highest overall efficiency reported in the literature was reported by *Yu et al.* [50], [51] who developed a micro-channel loop heat pipe PV/T. Similar to the micro-heat pipe array previously described, the loop heat pipe is made of aluminium and comprises rectangular channels with wicks. In this

apparatus, the condenser was not included in the PV/T module. Instead, a loop heat pipe was used to circulate the working fluid and convey the thermal energy to a double pipe heat exchanger. To limit the dry-out phenomenon that usual appears at the evaporator section of loop heat pipes, the authors developed a vapour-liquid separator. This simply consisted of adding holes in the liquid header to allow the condensate to return to the micro-channel. The micro-channel loop heat pipe based PV/T developed by *Yu et al.* [50], [51] is presented in Figure 2-9.

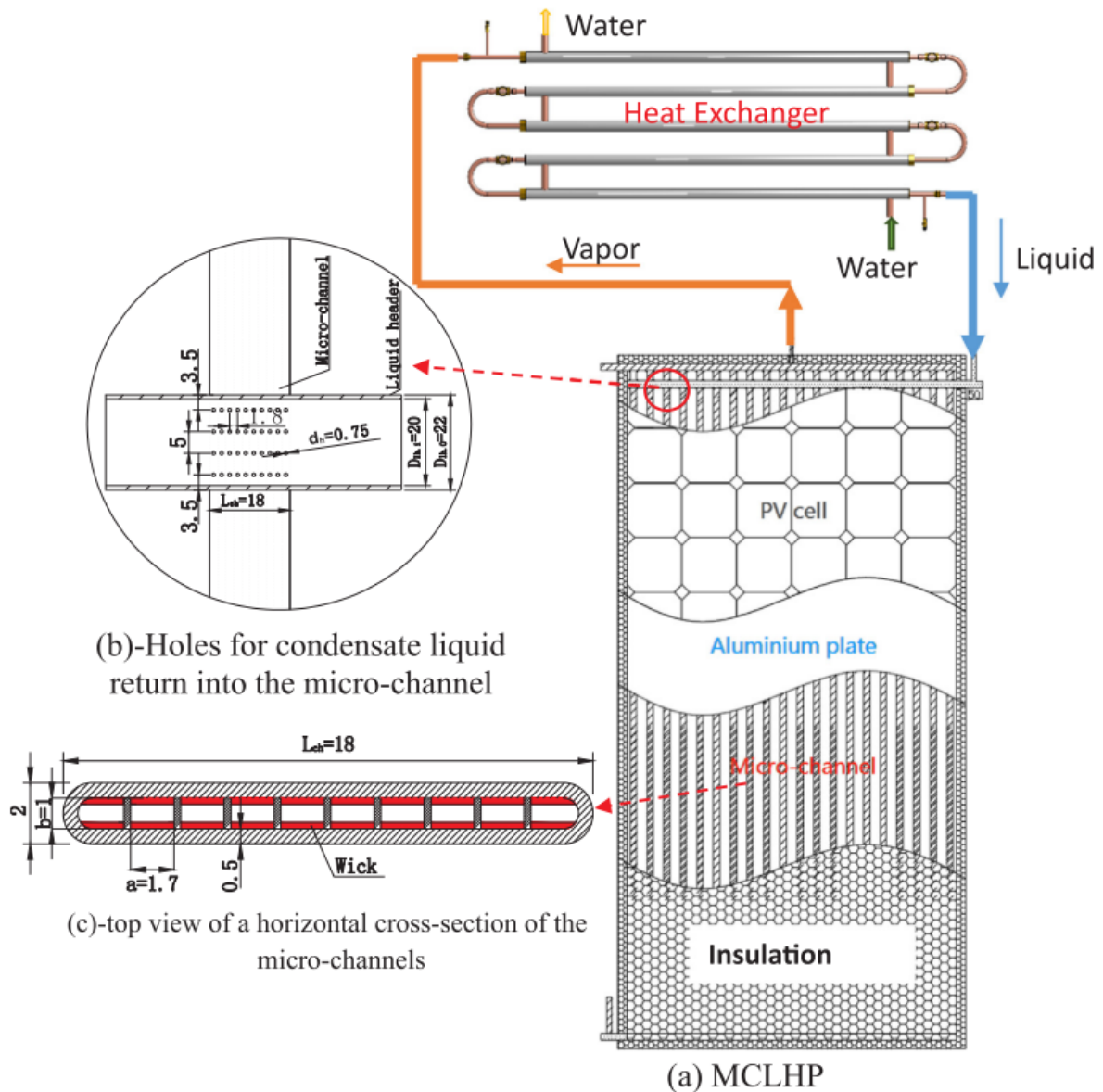


Figure 2-9. Micro-channel loop heat pipe based PV/T presented by *Yu et al.* [50], [51]

Unfortunately, the relevance of the vapour-liquid separator developed cannot be proved. Indeed, the published study does not permit a confirmation that dry-out did not appear, as the temperature measurements presented were very limited. It is worth noticing that an exceptional 17.0% of electrical efficiency was reached. This attests the high quality of the photovoltaic cells

used. The thermal performance of the micro-channel loop heat pipe reached a reasonable 49.7% of average thermal efficiency. Hence, by using high efficiency PV cells, the overall performance of the micro-channel loop heat pipe-based PV/T was 66.7%.

#### 2.1.4 Comparison of existing PV/T systems

To sum up the state of the art on the reported photovoltaic-thermal (PV/T) systems, Table 2-1 compares the works reviewed and reports the electrical, thermal, and overall performance of the PV/T modules.

Table 2-1. State of the Art on PV/T systems

Authors	PV/T technology	$\eta_{el}$	$\eta_{th}$	$\eta_{tot}$
<b>Air type PV/T collectors</b>				
<i>Tiwari and Sodha</i> [20]	Glazed PV/T air collector without Tedlar and single air channel	12%	25%	37%
<i>Sopian et al.</i> [21]	Double pass PV/T air collector	11%	50%	61%
<i>Othman et al.</i> [22]	Double pass PV/T air collector with a single fin	4%	58%	62%
<i>Jin et al.</i> [23]	Single pass PV/T air collector with rectangular channels	10%	55%	65%
<i>Bambrook and Sproul</i> [24]	Unglazed, single pass, open loop PV/T air collector	12%	55%	67%
<i>Kumar and Rosen</i> [25]	Double pass PV/T air collector with fins	15%	60%	75%
<b>Liquid type PV/T collectors</b>				
<i>Sun et al.</i> [26]	PV/T water collector with parallel tubes for the coolant	10%	35%	45%
<i>Tripathi and Tiwari</i> [27]	PV/T water collector with reflectors using an absorber and water tubes.	9%	37%	46%
<i>Kostic et al.</i> [28]	PV/T water collector with reflectors. The cooling water flows through copper tubes	5%	47%	52%
<i>Dupeyrat et al.</i> [29]	Single glazed PV/T water collector with direct lamination of PV cells on a metal heat exchanger	8%	50%	58%
<i>Lalovic</i> [30]	Water PV/T collector with a finned aluminium heat-exchange plate and copper tubes	4%	54%	58%
<i>Ji et al.</i> [31]	Flat plate glazed PV/T water collector using a flat-box Al-Alloy absorber plate with parallel passes	10%	49%	59%
<i>Sandnes and Rekstad</i> [32]	PV/T water collector with black plastic absorber and ceramic granulates in the water multi-channels	12%	55%	67%
<i>Coventry</i> [33]	Parabolic trough PV/T collector "CHAPS" with glass-on-metal mirrors and water with additives	11%	58%	69%
<i>Zondag et al.</i> [34]	Insulated two-absorber PV/T water collector	8%	66%	74%
<i>Fadhel et al.</i> [35]	PV/T water collector with a spiral flow absorber collector	12%	63%	75%
<i>Nahar et al.</i> [36]	PV/T water collector without absorber plate using encapsulation and Tedlar	11%	69%	80%
<i>Nasrin et al.</i> [37]	PV/T water collector with converging lens and multi-pass collector	11%	71%	82%

<b>Heat pipe-based PV/T collectors</b>				
<i>Tang and Zhao</i> [41]	Water cooled PV/T with micro heat pipe array	13%	/	/
<i>Deng et al.</i> [42], [43]	Water cooled PV/T with micro heat pipe array with micro fins, micro channels, and micro grooves	12%	32%	45%
<i>Gang et al.</i> [44], [45]	Water cooled PV/T with aluminium plate and nine cylindrical heat pipes	9%	42%	51%
<i>Moradgholi et al.</i> [46]	Water cooled PV/T with parallel cylindrical thermosyphons linked at the top and bottom	12%	44%	56%
<i>Hu et al.</i> [47]	Water cooled PV/T with aluminium plate and nine cylindrical thermosyphons	6%	50%	56%
<i>Jouhara et al.</i> [18], [48]	Water cooled PV/T multi-channel flat heat pipe (heat mat)	7%	49%	56%
<i>Modjinou et al.</i> [49]	Water cooled PV/T with aluminium micro heat pipe array	8%	51%	58%
<i>Wu et al.</i> [15]	Water cooled PV/T using 14 parallel, independent, circular, wicked heat pipes	8%	57%	66%
<i>Yu et al.</i> [50], [51]	Water cooled PV/T using a micro-channel loop heat pipe with wicks	17%	50%	67%

Compared to air type PV/T, it can be concluded that liquid type PV/T systems have reached better thermal performances. However, due to the possible freezing of the coolant, liquid type PV/T are not adopted for cold conditions. Heat pipe-based PV/T are currently being developed and improved to tackle the potential freezing of the coolant that could convey structural damage to the installation. In addition, heat pipe-based PV/T presents further advantages that are responsible for their penetration into the PV/T market such as guaranteeing an isothermal distribution of the panel, decreasing the differences of temperature within the solar panel modules, reducing the internal stresses of the PV cell, reducing the pumping power requirements, and increasing the life span of the PV/T system. Yet, it can be noted that the maximum overall performance of heat pipe-based PV/T is lower than for liquid type PV/T. The thermal efficiency of the heat pipe-based PV/T can, in particular, be further improved. Due to the recent introduction of heat pipes in PV/T, the heat pipe-based PV/T systems reported to date present significant technical differences. In many cases, the contact between the photovoltaic cell and the heat pipe is not optimum, the uniform temperature distribution is partial, and the thermal efficiency of the absorber is lower than for liquid type PV/T. These challenges confirm the progress that remains to be made in the promising field of heat pipe-based PV/T.

## 2.2 Multi-channel heat pipes

A multi-channel heat pipe describes a heat pipe or thermosyphon with parallel channels that are linked together in order to obtain uniform saturation conditions of the working fluid in all the channels. By allowing the circulation of the working fluid in the parallel channels, the working temperature of all the channels is similar, and the temperature profile does not vary between each leg of the heat pipe. Hence, multi-channel heat pipes have the potential of allowing a completely uniform temperature distribution on their surfaces. By combining this uniform temperature distribution characteristic with a flat external shape, multi-channel flat heat pipes become particularly suitable for PV/T applications.

In the literature, a few works on multi-channel heat pipes have been reported. Similar to the heat pipe investigated in this study, some heat pipes with parallel channels presented flat external shapes and have been used for surface cooling applications. However, heat pipes with parallel channels that are not linked and where each channel works independently cannot be considered as multi-channel heat pipes. For instance, many micro heat pipe arrays have been recently introduced as presented in the works by *Shittu et al.* [52], *Li et al.* [53], and *Sun et al.* [54]. Among others, such heat pipe arrays have been used for heat pipe-based PV/Thermoelectric systems that require a flat surface with high conductivity material to generate electricity from a temperature gradient by the Seebeck effect. *Diao et al.* [55] also used six parallel flat micro-heat pipe arrays to develop a new type of latent heat thermal energy storage. This apparatus with a micro-heat pipe array is presented in Figure 2-10.

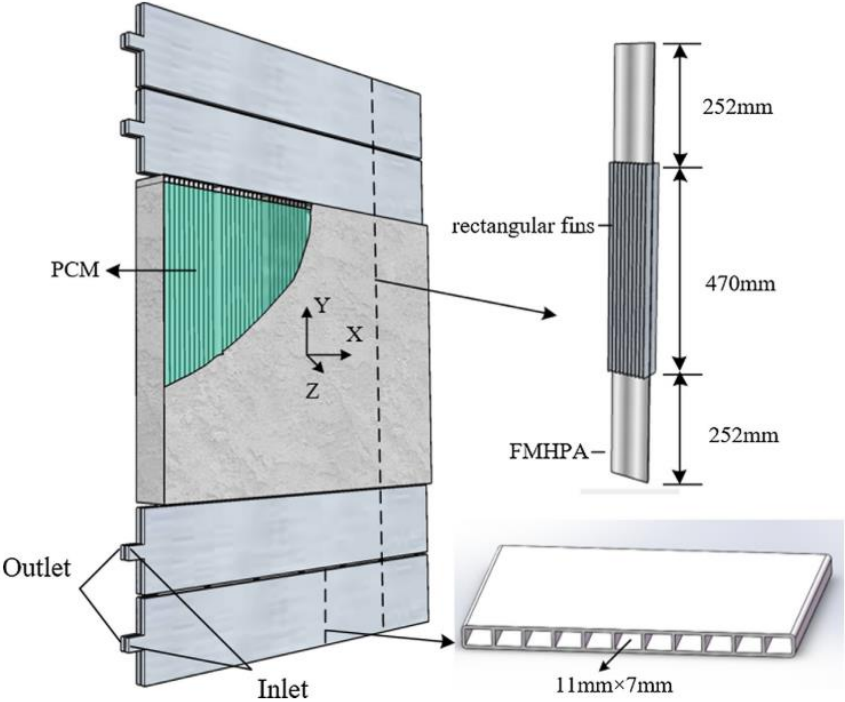


Figure 2-10. Micro-heat pipe array used for latent heat thermal energy storage, by *Diao et al.* [55]

The heat transfer area inside each channel was increased by incorporating rectangular fins. However, in all the heat pipe arrays presented, each channel works independently. Therefore, heat pipe arrays do not constitute a multi-channel heat pipe as the working fluid does not communicate between all the channels. Furthermore, the heat pipe arrays introduced have not been modelled to date. Indeed, in the current literature, the number of works reporting theoretical models of multi-channel heat pipes is limited. *Zhao et al.* [56] investigated the use of flat heat pipes with micro channels for battery management. The heat pipes were made of aluminium and are described as “ultra-thin” heat pipes by the authors. The channel structure comprised grooves. However, the internal structure was not reported and, even if the channels are likely to be connected, it cannot be confirmed from the publication that these heat pipes are multi-channel heat pipes. The flat aluminium heat pipes used acetone as a working fluid and are presented with battery packs in Figure 2-11.

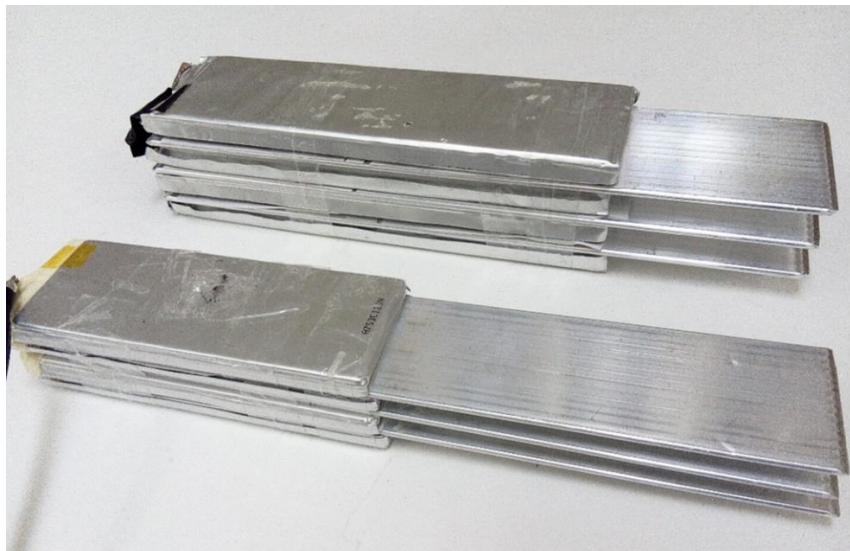


Figure 2-11. Micro-channel flat heat pipe presented by *Zhao et al.* [56]

In this investigation, the heat released by the battery packs was conveyed by the heat pipe to a heat sink. Five different heat sinks were tested to recover the thermal energy extracted: ambient air, horizontal fan cooling, vertical fan cooling, thermostat bath, and wet cooling. Yet, the experiment conducted by *Zhao et al.* [56] was focused on the battery management and, in this regard, the behaviour and performance of the micro-channel flat heat pipe have not been investigated. The micro-channel heat pipe was not modelled by the authors. In another study, *Zhao et al.* [57] presented an air-cooled multi-port flat heat pipe designed for the thermal management of a power battery. In the experiments, thermal energy was transferred from a wire heater to an air flow. The multi-port flat heat pipe used has been poorly described by the authors. Nevertheless, based on the pictures included in the manuscript, it seems that a confluence chamber links the bottom of six channels. At the condenser section, fins have been

placed to improve the heat transfer with the air stream. The air-cooled multi-port flat heat pipe used by *Zhao et al.* [57] can be seen in Figure 2-12.

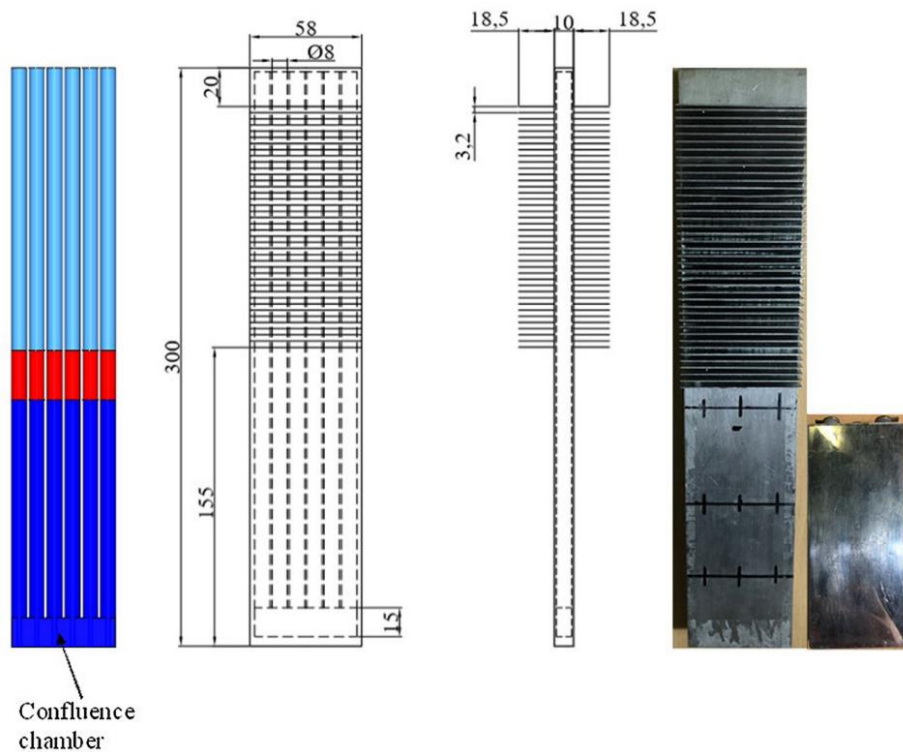


Figure 2-12. Air-cooled multi-port flat heat pipe developed by *Zhao et al.* [57]

Experimentally, factors such as the cooling and heating conditions, the heat pipe working fluid, and the filling ratio were investigated. The filling ratio represents the ratio of the liquid working fluid volume to the evaporator volume of the heat pipe. The working fluids tested were ammonia, acetone, and R134a. At a filling ratio of 50%, ammonia was the working fluid that achieved the best performance. It was also noted that the boiling resistance of acetone was significantly larger than that of ammonia and R134a. In comparison, the condensation resistances remained equivalent. As for the impact of the filling ratio, it was discovered experimentally that the thermal conductivity of the air-cooled multi-port flat heat pipe at a filling ratio of 50% was up to 1.6 times higher than the thermal conductivity at a filling ratio of 70%, and 2.22 times higher than that at 30%. The experimental evaporation and condensation heat transfer coefficients were compared with correlations from the literature. However, *Zhao et al.* [57] did not develop a predictive model based on two-phase heat transfer fundamentals. Similar to the heat mat presented for PV/T applications, *Jouhara et al.* [58] used a smaller scale multi-channel flat heat pipe for battery cooling purposes. By using this small flat heat pipe, the temperature of a battery was controlled and maintained within  $\pm 1^\circ\text{C}$  of the desired temperature. The smaller multi-channel flat heat mat used for battery management is shown in Figure 2-13.



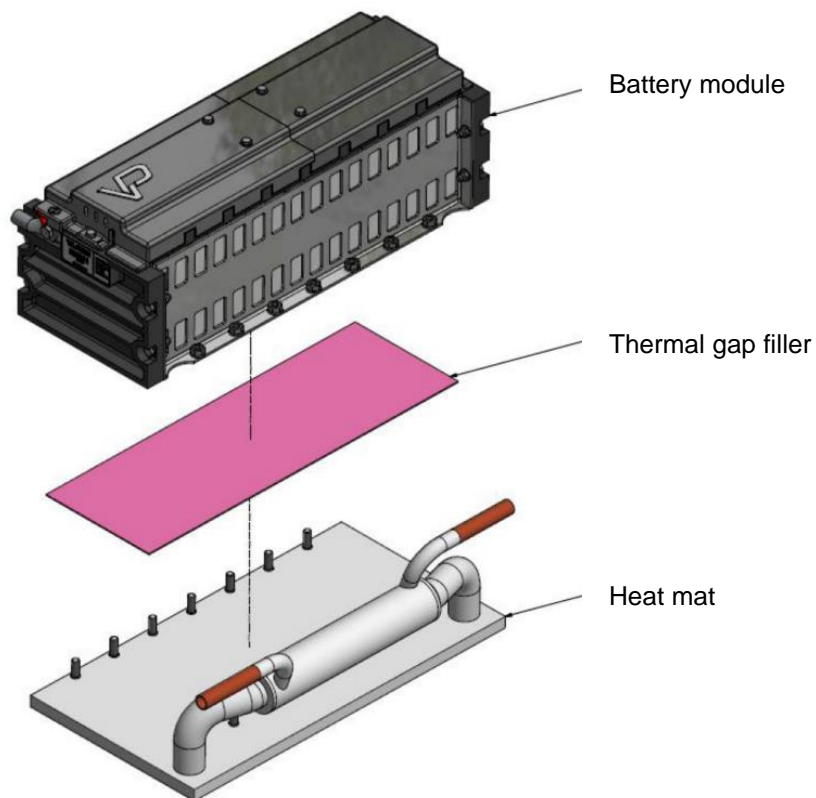
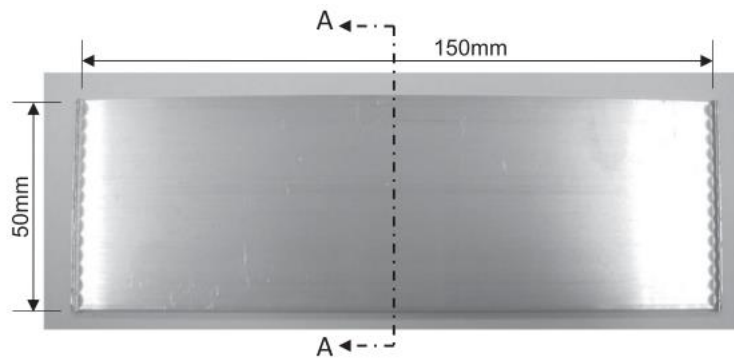
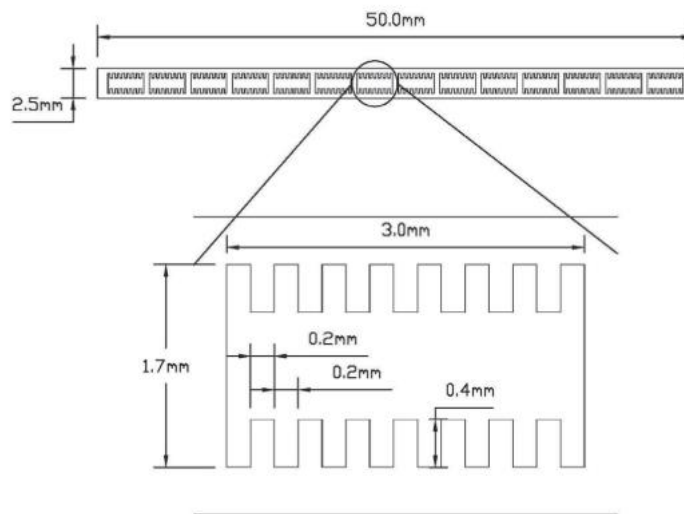


Figure 2-13. Smaller heat mat used for battery management, by *Jouhara et al.* [58]

In their work, *Jouhara et al.* [58] showed that the multi-channel flat heat pipe was able to remove 60% of the heat generated by the battery while guaranteeing a uniform temperature distribution. However, the multi-channel flat heat pipe has not been modelled theoretically. *Chen and Chou* [59] investigated the impact of the working fluid filling ratio and leakage on the thermal performance of flat plate heat pipes. The flat plate heat pipes were 150 mm long by 50 mm wide and were made by aluminium extrusion. The internal structure of the investigated flat heat pipe comprises parallel channels with grooves. The profile of the channels can be seen in Figure 2-14.



(a) An actual FPHP (top view)



(b) A-A cross-sectional view

Figure 2-14. Flat plate heat pipe developed by *Chen and Chou* [59]

According to the manufacturing process described by the authors, the flat plate heat pipe was first cut to the desired length and sealed at one end. Then, the channels were filled with working fluid and the other end of the heat pipe was closed. Therefore, it seems that the channels were not connected and that the flat plate heat pipe investigated by *Chen and Chou* [59] was not a multi-channel heat pipe. Thus, different saturation pressures can take place in the different channels. Acetone was selected as the working fluid. The best thermal performances were reached at a filling ratio of 25%. The thermal resistance of this flat plate heat pipe was 0.254 K/W. *Azad* [60] compared the thermal efficiency of three heat pipe solar collectors experimentally. Unfortunately, the description of the three-heat pipe solar collectors is imprecise, and there is a lack of clarity in the manuscript. Based on the work reported, it seems that the first heat pipe solar collector (Type I) consisted of a multi-channel heat pipe, in which at one end the parallel heat pipes were connected to a collector at the bottom, while at the other end they were linked to a shell and tube condenser at the top. The absorber was made of aluminium with fins. The second heat pipe solar collector (Type II) was made of independent parallel heat pipes not connected to each other. The condenser section was a succession of

double pipe heat exchangers. In the third solar collector (Type III), the heat pipe was also a multi-channel heat pipe and the condenser was a shell and tube exchanger. In Type II and Type III, the heat pipes were mechanically bonded to an aluminium absorber plate. The three heat pipe solar collectors are presented in Figure 2-15.

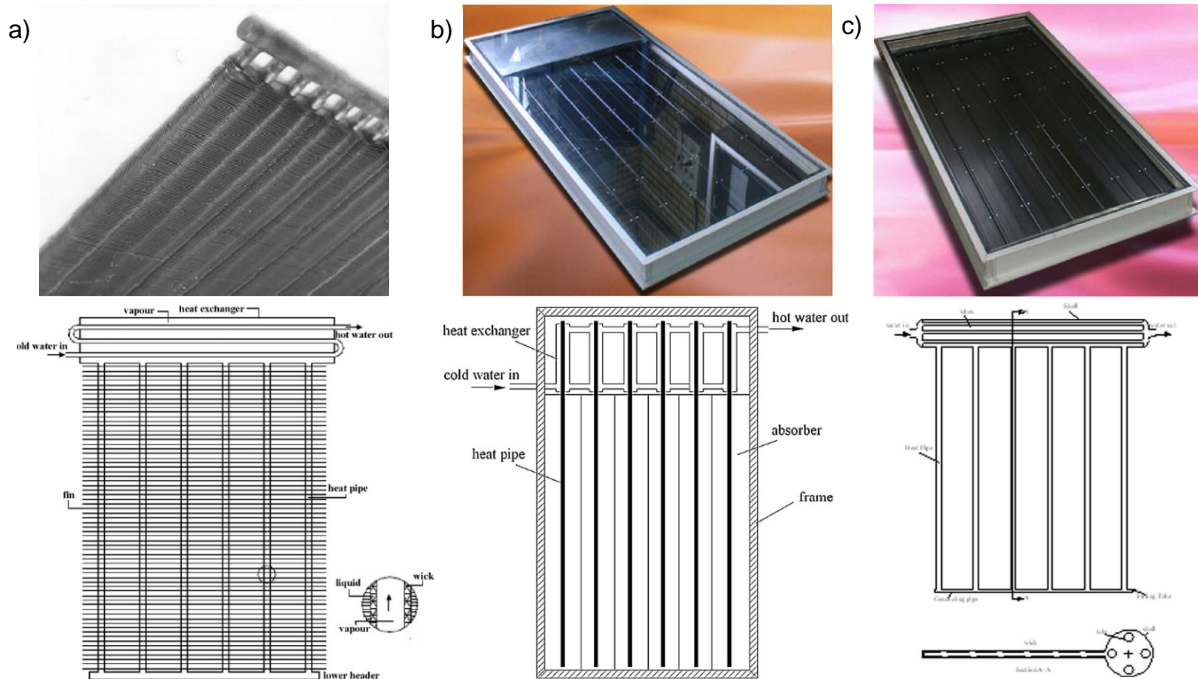


Figure 2-15. Heat pipe solar collectors presented by Azad [60]

The working fluid used in this experiment was ethanol and the filling ratio was identical for the three-heat pipe solar collectors. Despite the interest of this research, the results section was poor and only one graph with exact linear trends was presented. According to this graph, the efficiency of the solar collector Type I was higher at lower irradiation rates. Overall, the solar collector Type III had the highest average efficiency. It is worth noticing that, according to the authors, a weakness of the collectors Type I and Type III is that a leakage in one heat pipe implies that the whole heat pipe ceases to operate. However, the authors did not balance this statement by investigating the advantage of this design. The temperature differences of the three-heat pipe solar collectors were not presented. Hence, the experiments carried out by Azad [60] were too limited to make conclusions on the differences between the three solar collectors. Finally, Azad [60] did not propose a theoretical model of the heat pipe based solar collectors. Sun *et al.* [54] used a loop heat pipe with two vapour ascending tubes connecting the evaporator to the condenser section. The condenser consisted of a heat exchanger with several flat micro-channels. The multi-channel heat pipe developed by Sun *et al.* [54] is presented in Figure 2-16.

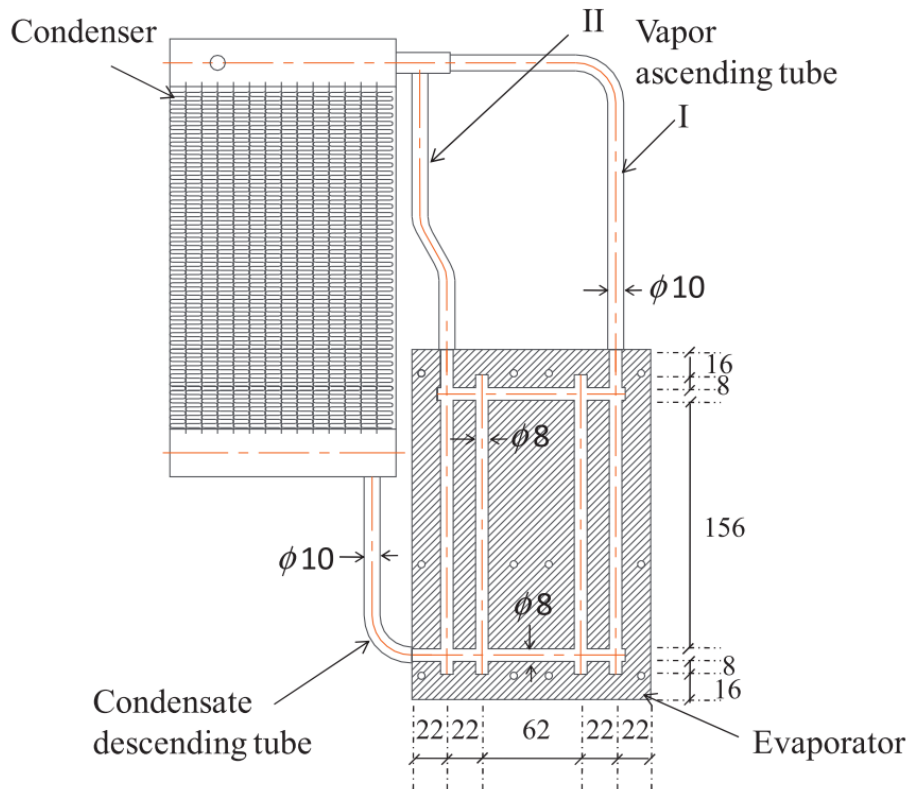


Figure 2-16. Multi-channel heat pipe developed by Sun *et al.* [54]

A theoretical model was developed by Sun *et al.* [54]. However, the authors considered the multi-channel thermosyphon as a single heat pipe and used an equivalent heat transfer area. Furthermore, the authors used single phase and two-phase flow convection correlations. Nevertheless, at a heat load between 100W and 200W, the condenser temperature of the heat pipe was predicted within an average relative error of 4.2%.

Yasuda *et al.* [61] visualized the working fluid flow in a flat plate pulsating heat pipe with 22 turns. The channels had a square shape cross section of dimensions 1.2mm x 1.2mm and the refrigerant used was R1336mzz. The filling ratio was selected to be 50% and the heat transfer rates investigated were 80W and 120W. The authors observed that the initial distribution of the refrigerant had no impact on its oscillation and performance during the start-up of the heat pipe. Furthermore, even if at 80W the working fluid is evenly distributed, at 120W, the working fluid is pushed away from the heating section. Almahmoud and Jouhara [62], [63] investigated the performance of a multi-channel heat pipe designed for waste heat recovery for the steel industry. In their apparatus, thermal energy was recovered by convection and radiation. The multi-channel heat pipe was made from fourteen stainless steel tubes connected at the top and bottom by collectors. The collectors were two horizontal stainless-steel tubes linking all the legs of the heat pipe to each other. Inside the top collector, a shell and tube heat exchanger with a coolant recovered the thermal energy. The radiative multi-channel heat pipe developed is presented in Figure 2-17.



Figure 2-17. Radiative multi-channel heat pipe developed by *Almahmoud and Jouhara* [62], [63]

A theoretical model was developed to predict the performance of the heat pipe and the temperatures in the system. This model included the resistances of the radiative source, the heat pipe, and the shell and tube condenser. To estimate the equivalent resistance of the heat pipe, an equivalent heat transfer area of boiling and condensation was taken, and the influence of each leg was not investigated. Nonetheless, for a heat transfer rate between 4500W and 8500W, the heat transfer rate was predicted within an error of 14.3%. The heat pipe temperatures were predicted within 3°C. Similarly, *Delpech et al.* [64] developed a multi-channel heat pipe for heat recovery in the ceramic industry. The multi-leg heat pipe was placed over hot ceramic tiles and absorbed heat by radiation and natural convection. The heat pipe was made of ten parallel stainless-steel tubes linked at the top and bottom by collectors allowing the liquid and vapour phases of the working fluid to communicate between the different legs. Inside the top header, a shell-and-tube heat exchanger allowed cooling water to recover the thermal energy transmitted by the heat pipe. The multi-channel heat pipe investigated by *Delpech et al.* [64] is presented in Figure 2-18.

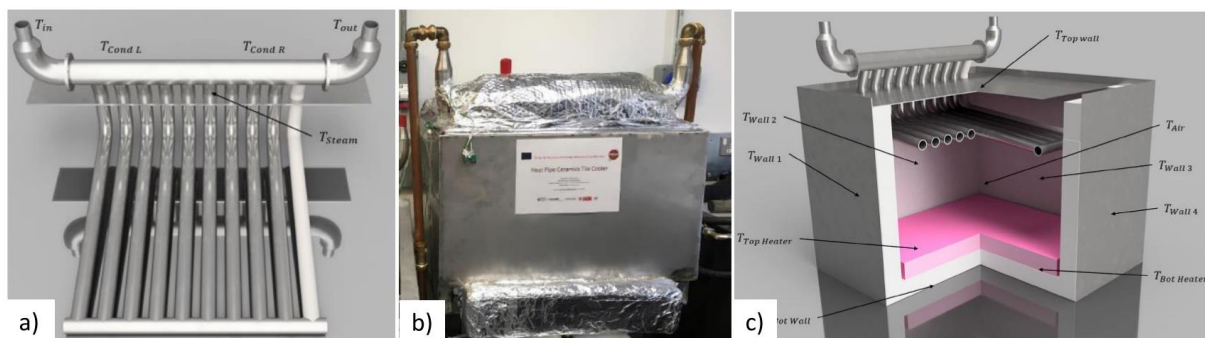


Figure 2-18. Multi-channel heat pipe developed by *Delpech et al.* [64]

*Delpech et al.* [64] developed a theoretical model including both radiative and natural convective heat sources. A detailed radiative thermal resistance analysis was presented. As for the multi-channel heat pipe, the evaporator and condenser resistances have been modelled

using boiling and condensation correlations on the equivalent heat transfer area. For a heat transfer rate in the range 470W-2435W, the average error associated with the heat transfer rate prediction was 7.5%.

From the preceding literature review on multi-channel heat pipes, it is noted that, among the several works published on this topic, the majority of the investigations available are experimentally based and usually focus more on the application of a multi-channel heat pipe than on the behaviour of the multi-channel heat pipe itself. Indeed, the impact of the multi-channel geometry and its influence has not yet been studied. Finally, the number of theoretical models developed to predict the performance of a multi-channel heat pipe is very limited. To date, it seems that only *Almahmoud and Jouhara* [62], [63], and *Delpech et al.* [64] have proposed theoretical models of a multi-channel heat pipe. Yet, these models considered an equivalent heat transfer area of boiling and condensation which means that the multi-channel geometry is considered to have no influence on the performance of the heat pipe, and that the temperature is uniform between all the legs and the collectors. However, this assumption remains to be verified. Furthermore, such models could be improved by differentiating the collectors and each legs of the heat pipe instead of considering an equivalent heat transfer area. Finally, no flat shape multi-channel heat pipe has been analytically modelled so far.

## 2.3 Computational fluid dynamic (CFD) modelling of heat pipes

With the development of software and the increase of calculating power, Computational Fluid Dynamic (CFD) simulation is a promising technique for investigating the behaviour of heat pipes. To model two-phase flow, source terms must be added to the software's transport equations to model evaporation and condensation; the use of such source terms is a necessity for the modelling of heat pipes. Several models exist, and it is not clear that one model performs better than the others. Hence, a review of the available models for the simulation of evaporation and condensation phenomena is relevant.

### 2.3.1 Phase change models and source terms

In this section, the different mass transfer source terms used to simulate phase change are reviewed. To simulate evaporation and condensation, two types of source terms are used. On the one hand, the mass source term of each phase (liquid and vapour) describes the mass transfer from one phase to the other. On the other hand, the energy source terms express the energy transfer occurring during the phase change mechanism. The energy source term  $S_E$  can be related to the mass source term  $S_M$  by:

$$S_E = i_{lv}S_M \quad (2-5)$$

with  $S_E$  the energy source term ( $\text{J/m}^3\text{s}$ ),  $S_M$  the mass source terms ( $\text{kg/m}^3\text{s}$ ), and  $i_{lv}$  the latent heat of vaporization ( $\text{J/kg}$ ). Hence, in the state of the art of the available phase change models, only the mass source terms are reported.

#### 2.3.1.1 Schrage model

Derived from the well-known *Hertz-Knudsen* [65] equation, the *Schrage* [66] model uses pressure and temperature of both phases to predict the mass flux at the liquid/vapour interface. The *Schrage* [66] model is based on the mass source term hereafter:

Table 2-2. *Schrage* [66] phase change model

Process	Condition	Mass source term
Evaporation and Condensation	None	$\dot{m}_{M,v} = -\dot{m}_{M,l} = \frac{2}{2 - \beta_c} \frac{\sqrt{M_{mol}}}{\sqrt{2\pi R_{gas}}} \left[ \beta_c \frac{P_v}{\sqrt{T_v}} - \beta_e \frac{P_{sat}(T_l)}{\sqrt{T_l}} \right]$ $S_M = \dot{m}_M \frac{A_{int}}{V}$

where  $\dot{m}_M$  is the mass transfer rate ( $\text{kg/m}^2\cdot\text{s}$ ),  $\beta_c$  and  $\beta_e$  a condensation and evaporation coefficient,  $M_{mol}$  the molecular weight ( $\text{kg/mol}$ ),  $R_{gas}$  the universal gas constant ( $\text{J/mol}\cdot\text{K}$ ),  $P_v$  the vapour pressure (Pa),  $T_v$  the vapour temperature (K),  $P_{sat}$  the saturation pressure (Pa),  $T_l$  the liquid temperature (K),  $S_M$  the mass source term,  $A_{int}$  the cell interfacial area ( $\text{m}^2$ ), and  $V$  the cell volume ( $\text{m}^3$ ). In practice, the complexity of the *Schrage* model [66] has discouraged

researchers from using it for their simulations. Instead, simpler versions of the *Schrage* [66] model have been derived to simulate phase change mechanisms, such as the *Lee* model [67].

### 2.3.1.2 Lee model

The most known and used multi-phase flow model is called the *Lee* model [67] and it was widely introduced in a work by *De Schepper et al.* [68][69] which is considered as a reference study in the domain of multi-phase flow modelling. The *Lee* model [67] is presented hereafter:

Table 2-3. *Lee* [67] phase change model

Process	Condition	Mass source term
Evaporation	$T_{mix} > T_{sat}$	$S_{M,l} = -S_{M,v} = -\beta_e \alpha_l \rho_l \frac{T_{mix} - T_{sat}}{T_{sat}}$
Condensation	$T_{sat} < T_{mix}$	$S_{M,l} = -S_{M,v} = \beta_c \alpha_v \rho_v \frac{T_{sat} - T_{mix}}{T_{sat}}$

where  $S_{M,l}$  and  $S_{M,v}$  are the liquid and vapour phase mass source terms (kg/m<sup>3</sup>s),  $\beta_e$  and  $\beta_c$  are the evaporation and condensation mass transfer coefficients (s<sup>-1</sup>),  $\alpha_l$  and  $\alpha_v$  the liquid and vapour phase volume fractions,  $\rho_l$  and  $\rho_v$  the liquid and vapour densities (kg/m<sup>3</sup>),  $T_{mix}$  the mixture temperature (K),  $T_{sat}$  the saturation temperature (K), and  $i_{lv}$  the latent heat of vaporization (J/kg). Apart from its simplicity, the *Lee* model [67] is described as a model with a lower physical meaning [70]. This is justified as the constants  $\beta_e$  and  $\beta_c$  are usually adapted by the authors to balance the evaporation and condensation mass transfers and limit the convergence issues. The exact values of the evaporation and condensation coefficients are:

$$\beta_e = \frac{6}{D_{sm}} \sqrt{\frac{M_{mol}}{2\pi R_{gas} T_{sat}}} \left( \frac{\rho_v}{\rho_l - \rho_v} \right) (i_{lv}) \quad (2-6)$$

$$\beta_c = \frac{6}{D_{sm}} \sqrt{\frac{M_{mol}}{2\pi R_{gas} T_{sat}}} \left( \frac{\rho_l}{\rho_l - \rho_v} \right) (i_{lv}) \quad (2-7)$$

with  $D_{sm}$  the Sauter mean diameter (m),  $M_{mol}$  the molecular weight (kg/kmole),  $R_{gas}$  the universal gas constant (J/mole.K),  $T_{sat}$  the saturation temperature (K),  $\rho_l$  and  $\rho_v$  the liquid and vapour densities (kg/m<sup>3</sup>), and  $i_{lv}$  the latent heat of vaporization (J/kg). Generally, the two mass transfer constants are set to  $\beta_e = \beta_c = 0.1 \text{ s}^{-1}$  [71]. However, in the literature, researchers have modified the condensation coefficient in order to obtain different condensation patterns. While the evaporation coefficient usually remains unchanged, the condensation coefficient  $\beta_c$  can vary from  $0.1 \text{ s}^{-1}$  to  $5000 \text{ s}^{-1}$  [72]. In this regard, *Kim et al.* [71] dedicated a study to investigate the optimum values of the condensation mass transfer coefficients. The authors compared simulations using four different values of condensation mass transfer coefficient  $\beta_c$ , and validated them with experimental data. The mass transfer coefficients investigated and their validation with experimental data are reported in Table 2-4.



Table 2-4. Investigation of the evaporation and condensation mass transfer coefficients values in the Lee model, from *Kim et al.* [71]

	Evaporation coefficient $\beta_e$	Condensation coefficient $\beta_c$	Comparison of the condenser temperature with experiments $\Delta T_c$
Case 1	0.1	0.1	15.3 °C
Case 2	0.1	$\beta_{c,old} \left\{ 1 - \left[ \frac{m_c - m_e}{\max(m_c, m_e)} \right] \right\}$	9.0 °C
Case 3	0.1	100	7.0 °C
Case 4	0.1	$\beta_e \times \frac{\rho_l}{\rho_v}$	4.3 °C

where  $\beta_e$  and  $\beta_c$  are the evaporation and condensation mass transfer coefficients ( $s^{-1}$ ),  $m_c$  is the total mass condensed (kg),  $m_e$  is the total mass evaporated (kg), and  $\rho_l$  and  $\rho_v$  are the liquid and vapour densities ( $kg/m^3$ ), respectively. According to this study, the best agreement with experimental data was obtained for Case 4. Therefore, *Kim et al.* [71] concluded that the condensation mass transfer coefficient value considering the density ratio was advised. In the expression of the *Lee* model [67], it can be noted that a value of the saturation temperature is required. In practice, researchers use a fixed value of saturation temperature which is commonly based on experimental data.

### 2.3.1.3 Wang model

*Wang et al.* [70] proposed a pressure based phase change model derived from the *Hertz-Knudsen* equation [65] with the objective of considering the influence of the hydrostatic pressure on boiling. Indeed, one of the limits of the *Lee* model [67] is that it does not consider the impact of the hydrostatic pressure on the fluid dynamics, which can be significant in the case of deep liquid pools. The authors decided to imply different conditions between evaporation from the surface and evaporation in the bulk liquid by introducing a pressure potential difference term  $\Delta P_i$ , which represents the superheating condition required for a bubble to grow from a nucleation site. These conditions are illustrated in Figure 2-19.

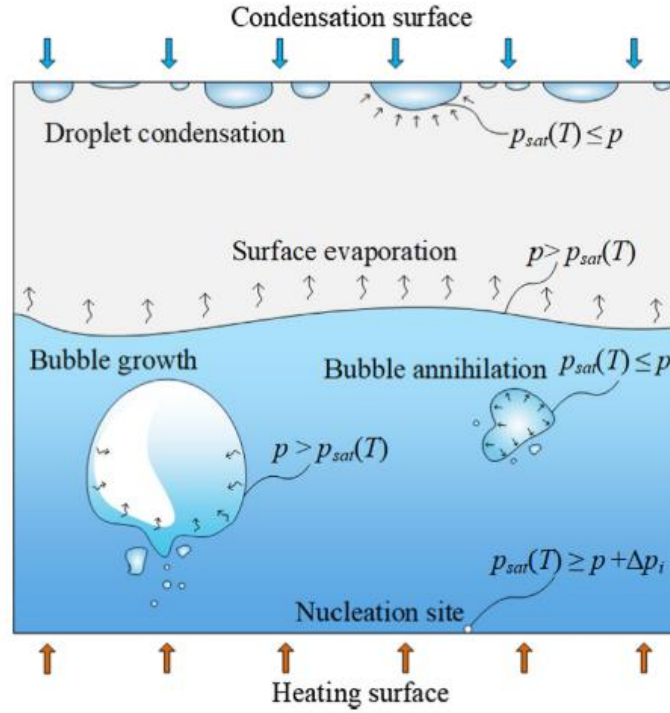


Figure 2-19. Pressure boundaries considered in the model by Wang *et al.* [70]

Based on the above conditions, the model by Wang *et al.* [70] is described in Table 2-5.

Table 2-5. Wang *et al.* [70] phase change model

Process	Condition	Mass source term
Evaporation – Nucleation site	$P_{sat}(T) \geq P_{mix} + \Delta P_i$	$S_{M,l} = -S_{M,v} = -\beta_e \alpha_l \sqrt{\rho_v} \frac{P_{sat}(T) - P_{mix}}{\sqrt{P_{mix}}}$
Evaporation – bulk	$P_{mix} < P_{sat}(T) < P_{mix} + \Delta P_i$	$S_{M,l} = -S_{M,v} = \begin{cases} -\beta_e \alpha_l \sqrt{\rho_v} \frac{P_{sat}(T) - P_{mix}}{\sqrt{P_{mix}}}, & 0 < \alpha_l < 1 \\ 0, & \alpha_l = 1 \end{cases}$
Condensation	$P_{sat}(T) \leq P_{mix}$	$S_{M,l \rightarrow v} = -S_{M,v \rightarrow l} = \beta_c \alpha_v \sqrt{\rho_v} \frac{P_{sat}(T) - P_{mix}}{\sqrt{P_{mix}}}$

where  $\beta_e$  is an empirical constant set to  $\beta_e = 0.5 \text{ s}^{-1}$ ,  $\beta_c$  is an empirical constant set to  $\beta_c = 1.5 \text{ s}^{-1}$ ,  $\alpha_l$  and  $\alpha_v$  the liquid and vapour phase volume fractions,  $\rho_l$  and  $\rho_v$  the liquid and vapour densities ( $\text{kg/m}^3$ ),  $P_{sat}(T)$  is the saturation pressure at a temperature  $T$  (Pa),  $P_{mix}$  is the mixture pressure (Pa), and  $i_{lv}$  the latent heat of vaporization (J/kg). The pressure potential difference  $\Delta P_i$  required for a bubble to grow in the cavity is estimated by [70]:

$$\Delta P_i = \frac{2\sigma_{lv}}{r_{cav}} \left( 1 + \frac{\rho_v}{\rho_l} \right) \quad (2-8)$$

with  $\sigma_{lv}$  the liquid surface tension (N/m), and  $r_{cav}$  the cavity radius (m). The cavity radius is usually in the range 1-10  $\mu\text{m}$  [70], [73]. The saturation pressure was calculated using an experimental based equation which depends on the temperature:

$$P_{sat}(T) = e^{\left( 90.483 - \frac{4669.7}{T} - 11.607 \ln(T) + 0.017194T \right)} \quad (2-9)$$

### 2.3.1.4 Nichita and Thome model

Also known as the “sharp interface model”, *Nichita and thome* [74] proposed a phase change model based on the Rankine-Hugoniot jump conditions [75]. The rate of mass transfer is defined according to the temperature and volume fraction gradients as:

Table 2-6. *Nichita and thome* [74] phase change model

Process	Condition	Mass source term
Evaporation and Condensation	None	$\dot{m}_{M,v} = -\dot{m}_{M,l} = \frac{(k_l \nabla T_l - k_v \nabla T_v) \cdot \vec{n}}{i_{lv}}$ $S_M = \dot{m}_M \frac{A_{int}}{V}$

with  $k_l$  and  $k_v$  the liquid and vapour thermal conductivity (W/m.K),  $T_l$  and  $T_v$  the liquid and vapour temperature (K), and  $i_{lv}$  the latent heat of vaporization (J/kg). The above model may be simplified by considering an effective thermal conductivity. Some other phase change models have also been reported by *Wen et al.* [75] and *Kharangate and Mudawar* [76] but are used less by researchers and thus not discussed in this work. The four phase change models reviewed are the most known and used mass transfer models that are discussed for the modelling of evaporation and condensation in heat pipes. In the above models, it can be noted that the phase change models commonly require values for the saturation pressure and/or temperature. In practice, these values are usually fixed by researchers and experimentally based.

### 2.3.2 Simulation of thermosyphons

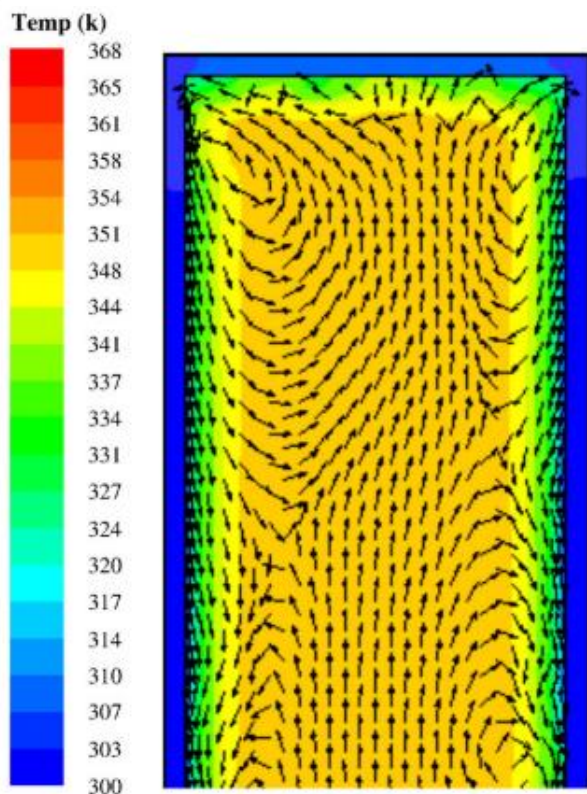
In the past twenty years, computational simulations of heat pipes have been intended to study and predict the two-phase cycle of the working fluid in heat pipes. The state of the art of available simulations of thermosyphons is presented hereafter in chronological order.

Differences of temperature between the presented simulations and experiments have been chosen as a criterion for estimating the accuracy of the simulations. The concept of relative error has been misused by researchers as the temperature in the denominator makes this information biased. Indeed, it is a common practice that researchers use temperatures in Kelvin which significantly decreases the relative error. For this reason, according to the author, it seems more relevant to compare the works available in the literature in terms of difference of temperature between the simulation and experimental data.

*Legierski et al.* [77] tried to simulate the transient behaviour of an horizontal wicked heat pipe. Experimental measurements from a thermographic camera and contact thermometers were taken to validate the simulation. For their simulation, *Legierski et al.* [77] used C-based user defined functions (UDF) including the *Hertz-Knudsen* [65] model to calculate the mass flux during evaporation. The evaporation coefficient used varied in the range [0.01:0.0001] and

was adjusted to best fit the experiments. Furthermore, the simulation used an experimental based temperature profile called “thermal excitation function” which makes the simulation semi-empirical. Therefore, this simulation does not permit any prediction. Finally, the simulation failed in modelling boiling and condensation and the fluid dynamics were not presented. *Zang et al.* [78] developed a two-dimensional model of a disk-shaped flat thermosyphon and compared it with experimental observations in a transparent flat thermosyphon. Only the vapour section was simulated. The saturation temperature was determined with the Clausius-Clapeyron equation using the initial temperature and pressure conditions. The evaporation and condensation heat exchange terms were implemented on the boundary condition instead of modifying the transport equations. Indeed, no mass source terms were implemented. Hence, no nucleation and bubble activity were simulated, and the model was single phase (no liquid). For these reasons, this simulation is considered irrelevant as a heat pipe simulation. *Rahmat and Hubert* [79] modelled a single triangular micro heat pipe and a 3D microchannel network. The ANSYS CFX phase change model included was used to simulate the phase change. It seems that source terms were used as they appear in the governing equations but were not explicitly formulated. Both constant heat flux and constant temperature boundary conditions were implemented, and a slip boundary condition was set for the vapour phase. The authors [79] reported that convergence of the simulation was challenging. The simulation was interrupted after 200 iterations or 9h of simulation, which is extremely low for a two-phase simulation. The limited number of iterations and the residual trend makes the “steady state” status of the results questionable. The simulation results were validated with the literature. However, this validation was poor, and the temperature comparison between the simulation and experimental data was not made. *Alizadehdakhel et al.* [80] simulated a 2D single thermosyphon by using the Lee model [67]. The coefficient  $\beta$  of the Lee model was set to its common value of  $\beta_e = \beta_c = 0.1 \text{ s}^{-1}$ . A constant heat flux boundary condition of up to  $30,000 \text{ W/m}^2$  was imposed on both evaporator and condenser sections of the thermosyphon. To consider the impact of non-condensable gases, the authors added the volume fraction of water vapour contained in the gas phase to the source term of *De Schepper et al.* [69]. The saturation temperature was set to 350K. The *Brackbill et al.* surface tension model [81] was used to describe the interactions between the phases. The simulation was compared to experimental data taken from a 1m long copper thermosyphon. Three heat transfer rates of 350W, 500W, and 700W were simulated. At the condenser, Filmwise condensation was observed and this seems to fit with expectations. The film forming and vapour velocity contours can be observed in Figure 2-20.

a) Velocity vectors and temperature profile



b) Vapour volume fraction

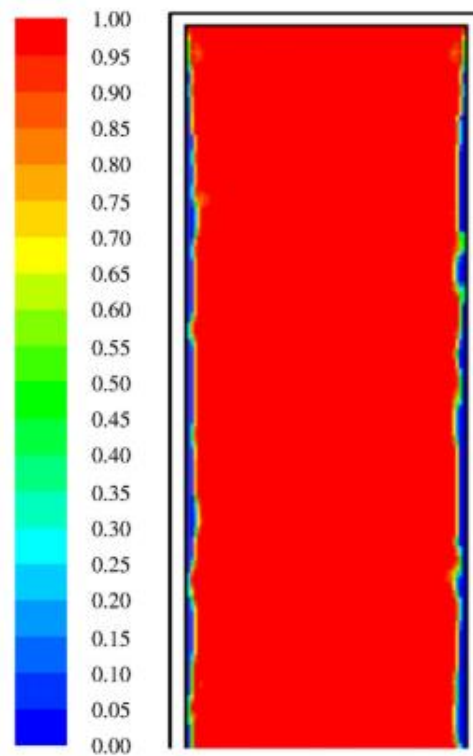


Figure 2-20. a) Vapour velocity contours and b) Filmwise condensation in the simulation by *Alizadehdakhel et al.* [80]

*Alizadehdakhel et al.* [80] observed that, at a heat transfer rate of 350W, the liquid phase in the condenser was negligible and very limited. At the evaporator, bubbles were observed forming a vapour layer near the wall and then moving to the centre of the thermosyphon. Also, the returning falling film was visualized. The simulation was validated with temperature measurements. Even if the temperature agreement was not characterized accurately by the authors, the temperature profile was in relatively good agreement for the evaporator and condenser sections, but a higher error was made on the adiabatic section as the temperature difference between experimental data and simulation was 16°C. The authors justified this discrepancy by potential heat losses taking place at the adiabatic section of their tested thermosyphon. At the evaporator and condenser, the temperature differences between simulation and experiments were 0.9°C, and 5.4°C. *Annamalai and Ramalingam* [82] numerically and experimentally investigated the performance of a one meter long copper heat pipe. The simulation was made with the software ANSYS and only steady-state conditions were studied. The saturation temperature was determined using the Clausius Clapeyron equation with a reference saturation pressure and temperature. At the liquid-vapour interface, a heat source term was added as a boundary condition. Only the temperature profile of the heat pipe was reported. Because no mass transfer was considered, boiling and condensation were not successfully modelled. For both evaporator and condenser, the temperature

prediction gave an error of 6°C. *Lin et al.* [83] numerically simulated a miniature oscillating heat pipe by using the Volume of Fluid method, the continuum surface force model, and a user-defined-function to implement the phase change process source terms. The source terms used were taken from the Lee model [67]. For their simulation, the authors [83] used a mixture model which seems more suitable for the special case of oscillating heat pipes due to the moving slugs of both liquid and vapour phases. The saturation temperature was taken from experiments and set to be around  $T_{sat} = 303\text{K}$ . A semi-transparent oscillating heat pipe made from silicon tubes was built to validate the CFD modelling of the oscillating heat pipe. However, the bubble motion and fluid dynamics were not used by *Lin et al.* [83] to validate their simulation. Indeed, in the work presented, only the temperature profiles were shown, and the fluid dynamics were not presented. Hence, one can raise doubt on the fact that boiling and condensation were successfully modelled. The only aspect that could be an indicator of a successful simulation of the oscillating heat pipe is the local oscillation of temperature in the geometry. However, the validation remains limited. On average, at the evaporator, the difference of temperature between the simulation and experimental data was 8.9°C and, at the condenser, this difference of temperature was 4.8°C. *Fadhl et al.* [84] simulated the operation of a single thermosyphon in 2D. To do so, the Volume of Fluid (VOF) method was used. In addition to the fluid properties, the Lee [67] source terms were incorporated into the UDF to model the mass and heat transfer between the phases. The continuum surface force (CSF) model by *Brackbill et al.* [81] was chosen to describe the interfacial surface tension between the liquid and vapour phases. *Fadhl et al.* [84] was one of the first researchers to report the numerical modelling of boiling and condensation, as shown in Figure 2-21 (a) and (b), respectively.

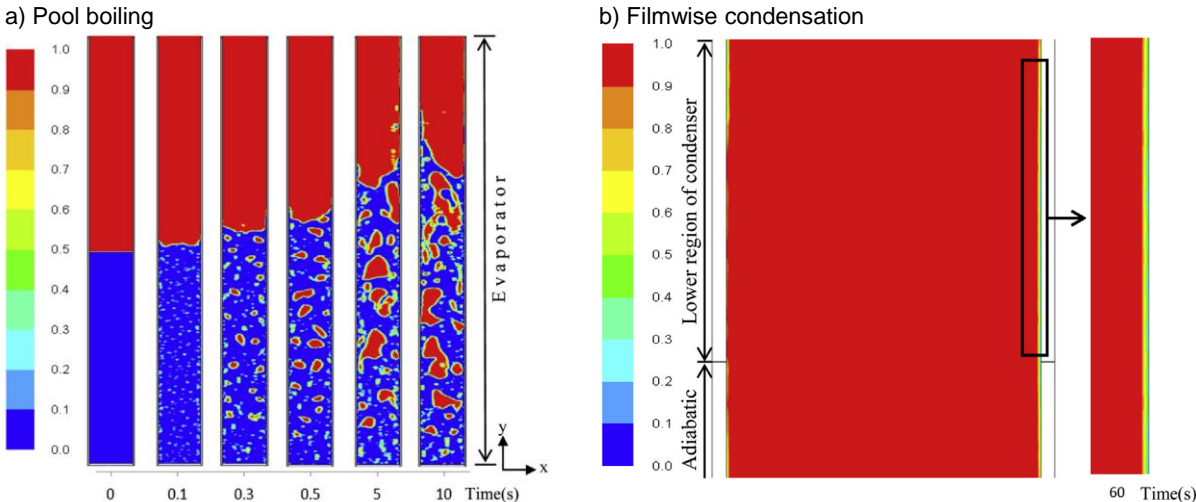


Figure 2-21: Volume fraction contours of vapour showing the modelling of pool boiling (a) and Filmwise condensation (b) in a thermosyphon, by *Fadhl et al.* [84]

At the evaporator, a constant heat flux boundary condition was defined whereas a forced convective heat transfer coefficient was applied on the condenser wall. In addition to the boundary conditions that can differ between the studies, the work by *Fadhl et al.* [84] also raises the question of implementing suitable initial conditions. Indeed, as shown in Figure 2-22 that presents the temperature profile of the thermosyphon, *Fadhl et al.* [84] decided to set the temperature of the liquid pool to the saturation temperature ( $T_{sat} = 373\text{K}$ ), whereas the vapour section was at a lower temperature around 340K. It is expected that this temperature was also used as the heat sink temperature as the condenser temperature does not decrease with time.

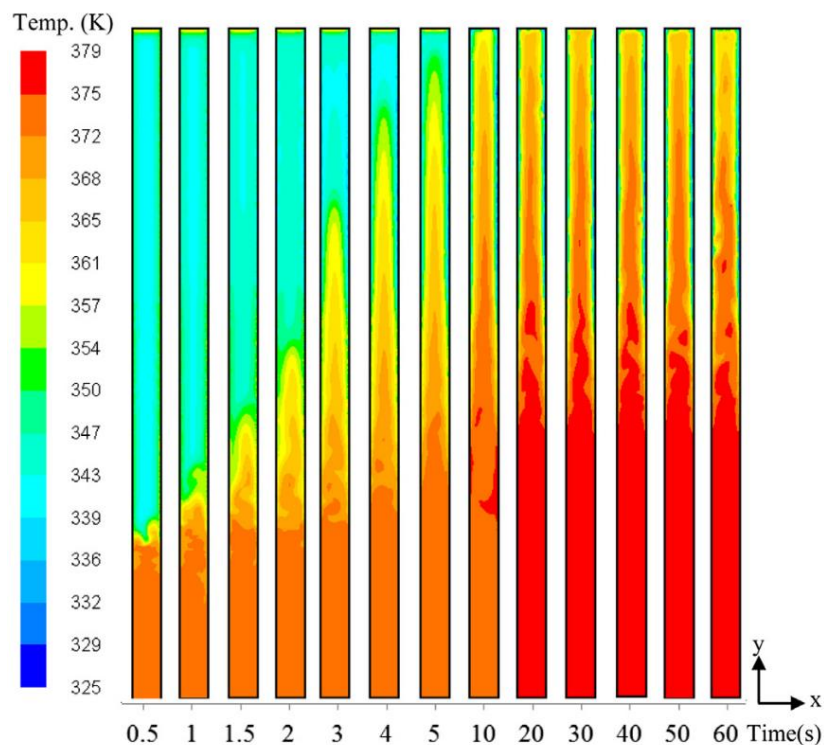


Figure 2-22. Temperature contour of the thermosyphon, by *Fadhl et al.* [84]

The simulation was validated with experiments taken from a copper, thermosyphon, 0.5m long, using distilled and degassed water as a working fluid. For all the heat transfer rates tested, the average differences of temperature between experimental data and the simulation at the evaporator, adiabatic, and condenser section were 27.6°C, 32.9°C, and 6.1°C, respectively. The average error made in the estimation of the thermosyphon thermal resistance was 79.6%. *Kafeel and Turan* [85], [86] simulated a vertical thermosyphon under steady state and pulsed heat increment conditions. An axi-symmetric mesh was used, which included the model of the cooling water jacket. To simulate the phase change, the *Lee* model [67] was implemented but the evaporation and condensation coefficients were modified. According to the authors [86], theoretically, the coefficients for evaporation and condensation should be different. Hence, in their study, *Kafeel and Turan* [86] decided to calculate the condensation relaxation parameter

while fixing the evaporation parameter. The condensation coefficient  $\beta_c$  was adapted at each time step based on the mass transfer occurring by using the following formula:

$$\beta_{c,new} = \beta_{c,old} - \beta_{c,old} \times \left[ \frac{m_c - m_e}{\max(m_c, m_e)} \right] \quad (2-10)$$

where  $m_c$  is the fluid mass condensing (kg) and  $m_e$  is the fluid mass evaporating (kg). The evaporation relaxation parameter was set to  $\beta_c = 0.1 \text{ s}^{-1}$ . The saturation temperature was set to 350K. The author mentioned that they implemented the condensation mass transfer only on the near-wall cells in order to obtain Filmwise condensation. A constant heat flux boundary condition of 12,000 W/m<sup>2</sup> was defined at the evaporator whereas forced convection took place at the condenser of the thermosyphon. In the studies reported, some surprising results were poorly analysed. For instance, the liquid vapour fraction at the evaporator is extremely low and no pool of liquid is visualized. Therefore, no boiling can be observed. This is a main limitation in the validation of the CFD simulation by *Kafeel and Turan* [85], [86]. Furthermore, the temperature validation of the simulation was very limited as only one temperature profile of the thermosyphon was reported and compared with experimental data. For these reasons, the CFD simulation of a thermosyphon and the proposed condensation relaxation parameter equation by *Kafeel and Turan* [86] is considered to be unvalidated. *Asmaie et al.* [87] simulated a thermosyphon using deionized water and CuO/water nanofluid as working fluids. The Volume of Fluid approach was adopted and the *Lee* model [67] source terms with a coefficient  $\beta = 0.1 \text{ s}^{-1}$  for both evaporation and condensation was implemented in a User Defined Function (UDF). However, it seems that there was an error in the source terms reported in their publication. The authors also reported that the impact of non-condensable gas was considered in the UDF code that was added to the transport equations. As for the boundary conditions of their simulation, *Asmaie et al.* [87] set constant heat flux conditions to both evaporator and condenser walls. In total, 450s were simulated with a time step of 0.001s. This time step is very high for a two-phase simulation, which means the simulation was relatively stable, and the boiling activity probably showed low turbulence. At the condenser, the falling film could be visualized. In addition, the velocity vectors showed that the liquid fraction goes down due to the gravity action, whereas the vapour stream goes up. This is presented in Figure 2-23.



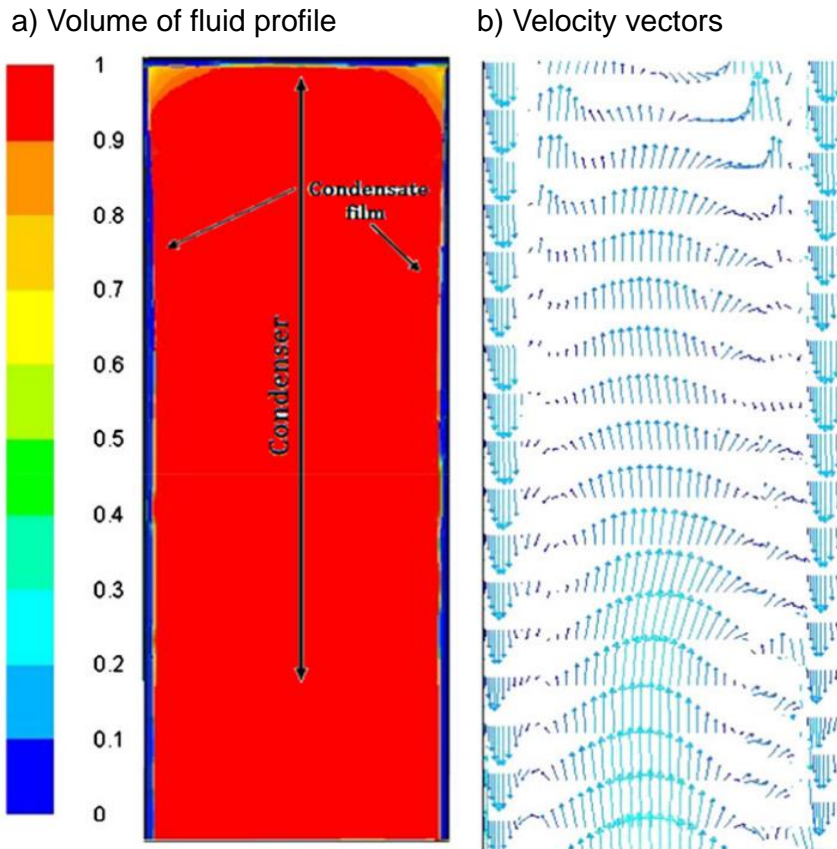


Figure 2-23. a) Volume of Fluid profile and b) Velocity vectors in the simulation of *Asmaie et al.* [87]

However, in the work by *Asmaie et al.* [87], the boiling fluid dynamics were not presented. Numerically, it was found that the condenser heat transfer coefficient was improved by 117%. This impact was lower at the evaporator. The simulations were validated with the experiments by *Liu et al.* [88]. At the evaporator, adiabatic section, and condenser, the difference of temperature between the simulation and the experiments were 5.1°C, 0.3°C, and 1.5°C, respectively. By using similar simulation parameters as in their previous work [84], *Fadhli et al.* [89] modelled a thermosyphon using R134a and R404a as working fluids. The thermosyphon was made of copper and was 500mm long. For the source terms, the *Lee* model [67] was implemented with an evaporation and condensation coefficient of  $\beta=0.1$ . Similar to their previous work, the boundary conditions considered a constant heat flux at the evaporator and a convection heat transfer coefficient at the condenser. However, the temperature of the coolant free stream was not reported. The saturation temperature was set to  $T_{sat} = 298\text{K}$ . As a result, the temperature and vapour volume fraction profiles can be seen in Figure 2-24.

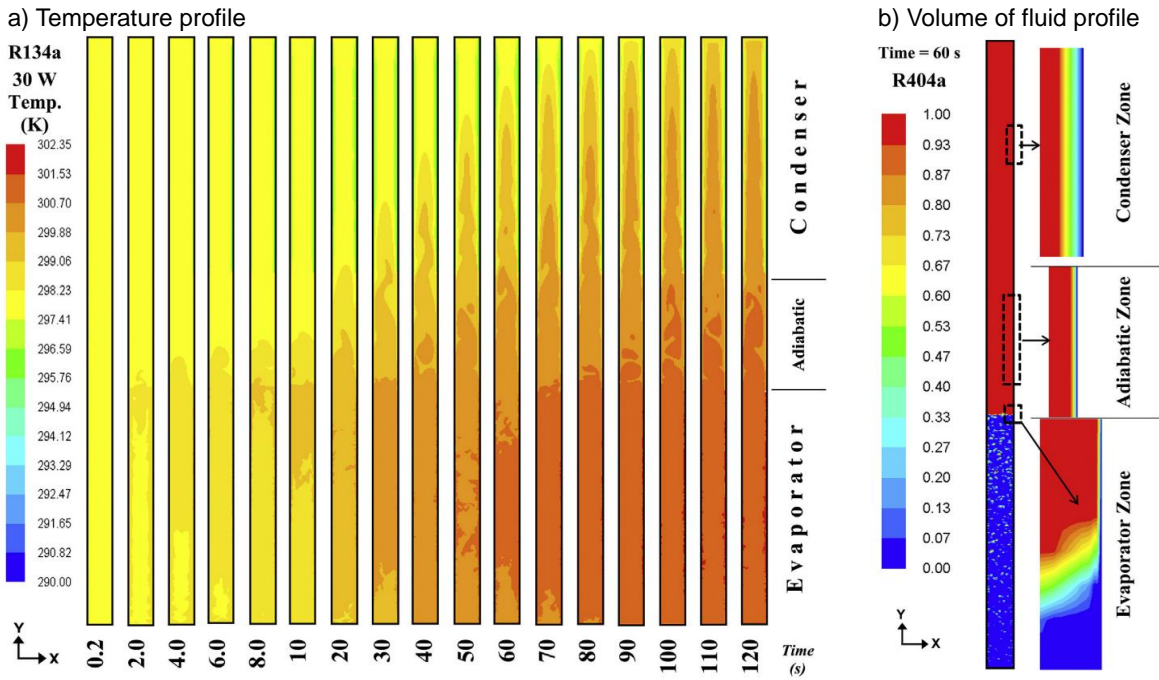


Figure 2-24. a) Temperature contour of the R134a thermosyphon, and b) Vapour phase contour of the R404a thermosyphon at a time  $t=60s$ , by *Fadhl et al.* [89]

At first, one can notice that the initial conditions implemented in this work were different from the initial conditions in the previous work presented by *Fadhl et al.* [84]. At time  $t=0s$ , the temperature is uniform in all the thermosyphon and equal to the saturation temperature defined. This makes more sense from a scientific point of view. However, from the temperature contour, note that the condenser temperature does not decrease significantly. This was already the case in the previous work presented by the authors [84]. In the simulations by *Fadhl et al.* [89], it seems that only a very restricted zone near the condenser wall is at a temperature lower than the saturation temperature, which allows Filmwise condensation to appear near the wall. Furthermore, *Fadhl et al.* [89] noted that bubbles in the R134a and R404a thermosyphons were significantly smaller than for the water thermosyphon. According to the authors, this was explained by a different value of the critical nucleation site radius. However, this is extremely doubtful as nucleation radii cannot be modelled to date and have not been simulated so far in the modelling of complete thermosyphons. Furthermore, the nucleation site radii would only impact the size of bubbles departing from the wall but would not impact the bubbles developing in the liquid bulk. According to the expression for the critical diameter of a bubble that was reported in the work by *Guichet et al.* [73], it is assumed that the size of the bubbles was smaller because of lower values of fluid surface tension, saturation temperature, and heat flux. The average temperature differences between the experiments and the simulation of the R134a thermosyphon were  $12.4^{\circ}C$  at the evaporator,  $3.5^{\circ}C$  at the adiabatic section, and  $5.9^{\circ}C$  at the condenser. As for the R404a thermosyphon, the difference of temperatures between the CFD and the experiments were  $18.9^{\circ}C$ ,  $6.3^{\circ}C$  and  $2.3^{\circ}C$  at the

evaporator, adiabatic, and condenser sections, respectively. The same year, *Fadhl* [90] published a thesis on the CFD simulation of thermosyphons. In addition to the two previously discussed works by *Fadhl et al.* [84], [89], this thesis includes the 3D modelling of geyser boiling in a thermosyphon [91] which was validated with observation from a transparent thermosyphon. *Kim et al.* [71] have investigated the impact of the condensation mass transfer time relaxation parameter in the *Lee* model [67] on the temperature distribution in a cylindrical thermosyphon. Four different values of the condensation coefficient were implemented and compared with experimental data. Water was used as a working fluid and a convective heat transfer boundary condition was selected for the condenser. It was found that the best performing mass transfer time relaxation parameter was obtained from:

$$\beta_c = \beta_e \left( \frac{\rho_l}{\rho_v} \right) \quad (2-11)$$

with  $\rho_l$  and  $\rho_v$  the liquid and vapour densities ( $\text{kg/m}^3$ ). In this case, the difference of temperature between the simulation and the experiments was  $4.3^\circ\text{C}$  at the condenser. Unfortunately, this comparison was not made for the adiabatic and evaporator sections. Nevertheless, boiling and condensation were both successfully simulated. *Wang et al.* [92] modelled a two-phase loop heat pipe using Dowtherm A as a working fluid. The loop heat pipe was mainly horizontal and positioned with a small angle to allow the working fluid circulation. This heat pipe was developed and used for a solar thermal collector. To simulate the working cycle of their loop heat pipe, *Wang et al.* [92] used the *Lee* model [67] with an evaporation coefficient  $\beta_e=0.1 \text{ s}^{-1}$  and a condensation coefficient of  $\beta_c=110 \text{ s}^{-1}$ . The value of the condensing coefficient was determined numerically. To do so, the authors calculated a ratio of the vapour pressure to the saturation pressure, and studied its evolution with an increase of the condenser coefficient  $\beta_c$ . The condenser coefficient  $\beta_c$  used for the simulation of the heat pipe was taken at the point where the vapour pressure was equal to the saturation pressure. The evaporator heat flux tested was in the range  $8.5\text{-}25.6 \text{ kW/m}^2$ . High temperatures were investigated with a saturation temperature up to  $T_{\text{sat}}=601.6 \text{ K}$ . Steady state conditions of the simulation were reached beyond 350s. At the condenser section, the condensation appeared in the form of droplets at the top wall of the condenser. At the bottom wall of the condenser, a stratified liquid was observed. The difference of temperature at the evaporator was  $0.3^\circ\text{C}$  between the simulation and the experiments. At the adiabatic section, this difference was about  $1.4^\circ\text{C}$ , depending on the location, whereas at the condenser, the absolute temperature error was  $5.5^\circ\text{C}$ . *Fertahi et al.* [93] simulated a two-phase closed thermosyphon by using the Volume of Fluid model and the *Lee* [67] source terms. They first validated their model by using the experiments by *Fadhl et al.* [84]. Indeed, this work was mainly based on the study by *Fadhl et al.* [84]. The saturation temperature was set to  $T_{\text{sat}}=373\text{K}$ . For this first simulation, the fluid dynamics were not presented, and only a temperature validation at the adiabatic and condenser section was

carried out. At the adiabatic section, the average difference of temperature between the simulation and the experiments was 36.2°C, whereas this difference decreased to 5.3°C for the condenser section. The model presented was then used to study the impact of fins on the performances of a TPCT. For this study, the temperature and Volume of Fluid contours were presented. The temperature and vapour fraction contour at a time  $t=30s$  are presented in Figure 2-25.

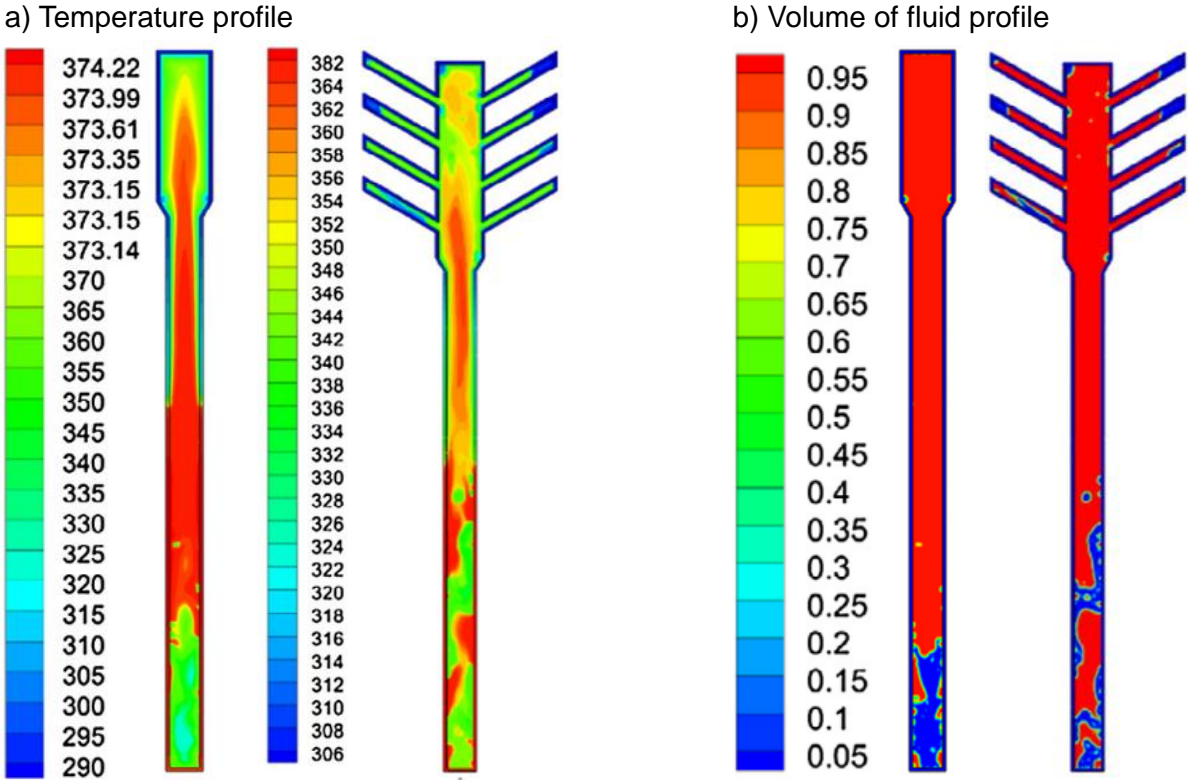


Figure 2-25. Temperature and Volume of fluid contour for a TPCT with and without fins at the condenser, from Fertahi et al. [93]

From the Volume of Fluid contours, it can be noted that condensation mainly appeared in the form of droplets, and that a condensate falling film cannot be visualized. Numerically, a heat transfer improvement of 16.05% was predicted by the incorporation of tilted fins at the condenser section. Yue et al. [94] simulated the evaporator of a microchannel separate heat pipe (MCSHP). The heat pipe investigated consisted of a vapour ascending pipe and liquid descending pipe, linked with multiple micro flat tubes with louvered fins. The material used was copper and the micro channel hydraulic diameter was about 1.09mm. The actual channel cross section shape was rectangular. R22 was selected as the working fluid. The Volume of Fluid technique with the Lee model [67] was used to simulate the phase change. However, the evaporation and condensation coefficients were reported to be tuned to match experimental data, and their values were not given by the authors. From the CFD simulation, it was observed that the boiling pattern evolved from small circular bubbles to larger vapour slugs with time.

The impact of the filling ratio on the evaporator liquid fraction was studied numerically. Condensation was not studied or visualized. The average temperature difference between the experiments and the simulation at the evaporator was 0.68°C.

*Temimy and Abdulrasool* [95] simulated a 3D thermosyphon at heat transfer rates between 20-120W with the objective of visualizing the interactions between the steam and condensate. The impact of the filling ratio was studied numerically. This work by *Temimy and Abdulrasool* [95] can be strongly criticised for several reasons. To start with, the source terms used to model the heat and mass transfer were not reported. Second, the interactions between the phases were not clearly visualized as no contour of the volume fraction of each phase (liquid and vapour) was presented. Instead, temperature profiles were used and assimilated by the authors as “phase interactions”. Indeed, in this work, boiling and condensation could not be observed. Finally, the authors [95] reported that the commonly known two-phase flow occurring in a thermosyphon did not occur. Instead of having a vapour stream flowing upwards in the core of the thermosyphon and observing the return of the condensate near the wall, their simulation showed that both phases were flowing near the wall. According to the authors, the liquid and vapour phases interact with each other and would push the phase with lower momentum to the centre of the thermosyphon. This disagrees with the commonly accepted two-phase flow pattern taking place in heat pipes. Moreover, no experiments were conducted to validate their simulation. Based on the above analysis, the simulation by *Temimy and Abdulrasool* [95] is considered to be wrong and the results doubtful. *Wang et al.* [96] decided to model super-long thermosyphons that can be used for geothermal applications. A 54 meter long 2D thermosyphon was simulated to validate their source terms derived from the *Hertz-Knudsen* [65] equation. Four different filling ratios were tested as the initial height of the liquid pool was set to 5m, 10m, 20m and 40m. In order to simulate 250s of operation and reach steady state conditions, each simulation took 2-3 months of calculation. A convection heat transfer boundary condition was applied for both evaporator and condenser sections. The vapour Volume of Fluid contours in the case of a liquid pool of 10m is presented in Figure 2-26.

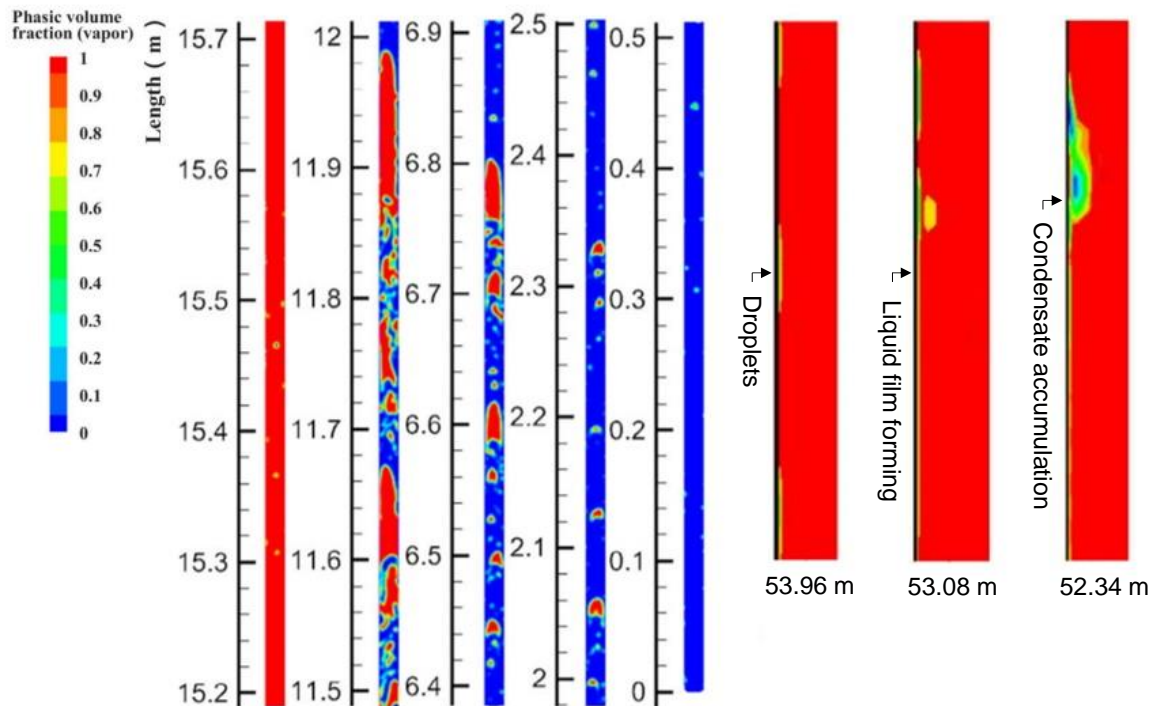


Figure 2-26. Vapour volume fraction contours, from *Wang et al.* [96]

As a visual validation, we can notice that no boiling occurs at the bottom of the liquid pool. This was expected by the authors as a result of the influence of pressure on the mass transfer. Indeed, as the pressure is higher at the bottom of the liquid pool, the development of bubbles is lower than near the surface. At the condenser section, different condensation mechanisms were witnessed. At the upper level of the condenser, condensation appears in the form of liquid droplets whereas a liquid film progressively forms downstream. Finally, a condensate accumulation can appear locally at the bottom of the condenser as the falling fluid goes down the wall. However, a weakness of the work done by *Wang et al.* [96] is the absence of experimental validation, which limits the impact and the relevance of the model implemented. *Wang et al.* [97] also used their model to simulate geyser boiling. Compared to the *Lee* model [67], the proposed model by *Wang et al.* [97] seemed to present a significantly different boiling pattern and showed the formation of large vapour bubbles generating geyser boiling. At the evaporator section, a high temperature zone was observed in the evaporator volume occupied by the vapour. Regardless of the presence of falling droplets, this portion of the thermosyphon remained at a temperature much higher than the rest of the wickless heat pipe. *Hosseinzadeh et al.* [98] experimentally and numerically studied the impact of a super-hydrophobic coating on the condenser wall on the performance of a two-phase closed thermosyphon. 1-Butanol was also added to the working fluid of the water-copper heat pipe. The super-hydrophobic coating increased the contact angle of droplets on the wall from  $59^\circ$  to  $165^\circ$ . For the simulation, the Volume of Fluid was used with a user defined function considering the two-phase heat transfer source terms. The *Lee* model [67] with the source terms by *De Schepper et al.* [69]

was used with an evaporation and condenser coefficient of  $\beta=0.1 \text{ s}^{-1}$ . Gravity was considered in the simulation. An experimental forced convection heat transfer coefficient was defined as the boundary condition at the condenser. The heat transfer rate studied was 250W. The phase fraction obtained by *Hosseinzadeh et al.* [98] is presented in Figure 2-27.

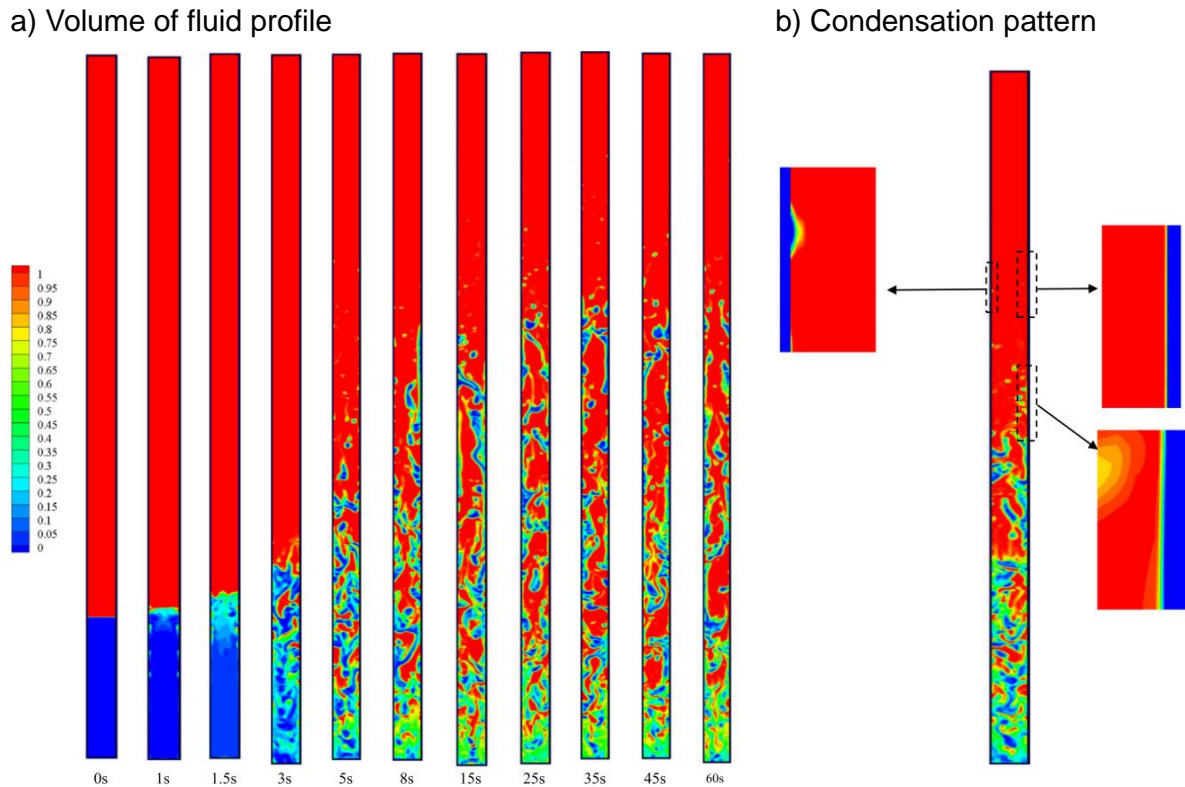


Figure 2-27. Vapour volume fraction contours, from *Hosseinzadeh et al.* [98]

Compared to previous works such as the study by *Fadhl et al.* , who implemented the exact same source terms and boundary conditions, it can be observed that the fluid dynamics obtained by *Hosseinzadeh et al.* [98] differ significantly. Indeed, the boiling pattern shows an exploding pool without real formation of bubbles. If this could be explained by a high heat transfer rate through the heat pipe during the start-up of the thermosyphon, one could expect the formation of bubbles. Instead, the whole volume of liquid vaporizes, starting from the liquid pool surface. This boiling pattern is surprising and disagrees with the commonly observed boiling pattern in heat pipes [73], [99]. By using super-hydrophobic coating, the condenser heat transfer coefficient was improved by 13.3% and the thermal resistance of the TPCT was reduced by 6.4%. The temperature differences between the simulation and the experiment were 4.5°C, 7.7°C, and 2.0°C for the evaporator, adiabatic, and condenser sections, respectively. *Wang et al.* [100] experimentally and numerically investigated the thermal performance and fluid dynamics of a novel horizontal radial heat pipe with an internally finned condenser. The heat pipe is similar to a double pipe heat exchanger where the coolant flows in the inner tube. The computational fluid dynamics simulation made was 2D and used the Volume of Fluid method. To model the mass and heat transfer, the *Lee* model [67] was

implemented with an evaporation coefficient of  $\beta_e=0.1 \text{ s}^{-1}$  and a condensation coefficient of  $\beta_c=110 \text{ s}^{-1}$ . A time step of 0.00005s was chosen which witnesses the difficulty in convergence of the implemented model and the need for a very low time step. The fluid dynamics were presented including the boiling and condensation pattern. Yet, only one profile of condensation was presented and no temperature validation was reported for the condenser section. At the evaporator, the average temperature difference between the experiments and the simulation was 5.0°C. Yet, the maximum error at one location of the evaporator rose to 8.2°C. *Tarokh et al.* [101] simulated a straight two-phase thermosyphon and numerically added a vortex generator in the vapour volume to improve the performance of the TPCT. By adding a vortex generator at different locations in the thermosyphon, the mixing is improved which increases the heat transfer. Water was used as the working fluid. The Volume of Fluid model with the *Lee* [67] model source terms were used to simulate the thermosyphon. The evaporation coefficient was set to  $\beta_e=0.1 \text{ s}^{-1}$  whereas the condensation coefficient  $\beta_c$  was based on the work by *Kim et al.* [71]. A constant heat flux was set at the evaporator while convection heat transfer was defined at the condenser of the thermosyphon. As for the initial conditions, the fluid region was patched at an initial temperature of  $T_{\text{sat}}=373.15\text{K}$ . In contrast, the wall was patched at a temperature of 315K to improve the simulation convergence during the early iterations. *Wei et al.* [102] simulated a microchannel  $\Omega$ -shape heat pipe under zero gravity. A user defined function was developed and included a code to modify the dynamic contact angle and a modified surface tension momentum source term. The *Lee* model was used for the mass and energy source terms and the empirical coefficients have been adapted to fit the experiment. Unfortunately, those coefficients have not been reported by the authors. The authors decided to focus more on the improvements provided by the improved continuum surface force model (CSF) and the applied dynamic contact angle. In their simulations, *Tarokh et al.* [101] found that condensation mainly appeared in the form of small droplets, and that a very thin film could be observed locally near the wall. The simulation was validated with the experiments by *Fadhl et al.* [84] before the impact of the vortex generator was studied. The average differences of temperature between the experiments and the simulation at the evaporator, adiabatic section, and condenser, were 3.7°C, 13.8°C and 15.8°C, respectively. When studying the vortex generator impact on the performance of the thermosyphon, it was found that the vortex generator had a more significant impact when placed in the adiabatic and condenser sections. Placing the vortex generator in these sections leads to a reduction of the thermal resistance by 3.5% and 3.3%, for the adiabatic and condenser sections, respectively.



### 2.3.3 Comparison of thermosyphon simulations

To sum up the state of the art on the available computational fluid dynamic (CFD) modelling of thermosyphons, Table 2-7 compares the reviewed works and reports the accuracy of each simulation when compared with experimental data.

Table 2-7. State of the art of available simulations of thermosyphons.

Simulation conducted			Results			
Authors	Year	Parameters	Phase simulation	Comparison with experiments		
				$\Delta T_e$	$\Delta T_a$	$\Delta T_c$
<i>Legierski et al.</i> [77]	2006	Horizontal wicked heat pipe simulated using the Hertz-Knudsen [65] model with an evaporation coefficient adjusted according to experiments. An experimental based “thermal excitation function” was used to fit experimental temperature profiles.	Semi-experimental Simulation, no boiling simulated.	Irrelevant simulation		
<i>Zang et al.</i> [78]	2009	Vapour section of a Disk-shaped flat thermosyphon simulated only with heat exchange considered on the boundary conditions. Single phase simulation.	Single phase simulation.	Irrelevant simulation		
<i>Rahmat and Hubert</i> [79]	2010	Triangular micro heat pipe simulated with the phase change model of ANSYS CFX.	Boiling modelled	Experimental validation limited		
<i>Alizadehdakhel et al.</i> [80]	2010	2D single thermosyphon simulated with the <i>Lee</i> [67] model with $\beta=0.1 \text{ s}^{-1}$ .	Boiling and condensation modelled.	1°C	16°C	5°C
<i>Annamalai and Ramalingam</i> [82]	2011	1m copper heat pipe simulated. Heat source term applied as a boundary condition at the vapour/liquid interface.	No boiling/condensation simulated.	6°C	/	6°C
<i>Lin et al.</i> [83]	2013	Miniature oscillating heat pipe simulated using the <i>Lee</i> [67] source terms using a mixture model.	No boiling/condensation simulated.	9°C	/	5°C
<i>Fadhl et al.</i> [84]	2013	Water thermosyphon simulated using the <i>Lee</i> [67] model with $\beta=0.1 \text{ s}^{-1}$ .	Boiling and condensation simulated.	28°C	33°C	6°C
<i>Kafeel and Turan</i> [85], [86]	2013	Thermosyphon simulated using the <i>Lee</i> [67] model with a condensation coefficient adapted with the mass transfer occurring.	Condensation simulated. Boiling not simulated.	Irrelevant simulation		

<i>Asmaie et al.</i> [87]	2013	Water and CuO/water nanofluid thermosyphon simulated using the Lee [67] model with $\beta=0.1 \text{ s}^{-1}$ .	Condensation simulated. Boiling not simulated.	5°C	0.3°C	2°C
<i>Fadhl et al.</i> [89]	2015	Modelling of two thermosyphons: R134a and R404a. Lee [67] model with $\beta=0.1 \text{ s}^{-1}$ .	Boiling and condensation simulated.	R134a TPCT		
				12°C	4°C	6°C
				R404a TPCT		
				19°C	6°C	2°C
<i>Kim et al.</i> [71]	2015	Modelling of a water thermosyphon using the Lee [67] model with $\beta_e=0.1 \text{ s}^{-1}$ and $\beta_c=\beta_e(\rho_l/\rho_v)$ .	Boiling and condensation simulated.	/	/	4°C
<i>Wang et al.</i> [92]	2017	Modelling of a Dowtherm A loop heat pipe using simulated with the Lee [67] model with $\beta_e=0.1 \text{ s}^{-1}$ and $\beta_c=110 \text{ s}^{-1}$ .	Boiling and condensation simulated.	0.3°C	1°C	6°C
<i>Fertahi et al.</i> [93]	2018	Modelling of a water thermosyphon using the Lee [67] model with $\beta=0.1 \text{ s}^{-1}$ .	Boiling and condensation simulated.	/	36°C	5°C
<i>Yue et al.</i> [94]	2018	Modelling of a R22 microchannel thermosyphon using the Lee [67] model.	Boiling simulated only	0.7°C	/	/
<i>Temimy and Abdulrasool</i> [95]	2019	Modelling of a water thermosyphon. The source terms used were not reported.	No boiling/condensation simulated.	Irrelevant simulation and no experimental validation		
<i>Wang et al.</i> [96]	2020	Modelling of a 54m long thermosyphon. New model based on the Hertz-Knudsen [65] equation, considering the impact of hydrostatic pressure.	Boiling and condensation simulated.	No experimental validation		
<i>Hosseinzadeh et al.</i> [98]	2020	Modelling of a Water thermosyphon using the Lee [67] model with $\beta=0.1 \text{ s}^{-1}$ .	Boiling and condensation simulated.	5°C	8°C	2°C
<i>Wang et al.</i> [100]	2020	Modelling of a water radial heat pipe using the Lee [67] model with $\beta_e=0.1 \text{ s}^{-1}$ and $\beta_c=110 \text{ s}^{-1}$ .	Boiling and condensation simulated.	5°C	/	/
<i>Wei et al.</i> [102]	2020	Modelling of a $\Omega$ -shape heat pipe with the Lee model and empirical coefficients adjusted with experiments	No Boiling and condensation observed	Irrelevant simulation		
<i>Tarokh et al.</i> [101]	2021	Modelling of a water thermosyphon using the Lee [67] model with $\beta_e=0.1 \text{ s}^{-1}$ and $\beta_c=\beta_e(\rho_l/\rho_v)$ .	Boiling and condensation simulated.	4°C	14°C	16°C

To conclude the state of the art of computational fluid dynamic simulations of heat pipes, significant discrepancies can be observed between the works. To simulate boiling and condensation of the working fluid, source terms from a phase change model are implemented. Even if different models exist, while simulating thermosyphons, the Lee model [67] is largely

preferred by researchers. Yet, even if the boiling coefficient is generally set to  $\beta_e=0.1 \text{ s}^{-1}$ , different values of condensation coefficient have been used. In all the works reviewed, the phase change model implemented required values of saturation pressure or temperature. A major limit identified is that the values of saturation pressure or temperature are experimentally based. This forces the model to reach equilibrium around the experimental saturation temperature and thus, limits the predictive character of the thermosyphon simulation. As mentioned by *Jouhara et al.* [91] and *Fadhl* [90], the simulation of two-phase flow inside heat pipes using CFD is still at an early stage. Researchers are still trying to develop and validate models that can be used in the future to fully predict the behaviour of thermosyphons. Nonetheless, it is clear that the progress made in this field opens new opportunities. In this study, efforts have been made to modify the *Lee* model [67] and use various values for the boiling and condensation coefficients to study their impact on the simulation. The *Lee* model is used to simulate thermosyphons with a multi-channel geometry which has not been investigated up to today.

## **2.4 Research gap identification**

Despite promising experimental results, the multi-channel flat heat pipe is a new technology, and its operation has not been investigated from a theoretical and numerical point of view to date. The two-phase mechanisms taking place in a multi-channel geometry remain to be understood and studied. To be used as a PV/T thermal absorber, the impact of factors such as various heat transfer rates and tilt angles must be investigated. In the literature, no analytical modelling of a multi-channel flat heat pipe is available to predict the performance of this technology by considering the two-phase heat transfer inside the multi-channel geometry. Finally, computational fluid dynamic (CFD) simulations of heat pipes are still at an early stage and multi-channel heat pipes have never been simulated numerically to date.

---

## Chapter 3 - Apparatus, experimental procedure, data reduction and error propagation

---

The two pieces of experimental apparatus tested within the framework of this research are presented in this chapter. To start with, a one of a kind three-leg heat pipe has been designed and manufactured. In this apparatus, the two-phase heat transfer is divided into three legs which are linked at the top and bottom by horizontal collectors. This test rig was specially built for the study of two-phase heat transfer in a multi-channel heat pipe layout and for the development of analytical and numerical models. In a second phase, a multi-channel flat heat pipe, which can be used for surface cooling applications, was tested. This flat heat pipe comprises an internal structure comparable to the three-leg heat pipe with parallel channels linked at the top and bottom by collectors. The two-phase heat transfer in the multi-channel flat heat pipe has been thoroughly studied and the models compared to the experimental data.

### **3.1 Three-leg multi-channel heat pipe apparatus**

#### **3.1.1 Apparatus**

##### *3.1.1.1 Heat transfer principle*

A three-leg heat pipe has been designed and manufactured to study and better understand the two-phase heat transfer in a multi-channel heat pipe. The three-leg heat pipe is a multi-channel heat pipe in its simplest form: parallel channels linked at the top and bottom by collectors. The collectors allow the working fluid circulation between the three parallel channels. Inside the three-leg heat pipe, a working fluid is maintained at saturation conditions and transfers thermal energy by a phase change cycle. In the tested three-leg heat pipe apparatus, heat is provided to the three-leg heat pipe of interest by the condensation of water vapour on the outside of the evaporator wall. At the top of the heat pipe, heat is extracted from the outside of the condenser wall by the boiling of liquid water. The heat transfer principle of the three-leg heat pipe of interest is schematized in Figure 3-1.

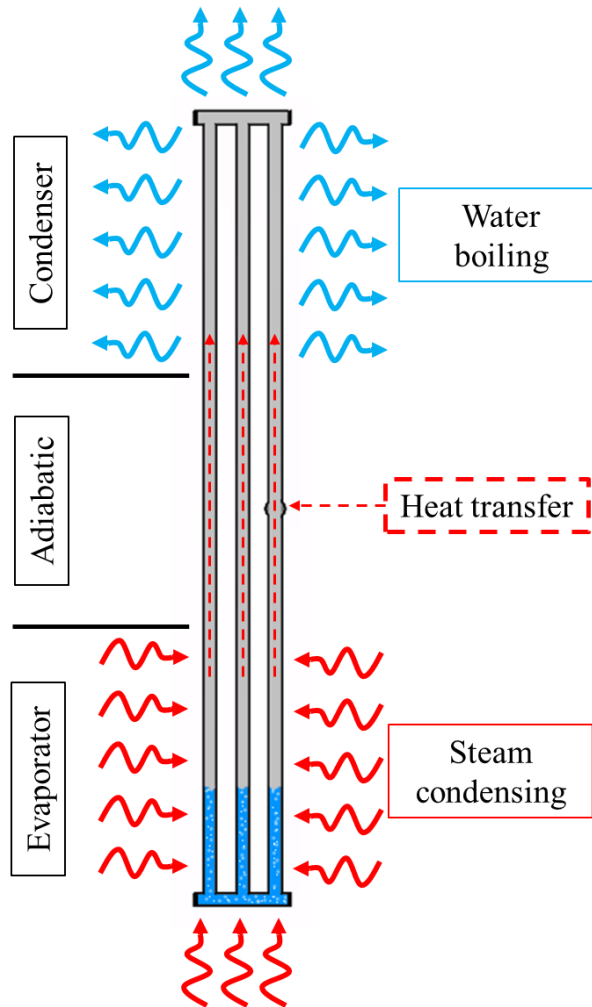


Figure 3-1. Heat transfer schematic in the three-leg multi-channel heat pipe

Inside the three-leg multi-channel heat pipe, the working fluid studied was R134a. This working fluid was chosen because the tested multi-channel flat heat pipe used for surface cooling applications also used R134a as a working fluid. The filling ratio  $FR$  of the three-leg heat pipe which represents the ratio between the liquid volume to the evaporator volume was set to 50%. By setting the filling ratio to 50%, half of the evaporator was filled by a liquid pool whereas the other half was occupied by vapour. In the two different sections, the evaporator and condenser, two heat transfer mechanisms take place, namely, pool boiling and falling film evaporation, respectively. Hence, the filling ratio of 50% was selected so that both pool boiling and falling film evaporation can be studied. Indeed, with this layout, thermocouples could be placed on both pool boiling and falling film regions.

As explained earlier, the heat source of the three-leg heat pipe of interest is vapour condensing. By doing so, a constant wall temperature boundary condition on the outer evaporator wall is achieved. A similar boundary condition is expected by extracting the heat at the top of the heat pipe with a boiling liquid pool at the condenser. This uniqueness of the

three-leg heat pipe prototype is a central idea in the design of the test rig and is expected to ease the development of models. To do so, the evaporator and condenser of the three-leg heat pipe were placed into pressurized cylinders charged with water as a working fluid. Those cylinders were therefore acting like heat pipes. At the bottom cylinder, electric heaters were used as a heat source to boil the water which condensed on the three-leg heat pipe evaporator. At the top cylinder, the heat from the three-leg heat pipe condenser forced the water to boil and evaporate. This vapour flow carrying energy under the form of latent heat condensed on a cooling coil inside which cold water circulates. Inside the coil, the cooling water extracted the energy by forced convection and transiently warmed up. The complete heat transfer principle of the three-leg heat pipe assembly is schematized in Figure 3-2.

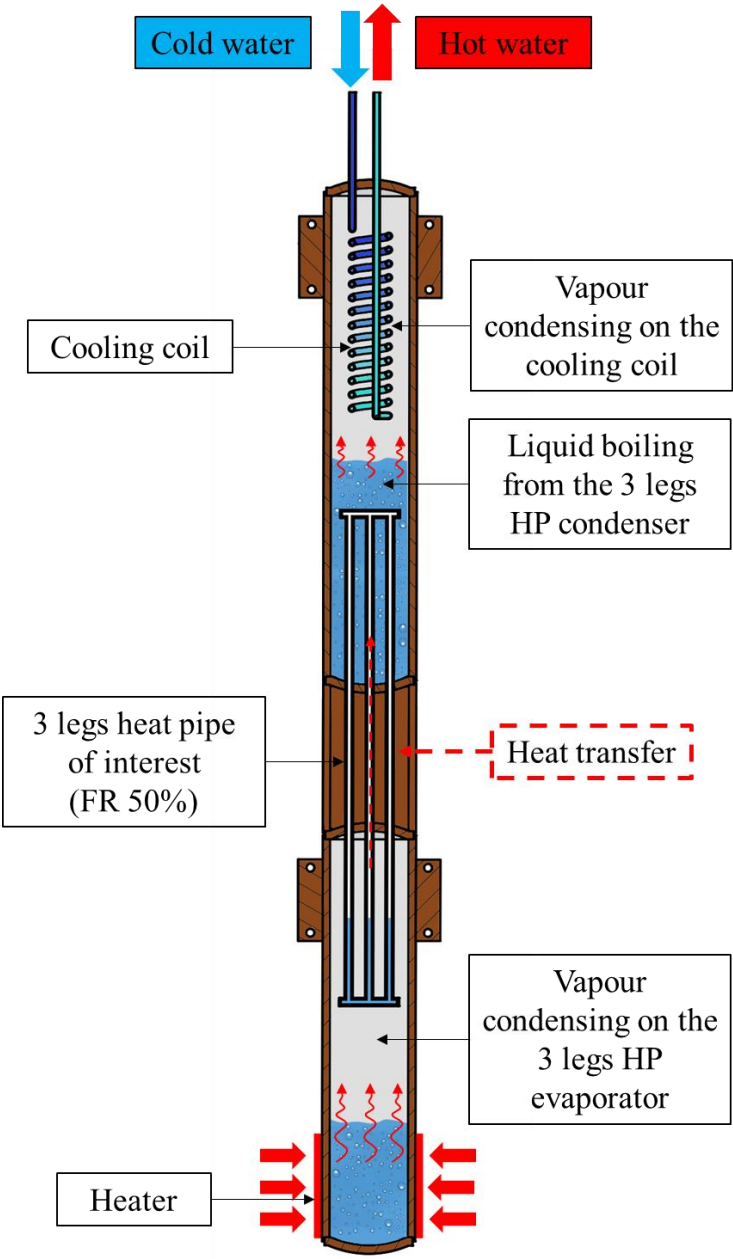


Figure 3-2. Heat transfer schematic in the three-leg multi-channel heat pipe assembly

### 3.1.1.2 Design stage

The three-leg heat pipe has been conceived, designed, sized, and manufactured under the framework of this research. After about 14 months, extensive discussions and reviews with the Heat Pipe and Thermal Management Research Group, the multiple design stages of the three-leg heat pipe have led to a final version of the design. Some design stages with previous versions considered are shown in Figure 3-3.

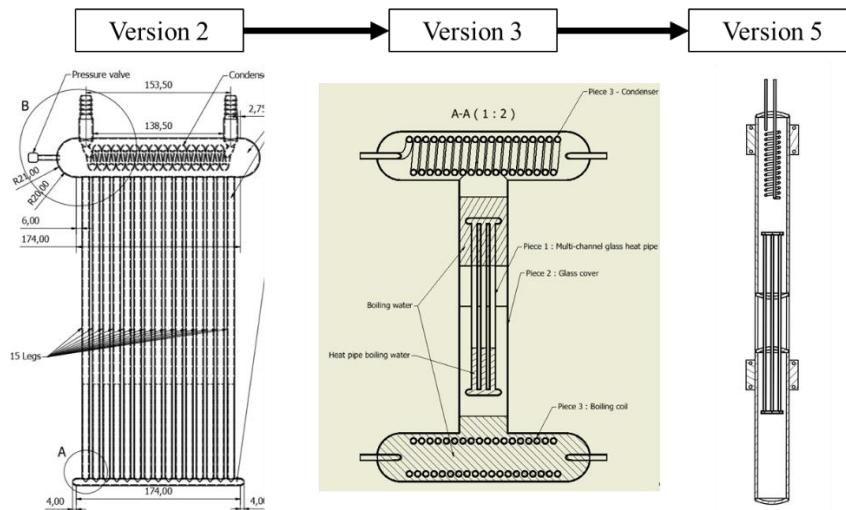


Figure 3-3. Design stages of the three-leg heat pipe

The design of the three-leg heat pipe has been adapted based on those considerations. Both Parts drawings and Assembly drawings have been produced internally for the manufacturing. An example of the final manufacturing drawings of the three-leg heat pipe design is shown in Figure 3-4.

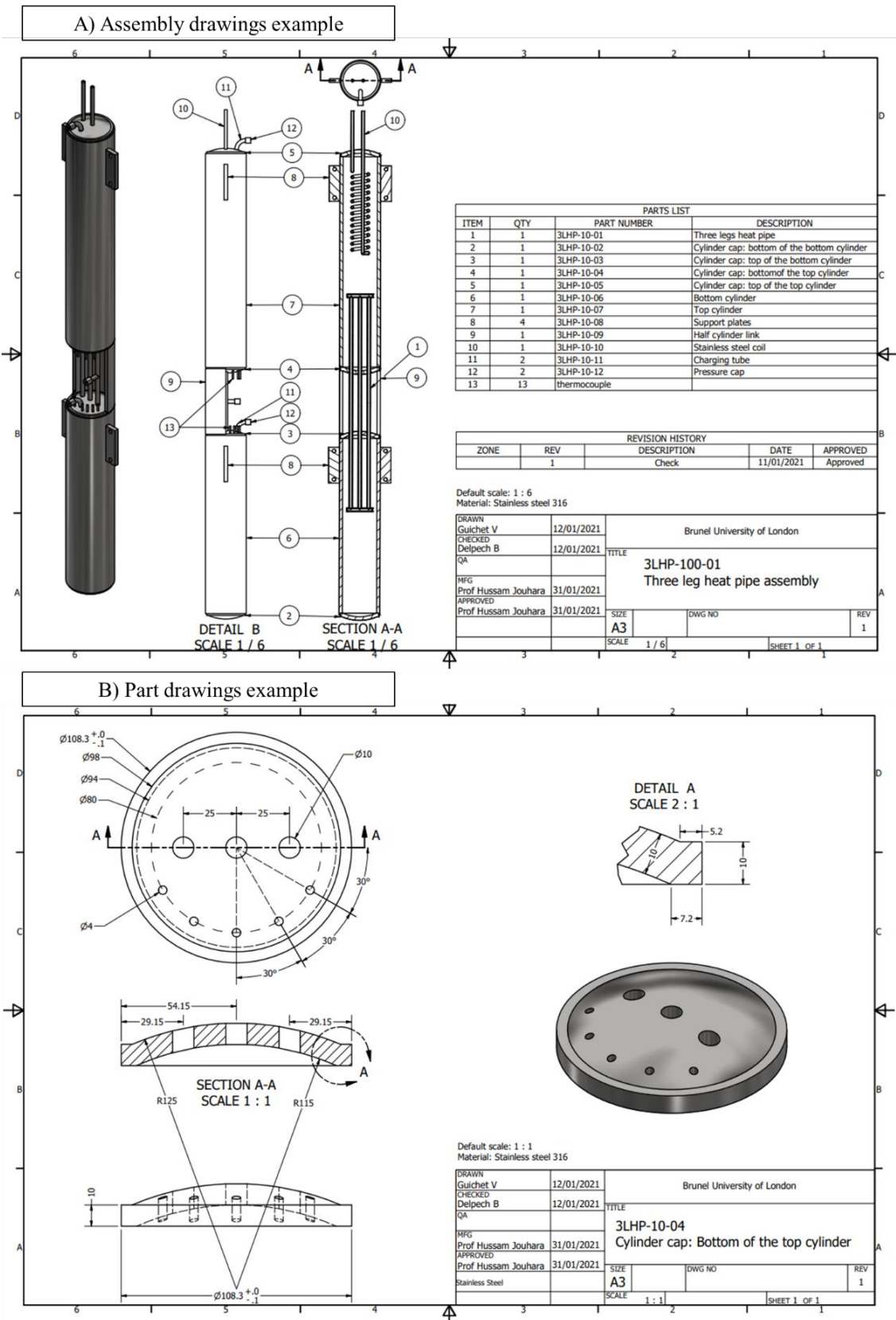


Figure 3-4. Manufacturing drawings of the three-leg heat pipe



### 3.1.1.3 Sizing calculation stage

In parallel with the physical layout of the test rig, an important stage in the design of the three-leg heat pipe is the sizing. Indeed, calculations had to be done for safety purposes and to guarantee the good operation of the prototype.

- **Thermal calculation**

To start with, a theoretical model of the three-leg heat pipe prototype was developed to estimate the temperature and pressure ranges of the working fluids inside the three-leg heat pipe. A brief description of the model is provided below and will be detailed further in the theoretical chapter of this thesis. The thermal resistance model presented in Figure 3-5 was used for predicting the system temperatures.

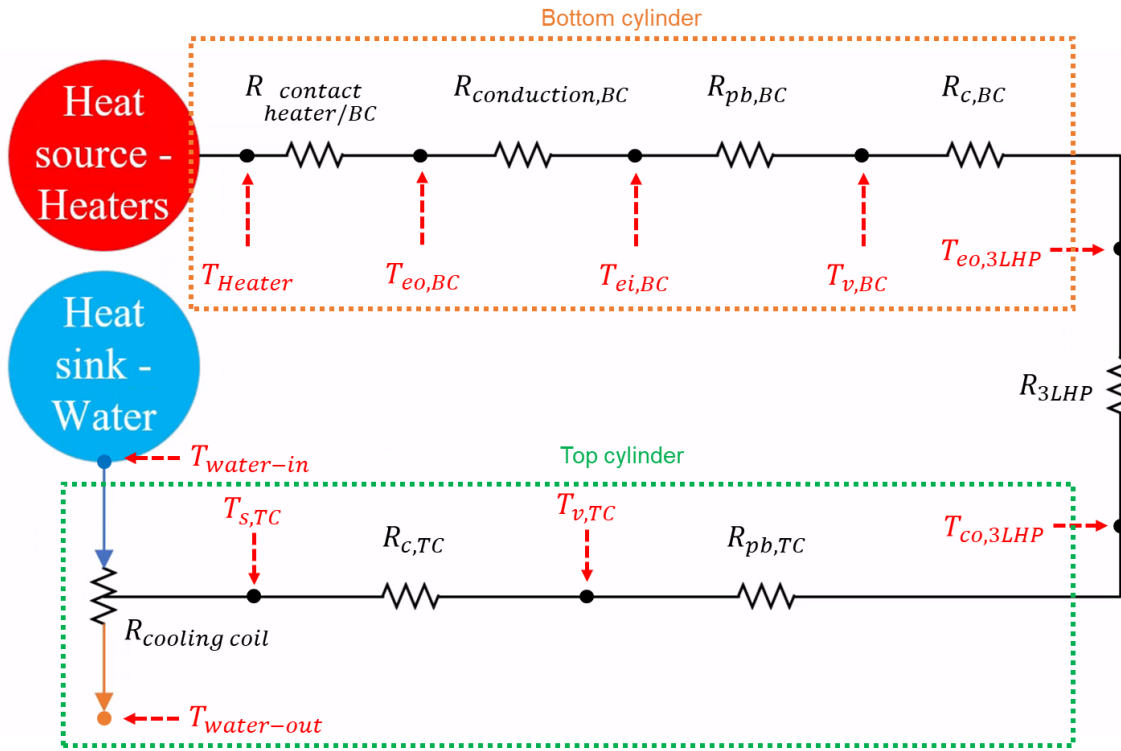


Figure 3-5. Three-leg heat pipe thermal resistance network used for sizing calculation

The usual radial conduction laws were used to estimate the conduction thermal resistances in the three-leg heat pipe [14]:

$$R_{conduction,} = \frac{\ln(D_o/D_i)}{2\pi k_w L} \quad (3-1)$$

with  $D_o$  the outside tube diameter (m),  $D_i$  the inside tube diameter (m),  $k_w$  the wall thermal conductivity (W/m.K), and  $L$  the heated length of the cylinder which is the length of cylinder in contact with the heater (m). The pool boiling and condensation resistances  $R_{pb}$  and  $R_c$  were calculated by estimating the corresponding heat transfer coefficient in:

$$R_{pb/c} = \frac{1}{h_{pb/c} A_{pb/c}} \quad (3-2)$$

where  $h_{pb/c}$  is the pool boiling/condensation heat transfer coefficient (W/m<sup>2</sup>K), and  $A_{pb/c}$  is the corresponding pool boiling/condensation heat transfer area (m<sup>2</sup>). To estimate the pool boiling heat transfer coefficient  $h_{pb}$ , the well-known correlation from *Rohsenow* [99] was used:

$$h_{pb,Rohsenow} = \left( \frac{q''_{pb}}{i_{lv}} \right)^{1-r} \left[ \frac{\mu_l}{\sqrt{g(\rho_l - \rho_v)}} \right]^r \frac{c_{p,l}}{C_{sf}} Pr_l^{-s} \quad (3-3)$$

where,

- ❖  $r = 1/3$
- ❖  $\begin{cases} s = n = 1 & \text{for water} \\ s = n = 1.7 & \text{for other fluids} \end{cases}$
- ❖  $C_{sf}$  is a constant depending on the solid – fluid characteristics

with  $q''_{pb}$  the pool boiling heat flux per unit surface area (W/m<sup>2</sup>),  $i_{lv}$  the latent heat of vaporization (J/kg),  $\mu_l$  the liquid dynamic viscosity (Pa.s),  $\sigma$  the liquid surface tension (N/m),  $g$  the gravitational acceleration (m/s<sup>2</sup>),  $\rho_l$  and  $\rho_v$  the density of the liquid and vapour phases respectively (kg/m<sup>3</sup>),  $c_{p,l}$  the specific heat of the liquid (J/kg.K), and  $Pr_l = \mu_l c_p / k$  the Prandtl number of the liquid. The constant  $C_{sf}$  depends on the solid/fluid characteristics. For water on stainless steel, the constant  $C_{sf}$  is taken as [99]:

$$C_{sf} = 0.008 \quad (3-4)$$

Regarding the estimation of the condensation heat transfer coefficient  $h_c$ , the well-known *Nusselt* correlation [103] was used:

$$h_c = 0.943 \left\{ \frac{\rho_l(\rho_l - \rho_v)i_{lv}gk_l^3}{\mu_l L_c (T_{sat} - T_w)} \right\}^{1/4} \quad (3-5)$$

where  $\rho_l$  and  $\rho_v$  are the density of the liquid and vapour phases respectively (kg/m<sup>3</sup>),  $i_{lv}$  is the latent heat of vaporization (J/kg),  $g$  the gravitational acceleration (m/s<sup>2</sup>),  $k_l$  is the liquid thermal conductivity (W/m.K),  $\mu_l$  is the liquid dynamic viscosity (Pa.s),  $L_c$  is the condenser length (m),  $T_{sat}$  is the saturation temperature (K), and  $T_w$  is the wall temperature (K). Finally, to estimate the forced convection heat transfer coefficient inside the cooling coil, usual forced convection laws could not be used. Indeed, in a helicoidal pipe, the forced convection heat transfer coefficient is increased due to a better mixing of the fluid generated by the centrifugal force, which creates a secondary flow pattern forcing the liquid particles to move to the outer wall and spiral back to the inner wall [104], [105]. Hence, a specific forced convection correlation for helicoidal pipes had to be used. For constant wall temperature condition and laminar flows, *Manlapaz and Churchill* [106] developed a correlation based on a regression analysis, which was used for the heat pipe and cooling coil sizing calculations:

$$Nu = \frac{h_{fc} D_i}{k_l} = \left[ \left( 3.657 + \frac{4.343}{\left( 1.0 + \frac{957}{De^2 Pr_l} \right)^2} \right)^3 + 1.158 \left( \frac{De}{\left( 1.0 + \frac{0.477}{Pr_l} \right)} \right)^{3/2} \right]^{1/3} \quad (3-6)$$

with  $h_{fc}$  the forced convection heat transfer coefficient,  $D_i$  the inside tube diameter (m),  $k_l$  the liquid thermal conductivity (W/m.K),  $De$  the Dean number, and  $Pr_l$  the liquid Prandtl number. The Dean number  $De$  is a dimensionless number equivalent to the Reynolds number  $Re$  with a coefficient considering the heat transfer improvement due to the helicoidal shape of the tube:

$$De = Re \left( \frac{r_{i,tube}}{r_{coil}} \right)^{1/2} \quad (3-7)$$

$$Re = \frac{\rho_l v D_i}{\mu_l} \quad (3-8)$$

with  $r_{i,tube}$  the radius of the circular pipe (m),  $r_{coil}$  the radius of the coil (m),  $\rho_l$  the liquid density (kg/m<sup>3</sup>),  $v$  the cooling water velocity (m/s),  $D_i$  the inside tube diameter (m), and  $\mu_l$  the liquid dynamic viscosity (Pa.s).

In this first model, which was used for sizing purposes only, the three-leg heat pipe resistance was calculated using an equivalent heat transfer area for the legs and collectors. To estimate the temperatures in the three-leg heat pipe at a given heat transfer rate, an iterative tool was built in Excel. The working principle of this iterative tool whose interface is shown in Annexe 1 is detailed later in the theoretical section of this thesis.

- **Pressure calculation**

The internal pressure of the cylinders was estimated from the estimated temperature range of the heat pipe and the working fluids used. The minimum wall thickness needed to handle the inner cylinder pressure can be determined from a force balance on a differential element of a pressurized cylinder wall. The force balance on the wall relates the radial stress  $\sigma_{r,w}$  and tangential stress  $\sigma_{\theta,w}$  in the cylinder to the internal pressure as [107]:

$$\sigma_{r,w} = \frac{r_i^2 P_i - r_o^2 P_o}{(r_o^2 - r_i^2)} - \frac{(P_i - P_o) r_i^2 r_o^2}{(r_o^2 - r_i^2) r^2} \quad (3-9)$$

$$\sigma_{\theta,w} = \frac{r_i^2 P_i - r_o^2 P_o}{(r_o^2 - r_i^2)} + \frac{(P_i - P_o) r_i^2 r_o^2}{(r_o^2 - r_i^2) r^2} \quad (3-10)$$

where  $r_i$  is the inner radius of the cylinder (m),  $r_o$  the outer radius of the cylinder (m),  $r$  the average radius of the cylinder (m),  $P_i$  the internal pressure (Pa), and  $P_o$  the outer pressure (Pa). These are known as the Lamé's equations [107]. For the cylinder to resist, the internal stress in the cylinder must be lower to the Yield tensile strength  $S_w$  allowable by the material. For safety, a security coefficient of  $s = 10$  was taken.

- **Finite Element Analysis (FEA) calculation**

In addition to the pressure calculation, Finite Element Analysis (FEA) has been conducted for sizing the three-leg heat pipe wall thickness of each part of the three-leg heat pipe using AUTODESK INVENTOR. An overview of the FEA analysis is provided in Figure 3-6.

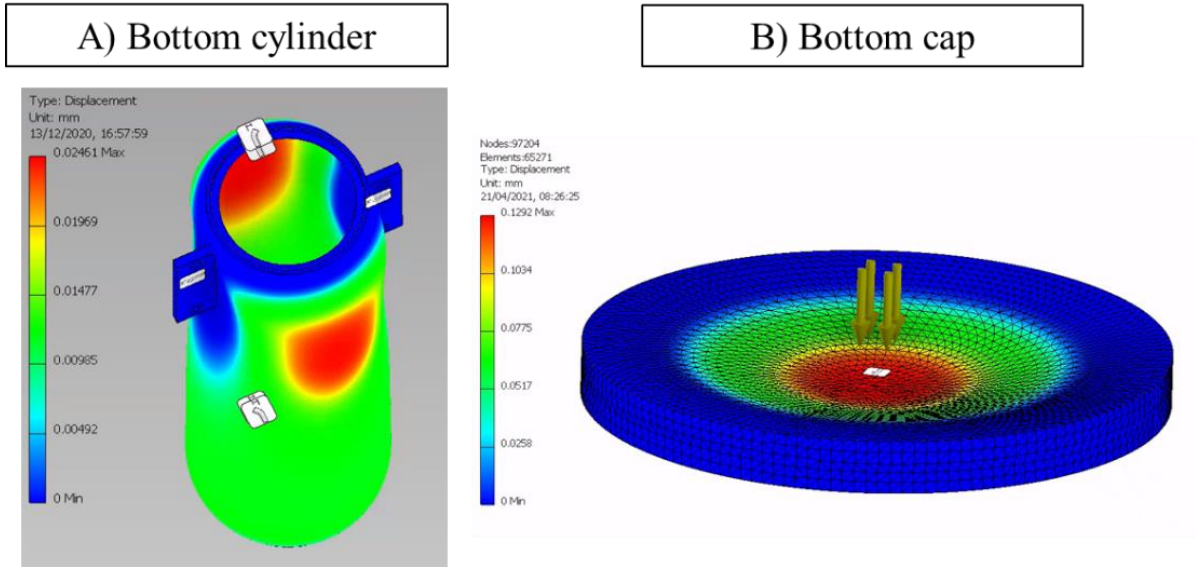


Figure 3-6. Finite element analysis of the three-leg heat pipe elements

Obviously, an important margin was taken in terms of pressure range applied inside the cylinders. The maximum pressure considered for the Finite Element Analysis was 150 bars. The wall thickness of the three-leg heat pipe was adjusted based on the stresses, displacement, and safety coefficients.

#### 3.1.1.4 Heat pipe limits check

Beyond the safety aspect of the three-leg heat pipe, the design must also be adapted to allow an optimal thermal performance of the test rig. Several heat pipe limits exist and must be checked to guarantee the good operation of the thermosyphon [108], [109]:

- Entrainment limit:

Due to high vapour velocities and shear stress at the liquid/vapour interface, the rising vapour flow can prevent the liquid condensate returning to the evaporator.

- Viscous limit:

At low temperatures, the viscous forces in the working fluid can be dominant and prevent the good start-up of the heat pipe.

- Sonic limit:

Under given conditions, the vapour velocity can become comparable to the speed of sound. In the case where the velocity of the vapour reaches the speed of sound, the heat transfer is choked. Hence, the vapour velocity must be maintained under a maximum value.

- Boiling limit:

The boiling limit corresponds to the transition between nucleate pool boiling and film boiling. At the maximum boiling heat flux, a vapour film blankets the wall surface and prevents heat transfer from the evaporator wall to the liquid pool.

- Dryout limit:

If the liquid volume (or filling ratio) is too low, a portion of the evaporator wall during the operation of the heat pipe may no longer be covered by liquid. Hence, a minimum liquid volume must be respected to avoid the appearance of dry patches.

- Vapour pressure limit

In heat pipes (or thermosyphons), a pressure drop in the vapour flow exists. This pressure drop increases with the heat transfer rate which, therefore, limits the heat transfer rate to a maximum value.

The equations used to check the heat pipe limits are reported in Annexe 2.

### 3.1.1.5 Manufacturing stage

Once validated, the drawings were sent to the manufacturer with the materials. The three-leg heat pipe is made from stainless steel 316. The cooling coil was also provided to the manufacturer to be welded inside the top cylinder. The manufacturing stages had to be done in a specific order. For instance, the cooling coil needed to be welded to the top cap before closing the top cylinder. One of the most crucial stages was the welding of the thermocouples on the legs of the three-leg heat pipe. This stage took place after the manufacturing of the three-leg heat pipe but was done before closing the top and bottom cylinders. Some pictures of the manufacturing process of the three-leg heat pipe are provided in Figure 3-7.

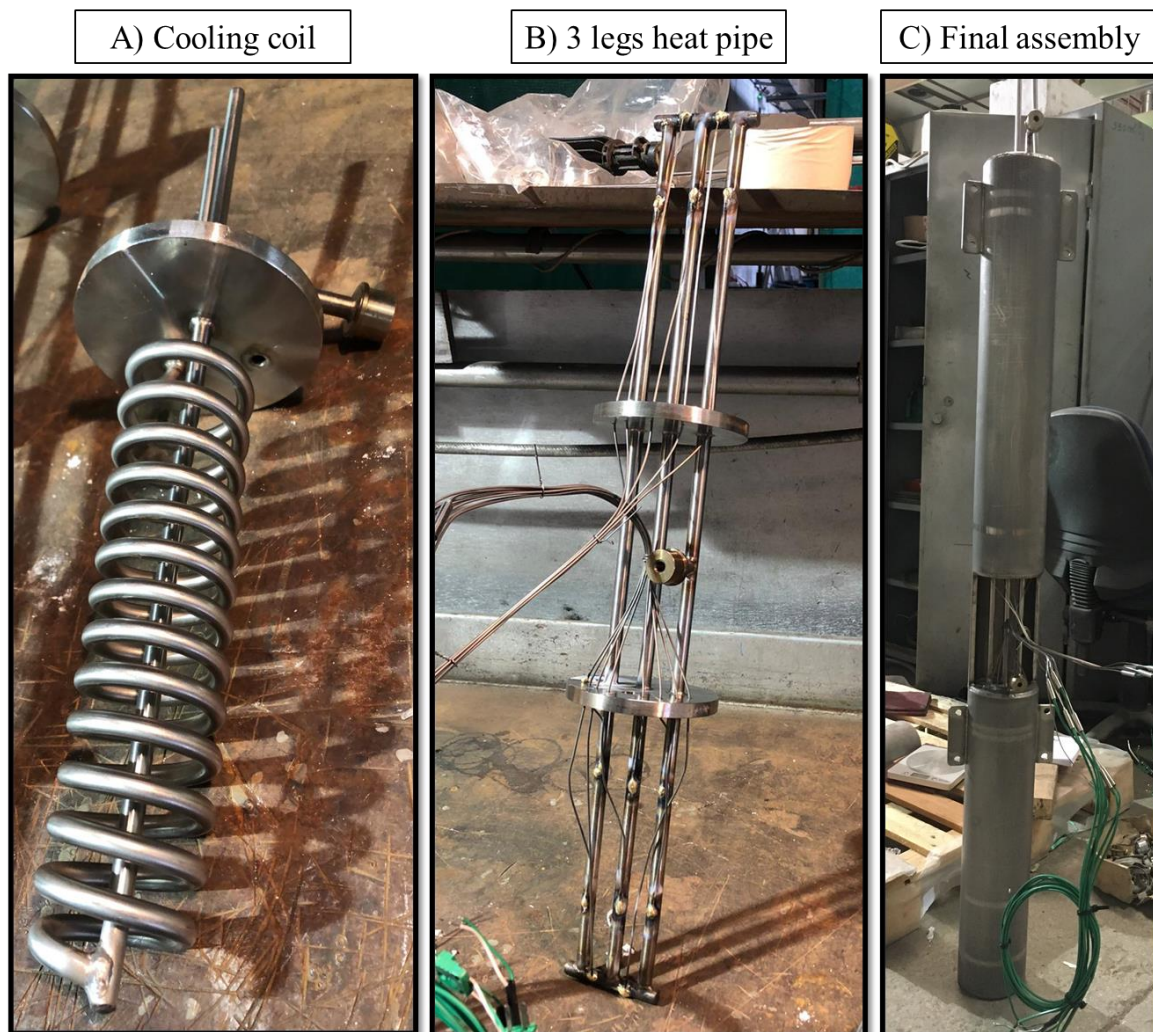


Figure 3-7. Manufacturing process of the three legs heat pipe prototype

The cooling coil shown in Figure 3-7 A) is shown after being welded to the top cap which closes the top cylinder. The three-leg heat pipe only is shown in Figure 3-7 B) and is shown with the thermocouples welded on the legs and passing through the cylinder caps. Lastly, the final three-leg heat pipe prototype is shown in Figure 3-7 C) with both top and bottom cylinders welded.

### 3.1.1.6 Final three-leg multi-channel heat pipe assembly

Once manufactured, the three-leg heat pipe was placed on a frame structure. The thermocouples passing through the cylinders were welded to seal the cylinders. Finally, after pressure testing the bottom cylinder, three-leg heat pipe, and top cylinder, each part of the assembly was charged with working fluid. Inside the three parallel legs, R134a was introduced as a working fluid as this refrigerant is used in the multi-channel flat heat pipe for surface cooling applications. This similarity aims at studying the two-phase heat transfer occurring in the three-leg heat pipe with similar conditions to a multi-channel flat heat pipe. In the same objective, the internal diameter of the three legs is 6mm which is similar to the flat heat pipe channels. In the top and bottom cylinders where only the boundary condition matters, water was used as a working fluid for environmental purposes and due to its temperature range compatibility. The complete three-leg multi-channel heat pipe test rig is shown in Figure 3-8.

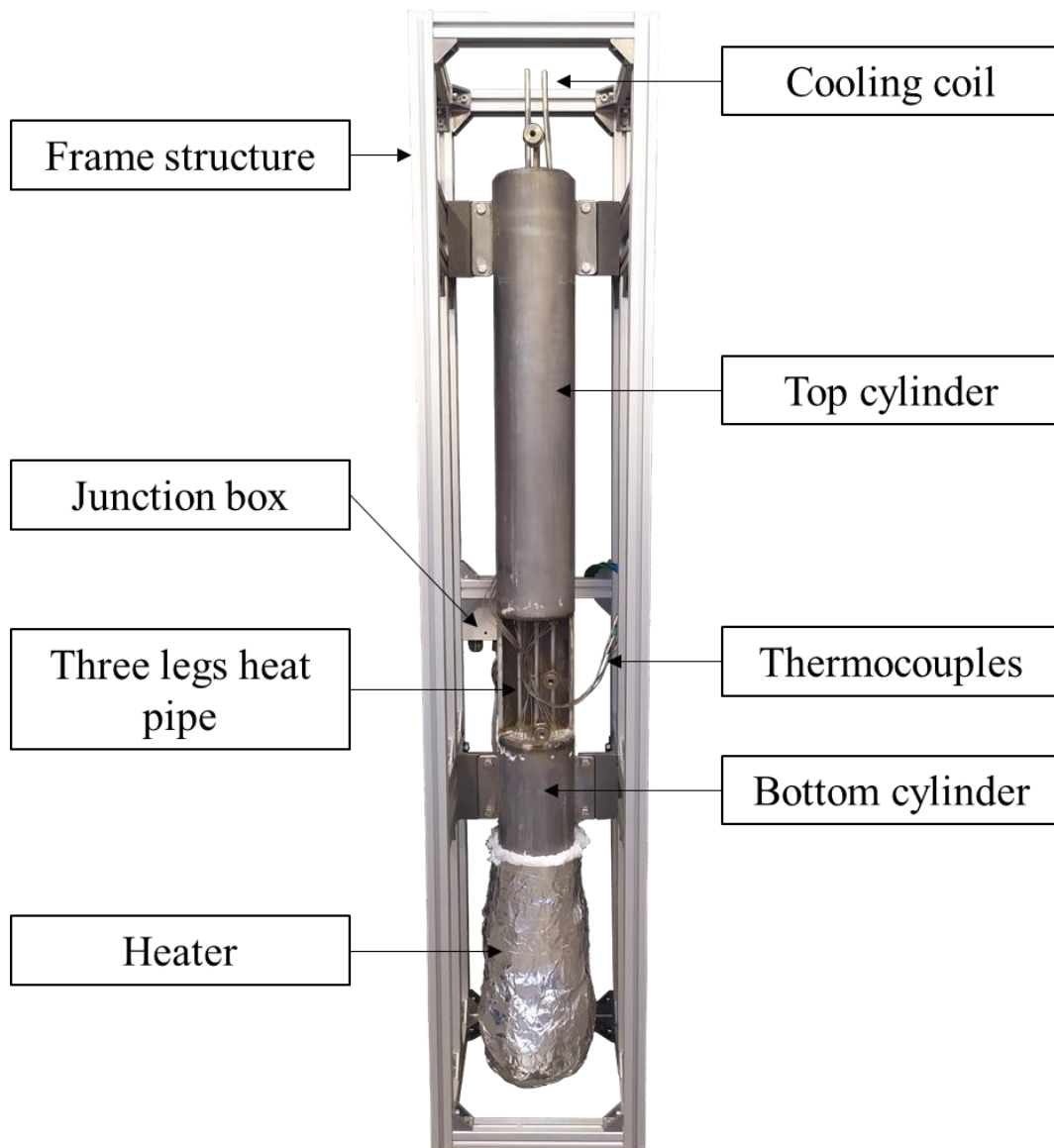


Figure 3-8. Three-leg multi-channel heat pipe apparatus

Two electric heaters were placed on the bottom cylinder to investigate the thermal performance of the three-leg heat pipe assembly. In order to study heat transfer rates in the range 0-1500W, two Omega 2-Piece Mica Insulated Band Heaters of 800W each were used and placed in parallel. A RS-GCS-040 silicone free thermal grease of thermal conductivity 4.0W/m.K was used at the interface to improve the contact between the heaters and the bottom cylinder. The two electric band heaters used on the three-leg heat pipe apparatus are shown in Figure 3-9.

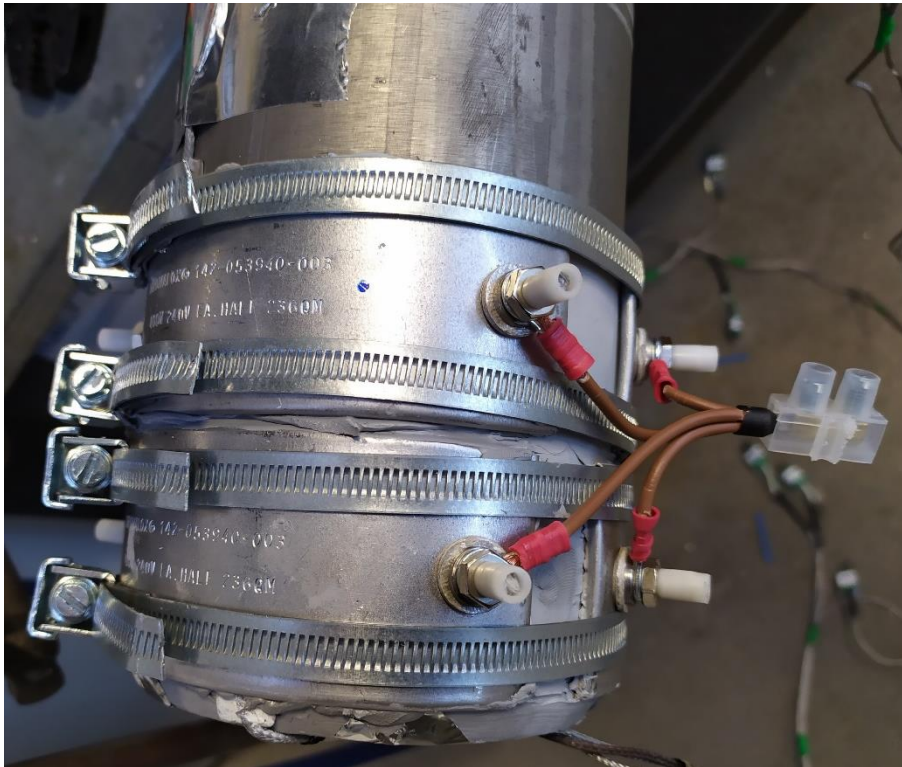


Figure 3-9. Omega 2-Piece Mica Insulated Band Heater 800W used on the three-leg heat pipe apparatus

As a heat sink, cold water was connected to the cooling coil and recovered heat by forced convection. To prevent thermal losses and decrease the length of each experiment, the whole three-leg heat pipe assembly was covered with thermal insulation.

### 3.1.2 Thermocouple locations

To investigate the thermal performances of the three-leg heat pipe, thermocouples have been welded on the legs and collectors of the heat pipe. The thermocouples used were K-type probe thermocouples 1.5mm diameter made for a temperature range of -30°C to +350°C. The locations of the thermocouples on the three-leg multi-channel heat pipe are shown in Figure 3-10.



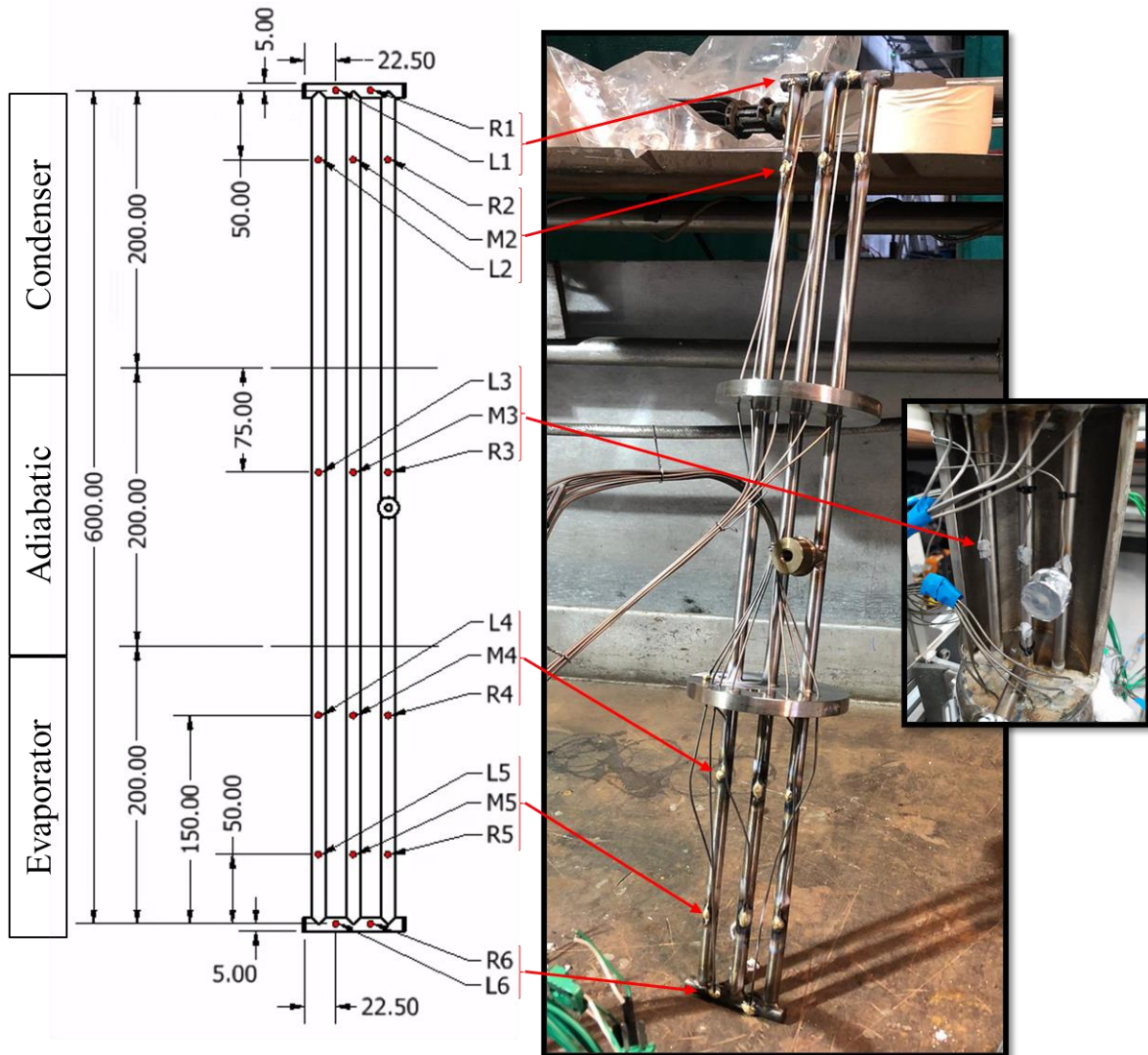


Figure 3-10. Thermocouple locations on the three-leg multi-channel heat pipe only

On the three-leg heat pipe, thermocouples situated on the left, middle and right legs are designated with a letter L, M, and R respectively. Starting from the bottom of the three-leg heat pipe, the thermocouples L6 and R6 are placed on the bottom collector. At a filling ratio of 50%, the pool boiling section of the evaporator is covered by the thermocouples L5, M5, and R5 for the left, middle and right legs. At the evaporator section which is not filled by the liquid pool, the thermocouples L4, M4, and R4 are located where falling film evaporation is expected to occur. For the adiabatic section, three thermocouples have been added once the assembly was done and are designated by L3, M3, and R3. The contact between those thermocouples and the legs have been improved by using thermal paste and the thermocouples have been thermally insulated. Thermocouples L2, M2, and R2 are placed on each leg of the condenser section of the three-leg heat pipe. Finally, thermocouples L1 and R1 are placed on the top collector. To check the good operation of the overall three-leg heat pipe assembly, other

thermocouples have been placed on the heater, bottom cylinder, top cylinder, and on the cooling water circuit. The exact locations of those thermocouples are shown in Figure 3-11.

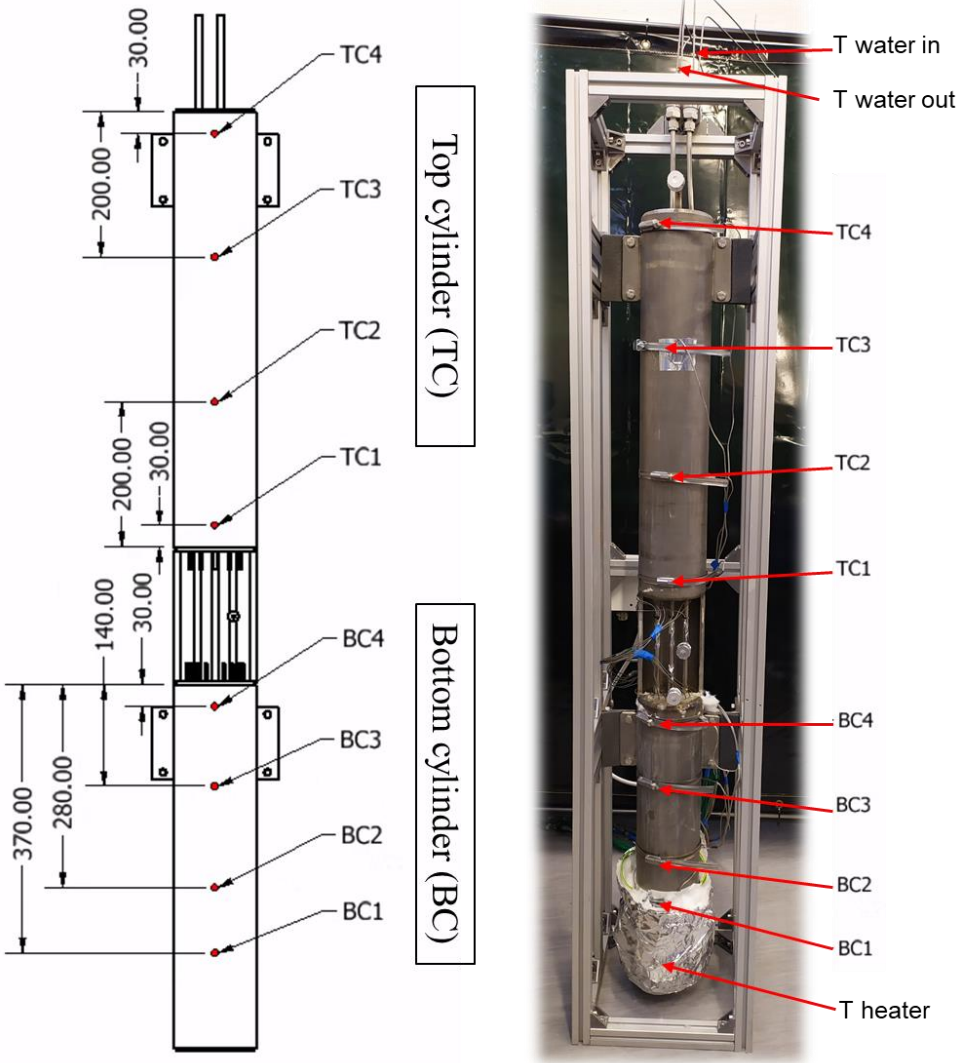


Figure 3-11. Thermocouple locations on the three-leg multi-channel heat pipe assembly

On the heater section, one thermocouple has been placed for each heater part to confirm and check their good operation. Four thermocouples were placed on the bottom cylinder at different heights and are designated by BC1, BC2, BC3, and BC4. BC1 is the thermocouple which is the closest to the water pool whereas the other thermocouples investigate the rise of the steam in the bottom cylinder. At the top cylinder, four thermocouples are also placed in a similar way with TC1 and TC2 measuring the water pool temperature while TC3 and TC4 are placed to measure the rising steam temperature. Finally, the water inlet and outlet temperatures are measured to obtain the heat transfer rate passing through the heat pipe. To improve the accuracy, two thermocouples are used for the cooling water inlet and two more for the water outlet. The summary of the thermocouples, including their labels and locations, are reported in Table 3-1.

Table 3-1. Thermocouples labels and locations on the three-leg multi-channel heat pipe

<b>Label</b>	<b>Full designation</b>	<b>Location</b>
1- Heater bot front	Front bottom heater	Front bottom heater
2- Heater bot back	Back bottom heater	Back bottom heater
3- Heater top front	Front top heater	Front top heater
4- Heater top back	Back top heater	Back top heater
5- BC4	Bottom cylinder – level 4	Bottom cylinder – level 4 – Vapour stream
6- BC3	Bottom cylinder – level 3	Bottom cylinder – level 3 – Vapour stream
7- BC2	Bottom cylinder – level 2	Bottom cylinder – level 2 – Vapour stream
8- BC1	Bottom cylinder – level 1	Bottom cylinder – level 1 – Pool
9- L6	Bottom collector left – level 6	3 Legs HP – Evaporator – Bottom collector left
10- R6	Bottom collector right – level 6	3 Legs HP – Evaporator – Bottom collector right
11- L5	Left leg – Level 5	3 Legs HP – Evaporator – Pool boiling - leg left
12- M5	Middle leg – Level 5	3 Legs HP – Evaporator – Pool boiling - leg middle
13- R5	Right leg – Level 5	3 Legs HP – Evaporator – Pool boiling - leg right
14- L4	Left leg – Level 4	3 Legs HP – Evaporator – Falling film - leg left
15- M4	Middle leg – Level 4	3 Legs HP – Evaporator – Falling film - leg middle
16- R4	Right leg – Level 4	3 Legs HP – Evaporator – Falling film - leg right
17- L3	Left leg – Level 3	3 Legs HP – Adiabatic – leg left
18- M3	Middle leg – Level 3	3 Legs HP – Adiabatic – leg middle
19- R3	Right leg – Level 3	3 Legs HP – Adiabatic – leg right
20- L2	Left leg – Level 2	3 Legs HP – Condenser – leg left
21- M2	Middle leg – Level 2	3 Legs HP – Condenser – leg middle
22- R2	Right leg – Level 2	3 Legs HP – Condenser – leg right
23- L1	Left leg – Level 1	3 Legs HP – Condenser – Top collector left
24- R1	Right leg – Level 1	3 Legs HP – Condenser – Top collector right
25- TC4	Top cylinder – level 4	Top cylinder – level 4 – Vapour stream
26- TC3	Top cylinder – level 3	Top cylinder – level 3 – Vapour stream
27- TC2	Top cylinder – level 2	Top cylinder – level 2 – Vapour stream
28- TC1	Top cylinder – level 1	Top cylinder – level 1 – Vapour stream
29- Water in 1	Water inlet n1	Cooling coil Water inlet n1
30- Water in 2	Water inlet n2	Cooling coil Water inlet n2
31- Water out 1	Water outlet n1	Cooling coil Water outlet n1
32- Water out 2	Water outlet n2	Cooling coil Water outlet n2

## 3.2 Multi-channel flat heat pipe apparatus

### 3.2.1 Apparatus

#### 3.2.1.1 Heat transfer principle

A simple system with a heat source and a heat sink has been assembled to investigate the thermal performance of the multi-channel flat heat pipe which can be used for surface cooling applications. At the bottom of the multi-channel flat heat pipe, two flat silicon heaters provide thermal energy to the heat pipe. On the other hand, at the top of the flat heat pipe, a cooling manifold inside which cold water is circulating recovers the heat transmitted by the heat pipe. The heat transfer principle of the multi-channel flat heat pipe assembly is presented in Figure 3-12.

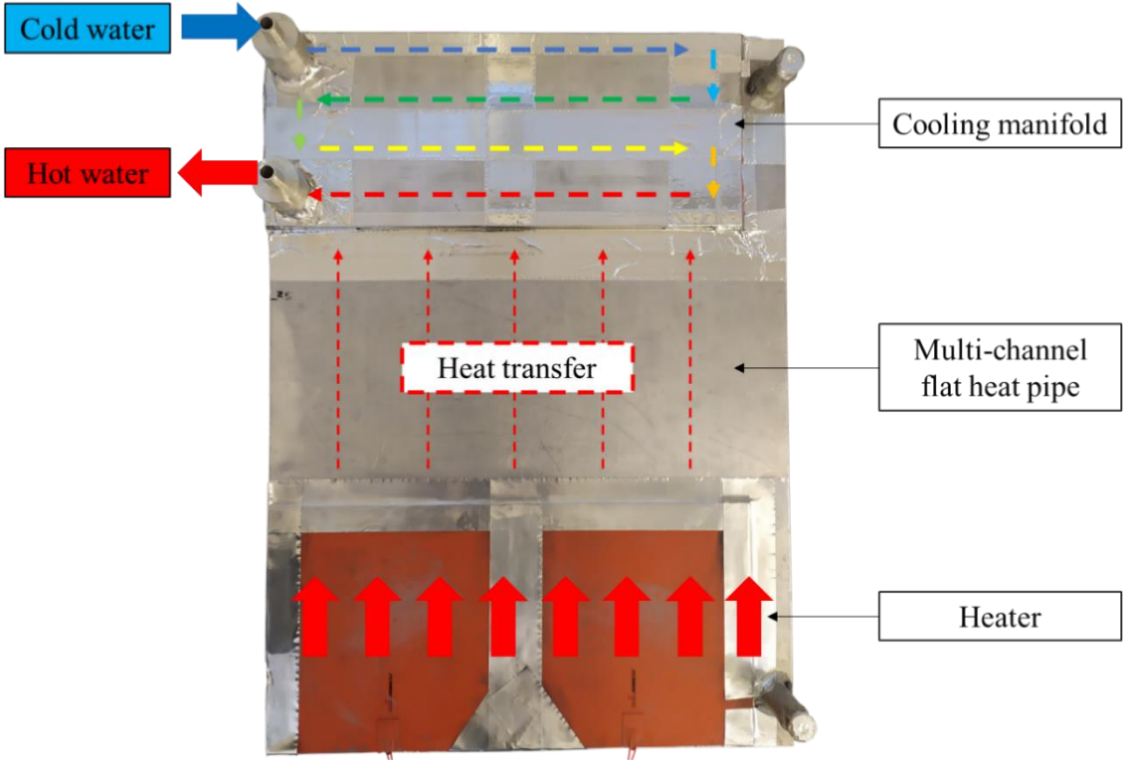


Figure 3-12. Heat transfer schematic of the multi-channel flat heat pipe assembly

At the bottom of the flat heat pipe, two flat silicon heaters transfer thermal energy by direct contact on the heat pipe. This contact is improved by using high thermal conductivity thermal paste to guarantee that the complete surface of the heater touches the flat heat pipe evaporator. At the condenser section, an identical thermal paste was used at the junction between the cooling manifold and the heat pipe. Cold water circulates inside the cooling manifold, hence heat is first transferred from the heat pipe to the cooling manifold by conduction through the material thickness and second, by forced convection between the cooling manifold material and the cooling water.

### 3.2.1.2 Multi-channel flat heat pipe assembly

The two independent elements of the multi-channel flat heat pipe assembly, namely (A) the multi-channel flat heat pipe investigated and (B) its cooling manifold are shown in detail in Figure 3-13.

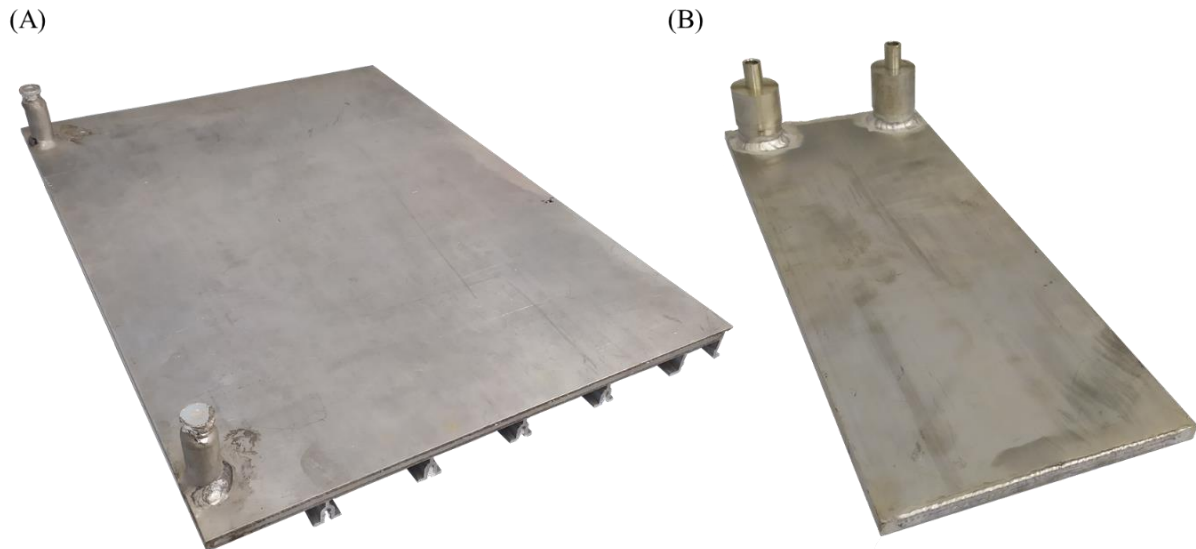


Figure 3-13. (A) Multi-channel flat heat pipe investigated and (B) its cooling manifold

The investigated multi-channel flat heat pipe is presented on the left-hand side. This heat pipe is made from an aluminium extrusion and comprises an internal channel network inside which the working fluid circulates. The multi-channel flat heat pipe has a rectangular surface of 680x497mm, and a thickness of 12mm. The two cylinders that can be seen on the surface of the flat heat pipe are the charging caps from which the working fluid was introduced inside the heat pipe. The working fluid used was R134a which is a reference refrigerant largely used for heat transfer purposes due to its performance and compatibility with aluminium. To determine the best working fluid for a wickless heat pipe, the figure of merit of each fluid can be estimated and this indicates which fluid best fits a given operating temperature [108]. For a temperature range within 0-70°C which is encountered in PV/T applications, R134a is suitable.

Several aluminium supports can be seen on the rear surface of the flat heat pipe. These supports were placed on the heat pipe so that it could be maintained in a horizontal position and be used as a shelf. Yet, in the framework of this research, these supports were not used.

The cooling manifold consists of a similar aluminium extrusion plate of dimensions 450x184mm. The thickness of the cooling manifold is 10mm. On top of the cooling manifold, two cylindrical connecting ports are used for the water inlet and outlet. The internal structure

of the cooling manifold comprises similar channels to the heat pipe, which are arranged in four passes. Each pass consists of four parallel channels as schematized in Figure 3-14.

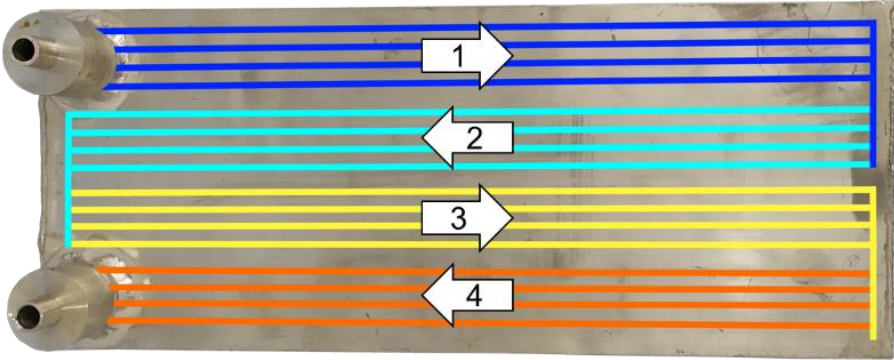


Figure 3-14. Cooling manifold internal structure

Regardless of the internal structure of the cooling manifold, in this research, the thermal performance of the manifold is only measured experimentally. The cooling manifold performance was not modelled theoretically to prevent any error propagation in order to focus only on the thermal performances of the multi-channel flat heat pipe.

The overall multi-channel flat heat pipe assembly, comprising the flat heaters, the multi-channel flat heat pipe, and the cooling manifold is shown in Figure 3-15 below.



Figure 3-15. Multi-channel flat heat pipe assembly with silicon flat heaters as a heat source and a cooling manifold as a heat sink

The evaporator section consists of two silicon flat heaters connected in series. Each Omega SRFG series flexible silicon heater has a dimension of 230x230mm with a maximum power of 820W. Thermal paste was also used at the interface between the heaters and the heat pipe. The thermal paste used is a RS-GCS-040 silicone free thermal grease of thermal conductivity 4.0W/m.K.

3.2.1.3 Internal structure of the multi-channel flat heat pipe

The working fluid circulates through a network of channels and grooves (or collectors) inside the multi-channel flat heat pipe. This structure has been designed to maximise the conduction heat transfer from the surface of the heat pipe to the working fluid, and to guarantee a uniform temperature profile of the heat pipe surface. The internal structure of the investigated heat pipe consists of 44 parallel channels directed from the heater to the cooling manifold. These channels are all connected to each other at the top and bottom of the heat pipe by two grooves. These collectors allow the circulation of the liquid and vapour phases of the working fluid between the parallel channels, and thus maintain a constant temperature on the surface of the multi-channel flat heat pipe. The design drawing of the investigated multi-channel flat heat pipe is presented in Figure 3-16.

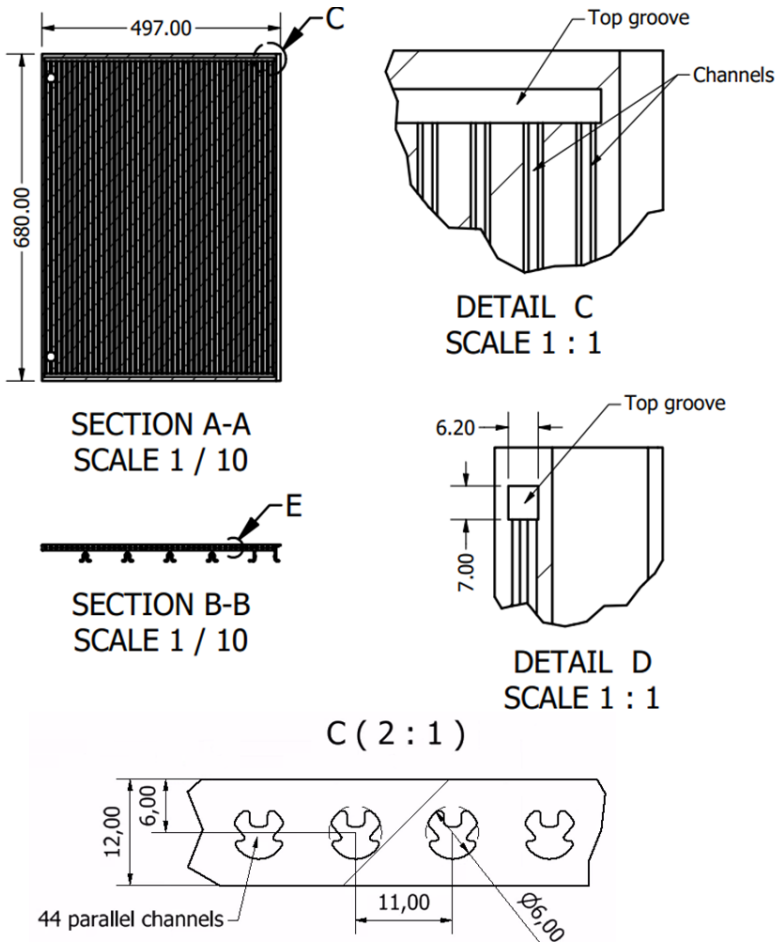


Figure 3-16. Multi-channel flat heat pipe drawing

The channel geometry used in the multi-channel flat heat pipe was designed and patented by *Jouhara and Lester* [110] under the International Patent n°WO2015193683 in 2015. This unique shape can be included in a circle of diameter 6mm and presents a symmetric axis through the heat pipe thickness. The channel detail and a picture of the channels are presented in Figure 3-17.



Figure 3-17. Channels of the multi-channel flat heat pipe

At the top of the channel cross-section, three metal teeth can be noted. These metallic surfaces aim at improving the conduction from the top surface to the working fluid inside the channel. Also, by using such a shape, the heat transfer area between the channel wall and the working fluid is increased. The bottom of the channel has a half circular shape which aims at recovering the liquid portion of the working fluid when the flat heat pipe is on a horizontal position. Indeed, the shape of this channel has been designed so that the multi-channel flat heat pipe can be used horizontally. Yet, in the framework of this research, the multi-channel flat heat pipe was mainly positioned vertically, which changes the impact of the channel shape compared to its original designed position. In contrast to the horizontal position of multi-channel flat heat pipe, the use of the heat pipe in a vertical or angled position means that the whole channel circumference will be occupied by liquid working fluid at the evaporator, and vapour at the adiabatic and condenser section. Hence, the impact of this channel shape on the two-phase heat transfer inside the heat pipe in this position is of interest in the research presented.

As mentioned earlier, the 44 parallel channels of the multi-channel flat heat pipe are linked together at the top and bottom of the heat pipe by collectors. These grooves have rectangular cross sections of dimensions 7x6.2 mm and are manufactured by extrusion of the side of the heat pipe with the heat pipe sealed by welding an end cap. Exceptionally, in Figure 3-18, a groove on a similar multi-channel heat pipe was extruded on the side and top of the heat pipe, which allowed the visualisation of the groove and of the parallel channels inside the flat heat pipe.





Figure 3-18. Open groove of the multi-channel flat heat pipe

In a vertical position, the groove situated at the bottom of the heat pipe is filled with the liquid phase of the working fluid and allows the liquid to circulate between the channels. At the top of the heat pipe, however, the groove is mainly filled with vapour. Yet, in the studied multi-channel assembly, the top groove is in contact with the cooling manifold, and, in this regard, condensation inside the top collector can also occur.

### 3.2.2 Thermocouple locations

Thermocouples have been placed on the heat pipe surface to investigate the thermal performance of the multi-channel flat heat pipe. The locations of the thermocouples are shown in Figure 3-19.

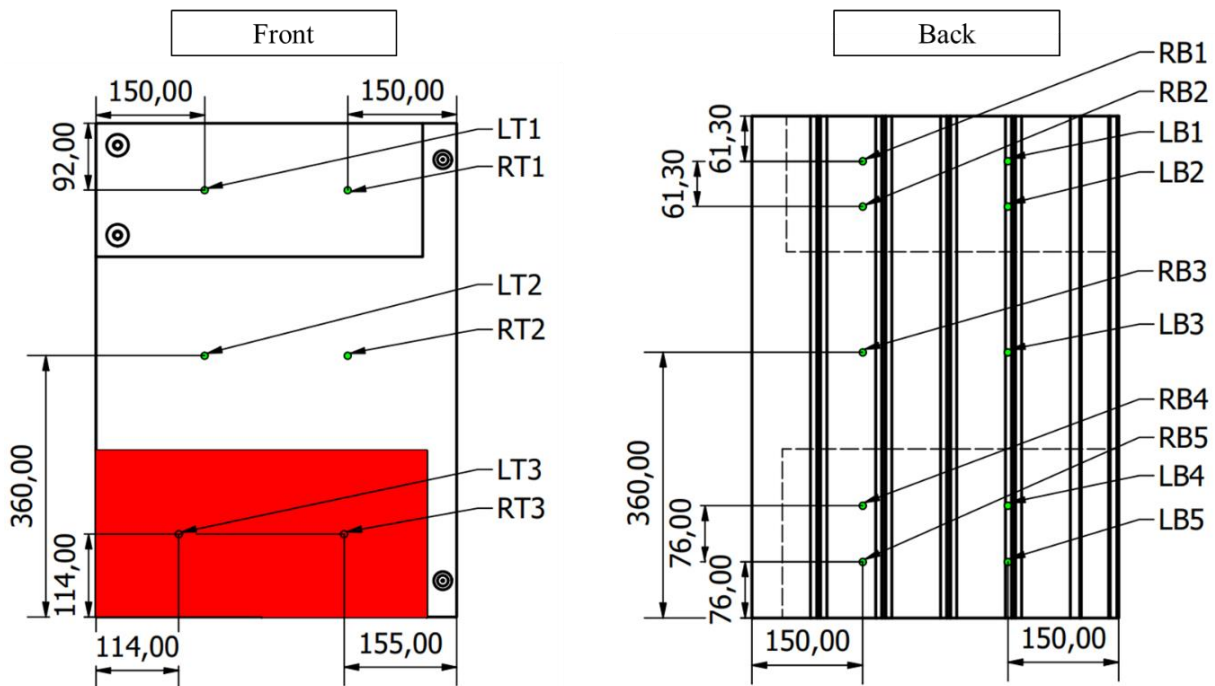


Figure 3-19. Thermocouple locations on the multi-channel flat heat pipe

On the front surface of the heat pipe, two thermocouples have been placed on the silicon heaters, on the adiabatic section of the flat heat pipe and on the cooling manifold. The two thermocouples situated on the heater have been placed for safety purposes to make sure that the temperature does not exceed the maximum temperature allowable (220°C). In order to measure the evaporator, adiabatic, and condenser temperatures, thermocouples have been mainly placed on the back surface of the heat pipe. Indeed, placing thermocouples at the interface between the flat heat pipe and the heaters, or between the heat pipe and the cooling manifold was impossible. To tackle this issue, thermal measurements have been made from the rear surface of the heat pipe. To make sure that the temperatures between the front and back surfaces of the heat pipe are similar, the measurement from the two thermocouples situated on the adiabatic section of the front surface were compared with two thermocouples at a similar location placed on the rear surface. On the back heat pipe surface of Figure 3-19, the heaters and cooling manifold locations are symbolized with dashed lines. The locations of the thermocouples at the evaporator and condenser section have been selected so that the temperature uniformity along the whole zone, in both x and y directions, was checked. In this regard, four thermocouples have been placed in a rectangular shape on both evaporator and condenser sections. The summary of the thermocouples, including their labels and locations are reported in Table 3-2.

Table 3-2. Thermocouples labels and location on the multi-channel flat heat pipe

<b>Label</b>	<b>Full designation</b>	<b>Location</b>
LT1	Left top – level 1	Cooling manifold surface - left
RT1	Right top – level 1	Cooling manifold surface - right
LT2	Left top – level 2	Top heat pipe surface – Adiabatic section - left
RT2	Right top – level 2	Top heat pipe surface – Adiabatic section - right
LT3	Left top – level 2	Heater surface - left
RT3	Right top – level 2	Heater surface - right
LB1	Left back – level 1	Back heat pipe surface – Condenser section – top left
RB1	Right back – level 1	Back heat pipe surface – Condenser section – top right
LB2	Left back – level 2	Back heat pipe surface – Condenser section – bottom left
RB2	Right back – level 2	Back heat pipe surface – Condenser section – bottom right
LB3	Left back – level 3	Back heat pipe surface – Adiabatic section - left
RB3	Right back – level 3	Back heat pipe surface – Adiabatic section - right
LB4	Left back – level 4	Back heat pipe surface – Evaporator section – top left
RB4	Right back – level 4	Back heat pipe surface – Evaporator section – top right
LB5	Left back – level 5	Back heat pipe surface – Evaporator section – bottom left
RB5	Right back – level 5	Back heat pipe surface – Evaporator section – bottom right

The thermocouples used were K-type leaf thermocouples made for surface temperature measurements. The stainless-steel leaf dimension was 13x25mm and the application range of these thermocouples is estimated to be from -30°C to +350°C. The leaf thermocouples were installed using thermal paste, a small piece of thermal insulation, and silver tape. The installation of the thermocouples on the flat heat pipe is shown in Figure 3-20.

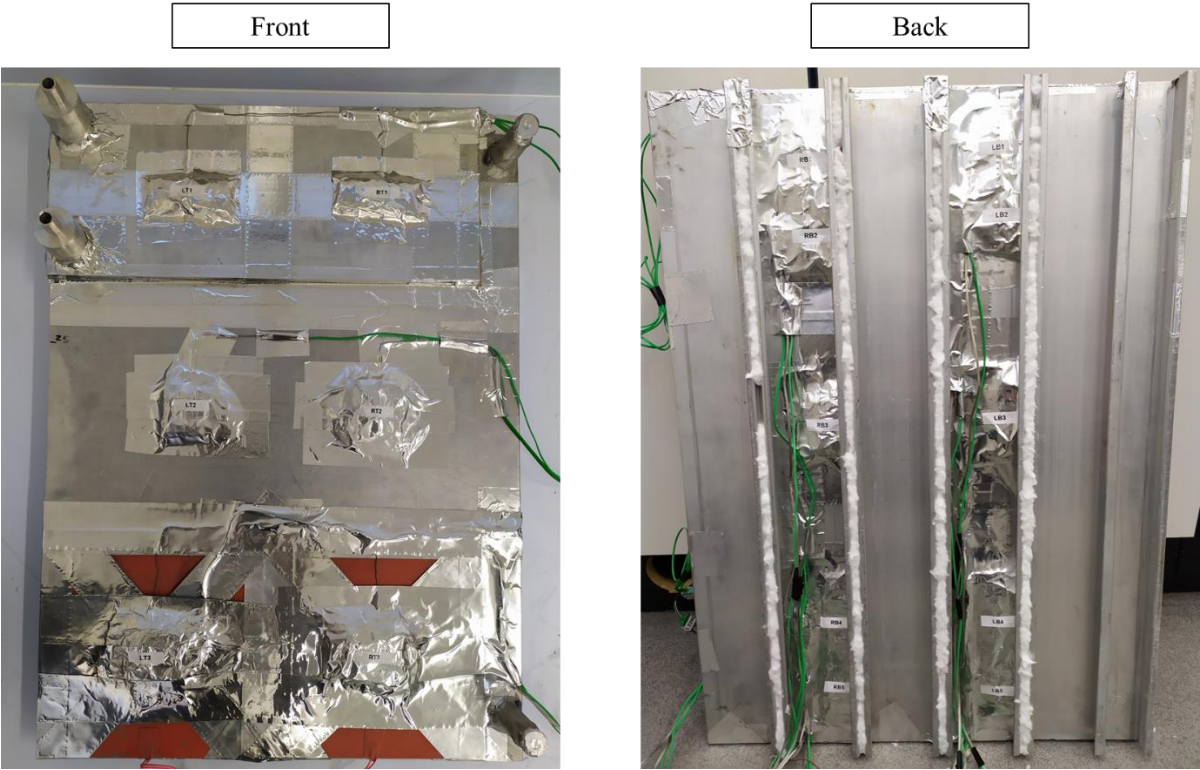


Figure 3-20. Installation of the thermocouples on the flat heat pipe

In addition to the thermocouples placed on the heat pipe surface, four probe thermocouples were placed on the cooling water line at the inlet and outlet of the cooling manifold. Each measurement was doubled to improve the measurement accuracy with two thermocouples placed on the cooling water inlet, and two on the outlet. These thermocouples were used to measure the thermal energy recovered by the cooling water.

### 3.3 Experimental test bench

To test the thermal performances of both the three-leg heat pipe and the multi-channel flat heat pipe, a test bench was built to investigate the impact of various factors such as different heat transfer rates, tilt angles, or cooling water flow rate. The experimental test bench is presented in Figure 3-21.

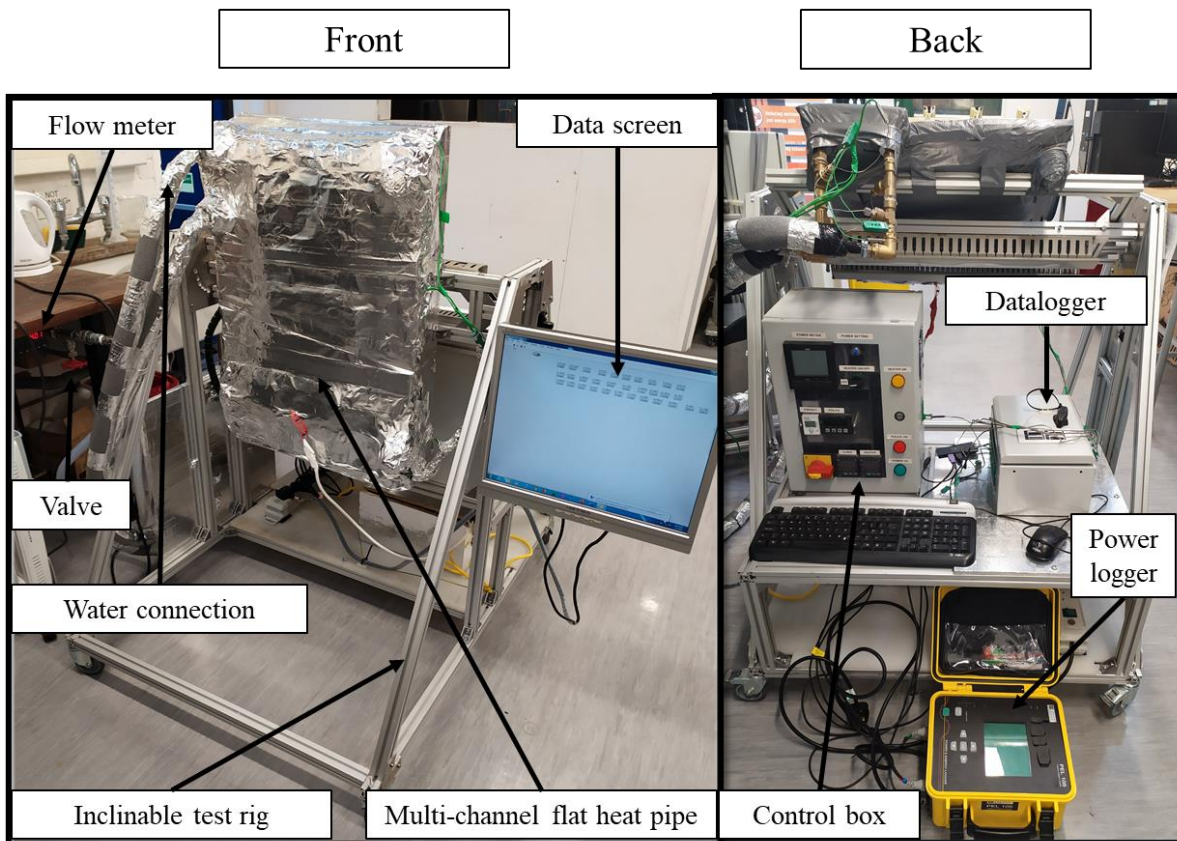


Figure 3-21. Experimental test bench while testing the multi-channel flat heat pipe

The test bench was made of an aluminium frame with a rotating axis that can be fixed at the desired angle. The heat pipe to be tested (either three leg heat pipe or flat heat pipe) was attached to the frame with a similar strut structure which facilitates the removal of the heat pipe. On the left side of the rig, the water connection was linked to the water supply. The water connection point comprised a flow meter Omega® Turbine Flow Sensors FTB371-G and a valve which allowed the regulation of the cooling water flow rate. At the back of the test rig, all the thermocouples of the system were linked to a data logger with two thermocouple modules NI-9213 and its computer. LabVIEW was used as software to visualise the data on the screen and for data recording. A control box was built to control the electric power sent to the heaters. This control box comprises three temperature controllers used for safety purposes only, and a power controller. To measure the electrical power with accuracy, a power logger PEL 105 was used to adjust the heater power and thus the heat transfer rate through the tested heat pipe. The experimental test bench is also shown in Figure 3-22 while the three-leg heat pipe was being tested.



Figure 3-22. Experimental test bench while testing the three-leg multi-channel heat pipe

The equivalent Piping and Instrumentation Diagram (P&ID) of the test bench is shown in Figure 3-23. The diagram is relevant regardless of which heat pipe apparatus is tested.

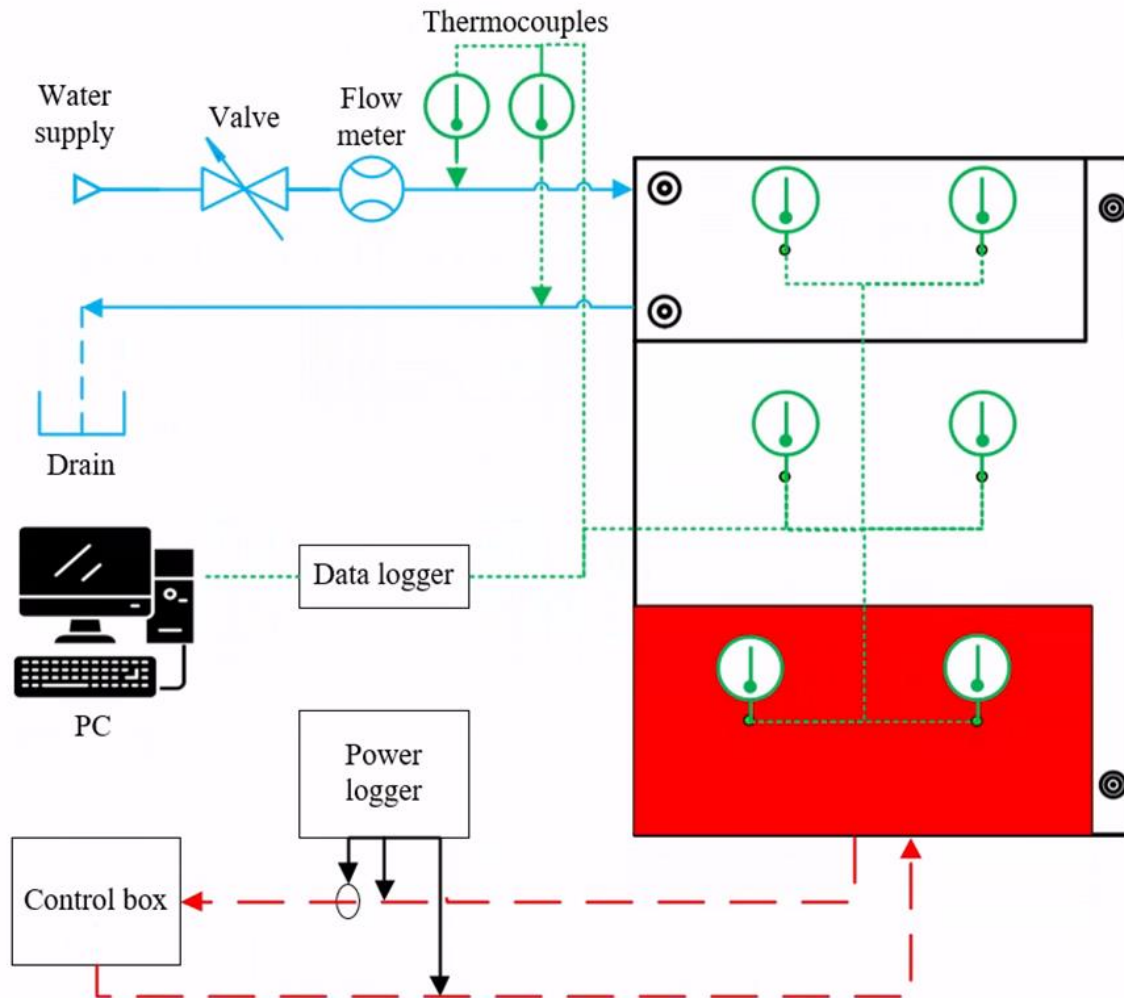


Figure 3-23. Piping and instrumentation diagram (P&ID) of the multi-channel flat heat pipe test rig

### 3.4 Experimental procedure

#### 3.4.1 Three-leg multi-channel heat pipe experimental procedure

In the multi-channel flat heat pipe used for surface cooling applications, different heat transfer rates take place due to the various boundary conditions imposed on the flat heat pipe. Hence, the channels need to transfer different amounts of heat by two-phase heat transfer. In this regard, different heat transfer rates must also be studied to evaluate the performance of the three-leg multi-channel heat pipe. In PV/T applications, the heat transfer rate of the multi-channel flat heat pipe is within 0-1500W. However, the multi-channel flat heat pipe comprises 44 parallel channels whereas our three-leg multi-channel heat pipe only consists of 3 parallel channels. By considering that the amount of heat transferred in each parallel channel is equal, the maximum heat transfer rate to test in the three-leg heat pipe was obtained by proportionality:

$$\text{Multi-channel flat heat pipe: } 44 \text{ channels} \rightarrow \dot{Q}_{max} = 1500 \text{ W} \quad (3-11)$$

$$\text{3 leg heat pipe: } 3 \text{ channels} \rightarrow \dot{Q}_{max} = 1500 \times \frac{3}{44} = 102.2 \text{ W} \quad (3-12)$$

Based on this approach, the heat transfer rate in the three-leg heat pipe was varied from 10W to 110W with an increment of 10W. Before starting the experiment, the cooling water flow was set to 1L/min. This water flow rate was selected as the lowest coolant flow rate generates the highest difference of temperature within the system, which reduces errors during temperature difference measurements. However, this needs to be balanced as lowering the coolant flow rate also increases all the temperatures in the test rig. For safety purposes, the three-leg heat pipe operating temperature should be maintained below 70°C when R134a is used. By selecting a cooling water flow rate of 1L/min, the heat pipe temperature was kept below 70°C while allowing a better accuracy of the thermal measurement. To measure the water flow rate accurately, 10 manual measurements of the flow were done at the beginning of each experiment and the average value was taken to estimate the heat transfer rate. For safety purposes, the control box powering the electric heaters was linked to three thermocouples and could automatically cut the electric power if one of the temperatures increased beyond its safety value. Safety temperature limits of 150°C for the heaters and 55°C for the three-leg heat pipe were set and these were large enough to conduct all the experiments normally. After making sure that the temperature was controlled as expected, the electric power was turned on. The electric power was measured and displayed on the power logger which was used to reach the desired electric power. Usually, for the testing of heat pipes and thermosyphons, once the heat source is switched on, the heat pipe temperature progressively increases until it stabilizes at steady state. In the case of the three-leg heat pipe apparatus, due to the low heat transfer rates investigated, the three heat pipe sections to be activated, and the thermal inertia of the apparatus, this usual protocol was unsuccessful. Indeed, at low heat transfer rates (20W), as shown in Figure 3-24, the three-leg heat pipe did not reach steady state after 6 hours of the experiment.

### Three legs heat pipe first protocol – heating only

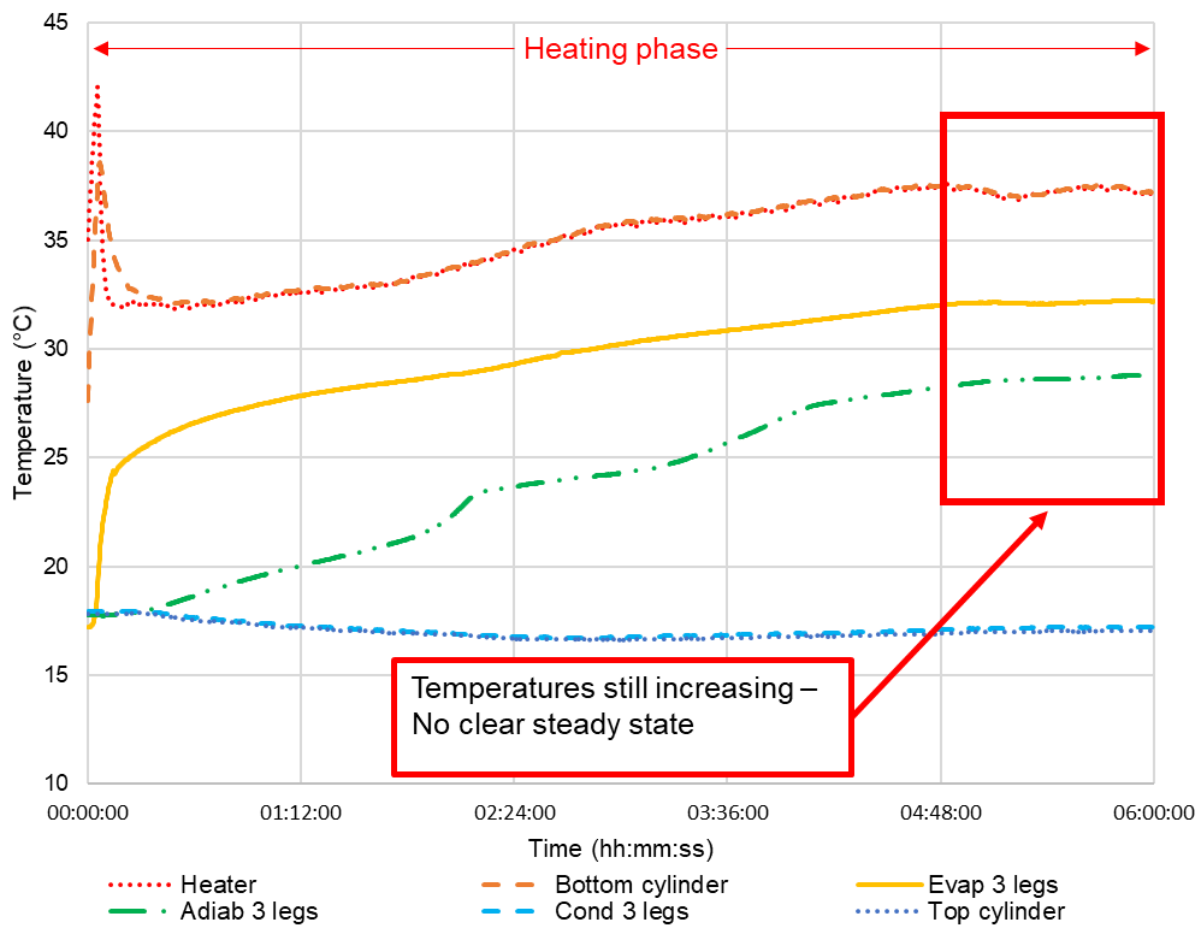


Figure 3-24. Usual heat pipe testing protocol – no steady state reached

In this regard, the experimental protocol of the three-leg heat pipe testing had to be adapted. Experimentally, it was observed that a certain amount of energy was required by the bottom cylinder, three-leg heat pipe, and top cylinder to be activated and start transmitting thermal energy. At low heat transfer rates, it could take several hours until a sufficient amount of energy was collected to start up the heat pipes and trigger the two-phase heat transfer. Based on this finding, to speed up the experimental process, a thermal boost was given to the three-leg heat pipe assembly in order to quickly trigger the two-phase heat transfer. At the beginning of each experiment, the electric heaters were switched on at a high heat transfer rate (~800W) until the three legs heat pipe adiabatic section reached 50°C. This stage took about 10 minutes. By doing so, the thermal energy accumulated inside the three-leg heat pipe assembly to allow the start-up of the bottom cylinder, three-leg heat pipe and top cylinder. This thermal boost stage was then followed by a rapid cooling stage during which the heater was switched off and the cooling water flow rate set to 5L/min. Once the three-leg heat pipe temperature returned to 40°C, the desired electric power was supplied to the heaters and the cooling water flow rate



was adjusted to 1L/min. The experiment was then recorded without modification until a clear steady state was reached as shown in Figure 3-25.

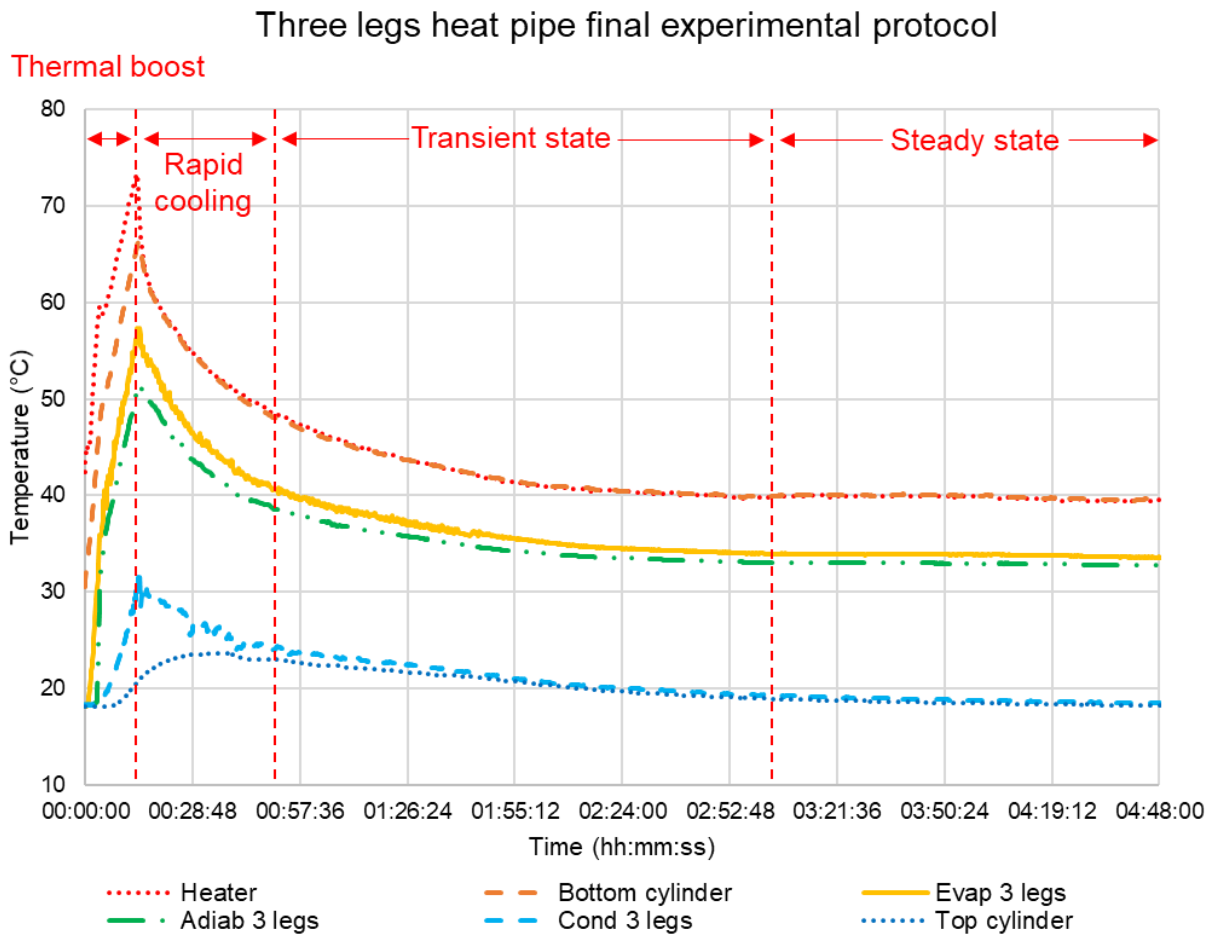


Figure 3-25. Three-leg heat pipe final experimental protocol

The experiment protocol shown in Figure 3-25 was obtained at a heat transfer rate of 20W which is similar to that of Figure 3-24. By comparing the two protocols, it can be seen that using a thermal boost and a rapid cooling at the start-up of the experiment permits a clear steady state to be reached and useful data obtained within 4-5 hours. In comparison, with a usual “heating only” experimental protocol, no clear steady state was reached after 6 hours. For higher heat transfer rates, the steady state can be reached even earlier. To improve the accuracy of the results and obtain more data, each experiment has been repeated a minimum of five times.

### 3.4.2 Multi-channel flat heat pipe experimental procedure

#### 3.4.2.1 Impact of the heat transfer rate

In surface cooling applications, the thermal performance of the heat pipe varies with the amount of thermal energy removed from the hot surface. In this regard, the impact of the heat

transfer rate on the thermal performance of the multi-channel flat heat pipe must be studied. The electrical power from the electrical heaters was adjusted from 100W to 1500W with an increment of 100W to draw the power map and study the impact of the heat transfer rate on the thermal performance of the multi-channel flat heat pipe. This range of heat transfer rates was selected as it corresponds to the heat transfer rate range occurring in a heat pipe-based PV/T system during the cooling of photovoltaic cells. The heat pipe was placed in a vertical position only. Before starting the experiment, the cooling water flow rate inside the cooling manifold was adjusted using the valve and the flow meter. Three different cooling water flow rates of 2L/min, 4L/min, and 6L/min were tested. Manual measurements of the water flow rate were taken to improve the flow rate measurement accuracy. Indeed, it was found that the flow rate measurement from the Omega® Turbine Flow Sensors FTB371-G was approximate and showed an error in the range of 5%. In this regard, for each experiment, six manual flow rate measurements were made and the standard deviation between each measurement was lower than 1%. Once the cooling water flow rate was circulating inside the cooling manifold, the power was turned on. For safety purposes, the control box comprised two temperature controllers and a “policeman” that can cut the power if the temperature of key elements in the system exceeds the maximum allowable temperature. The temperature limit for the silicon heaters was set to 220°C whereas the heat pipe temperature limit was set to 60°C. Power was delivered to the heaters in cases where the temperature safety criteria were verified. Once switched on, the power was adjusted with the dial from the power controller until the desired value could be read on the power logger. The system temperatures, including the temperature of the water, were recorded for 30 minutes until steady state was reached. To improve the accuracy of results, each experiment (electric power-cooling flow rate combination) was repeated four times which gives a total of 180 experiments.

#### *3.4.2.2 Impact of the tilt angle*

In the photovoltaic application of the multi-channel flat heat pipe, the device may be used with various tilt angles to maximise the electrical production from the photovoltaic cells. Yet, the tilt angle can also have an impact on the performance of the multi-channel flat heat pipe, which must be characterised. With this objective, the insulated multi-channel flat heat pipe assembly was tested at various angles: 90° (vertical), 45°, 20°, 10°, 5°, and 2° (close to horizontal). Such angles were selected as, in heat pipes, the impact of the tilt angle on the thermal performance is limited at angles higher than 20°. Indeed, the tilt angle is expected to significantly influence the thermal performances of the multi-channel flat heat pipe at low angles only (close to the horizontal). For this investigation, a cooling water flow rate of 3L/min was chosen. The electrical powers investigated were in the range 100W to 1500W. Indeed, it can be expected that the

impact of the tilt angle will be different at various heat transfer rates. Thus, different heat transfer rates were investigated.

### 3.4.2.3 *Infrared imaging*

Infrared imaging of the cooling device has been done to visualise and check the temperature uniformity characteristics when using a multi-channel flat heat pipe. Several experiments conducted aimed at studying the impact of various factors on the temperature distribution at the evaporator, adiabatic, and condenser sections of the multi-channel flat heat pipe. Hence, the infrared imaging tests conducted are listed below:

- Infrared imaging of the multi-channel flat heat pipe at 1000W

In this experiment, the objective was to investigate in detail the temperature distribution of all the multi-channel heat pipe sections (evaporator, adiabatic, and condenser). A fixed heat transfer rate of 1000W was chosen as this corresponds to a relatively high heat transfer rate for PV/T applications and generates a high heat pipe temperature which makes the visualisation easier. Both front and rear heat pipe surface have been observed. Indeed, due to the presence of the heaters and of the cooling manifold on the front surface of the heat pipe, the temperature uniformity of the evaporator and condenser section can only be observed from the rear surface. In this regard, the test rig had to be adapted to reverse the multi-channel heat pipe and observe both surfaces. The heat pipe orientation was kept vertical.

- Infrared imaging of the impact of the tilt angle

In this experiment, the front heat pipe surface was observed only. The heat transfer rate was kept at 1000W, but the tilt angle of the device was changed. The investigated tilt angles were 90° (vertical), 45°, 20°, 10°, 5°, and 2°.

- Infrared imaging of the impact of the heat transfer rate

In this experiment, the impact of the heat transfer rate was investigated, and the electrical power of the heaters was changed from 100W to 1500W. The power increment was 100W. To draw a power map of the flat heat pipe and observe the evaporator and condenser sections, the back surface of the multi-channel heat pipe was observed. The tilt angle of the heat pipe was kept at 90°.

- Infrared imaging of the transient warmup of the multi-channel flat heat pipe

In this experiment, the transient warmup of the multi-channel flat heat pipe was studied. To do so, infrared imaging pictures have been taken every 5s. The rear surface of the heat pipe was observed at a power of 1000W in a vertical position. Thermal imaging of the heat pipe surface

was taken for an experiment duration of 600s (10 minutes) after which the steady state of the heat pipe was reached.

- Infrared imaging of the multi-channel flat heat pipe with the cooling manifold situated on one side

In this experiment, the cooling manifold location was changed to the side of the heat pipe. This investigation aimed at verifying that the heat pipe temperature remains uniform in all the directions even if the heat sink is situated on the side of the heat pipe instead of being placed at the top. The device was maintained in a vertical position at a heat transfer rate of 1000W. The back surface of the multi-channel flat heat pipe was observed.

For all the above infrared experiments, the cooling water flow rate was maintained at 3L/min. The infrared camera used was a thermal camera FLIR C2 suitable for temperatures from -10°C to +150°C. The emissivity and infrared settings were automatically adjusted by the camera. To visualise the heat transfer on the front heat pipe surface, the thermal insulation and thermocouples have been removed. Only the layer of insulation above the heaters was kept as the high temperature difference between the heaters and the multi-channel flat heat pipe would have made the focus of the thermal camera impossible. The top surface of the cooling manifold was observed too. To visualise the back of the multi-channel flat heat pipe surface and observe the evaporator and condenser sections, thermal insulation was placed on the front heat pipe surface and was removed from the rear surface. The thermocouples were also removed, and the heat pipe surface cleaned. To avoid the reflection from the aluminium material of the multi-channel flat heat pipe, the surfaces to be observed were covered with masking tape. The modified test rig for the infrared imaging experiments is presented in Figure 3-26.

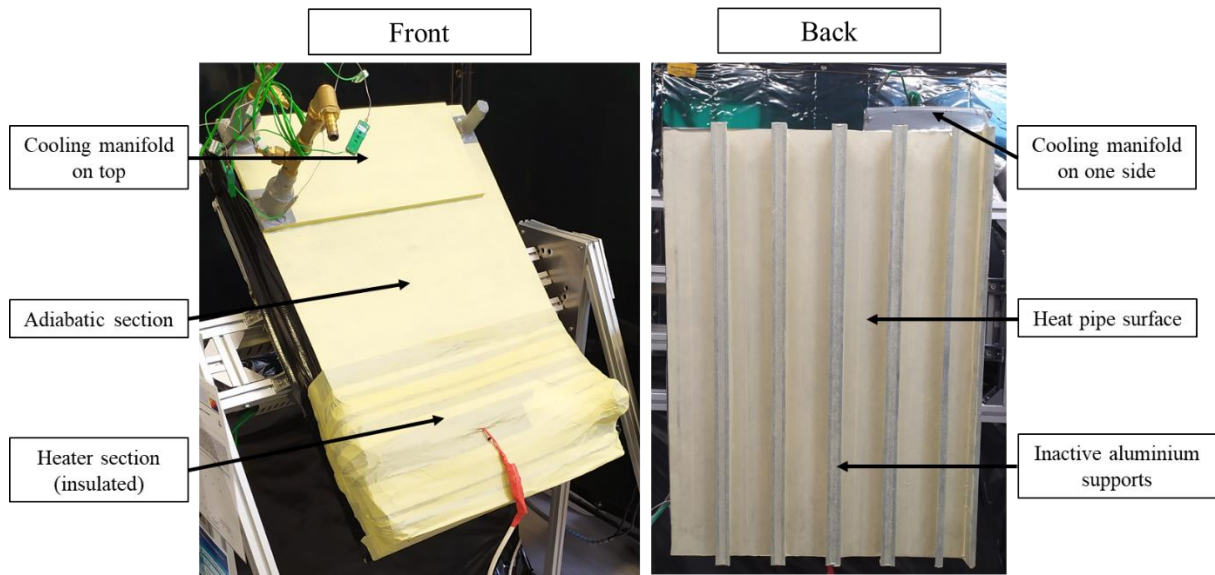


Figure 3-26. Front and back heat pipe surface set up during infrared imaging experiments.

### 3.5 Data reduction

The raw data from the power logger, cooling water flow rate measurements, and thermocouples were transformed to analyse the thermal performance of the heat pipes studied. In the following section, the equations used to reduce the raw data into meaningful variables such as thermal resistances and heat transfer coefficient are detailed.

#### 3.5.1 Heat transfer rate

In the objective of decreasing the flow rate measurement error from the flow meter used, the cooling water flow rate was measured manually. A volume of water from the experimental rig was recovered for 10s and measured multiple times. From those manual measurement, the cooling water flow rate  $\dot{m}_{water}$  in L/min was obtained by:

$$\dot{m}_{water} (L/min) = 0.006 * \left[ \frac{1}{n} \sum_{i=1}^n V_{water \text{ in } 10s, manual, i} \right] \quad (3-13)$$

where  $n$  is the number of manual measurements taken and  $V_{water \text{ in } 10s, manual}$  is the volume of cooling water recovered in 10s (ml). The cooling water mass flow rate can be expressed in kg/s with the following:

$$\dot{m}_{water} (kg/s) = \frac{\dot{m}_{water} * \rho_{water}}{60000} \quad (3-14)$$

with  $\dot{m}_{water}$  the cooling water flow rate (L/min), and  $\rho_{water}$  the cooling water density ( $kg/m^3$ ). Based on the cooling water mass flow rate, the heat transfer rate recovered by the cooling water and thus, the heat transfer rate transmitted through the heat transfer apparatus is given by:

$$\dot{Q} = \dot{m}_{water} c_{p,water} (T_{water,out} - T_{water,in}) \quad (3-15)$$

where  $\dot{Q}$  is the heat transfer rate through the system (W),  $\dot{m}_{water}$  is the water flow rate in the cooling manifold (kg/s),  $c_{p,water}$  is the specific heat of water (J/kg.K), and  $T_{water,out}$  and  $T_{water,in}$  are the water temperature at the outlet and inlet (K), respectively. Theoretically, this heat transfer rate is similar to the electrical power input measured from the power logger. Yet, in reality, a few watts are lost in the energy conversion and through the assembly thermal insulation.

### 3.5.2 Flat heat pipe cooling manifold thermal resistance

To subtract potential errors in modelling the cooling manifold and focus on the flat heat pipe only, the cooling manifold resistance was measured experimentally. The cooling manifold thermal resistance is determined using:

$$R_{cooling\ manifold} = \frac{1}{\dot{Q}} \times \frac{T_{water,in} - T_{water,out}}{\ln((T_s - T_{water,out})/(T_s - T_{water,in}))} \quad (3-16)$$

where  $R_{cooling\ manifold}$  is the cooling manifold thermal resistance (K/W),  $\dot{Q}$  is the total heat transfer rate through the system (W),  $T_{water,in}$  and  $T_{water,out}$  are the water inlet and outlet temperatures (K), and  $T_s$  is the surface temperature of cooling manifold in contact with the heat pipe (K).

### 3.5.3 Three-leg heat pipe top cylinder thermal resistance

Similarly, for the three-leg heat pipe test rig, the thermal resistance of the top cylinder which is the heat sink of the three-leg heat pipe was determined experimentally using:

$$R_{eq,TC} = \frac{1}{\dot{Q}} \times \frac{T_{water,in} - T_{water,out}}{\ln((T_{co,3LHP} - T_{water,out})/(T_{co,3LHP} - T_{water,in}))} \quad (3-17)$$

where  $R_{eq,TC}$  is the top cylinder thermal resistance (K/W),  $\dot{Q}$  is the total heat transfer rate through the system (W),  $T_{water,in}$  and  $T_{water,out}$  are the water inlet and outlet temperatures (K), and  $T_{co,3LHP}$  is the three-leg heat pipe outer condenser wall temperature (K).

### 3.5.4 Heat flux

In order to identify the best performing boiling and condensation correlation, the pool boiling, falling film boiling, and condensation heat flux were measured and calculated from:

$$q''_{pb} = \frac{\dot{Q}}{A_{pb}} \quad (3-18)$$

$$q''_{ffb} = \frac{\dot{Q}}{A_{ffb}} \quad (3-19)$$

$$q''_c = \frac{\dot{Q}}{A_c} \quad (3-20)$$

with  $q''_{pb}$ ,  $q''_{ffb}$ , and  $q''_c$  the pool boiling, falling film boiling, and condensation heat flux (W/m<sup>2</sup>),  $\dot{Q}$  the heat transfer rate (W), and  $A_{pb}$ ,  $A_{ffb}$ , and  $A_c$  the pool boiling, falling film boiling, and condensation heat transfer area (m<sup>2</sup>).

### 3.5.5 Heat pipe thermal resistances and heat transfer coefficients

The evaporator, adiabatic, and condenser temperatures are required to estimate the thermal resistances inside the heat pipe. Those temperatures are obtained experimentally by taking the average temperature of the relevant thermocouples in the region as:

$$T_{evaporator,pb} = \frac{1}{n} \sum_{i=1}^n T_{evaporator,pb,i} \quad (3-21)$$

$$T_{evaporator,ffb} = \frac{1}{n} \sum_{i=1}^n T_{evaporator,ffb,i} \quad (3-22)$$

$$T_{adiabatic} = \frac{1}{n} \sum_{i=1}^n T_{adiabatic,i} \quad (3-23)$$

$$T_{condenser} = \frac{1}{n} \sum_{i=1}^n T_{condenser,i} \quad (3-24)$$

In the above equations, the evaporator (pool boiling section), evaporator (falling film boiling section), adiabatic, and condenser temperatures  $T_{evaporator,pb}$ ,  $T_{evaporator,ffb}$ ,  $T_{adiabatic}$ , and  $T_{condenser}$  respectively, are obtained by doing the averages of a number  $n$  of thermocouple measurements in the relevant heat pipe region. Once the temperature of each heat pipe section is determined, the pool boiling resistance, falling film boiling resistance, condensation resistance, and total heat pipe resistance can be determined:

$$R_{pb} = \frac{(T_{evaporator,pb} - T_{adiabatic})}{\dot{Q}} \quad (3-25)$$

$$R_{ffb} = \frac{(T_{evaporator,ffb} - T_{adiabatic})}{\dot{Q}} \quad (3-26)$$

$$R_c = \frac{(T_{adiabatic} - T_{condenser})}{\dot{Q}} \quad (3-27)$$

$$R_{HP} = \frac{(T_{evaporator} - T_{condenser})}{\dot{Q}} \quad (3-28)$$

where  $R_{pb}$ ,  $R_{ffb}$ ,  $R_c$ , and  $R_{HP}$  the pool boiling, falling film boiling, condensation, and total heat pipe thermal resistances (K/W),  $T_{evaporator,pb}$ ,  $T_{evaporator,ffb}$ ,  $T_{adiabatic}$ , and  $T_{condenser}$  the evaporator (pool boiling section), evaporator (falling film boiling section), adiabatic, and

condenser temperatures (K), and  $\dot{Q}$  the heat transfer rate (W). Even if the notion of thermal resistance is relevant to characterise the thermal performance of heat pipes, two-phase heat transfer correlations are expressed in terms of heat transfer coefficients. Experimentally, the pool boiling, falling film boiling, and condensation heat transfer coefficients can be obtained from:

$$h_{pb} = \frac{1}{R_{pb}A_{pb}} \quad (3-29)$$

$$h_{ffb} = \frac{1}{R_{ffb}A_{ffb}} \quad (3-30)$$

$$h_c = \frac{1}{R_cA_c} \quad (3-31)$$

with  $h_{pb}$ ,  $h_{ffb}$ , and  $h_c$  the pool boiling, falling film boiling, and condensation heat transfer coefficients (W/m<sup>2</sup>K),  $R_{pb}$ ,  $R_{ffb}$ ,  $R_c$ , and  $R_{HP}$  the pool boiling, falling film boiling, condensation, and total heat pipe thermal resistances (K/W), and  $A_{pb}$ ,  $A_{ffb}$ , and  $A_c$  the pool boiling, falling film boiling, and condensation heat transfer area (m<sup>2</sup>).

### 3.6 Error propagation and standard deviation

Measurement errors from the sensors are being propagated while using data reduction equations. To estimate the error propagated to a given variable, the uncertainty of this variable needs to be deduced from the theoretical measurement errors. On the other hand, the standard deviation describes the actual experimental error which was observed while repeating similar experiments. In this section, the theoretical uncertainties and experimental standard propagation are estimated and compared.

#### 3.6.1 Uncertainties

In the following sections, the uncertainty, denoted  $S_x$ , represents the estimated error related to the variable  $x$ . The unit of the uncertainty  $S_x$  is the same as the related variable  $x$ . The estimated measurement uncertainties for the flat heat pipe experiments are listed in Table 3-3 hereafter.

Table 3-3. Estimated measurement uncertainties

Flow rate manual measurement	$S_{V_{water\ in\ 10s,manual}}$	2.5 ml
Thermocouple	$S_T$	0.2 K

Between two flow measurements of 10 seconds, it was observed that the maximum difference of water volume measured was 2.5 ml. The thermocouple inaccuracy was estimated by immersing several thermocouples in boiling water. The maximum difference of reading was estimated to be 0.2°C.



### 3.6.2 Error propagation

Measurement error is propagated through the data reduction equations used based on the measurement uncertainties. The uncertainty  $S_x$  related to the variable  $x$  for all the variables calculated in the experimental analysis are detailed in this section. The mass flow rate uncertainty  $S_{\dot{m}_{water}}$  can be calculated from:

$$S_{\dot{m}_{water}} = \frac{\rho_{water} \times 1e^{-7}}{\sqrt{n}} S_{V_{water\ in\ 10s,manual}} \quad (3-32)$$

where  $\rho_{water}$  is the cooling water density (kg/m<sup>3</sup>),  $n$  is the number of manual measurements, and  $S_{V_{water\ in\ 10s,manual}}$  is the uncertainty on the volume of water recovered within 10s. To calculate the heat transfer rate through the apparatus, the difference of cooling water temperature  $\Delta T_{water}$  is measured. The associated error is given as:

$$S_{\Delta T_{water}} = \sqrt{S_{T_{water,out}}^2 + S_{T_{water,in}}^2} = S_T \quad (3-33)$$

with  $S_{T_{water,out}}$  and  $S_{T_{water,in}}$  the error uncertainties related to the water outlet and water inlet temperature measurements (K). The error uncertainties related to the water inlet and outlet was reduced as two thermocouples were used for the inlet, and two for the outlet, respectively. Based on the last equation, the heat transfer rate uncertainty  $S_{\dot{Q}}$  can be obtained:

$$S_{\dot{Q}} = \dot{Q} \sqrt{\left(\frac{S_{\dot{m}_{water}}}{\dot{m}_{water}}\right)^2 + \left(\frac{S_{\Delta T_{water}}}{\Delta T_{water}}\right)^2} \quad (3-34)$$

where  $\dot{Q}$  is the heat transfer rate (W),  $S_{\dot{m}_{water}}$  the uncertainty related to the water mass flow rate  $\dot{m}_{water}$  (kg/s), and  $S_{\Delta T_{water}}$  the uncertainty related to the difference of cooling water temperature (K). Data reduction equations were used to estimate the cooling manifold thermal resistance. Hence, the uncertainty related to the experimental cooling manifold thermal resistance  $S_{R_{cooling\ manifold}}$  is to be calculated using:

$$S_{R_{cooling\ manifold}} = R_{cooling\ manifold} \times \quad (3-35)$$

$$\sqrt{\left(\frac{S_{\dot{Q}}}{\dot{Q}}\right)^2 + \left(\frac{S_{\Delta T_{water}}}{\Delta T_{water}}\right)^2 + \left(\frac{\sqrt{\frac{3/4 S_T^2}{(T_s - T_{water,out})^2} + \frac{3/4 S_T^2}{(T_s - T_{water,in})^2}}}{\ln((T_s - T_{water,out})/(T_s - T_{water,in}))}\right)^2}$$

In the above equation, the experimental cooling manifold thermal resistance uncertainty  $S_{R_{cooling\ manifold}}$  is related to the cooling manifold resistance  $R_{cooling\ manifold}$  (K/W),  $S_{\dot{Q}}$  is the uncertainty related to the heat transfer rate  $\dot{Q}$  (W),  $S_{\Delta T_{water}}$  the uncertainty related to the cooling water difference of temperature  $\Delta T_{water}$  (K),  $S_T$  the thermocouple's uncertainty (K),  $T_s$  the cooling manifold surface temperature in contact with the heat pipe (K), and  $T_{water,in}$  and

$T_{water,out}$  are the water inlet and outlet temperatures (K). The surface temperature  $T_s$  was obtained from four thermocouples which led to the  $\frac{3}{4}$  factor in the above expression. Similar to the cooling manifold thermal resistance for the flat heat pipe, the three-leg heat pipe top cylinder thermal resistance was obtained using the Log Mean Temperature Difference method. Hence, the uncertainty related to the experimental top cylinder thermal resistance  $S_{R_{eq,TC}}$  can be calculated from:

$$S_{R_{eq,TC}} = R_{eq,TC} \times \sqrt{\left(\frac{S_{\dot{Q}}}{\dot{Q}}\right)^2 + \left(\frac{S_{\Delta T_{water}}}{\Delta T_{water}}\right)^2 + \left(\frac{\sqrt{\frac{7/10 S_T^2}{(T_{co,3LHP} - T_{water,out})^2} + \frac{7/10 S_T^2}{(T_{co,3LHP} - T_{water,in})^2}}{\ln((T_{co,3LHP} - T_{water,out})/(T_{co,3LHP} - T_{water,in}))}\right)^2} \quad (3-36)$$

where the experimental top cylinder thermal resistance uncertainty  $S_{R_{eq,TC}}$  is related to the equivalent top cylinder resistance  $R_{eq,TC}$  (K/W),  $S_{\dot{Q}}$  is the uncertainty related to the heat transfer rate  $\dot{Q}$  (W),  $S_{\Delta T_{water}}$  the uncertainty related to the cooling water difference of temperature  $\Delta T_{water}$  (K),  $S_T$  the thermocouple's uncertainty (K),  $T_{water,in}$  and  $T_{water,out}$  are the water inlet and outlet temperatures (K) used to calculate the difference of water temperature  $\Delta T_{water}$  (K), and  $T_{co,3LHP}$  is the three-leg heat pipe outer condenser wall temperature (K).

To estimate the different heat pipe thermal resistances, the evaporator, adiabatic, and condenser heat pipe temperatures were obtained by taking the average of the relevant surface thermocouples. As an example, the uncertainty related to the evaporator, pool boiling section temperature  $S_{T_{evaporator,pb}}$  is calculated from:

$$S_{T_{evaporator,pb}} = \frac{S_T}{\sqrt{n}} \quad (3-37)$$

with  $S_T$  the thermocouples uncertainty (K), and  $n$  the number of relevant thermocouples used in the section. As the uncertainty equations are similar for all thermal resistances, the pool boiling section thermal resistance uncertainty  $S_{R_{pb}}$  only is detailed as an example and can be estimated using:

$$S_{R_{pb}} = R_{pb} \sqrt{\frac{S_{T_{evaporator,pb}}^2 + S_{T_{adiabatic}}^2}{(T_{evaporator,pb} - T_{adiabatic})^2} + \left(\frac{S_{\dot{Q}}}{\dot{Q}}\right)^2} \quad (3-38)$$

where  $R_{pb}$  is the pool boiling thermal resistance (K/W),  $S_{T_{evaporator,pb}}$  the temperature uncertainty of the evaporator, pool boiling section (K),  $S_{T_{adiabatic}}$  the temperature uncertainty of adiabatic section (K),  $T_{evaporator,pb}$  the evaporator, pool boiling section temperature (K),  $T_{adiabatic}$  the adiabatic section temperature (K), and  $S_{\dot{Q}}$  the uncertainty related to the heat transfer rate  $\dot{Q}$  (W).

### 3.6.3 Standard deviation

The uncertainties presented represent the theoretical errors that are made during the experiments. Those uncertainties are based on the estimated inaccuracies of the thermocouples and flow rate measurement which are propagated to the data. Yet, experimentally, the error between similar experiments differs from the estimations and can be studied in terms of standard deviation between the series. This method permits an estimate of the scatter of the data. Hence, it seems relevant to compare both theoretical errors (uncertainties) and observed experimental errors (standard deviation).

#### 3.6.3.1 Three-leg multi-channel heat pipe apparatus

For the three-leg multi-channel heat pipe experiments, the estimated and experimental errors made in the calculation of the heat transfer rate and equivalent top cylinder thermal resistance are presented in Figure 3-27.

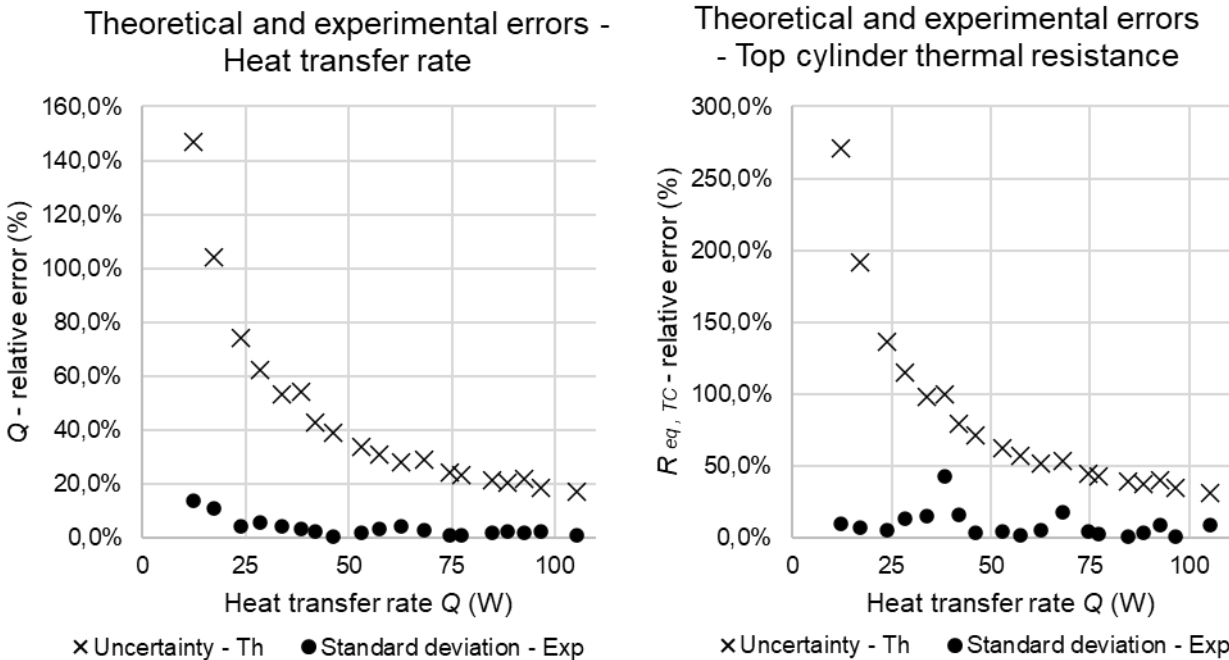


Figure 3-27. Theoretical and experimental errors of the heat transfer rate and equivalent top cylinder resistance during the multi-channel flat heat pipe experiments

Due to the low heat transfer rates investigated during the test of the three-leg heat pipe, the uncertainty during the estimation of the heat transfer rate is relatively high. Indeed, even if the cooling water flow rate was set to 1 L/min, at heat transfer rates lower than 25W, the difference of temperature between the cooling water inlet and outlet are very small. Hence, the relative error of the thermocouple accuracy is high which leads to uncertainties higher than 70% at heat transfer rates below 25W. With an increase in the heat transfer rate, the temperature difference in the cooling water increases and the temperature measurement error becomes less significant. This decrease of the theoretical uncertainty with the increase of the heat

transfer rate is also observed on the estimation of the thermal resistance of the top cylinder. Yet, experimentally, the standard deviation between similar experiments is lower than the theoretically estimated uncertainties. Indeed, while estimating the experimental heat transfer rate, a maximum standard deviation of 20% was observed. For the top cylinder thermal resistance, the maximum standard deviation measured was about 50%. This attests that the experimental results were close while repeating similar experiments. Overall, the standard deviation decreases with the increase of the heat transfer rate due to higher temperature differences between the heat pipe sections. Yet, for the estimation of the top cylinder thermal resistances, the standard deviation was higher at 35W and 65W due to the geyser boiling pattern. Figure 3-28 presents the uncertainties and standard deviation propagated to the boiling, condensation and total thermal resistances of the three-leg heat pipe.

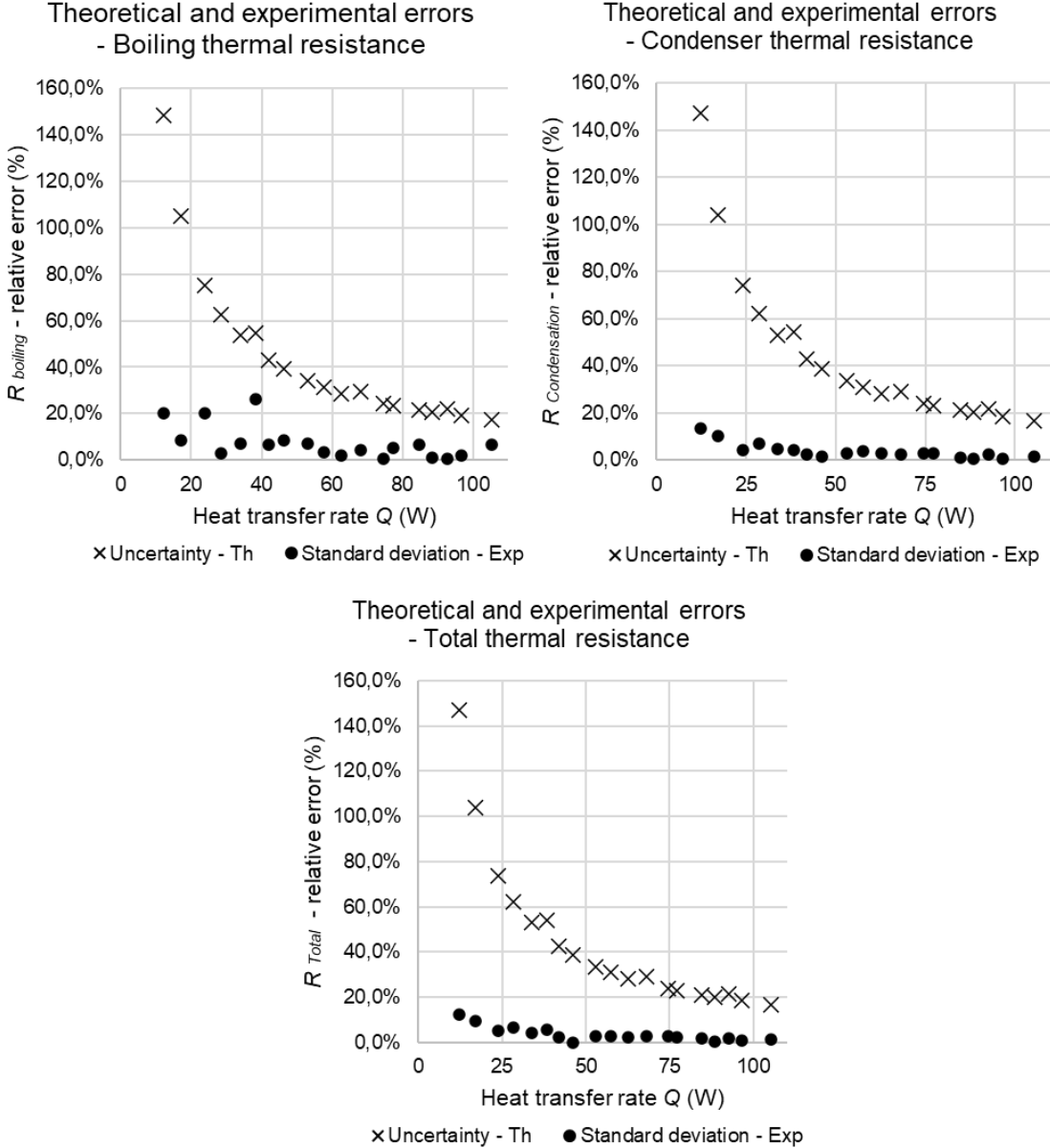


Figure 3-28. Theoretical and experimental errors of the boiling, condensation, and total thermal resistances during the three-leg heat pipe experiments

From Figure 3-28 it can be noted that the uncertainty for all the heat pipe resistances is similar and directly linked to the uncertainty on the estimation of the heat transfer rate. The theoretical uncertainties are higher than 70% below 25W. More interestingly, noticeable differences can be observed in the experimental standard deviation of the heat pipe. The experimental boiling resistance of the three-leg heat pipe is low and more difficult to measure accurately due to the low temperature difference between the evaporator and adiabatic sections. This led to a high standard deviation of up to 50% at heat transfer rates below 50W and justifies that a large number of experiments had to be carried out to obtain accurate results. The condensation and total thermal resistances of the three-leg heat pipe were more important and, as such, easier to measure experimentally. Therefore, for both condensation and total thermal resistance, the standard deviation between similar experiments was lower than 20% and the results were homogeneous.

### 3.6.3.2 Multi-channel flat heat pipe apparatus

For the multi-channel flat heat pipe experiments, the estimated and experimental errors made in the calculation of the heat transfer rate and cooling manifold resistance are presented in Figure 3-29.

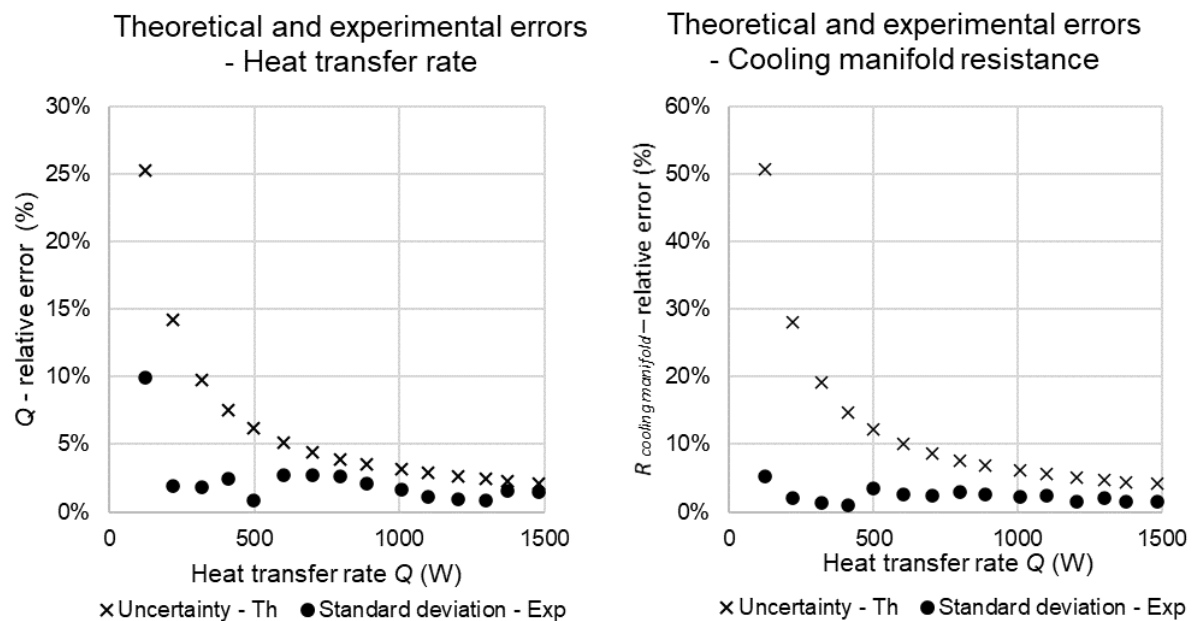


Figure 3-29. Theoretical and experimental errors of the heat transfer rate and cooling manifold resistance during the multi-channel flat heat pipe experiments

While calculating the heat transfer rate, an uncertainty of 32W was predicted but the experimental standard deviation was observed to be a maximum of 22W. The maximum theoretical error was 25% but the highest experimental error was measured to be 10%. Even if the error made on the cooling manifold resistance was estimated to be up to 50%, experimentally, the standard deviation between four series of experiments was lower than 10%.

The errors propagated to the boiling, condensation, and total thermal resistances of the multi-channel flat heat pipe are presented in Figure 3-30.

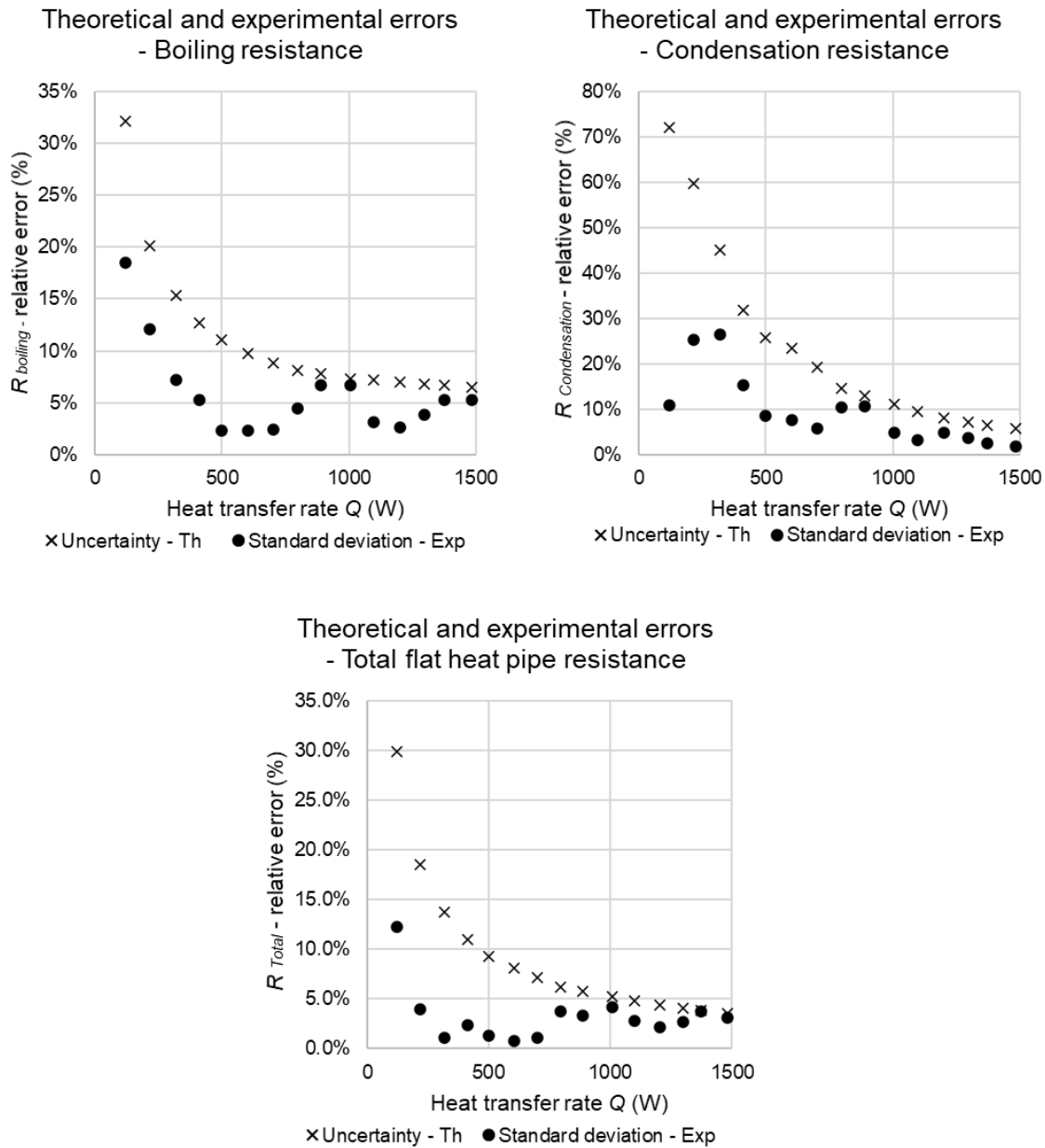


Figure 3-30. Theoretical and experimental errors of the boiling, condensation, and total flat heat pipe thermal resistance during the multi-channel flat heat pipe experiments

Happily, the experimental standard deviation for the boiling and condensation thermal resistances of the multi-channel flat heat pipe were lower than 20% and 30% respectively which guarantees a decent accuracy of the experimental results. Nevertheless, to reduce the inaccuracies, the number of data points was increased. From Figure 3-30, it can be noted that the experimental error was higher at low heat transfer rates. For instance, at a heat transfer rate of 100W, the experimental error on the total heat pipe thermal resistance was 12.2%. Yet, at heat transfer rates higher than 100W, the standard deviation between the four experimental series was lower than 5%.

# Chapter 4 - Theoretical modelling

In this chapter, first a review of the current knowledge of two-phase heat transfer occurring in single wickless heat pipes is reported. Based on the current knowledge of the two-phase cycle taking place in a single heat pipe, this cycle is then adapted to a multi-channel geometry and a new thermal resistance network derived. Finally, the proposed multi-channel heat pipe thermal resistance network is used to develop theoretical models of the two heat pipes investigated: the three-leg multi-channel heat pipe and the multi-channel flat heat pipe.

## 4.1 Two-phase heat transfer in single heat pipes

This section is based on two state of the art manuscripts published by the author of this thesis: *Guichet et al.* [73], [111].

### 4.1.1 Two-phase working cycle in a single thermosyphon

Heat pipes use the two-phase cycle of a working fluid to transfer large amounts of thermal energy. During this cycle, several mechanisms have been observed and studied by researchers. Even if such mechanisms are not fully understood to date, they seem to be clearly identified and are schematized in Figure 4-1.

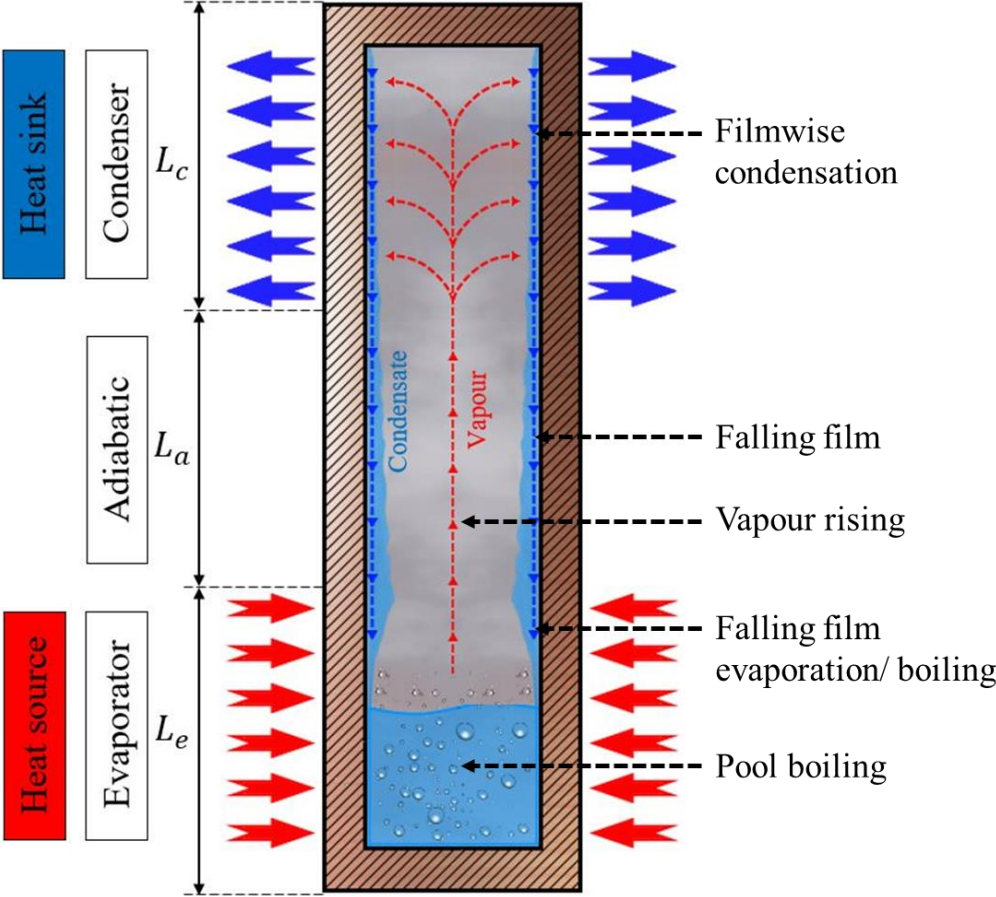


Figure 4-1. Two-phase working fluid cycle in a wickless heat pipe (thermosyphon)

At the bottom of the heat pipe, the working fluid is present under liquid form at saturated conditions. With the contact with a heat source, thermal energy is transferred by conduction through the heat pipe wall and makes the liquid pool boil. This mechanism is designated as pool boiling. Inside the pool, the motion of fluid observed is due to the boiling activity only and the creation of vapour bubbles inside the liquid bulk. Attracted by the temperature gradient inside the heat pipe, the generated vapour phase of the working fluid rises to the cold point of the condenser, thus, carrying latent energy. At the contact with the heat sink, the vapour condenses along the wall and releases its thermal energy. On the inside wall, a liquid condensate forms and becomes thicker at the bottom of the condenser. Indeed, a significant portion of the rising vapour condenses on the formed condensate itself. This phenomenon is designated as filmwise condensation. Under the action of gravity (thermosyphons) or wicks (heat pipes), the formed condensate returns to the evaporator. At the adiabatic section, no heat transfer takes place. However, due to the interactions with the rising vapour, the flow development evolves, and waves/turbulence can be formed in the falling condensate film. Once it reaches the evaporator section, in the case where the liquid pool does not occupy the whole evaporator volume (filling ratio  $FR < 100\%$ ), the condensate can get in contact with the heated wall. In this case, the falling film can evaporate and even boil before reaching the liquid pool. This heat transfer mechanism is designated as falling film evaporation and boiling.

#### 4.1.2 Equivalent thermal resistance network

The concept of thermal resistances is used to estimate the thermal performance of heat pipes. The heat pipe thermal resistance relates the heat transfer rate passing through the system to the temperatures of the heat pipe as:

$$\dot{Q} = \frac{(T_e - T_c)}{R_{hp}} \quad (4-1)$$

where  $\dot{Q}$  is the heat transfer rate through the system (W),  $T_e$  and  $T_c$  the evaporator and condenser temperatures (K), and  $R_{hp}$  the thermal resistance of the heat pipe (K/W). In the objective of theoretically predicting the thermal performance of a system, each heat transfer mechanism is described by a thermal resistance which is estimated using correlations. This approach is called the thermal resistance analogy. In the case of a single thermosyphon, the commonly adopted thermal resistance network is presented in Figure 4-2 [73], [105].



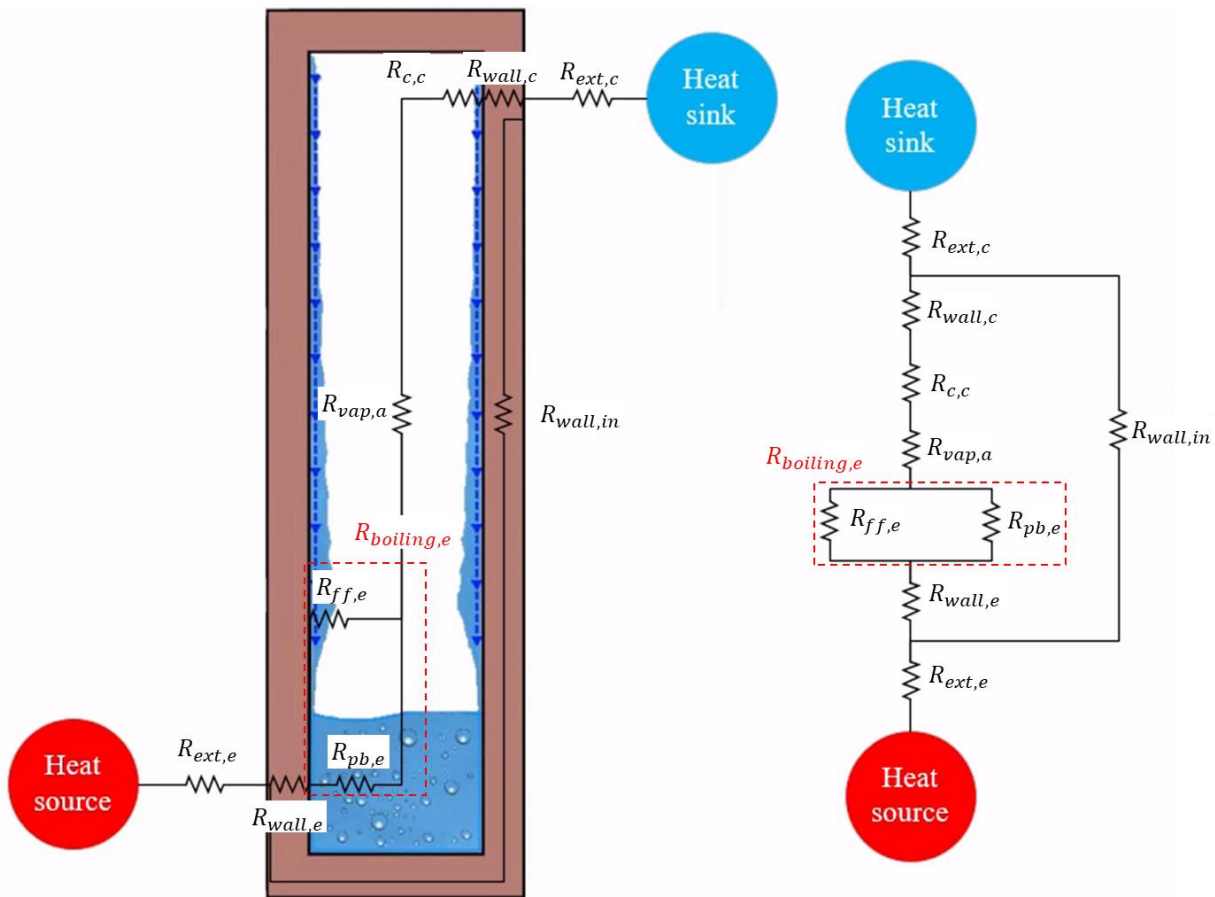


Figure 4-2. Single thermosyphon thermal resistance model

The analogy between the two-phase cycle of a thermosyphon and the equivalent thermal resistance network is presented on the left side of Figure 4-2, whereas, on the right, the thermal resistance network alone is shown. Depending on the nature of the heat source and of the heat sink, external thermal resistances  $R_{ext}$  are used and evaluate the heat transfer at the contact between the heat source and the thermosyphon, and between the thermosyphon and the heat sink. Typically, these thermal resistances can be contact thermal resistances between a heater and the thermosyphon, forced convection resistances, or even radiative resistances. As heat is received by the wall of the thermosyphon, thermal energy is transferred by conduction inside the wall in the radial and transverse directions. Hence, two radial conduction resistances  $R_{wall,e}$  (evaporator) and  $R_{wall,c}$  (condenser), and a transverse conduction resistance  $R_{wall,in}$  are included in the resistance network. Such conduction resistances can be calculated by validated conduction correlations. At the evaporator, the hot wall transfers heat to the working fluid by two mechanisms. At the bottom of the evaporator, thermal energy is used to make the liquid pool boil whereas at the top of the evaporator, the thermal energy received makes the falling film evaporate. These are represented by two parallel thermal resistances:  $R_{pb,e}$  which represents the pool boiling thermal resistance and  $R_{ffb,e}$  which represents the falling film boiling thermal resistance. These two parallel thermal resistances

form the equivalent boiling resistance of the thermosyphon. As the vapour rises along the heat pipe, minor changes of temperature can occur. This is schematized by the introduction of the vapour thermal resistance  $R_{vap,a}$ . In practice, this heat loss is very small and is usually neglected by researchers. Finally, to characterise the efficiency of the heat transfer at the condenser section, a condensation thermal resistance  $R_{c,c}$  is introduced.

Based on the thermal resistance network presented, the total thermal resistance of the heat pipe  $R_{hp}$  is calculated from:

$$R_{hp} = \left[ \frac{1}{R_{wall,in}} + \frac{1}{R_{wall,e} + R_{boiling,e} + R_{c,c} + R_{wall,c}} \right]^{-1} \quad (4-2)$$

and the equivalent boiling thermal resistance  $R_{boiling,e}$  given by:

$$\frac{1}{R_{boiling,e}} = \frac{1}{R_{pb,e}} + \frac{1}{R_{ffb,e}} \quad (4-3)$$

where  $R_{pb,e}$  and  $R_{ffb,e}$  are the pool boiling thermal resistance and falling film boiling thermal resistances (K/W), respectively.

If the theoretical equations used to estimate the conduction thermal resistances are well known and theoretically demonstrated, to estimate the two-phase thermal resistances of pool boiling, filmwise condensation, and falling film boiling, semi-empirical correlations must be used. Such correlations are usually given in terms of a heat transfer coefficient  $h$  which is used to calculate the corresponding thermal resistance as:

$$R = \frac{1}{hA} \quad (4-4)$$

with  $R$  the two-phase thermal resistance (K/W),  $h$  the two-phase heat transfer coefficient (W/m<sup>2</sup>K), and  $A$  the corresponding heat transfer area (m<sup>2</sup>). Then, the study of each two-phase mechanism aims at better understanding the physical behaviour of the heat transfer and developing suitable correlations to estimate the heat transfer coefficient. In the next sections, each two-phase heat transfer mechanism is studied separately, and the correlations developed to date are reported.

### 4.1.3 Pool boiling

Pool boiling refers to the phase change process of a static volume of fluid inside which the heat flux imposed on the surrounding walls generates the formation of vapour bubbles in the liquid pool. By undergoing a phase change from liquid to vapour, thermal energy is carried in the form of latent heat by the vapour bubbles created. The heat transfer is also greatly improved depending on the agitation of the bubbles that generates a mixing of the fluid. Hence, in pool boiling, the bubble dynamics, from their formation process, shapes and diameters, release frequency and density in the pool, rule pool boiling heat transfer. Studying the scientific phenomena related to bubbles provides the micro scale keys to better understand the different

boiling regimes and their corresponding pool boiling heat transfer coefficients on a macro scale. On a heat pipe perspective, studying these fundamentals provides guidance to improve the performance of the manufactured heat pipes, and understand the origin of the available correlations predicting the pool boiling heat transfer coefficient.

#### 4.1.3.1 *Bubble formation and nucleation process*

- **Nucleation process**

The nucleation process designates the process during which a bubble is created. Depending on the location of the vapour bubble, two types of nucleation processes exist. In the case where the bubble is created among the liquid bulk, the nucleation process is designated as “homogeneous nucleation”. In contrast, when the bubble is formed near the hot wall at the solid-liquid interface, the nucleation process is called “heterogeneous nucleation”. During a homogeneous nucleation process, local fluctuations of temperature within the volume of liquid can trigger the generation of a bubble with a diameter large enough for the bubble to persist. During this process, the amount of energy required is high, and the local temperature of the liquid must be significantly superior to the working fluid saturation point. In pool boiling, due to the higher amount of energy required, homogeneous nucleation processes are rare and heterogeneous nucleation largely prevails. In heterogeneous nucleation, the microscopic seeds of vapour called “nuclei” that initiate the formation of bubbles develop in microscopic cavities situated on the metal surface. This growth is favoured by the formation of a hot layer of fluid near the wall called “thermal layer”, in which the fluid temperature is higher due to the proximity with the hot surface. Depending on the surface aspect and roughness, the number of cavities and their dimensions vary which influences the heterogeneous process and this highlights the link between the boiling activity and the aspect of the surface. The influence of the cavities as nucleation sites must be studied to explain the lower level of energy needed for the development of a bubble under heterogeneous nucleation, which was observed by *Cole* [112] and *Rohsenow* [99]. In reality, during the injection of the liquid into the pool, small portions of gas remain trapped in microcavities. Then, the creation of a bubble is already initiated by the presence of a vapour nucleus in the cavity. Later, the development of a bubble only requires energy for the growth of the bubble seed into a larger bubble forming near the wall.

- **Bubble growth**

In most of the cases where the bubble forms under the heterogeneous nucleation process near the wall, several steps are identified during the growth of the bubble which conducts the vapour nucleus trapped in the cavity to form a bubble and get released from the wall. The cyclic bubble growth model by *Carey* [113] is presented in Figure 4-3, which identifies six stages leading to the departure of a bubble from a cavity.

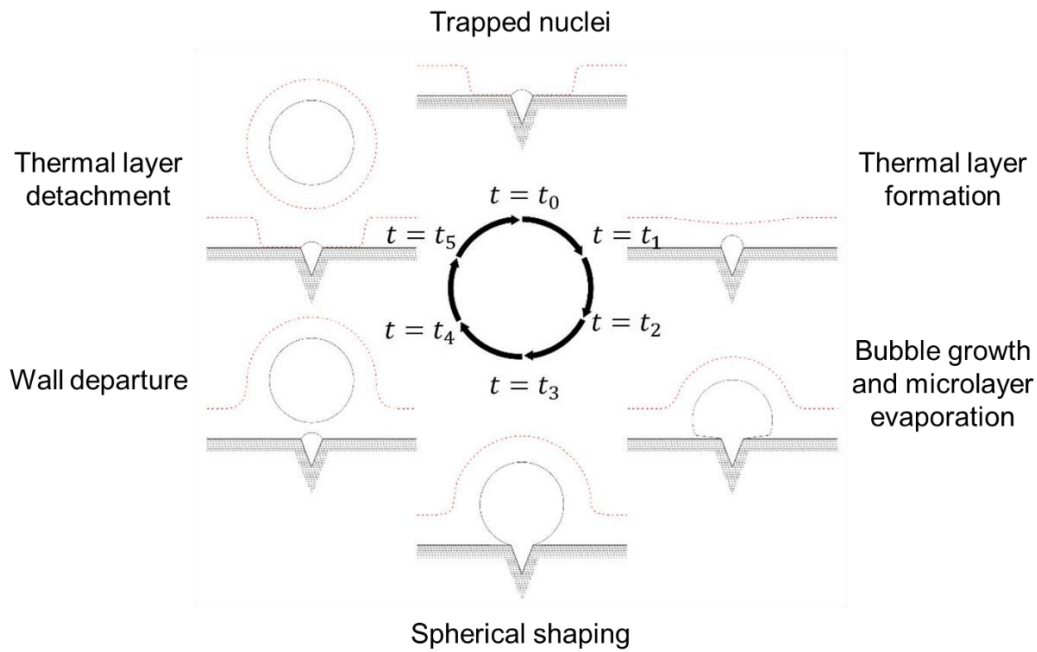


Figure 4-3. Cyclic model of bubble growth from a surface, adapted from Carey [24]

For purposes of clarity, each stage from  $t = t_0$  to  $t = t_5$  is detailed hereafter. At  $t = t_0$ , with the departure of the previous bubble, a vapour nucleus is left behind and trapped inside the cavity. Near the hot wall, the thermal layer which is the liquid volume at a higher temperature due to its proximity with the hot surface has been locally removed and entrained by the previous bubble. This stage is schematized in Figure 4-4.

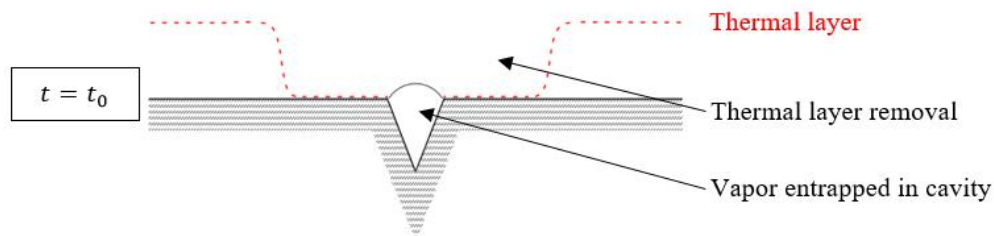


Figure 4-4. Bubble growth from a surface, stage  $t = t_0$

During a short period of time after the previous departure of a bubble, the new bubble does not grow. For a given waiting period, the thermal layer near the wall reforms. Colder liquid from the volume reaches the hot surface and locally warms up near the cavity. This is schematized in Figure 4-5.

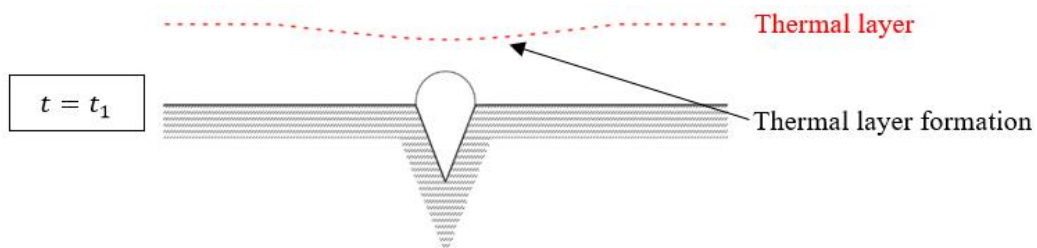


Figure 4-5. Bubble growth from a surface, stage  $t = t_1$

Once the thermal layer is formed, the higher liquid temperature near the cavity favours the growth of the vapour nucleus into a semi-circular bubble. At the interface between the vapour bubble and the liquid, a portion of the hot liquid from the thermal layer undergoes a phase change and turns to vapour. The growth of the bubble is significantly improved by the presence of a microlayer of liquid between the base of the semi-circular bubble and the hot surface. This very thin portion of liquid evaporates rapidly and is responsible for the quick growth of the bubble during this early stage. This is schematized in Figure 4-6.

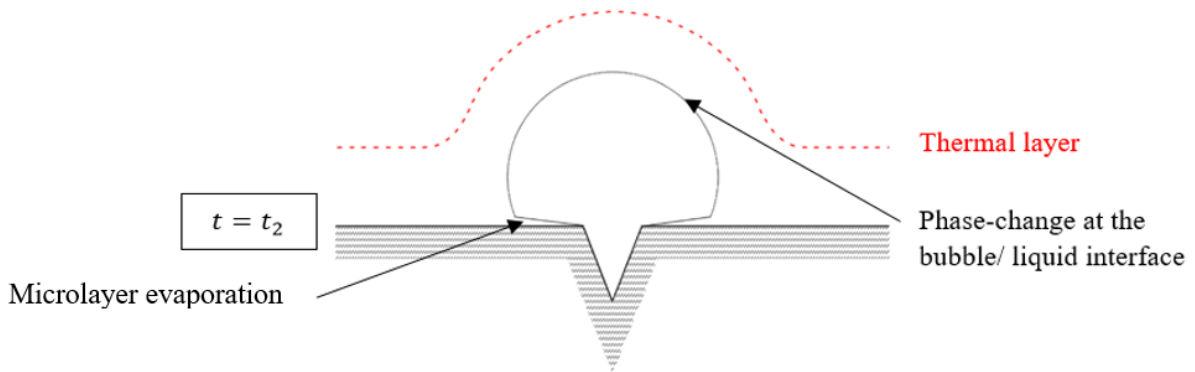


Figure 4-6. Bubble growth from a surface, stage  $t = t_2$

In a later stage of the growth of the vapour, the bubble takes a spherical shape and the presence of a microlayer at the base of the bubble disappears. Hence, the growth of the bubble slows down, and the vapour volume increases due to the phase change at the liquid-vapour interface only. This is schematized in Figure 4-7.

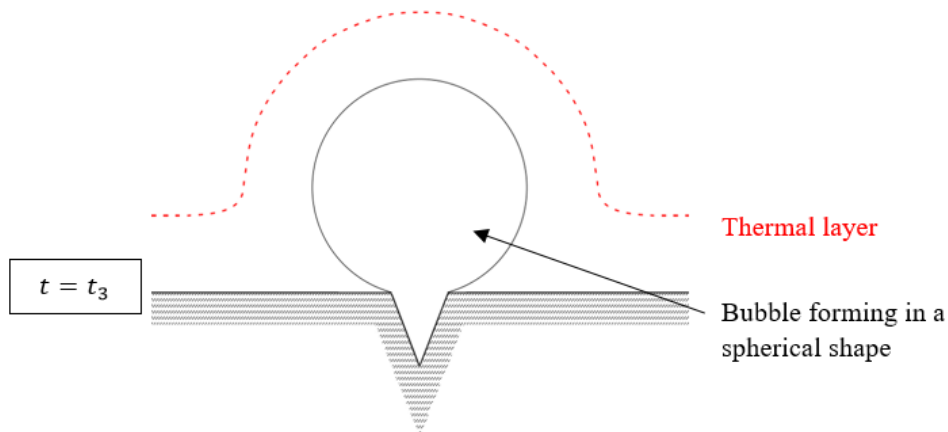


Figure 4-7. Bubble growth from a surface, stage  $t = t_3$

Once the bubble reaches its departure diameter, the bubble is dragged away by the buoyancy force and detaches from the cavity. While doing so, a small portion of vapour remains trapped in the cavity and will start the next heterogeneous nucleation process. This is schematized in Figure 4-8.

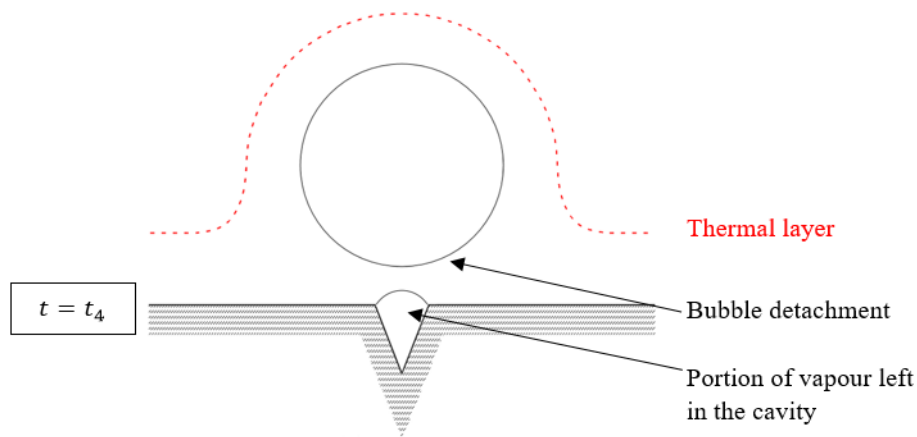


Figure 4-8. Bubble growth from a surface, stage  $t = t_4$

The last stage of a bubble departure is of importance to understand why boiling represents a high heat transfer potential, and how a high bubble activity can improve the boiling heat transfer coefficient of a thermosyphon. Once departing from the wall, a portion of the thermal layer is removed from the surface and carried away by the departing bubble. Two processes simultaneously occur: on the one hand, the superheated thermal layer around the bubble mixes with the liquid bulk whose temperature increases by enhanced convection, whereas, on the other hand, colder fluid from the liquid bulk is able to reach the hot surface and warms up by transient conduction. In addition, the rising bubble acts as an energy mover and mixes the liquid pool, thus, increasing the heat transfer potential. Finally, once the thermal layer is consumed by the liquid pool, the bubble itself conveys its energy as sensible heat transport. If the surrounding pool is at a temperature lower than the saturation point, the bubble will be consumed and delivers its energy by vapour to liquid phase change. However, if the pool temperature is high enough, the bubble will persist and rise to the pool surface. These combined phenomena responsible for the high heat transfer coefficients during pool boiling are represented in Figure 4-9.

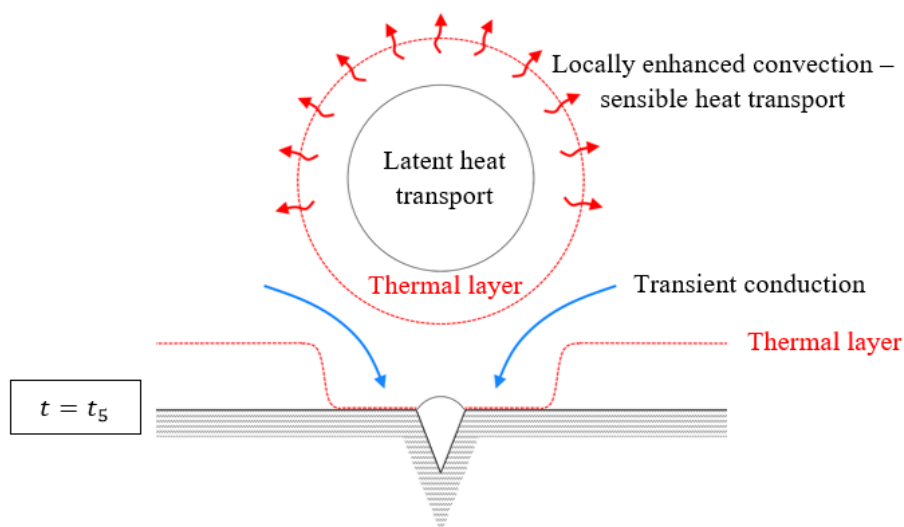


Figure 4-9 Bubble growth from a surface, stage  $t = t_5$ .

Finally, the formation process of a new bubble restarts by heterogeneous nucleation from the cavity. Thus, by the latent heat transport from the bubble, combined with the enhanced convection of the thermal layer removed from hot wall region, the transient conduction of the bulk liquid reforming the thermal layer, and the mixing of the pool due to the departure of bubbles, the bubble activity is responsible for the high heat transfer coefficients observed during boiling. In this regard, many parameters related to the bubble dynamics such as the departure diameter, frequency, and number of active nucleation sites are of interest when trying to predict pool boiling heat transfer coefficients.

- **Departure diameter and frequency**

An intensively studied parameter in the investigation of pool boiling is the estimation of the size and frequency of the bubble at its departure. By operating a force balance between the surface tension of the bubble and the buoyancy force, *Fritz* [114] showed that the bubble departure diameter  $D_d$  is proportional to the following:

$$D_d \propto \theta \sqrt{\frac{\sigma}{g(\rho_l - \rho_v)}} \quad (4-5)$$

where  $\theta$  is the surface contact angle ( $^\circ$ ),  $\sigma$  is the surface tension (N/m),  $g$  is the gravitational acceleration ( $\text{m/s}^2$ ), and  $\rho_l$  and  $\rho_v$  are the liquid and vapor densities ( $\text{kg/m}^3$ ). Based on the references [73], [105], [115]–[122], the *Cole* [123] correlation has been widely used for the prediction of the bubble departure diameter and is recommended:

$$D_d = 0.04 \times Ja \sqrt{\frac{\sigma}{g(\rho_l - \rho_v)}} \quad (4-6)$$

with  $Ja$  the Jakob number defined by:

$$Ja = \frac{[T_W - T_{sat}(P_l)]c_{p,l}\rho_l}{\rho_v i_{lv}} \quad (4-7)$$

and  $T_W$  the wall temperature (K),  $T_{sat}(P_l)$  the saturation temperature under the liquid pressure  $P_l$  (K),  $c_{p,l}$  the liquid specific heat (J/kg.K),  $\rho_l$  and  $\rho_v$  the liquid and vapor densities ( $\text{kg/m}^3$ ), and  $i_{lv}$  the latent heat of vaporization (J/kg). Despite some limits reported by researchers on the correlation by *Cole* [123], the prediction usually fits with experimental data with an error within  $\pm 30\%$ .

When studying the departure of bubbles from a single nucleation site, a cyclic process is repeated, and, under steady state conditions, it seems that bubbles leave the cavity with a given frequency. As explained by *Collier and Thome* [124] in Figure 4-10, the nucleate boiling activity from a single cavity consists of a waiting period and a bubble growth period.

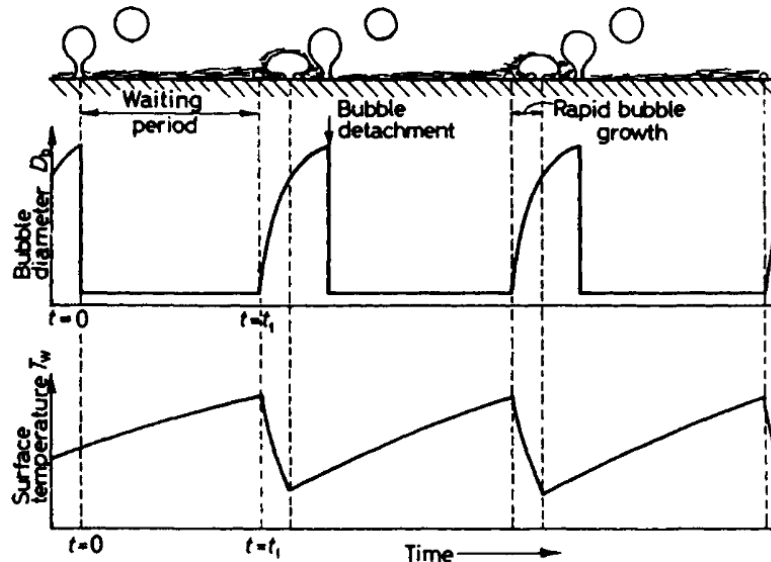


Figure 4-10. Bubble departure frequency, bubble growth period and waiting period, from *Collier and Thome* [78]

Based on the previously introduced phenomena such as the thermal layer formation, evaporation of the liquid micro layer, bubble growth and its departure, small and periodic fluctuations of the local wall temperature are detected. Then, based on the proposed model by *Collier and Thome* [124], it is understood that the bubble departure frequency is related to the time taken by the bubble growth and thus, to the bubble departure diameter. In this regard, correlations predicting the bubble departure frequency are usually correlated in terms of bubble departure diameter. Based on the references [73], [105], [119], [120], [125]–[127], the bubble departure frequency correlation by *Cole* [128] is also widely recommended. This correlation was obtained by balancing the buoyancy and drag force and the authors are considered as a main reference in the study of bubbles. The bubble departure frequency  $f_d$  was correlated by *Cole* [128] as:

$$f_d D_d^{1/2} = \left[ \frac{4g(\rho_l - \rho_v)}{3\rho_l} \right]^{1/2} \quad (4-8)$$

For the references studied, the accuracy of this correlation is reported as acceptable in most cases.

- **Number of active nucleation sites**

Even if the presence of cavities represents potential nucleation sites, some nucleation sites can be inactive and do not produce bubbles. In addition to the wall superheat needed to create a bubble from a trapped vapour nucleus, a second condition to the activity of a nucleation site is the entrapment of a small amount of gas in the microscopic cavity of the surface. Indeed, during the introduction of the liquid inside the pool or with the boiling activity, a cavity can be rewetted by the liquid phase, thus preventing future bubbles from being formed from this cavity. In this case, the nucleation site becomes inactive. The condition of the entrapment of a vapour nucleus depends on the contact angle of the advancing wave of liquid, and the geometry of



cavities. Then, surfaces with different aspects and roughness present various numbers of active nucleation sites under similar conditions. This highlights the relation between the aspect of the hot wall surface to the boiling activity and thus, to the pool boiling heat transfer coefficient. This fact has made the prediction of the number of active nucleation sites from a given surface tedious. Nevertheless, *Zhokhov* [129] tried to correlate the number of active nucleation site  $N_a$  without considering the surface aspect as:

$$\sqrt{N_a} = 25 \times 10^{-8} \left( \frac{i_{lv} \rho_v \Delta T}{T_{sat} \sigma} \right)^{1.5} \quad (4-9)$$

Yet, in their work, *Wang and Dhir* [130] showed that the number of active nucleation sites is related to the cavities' diameters, and that the density of nucleation sites with small diameters is higher than that of larger diameters. In accordance with this observation, *Mikic and Rohsenow* [131] proposed a correlation relating the number of active nucleation sites to the cavity radius on the surface:

$$N_a = C \left( \frac{r_{cav,max}}{r_{cav}} \right)^m = C r_{cav,max}^m \left( \frac{i_{lv} \rho_v}{2 T_{sat} \sigma} \right)^m \Delta T_{sat}^m \quad (4-10)$$

where  $C$  is an experiment-based constant often taken as  $C = 1 \text{ unit.m}^{-2}$ ,  $r_{cav,max}$  is the maximum active cavity radius on the surface (m), and  $m$  is a constant (typically,  $m = 6.5$ ). Based on the study of the number of nucleation site from a surface, it is highlighted that the aspect of the surface is highly related to the boiling activity. This interaction is partly responsible for discrepancies observed in the boiling activities carried out by various researchers and makes the prediction of pool boiling heat transfer coefficient challenging.

#### 4.1.3.2 Pool boiling regimes and boiling curves

Moving from a micro scale to a macro scale, looking at the overall liquid pool, different boiling regimes are observed. Depending on the temperature of the bulk liquid, boiling is first described as "subcooled" if the bulk liquid temperature is lower than the saturation point, and "saturated" when the bulk liquid temperature has reached the saturation point. In subcooled boiling, vapour bubbles can form near the wall where the thermal layer is at a saturation temperature, but the departing bubble collapses within the liquid bulk at a lower temperature. In contrast, during saturated boiling, the departing bubble persists in the liquid volume and reaches the surface of the pool. The pool boiling heat flux, which is proportional to the pool boiling heat transfer coefficient, varies, depending on the wall superheat. The pool boiling heat flux  $q''_{pb}$  is related to the pool boiling heat transfer coefficient  $h_{pb}$  as follows:

$$q''_{pb} = h_{pb}(T_W - T_{sat}) = h_{pb} \Delta T_{sat} \quad (4-11)$$

with  $T_W$  the wall temperature (K), and  $T_{sat}$  the saturation temperature (K). Depending on the boiling heat flux measured while increasing the wall superheat, different boiling regimes have been identified and are reported in the pool-boiling curve in Figure 4-11 [14].

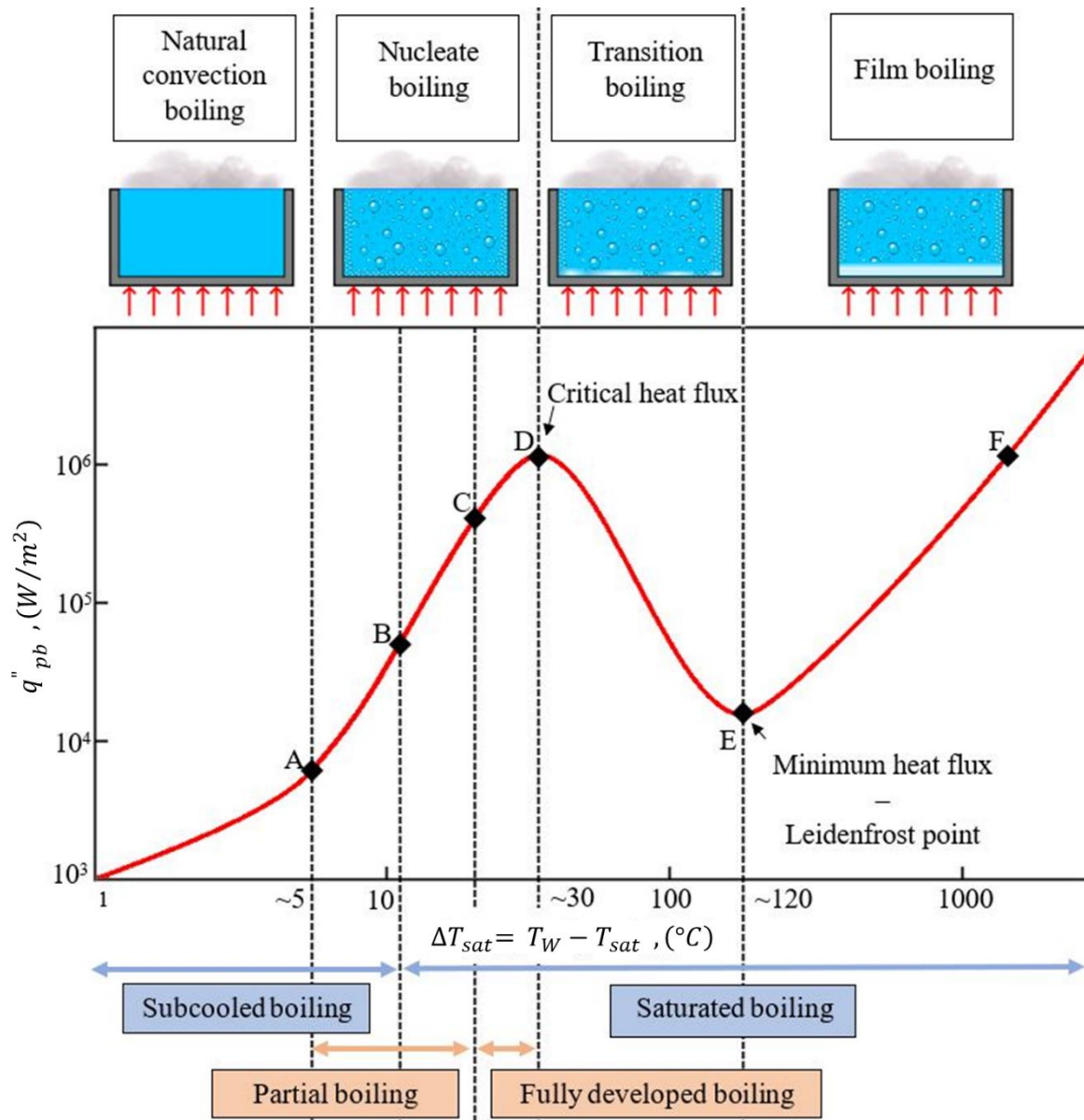


Figure 4-11. Pool boiling curve of water at 1 atm pressure, adapted from Yunus A. Cengel [20]

The pool boiling curve reveals that, for different values of wall superheat  $\Delta T_{sat}$ , the pool boiling heat flux  $q''_{pb}$  does not vary linearly. In particular, it is observed that increasing the wall superheat above a certain value may no longer increase the boiling heat flux. The optimum boiling regimes must be aimed with the objective of maximizing the pool boiling heat transfer coefficient. While increasing the wall superheat, the following pool boiling regimes can be found:

- **Natural convection boiling (to point A)**

At a wall superheat of only a few degrees ( $\Delta T_{excess} \leq 5^{\circ}C$ ), the bulk liquid temperature is lower than the saturation point. Only the thermal layer situated near the wall reaches the saturation temperature which is not sufficient for the growth and departure of bubbles. With an increase of the wall superheat, small bubbles forming on the surface may be seen but they do not leave

the surface. In natural convection boiling, the fluid motion is very limited and only natural convection streams are acting. Due to the very limited motion of the pool and non-formation of bubbles, natural convection boiling is avoided because the corresponding heat transfer coefficients are low.

- **Nucleate boiling (Point A to D)**

Once the wall superheat is high enough for bubbles to grow and depart from the wall, the pool boiling heat flux increases rapidly. With the previously described phenomena related to the growth and departure of bubbles, the heat transfer coefficient improves significantly and marks a transition to a new boiling regime called nucleate boiling. Despite its complexity, nucleate pool boiling has received a lot of attention as the heat transfer coefficients in this regime are high. Two-phase heat exchangers such as heat pipes and thermosyphons aim at nucleate pool boiling as their boiling regime. Yet, due to the appearance of various bubble phenomena, different regions exist in the pool boiling regime, and selecting the suitable wall superheat can result into a direct improvement of the nucleate pool boiling heat transfer coefficient. Some researchers such as *Nishikawa* [132] and *Merte et al.* [133] have observed that, with an increase in the wall superheat, the nucleate boiling heat flux becomes independent of factors such as the depth of the pool, tilt angle, and others. Two regions are designated as “partial boiling” and “fully developed boiling”. In partial boiling, also called isolated bubble region, each bubble forming, growing, and detaching from the hot surface rises independently. As the nucleate boiling transits to the fully developed region, bubbles start merging and form columns of vapour or larger vapour mushrooms. These bubble phenomena occurring during nucleate boiling were studied by *Gaertner* [134] whose model is presented in Figure 4-12.



Figure 4-12. Bubble phenomena during nucleate boiling regime, from *Gaertner* [95]

An interesting aspect of the bubble phenomena model proposed by *Gaertner* [134] is that it can be related to the pool boiling curve. Within the nucleate pool boiling region, three regions are identified:

- Subcooled and partial nucleate boiling (Point A to B):

In this region, discrete and isolated bubbles (Figure 4-12 (a)) are forming at the nucleation sites and depart from the wall. However, due to the subcooled nature of the pool, the bubbles are consumed by the bulk liquid, which warms it up more rapidly. Even if the boiling heat transfer coefficient progressively increases with the increase in bubble activity, the number and

volume of vapour bubbles are relatively small, and the stirring action remains limited. This stage corresponds to the increase of the boiling heat flux due to the generation and departure of the first isolated bubbles.

- Saturated and partial nucleate boiling (Point B to C):

With the generation of the first bubbles, the bulk liquid temperature increases rapidly, and the boiling regime becomes saturated. Then, the isolated bubbles no longer collapse in the liquid pool and reach the surface. The increase of the wall superheat also increases the bubble departure frequency and thus the turbulence of the liquid pool. As a result, the boiling heat flux increases sharply. Beyond a certain value, the bubble departure frequency may become high enough to see successive bubbles merging and forming stems of vapour. If placed in the same region, stems of vapour can also potentially merge and form small vapour mushrooms (Figure 4-12 (b)). This marks the transition from partial nucleate boiling to fully developed nucleate boiling.

- Saturated and fully developed nucleate boiling (Point C to D):

In saturated fully developed nucleate pool boiling, the vapour columns from adjacent nucleation sites merge and form large vapour mushrooms above a thin liquid layer at the base called “macro-layer” (Figure 4-12 (c)). The evaporation of this macro-layer of liquid explains the independence of the fully developed boiling regime regarding some factors such as the tilt angle, depth of pool, etc. At higher wall superheat, the dry-out of the liquid macro-layer underneath the vapour mushroom (Figure 4-12 (D)) slows down the improvement of the heat transfer coefficient and will eventually lead to a critical boiling heat flux after which the heat transfer coefficient reduces.

- **Critical heat flux (Point D)**

With the consumption of the liquid macro layer situated at the base of the vapour mushrooms, the hot wall comes in contact with the vapour phase. At a given point named “critical heat flux”, some researchers such as *Nukiyama* [135] observed the incapacity of the working fluid to receive more energy. As a result, the excess thermal energy from the heating surface cannot be dissipated and a sudden rise of temperature of the surface can occur. This phenomenon is designated as “burnout”. The physical reasons leading to the burnout phenomena have been widely studied but remain to be fully understood. Four hypotheses have been proposed to try to explain this decrease in the boiling heat flux beyond the critical heat flux. Yet, the consumption of the liquid layer which leaves the hot surface in contact with the vapour phase only seems the most popular explanation [105].

- **Transition boiling (Point D to E)**

Beyond the critical wall superheat, the portion of vapour in contact with the hot wall increases further and the pool boiling heat transfer coefficient decreases. Once the liquid volume near

the wall reaches zero, the boiling heat flux reaches a local minimum. This is known as the Leidenfrost point or minimum heat flux (Point E).

- **Film boiling (Point E to F)**

In film boiling, a vapour film blankets the hot wall and separates the liquid and the heating surface. Once the hot wall is in contact with the vapour phase only, a new mode of heat transfer becomes significant. Instead of dissipating its energy by direct contact, the wall mainly transfers thermal energy to the liquid by radiation through the layer of vapour.

In heat pipes and thermosyphons, the pool boiling regimes taking place at the evaporator section are natural convection boiling and nucleate boiling. Typically, natural convection boiling can be observed at the start-up of the heat pipe or at very low heat fluxes. Yet, because of the high values of heat transfer coefficients, nucleate boiling is targeted and appears rapidly after the start-up of the heat pipe. In the design consideration of heat pipes, the dry out limit related to the critical heat flux and burnout of the evaporator is to be considered to avoid the appearance of dry patches. Therefore, nucleate pool boiling heat transfer coefficient correlations must be studied to predict the thermal performance of heat pipes and thermosyphons.

#### 4.1.3.3 Pool boiling correlations

Researchers have developed correlations to predict the nucleate pool boiling heat transfer coefficient based on the current understanding of the micro and macro phenomena involved in nucleate pool boiling. Yet, because of the complex phenomena involved such as the bubble nucleation process, the diameter and departure frequency of bubbles, the influence of the surface aspect on boiling, the number of active nucleation sites and others, the nucleate pool boiling heat transfer coefficient is difficult to predict. Moreover, the difficulty of characterising the surface aspect have led to different experimental results for researchers who used so-called similar experimental conditions (same fluid, same surface material). As a result, many correlations for predicting the nucleate pool boiling heat transfer coefficient have been reported in the literature. The pool boiling heat transfer coefficient correlations reported to date are listed in Table 4-1.

Table 4-1. Nucleate pool boiling heat transfer coefficient  $h_{nb}$  correlations

Authors	Year	Frequency of use	Fluids	Correlation
Kruzhilin [136]	1947	Very low	All	$h_{pb} = 0.082 \left( \frac{k_l}{L_b} \right) \left( \frac{i_{lv} q''_{pb} \rho_v}{g T_{sat} k_l \rho_l - \rho_v} \right)^{0.7} \left( \frac{T_{sat} c_{p,l} \sigma \rho_l}{i_{lv}^2 \rho_v^2 L_b} \right)^{0.33} Pr_l^{-0.45}$ <p>where,</p> $\ast L_b = \left[ \frac{\sigma}{g(\rho_l - \rho_v)} \right]^{1/2}$

Rohsenow [137]	1 9 5 2	Very high	All	$h_{pb} = \left( \frac{q''_{pb}}{i_{lv}} \right)^{1-r} \left[ \frac{\mu_l}{\sqrt{g(\rho_l - \rho_v)}} \right]^r \frac{c_{p,l}}{C_{sf}} Pr_l^{-s}$ <p>where,</p> <ul style="list-style-type: none"> <li>❖ <math>r = 1/3</math></li> <li>❖ <math>\begin{cases} s = n = 1 \text{ for water} \\ s = n = 1.7 \text{ for other fluids} \end{cases}</math></li> <li>❖ <math>C_{sf}</math> is a constant depending on the solid-fluid characteristics</li> </ul>
McNelly [138]	1 9 5 3	Very low	All	$h_{pb} = 0.225 \left( \frac{q''_{pb} c_p}{i_{lv}} \right)^{0.69} \left( \frac{Pk_l}{\sigma} \right)^{0.31} \left( \frac{\rho_l}{\rho_v} - 1 \right)^{0.33}$
Forster and Zuber [139]	1 9 5 5	Medium	All	$h_{pb} = \frac{0.00122 \times \Delta T_{sat}^{0.24} \Delta P_{sat}^{0.75} c_{p,l}^{0.45} \rho_l^{0.49} k_l^{0.79}}{\sigma^{0.5} i_{lv}^{0.24} \mu_l^{0.29} \rho_v^{0.24}}$ <p>where,</p> <ul style="list-style-type: none"> <li>❖ <math>\Delta P_{sat} = P_v _{T=T_w} - P_v _{T=T_{sat}}</math> is the difference in saturation (vapour) pressure between the wall temperature and the saturation temperature.</li> </ul>
Tien [140]	1 9 6 2	Very low	All	$h_{pb} = 61.3 k_l Pr_l^{0.33} N_a^{0.5} \Delta T_{sat}$
Lienhard [141]	1 9 6 3	Very low	All	$h_{pb} = C k_l Pr^{1/3} \frac{\sqrt{\sigma g(\rho_l - \rho_v)/\rho_l^2} _{fluid}}{\sqrt{\sigma g(\rho_l - \rho_v)/\rho_l^2} _{water}} N_a^{1/3} (\Delta T_{sat})^{5/4}$ <p>where,</p> <ul style="list-style-type: none"> <li>❖ <math>C</math> is an empirical constant</li> </ul>
Mostinskii [142]	1 9 6 3	Low	All	$h_{pb} = 3.596 \times 10^{-5} P_{crit}^{0.69} (q''_{pb})^{0.7} F(P^*)$ <p>where,</p> <ul style="list-style-type: none"> <li>❖ <math>F(P^*) = 1.8P^{*0.17} + 4P^{*1.2} + 10P^{*10}</math></li> <li>❖ <math>P^* = P/P_{crit}</math></li> </ul>
Mikic and Rohsenow [131]	1 9 6 9	Low	All	$h_{pb} = 2N_a D_a^2 (\pi k_l c_{p,l} \rho_l f_d)^{1/2}$ <p>To estimate the value of bubble related factors <math>N_a</math>, <math>D_a</math> and <math>f_d</math>, authors proposed:</p> <ul style="list-style-type: none"> <li>❖ <math>N_a = r_s^m \left( \frac{i_{lv} \rho_v}{2T\sigma} \right)^m \Delta T_{sat}^m</math></li> <li>❖ <math>D_a = a \left[ \frac{\sigma}{g(\rho_l - \rho_v)} \right]^{1/2} \left( \frac{\rho_l c_{p,l} T_{sat}}{\rho_v i_{lv}} \right)^{5/4}</math></li> <li>❖ <math>f_d = \frac{0.6}{D_a} \left[ \frac{\sigma g(\rho_l - \rho_v)}{\rho_v^2} \right]^{1/4}</math></li> <li>❖ <math>\begin{cases} a = 1.5 \times 10^{-4} \text{ for water} \\ a = 4.65 \times 10^{-4} \text{ for other fluids} \end{cases}</math></li> <li>❖ <math>h_{nc}</math> is the natural convection heat transfer coefficient occurring on the surface not affected by bubbles.</li> <li>❖ <math>m</math> is a coefficient that can be obtained by measuring the cavity radius distribution or to fit experimental data.</li> </ul>
Danilova [143]	1 9 7 0	Very low	Freon	$h_{pb} = C \left( \frac{R_a}{R_{a0}} \right)^{0.2} (0.14 + 2.2P^*) q''_{pb}{}^{0.75}$ <p>where,</p> <ul style="list-style-type: none"> <li>❖ <math>C</math> is an empirical constant</li> </ul>
Labuntsov [144]	1 9 7 3	Medium	All	$h_{pb} = 0.075 \left[ 1 + 10 \left( \frac{\rho_v}{\rho_l - \rho_v} \right)^{0.67} \right] \left( \frac{k_l^2}{v_l \sigma T_{sat}} \right)^{0.33} q''_{pb}{}^{0.67}$
Imura et al. [145]	1 9	Very high	All	$h_{pb} = 0.32 \left( \frac{\rho_l^{0.65} k_l^{0.3} c_{p,l}^{0.7} g^{0.2}}{\rho_v^{0.25} i_{lv}^{0.4} \mu_l^{0.1}} \right) \left( \frac{P_v}{P_{atm}} \right)^{0.3} q''_{pb}{}^{0.4}$

	7 9			
Stephan and Preusser [146]	1 9 7 9	Very low	All	$h_{pb} = 0.1 \left( \frac{k_l}{D_d} \right) \left( \frac{q''_{pb} D_d}{k_l T_{sat}} \right)^{0.674} \left( \frac{\rho_v}{\rho_l} \right)^{0.156} \left( \frac{i_{lv} D_d^2}{\alpha_l^2} \right)^{0.371} \left( \frac{\alpha_l^2 \rho_l}{\sigma D_d} \right)^{0.35} \left( \frac{\mu_l c_{p,l}}{k_l} \right)^{-0.14}$
Stephan and Abdelsalam [147]	1 9 8 0	High	All	$\begin{cases} h_{pb} = 0.246 \frac{k_l}{D_d} \times 10^{-7} \times X_1^{0.673} X_3^{1.26} X_4^{-1.58} X_8^{5.22} \text{ for water} \\ h_{pb} = 0.0546 \frac{k_l}{D_d} \times X_1^{0.67} X_4^{0.248} X_5^{1.17} X_8^{-4.33} \text{ for hydrocarbons} \\ h_{pb} = 4.82 \frac{k_l}{D_d} \times X_1^{0.624} X_3^{0.374} X_4^{0.329} X_5^{0.257} X_7^{0.117} \text{ for cryogenic fluids} \\ h_{nb} = 207 \frac{k_l}{D_d} \times X_1^{0.745} X_5^{0.581} X_6^{0.533} \text{ for refrigerants} \end{cases}$ <p>where,</p> <ul style="list-style-type: none"> <li>❖ <math>X_1 = \left( \frac{q''_{pb} D_d}{k_l T_v} \right)</math>, <math>X_2 = \left( \frac{\alpha^2 \rho_l}{\sigma D_d} \right)</math>, <math>X_3 = \left( \frac{c_p T_v D_d^2}{\alpha^2} \right)</math>, <math>X_4 = \left( \frac{i_{lv} D_d^2}{\alpha^2} \right)</math></li> <li>❖ <math>X_5 = \left( \frac{\rho_v}{\rho_l} \right)</math>, <math>X_6 = \left( \frac{c_p \mu_l}{k_l} \right)</math>, <math>X_7 = \left( \frac{\rho_{l,w} c_{p,l,w} k_{l,w}}{\rho_l c_{p,l} k_l} \right)</math>, <math>X_8 = \left( \frac{\rho_l - \rho_v}{\rho_l} \right)</math></li> <li>❖ <math>10^{-4} \leq P^* \leq 0.9</math> and <math>\theta = 45^\circ</math> for water</li> <li>❖ <math>5.7 \times 10^{-3} \leq P^* \leq 0.9</math> and <math>\theta = 35^\circ</math> for hydrocarbons</li> <li>❖ <math>4 \times 10^{-3} \leq P^* \leq 0.97</math> and <math>\theta = 1^\circ</math> for cryogenic fluids</li> <li>❖ <math>3 \times 10^{-3} \leq P^* \leq 0.78</math> and <math>\theta = 35^\circ</math> for refrigerants</li> </ul>
Shiraishi et al. [148]	1 9 8 1	High	All	$h_{pb} = 0.32 \left( \frac{\rho_l^{0.65} k_l^{0.3} c_{p,l}^{0.7} g^{0.2}}{\rho_v^{0.25} i_{lv}^{0.4} \mu_l^{0.1}} \right) \left( \frac{P_v}{P_{atm}} \right)^{0.23} q''_{pb}{}^{0.4}$
Bier [149]	1 9 8 2	Very low	All	$h_{pb} = 3.596 \times 10^{-5} P_{crit}^{0.69} (q''_{pb})^{0.7} F(P^*)$ <p>where,</p> <ul style="list-style-type: none"> <li>❖ <math>F(P^*) = 0.7 + 2P^* \left( 4 + \frac{1}{1-P^*} \right)</math></li> <li>❖ <math>P^* = P/P_{crit}</math></li> </ul>
Nishikawa [150]	1 9 8 2	Medium	Refrigerants	$h_{pb} = 31.4 \frac{p_{crit}^{0.2}}{M_{mol}^{0.1} T_{crit}^{0.9}} \left( 8 \frac{R_p}{R_{p0}} \right)^{0.2(1-P^*)} \frac{P^{*0.23}}{(1-0.99P^*)^{0.9}} q''_{pb}{}^{0.8}$ <p>where,</p> <ul style="list-style-type: none"> <li>❖ <math>F(P^*) = 0.7 + 2P^* \left( 4 + \frac{1}{1-P^*} \right)</math></li> <li>❖ <math>R_p</math> is the Maximum peak height of the profile</li> <li>❖ The Maximum peak height reference <math>R_{p0}</math> should be taken as: <math>R_{p0} = 1 \times 10^{-6} m</math></li> <li>❖ <math>R_p = 0.125 \times 10^{-6} m</math></li> <li>❖ <math>P^* = P/P_{crit}</math></li> </ul>
Cooper [151]	1 9 8 4	High	All	$h_{pb} = 55 (q''_{pb})^{0.67} P^{*(0.12-0.2 \log R_{a,p})} (-\log P^*)^{-0.55} M_{mol}^{-1/2}$ <p>where,</p> <ul style="list-style-type: none"> <li>❖ <math>R_{a,p}</math> is an average roughness parameter expressed in <math>\mu m</math>. If unknown, a default value of <math>R_{a,p} = 1 \mu m</math> should be taken.</li> </ul>
Ueda et al. [152]	1 9 8 8	Low	Water, methanol, R113	$h_{pb} = C_{sf}^{-1} Pr_l^{-1.7} \left( \frac{c_{p,l}}{i_{lv}} q''_{pb} \right) \left( \frac{L_b}{i_{lv} \mu_l} q''_{pb} \right)^{-1/3}$ <p>where,</p> <ul style="list-style-type: none"> <li>❖ <math>L_b = \left[ \frac{\sigma}{g(\rho_l - \rho_v)} \right]^{1/2}</math></li> </ul>

				$\begin{cases} C_{sf} = 0.0098 \text{ for water} \\ C_{sf} = 0.0028 \text{ for methanol} \\ C_{sf} = 0.0047 \text{ for R - 113} \end{cases}$
Kutateladze [153]	1 9 9 0	High	All	$h_{pb} = 0.44Pr_l^{0.35} \left( \frac{k_l}{L_b} \right) \left( \frac{\rho_l}{\rho_l - \rho_v} \frac{P \times 10^{-4}}{\rho_v g i_{lv} \mu_l} q''_{pb} \right)^{0.7}$ <p>where,</p> $L_b = \left[ \frac{\sigma}{g(\rho_l - \rho_v)} \right]^{1/2}$
Kutateladze (new)	1 9 9 0	High	All	$h_{pb} = \left[ 3.37 \times 10^{-9} \frac{k_l}{L_b} \left( \frac{q''_{pb} c_{p,l}}{i_{lv}} \right)^2 M_*^{-4} \right]^{1/3}$ <p>where,</p> $L_b = \left[ \frac{\sigma}{g(\rho_l - \rho_v)} \right]^{1/2}$ $M_*^{-4} = \frac{(P/\rho_v)^2}{\sigma g / (\rho_l - \rho_v)}$
Groß [154]	1 9 9 0	Very low	All	$h_{pb} = 55 q''_{pb}{}^{0.7} [P^{*0.12} / ((-\log_{10} P^*)^{0.55} \sqrt{M_{mol}})]$ <p>where,</p> $P^* = P/P_{crit}$
Gorenflo et al. [155]	1 9 9 0	Medium	All except liquid helium	$h_{pb} = h_o F(P^*) (q''_{pb} / q_0'')^n (R_a / R_{a0})^{0.133}$ <p>where,</p> $\begin{cases} F(P^*) = 1.73P^{*0.27} + \left(6.1 + \frac{0.68}{1-P^*}\right) P^{*2} \text{ for water} \\ F(P^*) = 1.2P^{*0.27} + 2.5P^* + \frac{P^*}{1-P^*} \text{ for all other fluids except liquid helium} \end{cases}$ $\begin{cases} n = 0.9 - 0.3P^{*0.15} \text{ for water} \\ n = 0.9 - 0.3P^{*0.3} \text{ for all other fluids except liquid helium} \end{cases}$ $P^* = P/P_{crit}$ <p>The standard conditions in which <math>h_o</math> must be evaluated are: <math>P^* = 0.1</math>, <math>R_{a0} = 0.4 \times 10^{-6} m</math>, <math>q_0'' = 20,000 W \cdot m^{-2}</math></p> $h_{o,water} = 5600, h_{o,butane} = 3600$
Kaminaga et al. [156]	1 9 9 2	Very low	All	$h_{pb} = 22(\rho_v/\rho_l)^{0.4} R_{a,p}{}^{0.2(1-P^*)} h_{pb,Kutateladze}$ <p>where,</p> $h_{pb,Kutateladze} = 0.44Pr_l^{0.35} \left( \frac{k_l}{L_b} \right) \left( \frac{\rho_l}{\rho_l - \rho_v} \frac{P \times 10^{-4}}{\rho_v g i_{lv} \mu_l} q''_{pb} \right)^{0.7}$ $R_{a,p} \text{ is an average roughness parameter expressed in } \mu m.$
Leiner [157], Leiner and Gorenflo [158]	1 9 9 4	Medium	All except liquid helium	$h^*_{pb} = AF'(P^*) q''^n R^{*0.133}$ <p>where,</p> $h^*_{pb} = \frac{h_{pb}}{P_{crit}(R_{mol}/M_{mol}T_{crit})^{1/2}}$ $P^* = P/P_{crit}$ $q^* = \frac{q''_{nb}}{P_{crit}(R_{mol}T_{crit}/M_{mol})^{1/2}}$ $R^* = \frac{R_a}{(R_{mol}T_{crit}/P_{crit}N_{mol})^{1/3}}$ $F'(P^*) = 43000^{(n-0.75)} \left[ 1.2P^{*0.27} + \left(2.5 + \frac{1}{1-P^*}\right) P^* \right]$ $\begin{cases} n = 0.9 - 0.3P^{*0.15} \text{ for water} \\ n = 0.9 - 0.3P^{*0.3} \text{ for all other fluids except liquid helium} \end{cases}$ $A = 0.6161C^{0.1512} K^{0.4894}$ $C = \frac{c_{p,l} _{P^*=0.1}}{R}$



				<ul style="list-style-type: none"> <li>❖ <math>K = \frac{T_{crit} \ln(P^*)}{(1 - T_{crit})}</math></li> <li>❖ <math>c_{p,l} _{P_r=0.1}</math> is the molar specific heat capacity at <math>P^* = 0.1</math> expressed in <math>[J.kmol^{-1}.K^{-1}]</math></li> </ul> <p>If unknown, a default value <math>R_a = 0.4 \times 10^{-6} m</math> is recommended.</p>
Chowdhury et al. [159]	1997	Medium	Water, ethanol, R113	$\begin{cases} h_{pb} = 11.43(Re_b)^{0.72}(Pr_l)^{0.42} \left(\frac{\rho_v}{\rho_l}\right)^{0.5} \left(\frac{D_d}{D_i}\right) \left(\frac{k_l}{D_d}\right) \text{ for water} \\ h_{pb} = 495.7(Re_b)^{0.8}(Pr_l)^{0.5} \left(\frac{\rho_v}{\rho_l}\right)^{0.33} \left(\frac{k_l}{D_d}\right) \text{ for ethanol} \\ h_{pb} = 6(Re_b)^{0.78}(Pr_l)^{0.48} \left(\frac{\rho_v}{\rho_l}\right)^{0.58} \left(\frac{k_l}{D_d}\right) \text{ for Freon R - 113} \end{cases}$ <p>where,</p> <ul style="list-style-type: none"> <li>❖ <math>Re_b = \frac{q''_{pb} D_d}{\rho_v i_{lv} \nu_l}</math></li> </ul>
El-Genk and Saber [1]	1998	Medium	Water, methanol, Downtherm-A, R-11, R-113	$h_{nb} = (1 + 4.95\psi) \times h_{pb,Kutateladze}$ <p>where,</p> <ul style="list-style-type: none"> <li>❖ <math>h_{pb,Kutateladze} = 0.44 Pr_l^{0.35} \left(\frac{k_l}{L_b}\right) \left(\frac{\rho_l}{\rho_l - \rho_v} \frac{P \times 10^{-4}}{\rho_v g i_{lv} \mu_l} q''_{pb}\right)^{0.7}</math></li> <li>❖ <math>\psi = \left(\frac{\rho_v}{\rho_l}\right)^{0.4} \left[\frac{Pr_l \nu_l}{\sigma} \left(\frac{\rho_l^2}{\sigma g(\rho_l - \rho_v)}\right)^{1/4}\right]^{1/4}</math></li> <li>❖ <math>L_b = \left[\frac{\sigma}{g(\rho_l - \rho_v)}\right]^{1/2}</math></li> </ul>
Kiatsiroat et al. [160]	2000	Very low	Water, ethanol, TEG	$h_{pb} = C \left(\frac{\mu i_{lv}}{L_b \Delta T_{sat}}\right) \left(\frac{c_p \Delta T_{sat}}{i_{lv} Pr}\right)^{3n}$ <p>where,</p> <ul style="list-style-type: none"> <li>❖ <math>L_b = \left[\frac{\sigma}{g(\rho_l - \rho_v)}\right]^{1/2}</math></li> <li>❖ <math>\begin{cases} C = 18.688 \text{ for water} \\ C = 17.625 \text{ for ethanol} \\ C = 20.565 \text{ for triethylene glycol (TEG)} \end{cases}</math></li> <li>❖ <math>\begin{cases} n = 0.3572 \text{ for water} \\ n = 0.3300 \text{ for ethanol} \\ n = 0.3662 \text{ for triethylene glycol (TEG)} \end{cases}</math></li> </ul>
Ribatski and Jabardo [161]	2003	Very low	All	$h_{pb} = C \left(\frac{R_a}{R_{a0}}\right)^{0.2} P^{*0.45} [-\log(P^*)]^{-0.8} M^{-0.5} q''_{pb}{}^n$ <p>where,</p> <ul style="list-style-type: none"> <li>❖ <math>\begin{cases} C = 100 \text{ for copper} \\ C = 110 \text{ for brass} \\ C = 85 \text{ for stainless steel} \end{cases}</math></li> <li>❖ <math>n = 0.9 - 0.3P^{*0.2}</math></li> <li>❖ <math>P^* = P/P_{crit}</math></li> <li>❖ <math>R_{a0} = 1 \times 10^{-6} m</math></li> </ul>

Regarding the high number of nucleate pool boiling correlations, it may be difficult to identify and select the best model to predict a given pool boiling heat transfer. In the literature, it is observed that many scientists (see for instance refs: [14], [162]–[165]) only use and refer to the widely known pool boiling correlation by Rohsenow [137]. This is also justified as the most known correlations are also the most used ones which means that their accuracies, limits, and reliabilities are well-known. In contrast, many models have been reported by some authors but

haven't been used by other researchers. For such correlations, the accuracy of the model is uncertain. This fact is further amplified as pool boiling correlations are usually semi empirical correlations and often comprise constants which are adjusted to fit the author's experimental data. Therefore, when used by other researchers, large discrepancies between the correlation and the new set of experimental data can appear.

A large analysis of the literature has been conducted with the objective of providing first recommendations on the most accurate and reliable nucleate pool boiling heat transfer coefficient correlations. Based on the references [1], [125], [160], [166]–[174], the following recommendations are made [73]. Without considering its popularity, the first advised model is the correlation by *Rohsenow* [137] which shows a constant reliability and a good accuracy for most of the pool boiling situations. Obviously, its wide use is also an advantage as it permitted its reliability to be tested. Despite the relevance of the factors used in this correlation, the introduction of a coefficient  $C_{sf}$  that characterizes the surface-fluid interface gives flexibility to the correlation. Indeed, behind this constant  $C_{sf}$  are hidden the notion of surface aspect, cavities and porosity of the surface, number of active nucleation sites etc... If such surface related characteristics can be difficult to estimate, values of the coefficient  $C_{sf}$  reported by researchers can be used. Indeed, tables reporting a list of values for the coefficient  $C_{sf}$  can be found in heat transfer books such as *Cengel*. [14], *Incropera et al.* [165], *Rohsenow et al.* [105] or in the literature and they relate the fluid and solid material selected to a given value of the coefficient  $C_{sf}$ . For more meticulous researchers, the value of the  $C_{sf}$  coefficient can be estimated by studying surface characteristics, active nucleation sites, surface-liquid interactions or adapted from experimental measurements. A second correlation which is often used and recommended for the prediction of pool boiling heat transfer coefficient is the model developed by *Imura et al.* [145]. An important advantage of this model in the studied context of heat pipes is that this correlation was developed especially for thermosyphons. For thermosyphons with high filling ratios, the correlation by *Imura et al.* [145] showed an excellent accuracy to predict the pool boiling heat transfer coefficient occurring at the evaporator. Nevertheless, some limitations of this correlation are known. For instance, some inaccuracies of the prediction have been observed in the case of small diameter liquid pools. Hence, this correlation isn't advised for small diameter thermosyphons and should be used for wickless heat pipes with diameters larger than a few millimetres. The correlation by *Stephan and Abdelsalam* [147] is also strongly recommended as it was developed using a regression analysis on over 5000 pool boiling data points obtained by various researchers. This ensures the suitability of this correlation to predict various pool boiling situations and increases the probability that this correlation will predict the pool boiling heat transfer coefficient accurately. This correlation is also quite flexible regarding the working fluid used as the boiling dataset

used for the development of the correlation comprised data using water, R-113, Isopropanol and benzene. Unlike the correlation by *Imura et al.* [145], this correlation seems insensitive to the diameter of the pool. Finally, among the more recent works and models reported, the correlation from *El-Genk and Saber* [1] looks promising as it was also developed using a large database. Similar to the correlation by *Stephan and Abdelsalam* [147], experimental data points from the boiling of various fluids such as water, Dowtherm-A, ethanol, methanol, R-11 and R-113 were used. Like *Rohsenow* [137], *El-Genk and Saber* [1] introduced to their correlation a mixing coefficient  $\psi$  that accounts for the bubble mechanisms and activity. Nevertheless, this correlation is relatively new and its reliability on various boiling experiments remains to be confirmed at larger scale.

#### 4.1.4 Filmwise condensation

When the vapour rises to the condenser section of the thermosyphon, it gets in contact with a cold wall at a temperature lower than the saturation temperature. Therefore, a phase change from vapour state to liquid state takes place and the vapour condenses. According to the studies on condensation, two modes can be identified [14]:

- *Dropwise condensation*: In this mode of condensation, droplets form on the cold surface. However, the totality of the surface isn't covered by the condensate. Eventually, droplets will merge and flow down along the surface due to the influence of gravity.
- *Filmwise condensation*: In this mode of condensation, the whole surface is covered by a liquid condensate and a film is formed on the cold surface. Then, the phase change process takes place on the liquid film itself. Therefore, the thickness of the liquid film increases as it flows down along the condenser wall.

The conditions defining the presence of a given condensation mode are discussed by researchers. In his model, *Tanasawa* [175] presented a condensation mode map depending on the difference of temperature between the vapour and the cold wall (subcooling), and on the vapour velocity. This can be seen in Figure 4-13.

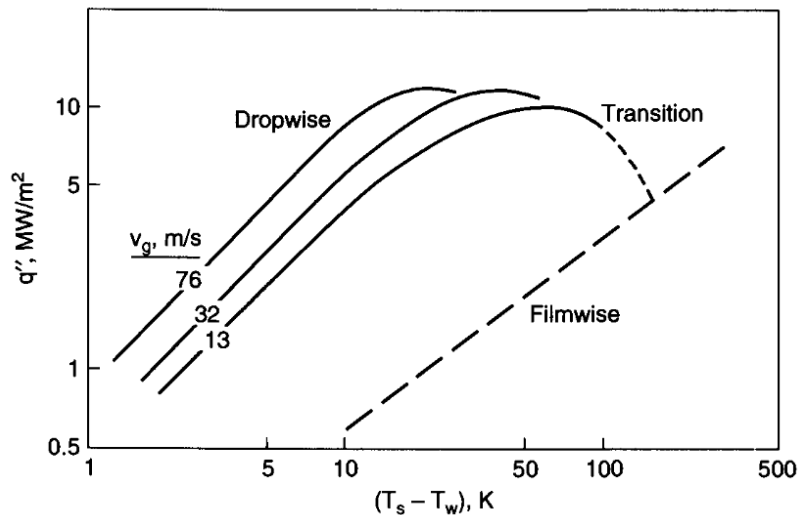


Figure 4-13. Map of the condensation modes by *Tanasawa* [175]

According to the condensation map proposed by *Tanasawa* [175], at low degrees of subcooling (meaning the cold wall temperature is slightly lower than the saturation temperature), dropwise condensation takes place. It is also noted that larger vapour velocities favour dropwise condensation. However, at lower vapour velocities and larger degrees of subcooling, the mass transfer is quicker than the departure of droplets and a liquid film is formed. Despite the higher values of the dropwise condensation heat transfer coefficient compared to filmwise condensation, in practice it is difficult to maintain a dropwise condensation mode for a long time [176]. Therefore, in the industry, typical condensers use filmwise condensation heat transfer. In heat pipes and thermosyphons, filmwise condensation also takes place, and, at steady state, the vapour condenses on the liquid condensate itself situated on the cold wall.

#### 4.1.4.1 Nusselt theory – Laminar film condensation on a vertical surface

Filmwise condensation was studied theoretically by *Nusselt* [103] in 1916 and is recognized as the reference in this domain. The *Nusselt* [103] theory is the foundation of the first condensation heat transfer coefficient correlation by *Nusselt* [103] which is still largely used to date and was also used by many researchers to develop their own correlations. The *Nusselt* [103] theory is reported and schematized in Figure 4-14 (adapted from [14], [105]).

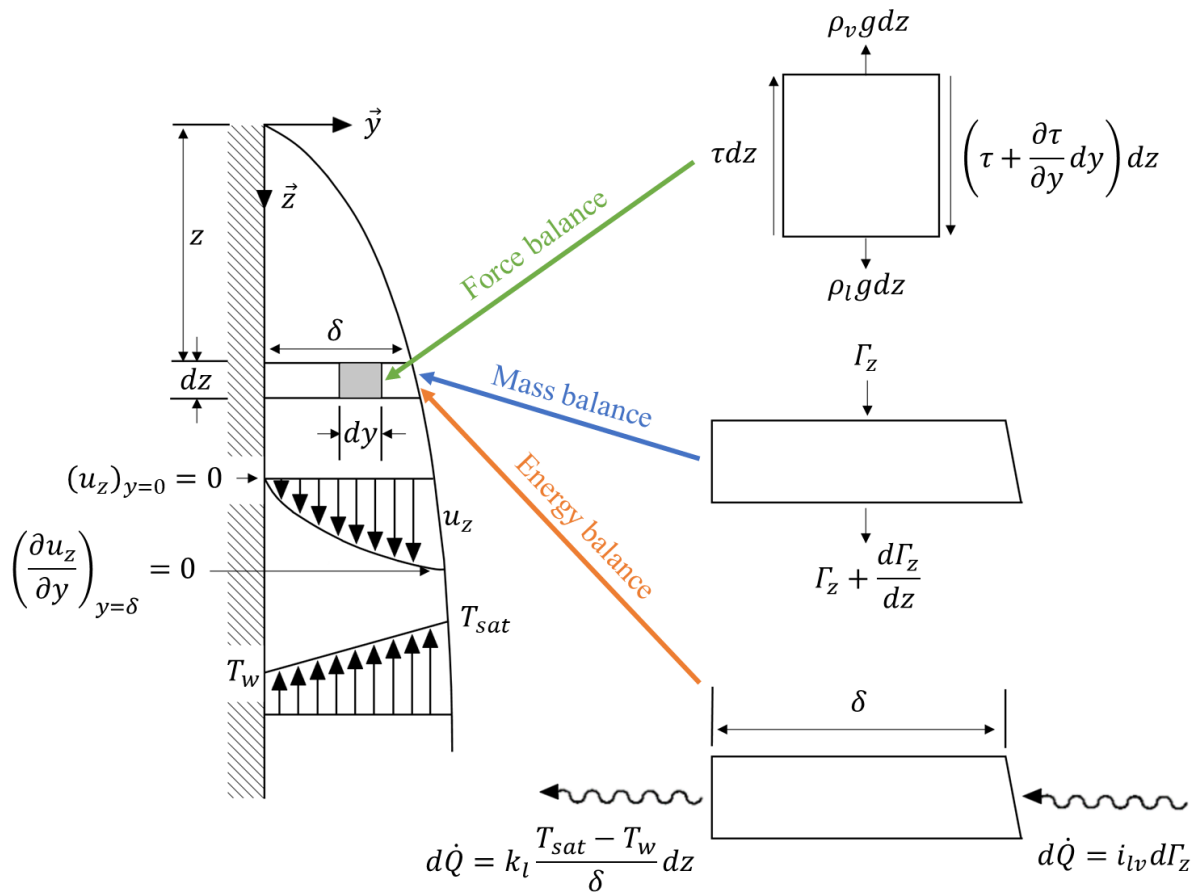


Figure 4-14. Nusselt [18] theory, film condensation on a vertical plate

The Nusselt analysis is valid under the following assumptions:

- The condensate flows down under the action of gravity
- The flow is laminar, and the fluid properties are constants in all directions
- The temperature of the liquid film at the liquid-wall interface is  $T_w$  and the temperature at the liquid-vapour interface is  $T_{sat}$
- The inertia forces are neglected
- The shear stress at the liquid-vapour interface is neglected. Hence, the velocity gradient at the liquid-vapour interface is zero:  $(\frac{\partial u_z}{\partial y})_{y=0} = 0$
- The heat transfer within the film occurs by pure conduction and the temperature distribution is assumed linear.

In the following, a force balance, mass balance and energy balance are operated on a 2D differential element of dimensions  $dy$ ,  $dz$ . The velocity vector coordinates in the  $y$  and  $z$  directions are denoted  $v_y$  and  $u_z$ . The other variables used are  $\tau$  the shear stress (N/m<sup>2</sup>),  $\mu_l$  the liquid dynamic viscosity (Pa.s),  $g$  the gravitational acceleration (m/s<sup>2</sup>),  $\rho_l$  and  $\rho_v$  the liquid and vapour densities (kg/m<sup>3</sup>),  $\delta$  the condensate thickness (m),  $\Gamma_z$  the mass flow rate per unit periphery (kg/m.s),  $\dot{Q}$  the heat transfer rate (W),  $i_{lv}$  the latent heat of vaporization (J/kg),  $h$  the heat transfer coefficient (W/m<sup>2</sup>.K),  $A$  the heat transfer area (m<sup>2</sup>),  $T_{sat}$  the saturation temperature

(K),  $T_w$  the wall temperature (K),  $k_l$  the liquid thermal conductivity (W/m.K),  $Re_f$  the film Reynolds number,  $q''$  the heat flux (W/m<sup>2</sup>), and  $L_c$  the condenser length (m).

- **Force balance**

By considering a force balance between the shear stress, the liquid weight, and the buoyancy force, the following equation arises [14], [105]:

$$\left(\tau + \frac{\partial \tau}{\partial y} dy\right) dz - \tau dz + \rho_l g(dz dy) - \rho_v g(dz dy) = 0 \quad (4-12)$$

The shear stress  $\tau$  in the condensate can be described by the Newton's law of viscosity:

$$\tau = \mu_l \frac{du_z}{dy} \quad (4-13)$$

Therefore, the force balance becomes:

$$\left(\mu_l \frac{du_z}{dy} + \mu_l \frac{d^2 u_z}{dy^2} dy\right) dz - \left(\mu_l \frac{du_z}{dy}\right) dz + \rho_l g(dz dy) - \rho_v g(dz dy) = 0 \quad (4-14)$$

which can be simplified as:

$$\mu_l \frac{d^2 u_z}{dy^2} + (\rho_l - \rho_v)g = 0 \quad (4-15)$$

By integrating, we have:

$$\mu_l \frac{du_z}{dy} = -(\rho_l - \rho_v)gy + C_1 \quad (4-16)$$

$$\left(\frac{du_z}{dy}\right)_{y=\delta} = 0 \rightarrow C_1 = (\rho_l - \rho_v)g\delta \quad (4-17)$$

Hence, the shear stress in the liquid condensate is expressed as:

$$\tau = \mu_l \frac{du_z}{dy} = (\rho_l - \rho_v)g(\delta - y) \quad (4-18)$$

This can be further integrated to obtain the velocity profile of the condensate:

$$u_z = \frac{(\rho_l - \rho_v)g}{\mu_l} \left(\delta y - \frac{1}{2}y^2\right) + C_2 \quad (4-19)$$

$$(u_z)_{y=0} = 0 \rightarrow C_2 = 0 \quad (4-20)$$

Therefore, the local vertical velocity  $u_z$  at a location  $y$  is [14], [105]:

$$u_z = \frac{(\rho_l - \rho_v)g}{\mu_l} \left(\delta y - \frac{1}{2}y^2\right) \quad (4-21)$$

Based on this, the mean falling film velocity at an altitude  $z$  can be obtained:

$$u_{z,mean} = \frac{1}{\delta} \int_0^\delta u_z dy = \frac{(\rho_l - \rho_v)g\delta^2}{3\mu_l} \quad (4-22)$$

- **Mass balance**

The mass flow rate per unit periphery  $\Gamma_z$  at an altitude  $z$  can be obtained by integrating on  $y$  the local flow rates at the altitude  $z$  [14].

$$\Gamma_z = \int_0^\delta \rho_l u_z dy = \frac{\rho_l(\rho_l - \rho_v)g\delta^3}{3\mu_l} \quad (4-23)$$

Then, the mass of liquid added to the condensate  $d\Gamma_z$  is also the variation of the mass flow rates between two altitudes.

$$\frac{d\Gamma_z}{dz} = \frac{d}{d\delta} \left[ \frac{\rho_l(\rho_l - \rho_v)g\delta^3}{3\mu_l} \right] \frac{d\delta}{dz} = \left[ \frac{\rho_l(\rho_l - \rho_v)g\delta^2}{\mu_l} \right] \frac{d\delta}{dz} \quad (4-24)$$

which gives the variation of mass  $d\Gamma_z$  with the variation of the condensate thickness as:

$$d\Gamma_z = \left[ \frac{\rho_l(\rho_l - \rho_v)g\delta^2}{\mu_l} \right] d\delta \quad (4-25)$$

- **Energy balance**

At steady state, the energy given to the condensate by vapour condensation is transmitted through the condensate thickness by conduction. The energy provided to the differential element by vapour condensation is given by the product of the latent heat  $i_{lv}$  and the added mass of the element  $d\Gamma_z$ :

$$d\dot{Q} = i_{lv}d\Gamma_z \quad (4-26)$$

On the other side of the differential element, at steady state, an equivalent amount of energy is transferred by conduction in the liquid. This is expressed by the Fourier's law as:

$$d\dot{Q} = k_l dz \frac{dT}{dy} = k_l dz \frac{T_{sat} - T_w}{\delta} \quad (4-27)$$

Therefore, the energy balance between the two above expressions gives:

$$i_{lv}d\Gamma_z = k_l dz \frac{T_{sat} - T_w}{\delta} \quad (4-28)$$

By rearranging,

$$\frac{d\Gamma_z}{dz} = \frac{k_l T_{sat} - T_w}{i_{lv} \delta} \quad (4-29)$$

- **Determining the condensate thickness  $\delta$**

By replacing the expression of the mass balance equation, the energy balance becomes:

$$\left[ \frac{\rho_l(\rho_l - \rho_v)g\delta^2}{\mu_l} \right] \frac{d\delta}{dz} = \frac{k_l T_{sat} - T_w}{i_{lv} \delta} \quad (4-30)$$

which is equivalent to

$$\delta^3 d\delta = \frac{\mu_l k_l (T_{sat} - T_w)}{\rho_l(\rho_l - \rho_v)g i_{lv}} dz \quad (4-31)$$

By integrating from  $z = 0$  where  $\delta = 0$  to  $z = z$  where  $\delta = \delta$ , the condensate thickness at a location  $z$  is obtained:

$$\delta = \left( \frac{4\mu_l k_l (T_{sat} - T_w) z}{\rho_l (\rho_l - \rho_v) i_{lv} g} \right)^{\frac{1}{4}} \quad (4-32)$$

Even if this expression of the falling film thickness is useful, it is common to express the condensate thickness depending on the Reynolds falling film number  $Re_f$  defined as:

$$Re_f = 4\Gamma_z / \mu_l \quad (4-33)$$

Then, by using this expression with the mass balance equation, we can reformulate:

$$Re_f = \frac{4 \rho_l (\rho_l - \rho_v) g \delta^3}{\mu_l} \quad (4-34)$$

And thus, by isolating the film thickness  $\delta$ :

$$\delta^3 = \frac{3\mu_l^2}{4\rho_l(\rho_l - \rho_v)g} Re_f \quad (4-35)$$

$\Leftrightarrow$

$$\delta = \left( \frac{3}{4} \frac{\mu_l^2}{\rho_l(\rho_l - \rho_v)g} \right)^{1/3} Re_f^{1/3} \quad (4-36)$$

In the case where  $\rho_v \ll \rho_l$ , this expression is often simplified as [177]–[180]:

$$\delta = \left( \frac{3\mu_l^2}{4\rho_l^2 g} \right)^{1/3} Re_f^{1/3} \quad (4-37)$$

This correlation is well known as the *Nusselt* [103] falling film thickness correlation.

- **Determining the heat transfer coefficient correlation**

According to the assumptions and Fourier's law, the local heat transfer coefficient  $h_z$  can be expressed by:

$$h_z = \frac{q''}{(T_{sat} - T_w)} = \frac{k_l}{\delta} \quad (4-38)$$

By introducing the expression of the falling film thickness  $\delta$ , it becomes:

$$h_z = \left( \frac{\rho_l (\rho_l - \rho_v) i_{lv} g k_l^3}{4\mu_l z (T_{sat} - T_w)} \right)^{\frac{1}{4}} \quad (4-39)$$

Finally, to obtain the value of the film condensation heat transfer coefficient over the whole condenser length  $L_c$ , the local heat transfer coefficient must be summed over the whole condenser's length:

$$h_{Nusselt} = \frac{1}{L_c} \int_0^{L_c} h_z dz = 4/3 h_{L_c} \quad (4-40)$$

which gives:



$$h_{Nusselt} = 4/3 h_{Lc} = \frac{4}{3} \left( \frac{\rho_l(\rho_l - \rho_v) i_{lv} g k_l^3}{4 \mu_l L_c (T_{sat} - T_w)} \right)^{1/4} = \frac{4}{3} \left( \frac{1}{4} \right)^{1/4} \left\{ \frac{\rho_l(\rho_l - \rho_v) i_{lv} g k_l^3}{\mu_l L_c (T_{sat} - T_w)} \right\}^{1/4} \quad (4-41)$$

By giving an approximated value of the constant, the well-known filmwise condensation heat transfer coefficient correlation by *Nusselt* [103] becomes:

$$h_{Nusselt} \approx 0.943 \left\{ \frac{\rho_l(\rho_l - \rho_v) i_{lv} g k_l^3}{\mu_l L_c (T_{sat} - T_w)} \right\}^{1/4} \quad (4-42)$$

#### 4.1.4.2 Filmwise condensation correlations

The *Nusselt* [103] heat transfer coefficient correlation is the most commonly used equation to predict filmwise heat transfer coefficients and, according to many researchers, performs very well for laminar and wavy-laminar falling films. Yet, some authors such as *McAdams* [181], *Chen et al.* [182] and *Oh and Revankar* [183] defend that, when compared to experimental data, the *Nusselt* [103] correlation underpredicts the filmwise condensation heat transfer coefficient by 15% to 20%. It must also be noted that the *Nusselt* theory is valid under certain assumptions only such as linear temperature distribution in the condensate, no shear stress at the vapour-liquid interface, or constant fluid properties which may lead to errors compared to real cases. In this regard, *Rohsenow* [184] proposed a correction to the latent heat of vaporization to consider the potential subcooling of the condensate. According to some, the 15-20% of condensation heat transfer coefficient underprediction made by the *Nusselt* [103] correlation could be explained by the appearance of small waves in the condensate that can increase the heat transfer. Indeed, even for small waves, *Kapitza* [185] showed that the formation of waves in the falling film leads to a reduced average of the film thickness which favours the condensation heat transfer. The longer the condenser length, the higher the turbulence in the falling film. Similar to forced convection, more turbulent falling films lead to improved heat transfer and a higher condensation heat transfer coefficient. In this regard, filmwise condensation correlations are distributed according to the falling film Reynolds number  $Re_f$  values in several turbulence regimes. Based on the references [105], [179], [186]–[189], the following falling film regimes seem relevant to classify the condensation correlations:

- $Re_f < 20 - 30$  : Laminar regime
- $30 - 50 < Re_f < 600$  : Laminar wavy regime
- $600 < Re_f < 1600$  : Wavy regime
- $1600 < Re_f < 3200$  : Turbulent regime
- $3200 < Re_f$  : Highly turbulent regime

For wavy and turbulent regimes, high discrepancies with the *Nusselt* theory can be observed as the assumptions no longer apply. Then, similar to boiling experiments, many semi-empirical condensation correlations have been developed. Such correlations may also present

differences depending on the working fluid used and experimental conditions under which the semi-empirical correlation was developed. The filmwise condensation heat transfer coefficient correlations reported to date are listed in Table 4-2.

Table 4-2. Filmwise condensation heat transfer coefficient  $h_c$  correlations

Authors	Year	Frequency of use	Fluids	Correlation
<b>Laminar falling film (<math>Re_f \leq 20 - 30</math>) and Wavy-laminar falling film (<math>20 - 30 \leq Re_f \leq 600</math>)</b>				
Nusselt [103]	1916	Very high	All	$h_{c,Nusselt} = 0.943 \left\{ \frac{\rho_l(\rho_l - \rho_v)i_{lv}gk_l^3}{\mu_l L_c(T_{sat} - T_w)} \right\}^{1/4}$
McAdams [181]	1942	Medium	All	$h_c = 1.13 \left\{ \frac{\rho_l(\rho_l - \rho_v)i_{lv}gk_l^3}{\mu_l L_c(T_{sat} - T_w)} \right\}^{1/4}$
Nusselt [103] corrected by Rohsenow [184]	1956	High	All	$h_c = 0.943 \left\{ \frac{\rho_l(\rho_l - \rho_v)i_{lv}'gk_l^3}{\mu_l L_c(T_{sat} - T_w)} \right\}^{1/4}$ <p>where,</p> <ul style="list-style-type: none"> <li>❖ Correction for a subcooled condensate: <math display="block">i_{lv}' = i_{lv} + \frac{3}{8} c_{pl}(T_{sat} - T_w)</math></li> <li>❖ Correction for a non-linear temperature distribution: <math display="block">i_{lv}' = i_{lv} + 0.68c_{pl}(T_{sat} - T_w)</math></li> <li>❖ Correction for a shear-stress dominating flow, linear temperature distribution and potential subcooling of the condensate: <math display="block">i_{lv}' = i_{lv} + \frac{1}{3} c_{pl}(T_{sat} - T_w)</math></li> <li>❖ Correction in the case where both gravity and shear stress are significant: <math display="block">h_c = (h_{correction:non-linear\ temperature}^2 + h_{correction:shearstress}^2)^{1/2}</math></li> </ul>
Rohsenow [184]	1956	High	All	$h_c = 1.51 \left( \frac{P_v}{P_{crit}} \right)^{0.14} \times 0.943 \left\{ \frac{\rho_l(\rho_l - \rho_v)gk_l^3}{\mu_l L_c(T_{sat} - T_w)} [i_{lv} + \frac{3}{8} c_{pl}(T_{sat} - T_w)] \right\}^{1/4}$ <p>where the fluid properties should be evaluated at a temperature:</p> <ul style="list-style-type: none"> <li>❖ <math>T = T_w + 0.31(T_{sat} - T_w)</math></li> </ul>
Kutateladze [190]	1963	Low	All	$h_c = 0.69 Re_{f,L_c}^{0.11} \times h_{Nusselt}$ <p>where,</p> <ul style="list-style-type: none"> <li>❖ <math>Re_{f,L_c} = \frac{4\Gamma_{L_c}}{\mu_l}</math></li> </ul>
Kutateladze [190]	1963	High	All	$h_c = \frac{Re_{f,L_c}/4}{1.47(Re_{f,L_c}/4)^{1.22} - 1.3} k_l \left( \frac{\mu_l^2}{\rho_l(\rho_l - \rho_v)g} \right)^{-1/3}$ <p>where,</p> <ul style="list-style-type: none"> <li>❖ <math>Re_{f,L_c} = \frac{4\Gamma_{L_c}}{\mu_l}</math></li> </ul>
Butterworth [191]	1981	Low	All	$h_c = 1.013 Re_{f,L_c}^{-0.22} k_l \left( \frac{\mu_l^2}{\rho_l(\rho_l - \rho_v)g} \right)^{-1/3}$ <p>where,</p> <ul style="list-style-type: none"> <li>❖ <math>Re_{f,L_c} = \frac{4\Gamma_{L_c}}{\mu_l}</math></li> </ul>
Butterworth [191]	1981	Medium	All	$h_c = \frac{Re_{f,L_c}^{-0.22}}{1.08 Re_{f,L_c}^{-0.22} - 5.2} k_l \left( \frac{\mu_l^2}{\rho_l(\rho_l - \rho_v)g} \right)^{-1/3}$ <p>where,</p> <ul style="list-style-type: none"> <li>❖ <math>Re_{f,L_c} = \frac{4\Gamma_{L_c}}{\mu_l}</math></li> </ul>

Wang and Ma [192]	1 9 9 1	High	All	$h_c = \left(\frac{L_c}{r_i}\right)^{\frac{\cos(\beta)}{4}} [0.54 + (5.68 \times 10^{-3}\beta)] h_{Nusselt}$ <p>where,</p> <ul style="list-style-type: none"> <li>❖ <math>\beta</math>: Inclination angle of the thermosyphon (°)</li> <li>❖ <math>L_c</math>: Condenser length (m)</li> <li>❖ <math>r_i</math>: Internal radius of the thermosyphon (m)</li> </ul>
Gross [193]	1 9 9 2	High	All	$h_c = \left( (0.925 f_d Re_{f,max}^{-1/3})^2 + (0.044 Pr_l^{2/5} Re_{f,max}^{1/6})^2 \right)^{1/2} \times k_l \left( \frac{\mu_l^2}{\rho_l(\rho_l - \rho_v)g} \right)^{-1/3}$ <p>where,</p> <ul style="list-style-type: none"> <li>❖ <math>f_d = (1 - 0.63(P_v/P_{crit})^{3.3})^{-1}</math></li> <li>❖ <math>Re_{f,max} = Re_f = \frac{\dot{Q}}{\pi D_i i_{lv} \mu_l}</math></li> </ul>
Schnabel and Palen [194]	1 9 9 8	Low	All	$h_c = 0.693 \left( \frac{1 - \rho_v/\rho_l}{Re_f/4} \right)^{1/3} k_l \left( \frac{\mu_l^2}{\rho_l(\rho_l - \rho_v)g} \right)^{-1/3}$ <p>where,</p> <ul style="list-style-type: none"> <li>❖ <math>Re_{f,L_c} = \frac{4\Gamma_{L_c}}{\mu_l}</math></li> </ul>
Hussein et al. [195]	2 0 0 1	Low	All	$h_c = \left(\frac{L_c}{D_i}\right)^{\frac{1}{4}(\cos(\beta))^{0.358}} [0.997 - 0.334(\cos(\beta))^{0.108}] h_{Nusselt}$ <p>where,</p> <ul style="list-style-type: none"> <li>❖ <math>\beta</math>: Inclination angle of the thermosyphon (°)</li> <li>❖ <math>L_c</math>: Condenser length (m)</li> <li>❖ <math>D_i</math>: Internal diameter of the thermosyphon (m)</li> </ul>
Fiedler and Auracher [196]	2 0 0 4	Low	R134a	$h_c = \left(\frac{L_c}{r_i}\right)^{\cos(\beta/4)} [0.125 + (1.46 \times 10^{-2}\beta) - (7.27 \times 10^{-5}\beta^2)] h_{Nusselt}$ <p>where,</p> <ul style="list-style-type: none"> <li>❖ <math>\beta</math>: Inclination angle of the thermosyphon (°)</li> <li>❖ <math>L_c</math>: Condenser length (m)</li> <li>❖ <math>r_i</math>: Internal radius of the thermosyphon (m)</li> </ul>
<b>Wavy falling film (<math>600 \leq Re_f \leq 1600</math>)</b>				
Kutateladze [190]	1 9 6 3	Low	All	$h_c = 0.69 Re_{f,L_c}^{0.11} \times h_{Nusselt}$ <p>where,</p> <ul style="list-style-type: none"> <li>❖ <math>Re_{f,L_c} = \frac{4\Gamma_{L_c}}{\mu_l}</math></li> </ul>
Kutateladze [190]	1 9 6 3	High	All	$h_c = \frac{Re_{f,L_c}/4}{1.47(Re_{f,L_c}/4)^{1.22} - 1.3} k_l \left( \frac{\mu_l^2}{\rho_l(\rho_l - \rho_v)g} \right)^{-1/3}$ <p>where,</p> <ul style="list-style-type: none"> <li>❖ <math>Re_{f,L_c} = \frac{4\Gamma_{L_c}}{\mu_l}</math></li> </ul>
Butterworth [191]	1 9 8 1	Low	All	$h_c = 1.013 Re_{f,L_c}^{-0.22} k_l \left( \frac{\mu_l^2}{\rho_l(\rho_l - \rho_v)g} \right)^{-1/3}$ <p>where,</p> <ul style="list-style-type: none"> <li>❖ <math>Re_{f,L_c} = \frac{4\Gamma_{L_c}}{\mu_l}</math></li> </ul>
Butterworth [191]	1 9 8 1	Medium	All	$h_c = \frac{Re_{f,L_c}^{-0.22}}{1.08 Re_{f,L_c}^{-0.22} - 5.2} k_l \left( \frac{\mu_l^2}{\rho_l(\rho_l - \rho_v)g} \right)^{-1/3}$ <p>where,</p> <ul style="list-style-type: none"> <li>❖ <math>Re_{f,L_c} = \frac{4\Gamma_{L_c}}{\mu_l}</math></li> </ul>
Uehara et al. [197]	1 9 8 3	Low	All	$h_c = 1.013 Re_{f,\beta}^{-1/3} k_l \left( \frac{\mu_l^2}{\rho_l(\rho_l - \rho_v)g} \right)^{-1/3}$ <p>where,</p> <ul style="list-style-type: none"> <li>❖ <math>Re_{f,\beta} = \frac{\dot{Q}}{\pi D_i i_{lv} \mu_l} \times f_\beta</math></li> <li>❖ <math>f_\beta = 1</math> for vertical tube</li> <li>❖ <math>f_\beta = 2.87 \left( \frac{D_i}{L_c \sin(\beta)} \right)</math> for inclined tube with <math>10^\circ &lt; \beta</math></li> </ul>

Chun and Kim [198]	1 9 9 1	Low	Fluids with $1.75 < Pr_l < 5.0$	$h_c = [1.33Re_{f,L_c}^{-1/3} + 9.56 \times 10^{-6}Re_{f,L_c}^{0.89}Pr_l^{0.94} + 8.22 \times 10^{-2}]k_l \left( \frac{\mu_l^2}{\rho_l(\rho_l - \rho_v)g} \right)^{-1/3}$ <p>where,</p> <ul style="list-style-type: none"> <li>❖ <math>Re_{f,L_c} = \frac{4\Gamma_{L_c}}{\mu_l}</math></li> </ul>
Gross [193]	1 9 9 2	High	All	$h_c = \left( (0.925f_dRe_{f,max}^{-1/3})^2 + (0.044Pr_l^{2/5}Re_{f,max}^{1/6})^2 \right)^{1/2} k_l \left( \frac{\mu_l^2}{\rho_l(\rho_l - \rho_v)g} \right)^{-1/3}$ <p>where,</p> <ul style="list-style-type: none"> <li>❖ <math>f_d = (1 - 0.63(P_v/P_{crit})^{3.3})^{-1}</math></li> <li>❖ <math>Re_{f,max} = Re_f = \frac{q}{\pi D_{i,v}\mu_l}</math></li> </ul>
Nozhat [199]	1 9 9 5	Low	All	$h_c = 0.87Re_{f,L_c}^{0.07} \times h_{Nusselt}$ <p>where,</p> <ul style="list-style-type: none"> <li>❖ <math>Re_{f,L_c} = \frac{4\Gamma_{L_c}}{\mu_l}</math></li> </ul>
Schnabel and Palen [194]	1 9 9 8	Low	All	$h_c = (h_{laminar}^2 + h_{turbulent}^2)^{1/2}$ $h_{laminar} = 0.693 \left( \frac{1 - \rho_v/\rho_l}{Re_f/4} \right)^{1/3} k_l \left( \frac{\mu_l^2}{\rho_l(\rho_l - \rho_v)g} \right)^{-1/3}$ $h_{turbulent} = \frac{0.0283(Re_f/4)^{7/24}Pr_l^{1/3}}{1 + 9.66(Re_f/4)^{-3/8}Pr_l^{-1/6}} k_l \left( \frac{\mu_l^2}{\rho_l(\rho_l - \rho_v)g} \right)^{-1/3}$ <p>where,</p> <ul style="list-style-type: none"> <li>❖ <math>Re_{f,L_c} = \frac{4\Gamma_{L_c}}{\mu_l}</math></li> </ul>
Hashimoto and Kaminaga [200]	2 0 0 2	Medium	All	$h_c = 0.85Re_f^{0.1} \exp\left(-6.7 \times 10^{-5} \frac{\rho_l}{\rho_v} - 0.6\right) h_{Nusselt}$ <p>where,</p> <ul style="list-style-type: none"> <li>❖ <math>Re_{f,L_c} = \frac{4\Gamma_{L_c}}{\mu_l}</math></li> </ul>
Jouhara and Robinson [169]	2 0 1 0	Medium	Water, FC-84, FC-77, FC-3283	$h_c = 0.85Re_f^{0.1} \exp\left(-6.7 \times 10^{-5} \frac{\rho_l}{\rho_v} - 0.14\right) h_{Nusselt}$ <p>where,</p> <ul style="list-style-type: none"> <li>❖ <math>Re_f = \frac{4\dot{Q}}{\pi D_{i,v}\mu_l}</math></li> </ul>
<b>Turbulent falling film (<math>1600 \leq Re_f \leq 3200</math>) and Highly turbulent falling film (<math>3200 \leq Re_f</math>)</b>				
Labuntsov [201]	1 9 5 7	Medium	All	$h_c = 0.0306Re_{f,L_c}^{1/4}Pr_l^{1/2}k_l \left( \frac{\mu_l^2}{\rho_l(\rho_l - \rho_v)g} \right)^{-1/3}$ <p>where,</p> <ul style="list-style-type: none"> <li>❖ <math>Re_{f,L_c} = \frac{4\Gamma_{L_c}}{\mu_l}</math></li> </ul>
Uehara et al. [197]	1 9 8 3	Low	All	$h_c = 0.044Pr_l^{2/5}Re_{f,\beta}^{1/6}k_l \left( \frac{\mu_l^2}{\rho_l(\rho_l - \rho_v)g} \right)^{-1/3}$ <p>where,</p> <ul style="list-style-type: none"> <li>❖ <math>Re_{f,\beta} = \frac{\dot{Q}}{\pi D_{i,v}\mu_l} \times f_\beta</math></li> <li>❖ <math>f_\beta = 1</math> for vertical tube</li> <li>❖ <math>f_\beta = 2.87 \left( \frac{D_i}{L_c \sin(\beta)} \right)</math> for inclined tube with <math>10^\circ &lt; \beta</math></li> </ul>
Chun and Kim [198]	1 9 9 1	Low	Fluids with $1.75 < Pr_l < 5.0$	$h_c = [1.33Re_{f,L_c}^{-1/3} + 9.56 \times 10^{-6}Re_{f,L_c}^{0.89}Pr_l^{0.94} + 8.22 \times 10^{-2}]k_l \left( \frac{\mu_l^2}{\rho_l(\rho_l - \rho_v)g} \right)^{-1/3}$ <p>where,</p> <ul style="list-style-type: none"> <li>❖ <math>Re_{f,L_c} = \frac{4\Gamma_{L_c}}{\mu_l}</math></li> </ul>
Gross [193]	1 9 9 2	High	All	$h_c = \left( (0.925f_dRe_{f,max}^{-1/3})^2 + (0.044Pr_l^{2/5}Re_{f,max}^{1/6})^2 \right)^{1/2} k_l \left( \frac{\mu_l^2}{\rho_l(\rho_l - \rho_v)g} \right)^{-1/3}$

				where, $\diamond f_d = (1 - 0.63(P_v/P_{crit})^{3.3})^{-1}$ $\diamond Re_{f,max} = Re_f = \frac{\dot{Q}}{\pi D_{i,v} \mu_l}$
<i>Schnabel and Palen</i> [194]	1998	Low	All	$h_c = \frac{0.0283(Re_f/4)^{7/24} Pr_l^{1/3}}{1 + 9.66(Re_f/4)^{-3/8} Pr_l^{-1/6}} k_l \left( \frac{\mu_l^2}{\rho_l(\rho_l - \rho_v)g} \right)^{-1/3}$ where, $\diamond Re_{f,L_c} = \frac{4\Gamma_{L_c}}{\mu_l}$
<i>Hashimoto and Kaminaga</i> [200]	2002	Medium	All	$h_c = 0.85 Re_f^{0.1} \exp\left(-6.7 \times 10^{-5} \frac{\rho_l}{\rho_v} - 0.6\right) h_{Nusselt}$ where, $\diamond Re_f = \frac{4\dot{Q}}{\pi D_{i,v} \mu_l}$
<i>Jouhara and Robinson</i> [169]	2010	Medium	Water, FC-84, FC-77, FC-3283	$h_c = 0.85 Re_f^{0.1} \exp\left(-6.7 \times 10^{-5} \frac{\rho_l}{\rho_v} - 0.14\right) h_{Nusselt}$ where, $\diamond Re_f = \frac{4\dot{Q}}{\pi D_{i,v} \mu_l}$

Similar to the analysis made on the pool boiling correlations, in the following, recommendations are provided on the most suitable filmwise condensation heat transfer coefficient correlations to be used [111]. Such recommendations are given based on a large analysis of the literature ([105], [169], [174], [182], [193], [195], [196], [202]–[206]). For strictly laminar filmwise condensation ( $Re_f \leq 20 - 30$ ), the corrected correlation by *Nusselt* [103] with the latent heat correction from *Rohsenow* [184] is advised by researchers. This correlation seems to combine the advantages of the *Nusselt* [103] correlation while accounting for the subcooling of the condensate and the non-linear temperature distribution in the condensate. Yet, when using this model, attention must be paid to the regime of the condensate as the appearance of small waves on the falling film is likely to lead to an underprediction of the condensation heat transfer coefficient by 15-20% [181]–[183]. In thermosyphons, due to the counter-current of the rising vapour, turbulence and waves are likely to appear along the condensate. In this regard, for wavy-laminar regimes, the correlation from *Rohsenow* [184] may be preferred to the *Nusselt* [103] correlation. This correlation consists of the corrected form of the *Nusselt* [103] equation with the addition of a coefficient including a ratio of the vapour pressure to the critical pressure of the fluid. Another correlation that can be used for wavy-laminar condensates is the correlation by *McAdams* [181] which simply consists of correcting the *Nusselt* [103] correlation by a 20% factor. Even if this correlation may not consider additional fluid related factors, the correlation by *McAdams* [181] can be a simple way to estimate the filmwise condensation heat transfer coefficient during wavy-laminar regimes. For wavy films ( $600 \leq Re_f \leq 1600$ ) and turbulent falling films ( $1600 \leq Re_f$ ), the correlations by *Kutateladze* [190] and *Labuntsov* [201] are commonly used and advised by researchers. Some models have also been reported as very suitable under certain conditions. For instance, the correlation by *Gross* [193] was developed using a large database of condensation data from various fluids and is expected to

be accurate for a large range of working fluids. For low condensation heat fluxes, the recent correlation from *Jouhara and Robinson* [169] shows promising results and, despite its recent release, is already used by many researchers. Finally, in the case where the cold wall is inclined, the correlations by *Hussein et al.* [195] and *Wang and Ma* [192] use the tilt angle as a factor and are relevant.

#### 4.1.5 Falling film warmup, evaporation and boiling.

In the case where the filling ratio is lower than 100%, as the falling condensate returns to the evaporator of the thermosyphon, it reaches a portion of the heat pipe wall which is in contact with the heat source. As the condensate flows along the evaporator wall which is not filled by the liquid pool, the condensate warms up, and heat transfer from the hot wall to the falling film takes place. Often, the warmup of this falling film is neglected by researchers who consider that only pool boiling occurs at the evaporator. Yet, according to *Jafari et al.* [168], neglecting the warmup and evaporation of the falling film can lead to errors of up to 100% in the prediction of the boiling thermal resistance. The phenomenon of falling film evaporation becomes more significant with lower filling ratios as reducing the filling ratio means reducing the height of the liquid pool and thus increasing the length of the heated evaporator wall along which the condensate flows. With the contact of the hot evaporator wall, the falling film warms up and can eventually evaporate or boil before reaching the pool. In falling film evaporation or boiling, heat transfer coefficients as high as condensation heat transfer coefficients can be reached. In this regard, correlations describing the falling film warmup, evaporation and boiling must be studied.

##### 4.1.5.1 Falling film warmup and evaporation mechanism

Once the falling film reaches the evaporator wall, two cases can occur. First, in the case where the condensate is subcooled, the falling film warms up without phase change occurring. This can be designated as “sensible heating” [207]. Second, in the case where the condensate reaches the saturation temperature, evaporation of the falling film is triggered. The mass transfer from the liquid falling film to rising vapour consumes the condensate whose thickness progressively decreases. Both sensible heating and evaporation of the condensate are usually studied separately with their own sets of correlations. Indeed, when a phase change occurs, heat transfer coefficients are usually higher than during sensible heating of the condensate. In falling film heat transfer, correlations are usually given in terms of a dimensionless heat transfer coefficient  $h^*$  defined by:

$$h^* = \frac{h_{ff} l_0}{k_l} \quad (4-43)$$

where  $h$  is the falling film heat transfer coefficient ( $W/m^2.K$ ),  $k_l$  is the liquid thermal conductivity ( $W/m.K$ ), and  $l_0$  is the viscous length scale (m) given by:

$$l_0 = \left( \frac{\mu_l^2}{\rho_l^2 g} \right)^{1/3} \quad (4-44)$$

with  $\mu_l$  the liquid dynamic viscosity (Pa.s),  $\rho_l$  the liquid density (kg/m<sup>3</sup>), and  $g$  the gravitational acceleration (m/s<sup>2</sup>). It can be observed that the characteristic group  $l_0$  is typical of the film thickness correlations, which indicates the direct link between the falling film heat transfer coefficient and condensate thickness.

#### 4.1.5.2 Falling film warmup and evaporation correlations

In this section, the correlations to date for sensible heating of the falling film and falling film evaporation are reported. Some recommendations are also provided based on the literature. Similar to condensation heat transfer, the falling film heat transfer coefficient varies regarding the flow regime of the condensate. Hence, the correlations are classified regarding the falling film Reynolds number. The heat transfer coefficient correlations for the warmup of a subcooled condensate are listed in Table 4-3.

Table 4-3. Falling film warmup (sensible heating) heat transfer coefficient  $h_{ff}$  correlations

Authors	Year	Frequency of use	Fluids	Correlation
<b>Laminar falling film (<math>Re_f \leq 20 - 30</math>) and Wavy-laminar falling film (<math>20 - 30 \leq Re_f \leq 600</math>)</b>				
Wilke [208]	1962	Very high	Water, Glycol-water	$h^* = 2.27 Re_f^{-1/3}$ where, ❖ $Re_f \leq 2460 Pr_l^{-0.646}$
Hewitt and Hall-Taylor [209]	1994	Medium	All	$h^* = \frac{280}{141} \left( \frac{4}{3} \right)^{1/3} Re_f^{-1/3}$ where, ❖ $Re_f \leq 20 - 30$
<b>Wavy falling film (<math>600 \leq Re_f \leq 1600</math>)</b>				
Wilke [208]	1962	Very high	Water, Glycol-water	$h^* = 3.23 \times 10^{-2} Re_f^{1/5} Pr_l^{0.344}$ where, ❖ $2460 Pr_l^{-0.646} \leq Re_f < 1600$
<b>Turbulent falling film (<math>1600 \leq Re_f \leq 3200</math>)</b>				
Wilke [208]	1962	Very high	Water, Glycol-water	$h^* = 1.02 \times 10^{-3} Re_f^{2/3} Pr_l^{0.344}$ where, ❖ $1600 \leq Re_f < 3200$
Gimbutis [210]	1974	Medium	All	$h^* = (0.165 Re_f^{0.16} - 0.4) Pr_l^{0.34} \left( \frac{Pr_l}{Pr_{l,wall}} \right)^{0.25}$ where, ❖ $2,800 \leq Re_f \leq 70,000$ ❖ $4.3 \leq Pr_l \leq 8.4$
Mudawwar and El-Masri [187]	1986	Medium	Water	$h^* = 0.1 Re_f^{0.14} Pr_l^{0.35}$ where, ❖ $2,000 \leq Re_f \leq 10,000$
Shmerler and Mudawwar [211]	1988	High	Water	$h^* = 1.06 \times 10^{-2} Re_f^{0.3} Pr_l^{0.63}$ where, ❖ $2,480 \leq Re_f \leq 39,430$ ❖ $2.55 \leq Pr_l \leq 7.2$
<b>Highly turbulent falling film (<math>3200 \leq Re_f</math>)</b>				

<i>Wilke</i> [208]	1 9 6 2	Very high	Water, Glycol- water	$h^* = 8.71 \times 10^{-3} Re_f^{2/5} Pr_l^{0.344}$ where, ❖ $3200 \leq Re_f$
<i>Gimbutis</i> [210]	1 9 7 4	Medium	All	$h^* = (0.165 Re_f^{0.16} - 0.4) Pr_l^{0.34} \left( \frac{Pr_l}{Pr_{l,wall}} \right)^{0.25}$ where, ❖ $2,800 \leq Re_f \leq 70,000$ ❖ $4.3 \leq Pr_l \leq 8.4$
<i>Mudawwar and El-Masri</i> [187]	1 9 8 6	Medium	Water	$h^* = 0.1 Re_f^{0.14} Pr_l^{0.35}$ where, ❖ $2,000 \leq Re_f \leq 10,000$
<i>Shmerler and Mudawwar</i> [211]	1 9 8 8	High	Water	$h^* = 1.06 \times 10^{-2} Re_f^{0.3} Pr_l^{0.63}$ where, ❖ $2,480 \leq Re_f \leq 39,430$ ❖ $2.55 \leq Pr_l \leq 7.2$
<i>Al-Najem et al.</i> [212]	1 9 9 8	Medium	All	$h^* = 6.832 \times 10^{-4} \left( Re_f^{0.4829} Pr_l^{0.93717} - \frac{21,817.84}{Re_f} \right)$ where, ❖ $4,000 \leq Re_f \leq 20,000$ ❖ $1.8 \leq Pr_l \leq 5.5$

Based on the references [187], [212]–[216], the most used correlations for the estimation of the falling film warmup heat transfer coefficient are the correlations by *Wilke* [208]. *Narvaez-Romo et al.* [217] conducted a literature review and mainly discussed the correlations from *Wilke* [208] for non-evaporating films. *Fujita and Ueda* [214] compared experimental data of the warmup of a subcooled falling film flowing along a heated tube. Despite a slight over prediction, the model by *Wilke* [208] was reported to be accurate. A similar conclusion was made by *Mudawwar and El-Masri* [187] using water and water ethylene glycol. For turbulent falling films, the correlation from *Shmerler and Mudawwar* [211] was also reported to show a good accuracy and presented a satisfactory agreement with the data from *Fujita and Ueda* [214]. In the case where the falling film isn't subcooled and starts to evaporate, different correlations are used. The falling film evaporation heat transfer coefficient correlations are listed in Table 4-4.

Table 4-4. Falling film evaporation heat transfer coefficient  $h_{ff}$  correlations

Authors	Year	Frequency of use	Fluids	Correlation
<b>Laminar falling film (<math>Re_f \leq 20 - 30</math>) and Wavy-laminar falling film (<math>20 - 30 \leq Re_f \leq 600</math>)</b>				
<i>Nusselt</i> [218]	1 9 1 6	Very high	All	$h^* = \left( \frac{4}{3} \right)^{1/3} Re_f^{-1/3}$ where, ❖ $Re_f \leq 20 - 30$
<i>Wilke</i> [208]	1 9 6 2	Very high	Water, Glycol- water	$h^* = 1.76 Re_f^{-1/3}$ where, ❖ $Re_f \leq 2460 Pr_l^{-0.646}$
<i>Ahmed et al.</i> [219]	1 9	Low	All	$h^* = 6.92 \times 10^{-3} Re_f^{0.345} Pr_l^{0.4}$ where, ❖ $3 \leq Re_f \leq 10,250$



	63			❖ $3.6 < Re_f < 950$
<i>Chun and Seban</i> [220]	1971	High	All	$h^* = 0.606(Re_f/4)^{-1/3}$ where, ❖ $Re_f \leq 2.44Ka^{-1/11}$
<i>Alhusseini et al.</i> [215]	1998	Low	Propylene-Glycol, Water	$h^* = 2.65Re_f^{-0.158}Ka^{0.0563}$ where, ❖ $Re_f \leq 600$
<i>Wadekar</i> [221]	2000	Low	High Prandtl number fluids	$h^* = 9.7 \times 10^{-3}Re_f^{0.29}Pr_l^{0.63}$ where, ❖ $Re_f \leq 21,000$ ❖ $1.77 \leq Pr_l \leq 5.7$
<b>Wavy falling film (<math>600 \leq Re_f \leq 1600</math>)</b>				
<i>Wilke</i> [208]	1962	Very high	Water, Glycol-water	$h^* = 3.23 \times 10^{-2}Re_f^{1/5}Pr_l^{0.344}$ where, ❖ $2460Pr_l^{-0.646} \leq Re_f < 1600$
<i>Ahmed et al.</i> [219]	1963	Low	All	$h^* = 6.92 \times 10^{-3} * Re_f^{0.345}Pr_l^{0.4}$ where, ❖ $3 \leq Re_f \leq 10,250$ ❖ $3.6 \leq Pr_l \leq 950$
<i>Chun and Seban</i> [220]	1971	High	All	$h^* = 0.606(Re_f/4)^{-0.22}$ where, ❖ $2.44Ka^{-1/11} \leq Re_f \leq 5800Pr_l^{-1.06}$
<i>Cerza and Sernas</i> [188]	1988	Medium	Water	$h^* = \left(\frac{4}{3}\right)^{1/3} Re_f^{-1/3} \left[1 - 0.72 \times \exp\left(-13.7 \frac{y}{Pe\delta}\right)\right]^{-1}$ where, ❖ $\delta = \left(\frac{3\mu_l^2}{4\rho_l^2g}\right)^{1/3} Re_f^{1/3}$ : calculated with the laminar expression of <i>Nusselt</i> [218] correlation in the source paper ❖ $y$ : distance downstream ❖ $Pe = Re_f Pr = (4\Gamma/\mu)Pr$ : Film Peclet modulus ❖ $Re_f \leq 1600$
<i>Parken et al.</i> [222]	1990	Low	Water	$h^* = 3.8 \times 10^{-2}Re_f^{0.15}Pr_l^{0.53}$ where, ❖ $600 \leq Re_f \leq 1650$
<i>Numrich</i> [223]	1995	Low	Aqueous solutions	$h^* = 3 \times 10^{-3}Re_f^{0.44}Pr_l^{0.4}$ where, ❖ $1,200 \leq Re_f \leq 41,000$ ❖ $Pr_l \leq 52$
<i>Alhusseini et al.</i> [215]	1998	Low	Propylene-Glycol, Water	$h^* = 2.65Re_f^{-0.158}Ka^{0.0563}$ where, ❖ $600 \leq Re_f \leq 1600$ ❖ $1.7 \leq Pr_l \leq 47$
<i>Wadekar</i> [221]	2000	Low	High Prandtl number fluids	$h^* = 9.7 \times 10^{-3}Re_f^{0.29}Pr_l^{0.63}$ where, ❖ $Re_f \leq 21,000$ ❖ $1.77 \leq Pr_l \leq 5.7$
<i>Ye et al.</i> [213]	2002	Medium	Water	$h^* = 4.62 \times 10^{-3}Re_f^{0.429}Pr_l^{1/3}$ where, ❖ $800 \leq Re_f \leq 7,000$ ❖ $2.55 \leq Pr_l \leq 7.2$
<b>Turbulent falling film (<math>1600 \leq Re_f \leq 3200</math>)</b>				
<i>Wilke</i> [208]	1962	Very high	Water, Glycol-water	$h^* = 1.02 \times 10^{-3}Re_f^{2/3}Pr_l^{0.344}$ where, ❖ $1600 \leq Re_f \leq 3200$

Ahmed et al. [219]	1 9 6 3	Low	All	$h^* = 6.92 \times 10^{-3} * Re_f^{0.345} Pr_l^{0.4}$ where, ❖ $3 \leq Re_f \leq 10,250$ ❖ $3.6 \leq Pr_l \leq 950$
Chun and Seban [220]	1 9 7 1	Very high	All	$h^* = 3.8 \times 10^{-3} Re_f^{0.4} Pr_l^{0.65}$ where, ❖ $5800 Pr_l^{-1.06} \leq Re_f$
Mudawwar and El-Masri [187]	1 9 8 6	Medium	Water	$h^* = 4.2 \times 10^{-2} Re_f^{0.17} Pr_l^{0.53}$ where, ❖ $2,000 \leq Re_f \leq 20,000$
Cerza and Sernas [188]	1 9 8 8	Medium	Water	$h^* = \left(\frac{4}{3}\right)^{1/3} Re_f^{-1/3} \left[1 - 0.72 \times \exp\left(-13.7 \frac{y}{Pe\delta}\right)\right]^{-1} \left[1 + (1.9 \times 10^{-7}) Re_f^{1.7}\right]$ where, ❖ $\delta = \left(\frac{3\mu^2}{4\rho^2 g}\right)^{1/3} Re_f^{1/3}$ : Calculated with laminar expression in the source paper ❖ $y$ : distance downstream ❖ $Pe = Re_f Pr = (4\Gamma/\mu) Pr$ : Film Peclet modulus ❖ $1600 \leq Re_f$
Shmerler and Mudawwar [211]	1 9 8 8	High	Water	$h^* = 3.8 \times 10^{-3} Re_f^{0.35} Pr_l^{0.95}$ where, ❖ $4,990 \leq Re_f \leq 37,620$ ❖ $1.75 \leq Pr_l \leq 5.42$
Numrich [223]	1 9 9 5	Low	Aqueous solutions	$h^* = 3 \times 10^{-3} Re_f^{0.44} Pr_l^{0.4}$ where, ❖ $1,200 \leq Re_f \leq 41,000$ ❖ $Pr_l \leq 52$
Alhusseini et al. [215]	1 9 9 8	Low	Propylen e-Glycol, Water	$h^* = \frac{Pr\delta^{*1/3}}{A_1 Pr^{3/4} + A_2 Pr^{1/2} + A_3 Pr^{1/4} + A_4 + A_5 Ka^{1/2} Pr^{1/2}}$ Where, ❖ $A_1 = 9.17$ ❖ $A_2 = 0.328\pi(130 + \delta^*)$ ❖ $A_3 = 0.289(152100 + 2340\delta^* + 7\delta^{*2})/\delta^{*2}$ ❖ $A_4 = (2.51 \times 10^6 \delta^{*1/3} Ka^{-0.173})/(Re_f^{3.49} Ka^{0.0675})$ ❖ $A_5 = 8.82 + 3 \times 10^{-4} Re_f$ ❖ $\delta^* = 94.6 \times 10^{-3} Re_f^{0.8}$ ❖ $1600 \leq Re_f$
Wadekar [221]	2 0 0 0	Low	High Prandtl number fluids	$h^* = 9.7 \times 10^{-3} Re_f^{0.29} Pr_l^{0.63}$ where, ❖ $Re_f \leq 21,000$ ❖ $1.77 \leq Pr_l \leq 5.7$
Ye et al. [213]	2 0 0 2	Medium	Water	$h^* = 4.62 \times 10^{-3} Re_f^{0.429} Pr_l^{1/3}$ where, ❖ $800 \leq Re_f \leq 7,000$ ❖ $2.55 \leq Pr_l \leq 7.2$
<b>Highly turbulent falling film (<math>3200 \leq Re_f</math>)</b>				
Dukler [224]	1 9 6 1	Low	All	$h^* = \{0.110 - [0.565/(Pr_l + 5.47)]\} Re_f^{0.231}$ where, ❖ $9,000 \leq Re_f$
Wilke [208]	1 9 6 2	Very high	Water, Glycol-water	$h^* = 8.71 \times 10^{-3} Re_f^{2/5} Pr_l^{0.344}$ where, ❖ $3200 \leq Re_f$
Ahmed et al. [219]	1 9	Low	All	$h^* = 6.92 \times 10^{-3} Re_f^{0.345} Pr_l^{0.4}$ where,

	6 3			<ul style="list-style-type: none"> <li>❖ <math>3 \leq Re_f \leq 10,250</math></li> <li>❖ <math>3.6 \leq Re_f \leq 950</math></li> </ul>
<i>Herbert and Sterns</i> [225]	1 9 6 8	Low	All	$h^* = 8.54 \times 10^{-4} Re_f^{0.65}$ where, <ul style="list-style-type: none"> <li>❖ <math>3,000 \leq Re_f \leq 20,000</math></li> </ul>
<i>Struve</i> [226]	1 9 6 9	Low	Water	$h^* = 7.9 \times 10^{-3} Re_f^{0.41}$ where, <ul style="list-style-type: none"> <li>❖ <math>9,000 \leq Re_f</math></li> </ul>
<i>Elle</i> [227]	1 9 7 0	Low	Water	$h^* = 9.2 \times 10^{-3} Re_f^{0.4}$ where, <ul style="list-style-type: none"> <li>❖ <math>6,000 \leq Re_f</math></li> </ul>
<i>Chun and Seban</i> [220]	1 9 7 1	Very high	All	$h^* = 3.8 \times 10^{-3} Re_f^{0.4} Pr_l^{0.65}$ where, <ul style="list-style-type: none"> <li>❖ <math>5800 Pr_l^{-1.06} \leq Re_f</math></li> </ul>
<i>Schnabel and Schlunder</i> [228]	1 9 8 0	Low	All	$h^* = 3.6 \times 10^{-3} Re_f^{0.4} Pr_l^{0.65}$ where, <ul style="list-style-type: none"> <li>❖ <math>40,000 \leq Re_f</math></li> <li>❖ <math>Pr_l \leq 7</math></li> </ul>
<i>Mudawwar and El-Masri</i> [187]	1 9 8 6	Medium	Water	$h^* = 4.2 \times 10^{-2} Re_f^{0.17} Pr_l^{0.53}$ where, <ul style="list-style-type: none"> <li>❖ <math>2,000 \leq Re_f \leq 20,000</math></li> <li>❖ <math>0.98 \leq Pr_l \leq 6.96</math></li> </ul>
<i>Cerza and Sernas</i> [188]	1 9 8 8	Medium	Water	$h^* = \left(\frac{4}{3}\right)^{1/3} Re_f^{-1/3} \left[1 - 0.72 \times \exp\left(-13.7 \frac{y}{Pe\delta}\right)\right]^{-1} \left[1 + (1.9 \times 10^{-7}) Re_f^{1.7}\right]$ where, <ul style="list-style-type: none"> <li>❖ <math>\delta = \left(\frac{3\mu^2}{4\rho^2g}\right)^{1/3} Re_f^{1/3}</math>: Calculated with laminar expression in the source paper</li> <li>❖ <math>y</math>: distance downstream</li> <li>❖ <math>Pe = Re_f Pr = (4\Gamma/\mu)Pr</math>: Film Peclet modulus</li> <li>❖ <math>1600 \leq Re_f</math></li> </ul>
<i>Shmerler and Mudawwar</i> [211]	1 9 8 8	High	Water	$h^* = 3.8 \times 10^{-3} Re_f^{0.35} Pr_l^{0.95}$ where, <ul style="list-style-type: none"> <li>❖ <math>4,990 \leq Re_f \leq 37,620</math></li> <li>❖ <math>1.75 \leq Pr_l \leq 5.42</math></li> </ul>
<i>Holmberg et al.</i> [229]	1 9 9 1	Low	Lithium bromide-water	$h^* = 1.2 \times 10^{-2} Re_f^{0.265} Pr_l^{0.52}$ where, <ul style="list-style-type: none"> <li>❖ <math>6,000 \leq Re_f</math></li> <li>❖ <math>2.2 \leq Pr_l \leq 8.2</math></li> </ul>
<i>Asblad and Bertsson</i> [216]	1 9 9 1	Low	All	$h^* = 1.2 \times 10^{-2} Re_f^{0.28} Pr_l^{0.53}$ where, <ul style="list-style-type: none"> <li>❖ <math>27,000 \leq Re_f</math></li> <li>❖ <math>1.8 \leq Pr_l \leq 5.7</math></li> </ul>
<i>Numrich</i> [223]	1 9 9 5	Low	Aqueous solutions	$h^* = 3 \times 10^{-3} Re_f^{0.44} Pr_l^{0.4}$ where, <ul style="list-style-type: none"> <li>❖ <math>1,200 \leq Re_f \leq 41,000</math></li> <li>❖ <math>Pr_l \leq 52</math></li> </ul>
<i>Alhusseini et al.</i> [215]	1 9 9 8	Low	Propylene-Glycol, Water	$h^* = \frac{Pr\delta^{*1/3}}{A_1 Pr^{3/4} + A_2 Pr^{1/2} + A_3 Pr^{1/4} + A_4 + A_5 Ka^{1/2} Pr^{1/2}}$ where, <ul style="list-style-type: none"> <li>❖ <math>A_1 = 9.17</math></li> <li>❖ <math>A_2 = 0.328\pi(130 + \delta^*)</math></li> <li>❖ <math>A_3 = 0.289(152100 + 2340\delta^* + 7\delta^{*2})/\delta^{*2}</math></li> <li>❖ <math>A_4 = (2.51 \times 10^6 \delta^{*1/3} Ka^{-0.173}) / (Re_f^{3.49} Ka^{0.0675})</math></li> </ul>

				<ul style="list-style-type: none"> <li>❖ <math>A_5 = 8.82 + 3 \times 10^{-4} Re_f</math></li> <li>❖ <math>\delta^* = 94.6 \times 10^{-3} Re_f^{0.8}</math></li> <li>❖ <math>1600 \leq Re_f</math></li> </ul>
Wadekar [221]	2000	Low	High Prandtl number fluids	$h^* = 9.7 \times 10^{-3} Re_f^{0.29} Pr_l^{0.63}$ where, <ul style="list-style-type: none"> <li>❖ <math>Re_f \leq 21,000</math></li> <li>❖ <math>1.77 \leq Pr_l \leq 5.7</math></li> </ul>
Ye et al. [213]	2002	Medium	Water	$h^* = 4.62 \times 10^{-3} Re_f^{0.429} Pr_l^{1/3}$ where, <ul style="list-style-type: none"> <li>❖ <math>800 \leq Re_f \leq 7,000</math></li> <li>❖ <math>2.55 \leq Pr_l \leq 7.2</math></li> </ul>
Kharangate et al. [207]	2015	Low	Water	$h^* = 4.4 \times 10^{-4} Re_f^{0.598} Pr_l^{0.975}$ where, <ul style="list-style-type: none"> <li>❖ <math>4,990 \leq Re_f \leq 37,620</math></li> <li>❖ <math>1.75 \leq Pr_l \leq 5.42</math></li> </ul>
Gourdon et al. [230]	2016	Low	Aqueous solution	$h^* = 8.5 \times 10^{-3} Re_f^{0.2} Pr_l^{0.65}$ where, <ul style="list-style-type: none"> <li>❖ <math>2 \leq Pr_l \leq 800</math></li> </ul>
Xue and Zhang [231]	2018	Low	Water	$h^* = 2.01 \times 10^{-3} Re_f^{0.35} Pr_l^{0.53}$ where, <ul style="list-style-type: none"> <li>❖ <math>3,000 \leq Re_f \leq 15,000</math></li> <li>❖ <math>2 \leq Pr_l \leq 10</math></li> </ul>
Kandlikar [232]	2018	Medium	All	$h^* = 8.7 \times 10^{-3} Re_f^{0.4} Pr_l^{0.344}$ where, <ul style="list-style-type: none"> <li>❖ <math>3200 \leq Re_f</math></li> </ul>

According to the references [187], [212]–[216], the correlation by *Nusselt* [218] should be kept for strictly laminar evaporating falling films only. Indeed, similar to condensation, the appearance of small waves in the falling film quickly generate a discrepancy of the data with the *Nusselt* [218] correlation which tends to underpredict the heat transfer coefficient. For wavy and turbulent evaporating falling films, the correlation by *Chun and Seban* [220] is reported to fit well with experimental data. Similar to boiling and condensation, *Chun and Seban* [220] developed this correlation from a large data base so that this correlation fits most of the falling film evaporation cases. Nevertheless, this correlation is not advised for Reynolds number higher than  $Re_f > 10,000$ . For highly turbulent falling film evaporation, the correlations from *Mudawwar and El-Masri* [187] and *Shmerler and Mudawwar* [211] should be preferred.

#### 4.1.5.3 Falling film boiling mechanism

In the case of high heat fluxes, bubbles can appear in the falling film itself. In this case, heterogeneous nucleation takes place, and bubbles form near the wall. Like pool boiling, a nucleus trapped inside a cavity grows due to the transient conduction, thermal layer removal, and locally enhanced convection. However, unlike pool boiling, bubbles keep growing after their departure as they flow downwards. *Cerza and sernas* [233] worked extensively on falling film boiling and proposed a model. This model is presented in Figure 4-15.

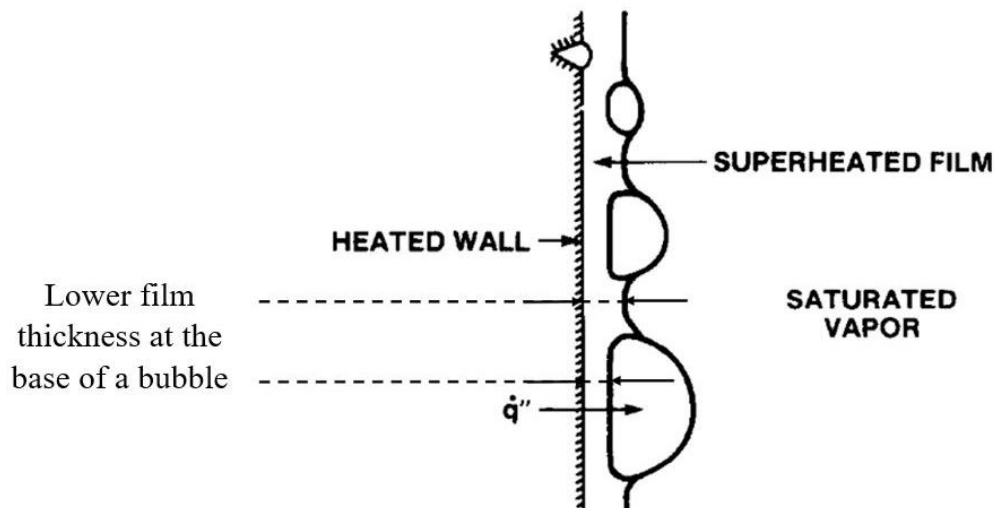


Figure 4-15. Falling film boiling, model by *Cerza and Sernas* [233]

First observed by *Parken* [234] and then confirmed by *Sernas and Stanzione* [235], the falling film thickness at the base of a bubble is lower than the average falling film thickness. Then, the falling film heat transfer at the base of the bubble is improved. Furthermore, according to *Cerza and sernas* [233] the bubble motion is faster than that of the liquid film. Hence, the base of the bubble is periodically in contact with a new portion of liquid which rapidly increases in temperature due to its reduced thickness. According to the model by *Cerza and sernas* [233], the higher heat transfer coefficient in falling film boiling can be explained by the improved transient conduction at the bubble's base. In the case of falling film boiling in a tube, an important factor to consider is the burst of bubbles. At low heat flux, most of the bubbles burst by themselves. However, at high heat flux the burst of a bubble can release small droplets of liquid which can trigger the burst of surrounding bubbles. In the case of falling film boiling inside tubes with small diameters, the bubble burst chain reaction can be important [189]. With an increase of the boiling activity, *Fujita and Ueda* [189] observed that the falling film boiling heat transfer coefficient becomes independent from the Reynolds number and fits well with flow boiling correlations.

#### 4.1.5.4 Falling film boiling correlations

The correlations reported to date for falling film boiling have been divided in two main categories: low heat flux and high heat flux. At relatively low heat flux, the falling film boiling heat transfer coefficient is linked to the flow regime and depends on the falling film Reynolds number. However, at high heat fluxes, the high boiling activity makes the heat transfer coefficient independent of the flow regime [189]. In this case, one correlation can be used for all falling film Reynolds numbers. The reported falling film boiling correlations are listed in Table 4-5.

Table 4-5. Falling film boiling heat transfer coefficient  $h_{ff}$  correlations

Authors	Year	Frequency of use	Fluids	Correlation
<b>Laminar and Wavy-laminar falling film (<math>Re_f \leq 600</math>) – Relatively low heat flux</b>				
Chun and Seban [220]	1971	High	All	$h^* = 0.606(Re_f/4)^{-1/3}$ where, ❖ $0.3 \times 10^5 \leq q_{ffb}'' \leq 0.7 \times 10^5 \text{ W.m}^{-2}$ ❖ $Re_f \leq 2.44Ka^{-1/11}$ ❖ $Ka = g\mu^4/\rho\sigma^3$
<b>Wavy falling film (<math>600 \leq Re_f \leq 1600</math>) – Relatively low heat flux</b>				
Chun and Seban [220]	1971	High	All	$h^* = 0.606(Re_f/4)^{-0.22}$ where, ❖ $0.3 \times 10^5 \leq q_{ffb}'' \leq 0.7 \times 10^5 \text{ W.m}^{-2}$ ❖ $2.44Ka^{-1/11} \leq Re_f \leq 5800Pr_l^{-1.06}$ ❖ $Ka = g\mu^4/\rho\sigma^3$
Fujita and Ueda [189]	1978	Medium	Water	$h^* = 0.90(Re_f)^{-0.22}$ where, ❖ $0.3 \times 10^5 \leq q_{ffb}'' \leq 0.7 \times 10^5 \text{ W.m}^{-2}$ ❖ $1000 \leq Re_f \leq 3200$
<b>Turbulent falling film (<math>1600 \leq Re_f \leq 3200</math>) – Relatively low heat flux</b>				
Chun and Seban [220]	1971	Very High	All	$h^* = 3.8 \times 10^{-3} Re_f^{0.4} Pr_l^{0.65}$ where, ❖ $0.3 \times 10^5 \leq q_{ffb}'' \leq 0.7 \times 10^5 \text{ W.m}^{-2}$ ❖ $5800Pr_l^{-1.06} \leq Re_f$
Fujita and Ueda [189]	1978	Medium	Water	$h^* = 0.90(Re_f)^{-0.22}$ where, ❖ $0.3 \times 10^5 \leq q_{ffb}'' \leq 0.7 \times 10^5 \text{ W.m}^{-2}$ ❖ $1000 \leq Re_f \leq 3200$
<b>Highly turbulent falling film (<math>3200 \leq Re_f</math>) - Relatively low heat flux</b>				
Chun and Seban [220]	1971	Very High	All	$h^* = 3.8 \times 10^{-3} Re_f^{0.4} Pr_l^{0.65}$ where, ❖ $0.3 \times 10^5 \leq q_{ffb}'' \leq 0.7 \times 10^5 \text{ W.m}^{-2}$ ❖ $5800Pr_l^{-1.06} \leq Re_f$
Fujita and Ueda [189]	1978	Medium	Water	$h^* = 6 \times 10^{-3} Re_f^{0.4}$ where, ❖ $0.3 \times 10^5 \leq q_{ffb}'' \leq 0.7 \times 10^5 \text{ W.m}^{-2}$ ❖ $3200 \leq Re_f$
<b>For all <math>Re_f</math> (independent of the falling film regime) – High heat flux</b>				
Kopchikov [236]	1969	Low	Water, ethanol, benzene, carbon tetrachloride	$h^* = 0.1 \left( \frac{k_l i_{lv} \rho_v}{\sigma T_{sat}} q_{ffb}'' \right) \frac{1}{k_l} \left( \frac{\mu_l^2}{\rho_l^2 g} \right)^{1/3}$
Fujita and Ueda [189]	1978	Medium	Water	$h^* = 1.24 q_{ffb}''^{0.741} \frac{1}{k_l} \left( \frac{\mu_l^2}{\rho_l^2 g} \right)^{1/3}$ where, ❖ $2 \times 10^5 \text{ W.m}^{-2} \leq q_{ffb}''$

<p><i>Cerza and Sernas</i> [188]</p>	<p>1 9 8 8</p>	<p>Medium</p>	<p>Water</p>	$h^* = \left(\frac{4}{3}\right)^{1/3} Re_f^{-1/3} \left[1 - 0.72 \exp\left(-13.7 \frac{y}{Pe\delta}\right)\right]^{-1} \times \left[1 + (1.9 \times 10^{-7}) Re_f^{1.7}\right] \times \left[1 + (0.05) \left(\frac{q_w'' - q_{incip}''}{q_{incip}''}\right)^{1.36}\right]$ <p>where,</p> <ul style="list-style-type: none"> <li>❖ <math>\delta = \left(\frac{3\mu_l^2}{4\rho_l^2 g}\right)^{1/3} Re_f^{1/3}</math> : Falling film thickness</li> <li>❖ <math>y</math> : Distance downstream of the heated section of the tube</li> <li>❖ <math>Pe = Re_f Pr = (4\Gamma/\mu) Pr</math> : Film Peclet modulus</li> <li>❖ <math>q_{incip}'' = 14.2 \text{ kW/m}^2</math>: Boiling incipient heat flux, determined experimentally (first bubble created)</li> </ul>
<p><i>El-Genk and Saber</i> [237]</p>	<p>1 9 9 9</p>	<p>Medium</p>	<p>Water, ethanol, methanol, Downtherm-A, R-11, R-113</p>	$h^* = \left(\frac{4}{3}\right)^{1/3} Re_f^{-1/3} (h_x^3 + h_{ffb}^3)^{1/3}$ $h_x = \left(\frac{4}{3}\right)^{1/3} Re_f^{-1/3} \left(\frac{k_l}{L_f}\right)$ $h_{ffb} = 1.155 \times 10^{-3} \left(\frac{k_l}{L_b}\right) N_\mu^{0.33} Pr_l^{0.35} \left(\frac{q_{ffb}'' L_b \rho_l}{\rho_v i_{lv} \mu_l}\right)^{0.7} \left(\frac{PL_b}{\sigma}\right)^{0.7}$ <p>where,</p> <ul style="list-style-type: none"> <li>❖ <math>L_f = \left(\frac{\mu_l^2}{g\rho_l(\rho_l - \rho_v)}\right)^{1/3}</math> : Liquid film thickness scale</li> <li>❖ <math>L_b = [\sigma/g(\rho_l - \rho_v)]^{1/2}</math> : Bubble length scale</li> <li>❖ <math>N_\mu = \frac{\mu_l}{(\sigma\rho_l L_b)^{0.5}}</math> : Viscosity number</li> </ul>
<p><i>Gogonin</i> [238]</p>	<p>2 0 0 6</p>	<p>Low</p>	<p>Water</p>	$h^* = 0.01 \left(\frac{\mu_l^2}{\rho_l^2 g}\right)^{1/3} L_b^{-1} Re_{fb}^{0.8} Pr_l^{1/3} b K_t^{0.4} \bar{R}_z^{-0.2} \left(\frac{k_l c_{p,l} \rho_l}{k_w c_{p,w} \rho_w}\right)^{-0.2}$ $b = \left[1 + 10 \left(\frac{\rho_v}{\rho_l - \rho_v}\right)^{2/3}\right]$ $K_t = \frac{(i_{lv} \rho_v)^2 L_b}{c_{p,l} T_{sat} \rho_l \sigma}$ $\bar{R}_z = R_z / L_f$ $L_f = \left(\frac{\mu_l^2}{g\rho_l(\rho_l - \rho_v)}\right)^{1/3}$ <p>where,</p> <ul style="list-style-type: none"> <li>❖ <math>Re_{fb} = \frac{q_{ffb}'' L_b \rho_l}{i_{lv} \rho_v \mu_l}</math>: falling film boiling Reynolds number</li> <li>❖ <math>L_b = [\sigma/g(\rho_l - \rho_v)]^{1/2}</math> : Bubble length scale</li> <li>❖ <math>Pr = c_p \mu_l / k_l</math>: Prandtl number</li> <li>❖ <math>K_t</math>: Thermal similarity criterion</li> <li>❖ <math>\bar{R}_z</math>: Scale of relative roughness</li> <li>❖ <math>R_z</math>: Height of irregularities of the surface (<math>\mu\text{m}</math>)</li> <li>❖ <math>L_f</math>: Liquid film thickness scale</li> </ul>

Based on relevant work from the literature [105], [188], [189], [236]–[238], the following recommendations are made on falling film boiling correlations. At low heat flux, the boiling activity is relatively low and can be approached with enhanced falling film evaporation correlations. Indeed, the correlations from *Fujita and Ueda* [189] are based on falling film evaporation correlations with the addition of a term considering the heat transfer improvement from the boiling activity. In the literature, the correlations from *Fujita and Ueda* [189] are the most recommended for low heat flux falling film boiling. The correlation by *Chun and Seban* [220] is also commonly used but tends to underestimate the heat transfer coefficient by 10%. At high heat flux, the heat transfer coefficient is mainly related to the heat flux and becomes

independent of the flow regime. The correlation by *Fujita and Ueda* [189] is reported to be in good agreement with experimental data and an average error of 10% with the predictions is usually observed. The correlation by *El-Genk and Saber* [237] can also be used as its accuracy is reported to be acceptable. However, its more complex form makes it less convenient to use and the accuracy of the prediction is not improved compared to the correlation by *Fujita and Ueda* [189]. A similar conclusion is made on the correlation by *Cerza and Sernas* [188] who took into account the thermal entry length of the flow development in their model. Finally, the work by *Gogonin* [238] should be noted as this model relates the falling film heat transfer coefficient to the surface characteristics. Like pool boiling correlations, relating the boiling activity to the surface aspect has been proved to be relevant. However, in practice, such correlations are difficult to use and surface characteristics difficult to estimate.

## **4.2 Multi-channel heat pipe model**

In the previous section, the commonly used thermosyphon thermal resistance model (Figure 4-2) was presented, that permits estimates of the temperature inside a single thermosyphon. To predict each thermal resistance inside the thermosyphon, two-phase correlations need to be used and they have been reported. However, the commonly used thermosyphon thermal resistance model is not relevant to model multi-channel heat pipes, and it needs to be adapted to suit the multi-channel geometry. In this section, the development of a new multi-channel heat pipe thermal resistance model is proposed and detailed.

### **4.2.1 Geometry**

In the objective of predicting the thermal performance of a multi-channel flat heat pipe to be used for surface cooling applications, the two-phase phenomena described previously must be studied in a new multi-channel geometry. Inside the flat heat pipe, the working fluid circulates in multiple parallel channels. In addition to the parallel channels inside which the working fluid evaporates and condenses, two collectors placed at the bottom and at the top of the parallel channels link the channels together. The multi-channel geometry of interest is schematized in Figure 4-16 below.



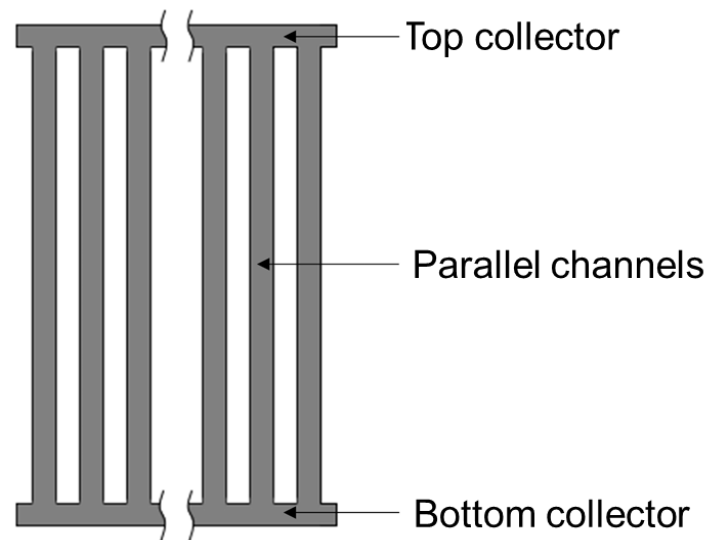


Figure 4-16. Multi-channel geometry schematic

For the development of the theoretical model, the horizontal tubes linking the parallel channels at the two extremities will be designated as top and bottom collectors.

#### **4.2.2 Two-phase working cycle in a multi-channel geometry**

Based on the current knowledge on two-phase heat transfer in thermosyphons, the two-phase cycle can be adapted to the new multi-channel geometry of interest. This adapted two-phase cycle will be used for the development of the theoretical model and it is presented in Figure 4-17.

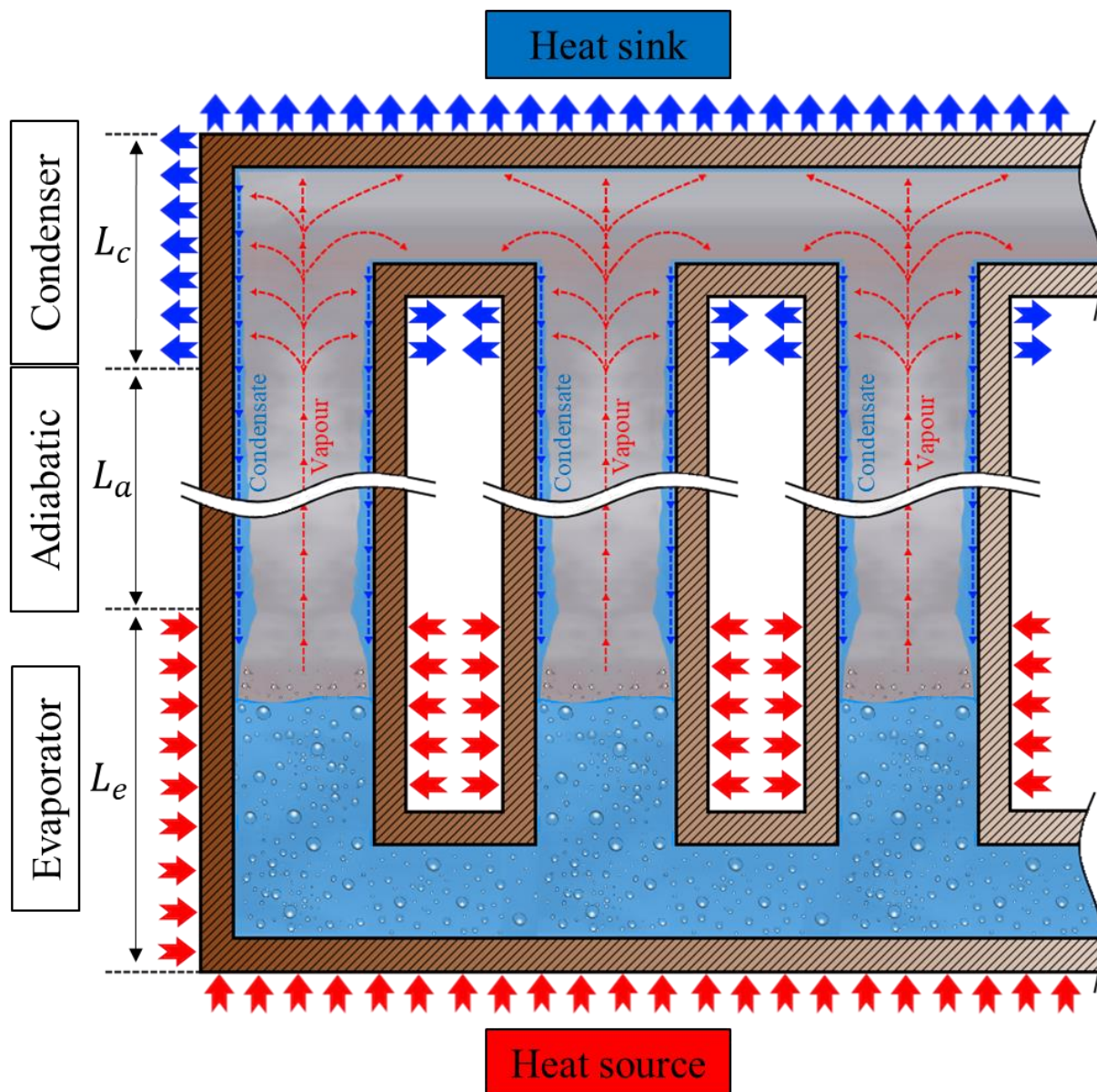


Figure 4-17. Two-phase working fluid cycle in a multi-channel geometry

The first difference of a multi-channel geometry from a single thermosyphon is that the liquid pool is separated into two main sections. At the very bottom of the multi-channel heat pipe, the bottom collector is filled with the liquid phase of the working fluid. Yet, a significant portion of the liquid pool is situated inside the parallel channels. Because all the channels are connected by the bottom collector, under saturation conditions, the whole liquid pool is at a constant temperature. Hence, on a horizontal axis, the temperature distribution is expected to be uniform. As the overall liquid pool evaporates at a similar temperature, the adiabatic section filled with vapour is also expected to present a uniform temperature distribution, regardless of the channel location. Indeed, in a vertical and balanced position in which the size of the pool is the same in all the parallel channels, there is no apparent reason for the rising vapour stream to differ between two parallel channels. In the case where the heat sink is placed at the top of

the multi-channel heat pipe and covers the whole width of the heat pipe surface, condensation is expected to occur on the whole length of the top collector and in all the parallel channels. Similar to the pool boiling section, the condensation area inside the multi-channel geometry comprises a condensation area inside the channels and a condensation area inside the top collector. Again, prior to the experimental investigations, the condensation is expected to be uniform on a horizontal axis. Hence, a condensate is expected to form inside all the parallel channels and the thickness of the condensate to be similar in all the channels.

Even if the conducted investigation and theoretical model developed have been considering a heat sink placed at the top of the multi-channel heat pipe, in the case where the heat sink would be placed on one side of the heat pipe surface only, some phenomena are expected to differ. With the heat sink placed on one side only of the multi-channel heat pipe, condensation would occur only inside the channels in contact with the cold area. Hence, the totality of the condensate would accumulate in those channels while other channels' walls remain dry. Nonetheless, due to the top collector connecting the channels, the rising vapour from all the channels would go through the top collector to reach the cold point of the heat pipe, thus, maintaining a uniform adiabatic section temperature. Yet, as the condensate is located in a few channels only, the thickness of the condensate is expected to increase for a similar heat and mass transfer. Moreover, whilst the condensate returns to the liquid pool by gravity, falling film evaporation and boiling would only take place in the channels where a condensate is forming. In addition, this falling film heat transfer is expected to differ significantly due to the increased thickness of the condensation layer near the wall.

### **4.2.3 Equivalent thermal resistance network**

Based on the expected two-phase flow working fluid cycle in a multi-channel geometry described above, in the case where the heat sink is placed at the top of the multi-channel heat pipe and covers the whole width of the heat pipe surface, an equivalent thermal resistance model was developed and is presented on two parallel channels in Figure 4-18 hereafter.

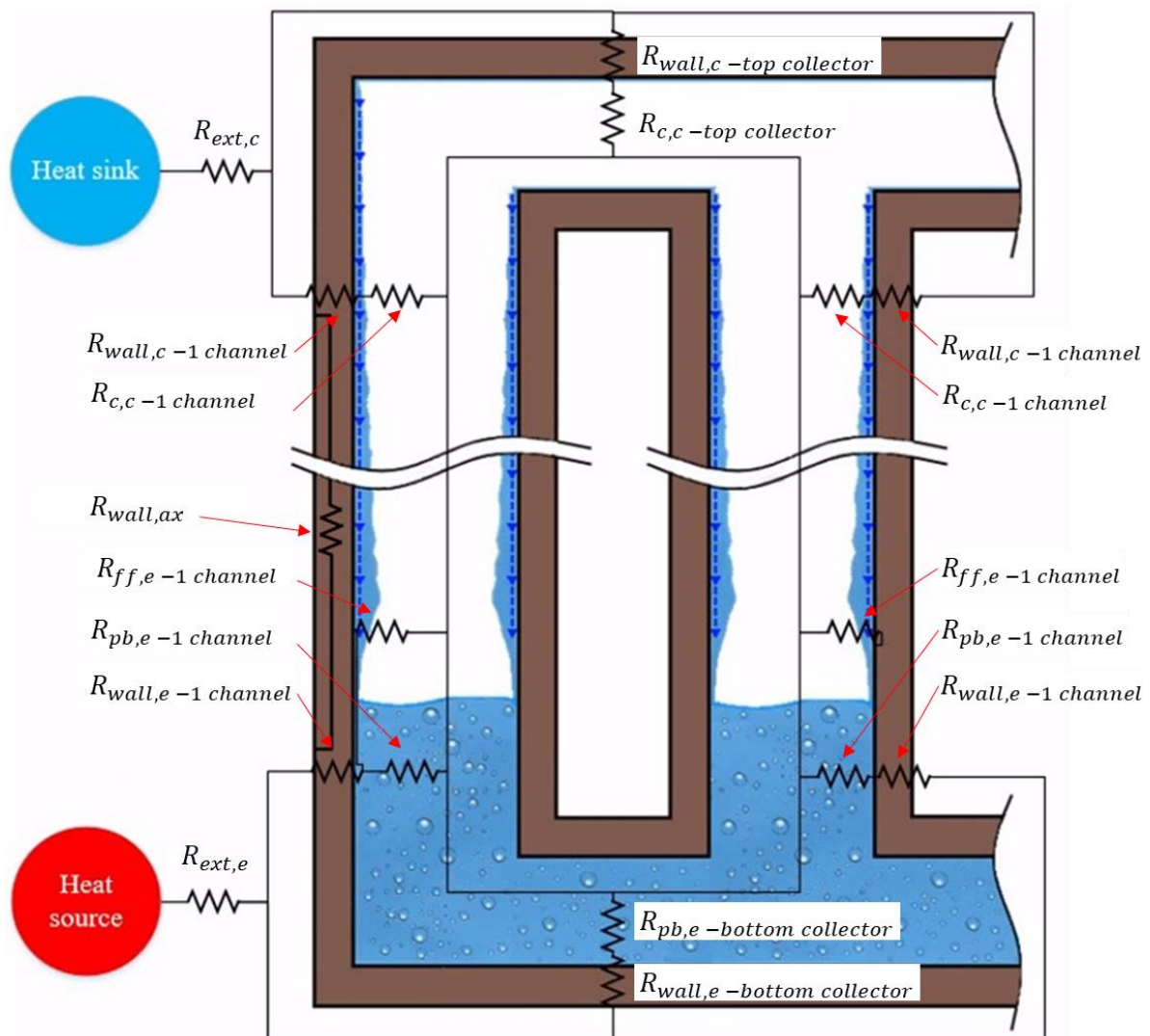


Figure 4-18. Schematized development of the theoretical model of a multi-channel heat pipe

Starting from the heat source, an external resistance  $R_{ext,e}$  describes the interface between the heat source and the heat pipe. This can be a contact resistance, forced convection or even radiation. Heat is then transmitted by conduction through the heat pipe wall. Two conductive sections can be differentiated due to the thermosyphon geometry: conduction through the bottom collector wall and conduction through the channel wall. Indeed, the diameter and wall thickness of the bottom collector can be different from that of the channels. Hence, one conductive thermal resistance for the bottom collector  $R_{wall,e-bottom collector}$  and one conductive thermal resistance for each channel  $R_{wall,e-1 channel}$  are considered in parallel. These resistances permit the temperature of the inner evaporator wall for both bottom collector and channels to be obtained. The thermal energy is then transferred from the hot wall with both pool boiling and falling film evaporation/boiling mechanisms. In the bottom collector, pool boiling only occurs as the collector is filled with liquid. Hence, a pool boiling resistance at the bottom collector  $R_{pb,e-bottom collector}$  describes the heat transfer from the hot bottom collector wall to the liquid pool. Similar pool boiling resistances can be found in the parallel channels

$R_{pb,e-1\ channel}$  in the channel section which is filled with liquid. These resistances are also linked to the bottom collector pool boiling resistance as the temperature of the liquid pool is considered to be uniform. In the case where the filling ratio is lower than 100%, a section of the channel is not filled by the liquid pool. Hence, falling film evaporation or boiling takes place where the hot wall transmits its energy to the condensate returning to the liquid pool. This is represented by the resistance  $R_{ff,e-1\ channel}$ . The vapour generated at the evaporator rises to the condenser section in the parallel channels. Here, the vapour resistance symbolizing the slight change of vapour temperature is neglected. Like the evaporator section, the condenser section of the heat pipe consists of a condensation area in the top collector and a condensation area in the parallel channels. In this regard, a condensation thermal resistance in the top collector  $R_{c,c-top\ collector}$  is placed in parallel with the condensation thermal resistances in the channels  $R_{c,c-1\ channel}$ . These thermal resistances are followed by conduction resistances at the top collector  $R_{wall,c-top\ collector}$  and in the channels  $R_{wall,c-1\ channel}$ . Even if most of the heat transfer is made through the phase change process of the working fluid, due to the conductivity of the heat pipe material, heat can also be transferred by axial conduction. Usually, axial conduction resistances  $R_{wall,ax}$  are very high compared to the parallel equivalent two-phase thermal resistance and can thus be neglected. Yet, in the case where the adiabatic section length is small, the axial thermal resistance of the heat pipe can have a small impact on the prediction. The different thermal resistances included in the thermal resistance model of a multi-channel heat pipe are summarized in Table 4-6.

Table 4-6. List of the thermal resistances included in the multi-channel thermal resistance model.

<b>Name</b>	<b>Type</b>	<b>Location</b>
$R_{ext,e}$	Contact, forced convection or radiation	External resistance between the heat source and the heat pipe evaporator
$R_{wall,e-bottom\ collector}$	Conduction	Radial conduction through the bottom collector wall (evaporator)
$R_{wall,e-1\ channel}$	Conduction	Radial conduction through the wall of a single channel (evaporator)
$R_{pb,e-bottom\ collector}$	Pool boiling	Pool boiling in the bottom collector (evaporator)
$R_{pb,e-1\ channel}$	Pool boiling	Pool boiling in a single channel (evaporator)
$R_{ff,e-1\ channel}$	Falling film warmup/ evaporation/ boiling	Falling film warmup / evaporation / boiling in a single channel (evaporator)
$R_{c,c-top\ collector}$	Condensation	Condensation in the top collector (condenser)
$R_{c,c-1\ channel}$	Condensation	Condensation in a single channel (condenser)
$R_{wall,c-top\ collector}$	Conduction	Radial conduction through the top collector wall (condenser)
$R_{wall,c-1\ channel}$	Conduction	Radial conduction through the wall of a single channel (condenser)
$R_{wall,ax}$	Conduction	Axial conduction in the heat pipe wall (evaporator / adiabatic / condenser)

The thermal resistance model that was introduced and illustrated in Figure 4-18 with two parallel channels can be extended to any multi-channel heat pipe with a bottom collector, a top collector, and a given number of parallel channels. The multi-channel heat pipe thermal resistance model proposed is presented in Figure 4-19.

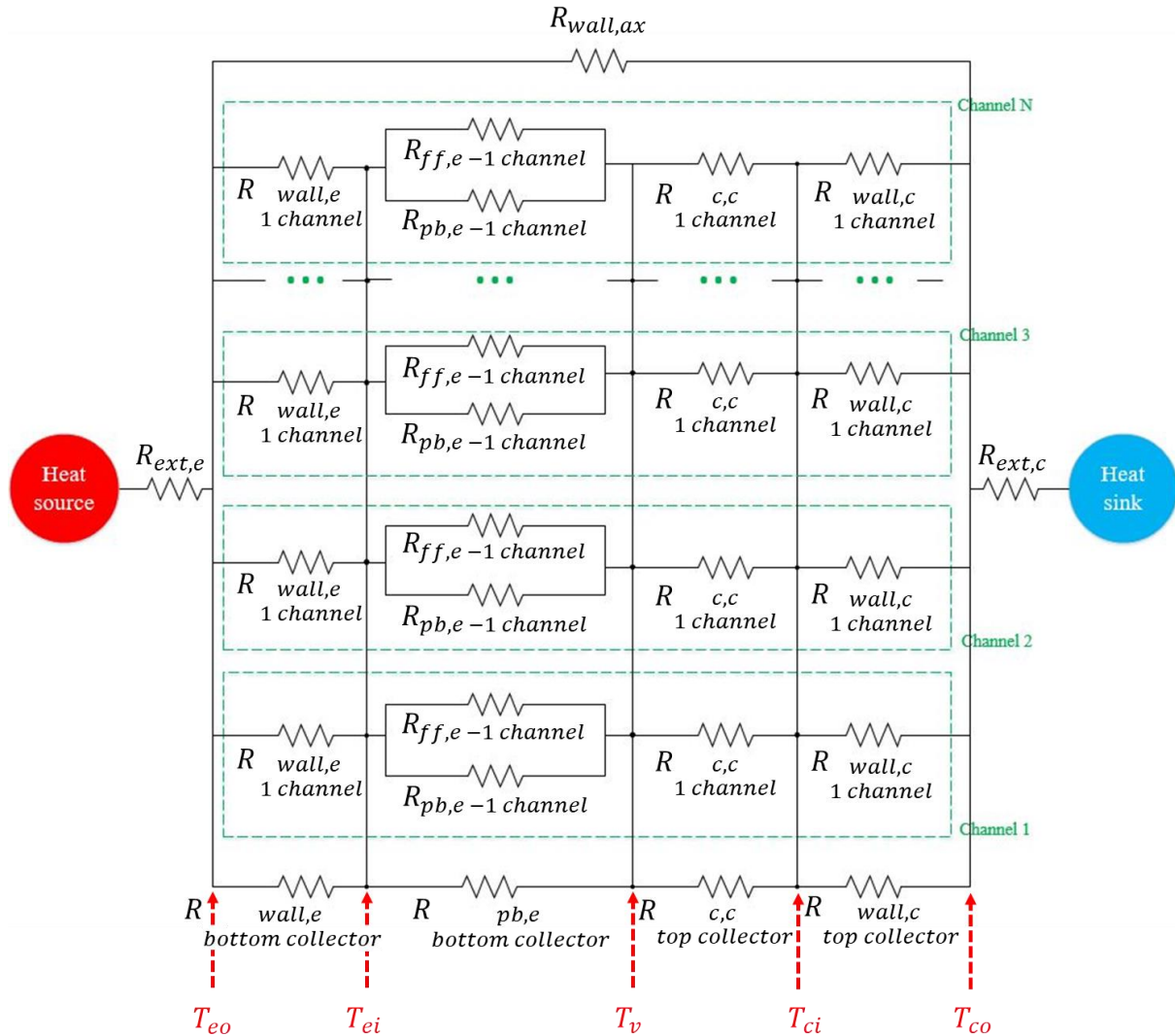


Figure 4-19. Multi-channel heat pipe thermal resistance model

In the multi-channel heat pipe thermal resistance proposed, heat is transferred from the left with the heat source to the heat sink on the right. After the external resistances, from left to right, the thermal resistances of the heat pipe consist of the conduction resistances at the evaporator, boiling resistances, condensation thermal resistances and finally conduction resistances at the condenser. The heat pipe temperatures are obtained at the nodes between all the thermal resistances and are indicated in red. The temperature  $T_{eo}$  is the outer evaporator temperature,  $T_{ei}$  is the inner evaporator temperature,  $T_v$  is the vapour temperature,  $T_{ci}$  is the inner condenser temperature, and  $T_{co}$  is the outer condenser temperature. The heat transfer taking place at the bottom collector and top collector are represented at the bottom of the thermal resistance model. Such heat transfer takes place in parallel with the channels. For

each channel, five thermal resistances are included in the thermal resistance model of the overall multi-channel flat heat pipe. Each channel of the multi-channel heat pipe is circled with green dashed lines in Figure 4-19. These resistances must be placed in parallel for each channel in the multi-channel heat pipe of interest. Finally, the axial conduction thermal resistance is represented at the top of the thermal resistance model.

The proposed thermal resistance model of a multi-channel heat pipe was developed so that it can be adapted to every heat pipe comprising parallel channels which are linked at the top and bottom by collectors. The number of channels can be adapted to suit a given heat pipe. Then, for each heat pipe, suitable correlations must be used to estimate each thermal resistance. For instance, radial and axial conduction thermal resistances are directly linked to the heat pipe geometry, channel diameters and other factors. External thermal resistances must be estimated depending on the type of contact between the multi-channel heat pipe and the heat source or heat sink. In the next sections, this multi-channel heat pipe thermal resistance network was used to model the two pieces of experimental apparatus tested in this research: 1) a three-leg heat pipe and 2) a multi-channel flat heat pipe.

### **4.3 Theoretical modelling of the three-leg multi-channel heat pipe apparatus**

#### **4.3.1 Equivalent thermal resistance network of the overall apparatus**

Electric heaters are used at the bottom cylinder to boil saturated water to transmit thermal energy to the three-leg multi-channel heat pipe. The steam generated rises inside the thermally insulated bottom cylinder and condenses on the legs of the three-leg heat pipe. By doing so, steam yields its latent energy to the three-leg heat pipe. To extract the energy from the three-leg heat pipe, the condenser is contained inside a top cylinder where saturated water boils. The steam created rises inside the top cylinder and condenses on a cold coil through which cooling water circulates and extracts heat from the system. The equivalent thermal resistance network of the complete three-leg multi-channel heat pipe assembly based on this operation is presented in Figure 4-20.

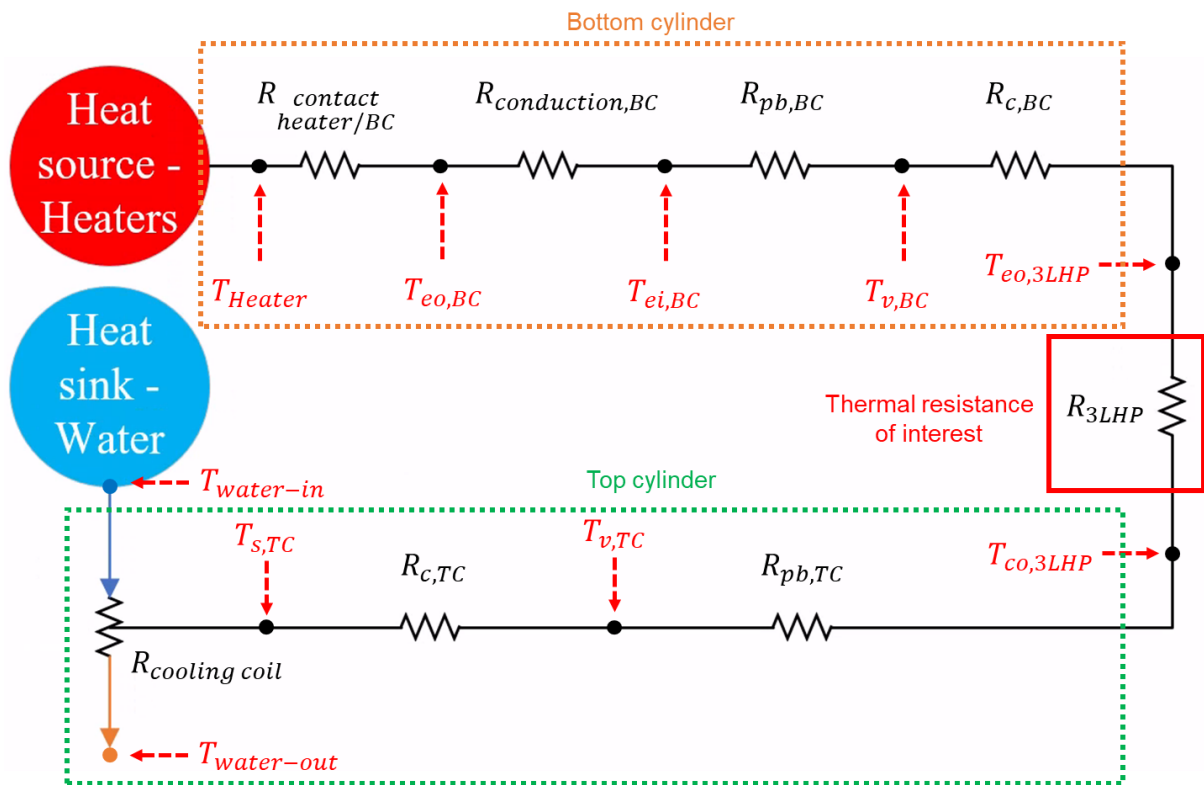


Figure 4-20. Thermal resistance network of the multi-channel three-leg heat pipe assembly

In the three-leg heat pipe assembly thermal resistance network proposed, a contact resistance  $R_{contact\ heater/BC}$  accounts for the difference of temperature between the electric heaters  $T_{heater}$  and the outer temperature of the bottom cylinder evaporator  $T_{eo,BC}$ . Thermal energy is then conducted radially through the bottom cylinder wall which is represented by the thermal resistance  $R_{conduction,BC}$ . This thermal resistance is used to obtain the bottom cylinder inner evaporator wall temperature  $T_{ei,BC}$  which is in contact with the saturated water. The pool boiling thermal resistance of the bottom cylinder  $R_{pb,BC}$  can then be estimated to obtain the steam temperature in the bottom cylinder  $T_{v,BC}$ . To finish with the bottom cylinder which represents the heat source to the three-leg heat pipe, the vapour condenses on the three-leg heat pipe evaporator  $T_{eo,3LHP}$  with a condensation thermal resistance  $R_{c,BC}$ . The thermal energy provided by the bottom cylinder is then transmitted by the three-leg heat pipe which is the main focus of this apparatus. The three-leg heat pipe thermal resistance of interest  $R_{3LHP}$  is encircled in red in Figure 4-20. To remove the heat from the three-leg heat pipe outer condenser wall  $T_{co,3LHP}$ , the condenser is immersed in the top cylinder saturated water pool which boils with a thermal resistance  $R_{pb,TC}$ . The top cylinder steam at a temperature  $T_{v,TC}$  then condenses on the cold cooling coil wall at a temperature  $T_{s,TC}$ . The latent heat given is then transmitted through the coil wall by conduction and then by forced convection between the inner coil wall and the cooling water. This cooling coil thermal resistance  $R_{cooling\ coil}$  relates the coil wall temperature  $T_{s,TC}$  to the cooling water temperatures  $T_{water-in}$  and  $T_{water-out}$ .



For simplicity, the thermal resistance network of the three-leg heat pipe assembly can be simplified by considering one equivalent thermal resistance for the bottom cylinder  $R_{eq,BC}$ , the three-leg heat pipe thermal resistance of interest  $R_{3LHP}$ , and an equivalent thermal resistance for the top cylinder  $R_{eq,TC}$ . The equivalent thermal resistance network of the three-leg heat pipe assembly is shown in Figure 4-21.

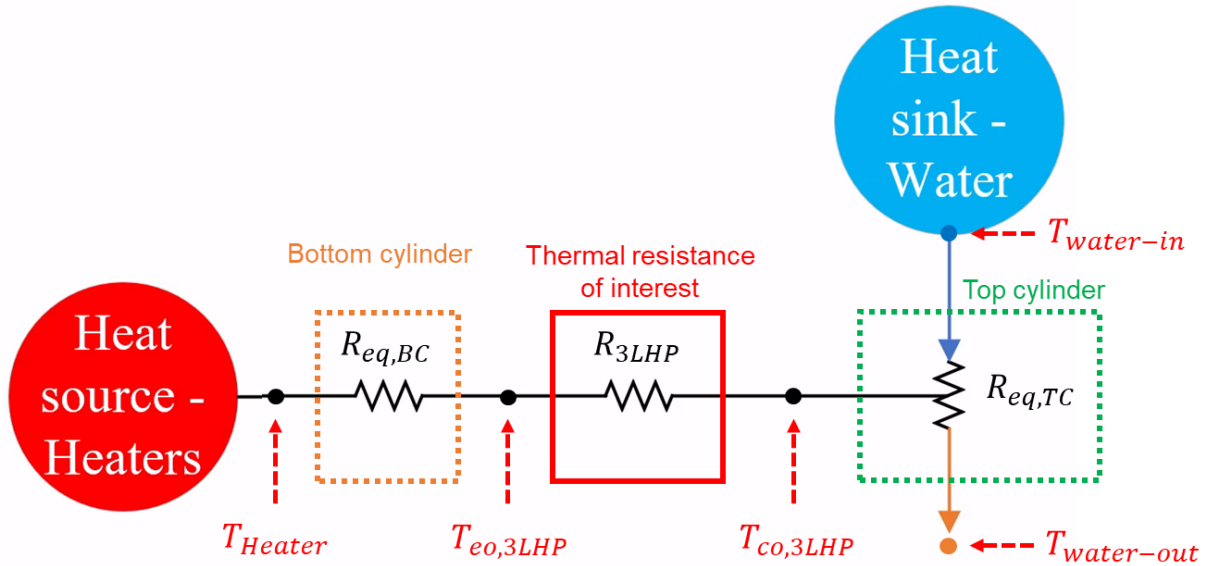


Figure 4-21. Equivalent thermal resistance network of the multi-channel three-leg heat pipe assembly

The bottom and top cylinder equivalent thermal resistances are therefore given by:

$$R_{eq/BC} = R_{contact\ heater/BC} + R_{conduction,BC} + R_{pb,BC} + R_{c,BC} \quad (4-45)$$

$$R_{eq/TC} = R_{pb,TC} + R_{c,TC} + R_{cooling\ coil} \quad (4-46)$$

In practice, the iterative tool developed does not need to calculate all the above resistances to predict the thermal performance of the three-leg heat pipe. To start with, the theoretical model is an iterative tool which assumes the hottest temperature of a given thermal resistance network and then adjusts it to respect an energy balance criterion. Yet, the hottest temperature can be taken at different locations. In the case of this study, as the thermal resistance of interest is the three-leg heat pipe thermal resistance  $R_{3LHP}$ , all the thermal resistances upstream are not needed. Then, the hottest temperature used by the developed iterative model is the outer evaporator temperature of the three-leg heat pipe  $T_{eo,3LHP}$ . The bottom cylinder thermal resistances are therefore not required. Regarding the top cylinder, the thermal resistances are needed by the iterative model to check the energy balance with the heat sink. However, errors in the estimation of the top cylinder thermal resistances would generate errors in the modelling of the three-leg multi-channel heat pipe thermal resistance of interest. Hence, to prevent the appearance of errors while modelling the top cylinder, which is not the focus of this study, the equivalent thermal resistance of the top cylinder was measured experimentally. To sum up the

three-leg heat pipe iterative model operation, the use of each thermal resistance in the iterative tool is listed in Table 4-7.

Table 4-7. Use of each thermal resistance by the iterative model

Thermal resistance	Status
Bottom cylinder: $R_{eq/BC}$	Not needed by the iterative model
3 leg heat pipe: $R_{3LHP}$	Predicted theoretically
Top cylinder: $R_{eq/TC}$	Used by the iterative model, measured experimentally

### 4.3.2 Heat source – Bottom cylinder

The thermal resistances of the bottom cylinder, which represents the heat source of the three-leg heat pipe, are detailed in this section. As the theoretical modelling of the three-leg heat pipe only is focused here, the thermal resistances inside the bottom cylinder have not been estimated theoretically. Nevertheless, these thermal resistances could be predicted with the equations reported in this section. These equations were used during the thermal design of the apparatus.

#### 4.3.2.1 Contact resistance between the heater and bottom cylinder

A contact thermal resistance  $R_{contact\ heater/BC}$  is used to take into consideration the quality of the contact interface between the electric heaters and the bottom cylinder wall. This resistance can be estimated by considering the conduction through the thermal paste layer as:

$$R_{contact\ heater/BC} = \frac{\delta_{tp}}{k_{tp}A_{heaters}} \quad (4-47)$$

where  $\delta_{tp}$  is the thermal paste thickness (m),  $k_{tp}$  the thermal paste thermal conductivity (W/m.K), and  $A_{heaters}$  the contact surface area (m<sup>2</sup>).

#### 4.3.2.2 Radial conduction resistance at the bottom cylinder

Usual conduction laws can be used to estimate the radial conduction through the bottom cylinder wall  $R_{conduction,BC}$  [14]:

$$R_{conduction,BC} = \frac{\ln(D_o/D_i)}{2\pi k_w L_e} \quad (4-48)$$

with  $D_o$  the outside tube diameter of the bottom cylinder (m),  $D_i$  the inside tube diameter of the bottom cylinder (m),  $k_w$  the wall thermal conductivity (W/m.K), and  $L_e$  the evaporator length of the bottom cylinder which is the length of cylinder in contact with the heater (m).

#### 4.3.2.3 Pool boiling resistance at the bottom cylinder

A pool boiling heat transfer coefficient correlation must be used to estimate the water pool boiling thermal resistance  $R_{pb,BC}$  inside the bottom cylinder:

$$R_{pb,BC} = \frac{1}{h_{pb}A_{pb,BC}} \quad (4-49)$$

In the above equation,  $h_{pb}$  is a pool boiling heat transfer coefficient (W/m<sup>2</sup>K), and  $A_{pb,BC}$  is the pool boiling heat transfer area (m<sup>2</sup>). A correlation such as the *Rohsenow* [99] correlation must be used to estimate the pool boiling heat transfer coefficient.

#### 4.3.2.4 Condensation resistance at the bottom cylinder

Like the pool boiling thermal resistance, the condensation thermal resistance in the bottom cylinder  $R_{c,BC}$  can be estimated using a condensation heat transfer coefficient correlation:

$$R_{c,BC} = \frac{1}{h_c A_{c,BC}} \quad (4-50)$$

where  $h_c$  is a condensation heat transfer coefficient (W/m<sup>2</sup>K), and  $A_{c,BC}$  is the condensation heat transfer area (m<sup>2</sup>) which is the evaporator surface of the three-leg heat pipe. The *Nusselt* [103] correlation can be used to estimate the condensation heat transfer coefficient.

### 4.3.3 Three-leg multi-channel heat pipe model

The three-leg heat pipe of interest is modelled in this section. The model is fully theoretical and the discrepancies between the iterative model and the experiments are generated here. The multi-channel thermal resistance model proposed in Figure 4-19 is used to estimate the thermal resistance of the three-leg multi-channel heat pipe  $R_{3LHP}$ . In the case of the three-leg heat pipe, 3 vertical channels are connected in parallel and are included in the thermal resistance model. In this thermal resistance model, correlations had to be integrated to estimate each thermal resistance and they are listed in this section.

#### 4.3.3.1 Radial conduction resistance

Usual conduction laws in tubes are applied to estimate the radial conduction resistance from the outer evaporator wall to the inner evaporator wall. Hence, the following equation is used to estimate the radial conduction resistance of each channel  $R_{wall,e-1\ channel}$  or of the bottom collector  $R_{wall,e-bottom\ collector}$  [14]:

$$R_{wall,e-1\ channel} = \frac{\ln(D_{o,1\ channel}/D_{i,1\ channel})}{2\pi k_w L_{e,1\ channel}} \quad (4-51)$$

with  $D_{o,1\ channel}$  the outer diameter of the channel tube (m),  $D_{i,1\ channel}$  the inner diameter of the channel tube (m),  $k_w$  the wall thermal conductivity (W/m.K), and  $L_{e,1\ channel}$  the evaporator length of the channel (m). The same equation is used for the bottom collector.

#### 4.3.3.2 Axial conduction resistance

Axial conduction along the three channels length is considered for the axial conduction thermal resistance  $R_{wall,ax}$  of the three-leg heat pipe. In heat pipes and thermosyphons, the axial conduction thermal resistance is given by [108]:

$$R_{wall,ax} = \frac{(L_a + 0.5L_c + 0.5L_e)}{k_{alum} A_{cs}} \quad (4-52)$$

where  $L_e$ ,  $L_a$ ,  $L_c$  the evaporator, adiabatic, and condenser length respectively (m), and  $A_{cs}$  the cross-section area of the heat pipe which is filled by solid material. In the three-leg heat pipe, the cross-section area is the sum of the cross-section areas of each parallel leg.

#### 4.3.3.3 Pool boiling resistance

In the three-leg heat pipe, pool boiling simultaneously takes place in the bottom collector and in the three parallel legs. Again, the respective heat transfer coefficient must be predicted to estimate the pool boiling thermal resistances. After comparing the existing pool boiling correlations, the correlation from *Shiraishi et al.* [148] was used to predict the bottom collector pool boiling resistance  $R_{pb,e-bottom collector}$ :

$$R_{pb,e-bottom collector} = \frac{1}{h_{pb,Shiraishi} A_{pb,e-bottom collector}} \quad (4-53)$$

$$h_{pb,Shiraishi} = 0.32 \left( \frac{\rho_l^{0.65} k_l^{0.3} c_{p,l}^{0.7} g^{0.2}}{\rho_v^{0.25} i_{lv}^{0.4} \mu_l^{0.1}} \right) \left( \frac{P_v}{P_{atm}} \right)^{0.23} q_{pb}''^{0.4} \quad (4-54)$$

where  $h_{pb,Shiraishi}$  is the pool boiling heat transfer coefficient predicted by the correlation from *Shiraishi et al.* [148] (W/m<sup>2</sup>K),  $A_{pb,e-bottom collector}$  is the pool boiling area in the bottom collector (m<sup>2</sup>),  $\rho_l$  and  $\rho_v$  the liquid and vapour densities (kg/m<sup>3</sup>),  $k_l$  the liquid thermal conductivity (W/m.K),  $c_{p,l}$  the specific heat (J/kg.K),  $g$  the gravitational acceleration (m/s<sup>2</sup>),  $i_{lv}$  the latent heat of vaporization (J/kg),  $\mu_l$  the liquid dynamic viscosity (Pa.s),  $P_v$  the saturated vapour pressure (Pa),  $P_{atm}$  the atmospheric pressure (Pa), and  $q_{pb}''$  the pool boiling heat flux (W/m<sup>2</sup>). For the pool boiling resistance of a leg  $R_{pb,e-1 channel}$ , the *Imura et al.* [145] correlation was used:

$$R_{pb,e-1 channel} = \frac{1}{h_{pb,Imura} A_{pb,e-1 channel}} \quad (4-55)$$

$$h_{pb,Imura} = 0.32 \left( \frac{\rho_l^{0.65} k_l^{0.3} c_{p,l}^{0.7} g^{0.2}}{\rho_v^{0.25} i_{lv}^{0.4} \mu_l^{0.1}} \right) \left( \frac{P_v}{P_{atm}} \right)^{0.3} q_{pb}''^{0.4} \quad (4-56)$$

with  $h_{pb,Imura}$  the pool boiling heat transfer coefficient predicted by the correlation from *Imura et al.* [145] (W/m<sup>2</sup>K), and  $A_{pb,e-1-channel}$  is the pool boiling area in one leg (m<sup>2</sup>),

#### 4.3.3.4 Falling film boiling resistance

Unexpectedly, the three-leg experimental data revealed that only pool boiling occurred at the evaporator. Indeed, depending on the charging of the heat pipe, the temperatures at the top of the evaporator were found similar than that of the bottom of the legs. The experimental heat transfer coefficients measured did not exhibit a falling film behaviour which is shown in the results section. In this regard, the falling film resistances were not considered for the prediction of the three-leg heat pipe performances and only pool boiling correlations were used.

#### 4.3.3.5 Condensation resistance

The correlation by *Schnabel and Palen* [194] was implemented in the model for the condensation thermal resistances in the legs  $R_{c,c-1 channel}$  and in the top collector  $R_{c,c-top collector}$ :

$$R_{c,c-1 channel} = \frac{1}{h_{c,Schnabel} A_{c,c-1 channel}} \quad (4-57)$$

$$R_{c,c-top collector} = \frac{1}{h_{c,Schnabel} A_{c,c-top collector}} \quad (4-58)$$

$$h_c = \frac{0.0283(Re_f/4)^{7/24} Pr_l^{1/3}}{1 + 9.66(Re_f/4)^{-3/8} Pr_l^{-1/6}} k_l \left( \frac{\mu_l^2}{\rho_l(\rho_l - \rho_v)g} \right)^{-1/3} \quad (4-59)$$

where,

- $Re_{f,L_c} = \frac{4\Gamma_{L_c}}{\mu_l}$

In the above equations,  $h_{c,Schnabel}$  is the condensation heat transfer coefficient predicted by the correlation from *Schnabel and Palen* [194],  $A_{c,c-1 channel}$  is the condensation area in a single leg (m<sup>2</sup>),  $A_{c,c-top collector}$  is the condensation area in the top collector (m<sup>2</sup>),  $Re_f$  the falling film Reynolds number,  $\Gamma_{L_c}$  the mass flow rate of liquid per unit periphery (kg/m.s),  $\mu_l$  the liquid dynamic viscosity (Pa.s),  $\rho_l$  and  $\rho_v$  the liquid and vapour densities (kg/m<sup>3</sup>), and  $g$  the gravitational acceleration (m/s<sup>2</sup>).

#### 4.3.4 Heat sink – Top cylinder

The thermal resistances of the top cylinder which represents the heat sink of the three-leg heat pipe are detailed in this section. To prevent the transmission of errors to the three-leg multi-channel heat pipe model, the equivalent thermal resistance of the top cylinder has been measured experimentally and fed to the thermal model. By doing so, the errors made between the theoretical model and the experiments were only caused by the theoretical modelling of the three-leg multi-channel heat pipe. The top cylinder thermal resistances equations are reported hereafter.

##### 4.3.4.1 Pool boiling resistance at the top cylinder

Similar to the bottom cylinder, a pool boiling heat transfer coefficient correlation must be used to estimate the water pool boiling thermal resistance  $R_{pb,TC}$  inside the top cylinder:

$$R_{pb,TC} = \frac{1}{h_{pb} A_{pb,TC}} \quad (4-60)$$

with  $h_{pb}$  a pool boiling heat transfer coefficient (W/m<sup>2</sup>K), and  $A_{pb,TC}$  the pool boiling heat transfer area (m<sup>2</sup>) which corresponds to the three-leg heat pipe condenser.

#### 4.3.4.2 Condensation resistance at the top cylinder

The condensation thermal resistance in the top cylinder  $R_{c,TC}$  is estimated using:

$$R_{c,TC} = \frac{1}{h_c A_{c,TC}} \quad (4-61)$$

where  $h_c$  is a condensation heat transfer coefficient (W/m<sup>2</sup>K), and  $A_{c,TC}$  is the condensation heat transfer area (m<sup>2</sup>) which corresponds to the cooling coil surface. Experimentally, the condensation heat transfer coefficient in the top cylinder could not be measured as the wall temperature of the cooling coil inside the top cylinder was not measured.

#### 4.3.4.3 Cooling coil resistance in the top cylinder

Two types of heat transfer must be used to predict the thermal resistance of the cooling coil. First, a conduction thermal resistance  $R_{conduction,coil}$  must be considered to calculate the inner wall temperature of the cooling manifold. Based on this temperature, forced convection laws can be applied to estimate the forced convection thermal resistance  $R_{fc,coil}$ . Then, the cooling coil thermal resistance  $R_{cooling\ coil}$  can be estimated by:

$$R_{cooling\ coil} = R_{conduction,coil} + R_{fc,coil} \quad (4-62)$$

The radial conduction thermal resistance can be estimated with [14]:

$$R_{conduction,coil} = \frac{\ln(D_o/D_i)}{2\pi k_w L_e} \quad (4-63)$$

with  $D_o$  is the outer tube diameter of the coil (m),  $D_i$  the inside tube diameter of the coil (m),  $k_w$  the wall thermal conductivity (W/m.K), and  $L_e$  the coil length (m). The forced convection thermal resistance of the coil can be expressed with:

$$R_{conduction,coil} = \frac{1}{h_{fc} A_{fc}} \quad (4-64)$$

where  $h_{fc}$  is the forced convection heat transfer coefficient (W/m<sup>2</sup>K), and  $A_{fc}$  is the forced convection heat transfer area (m<sup>2</sup>). Suitable correlations must be used to estimate the forced convection heat transfer coefficient  $h_{fc}$ . For internal forced convection, the correlation to use differs depending on the cooling water Reynolds number which dictates the flow turbulence. For straight tubes, the forced convection correlations by *Zukauskas* [14], [239] can be used. However, in the case of helicoidal pipes such as the cooling coil used in the assembly, the forced convection heat transfer coefficient is increased due to a better mixing of the fluid generated by the centrifugal force which creates a secondary flow pattern forcing the liquid particles to move to the outer wall and spiral back to the inner wall [104], [105]. To take this aspect into consideration, a coil friction factor is introduced and represents the heat transfer coefficient improvement compared to a straight tube. To estimate the laminar friction factor in a coil, the correlation by *Manlapaz and Churchill* [240] is advised. For turbulent flows, the coil friction factor can be estimated by the *Srinivasan et al.* [241] correlation.

#### 4.3.4.4 Equivalent heat sink thermal resistance

In practice, the thermal resistances inside the top cylinder were not modelled theoretically. To prevent the transmission of errors, the equivalent thermal resistance of the top cylinder  $R_{eq,TC}$  was measured experimentally and fed to the iterative model. The equivalent thermal resistance of the top cylinder was obtained experimentally using:

$$R_{eq,TC} = \frac{1}{\dot{Q}} \times \frac{T_{water,in} - T_{water,out}}{\ln\left(\frac{T_{co,3LHP} - T_{water,out}}{T_{co,3LHP} - T_{water,in}}\right)} \quad (4-65)$$

where  $R_{eq,TC}$  is the top cylinder thermal resistance (K/W),  $\dot{Q}$  is the total heat transfer rate through the system (W),  $T_{water,in}$  and  $T_{water,out}$  are the water inlet and outlet temperatures (K), and  $T_{co,3LHP}$  is the three-leg heat pipe outer condenser wall temperature (K). Figure 4-22 shows the experimental equivalent resistance of the heat sink of the three-leg heat pipe assembly.

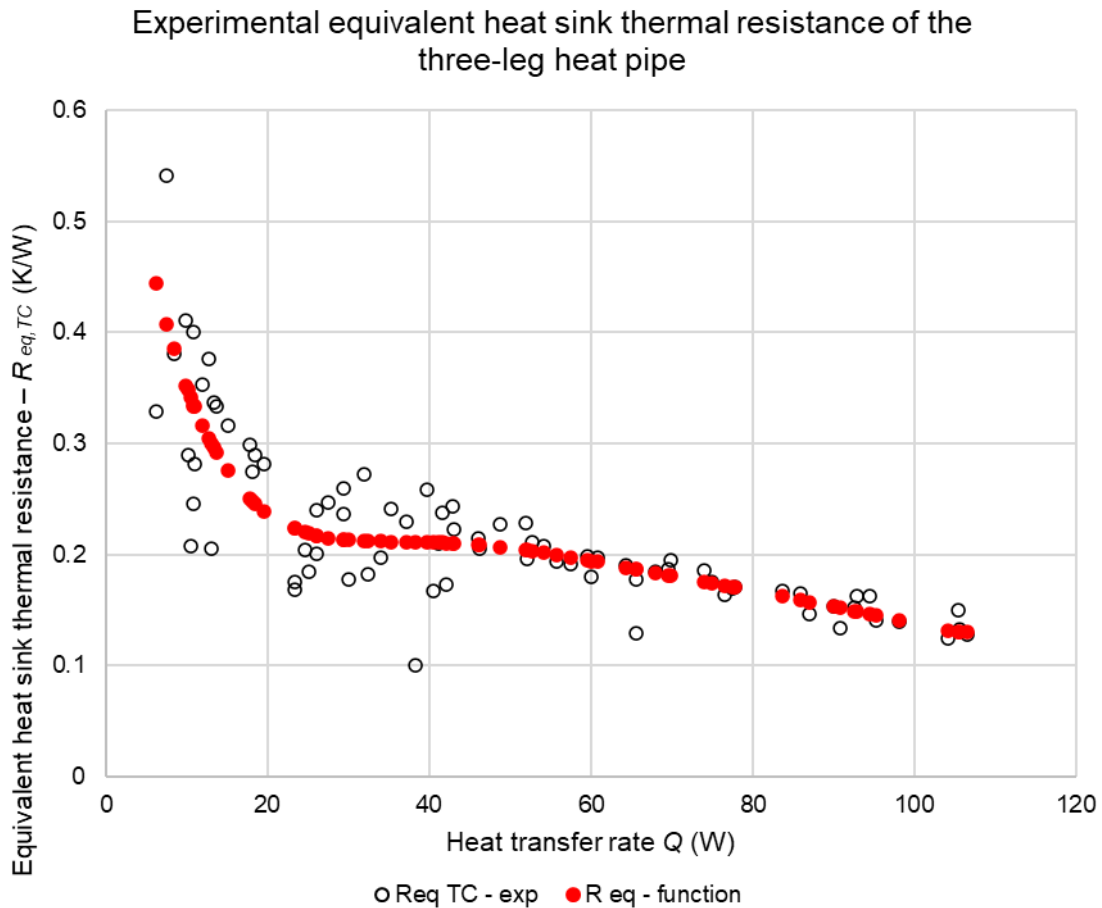


Figure 4-22. Experimental equivalent heat sink thermal resistance of the three-leg heat pipe and respective approached function

Figure 4-22 shows the measured thermal resistance of the heat sink with black markers whereas the corresponding correlated function is shown in red. The equivalent thermal resistance of the heat sink  $R_{eq,TC}$  was correlated from the experimental measurements as:

$$R_{eq,TC} = 8.73 \times 10^{-12} \dot{Q}^6 - 3.59 \times 10^{-9} \dot{Q}^5 + 5.96 \times 10^{-7} \dot{Q}^4 - 5.07 \times 10^{-7} \dot{Q}^3 \quad (4-66)$$

$$+ 2.30 \times 10^{-3} \dot{Q}^2 - 5.27 \times 10^{-2} \dot{Q} + 0.69$$

with  $\dot{Q}$  the heat transfer rate (W). This function was then used in the theoretical model to complete the thermal resistance network presented in Figure 4-21 and operate the energy balance.

## 4.4 Theoretical modelling of the multi-channel flat heat pipe apparatus

### 4.4.1 Equivalent thermal resistance network of the assembly

To test the multi-channel flat heat pipe, heat is transmitted from flat heaters placed at the bottom of the heat pipe to a cooling manifold placed at the top. Cold water is used as a heat sink and dissipates the heat while circulating in the manifold. To validate the thermal resistance model of the multi-channel heat pipe, the overall system must be modelled to operate an energy balance between the heat source and heat sink. For the modelling of the multi-channel flat heat pipe assembly, the equivalent thermal resistance network presented in Figure 4-23 was used.

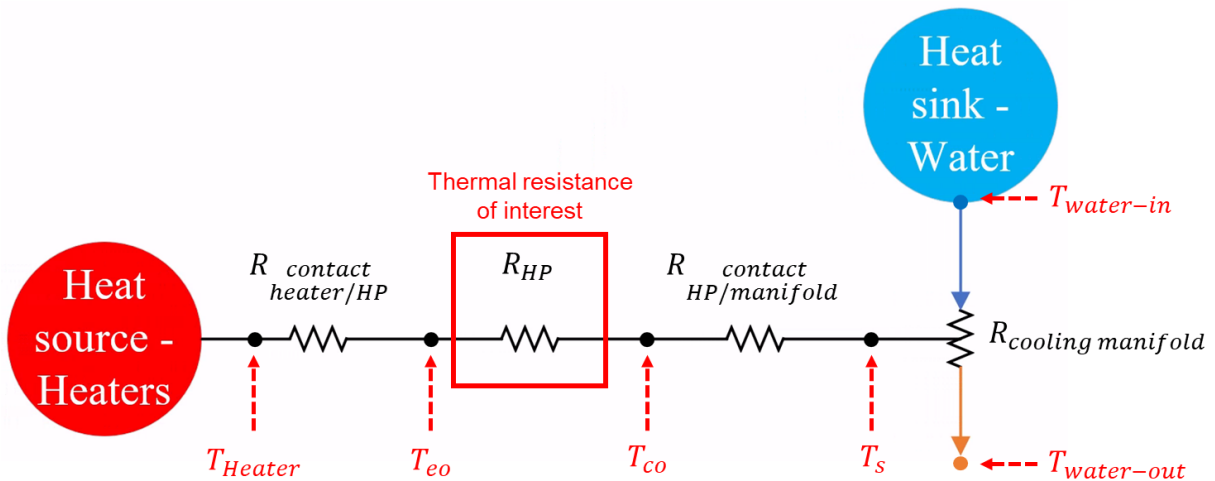


Figure 4-23. Thermal resistance network of the multi-channel flat heat pipe assembly

In the thermal resistance model proposed, the contact between the heaters and the heat pipe is described by a contact thermal resistance  $R_{contact\ heater/HP}$ . This contact is responsible for the difference of temperature between the silicon heaters  $T_{heater}$  and the outside temperature of the evaporator of the multi-channel flat heat pipe  $T_{eo}$ . The multi-channel flat heat pipe thermal resistance of interest  $R_{HP}$  (in red) is described using the multi-channel heat pipe thermal resistance model and suitable correlations detailed later in this section. Between the cooling manifold and the heat pipe condenser, a contact resistance  $R_{contact\ HP/manifold}$  describes the quality of the interface and potential differences of temperature between the outer condenser temperature of the heat pipe  $T_{co}$  and the surface temperature of the cooling manifold  $T_s$ . Finally, to describe the heat recovery from the cooling manifold to the cooling



water, a forced convection thermal resistance  $R_{cooling\ manifold}$  relates the surface temperature of the cooling manifold  $T_s$  to the water inlet and outlet temperatures  $T_{water-in}$  and  $T_{water-out}$ . Each thermal resistance and the equations used are described hereafter.

#### 4.4.2 Heat source

In practice, differences of temperature can be seen between the temperature of the heaters and the temperature of the heat pipe evaporator. This can be due to two main reasons: 1) potential losses of energy to the environment if the thermal insulation isn't perfect and 2) a thermal resistance at the contact interface. In the theoretical model, the losses are assumed to be negligible. To describe the contact thermal resistance, one dimensional conduction through the thermal paste layer can be considered. Then, the contact resistance can be estimated using:

$$R_{contact\ heater/HP} = \frac{\delta_{tp}}{k_{tp}A_{heaters}} \quad (4-67)$$

where  $\delta_{tp}$  is the thermal paste thickness (m),  $k_{tp}$  the thermal paste thermal conductivity (W/m.K), and  $A_{heaters}$  the contact surface area (m<sup>2</sup>). In practice, the contact thermal resistances are very small and can often be neglected without significant changes in the predictions.

#### 4.4.3 Multi-channel flat heat pipe model

The multi-channel thermal resistance model proposed in Figure 4-19 is used to estimate the thermal resistance of the multi-channel heat pipe  $R_{HP}$ . In the case of the multi-channel flat heat pipe, 44 channels are connected in parallel and are included in the thermal resistance model. In this thermal resistance model, correlations had to be integrated to estimate each thermal resistance and they are listed in this section.

##### 4.4.3.1 Radial conduction resistance

Special equations describing conduction heat transfer from a flat surface to a channel situated inside the material are used to determine the radial conduction resistances from the heat pipe outer surface to each channel  $R_{wall,e-1\ channel}$  or to the bottom collector  $R_{wall,e-bottom\ collector}$ . In this regard, the channels are incorporated as cylinders with a hydraulic diameter  $D_h$  calculated from:

$$D_h = \frac{4A_{cs}}{p} \quad (4-68)$$

with  $A_{cs}$  the cross-sectional area of the channel (m<sup>2</sup>), and  $p$  the perimeter of the channel (m). For complex geometries, the axial conduction resistance is obtained from a shape factor  $S$  as:

$$R_{wall,e-1\ channel} = \frac{1}{k_{alum}S} \quad (4-69)$$

where  $k_{alum}$  the aluminium thermal conductivity (W/m.K). In the case of the flat heat pipe, the shape factor must consider conduction from the flat surface to one of the parallel cylinders situated inside the material. The geometry of interest is schematized in Figure 4-24.

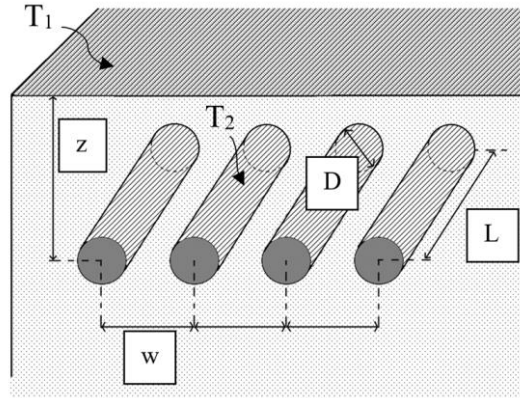


Figure 4-24. Radial conduction geometry of the multi-channel flat heat pipe considered

Based on Figure 4-24, the conduction shape factor  $S$  for the geometry of interest is given by [14]:

$$S = \frac{2\pi L}{\ln\left(\frac{2w}{\pi D} \sinh \frac{2\pi z}{w}\right)} \quad (\text{for each channel}) \quad (4-70)$$

with  $z$  the material thickness between the surface and the channel axis (m),  $w$  the pitch between each parallel channel (m),  $D$  the diameter of the channel (m), and  $L$  the length of the parallel channels (m). Then, for each channel, the radial conduction thermal resistance is [14]:

$$R_{wall,e-1 \text{ channel}} = \frac{1}{k_{alum} S} = \frac{\ln\left(\frac{2w}{\pi D} \sinh \frac{2\pi z}{w}\right)}{k_{alum} 2\pi L} \quad (\text{for each channel}) \quad (4-71)$$

One must be aware that the length of the channel in the above equation must correspond to the heated length of the channel. Again, the diameter of the channel is estimated using the hydraulic diameter. To calculate the axial conduction thermal resistance to the bottom collector, the same shape factor can be used but the parameters such as the length and diameter of the collector must be adapted. Similar equations have been used to estimate the radial conduction resistances at the condenser of the multi-channel flat heat pipe by adapting the length of the channels in contact with the heat sink.

#### 4.4.3.2 Axial conduction resistance

In the case of the multi-channel flat heat pipe, the axial conduction thermal resistance  $R_{wall,ax}$  consists of conduction inside a plain sheet of metal with a given length and thickness. The axial conduction thermal resistance can be estimated by [108]:

$$R_{wall,ax} = \frac{(L_a + 0.5L_c + 0.5L_e)}{k_{alum} A_{cs}} \quad (4-72)$$

where  $L_e$ ,  $L_a$ ,  $L_c$  the evaporator, adiabatic, and condenser length respectively (m), and  $A_{cs}$  the cross-section area of the heat pipe which is filled by solid material only.

#### 4.4.3.3 Boiling resistance

In the flat heat pipe assembly, the silicon heaters cover the section of the channels that is filled by liquid only. In this regard, only pool boiling is occurring, and the falling film thermal resistances need to be removed from the multi-channel heat pipe thermal resistance network. To estimate the pool boiling resistance of the multi-channel flat heat pipe, many correlations were compared, and they are presented in the results section. After comparison, the correlation chosen for the boiling thermal resistance prediction is that by *Rohsenow* [137]:

$$R_{pb,e-1\ channel} = \frac{1}{h_{pb,Rohsenow} A_{pb,e-1\ channel}} \quad (4-73)$$

$$h_{pb,Rohsenow} = \left( \frac{q''_{pb}}{i_{lv}} \right)^{1-r} \left[ \mu_l / \sqrt{\frac{\sigma}{g(\rho_l - \rho_v)}} \right]^r \frac{c_{p,l}}{C_{sf}} Pr_l^{-s} \quad (4-74)$$

where,

- ❖  $r = 1/3$
- ❖  $\begin{cases} s = n = 1 \text{ for water} \\ s = n = 1.7 \text{ for other fluids} \end{cases}$
- ❖  $C_{sf}$  is a constant depending on the solid-fluid characteristics

In the *Rohsenow* [137] equation,  $h_{pb,Rohsenow}$  is the nucleate boiling heat transfer coefficient (W/m<sup>2</sup>K) estimated from the Rohsenow correlation,  $A_{pb,e-1\ channel}$  the pool boiling heat transfer area (m<sup>2</sup>),  $q''_{pb}$  the pool boiling heat flux (W/m<sup>2</sup>),  $i_{lv}$  the latent heat of vaporization (J/kg),  $\mu_l$  the liquid dynamic viscosity (Pa.s),  $\sigma$  the liquid surface tension (N/m),  $g$  the gravitational acceleration (m/s<sup>2</sup>),  $\rho_l$  and  $\rho_v$  the liquid and vapour densities (kg/m<sup>3</sup>),  $c_{p,l}$  the specific heat (J/kg.K), and  $Pr_l$  the liquid Prandtl number. For an R134a/aluminium interface, the constant  $C_{sf}$  was taken as  $C_{sf} = 0.013$  [105]. To obtain the pool boiling resistance in the bottom collector  $R_{pb,e-bottom\ collector}$ , the same correlation was used and the pool boiling heat transfer area was adapted accordingly.

#### 4.4.3.4 Condensation resistance

At the condenser section, the cooling manifold covers the top collector and a portion of each parallel channel. Condensation correlations must be used for both condensation areas and the thermal resistances of the collector and channels. Similar to the boiling resistance, the correlations reported to date have been integrated and compared. After comparison, the correlation by *Hussein et al.* [195] was found to be the most suitable and was used to estimate the condensation thermal resistances:

$$R_{c,c-1\ channel} = \frac{1}{h_{c,Hussein} A_{c,c-1\ channel}} \quad (4-75)$$

$$h_{c,Hussein} = \left(\frac{L_c}{D_i}\right)^{\frac{1}{4}}(\cos(\beta))^{0.358} [0.997 - 0.334(\cos(\beta))^{0.108}]h_{c,Nusselt} \quad (4-76)$$

where,

$$h_{c,Nusselt} = 0.943 \left\{ \frac{\rho_l(\rho_l - \rho_v)i_{lv}gk_l^3}{\mu_l L_c (T_{sat} - T_w)} \right\}^{1/4}$$

In the above equations,  $h_{c,Hussein}$  is the condensation heat transfer coefficient (W/m<sup>2</sup>K) estimated with the *Hussein et al.* [195] correlation,  $A_{c,c-1 channel}$  the condensation heat transfer area (m<sup>2</sup>),  $L_c$  the condenser length (m),  $D_i$  the internal diameter of the heat pipe (m),  $\beta$  the inclination angle of the heat pipe (°),  $h_{c,Nusselt}$  the condensation heat transfer coefficient (W/m<sup>2</sup>K) estimated with the *Nusselt* [103] correlation,  $\rho_l$  and  $\rho_v$  the liquid and vapour densities (kg/m<sup>3</sup>),  $i_{lv}$  the latent heat of vaporization (J/kg),  $g$  the gravitational acceleration (m/s<sup>2</sup>),  $k_l$  the liquid thermal conductivity (W/m.K),  $\mu_l$  the liquid dynamic viscosity (Pa.s),  $T_{sat}$  the saturation temperature (K), and  $T_w$  the wall temperature (K). Again, the condensation thermal resistance of the top collector  $R_{c,c-top collector}$  is obtained with the same correlation by adapting the geometrical variables.

#### 4.4.3.5 Overall heat pipe thermal resistance

The thermal resistance network of the multi-channel flat heat pipe is then reduced to obtain the overall thermal resistance of the multi-channel flat heat pipe  $R_{HP}$ . To do so, the thermal resistance network of the multi-channel flat heat pipe can be simplified as shown in Figure 4-25.

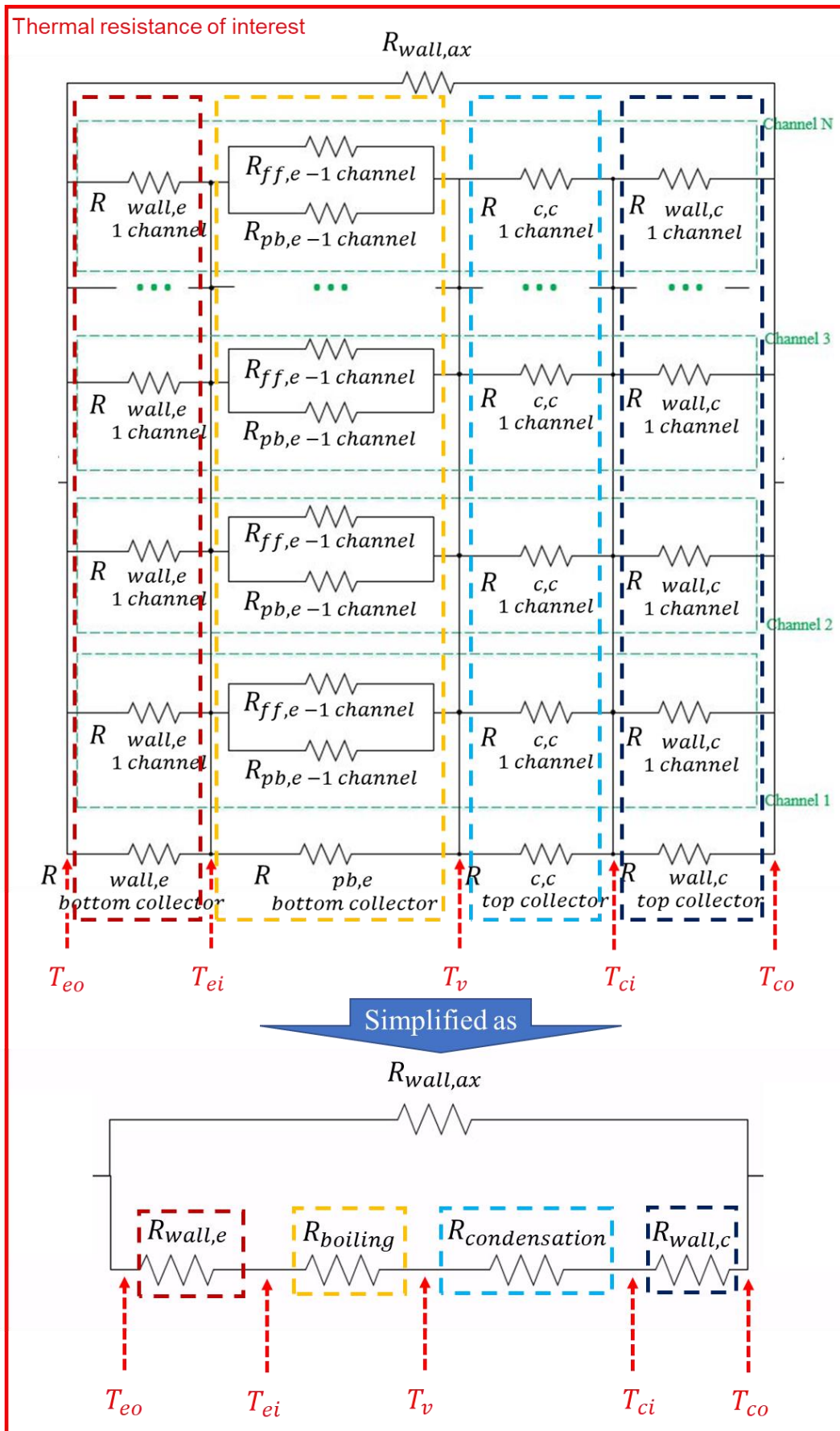


Figure 4-25. Multi-channel flat heat pipe thermal resistance simplification

Based on this thermal resistance simplification, the multi-channel flat heat pipe thermal resistance  $R_{HP}$  can be expressed as:

$$\frac{1}{R_{HP}} = \frac{1}{R_{wall,ax}} + \frac{1}{(R_{wall,e} + R_{boiling} + R_{condensation} + R_{wall,c})} \quad (4-77)$$

where  $R_{wall,ax}$  is the axial conduction resistance,  $R_{wall,e}$  is the equivalent radial conduction thermal resistance through the evaporator wall,  $R_{boiling}$  the equivalent boiling resistance,  $R_{condensation}$  the equivalent condensation resistance, and  $R_{wall,c}$  the equivalent radial conduction thermal resistance through the condenser wall (K/W). Knowing that in the case of the multi-channel flat heat pipe investigated, no falling film boiling or evaporation took place, the equivalent thermal resistances are obtained using:

$$R_{wall,e} = \frac{R_{wall,e-1\ channel} \times R_{wall,e-bottom\ collector}}{nR_{wall,e-bottom\ collector} + R_{wall,e-1\ channel}} \quad (4-78)$$

$$R_{boiling} = \frac{R_{pb,e-1\ channel} \times R_{pb,e-bottom\ collector}}{nR_{pb,e-bottom\ collector} + R_{pb,e-1\ channel}} \quad (4-79)$$

$$R_{condensation} = \frac{R_{c,c-1\ channel} \times R_{c,c-bottom\ collector}}{nR_{c,c-bottom\ collector} + R_{c,c-1\ channel}} \quad (4-80)$$

$$R_{wall,c} = \frac{R_{wall,c-1\ channel} \times R_{wall,c-bottom\ collector}}{nR_{wall,c-bottom\ collector} + R_{wall,c-1\ channel}} \quad (4-81)$$

In the above equations,  $n$  is the number of channels in the multi-channel flat heat pipe.

#### 4.4.4 Heat sink

Once the temperature of the outer wall of the heat pipe  $T_{co}$  is obtained, the temperature of the cooling manifold surface and of the cooling water must be obtained. First, a contact area with thermal paste is found between the heat pipe surface and the cooling manifold surface. Even if the two aluminium surfaces are in direct contact with a thin layer of thermal paste, the contact may not be perfect, and a slight difference of temperature between the two surfaces can be observed. In this regard, a contact resistance  $R_{contact\ HP/manifold}$  is considered and can be estimated from:

$$R_{contact\ HP/manifold} = \frac{\delta_{tp}}{k_{tp}A_{manifold}} \quad (4-82)$$

with  $\delta_{tp}$  the thermal paste thickness (m),  $k_{tp}$  the thermal paste thermal conductivity (W/m.K), and  $A_{manifold}$  the cooling manifold contact surface area (m<sup>2</sup>). Then, the surface temperature of the cooling manifold  $T_s$  can be related to the cooling water temperature inside the cooling manifold using the logarithmic mean temperature difference (LMTD) method. The thermal resistance of the cooling manifold  $R_{cooling\ manifold}$  was determined experimentally to avoid potential errors in the modelling of the cooling manifold thermal resistance that would propagate to the heat pipe model. Obviously, the thermal resistance of the cooling manifold

depends on the cooling water flow rate as higher flow rates and Reynolds number enhance the forced convective heat transfer. In this regard, the cooling manifold thermal resistance was measured for the three cooling water flow rates used in the experiments: 2L/min, 4L/min, and 6L/min. This experimental cooling manifold thermal resistance was then correlated by equations and integrated to the model. The experimental cooling manifold thermal resistance and the correlated functions are presented in Figure 4-26.

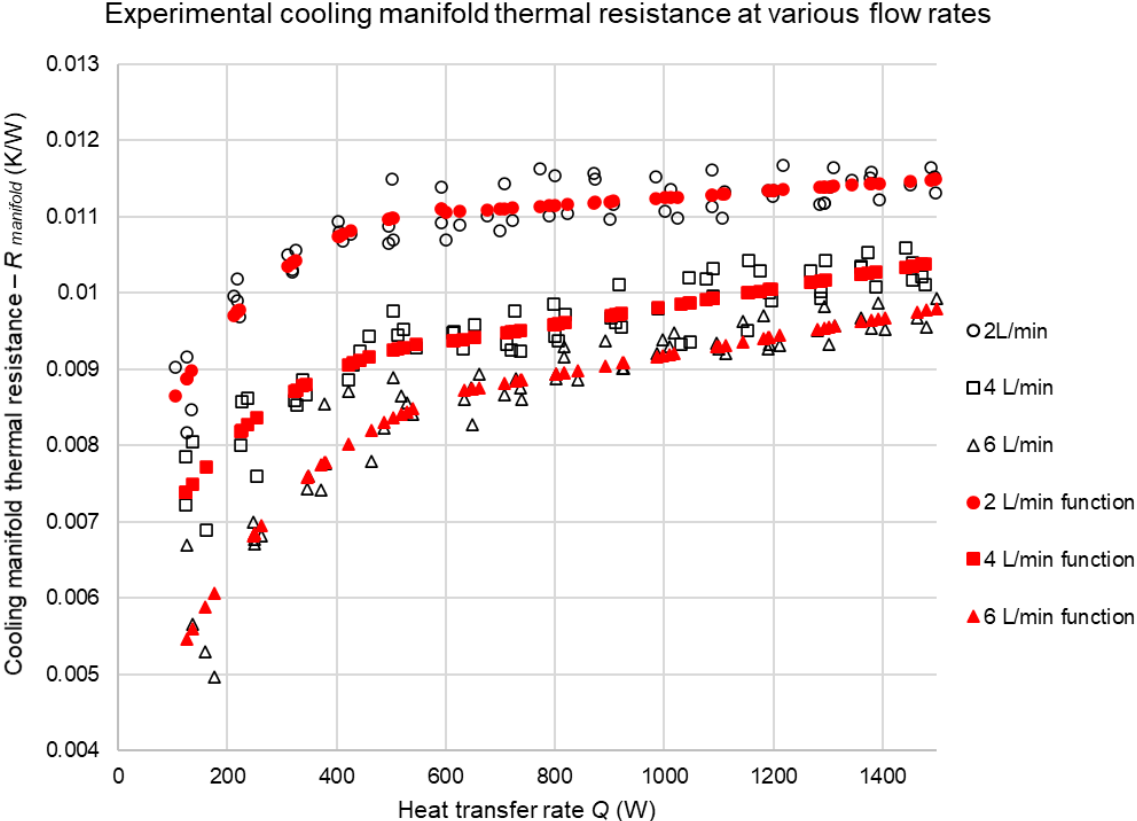


Figure 4-26. Experimental cooling manifold thermal resistance and respective correlated functions

From Figure 4-26, the experimental cooling manifold thermal resistances are represented in black markers whereas the correlated functions are in red. As expected, the thermal resistance of the cooling manifold differs significantly at different coolant flow rates. Hence, three series for 2L/min, 4L/min, and 6L/min are shown with circles, squares, and triangles, respectively. At higher flow rates, the cooling manifold thermal resistance decreases due to an improved forced convection heat transfer coefficient. The measured thermal resistance of the cooling manifold is not linear with the change of heat transfer rate. In particular, below heat transfer rates of around 600W, the cooling manifold thermal resistance drops. Scientifically, this shows an error in the measurements as the cooling manifold thermal resistance consists of conduction and forced convection resistances only and thus should only be influenced by the cooling water flow rate. In the case studied, the variation of cooling manifold thermal resistance with the heat transfer rate can be explained by the interaction with the heat pipe or potential thermal losses. It is likely that the cooling manifold surface temperature measurement was influenced by the

heat pipe surface temperature. Indeed, the measurement of the hot surface temperature of the cooling manifold had to be taken at the interface between the cooling manifold and heat pipe, which makes it laborious. Another factor that may have influenced the measurements are thermal losses which can vary with the heat transfer rate. Nevertheless, the measured experimental values of the cooling manifold thermal resistances have been used for the theoretical model so that the experimental and theoretical thermal resistances of the heat pipe are not influenced by a different cooling manifold thermal resistance. To improve the accuracy of the cooling manifold thermal resistance functions, each series has been divided into two equations for different heat transfer ranges. The cooling manifold thermal resistance  $R_{cooling\ manifold}$  was correlated as described in Table 4-8.

Table 4-8. Cooling manifold thermal resistance correlated functions

Conditions	$R_{cooling\ manifold}$ correlated function
<b>2 L/min</b>	
$\dot{Q} < 600$	$R_{cooling\ manifold} = (-4.46635 \times 10^{-15})\dot{Q}^4 + (1.816534612 \times 10^{-11})\dot{Q}^3$ $+ (-2.665176019084 \times 10^{-8})\dot{Q}^2 + (1.70542991096301 \times 10^{-5})\dot{Q}$ $+ 7.1217407864622 \times 10^{-3}$
$600 < \dot{Q}$	$R_{cooling\ manifold} = (4.833211829596 \times 10^{-7})\dot{Q} + 1.07605097655724 \times 10^{-2}$
<b>4 L/min</b>	
$\dot{Q} < 600$	$R_{cooling\ manifold} = (-4.27444 \times 10^{-15})\dot{Q}^4 + (1.638924747 \times 10^{-11})\dot{Q}^3$ $+ (-2.262339641124 \times 10^{-8})\dot{Q}^2 + (1.44041688084279 \times 10^{-5})\dot{Q}$ $+ 5.91576496171534 \times 10^{-3}$
$600 < \dot{Q}$	$R_{cooling\ manifold} = (1.17120317947527 \times 10^{-6})\dot{Q} + 8.64653310422441 \times 10^{-3}$
<b>6 L/min</b>	
$\dot{Q} < 600$	$R_{cooling\ manifold} = (-3.94335 \times 10^{-15})\dot{Q}^4 + (1.667795959 \times 10^{-11})\dot{Q}^3$ $+ (-2.623133389642 \times 10^{-8})\dot{Q}^2 + (1.93157060561482 \times 10^{-5})\dot{Q}$ $+ 3.4035236753789 \times 10^{-3}$
$600 < \dot{Q}$	$R_{cooling\ manifold} = (1.2377819954102 \times 10^{-6})\dot{Q} + 7.93912796631387 \times 10^{-3}$

## 4.5 Working fluid properties

Fluid characteristics are needed to calculate the boiling and condensation thermal resistances in the theoretical model of the multi-channel flat heat pipe. Depending on the temperature, the fluid characteristics can change and bring differences in the heat transfer coefficient. Hence, to calculate the two-phase heat transfer coefficients, the working fluid characteristics were calculated automatically based the temperature. In the case of the multi-channel flat heat pipe, R134a was used as a working fluid. Thus, the R134a properties have been correlated in terms of temperature using the National Institute of Standards and Technology (NIST) software and properties [242]. The working fluid properties correlated with functions are the saturated vapour



pressure  $Pv_{R134a}$ , the liquid density  $\rho_{l,R134a}$ , the vapour density  $\rho_{v,R134a}$ , the latent heat of vaporization  $i_{lv,R134a}$ , the liquid specific heat  $c_{p,R134a}$ , the liquid thermal conductivity  $k_{R134a}$ , the surface tension  $\sigma_{R134a}$ , the liquid dynamic viscosity  $\mu_{l,R134a}$ , the vapour dynamic viscosity  $\mu_{v,R134a}$ . The R134a properties used for the theoretical model are provided in Annexe 3 and the fluid variables and their corresponding function names are listed in Table 4-9.

Table 4-9. Working fluid characteristics and corresponding functions' names.

Variable	Description	Function name
$Pv_{R134a}$	Saturated vapour pressure	Pv_R134a
$\rho_{l,R134a}$	Liquid density	rho_liq_R134a
$\rho_{v,R134a}$	Vapour density	rho_vap_R134a
$i_{lv,R134a}$	Latent heat of vaporization	hfg_R134a
$c_{p,R134a}$	Liquid specific heat	cp_R134a
$k_{R134a}$	Liquid thermal conductivity	K_R134a
$\sigma_{R134a}$	Surface tension	surftension_R134a
$\mu_{l,R134a}$	Liquid dynamic viscosity	viscos_liq_R134a
$\mu_{v,R134a}$	Vapour dynamic viscosity	viscos_vap_R134a

In addition to the working fluid properties, the cooling water specific heat  $c_{p,water}$  was also calculated automatically, based on the temperature.

## 4.6 Energy balance and iterative model

### 4.6.1 Energy balance

Two iterative Excel models have been developed with VBA coding and macros for the theoretical modelling of the two multi-channel heat pipes. The models permit the calculation of all the thermal resistances in the overall thermal resistance network for the system, including the resistance of interest: the multi-channel heat pipe thermal resistance. The two iterative Excel models follow the same calculation procedure and only the correlations previously detailed differ. For simplicity and to avoid redundancy, in what follows, the iterative model calculation procedure is presented in the case where the multi-channel flat heat pipe performance was predicted. To do so, the thermal resistance and temperatures in the systems cannot be solved explicitly and iterations must be done. For instance, based on a heat source temperature upstream, the logic of a thermal resistance system is to determine the next thermal resistance which allows us to calculate the temperature downstream. However, in the case of boiling and condensation, the thermal resistances depend on both upstream and downstream temperatures. Hence, to estimate two-phase thermal resistances, the temperature must first be estimated randomly and are then refined by successive iterations. Again, iterations must be done to determine the first temperature in the thermal resistance model. The upstream temperature is first estimated randomly and then refined until an energy balance is reached. Indeed, the cooling manifold surface temperature in the system  $T_s$  can be used to calculate the recovered heat transfer rate  $\dot{Q}_{calculated}$  based on the log mean

temperature difference (LMTD) method. This can also be designated by  $\dot{Q}_n$  in reference to the heat transfer rate calculated at the iteration number  $n$ . This is given by:

$$\begin{aligned}\dot{Q}_{calculated} = \dot{Q}_n &= \frac{1}{R_{cooling\ manifold}} \Delta T_{LMTD} \\ &= \frac{1}{R_{cooling\ manifold}} \times \frac{T_{water-in} - T_{water-out}}{\ln \left[ \frac{(T_s - T_{water-out})}{(T_s - T_{water-in})} \right]}\end{aligned}\quad (4-83)$$

The temperature of the water outlet temperature  $T_{water-out}$  can be determined using the heat transfer rate  $\dot{Q}$  provided to the system:

$$T_{water-out} = T_{water-in} + \frac{\dot{Q}}{\dot{m}_{water} c_{p,water}} \quad (4-84)$$

with  $T_{water-in}$  the water inlet temperature (K),  $\dot{Q}$  the heat transfer rate (W),  $\dot{m}_{water}$  the cooling water mass flow rate (kg/s), and  $c_{p,water}$  the cooling water specific heat (J/kg.K). Then, at each end of iteration, the first temperature in the thermal resistance model is changed until the heat transfer calculated from the thermal resistance model  $\dot{Q}_{calculated}$  is equal to the heat transfer rate  $\dot{Q}$  at which we want to predict the heat pipe performance:

$$\dot{Q}_{calculated} = \dot{Q} \quad (4-85)$$

#### 4.6.2 Simplified flowchart of the iterative model

A simplified flowchart explaining the iterative Excel tool calculation procedure is presented in Figure 4-27 to better understand the theoretical model procedure.

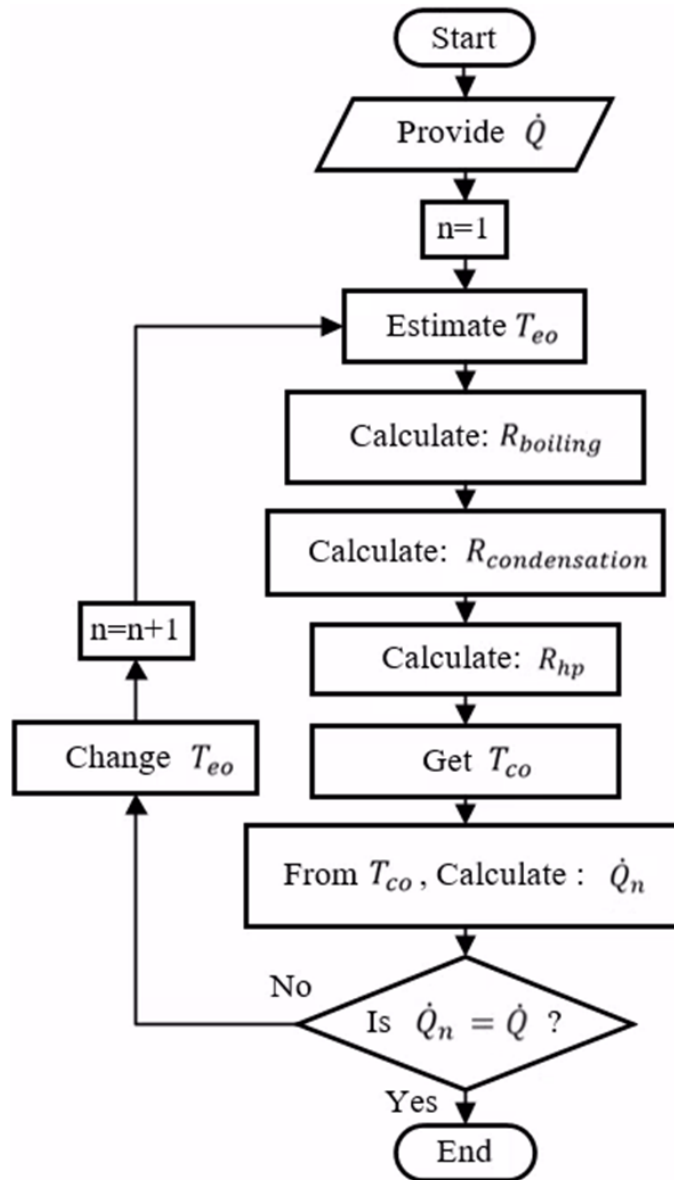


Figure 4-27. Simplified flow chart of the theoretical model calculation procedure

In the iterative model,  $n$  designates the number of the current iteration. First, the heat transfer rate  $\dot{Q}$  at which the system temperature and thermal resistances must be estimated is provided to the tool. At the first iteration ( $n = 1$ ), the outer evaporator temperature of the heat pipe  $T_{eo}$  is first estimated randomly. After calculating the conduction resistance at the evaporator, the boiling resistance is estimated with an internal iteration. Then, the condensation thermal resistance is also estimated using an internal iteration. Once all the thermal resistances in the multi-channel heat pipe have been estimated, the total heat pipe thermal resistance  $R_{HP}$  is calculated from the multi-channel thermal resistance network proposed (Figure 4-19). After obtaining the thermal resistance of the heat pipe, the outer condenser temperature of the heat pipe  $T_{co}$ , which is in contact with the cooling manifold, is determined. Based on this temperature, the log mean temperature difference (LMTD) method is used around the cooling

manifold to estimate the heat transfer rate recovered by the cooling water  $\dot{Q}_n$ . This calculated heat transfer rate  $\dot{Q}_n$  obtained at the iteration  $n$  is then compared to the input heat transfer rate  $\dot{Q}$  until an energy balance is obtained. If the calculated heat transfer rate  $\dot{Q}_n$  is higher than the target heat transfer rate  $\dot{Q}$ , the previously estimated outer evaporator temperature of the heat pipe  $T_{eo}$  was too high and is decreased. In contrast, if the calculated heat transfer rate  $\dot{Q}_n$  is lower than the target heat transfer rate  $\dot{Q}$ , the previously estimated outer evaporator temperature of the heat pipe  $T_{eo}$  was too low and is increased. This step is repeated until an acceptable energy balance is reached (within 0.1%) and the estimated system temperatures permit the recovery of the target heat transfer rate  $\dot{Q}$ .

#### **4.6.3 Detailed flowchart of the iterative model**

One must be aware that the previously presented flow chart was simplified for accessibility and to provide an overall understanding of the calculation procedure. However, many operations operated by the iterative model were omitted. Figure 4-28 presents the detailed iterative model procedure. In this flowchart, the user inputs provided to the model are in green parallelograms. The blue rectangles represent an operation done by the model. The orange diamonds represent tests done by the model. Finally, the model outputs are listed in the purple rectangle.

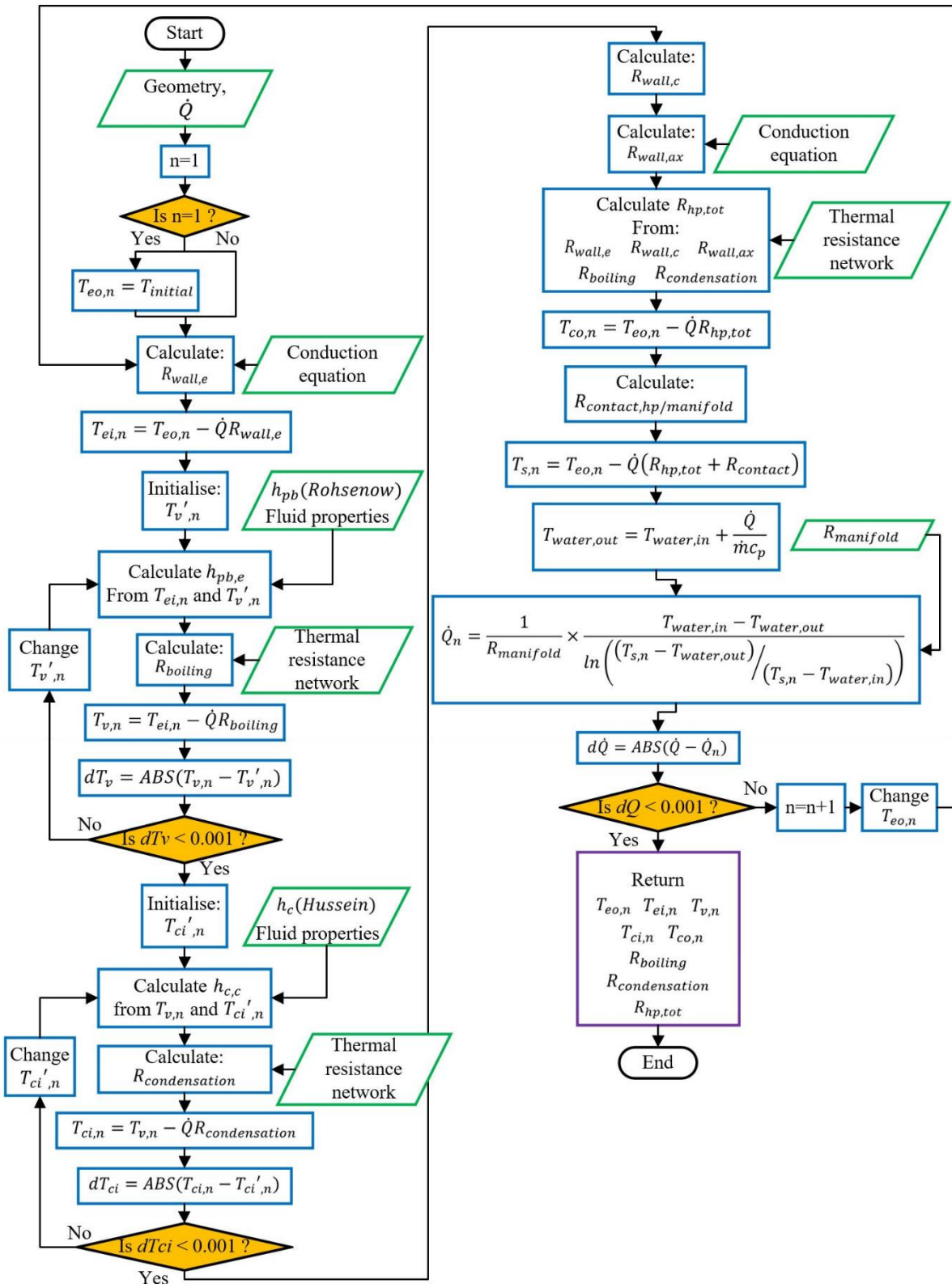


Figure 4-28. Detailed flowchart of the theoretical model calculation procedure

The above model will be described step by step, starting from the top left corner. First, the geometry of the multi-channel heat pipe must be provided. This includes the length, shapes, and diameters of the top collector, bottom collector, and parallel channels. The number of

parallel channels must also be provided. The heat transfer rate  $\dot{Q}$  at which we want to predict the system performance is then indicated. During the initialization occurring at the first iteration ( $n = 1$ ), the outer evaporator temperature  $T_{eo,n}$  is first initialized to a random value. This value has no influence on the final model output. The only differences that can occur between two different values of initial outer evaporator temperature is the speed of convergence of the model. For initial temperatures close to the solution, the number of iterations is usually lower and the model convergence quicker. Based on the outer evaporator temperature of the multi-channel heat pipe  $T_{eo,n}$ , the conduction thermal resistance at the evaporator  $R_{wall,e}$  is estimated and used to calculate the inner evaporator temperature  $T_{ei,n}$ . Then, the boiling thermal resistance  $R_{boiling}$  must be estimated to calculate the vapour temperature  $T_{v,n}$ . However, this thermal resistance cannot be calculated without the vapour temperature as most of the boiling heat transfer coefficient correlations use the difference of temperature between the vapour and the wall:  $\Delta T_{sat}$ . To overcome this issue, a tool vapour temperature  $T'_{v,n}$  is used. First estimated randomly, the tool vapour temperature  $T'_{v,n}$  is used to calculate the boiling thermal resistance  $R_{boiling}$ . This boiling thermal resistance is also calculated using the working fluid properties automatically estimated at the temperature  $T'_{v,n}$ . Once the boiling thermal resistance  $R_{boiling}$  is obtained, the vapour temperature  $T_{v,n}$  is calculated. However, this temperature can be significantly different from the tool vapour temperature  $T'_{v,n}$  which was used to calculate the boiling thermal resistance. Hence, the two vapour temperatures are compared by calculating the vapour temperature difference  $dT_v$ . Based on this indicator, the tool vapour temperature  $T'_{v,n}$  is changed by internal iteration until the error between the tool vapour temperature  $T'_{v,n}$  and the vapour temperature  $T_{v,n}$  is lower than 0.1%. Once the iterations for the boiling resistance have reached convergence and that an equilibrium is found between the vapour temperature  $T_{v,n}$ , the tool vapour temperature  $T'_{v,n}$ , and the boiling thermal resistance  $R_{boiling}$ , the condensation thermal resistance must be estimated to determine the internal condenser wall temperature  $T_{ci,n}$ . Similar to the boiling thermal resistance, iterations are needed to determine the condensation thermal resistance  $R_{condensation}$  which depends on the wall temperature  $T_{ci,n}$ . In this regard, a tool internal condenser wall temperature  $T'_{ci,n}$  is first used to estimate the condensation thermal resistance  $R_{condensation}$  which is then used to calculate the actual inner condenser wall  $T_{ci,n}$ . This condenser wall temperature is then compared to the tool condenser wall temperature by calculating the inner condenser wall difference  $dT_{ci}$ . Based on this variable, iterations are made until an equilibrium between the tool internal condenser wall temperature  $T'_{ci,n}$  and the inner condenser wall  $T_{ci,n}$  is reached. When the inner condenser wall difference  $dT_{ci}$  is lower than 0.1%, the inner condenser wall  $T_{ci,n}$  is considered to be converged. The next step operated by the tool is to calculate the radial

conduction thermal resistance at the condenser  $R_{wall,c}$  and axial conduction thermal resistance  $R_{wall,ax}$ . Once done, all the thermal resistances in the multi-channel heat pipe thermal resistance network at the iteration  $n$  are obtained, and the total thermal resistance of the multi-channel heat pipe  $R_{HP}$  is calculated from the thermal resistance network. This thermal resistance permits the outer condenser temperature  $T_{co,n}$  to be obtained. With the estimation of the interface thermal resistance between the heat pipe and the cooling manifold  $R_{contact\ HP/manifold}$ , the surface temperature of the cooling manifold  $T_{s,n}$  is obtained. Based on surface temperature of the cooling manifold  $T_{s,n}$ , the last calculation steps in the  $n$  iteration consist of estimating the recovered heat transfer rate  $\dot{Q}_n$ . To start with, the outlet cooling water temperature  $T_{water,out}$  is determined using Newton's law of cooling. Then, the recovered heat transfer rate  $\dot{Q}_n$  is estimated based on the log mean temperature difference (LMTD) method, the surface temperature of the cooling manifold  $T_{s,n}$ , the thermal resistance of the cooling manifold  $R_{cooling\ manifold}$ , and the cooling water temperatures. This calculated heat transfer rate is then compared to the target heat transfer rate  $\dot{Q}$  with the variable  $d\dot{Q}$ . In the case where the estimated temperatures in the system are too high, the recovered heat transfer rate  $\dot{Q}_n$  will be higher than the target heat transfer rate  $\dot{Q}$ . Obviously, the opposite is found if the estimated system temperatures are too low. Based on this indicator  $d\dot{Q}$ , the outer evaporator temperature  $T_{eo,n}$ , which is the upstream temperature in the model, is modified. This indicates the transition to the next overall iteration  $n + 1$  of the model. The outer evaporator temperature  $T_{eo,n}$  and all the downstream temperatures in the system are constantly adjusted and calculated at each iteration until an equilibrium is reached between the system temperatures, the recovered heat transfer rate  $\dot{Q}_n$ , and the target heat transfer rate  $\dot{Q}$ . Again, as a criterion, steady state is considered to be reached when the difference between the recovered and target heat transfer rates  $d\dot{Q}$  is lower than 0.1%. When the overall equilibrium of the thermal resistance model is reached, all the predicted temperatures in the heat pipe and thermal resistances values are returned. A picture of the multi-channel flat heat pipe Excel model interface is provided in Annexe 4.

---

# Chapter 5 - Computational fluid dynamics (CFD) modelling

---

## 5.1 Methods for CFD modelling of two-phase flow

### 5.1.1 Introduction to computational fluid dynamics (CFD)

Computational Fluid Dynamics (CFD) is a computational modelling technique which consists of studying the behaviour of a system by solving a set of mathematical equations on very small volumes of the geometry. Once introducing a 2D or 3D geometry to the software, the system of interest is converted into a Mesh which divides the overall geometry into multiple cells. For fluid dynamics, the volume of interest that needs to be meshed is the fluid volume. Based on the user inputs such as the simulation models and boundary conditions, the Navier-Stokes equations are solved for each control volume so that the physical conservation laws are respected. In the case where only one species is studied, this set of transport equations consists of [105]:

- 1- The **continuity equation** (conservation of mass)
- 2- The **equation of motion** (conservation of momentum)
- 3- The **energy equation** (conservation of energy)

As the mass of each control volume is constant, the sum of the internal mass variation and of the mass going in or out of the volume is null. Hence, the **continuity equation** for each cell is given by [105]:

$$\frac{\partial \rho}{\partial t} + \vec{\nabla} \cdot (\rho \vec{V}) = 0 \quad (5-1)$$

where  $\rho$  is the fluid density (kg/m<sup>3</sup>), and  $\vec{V}$  is the velocity vector (m/s). For a Newtonian fluid, the **equation of motion** is as follows [105]:

$$\frac{\partial \rho \vec{V}}{\partial t} = -\rho (\vec{\nabla} \cdot \vec{V}) \vec{V} - \vec{\nabla} P + \vec{\nabla} \cdot \vec{\tau} + \rho \vec{g} \quad (5-2)$$

with  $\rho$  the fluid density (kg/m<sup>3</sup>),  $\vec{V}$  the velocity vector (m/s),  $P$  the pressure (Pa),  $\vec{\tau}$  the stress tensor due to the fluid viscosity (N/m<sup>2</sup>), and  $\vec{g}$  the volumetric force vector including gravity, magnetic, electrostatic forces among others (m/s<sup>2</sup>). For a stationary control volume through which a fluid is flowing, the **energy equation** is expressed by:

$$\frac{\partial}{\partial t} \rho (\vec{U} + 1/2 V^2) = -\vec{\nabla} \cdot \rho \vec{V} (\vec{U} + 1/2 V^2) - \vec{\nabla} \cdot \vec{q}'' + \rho (\vec{V} \cdot \vec{g}) - \vec{\nabla} \cdot P \vec{V} + \vec{\nabla} \cdot (\vec{\tau} \vec{V}) + q'''_g \quad (5-3)$$

where  $\vec{U}$  is the internal energy vector (J/kg),  $\vec{V}$  the velocity vector (m/s),  $\rho$  the fluid density (kg/m<sup>3</sup>),  $\vec{q}''$  the heat flux (W/m<sup>2</sup>),  $\vec{g}$  the volumetric force vector (m/s<sup>2</sup>),  $P$  the pressure (Pa),  $\vec{\tau}$  the stress tensor (N/m<sup>2</sup>), and  $q'''_g$  the volumetric heat source (W/m<sup>3</sup>). The transport equations are



detailed further and projected in rectangular coordinates in Annexe 5. In practice, the transport equations are calculated by the solver under the form of tensors. With the increase of computational power in the last decades, CFD solvers are able to reduce their calculation times and to predict the fluid behaviour for meshes with a high number of elements. This permits the simulation of more complex geometries, flows and heat transfer and is making possible the investigation of heat pipes and two-phase heat transfer using CFD.

**5.1.2 Multi-phase flow modelling**

Specific simulation methods must be used for the steady state or transient (time dependent) simulation of multi-phase flows such as the one taking place in heat pipes. In the case of two-phase heat transfer where a phase change process is used to carry energy under the form of latent heat, the transport equations must be modified to account for the heat and mass transfer between the liquid and vapour phases. In multi-phase flow, multiple domains are used: the super domain is similar to the single-phase flow domain and contains threads inside which the phase-independent information about each element in the geometry (material, property ...) are stored. For each phase in the simulation, a subdomain is created and contains sub-threads for each element in the geometry which describes the phase-dependent data. Finally, an interaction domain is used to allow an interaction between the phase domains and the super domain. The previously described structure of multi-phase simulation is schematized in Figure 5-1 [243].

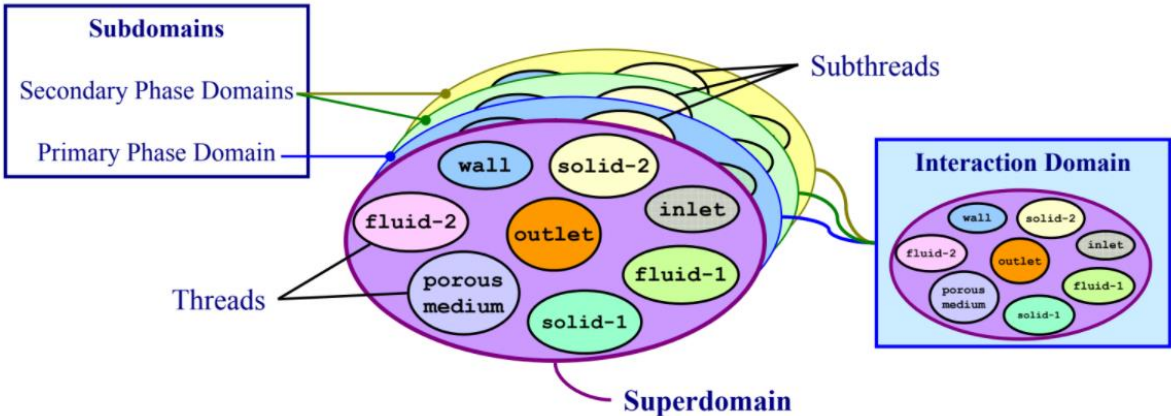


Figure 5-1. Multi-phase flow data structure

There are two approaches for the simulation of multiphase flows: the Euler-Lagrange and Euler-Euler approach [244]. In the Euler-Lagrange approach, the fluid phase is treated as a continuum whereas the dispersed phase is tracked by considering the particles, bubbles, droplets etc... This dispersed phase can interact with the fluid phase in terms of mass, energy, and momentum. An important assumption in the Euler-Lagrange model is that the dispersed phase occupies a volume fraction which is much lower than that of the fluid volume fraction. In this regard, the Euler-Lagrange approach is not advised for the simulation of heat pipes or

thermosyphons inside which some cells can be fully occupied by the liquid or vapour phase. In the Euler-Euler approach, the different phases are considered as interpenetrating continua. The volume of one phase cannot be occupied by another phase. In this regard, the flow field is described in terms of phase volume fraction which represents the ratio of the volume occupied by the given phase to the total cell volume. Hence, the sum of all the volume fractions is equal to one. The transport equations are adapted and solved for each phase.

In the Euler-Euler approach, which is more suitable for the simulation of heat pipes and thermosyphons, there are three main multiphase models [244]: the Volume of Fluid (VOF) model, the Mixture model, and the Eulerian model. The VOF model is a surface-tracking technique which focuses on the position of the interface between the phases. The volume fraction of each phase is determined for all the cells in the domain and a single momentum equation is shared by the phases. The volume fraction is a function of space and time. As a difference, in the mixture model, relative velocities are given to describe the dispersed phases. Finally, the Eulerian model is the most complex Euler-Euler model and solves several momentum and continuity equations for each phase. Exchange coefficients are used for the interaction between the phases. For the simulation of heat pipes and thermosyphons, the Euler-Euler VOF model is commonly used [77], [80], [94], [96]–[98], [100], [102], [82], [84]–[87], [89], [92], [93] due to its capability of tracking the bubble and droplet interfaces and due to its simplicity.

### 5.1.3 Volume of Fluid (VOF) model and source terms

As previously introduced, the Volume of Fluid (VOF) model is a Euler-Euler model which relies on the fact that the different phases or fluids are not interpenetrating. Then, the VOF model is used to define and track the interface between the phases. As such, the notion of volume fraction is introduced and is central to the Volume of Fluid model. For each cell, the sum of all the phase volume fractions sum to unity. For the simulation of two-phase heat transfer, the model considers the liquid and vapour phases of a fluid. As such,  $\alpha_l$  and  $\alpha_v$  represent the volume fraction of the liquid and vapour phases only. Then, for each computational cell, the VOF model can be expressed as follows:

$$\begin{cases} \alpha_l = 1 & \alpha_v = 0 & \text{The cell is filled with liquid} \\ \alpha_l = 0 & \alpha_v = 1 & \text{The cell is filled with vapor} \\ 0 < \alpha_l, \alpha_v < 1 & & \text{The cell contains both liquid and vapour} \end{cases} \quad (5-4)$$

It must be known that in the Volume of Fluid model, no void volume is accepted, and that the volume is always occupied by at least one of the phases. Based on the volume fraction, the variables and properties for the cells are volume-averaged and one set of Navier-Stokes equations is solved through the domain [244]. To account for the heat and mass transfer between the liquid and vapour phases, source terms can be added to the transport equation of the VOF model. In this regard, for the two-phase simulation of heat pipes and

thermosyphons, the adapted transport equations using the VOF model and source terms are given as follows:

- **VOF Continuity equation:**

For the liquid phase ( $l$ ), the VOF continuity equation with source terms is [76], [94], [96], [244]–[246]:

$$\frac{\partial(\rho_l \alpha_l)}{\partial t} + \vec{\nabla}(\rho_l \alpha_l \vec{V}) = S_{M,l} \quad (5-5)$$

where  $\rho_l$  is the liquid density (kg/m<sup>3</sup>),  $\alpha_l$  the liquid volume fraction,  $\vec{V}$  the velocity vector (m/s), and  $S_{M,l}$  the liquid phase mass source term (kg/m<sup>3</sup>s). A similar continuity equation is solved for the vapour phase.

- **VOF Equation of motion:**

The momentum equation for the VOF model is [76], [94], [96], [244]–[246]:

$$\frac{\partial}{\partial t}(\rho \vec{V}) + \vec{\nabla}(\rho \vec{V} \vec{V}) = -\vec{\nabla} \cdot P + \vec{\nabla}[\mu(\vec{\nabla} \vec{V} + \vec{\nabla} \vec{V}^T)] + \rho \vec{g} + \vec{F}_{CSF} \quad (5-6)$$

with  $\rho$  the fluid density (kg/m<sup>3</sup>),  $\vec{V}$  the velocity vector (m/s),  $P$  the pressure (Pa),  $\mu$  the dynamic viscosity (Pa.s),  $\vec{g}$  the volumetric force vector (m/s<sup>2</sup>), and  $\vec{F}_{CSF}$  the continuum surface force (CSF) accounting for the surface tension along the interface (N). The fluid properties for the momentum equation are averaged between the liquid and vapour phase as:

$$\mu = \alpha_l \mu_l + \alpha_v \mu_v \quad (5-7)$$

$$\rho = \alpha_l \rho_l + \alpha_v \rho_v \quad (5-8)$$

with  $\alpha_l$  and  $\alpha_v$  the liquid and vapour phase fractions,  $\mu_l$  and  $\mu_v$  the liquid and vapour dynamic viscosities (Pa.s), and  $\rho_l$  and  $\rho_v$  the liquid and vapour densities (kg/m<sup>3</sup>). To model the surface tension between the phases, *Brackbill et al.* [81] developed a model that interprets the surface tension as a continuous effect across the phase interface instead of a boundary condition. The continuum surface force (CSF) model by *Brackbill et al.* [81] has been largely used for the simulation of boiling and condensation [76], [89], [90], [94], [96], [245]–[247]. The continuum surface force is given by [81]:

$$\vec{F}_{CSF} = 2\sigma_{lv} \frac{\alpha_l \rho_l C_v \vec{\nabla} \alpha_v + \alpha_v \rho_v C_l \vec{\nabla} \alpha_l}{\rho_l + \rho_v} \quad (5-9)$$

with  $\sigma_{lv}$  the surface tension (N/m), and  $C$  the surface curvature.

- **VOF Energy equation:**

The energy equation for the VOF model is [76], [90], [94], [96], [244]–[246]:

$$\frac{\partial}{\partial t}(\rho U) + \vec{\nabla} \cdot [(\rho U + P) \vec{V}] = \vec{\nabla} \cdot (k \vec{\nabla} T) + S_E \quad (5-10)$$

with  $\rho$  the fluid density (kg/m<sup>3</sup>),  $U$  the internal energy (J/kg),  $P$  the pressure (Pa),  $\vec{V}$  the velocity vector (m/s),  $k$  the fluid thermal conductivity (W/m.K),  $T$  the temperature (K), and  $S_E$  is the

energy source term (J/m<sup>3</sup>s). Again, the fluid thermal conductivity is taken as the volume average:

$$k = \alpha_l k_l + \alpha_v k_v \quad (5-11)$$

with  $k_l$  and  $k_v$  the liquid and vapour thermal conductivities (W/m.K). Both temperature and internal energy are treated as mass-averaged variables by the VOF model. The mass averaged internal energy  $U$  is expressed by:

$$U = \frac{\alpha_l \rho_l U_l + \alpha_v \rho_v U_v}{\alpha_l \rho_l + \alpha_v \rho_v} \quad (5-12)$$

where  $U_l$  and  $U_v$  are given by the caloric equation of state [90], [248]:

$$U_l = c_{v,l}(T - T_{sat}) \quad (5-13)$$

$$U_v = c_{v,v}(T - T_{sat}) \quad (5-14)$$

with  $c_v$  the specific heat at constant volume (J/kg.K), and  $T_{sat}$  the saturation temperature (K). The last step in the definition of the multi-phase model using the Volume of Fluid approach is the definition of mass and energy source terms. If researchers are rather unanimous with the use of the VOF model to simulate heat pipes, different source terms have been implemented. For instance, *Schrage* [66], *Lee* [67], *Wang et al.* [70], and *Nichita and thome* [74] developed models to calculate the energy and mass transfer source terms. Yet, the use of the *Lee* [67] model largely dominates in the available simulation of heat pipes and thermosyphons as fourteen out of twenty of the reported heat pipe simulations use this model. Many authors have concluded that the *Lee* [67] model was suitable to model boiling and condensation [71], [80], [100]–[102], [83], [85]–[87], [89], [92], [94], [98]. In this regard, for the definition of source terms, the *Lee* [67] model is studied.

#### 5.1.4 Lee model for two-phase heat transfer and source terms

The *Lee* [67] model is the most known source terms model and was mainly introduced by *De Schepper et al.* [68], [69]. For each cell, the temperature of the mixture is compared with a saturation temperature  $T_{sat}$ . If the temperature of the mixture is below the saturation temperature, condensation takes place. On the contrary, boiling or evaporation occurs if the mixture temperature is higher than the saturation temperature. The *Lee* [67] model source terms are given by [68], [69], [244]:

- **Evaporation**  $T_{mix} > T_{sat}$  :

$$S_{M,l} = -S_{M,v} = -\beta_e \alpha_l \rho_l \frac{T_{mix} - T_{sat}}{T_{sat}} \quad (5-15)$$

- **Condensation**  $T_{mix} < T_{sat}$  :

$$S_{M,l} = -S_{M,v} = \beta_c \alpha_v \rho_v \frac{T_{sat} - T_{mix}}{T_{sat}} \quad (5-16)$$

where  $S_{M,l}$  and  $S_{M,v}$  are the liquid and vapour phase mass source terms ( $\text{kg/m}^3\text{s}$ ),  $\beta_e$  and  $\beta_c$  are the evaporation and condensation mass transfer coefficients ( $\text{s}^{-1}$ ),  $\alpha_l$  and  $\alpha_v$  the liquid and vapour phase volume fractions,  $\rho_l$  and  $\rho_v$  the liquid and vapour densities ( $\text{kg/m}^3$ ),  $T_{mix}$  the mixture temperature (K),  $T_{sat}$  the saturation temperature (K), and  $i_{lv}$  the latent heat of vaporization (J/kg). For both evaporation and condensation, the energy source term  $S_E$  is the product of the mass source term with the latent heat:

$$S_E = i_{lv}S_M \quad (5-17)$$

with  $S_E$  is the energy source term ( $\text{J/m}^3\text{s}$ ),  $S_M$  the mass source terms ( $\text{kg/m}^3\text{s}$ ), and  $i_{lv}$  the latent heat of vaporization (J/kg). The evaporation and condensation coefficients  $\beta_e$  and  $\beta_c$  are given by [244]:

$$\beta_e = \frac{6}{D_{sm}} \sqrt{\frac{M_{mol}}{2\pi R_{gas} T_{sat}}} \left( \frac{\rho_v}{\rho_l - \rho_v} \right) (i_{lv}) \quad (5-18)$$

$$\beta_c = \frac{6}{D_{sm}} \sqrt{\frac{M_{mol}}{2\pi R_{gas} T_{sat}}} \left( \frac{\rho_l}{\rho_l - \rho_v} \right) (i_{lv}) \quad (5-19)$$

with  $D_{sm}$  the Sauter mean diameter (m),  $M_{mol}$  the molecular weight (kg/kmole),  $R_{gas}$  the universal gas constant (J/mole.K),  $T_{sat}$  the saturation temperature (K),  $\rho_l$  and  $\rho_v$  the liquid and vapour densities ( $\text{kg/m}^3$ ), and  $i_{lv}$  the latent heat of vaporization (J/kg). In practice, the evaporation and condensation coefficients are defined by the user and the default value is  $\beta_e = \beta_c = 0.1 \text{ s}^{-1}$  [71]. However, in the literature, researchers have varied the condensation coefficient  $\beta_c$  up to  $5000 \text{ s}^{-1}$  [72]. The evaporation coefficient is usually kept at its default value.

### 5.1.5 User defined functions (UDF)

To implement source terms which are not included in the default CFD solver, user defined functions (UDF) can be developed and integrated into the solver. A UDF is a C code routine programmed by the user which can be dynamically linked to the solver [249]. Multiple types of UDF exist and allow users to define their own boundary conditions, materials and properties, initial conditions, time dependent variables, physical and chemical reactions, and source terms. Once linked to the solver, user defined functions can be used at the initialisation, during each iteration, or at the end of the calculation. In the case of two-phase heat transfer modelling, UDFs are used to adapt the fluid properties and to define the mass and heat transfer source terms. In this regard, at each iteration, the UDF input is integrated by the solver and supplied to the material properties and transport equations. The calculation flow chart of a typical CFD solver with the different UDF inputs are schematized in Figure 5-2 (adapted from [249]).

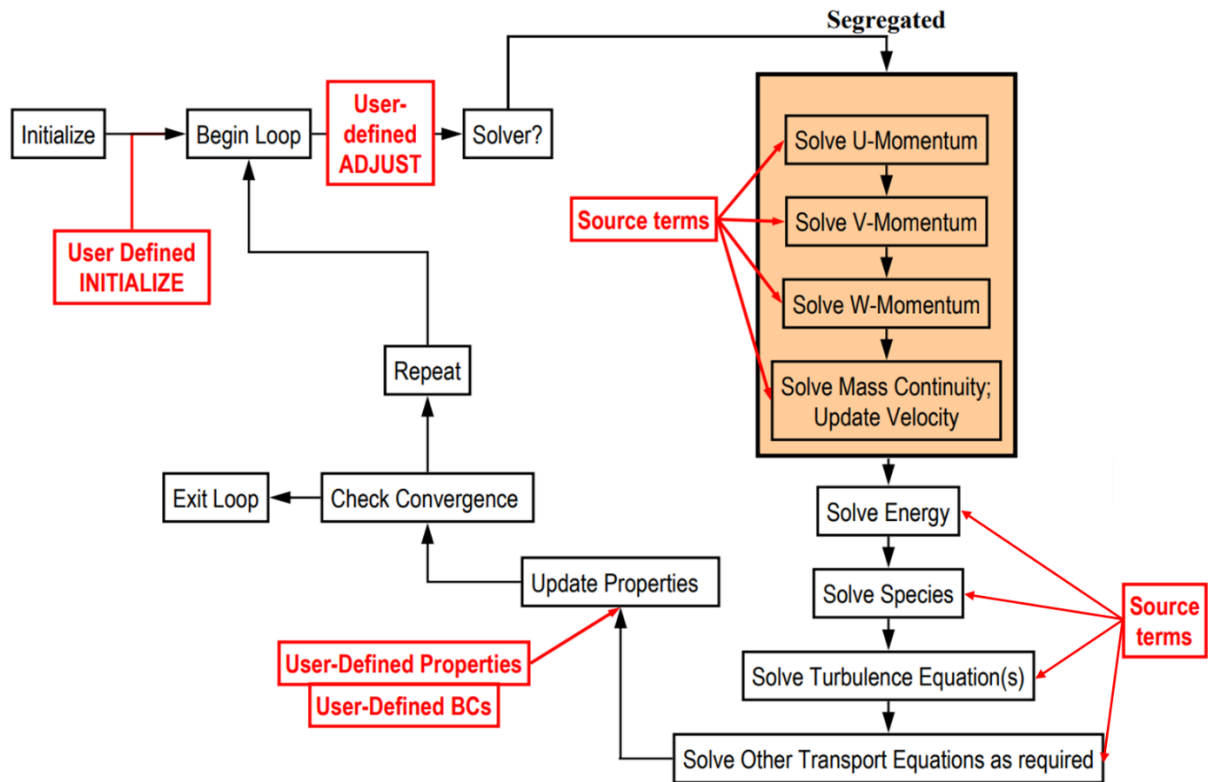


Figure 5-2. User defined inputs to the ANSYS Fluent solver, adapted from [249]

To link a C code UDF to the CFD solver, UDFs can either be interpreted or compiled. If interpreted, the UDF code is integrated into an intermediate, architecture-independent machine code. If this additional layer of code implies a performance penalty, interpreted UDF can be easily shared between different architectures, simulations, systems, and event solver versions. Yet, interpreted UDFs have limitations and do not have access to direct data structure references [244]. On the other hand, compiled UDFs are directly integrated into the solver source code and work in a similar manner. An internal script is called to allow a compiler to build an object code library containing the native machine language translation of the higher-level C source code. Once the library is built, the compiled UDF must be loaded to be used in the simulation. Due to the local creation of a library, compiled UDF cannot be transferred between simulation and must be compiled again. If compiling a UDF is more difficult than interpreting, a compiled UDF leads to a gain in computational time and has a direct access to the data structures [244], [250].

## 5.2 CFD simulation of the three-leg multi-channel heat pipe

### 5.2.1 Objectives

The objectives of the CFD simulation of the three-leg heat pipe are to develop, test, and determine the most suitable method to simulate the operation of heat pipes on ANSYS FLUENT 2020. By using the Volume of Fluid (VOF) approach, three different versions of the Lee model have been integrated and compared: 1) the integrated Lee model of ANSYS, 2) the usual Lee model using UDF, and 3) a modified Lee model using UDF. In addition to the Lee model's comparison, the suitable boundary conditions for the simulation of heat pipes are also determined. Finally, the value of the condensation mass transfer coefficient needed for the source terms of the Lee model is investigated.

### 5.2.2 Geometry

For the CFD simulation of the three-leg heat pipe, a 2D geometry is considered. This was preferred to the 3D geometry to significantly reduce the number of elements in the mesh and thus reduce the simulation time. The dimensions of the three-leg heat pipe geometry considered for the simulations are based on the three-leg multi-channel heat pipe prototype and shown in Figure 5-3.

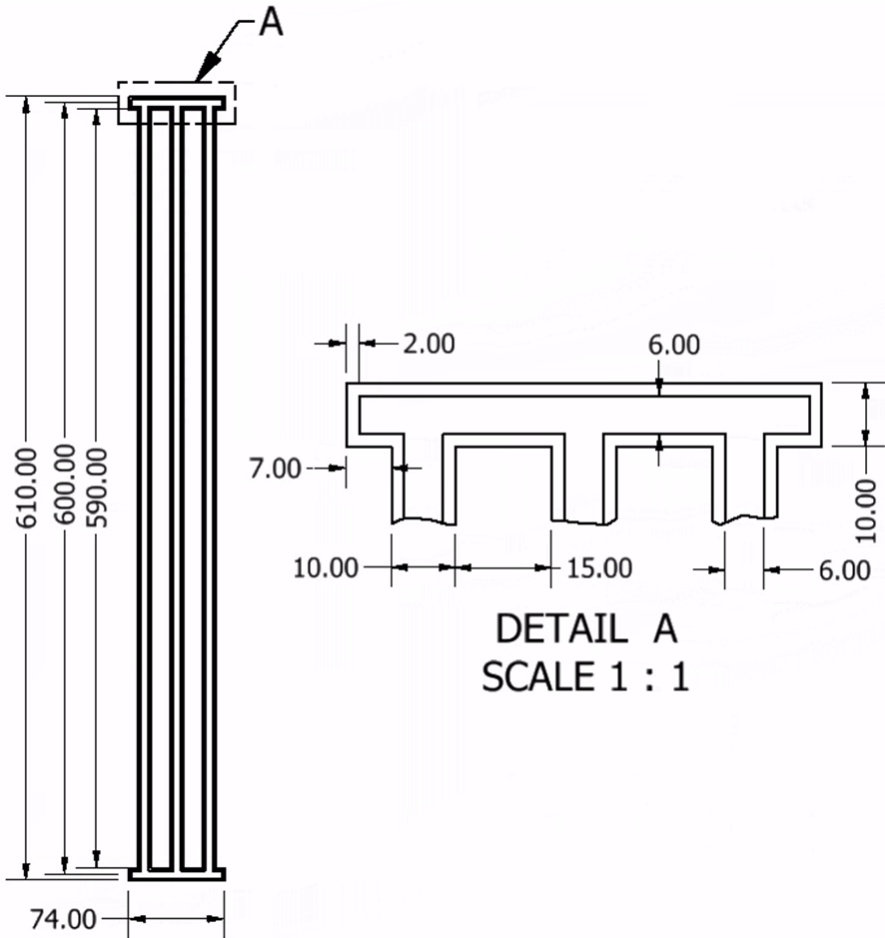


Figure 5-3. Three-leg heat pipe geometry considered for CFD simulation

### 5.2.3 UDF development for two-phase heat transfer

To simulate multi-phase flows and heat transfer, the Lee model is used. Even if an included Lee model is available in ANSYS, many researchers have reported that this included model was not capable of simulating heat pipes [71], [80], [84], [87], [90]. In this regard, UDFs have been coded in C to define the Lee model source terms and link them to the solver. This section presents the UDF codes developed.

#### 5.2.3.1 Lee model UDF

In the development of UDFs, different coding structures are made available by ANSYS to integrate a UDF into the solver. For the integration of source terms into the transport equations, the DEFINE\_SOURCE structure is used to estimate the source term to be applied on a given species in the simulation which means that, for the definition of the mass source terms, two DEFINE\_SOURCE structures must be used: one for the vapour phase and one for the liquid phase. The DEFINE\_SOURCE structure for the vapour mass source term is presented in Figure 5-4.

```
133 /*-----*/
134 /* UDF for vapour mass source terms*/
135
136 DEFINE_SOURCE(vap_src, cell, pri_th, dS, eqn)
137 {
138 /*defining variables */
139 Thread *mix_th, *sec_th;
140 real m_dot_v;
141 real T_SATv;
142
143 /* defining the mixture thread, primary phase thread, and secondary phase
   thread*/
144 mix_th = THREAD_SUPER_THREAD(pri_th);
145 sec_th = THREAD_SUB_THREAD(mix_th, 1);
146
147 /*Defining the saturation temperature Tsat */
148 T_SATv = 300;
149
150 /*Initialisation*/
151 m_dot_v=0.;
152
153 /*Calculation the vapour mass source term during evaporation/boiling*/
154 if(C_T(cell, mix_th)>T_SATv)
155 {
156 m_dot_v = 0.1*C_VOF(cell, sec_th)*C_R(cell, sec_th)*fabs(C_T(cell, sec_th) -
   T_SATv)/T_SATv;
157 dS[eqn] = 0.;
158 }
159
160 /*Calculation the vapour mass source term during Condensation*/
161 if(C_T(cell, mix_th)<T_SATv)
162 {
163 m_dot_v = -(0.1)*C_VOF(cell, pri_th)*C_R(cell, pri_th)*fabs(T_SATv-C_T
   (cell,pri_th))/T_SATv;
164 dS[eqn] = -(0.1)*C_R(cell, pri_th)*fabs(C_T(cell, pri_th) - T_SATv)/T_SATv;
165 }
166
167 /*Returning the vapour mass source term*/
168 return m_dot_v ;
169 }
```

Figure 5-4. Vapour phase mass source term UDF for Lee model



The DEFINE\_SOURCE structure takes five arguments which are the UDF name (vap\_src), the cell index which identifies the cell on which the source term will be applied (cell), the cell thread (pri\_th), an array that contains the derivative of the source term (dS), and the equation number (eqn). Among those five arguments, the name and equation number are provided by the user, the cell index and the cell thread are the inputs needed by the structure to apply the source terms, and the derivative term is an output used to enhance the stability of the solver. Inside the DEFINE\_SOURCE UDF, several operations can be seen. At first, the variables and threads needed for the calculation of the source terms are defined (Figure 5-4, line 138 to 146). The saturation temperature at which the phase change must occur is then provided (Figure 5-4, line 148) and the vapour mass source term  $m_{\dot{v}}$  is initialised to zero (Figure 5-4, line 151). The main criterion, during which the calculation of source term is done, starts in Figure 5-4, line 154. Before calculating the vapour source term, the solver must determine if evaporation or condensation takes place by comparing the cell temperature to the saturation temperature (Figure 5-4, line 154 & 161). Once done, the suitable vapour mass source term  $m_{\dot{v}}$  is calculated. For the estimation of the source term, the vapour phase volume fraction and densities are obtained from the command C\_VOF and C\_R, respectively. In the case where boiling takes place, vapour mass is added, and the source term is positive whereas, when condensation happens, vapour is removed, and the mass source term is negative. In both evaporation and condensation, a derivative term dS is then calculated and provided to the solver to enhance the stability of the transport equation. The vapour source term  $m_{\dot{v}}$  is finally returned by the UDF to the solver in Figure 5-4, line 168. To complete the Lee model UDF, two other DEFINE\_SOURCE structures have been included which are the liquid phase mass source term and the energy source term. If both structures are very similar to that of the vapour mass source term presented in Figure 5-4, the energy source term comprises a slight difference as it uses the latent heat of the fluid to calculate the source term.

#### 5.2.3.2 Modified Lee model UDF

One identified limit from the commonly used Lee model is the needed user input which determines the saturation temperature. Indeed, by doing so, the predictive nature of the simulation of heat pipes is limited as researchers usually provide the saturation temperature based on experimental measurements. With the objective of having a computational based value of the saturation temperature, a modified Lee model UDF was coded. This UDF is similar to the commonly used Lee model as it uses three DEFINE\_SOURCE structures that calculate the vapour and liquid phase mass transfer source terms and the energy source term. In the modified Lee model that was investigated, a fourth structure was integrated to calculate the saturation temperature from the simulation itself. The objective of this structure is to measure the average temperature of a zone inside the heat pipe and to take this as the new saturation temperature. The idea behind this is that an equilibrium could be found between the saturation

temperature and the mass transfer coefficients in the Lee model which would lead to a convergence of the computational based saturation temperature and of the heat pipe temperatures. To investigate this idea, a new structure was developed, designated by DEFINE\_EXECUTE\_AT\_END. This structure is called by the Fluent solver at the end of each iteration to measure the average temperature of a zone and conveys this value to the saturation temperature variable. The developed structure allowing the temperature measurement from the simulation and the use of this value as the saturation temperature is presented in Figure 5-5 and Figure 5-6.

```

1  /*-----*/
2  /* UDF for computational based Tsat with a temperature measurement*/
3
4  /* Global variable to be used between the commands*/
5  real Tsat_sensor;
6
7  DEFINE_EXECUTE_AT_END(Tsatsensor) /* UDF to hook*/
8  {
9  /*defining variables*/
10 #if !RP_HOST
11     real thermosensor_coordinate[ND_ND];
12     real thermosensor_temperature;
13     real xmin;
14     real xmax;
15     real ymin;
16     real ymax;
17     real zmin;
18     real zmax;
19     real x, y, z;
20     real time = RP_Get_Real("flow-time");
21     int nt; /* nt is the number of temperature measurement (counting) */
22
23     /* Defining cells, thread and domain */
24     cell_t c;
25     Domain* d;
26     Thread* t;
27     d = Get_Domain(1);
28
29     /* Defining thermocouple zone where the temperature measurement is taken
30     from; Temperature measurement located at coordinates (x,y,z) =
31     (0.050,0.280,0.050) */
32     xmin = 0.002;
33     xmax = 0.072;
34     ymin = 0.002;
35     ymax = 0.008;
36     zmin = -1000;
37     zmax = 1000;
38
39     /* Initializing sensor temperature and number of temperature
40     measurements nt */
41     thermosensor_temperature = 0;
42     nt = 0;
43
44     /* Begin loop to determine the temperature at the centroid of cells near
45     the thermocouple */
46     thread_loop_c(t, d)
47     {
48         /*looping within all the cells of the domain*/
49         begin_c_loop(c, t)
50         {
51             C_CENTROID(thermosensor_coordinate, c, t);
52             x = thermosensor_coordinate[0];
53             y = thermosensor_coordinate[1];
54             z = thermosensor_coordinate[2];

```

Figure 5-5. Modified Lee model UDF with computational saturation temperature (part1)

```

52      /* If cell is within the thermocouple zone: */
53      if ((x >= xmin) && (x <= xmax))
54      {
55          if ((y >= ymin) && (y <= ymax))
56          {
57              if ((z >= zmin) && (z <= zmax))
58              {
59                  /* get thermocouple temperature */
60                  thermosensor_temperature = thermosensor_temperature +
C_T(c, t);
61                  /* count number */
62                  nt = nt + 1;
63              }
64          }
65      }
66      }
67      end_c_loop(c, t)
68  }
69
70  /* Averaging thermocouple temperature */
71  thermosensor_temperature = thermosensor_temperature / nt;
72  /* Transmitting to global variable*/
73  if(time<0.00001)
74  {
75      Tsat_sensor=290;
76  }
77  else
78  {
79      Tsat_sensor=thermosensor_temperature;
80  }
81  /*Displaying the Tsat temperature in the ANSYS window*/
82  Message0("Tsat_sensor: %g \n", Tsat_sensor);
83 #endif
84 }

```

Figure 5-6. Modified Lee model UDF with computational saturation temperature (part2)

The development and coding of this DEFINE\_EXECUTE\_AT\_END structure was more difficult than the previously discussed source term structure as this new structure needs to access different levels of the solver such as the host, the node 0 and the nodes. This had to be done so that the developed UDF could be compiled and hooked to the solver which runs in parallel mode. The DEFINE\_EXECUTE\_AT\_END does not use any inputs from the solver and aims at changing a global variable called “Tsat\_sensor” which is outside the structure and therefore can also be used by any source term structure. Similarly to most of the structure, the first lines of codes consist of declaring the variables (Figure 5-5, line 11 to 27). A “time” variable is obtained from the transient simulation (Figure 5-5, line 20) and is later used to define a criterion that prevents the failure of the UDF at the early stage of the simulation. The number of temperature measurement is also counted using the variable “nt” and is used to calculate the temperature average of the zone (Figure 5-5, line 21). The 3D coordinates of the heat pipe zone within which the average temperature will be measured are defined from lines 30 to 35. After initialising the variables, the UDF needs to loop through all the cells in the simulation (Figure 5-5, line 45 to 50) and if the coordinates of the selected cell are within the zone of interest (Figure 5-6, line 53 to 58), a new temperature measurement is taken (Figure 5-6, line 60). The number of temperature measurement is also increased by 1 (Figure 5-6, line 62).

After looping through all the cells in the heat pipe domain and taking a number “nt” of temperature measurement, the average temperature of the zone is calculated (Figure 5-6, line 71). Theoretically, the UDF code could end here as the temperature was measured. However, in practice, the UDF was creating a simulation failure during the initialisation. Indeed, when the simulation time is 0s, an initial value for the saturation temperature must be indicated. In this regard, a test was added to the UDF (Figure 5-6, line 73 to 80) inside which an initial value for the saturation temperature is given if the simulation time is lower than 0.00001s. If the simulation time is higher, the saturation temperature is defined as the average temperature measured in the defined zone. Once defined by the DEFINE\_EXECUTE\_AT\_END, the computational based value of the saturation temperature “Tsat\_sensor” is then used by the three DEFINE\_SOURCE structures to calculate the phase change source terms.

### 5.2.3.3 Properties UDF

R134a was implemented as the working fluid in the heat pipe simulations carried out. To do so, the properties of R134a have been extracted from the National Institute of Standards and Technology (NIST) database [242]. Those properties have been correlated in terms of temperature and then integrated into the UDF so that they can vary with the heat pipe temperature. The correlated R134a properties are listed in Table 5-1 and Table 5-2.

- **R134a liquid phase properties:**

Table 5-1. R134a liquid phase properties

$\rho_l = (-3.18 \times 10^{-7}) \times T^5 + (5.00 \times 10^{-4}) \times T^4 + (-0.31 \times 10^{-4}) \times T^3 + (9.83 \times 10^1) \times T^2 + (1.54 \times 10^4) \times T + (9.63 \times 10^5)$	(5-20)
$c_{p,l} = (1.38 \times 10^{-6}) \times T^5 + (-2.14 \times 10^{-3}) \times T^4 + (1.32) \times T^3 + (-4.07 \times 10^2) \times T^2 + (6.28 \times 10^4) \times T + (-3.86 \times 10^6)$	(5-21)
$k_l = (1.52 \times 10^{-9}) \times T^3 + (-2.81 \times 10^{-7}) \times T^2 + (-5.94 \times 10^{-4}) \times T + 2.45 \times 10^{-1}$	(5-22)
$\mu_l = (-1.14 \times 10^{-12}) \times T^4 + (1.34 \times 10^{-9}) \times T^3 + (-5.78 \times 10^{-7}) \times T^2 + (1.05 \times 10^{-4}) \times T + (-6.29 \times 10^{-3})$	(5-23)
$\sigma_l = (4.22 \times 10^{-13}) \times T^5 + (-6.55 \times 10^{-10}) \times T^4 + (4.07 \times 10^{-7}) \times T^3 + (-1.26 \times 10^{-4}) \times T^2 + (1.94 \times 10^{-2}) \times T + (-1.15)$	(5-24)

- **R134a vapour phase properties:**

Table 5-2. R134a vapour phase properties

$\rho_v = (3.31 \times 10^7) \times T^5 + (-5.21 \times 10^{-4}) \times T^4 + (3.27 \times 10^{-1}) \times T^3 + (-1.03 \times 10^1) \times T^2 + (1.60 \times 10^4) \times T + (-1.00 \times 10^6)$	(5-25)
$c_{p,v} = (1.89 \times 10^{-7}) \times T^6 + (-3.55 \times 10^{-4}) \times T^5 + (2.78 \times 10^{-1}) \times T^4 + (1.16 \times 10^2) \times T^3 + (2.71 \times 10^4) \times T^2 + (-3.38 \times 10^6) \times T + (1.75 \times 10^8)$	(5-26)
$k_v = (5.86 \times 10^{-13}) \times T^6 + (-1.10 \times 10^{-9}) \times T^5 + (8.62 \times 10^{-7}) \times T^4 + (-3.60 \times 10^{-4}) \times T^3 + (8.42 \times 10^{-2}) \times T^2 + (-1.05 \times 10^1) \times T + (5.45 \times 10^2)$	(5-27)
$\mu_v = (5.57 \times 10^{-16}) \times T^6 + (-1.06 \times 10^{-12}) \times T^5 + (8.36 \times 10^{-10}) \times T^4 + (-3.51 \times 10^{-7}) \times T^3 + (8.29 \times 10^{-5}) \times T^2 + (-1.04 \times 10^{-2}) \times T + (5.44 \times 10^{-1})$	(5-28)

The R134a properties have been integrated into the UDF by using the DEFINE\_PROPERTY structure. To get the temperature of a given cell, the UDF uses the command C\_T. The UDF comprising the R134a properties is presented in Annexe 6.

#### *5.2.3.4 Compiling and interpreting UDF*

In the simulation of the two-phase heat transfer in the three-leg heat pipe, three types of Lee models have been used: solver integrated Lee model, usual Lee model, and modified Lee model. For each type of Lee model, a different UDF was used: for the integrated Lee model, a UDF comprising the R134a properties only was used. For the usual Lee model and modified Lee models, the corresponding UDFs comprising the R134a properties, and the source terms calculation were used. The UDFs were directly interpreted to integrate the R134a properties UDF and the usual Lee model UDF into the ANSYS solver. However, for the modified Lee model UDF, the function had to be compiled and parallelized using Visual Studio 2019 to access deeper solver structures. The complete modified Lee model UDF is provided in Annexe 7.

### **5.2.4 Mesh sensitivity analysis**

#### *5.2.4.1 Objective*

In finite element analysis, the meshing of the geometry has a significant impact on the simulation convergence, speed, and accuracy. A coarser mesh reduces the simulation time and facilitates the calculation convergence, but a finer mesh is more accurate. In particular, the mesh size must be adapted to model and capture the near wall phenomena occurring during boiling and condensation. In this regard, a mesh sensitivity analysis of the three-leg heat pipe was carried out. This aimed at identifying the optimum mesh which guarantees accurate simulations with a reasonable calculation time.

#### *5.2.4.2 Meshing*

Five meshes have been used for simulation to study the mesh sensitivity analysis of the three-leg heat pipe and compared: Very coarse, Coarse, Medium, Fine, and Very fine. For each mesh, the size of the hexahedron elements used varied from 0.7mm to 0.4mm. To capture the near wall phenomena, inflation layers have been added near the walls. Inflation layers have the advantage of greatly improving the simulation accuracy near the walls but are demanding in terms of calculation power. Several inflation layers were tried for the different meshes tested. The size of the first inflation layer was determined automatically by the Fluent solver from the growth rate and number of layers requested. The five meshes of the three-leg heat pipe compared are shown in Figure 5-7.



Mesh	Elements	Element's size (mm)	Inflation layers	Overview
Very coarse	52331	0.7	3	
Coarse	108056	0.5	5	
Medium	145528	0.5	10	
Fine	203304	0.4	10	
Very fine	252805	0.4	15	

Figure 5-7. Three-leg heat pipe – mesh comparison

Several mesh metrics need to be checked to estimate the suitability of a mesh. Indeed, the quality of the mesh and the shape of each cell have a significant impact on the convergence and accuracy of the simulation. The most known and mainly used mesh metrics are the Skewness, Aspect ratio, Squish index, average Orthogonal quality, and average Element quality [244]:

- Skewness is the difference between the cell shape and the shape of an equivalent cell with the same volume and equilateral sides. The skewness of a cell should be kept below 0.95 and the average skewness of the mesh below 0.33 [244].
- Aspect ratio is a measure of the stretching of the cell. For cells situated far from the walls, the aspect ratio is advised to be kept below 5. However, for cells inside the boundary layer near the wall, the aspect ratio can be up to 10 [244].
- Squish index is calculated using vectors from the cell centroid to each face of the cell. The squish index is comprised between 0 and 1 and should be as close to 0 as possible. The maximum squish index must be less than 0.99 [244].
- Orthogonal quality uses vector measurements to describe how close the cell angles are to an optimum angle for the simulation. The orthogonal quality ranges from 0 to 1 with 1 being the optimum orthogonal quality. The minimum orthogonal quality is advised to be more than 0.1 [244].
- Element quality is a modified ratio of the cell volume to the sum of the cell edge's length. The element quality indicator is comprised from 0 to 1 with 1 being a perfect cube or square. The element quality is recommended to be higher than 0.6 [244].

The mesh metrics were checked for all the three-leg heat pipe meshes, and they are provided in Annexe 8. Another factor that is worth checking during the meshing is the  $y^+$  value which describes the quality of the interaction between the solid wall and the first cells in the fluid domain (boundary layer). The  $y^+$  value is a non-dimensional distance from the wall to the first mesh node. This indicator is usually used to ensure that the near wall mesh is suitable with a particular turbulence model.

#### 5.2.4.3 Settings and UDF implemented

The mesh sensitivity analysis simulations carried out are transient simulations with a total time of 30s. Gravity was enabled and R134a was used as a working fluid with the properties provided in the UDF. The solid material was selected as steel. For the multi-phase model, the explicit Volume of Fluid approach with implicit body force was selected. The modified Lee model UDF was compiled, and the mass energy source terms were linked to the solver. Following previous simulations by *Fadhl* [89], [90], a laminar turbulence model was used. The working fluid surface tension was calculated using the UDF equation and the wall adhesion and jump adhesion were selected. Again, following recommendations by *Fadhl* [89], [90], the

SIMPLE algorithm was combined with a first-order upwind scheme for the momentum and energy calculations. Geo-Reconstruct and PRESTO discretization were used for the volume fraction and pressure interpolation scheme. The under-relaxation factors for pressure, density, body force, momentum, and energy were respectively 0.1, 0.5, 0.4, and 0.5. The boundary conditions were calculated so that a heat transfer rate of 1000W is transferred, which gives a heat flux for both evaporator and condenser of  $764.5 \text{ W/m}^2$  (with a negative sign for the condenser). The simulation was initialised at a temperature of 290 K and the corresponding saturation pressure for R134a at this temperature (518,149 Pa). The saturation temperature was defined with the hooked UDF and was therefore equal to 290K at  $t=0\text{s}$ . The filling ratio was 50% which means that half of the evaporator volume is filled with liquid. To record the temperature evolution at different locations of the three-leg heat pipe, temperature measurements have been taken on the middle leg by using reports at distance intervals of 50mm. Finally, for the calculation setting, a variable time step was adjusted by the solver to maintain a global courant number lower than 1 and the end time was defined as 30s.

5.2.4.4 Mesh sensitivity analysis results

Starting from a temperature of 290K at  $t=0\text{s}$ , the three-leg heat pipe temperatures transiently evolve with time as shown in Figure 5-8.

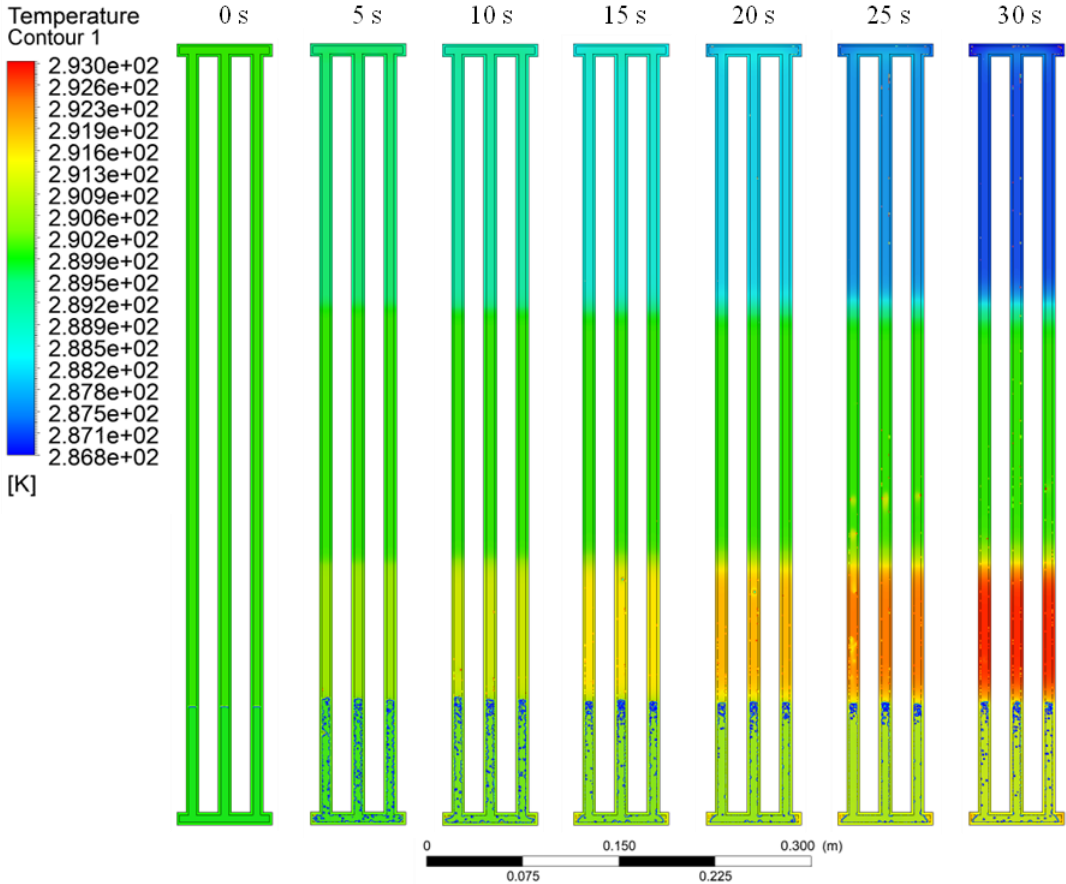


Figure 5-8. Temperature evolution in the three-leg heat pipe during the mesh sensitivity analysis simulations



At the bottom of the three-leg heat pipe, the formation of bubbles in the liquid pool can be seen due to the contact with the heat source, and the evaporator temperature increases. In contrast, the temperature of the condenser decreases due to the negative heat flux boundary condition implemented. Even if this behaviour isn't possible in practice, this boundary condition was implemented during the mesh sensitivity analysis simulations to impose a higher temperature gradient inside the heat pipe, force the condensation to take place, and therefore investigate more accurately the impact of the mesh on the simulations. Indeed, as presented in Figure 5-9, the temperature of the three-leg heat pipe simulated after 20s varies based on the mesh used.

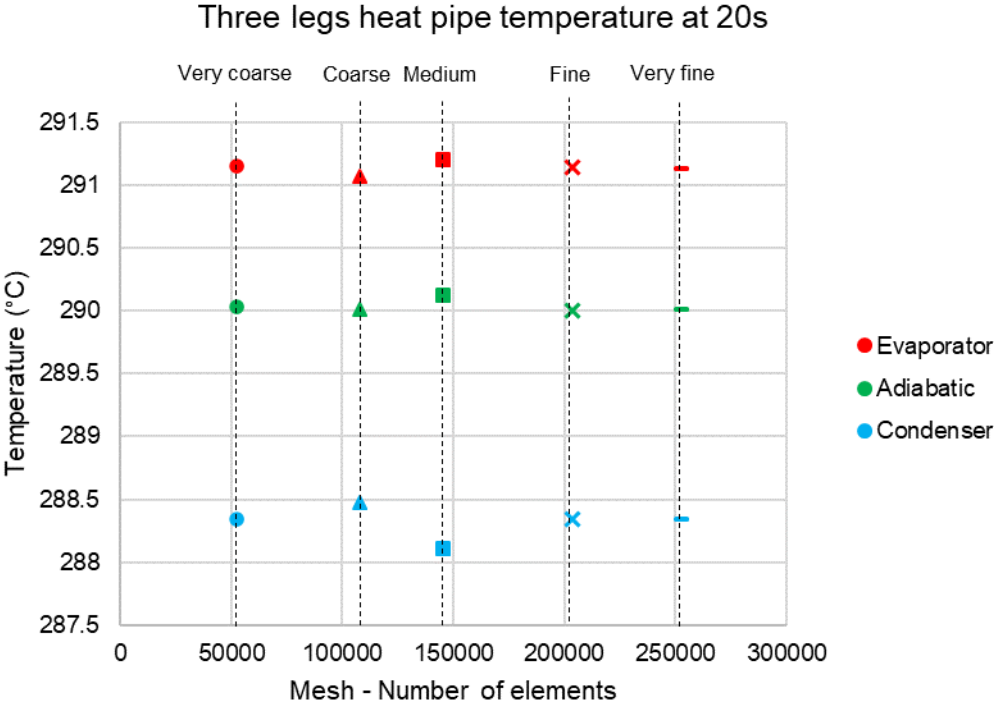


Figure 5-9. Mesh sensitivity analysis – heat pipe temperature after 20s

In Figure 5-9, the temperature of the evaporator, adiabatic, and condenser sections of the heat pipe are represented with red, green, and blue markers. Temperatures from the Very coarse mesh, Coarse mesh, Medium mesh, Fine mesh, and Very fine mesh are displayed with circles, triangles, squares, crosses, and hyphen markers respectively. With the increase of elements in the mesh, the heat pipe temperature converges to a given value. To obtain an accurate simulation, the selected mesh must guarantee that the temperatures of the heat pipe converge to a value which is close to that of the finer mesh. Even if the Very coarse mesh simulation is surprisingly accurate and gives temperatures which are close to the Very fine mesh values, significant differences can be noted for the Coarse and Medium mesh. When refining the mesh and increasing the number of elements up to 200 000, the temperatures seem to converge close to the target value. The average temperature difference between all the meshes investigated and the finer mesh temperatures are shown in Figure 5-10.

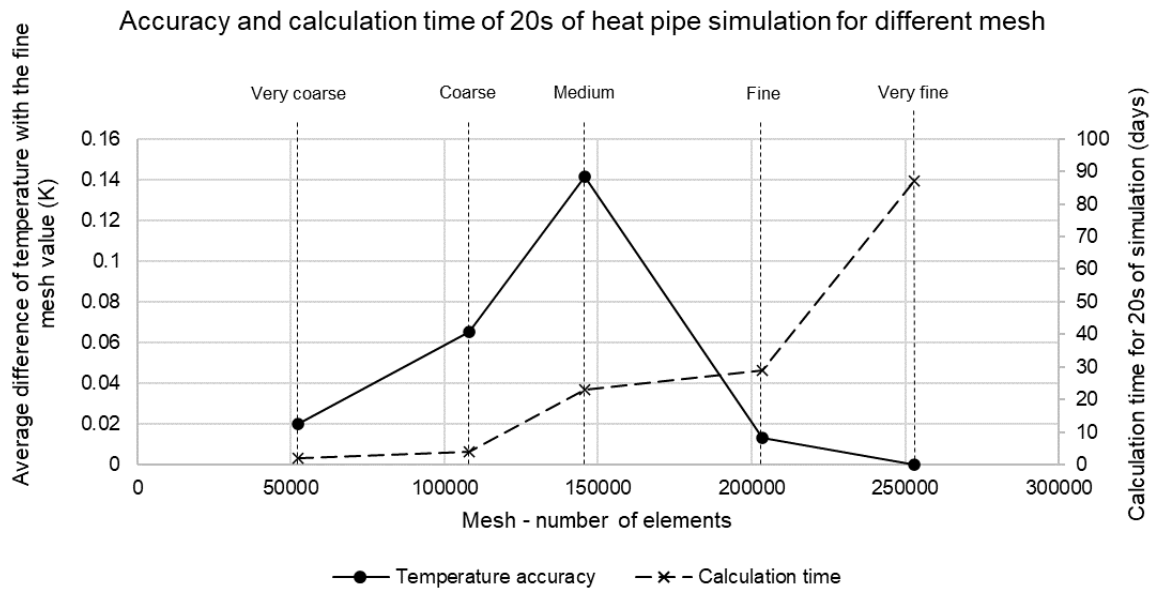


Figure 5-10. Mesh sensitivity analysis – Accuracy and calculation time for 20s simulated with different meshes

It is noted that the average temperature difference with the Very fine mesh increases when increasing the mesh number of elements from 50 000 to 150 000 and then significantly decreases beyond 200 000 elements. The maximum average temperature difference of 0.15°C is obtained for the Medium mesh and gives an estimation of the temperature accuracy of the simulation. For all the other meshes, the temperature difference is lower than 0.08°C which is relatively low in comparison to the accuracy of physical temperature sensors. Hence, it seems that the error made by the selection of the mesh has a low impact on the temperature validation of a simulation. Another factor that must be considered at the start of a series of two-phase flow simulations is the calculation time. Indeed, the complex two-phase mechanisms usually imply long calculation times, which can become a major obstacle if the selected mesh is too fine. The calculation time needed to calculate 20s of the three-leg heat pipe operation is displayed in Figure 5-10 on a secondary axis. Obviously, this calculation time increases when increasing the number of elements in the mesh and, in particular, the number of inflation layers. For the Very coarse and Coarse mesh, the calculation time is reasonable and only a few days of calculation are needed to simulate 20s of heat pipe operation. However, for the Medium and Fine mesh, the calculation time required increases drastically as a minimum of 25 days of calculation are needed to simulate 20s. For the Very fine mesh, 87 days were needed to run a similar simulation. To balance the simulation accuracy and calculation time, the Coarse mesh was selected to investigate the impact of the boundary conditions and compare the different Lee models as an absolute accuracy wasn't needed. However, to investigate the impact of the saturation temperature and condensation heat transfer coefficient, a finer mesh was required to allow an accurate simulation of the boiling and condensation mechanisms. In this regard,

the Fine mesh was used for investigating the impact of the saturation temperature and condensation coefficient.

## **5.2.5 Boundary condition comparison**

### *5.2.5.1 Objective*

Researchers have imposed different boundary conditions in the simulation of heat pipes. If a constant heat flux is usually imposed on the evaporator wall, both heat flux and convection heat transfer coefficient have been implied as boundary conditions on the condenser wall. To bring clarity and select the suitable boundary condition, both constant heat flux and convection heat transfer coefficient have been imposed on the three-leg heat pipe condenser wall and the results compared.

### *5.2.5.2 Settings*

The coarse mesh was used for the boundary condition investigation. A constant heat flux of  $764.5 \text{ W/m}^2$  was imposed on the evaporator wall, which corresponds to a heat transfer rate of  $1000 \text{ W}$ . For the constant heat flux boundary condition simulation, a heat flux of  $-764.5 \text{ W/m}^2$  was set on the condenser wall. For the convection heat transfer coefficient simulation, a convective heat transfer coefficient was imposed at the condenser. This heat transfer coefficient was calculated based on the boiling heat sink in the top cylinder of the three-leg heat pipe. At the top cylinder, water boils and absorbs the heat released from the three-leg heat pipe. As the water is at saturation condition in the top cylinder, the free stream temperature was set to the ambient temperature of  $290 \text{ K}$ . The heat transfer coefficient was estimated using the pool boiling correlation from Rohsenow [137] using water as a working fluid ( $h_{convection} = 139.5 \text{ W/m}^2 \cdot \text{K}$ ). In the three-leg heat pipe, R134a was used with a filling ratio  $FR=50\%$  and the modified Lee model was implemented for two-phase heat transfer. The simulation was initialized at  $290 \text{ K}$ .

### *5.2.5.3 Boundary condition comparison results*

The temperature profile of the three-leg heat pipe after 30s is presented in Figure 5-11 for both simulations. Both heat flux and heat transfer coefficient boundary condition simulations are displayed with a similar temperature range from  $287 \text{ K}$  to  $293 \text{ K}$ . It is observed that, in the case where a heat flux is imposed on the condenser wall, the condenser temperature decreases at values below the initial temperature of the heat pipe. In practice, this behaviour cannot be observed, and the three-leg heat pipe only transfers heat from bottom to top. The only possibility that could lead to a decrease of the condenser wall temperature is to impose a cooling of the wall with cold water. However, in the case of the three-leg heat pipe, the condenser is situated inside a liquid water pool in the top cylinder. Hence, the temperature of the pool in the top cylinder cannot decrease. It is therefore concluded that the convective heat transfer coefficient boundary condition at the condenser is more relevant to simulate the

physical behaviour of the three-leg heat pipe. This boundary condition is also more suitable to observe the transient warmup of the heat pipe.

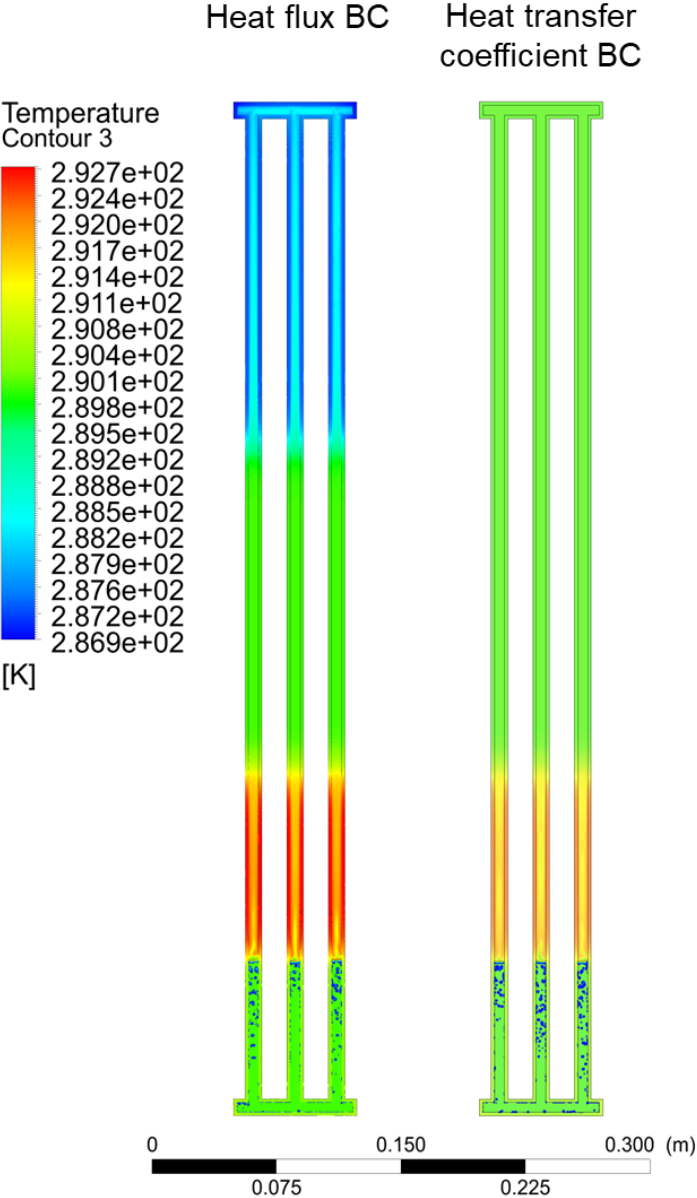


Figure 5-11. Boundary condition comparison

**5.2.6 Lee models comparison**

*5.2.6.1 Objective*

In most of the up-to-date reported work on heat pipe simulation, the Included Lee model of ANSYS has been described as unable to simulate the operation of heat pipes and UDFs have been preferred to model the two-phase heat transfer [70], [83], [84], [87], [89], [90], [102], [251]. However, with the updates of ANSYS, the Lee model provided has been modified. The different models have been implemented and compared with the objective of studying the capability of both the included Lee model and Lee model UDF to simulate two-phase heat transfer. The

modified Lee model was also tested to study its transient behaviour and the evolution of the computational based saturation temperature.

#### 5.2.6.2 Settings

For the Lee model comparison, the included Lee model, Lee model using UDF, and modified Lee model have been implemented to the explicit Volume of Fluid approach with implicit body force option. The saturation temperature for the included Lee model and UDF Lee model was fixed at 290K. For the modified Lee model, the saturation temperature was also initialized at 290K. R134a was used as a working fluid with a filling ratio  $FR=50\%$ . Based on the boundary condition comparison study, a constant heat flux of  $764.5 \text{ W/m}^2$  was imposed on the evaporator's wall whereas a heat transfer coefficient of  $139.5 \text{ W/m}^2\cdot\text{K}$  with a free stream temperature of 290K was imposed on the condenser's wall.

#### 5.2.6.3 Lee model comparison results

The temperature contour of the three-leg heat pipe after 20s of simulation is presented in Figure 5-12 for the three versions of the Lee model investigated. A similar temperature legend ranging from 290K to 292K is used to compare the three models. A Volume of Fluid contour was also added by transparency to visualize the boiling and condensation inside the three-leg heat pipe. Starting from the bottom of the heat pipe, the formation of vapour bubbles can be seen in the pool of the three simulations. For the included Lee model, the liquid level is slightly higher in the middle leg which could be due to a slightly higher bubble activity in the middle leg. Nevertheless, vapour bubbles can clearly be seen in the left and right legs too. For the UDF Lee model simulation, surprisingly, a much higher bubble activity is observed in the left leg whereas vapour bubbles can only be seen near the surface in the middle and right legs. No real explanation can be provided to justify this discrepancy with the other simulations as the same mesh and same simulation settings were implemented. This witnesses how variable and inconstant transient simulations of two-phase heat transfer can be. For the modified Lee model simulation, bubbles are evenly spread between the three legs and the liquid surface height is the same for all the legs. Around the liquid pool, the hot wall temperature can be noticed but the pool temperature remains very close to the initial temperature of 290K. On the upper section of the evaporator, which is not filled with liquid, a significant rise of temperature is observed for all simulations. It seems that, unlike observations in heat pipes, the hot evaporator wall is not cooled by the presence of a liquid condensate situated near the wall. The formation of a condensate liquid film is not observed for any of the Lee models investigated. In addition, it is observed that the temperatures of the adiabatic and condenser sections remain at 290K, which is the saturation temperature implemented. It is therefore concluded that, as the saturation temperature was also the initial temperature of the heat pipe,

the formation of vapour was limited, and condensation did not take place. As a result, heat was not transmitted, and the heat pipe temperature remained constant.

### Lee model comparison Three leg heat pipe after 20s

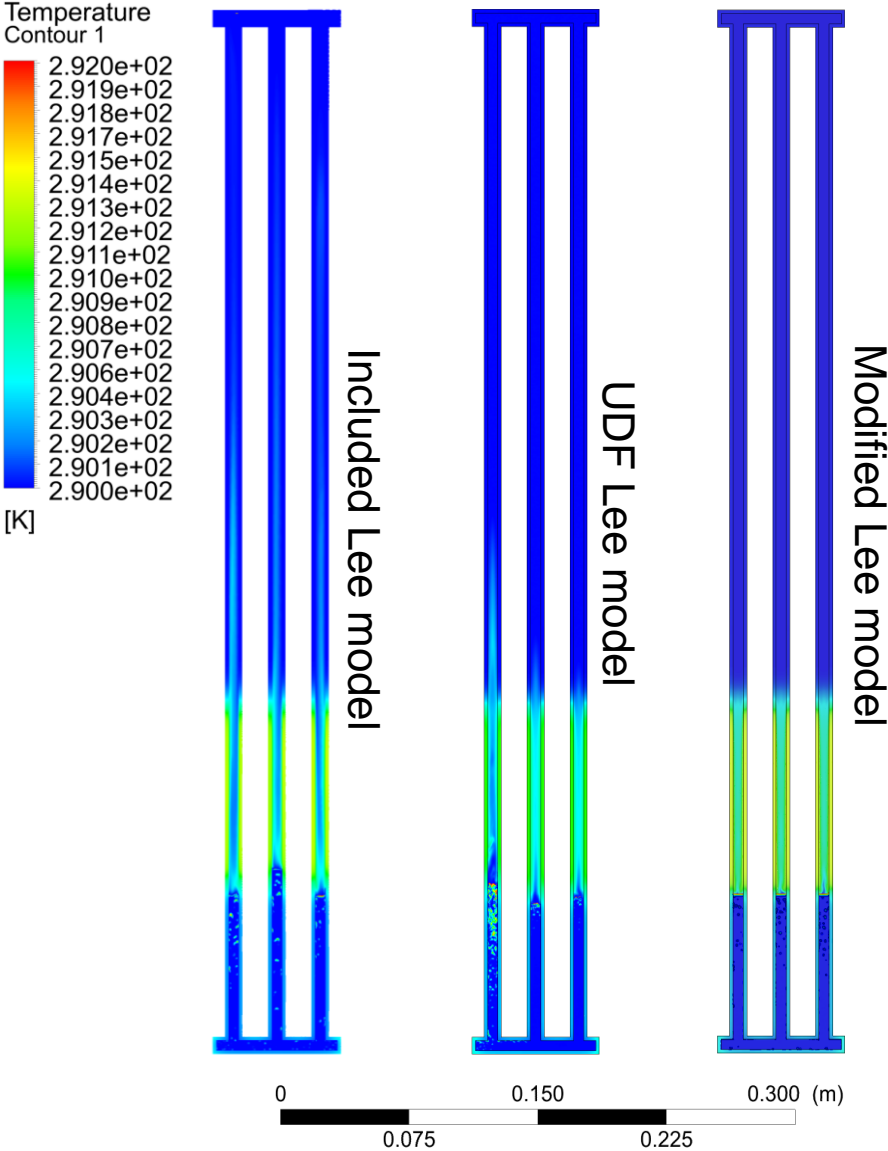


Figure 5-12. Lee model comparison

In this investigation, no significant differences could be noted regarding the comparison between the three Lee models. Unexpectedly, it was observed that the saturation temperature of the Modified Lee model remained constant and fixed at 290K. Indeed, as the saturation temperature is defined based on the pool temperature and that the pool temperature remains constant, no evolution took place. This behaviour could have been different by modifying the coordinates of the zone inside which the saturation temperature value was taken. In the included Lee model simulation, boiling was successfully modelled, and a rising vapour stream was visualized in each leg of the heat pipe. This model was selected for the heat pipe

simulation as the included Lee model also requires less computational effort than the UDF Lee models.

## **5.2.7 Saturation temperature comparison**

### *5.2.7.1 Objective*

The impact of the saturation temperature input provided to the Lee model is studied in this section. In the previously presented Lee model comparison, the saturation temperature specified was set at 290 K and the heat pipe temperature remained close to this value. However, by changing the saturation temperature value provided to the Lee model, the heat pipe temperatures are expected to stabilize around a different value. This dependence of the simulation's results to the saturation temperature input is studied here and could represent a significant limit of the Lee model in the numerical prediction of heat pipe temperatures.

### *5.2.7.2 Settings*

Two similar transient simulations using the included Lee model and Volume of Fluid approach were conducted to study the influence of the saturation temperature. In the first simulation, the saturation temperature was kept at 290 K whereas, for the second simulation, the saturation temperature input was set to 300 K. The boundary conditions remained unchanged with a constant heat flux heat source of  $764.5 \text{ W/m}^2$  and a convection heat transfer coefficient of  $139.5 \text{ W/m}^2\cdot\text{K}$  with a free stream temperature of 290 K for the heat sink. Both simulations were initialized at a temperature 290 K at  $t=0\text{s}$  and R134a was used as a working fluid.

### *5.2.7.3 Saturation temperature comparison results*

The temperature profile of the simulated three-leg heat pipe after 30s is presented in

Figure 5-13. The simulation where the saturation temperature input was 290 K is shown on the left-hand side, whereas the simulation with a saturation temperature input at 300 K is presented on the right-hand side. When the saturation temperature is set at 290 K, it is observed that the adiabatic and condenser section temperatures remain constant at 290 K. Only a section of the evaporator which is not occupied by the liquid pool experiences a temperature increase of up to  $3^\circ\text{C}$ . It is also noted that the vapour temperature in this section remains at a lower temperature than the wall. The simulation where the saturation temperature was set to 300 K presents a very different temperature profile. When the saturation temperature is set to 300 K, the vapour volume temperature significantly increases. In this case, heat transfer is observed and the rising vapour transiently warms-up and carries energy to the condenser section of the heat pipe. The vapour temperature is highest near the evaporator section and progressively decreases as it rises. Surprisingly, despite a saturation temperature value of 300 K, it is observed that the liquid pool remains at a temperature close to the initial temperature (290 K). This highlights the low physical consistency of the Lee model simulation as, in practice, the rising vapour cannot reach temperatures higher than that of the boiling liquid pool. As both

phases are treated independently by the solver, physical contradictions can appear in such simulations. Another detail which highlights the low physical meaning of such simulations is that, in the simulation with  $T_{sat} = 300\text{ K}$ , the evaporator wall temperature remains at temperatures lower than that of the rising vapour. As a conclusion, it seems that the saturation temperature setting forces the working fluid vapour volume temperature to increase and stabilize around the value provided. This is imposed on the simulation regardless of the boundary conditions and physical phenomena occurring at the evaporator and condenser.

Saturation temperature comparison  
Three leg heat pipe after 30s

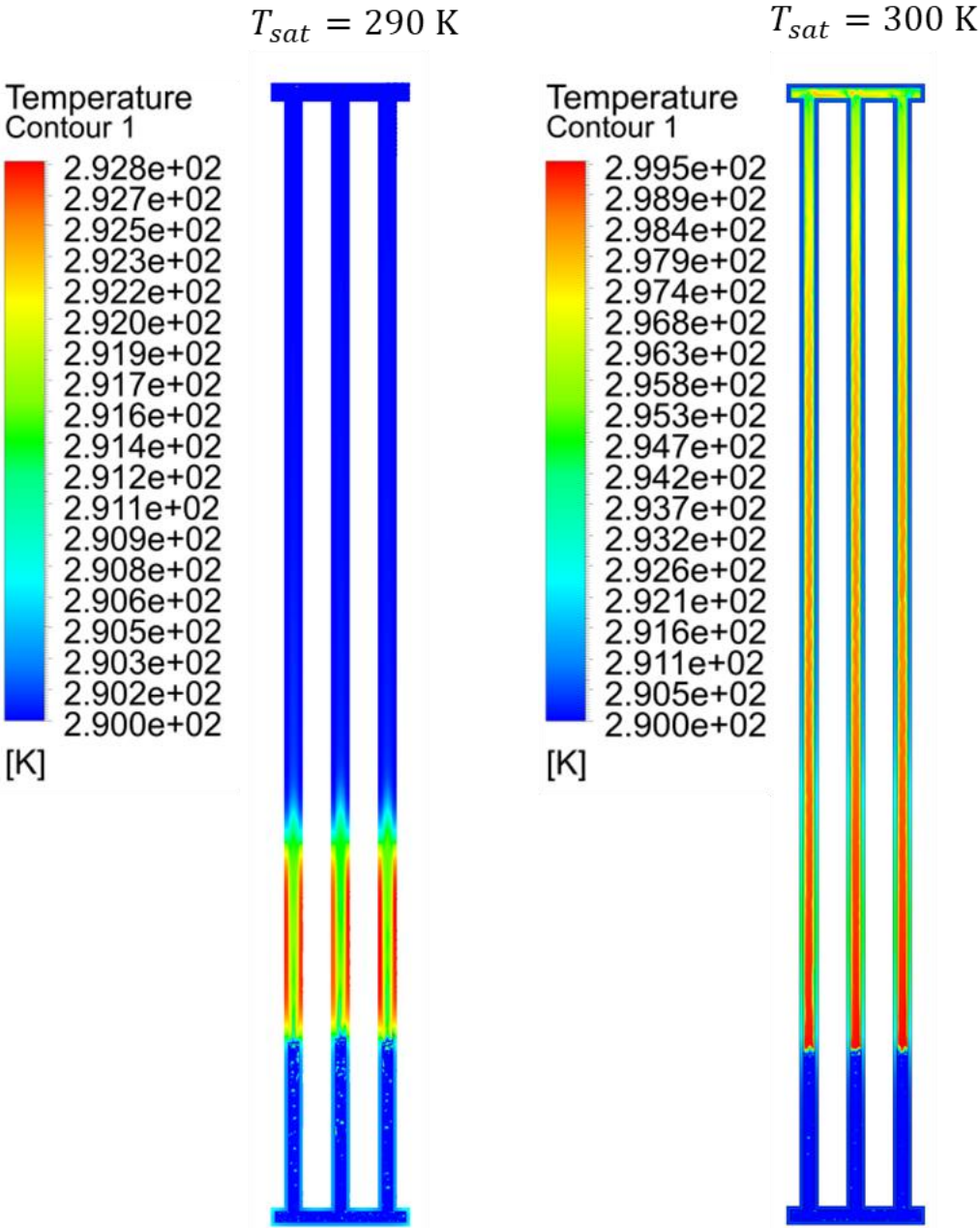


Figure 5-13. Saturation temperature comparison



The transient warmup of the simulated three-leg heat pipe with a saturation temperature of 290 K is presented in Figure 5-14.

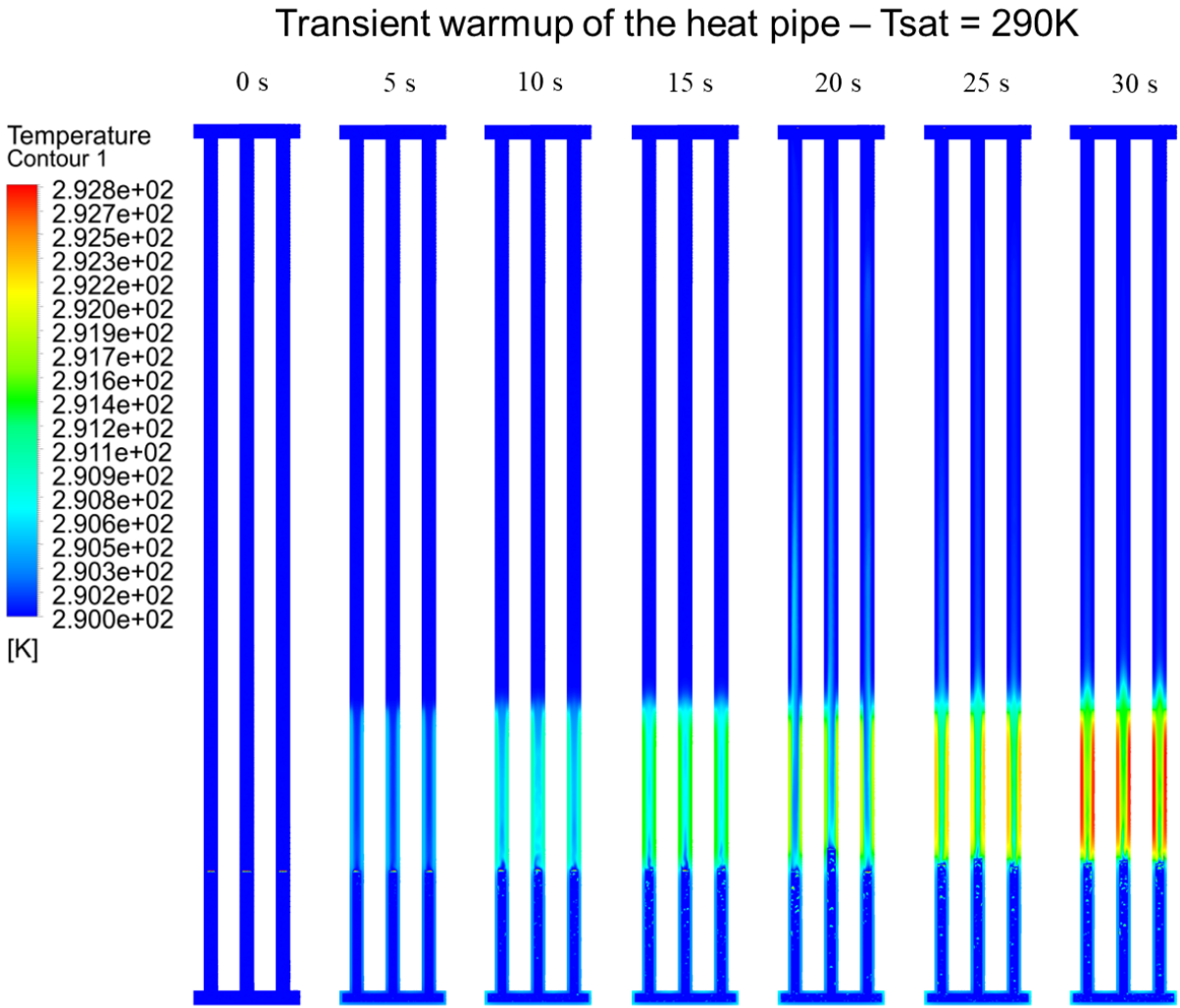


Figure 5-14. Transient warmup of the three-leg heat pipe with  $T_{sat}=290K$

The temperature contours of the three-leg heat pipe simulation reveal that the temperatures of the liquid pool, adiabatic section, and condenser section remain constant at 290 K. When the saturation temperature is set at the initial temperature of the heat pipe, only the evaporator section which is not filled with liquid shows a progressive increase of temperature. It seems that, despite the formation of vapour bubbles, the liquid pool remains at the initial temperature set. On the condenser section, no change of temperature is observed as the saturation temperature, initial temperature, and free stream temperature of the heat sink were all set to 290 K.

As a comparison, the transient temperature contours of the three-leg heat pipe, when a saturation temperature of 300 K was used, are presented in Figure 5-15.

## Transient warmup of the heat pipe – $T_{sat} = 300\text{K}$

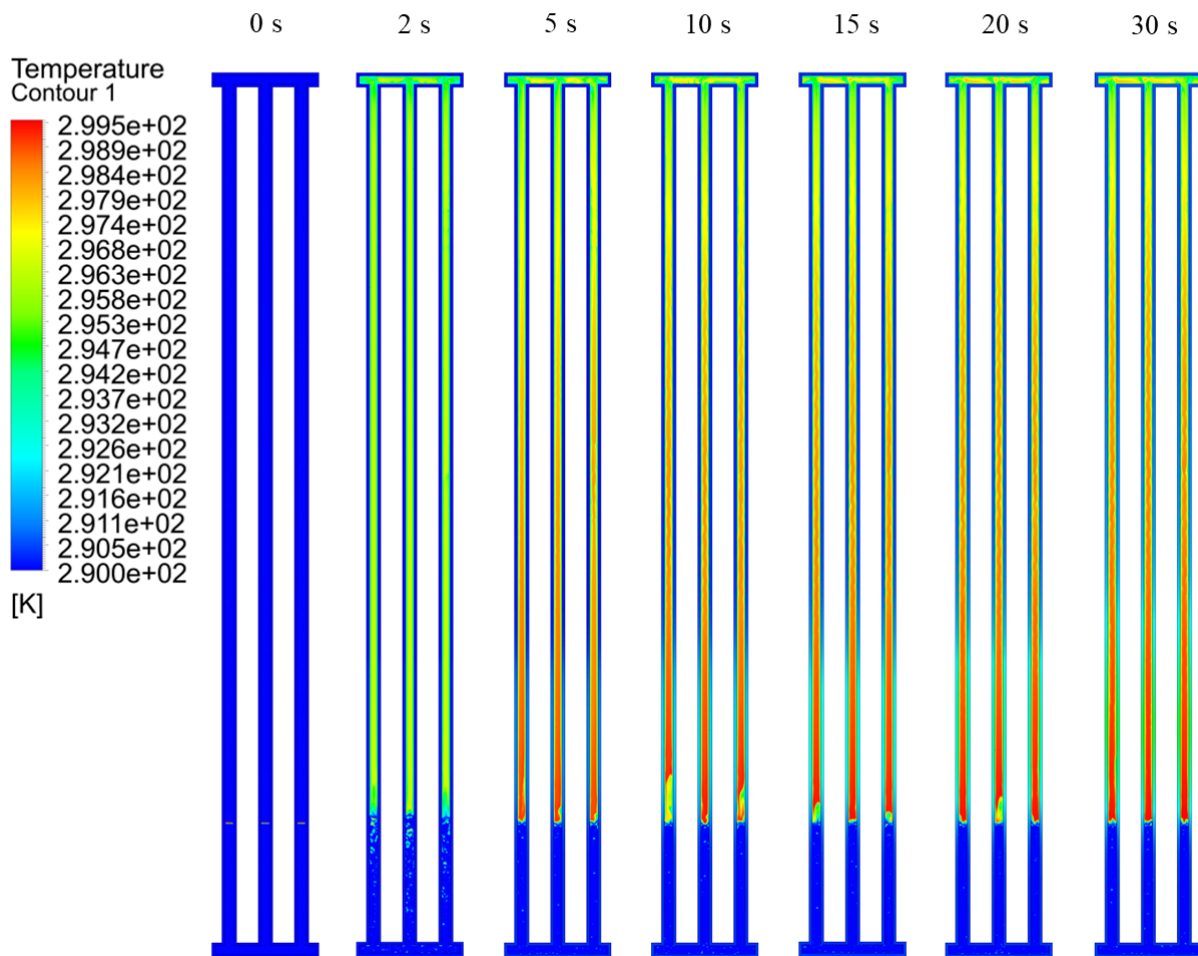


Figure 5-15. Transient warmup of the three-leg heat pipe with  $T_{sat}=300\text{K}$

The transient temperature contours of the simulation at  $T_{sat} = 300\text{ K}$  clearly show the formation of bubbles inside the R134a liquid pool after a few seconds. Simultaneously, the whole vapour volume immediately starts to warm up. However, the temperature increase of the vapour volume is forced by external means and is not physically related to the evaporator's wall temperature. The implemented Lee model forces the vapour phase to converge to temperatures close to the given saturation temperature. Again, it is seen that, despite a change in the saturation temperature, the liquid pool temperature remains at its initial temperature. The transient temperature contours of the heat pipe reveal that the simulated vapour temperature is very uniform after a few seconds. Yet, with an increase of the simulation time, a zone with higher temperatures can be detected at the evaporator section which is not filled with liquid. In addition, a colder zone progressively forms at the top of the heat pipe where the heat sink extracts thermal energy.

To conclude, the comparison of two identical simulations with different saturation temperature inputs revealed that the Lee model forces the vapour volume to converge to temperatures

close to the saturation temperature provided by the user. This is done regardless of the surrounding heat source and heat sink temperatures. Indeed, it was shown that the vapour volume can be forced to reach temperatures higher than the evaporating liquid pool itself, which has no physical meaning. In addition to the poor physical consistency of such simulation, the predictive nature of the two-phase simulation using the Lee model is limited. In practice, the saturation temperature input provided by the user is usually derived from experiments and is commonly used to adjust the heat pipe simulation and suit experimental data.

### 5.2.8 Condensation coefficient comparison

Other factors from the Lee model which have been adjusted by researchers are the evaporation and condensation mass transfer coefficients  $\beta_e$  and  $\beta_c$ . Indeed, in the literature, the condensation mass transfer coefficient in particular has been set to values from  $\beta_c = 0.1 \text{ s}^{-1}$  to  $\beta_c = 5000 \text{ s}^{-1}$  [72]. Yet, according to the Lee [67] model source terms [68], [69], [244], the adjusted mass transfer coefficients are directly related to the energy equation and thus to simulated temperatures:

- **Energy source term - Evaporation**  $T_{mix} > T_{sat}$  :

$$S_E = -\beta_e i_{lv} \alpha_l \rho_l \frac{T_{mix} - T_{sat}}{T_{sat}} \quad (5-29)$$

- **Energy source term - Condensation**  $T_{mix} < T_{sat}$  :

$$S_E = \beta_c i_{lv} \alpha_v \rho_v \frac{T_{sat} - T_{mix}}{T_{sat}} \quad (5-30)$$

where  $S_E$  is the energy source term ( $\text{J/m}^3\text{s}$ ),  $\beta_e$  and  $\beta_c$  are the evaporation and condensation mass transfer coefficients ( $\text{s}^{-1}$ ),  $\alpha_l$  and  $\alpha_v$  the liquid and vapour phase volume fractions,  $\rho_l$  and  $\rho_v$  the liquid and vapour densities ( $\text{kg/m}^3$ ),  $T_{mix}$  the mixture temperature (K),  $T_{sat}$  the saturation temperature (K), and  $i_{lv}$  the latent heat of vaporization ( $\text{J/kg}$ ).

Unfortunately, in the time frame of this research, the simulation of the three-leg heat pipe with various condensation mass transfer coefficients was not conducted due to a lack of time. However, the published study from Kim *et al.* [71] permits conclusions to be drawn on the impact of the condensation mass transfer on the simulation of a heat pipe. Kim *et al.* [71] simulated a single thermosyphon using the Lee [67] model and fixed the evaporation mass transfer coefficient to  $\beta_e = 0.1 \text{ s}^{-1}$ . However, four different values of condensation mass transfer coefficient  $\beta_c$  were used in their CFD simulations. The four conducted simulations were compared to the experimental data by Fadhl *et al.* [84]. The comparison between the experimental data and the thermosyphon simulations conducted with four different values of the condensation mass transfer  $\beta_c$  is shown in Figure 5-16.

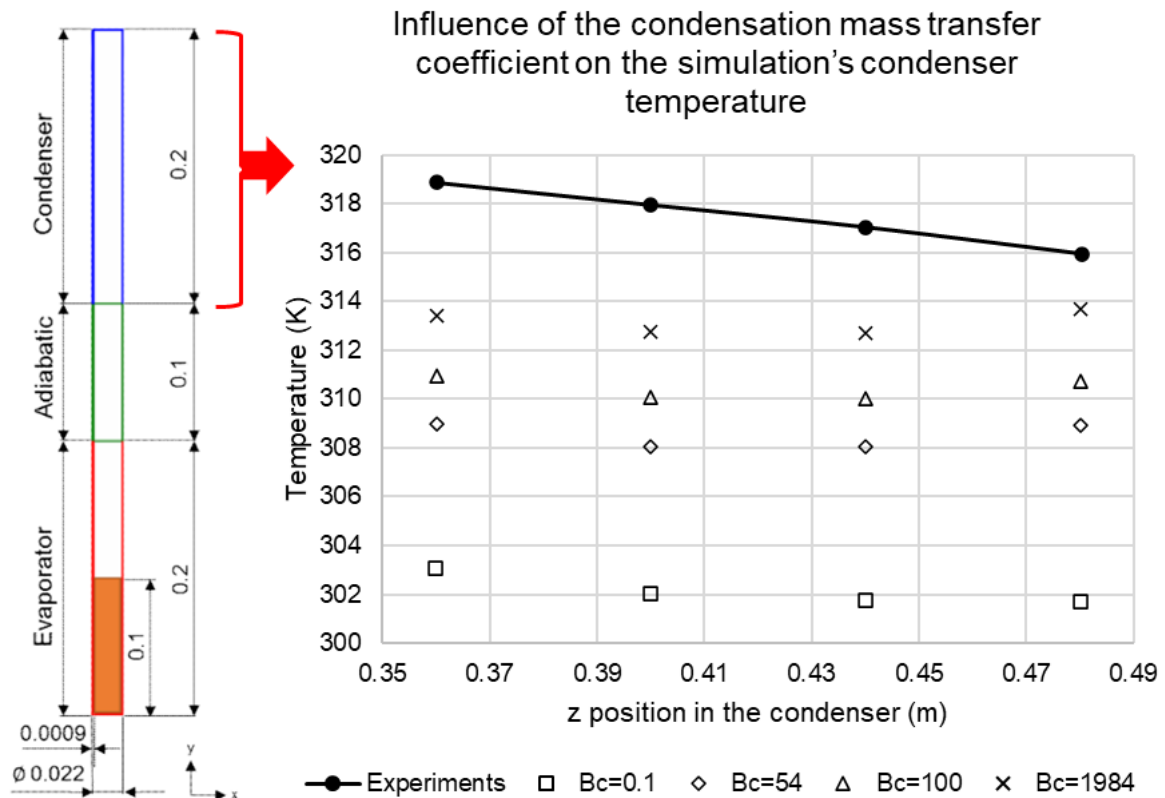


Figure 5-16. Condenser temperature simulated at different condensation mass transfer coefficient  $\beta_c$ , adapted from *Kim et al.* [71]

Only the condenser temperatures are studied in Figure 5-16. The experimental data from *Fadhi et al.* [84] are represented with a black line and circular markers whereas the CFD simulation results are displayed without lines. It is observed that, by changing the value of the condensation mass transfer coefficient  $\beta_c$ , the simulated condenser temperature changes significantly. According to the simulations by *Kim et al.* [71], increasing the value of the condensation mass transfer coefficient results in an increase in the condenser temperature. Indeed, for a condensation mass transfer coefficient  $\beta_c = 0.1 \text{ s}^{-1}$ , the simulated condenser temperature is 302 K whereas, for a condensation mass transfer coefficient  $\beta_c = 1984 \text{ s}^{-1}$ , the simulated condenser temperature increases to 313 K.

The temperature difference between each simulation and the experimental data is shown in Figure 5-17.

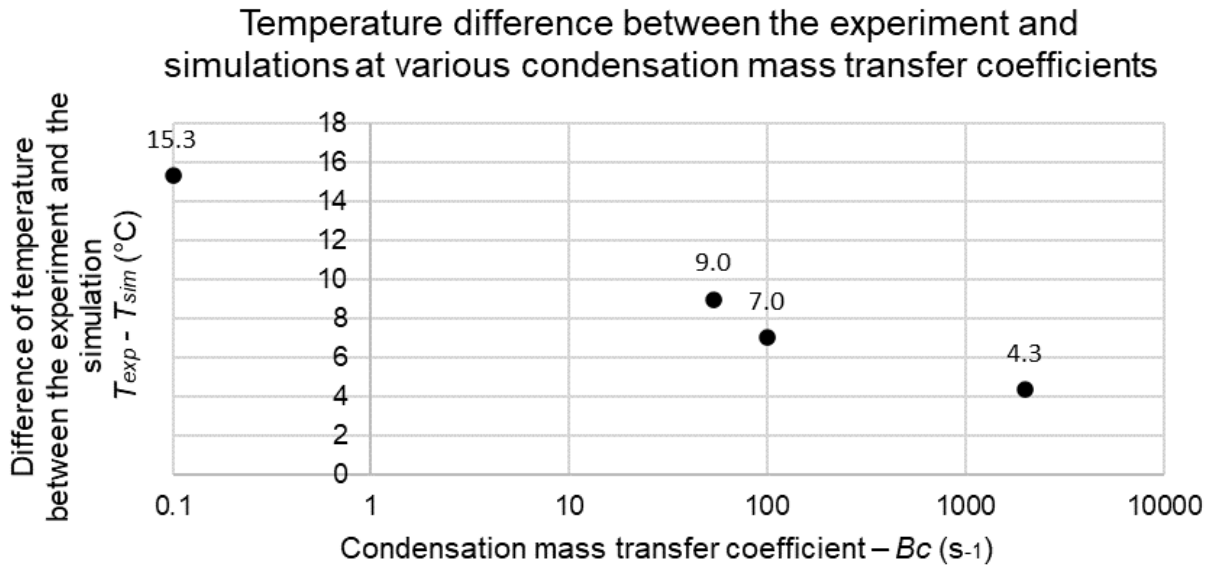


Figure 5-17. Difference of temperature between the simulations and experimental data at various condensation mass transfer coefficients

Figure 5-17 reveals that, by adjusting the condensation mass transfer coefficient, the difference of temperature between a simulation and experimental data can be reduced significantly. Indeed, when the condensation mass transfer coefficient is  $\beta_c = 0.1 s^{-1}$ , the temperature discrepancy between the experiment and simulation is up to  $15.3^{\circ}C$  whereas, when increasing the condensation mass transfer coefficient to  $\beta_c = 1984 s^{-1}$ , the difference of temperature between the experimental data and the simulation is down to  $4.3^{\circ}C$ . This proves that the condensation mass transfer coefficient  $\beta_c$  can be used to adjust the simulation temperature to agree with experimental data.

### 5.2.9 Conclusion and limitations of the Lee model for the three-leg heat pipe simulation

In this section, the CFD simulation of the three-leg heat pipe operating cycle has been addressed by using the Volume of Fluid (VOF) approach and implementing the Lee [67] model source terms to the transport equations.

A convection heat transfer coefficient boundary condition on the condenser's wall was found to be the most relevant boundary condition to apply and observe the transient warmup of the heat pipe. Indeed, a negative heat flux boundary condition results in a condenser's temperature decreasing below the initial temperature of the heat pipe which is physically impossible.

As the integrated Lee model of previous versions of ANSYS has often been described by researchers as unable to simulate heat pipes [71], [80], [84], [87], [90], three different versions of the Lee model have been integrated and compared: 1) the integrated Lee model of ANSYS\_2020, 2) the usual Lee model using UDF, and 3) a modified Lee model using UDF. According to the simulations carried out, little difference could be detected between the

included Lee model of ANSYS\_2020 and the user defined function (UDF) versions of the Lee model. Boiling was observed in the liquid pool and the vapour source terms generated an increase of temperature in the evaporator section which was filled with vapour. As the included Lee model requires a lower computational effort, this model was selected.

By manipulating the Lee model source terms, it was concluded that this approach to simulating two-phase heat transfer in heat pipes shows low physical consistency. Indeed, mass and energy source terms operate independently and are not necessarily linked. This can lead to an unacceptable physical behaviour of the simulation such as a liquid pool temperature being lower than the generated vapour temperature.

A limiting factor on the predictive nature of the Lee model simulations is the saturation temperature input required from the user. It was shown that the vapour phase temperature of the simulated three-leg heat pipe converges to the saturation temperature input indicated. To date, the saturation temperature to be used in the Lee model cannot be predicted using CFD software and researchers have derived this parameter from experimental data.

In addition to the saturation temperature parameter, two other parameters are often adjusted by researchers: the evaporation and condensation mass transfer coefficients  $\beta_e$  and  $\beta_c$ . Yet, as shown in the Lee model energy source terms and highlighted by the simulations from *Kim et al.* [71], these coefficients have a direct impact on the simulated evaporator and condenser temperatures. The evaporation and condensation mass transfer coefficients  $\beta_e$  and  $\beta_c$  of the Lee model can therefore be respectively adjusted to fit the simulated evaporator and condenser temperatures with experimental data.

The input parameters from the Lee model and how these can be adjusted to fit a heat pipe simulation to experimental data are shown in Figure 5-18. The saturation temperature input first determines the vapour temperature of the simulated heat pipe's adiabatic section. Then, the evaporation and condensation mass transfer coefficients can be modified to adjust the evaporator and condenser temperature, respectively.

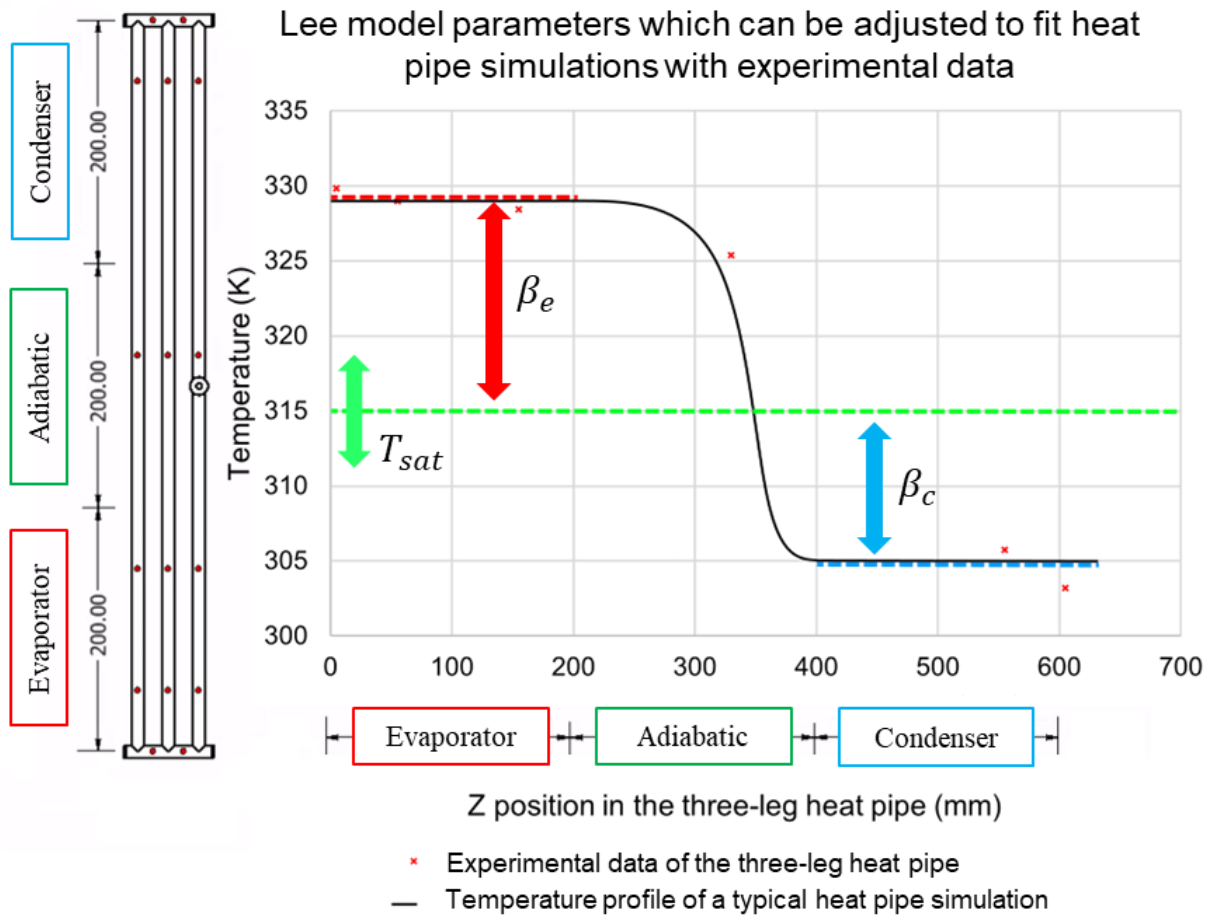


Figure 5-18. Lee model parameters adjustment to fit heat pipe simulation to experimental data

As a conclusion, the *Lee* [67] model is found unable of predicting a heat pipe temperature. Instead, this CFD approach for simulating two-phase heat transfer is a semi-empirical model. Indeed, even if the mass transfer coefficients can be kept to their default value of  $\beta_e = \beta_c = 0.1s^{-1}$ , a saturation temperature input is still required and cannot be predicted by ANSYS. This model is often used to fit heat pipe simulations with experimental data by adjusting the saturation temperature  $T_{sat}$ , the evaporation mass transfer coefficient  $\beta_e$ , and the condensation mass transfer coefficient  $\beta_c$ . The model presents a low physical coherence as the appearance of bubbles, generation of condensation, and temperatures in both liquid and vapour volumes can be managed independently. Finally, despite the simulation of vapour bubbles at the evaporator or liquid condensate near the condenser's wall, it is unlikely that the simulated mechanisms are close to experimental observations as such mechanisms are linked to the microscopic aspect of the surface which, to date, isn't considered by CFD software.

In this regard, instead of investigating the simulation of the complete multi-channel flat heat pipe working cycle, in the next sections, local simulations of a single channel of the multi-channel flat heat pipe are conducted.

### 5.3 Single channel simulations

#### 5.3.1 Objectives

The multi-channel flat heat pipe used for surface cooling application uses a unique channel shape which aims at improving the heat transfer from the top surface to the working fluid. If this channel shape was conceived to improve the heat pipe performance when its orientation is close to horizontal, the impact of the channel shape is different from the case where the flat heat pipe is used vertically. Local scale CFD simulations can help to investigate and visualize how two-phase heat transfer occurs from the hot surface to the working fluid inside the channel. Furthermore, in the theoretical modelling of the channel, correlations assimilate the channel cross-section to a circle with an equivalent hydraulic diameter. However, discrepancies between this simplification and the real channel temperature distribution, velocity profile, and two-phase mechanism are expected. In this section, the local influence of the channel shape on the conduction thermal resistance, temperature distribution, velocity profile, and boiling mechanisms is studied and compared with the case of a circular channel with equivalent hydraulic diameter and equivalent perimeter.

#### 5.3.2 Mesh sensitivity analysis

##### 5.3.2.1 Geometry

A single channel 200mm long was designed and introduced to ANSYS to study the impact of the channel shape on the two-phase heat transfer in the flat heat pipe. As shown in Figure 5-19, both solid and liquid volumes are considered so that the heat source can be applied on the top surface of the channel only.

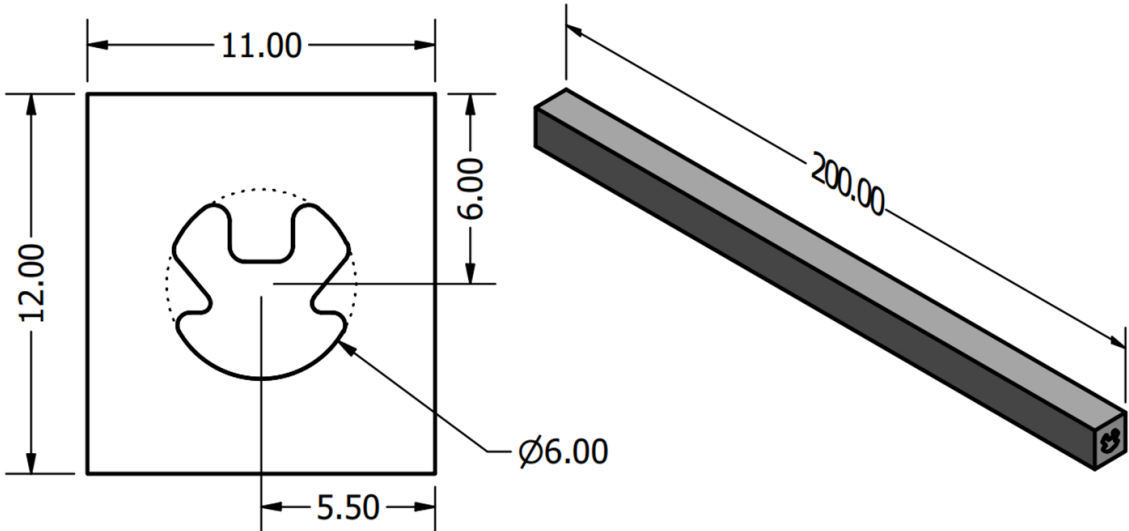


Figure 5-19. Single channel simulation geometry



### 5.3.2.2 Meshing

A mesh sensitivity analysis has been conducted to study the stability and accuracy of the single channel mesh. Four meshes have been compared: Very coarse, Coarse, Medium, and Fine. For those meshes, the element size has been reduced from 0.5mm to 0.15mm. Moreover, to improve the capture of the near wall phenomena, the number of inflation layers in the fluid volume has been changed from 3 to 14. The 4 meshes studied for the mesh sensitivity analysis of the single channel simulation are presented in Figure 5-20.

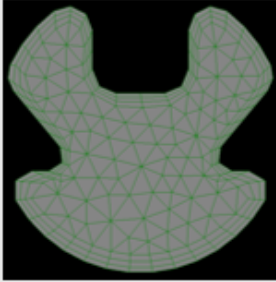
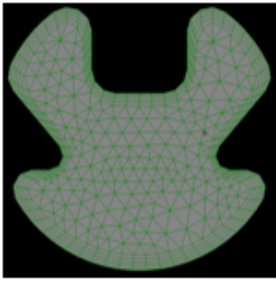
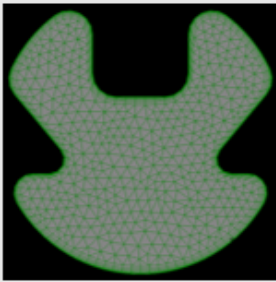
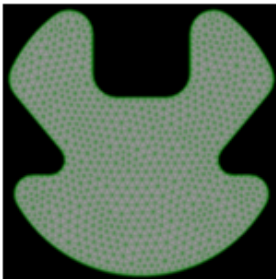
Mesh	Elements	Element's size (mm)	Inflation layers	Overview
Very coarse	301 357	0.5	3	
Coarse	1115718	0.3	5	
Medium	3134150	0.2	7	
Fine	9524145	0.15	14	

Figure 5-20. Single channel – mesh comparison

The mesh metrics of the investigated meshes are also provided in Annexe 9.

### 5.3.2.3 Settings

A forced convective simulation has been done to conduct the mesh sensitivity analysis of the single channel. The simulation is a single-phase steady state simulation estimating the warmup of rising steam inside a heated channel. Water vapour was used as a working fluid with an inlet velocity of 0.35 m/s which corresponds to a Reynolds number of  $Re=250$ . Regarding the thermal boundary condition, steam enters in the channel at a saturation temperature of 373.15 K and a heat flux of  $50 \text{ W/m}^2$  is imposed on the top wall. A similar simulation was conducted for the four meshes and temperature measurements were taken at distances of 0, 50, 100, 150, and 200mm at the centre of the channel.

### 5.3.2.4 Mesh sensitivity analysis results

The steam temperature taken from the middle of the channel at a location of 150mm from the channel inlet is presented in Figure 5-21 .

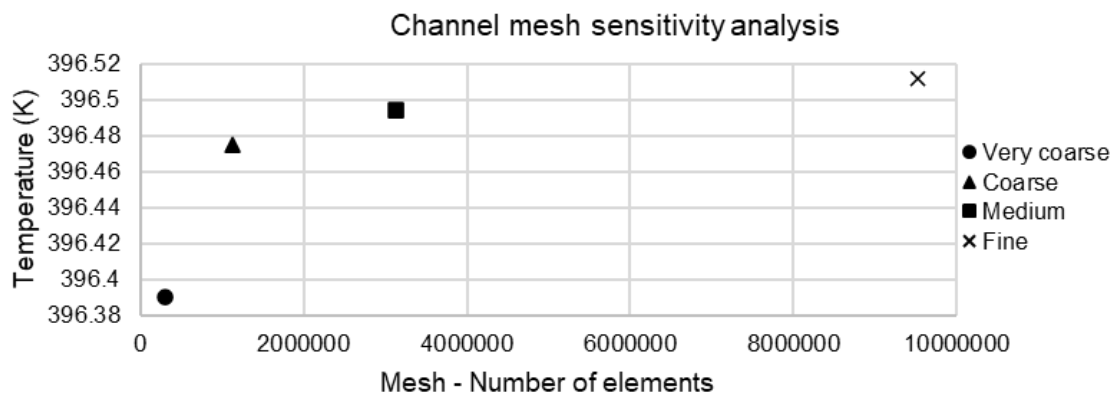


Figure 5-21. Single channel - mesh sensitivity analysis

In Figure 5-21, the channel temperatures for the Very coarse, Coarse, Medium, and Fine meshes are displayed with circle, triangle, square, and cross markers. A clear convergence to a temperature close to 396.52 K can be seen as the number of elements in the mesh increases. If an important error is made with the Very coarse mesh, both Coarse and Medium mesh results can be discussed. For both meshes, the number of elements is reasonable and below  $4e^6$  elements. Yet, the temperature difference between the Fine mesh and the Coarse mesh is 0.037 K whereas it is down to 0.018 K for the medium mesh. As this accuracy improvement remains reasonable in terms of increase of the number of elements, the medium mesh was selected for the single channel simulations. A circular channel was also meshed with a similar element size and number of inflation layer as the channel medium mesh for comparison. The selected Medium mesh and its mesh metrics are detailed in Annexe 10.

### 5.3.3 Conduction profile comparison

The conduction thermal resistance of the channel is investigated in this section. Attention is given to the temperature profile in the solid cross-section of the channel. The channel shape is also compared to two circular channels: a channel whose diameter equals the hydraulic diameter of the channel, and a circular channel whose perimeter equals the channel perimeter.

#### 5.3.3.1 Simulation settings

A steady single phase simulation using water vapour only was carried out to investigate the conduction profile of the heat pipe channel. Gravity was considered and the inlet velocity of the steam was calculated for a Reynolds number of  $Re=250$  which gives a steam velocity at the inlet of 0.35 m/s. The flow field is considered to be laminar, and the energy equation was used. Regarding the thermal boundary condition of the simulation, a constant heat flux of  $50 \text{ W/m}^2$  was imposed on the top wall whereas the other walls were considered adiabatic.

#### 5.3.3.2 Results

The temperature contour of the solid channels investigated is shown in Figure 5-22 below.

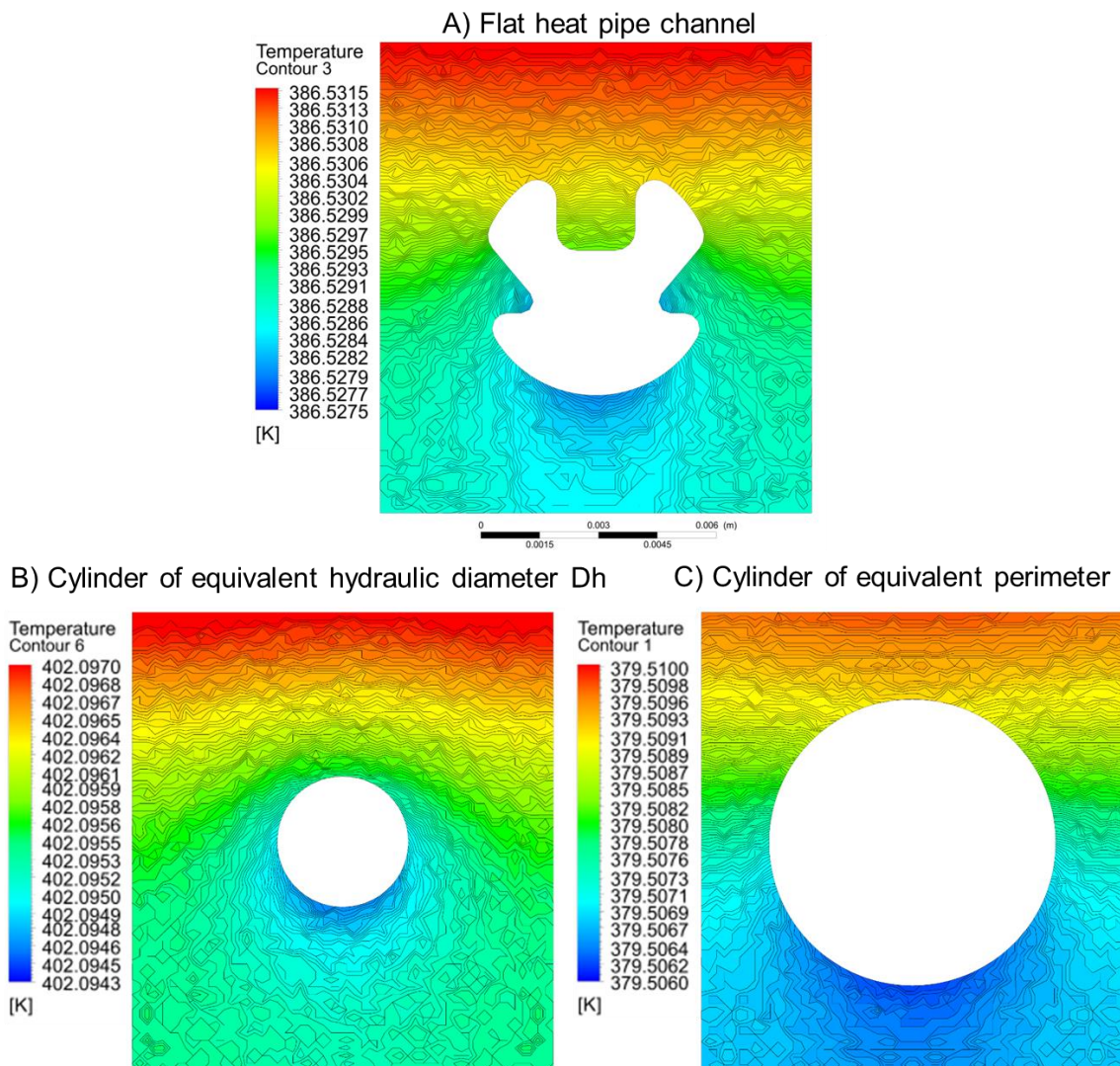


Figure 5-22. Temperature profile of the flat heat pipe channel cross-section and comparison with circular channels

From Figure 5-22 it is observed that, when the top surface of the channel only is heated, the temperature difference between the top and the bottom of the profile varies with the size of the channel. When the channel has a smaller diameter (tube with equivalent hydraulic diameter), the side and bottom zones of the cross-section present higher temperatures. In contrast, the temperature profile of the cylindrical channel with an equivalent perimeter shows that the temperature is much lower in the bottom half of the cross-section. It is also noted that the temperature profile shows a curvature that is more important for smaller diameters and leads to higher temperatures on each side of the profile. Regarding the temperature profile of the multi-channel flat heat pipe's channel, it is observed that the top half of the channel which presents the largest heat transfer area with the highest temperatures diffuses the heat with the three "teeth" of the channel. Some temperature indicators are provided in Table 5-3 to provide some details about the conduction profile of the channels investigated.

Table 5-3. Temperature measurement in the conduction profile of simulated channels

	<b>Diameter</b>	<b>Perimeter</b>	$T_{solid,avg}$	$T_{solid,max} - T_{solid,min}$	$T_{solid,avg} - T_{liquid,avg}$
	(mm)	(mm)	(K)	(K)	(K)
<b>A) Flat heat pipe channel</b>	3.43 ( $D_h$ )	23.48	386.5	0.00355	1.59
<b>B) Cylinder of equivalent hydraulic diameter</b>	3.43	10.76	402.1	0.00245	2.96
<b>C) Cylinder of equivalent perimeter</b>	7.47	23.48	379.5	0.00351	2.72

Even if the hydraulic diameters are similar, the modelling of the channel by a cylinder with a similar ratio between the perimeter and its cross-sectional area presents significant differences. Indeed, the heat transfer area between the solid and the liquid is more than twice in the case of the flat heat pipe's channel. The average temperature of the solid material in the cross-section seems directly related to the size of the liquid area as increasing the liquid passage for a constant velocity increases the cooling water flow rate. More interestingly, the difference of temperature between the maximum and minimum temperature of the solid indicates that the temperature profile of the channel with equivalent hydraulic diameter (B) is more uniform. Both channel (A) and the cylindrical channel with equivalent perimeter (C) have a similar difference of temperature between the maximum and minimum temperatures of the solid which means that, in terms of temperature uniformity, the flat heat pipe's channel (A) is much closer to a cylinder with an equivalent perimeter (C). Interestingly, the difference of temperature between the solid and liquid sections of each channel indicate that the fluid temperature is the closest to that of the solid in the case of the flat heat pipe channel. For both cylindrical channels, the fluid temperature isn't as close as that of the solid wall. This indicates

that, even if the conduction thermal resistance of the flat heat pipe channel may not be optimum compared to the cylindrical channels, the convection thermal resistance seems to compensate and is lower for the flat heat pipe channel than for usual cylindrical channels. To sum up the conduction observations, the conduction thermal resistances for the three channels investigated were calculated and are reported in Table 5-4.

Table 5-4. Conduction thermal resistances of the 3 investigated channels

A) Flat heat pipe channel	Conduction thermal resistances (K/W)	
	0.298	(CFD)
B) Cylinder of equivalent hydraulic diameter	0.271	(Theory)
C) Cylinder of equivalent perimeter	0.210	(Theory)

In Table 5-4, the conduction thermal resistance of the flat heat pipe channel (A) was determined from 10 CFD simulations whereas the cylindrical channels' conduction thermal resistances were determined theoretically from commonly used equations. In order to be able to determine the conduction thermal resistance of the channel of the multi-channel flat heat pipe, a correcting factor  $F_{correction}$  is introduced to the normally used conduction equation [14]:

$$R_{wall,e-1 channel} = \frac{1}{k_{alum} F_{correction} S} \tag{5-31}$$

$$= \frac{\ln\left(\frac{2w}{\pi D} \sinh \frac{2\pi z}{w}\right)}{k_{alum} F_{correction} 2\pi L} \quad (for\ each\ channel)$$

where  $k_{alum}$  is the aluminium thermal conductivity (W/m.K),  $S$  a shape factor,  $z$  the material thickness between the surface and the channel axis (m),  $w$  the pitch between each parallel channel (m),  $D$  the diameter of the channel (m), and  $L$  the length of the parallel channels (m) as indicated in Figure 5-23.

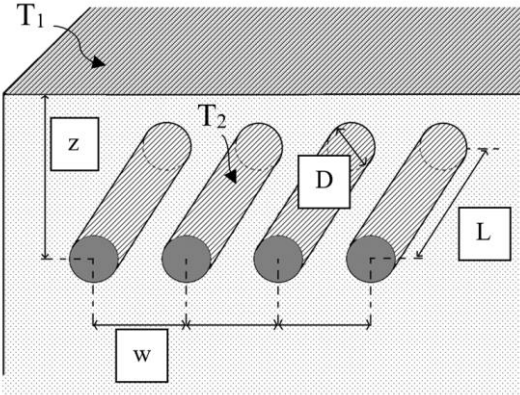


Figure 5-23. Conduction parameters to determine the conduction resistance for one channel

By measuring the average temperature of the heated surface and of the channel wall, the flat heat pipe conduction resistance was measured from the CFD simulation by:

$$R_{wall,e-1 channel} = \frac{(T_{heated surface,avg} - T_{channel wall,avg})}{\dot{Q}} \quad (5-32)$$

where  $\dot{Q}$  is the heat transfer rate passing through the channel's wall. Then, from the measurement of the channel's conduction thermal resistance, the correction factor introduced to the usual conduction equation was determined using:

$$F_{correction} = \frac{\ln\left(\frac{2w}{\pi D} \sinh \frac{2\pi z}{w}\right)}{k_{alum} 2\pi L R_{wall,e-1 channel}} \quad (5-33)$$

The conduction thermal resistance of the flat heat pipe channel is displayed in Figure 5-24 from 10 CFD simulations for heat flux varying from 1000 W/m<sup>2</sup> to 9000 W/m<sup>2</sup> which corresponds to heat transfer rates from 0.1 W to 1 W.

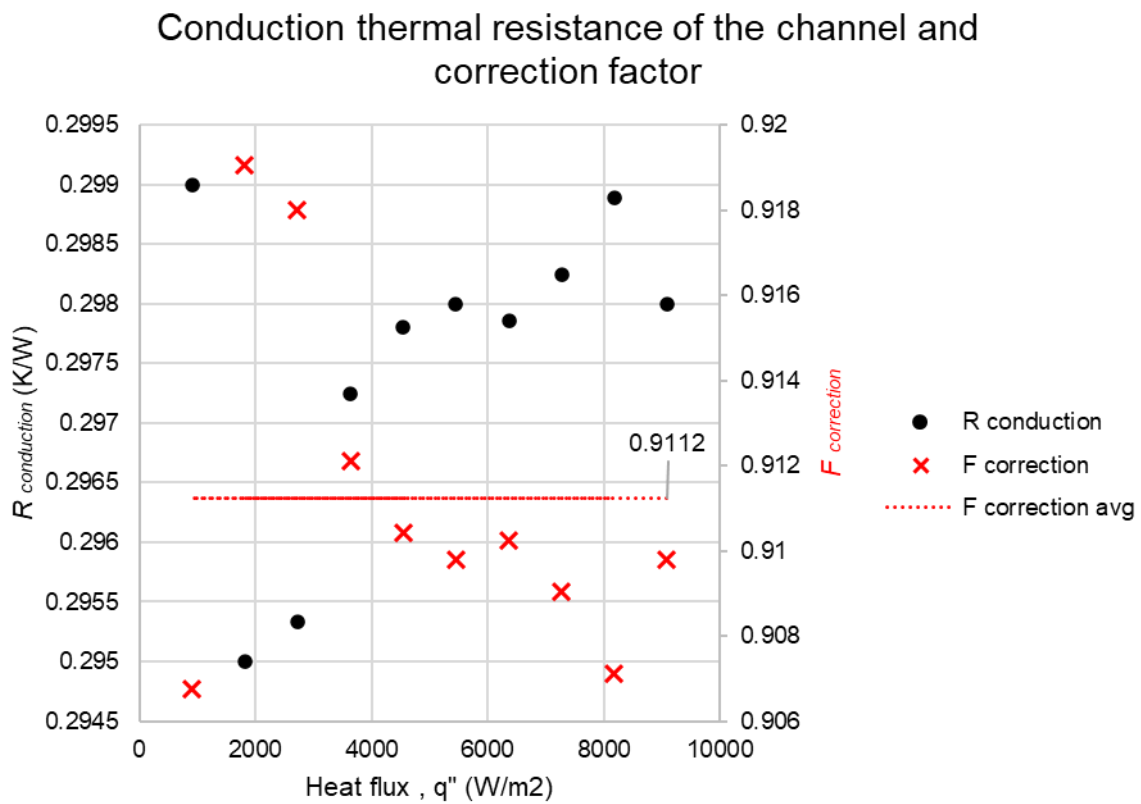


Figure 5-24. Conduction thermal resistance of the flat heat pipe channel (from CFD) and corresponding correction factor

The corresponding correction factor which allows the theoretical calculation of the flat heat pipe channel's conduction thermal resistance is also displayed in Figure 5-24 with red cross markers. It is observed that the measured conduction thermal resistance from the CFD simulations at various heat fluxes varies within 0.45%. Similarly, the same small fluctuations have been transmitted to the calculated correction factor. Yet, the standard deviation is small and the proposed correction factor to calculate the conduction thermal resistance of the multi-channel flat heat pipe channel is estimated to be:

$$F_{correction} = 0.9112 \quad (5-34)$$

### 5.3.4 Velocity profile comparison

In this section, the velocity profile of the vapour phase inside the multi-channel flat heat pipe's channel is investigated. This aims at understanding the flow pattern of the rising vapour at the adiabatic section of the multi-channel flat heat pipe. The velocity contour is compared with cylindrical channels of equivalent hydraulic diameter and equivalent perimeter. Two boundary conditions are implemented to compare the three channels: similar inlet velocity and similar flow rate.

#### 5.3.4.1 Simulation settings

Steam was used to carry out a single-phase simulation to investigate the velocity profile of the rising vapour inside the multi-channel flat heat pipe. Gravity was not considered for these simulations, and, for the water vapour inlet, two boundary conditions have been implemented: similar velocity and similar flow rate. Implementing a similar inlet velocity permits the impact of the channel's shape on the flow development to be studied. Yet, in heat pipes, the mass flow rate of the working fluid inside the channel is linked to the heat transfer rate. Therefore, it seems relevant also to compare the three channels with a similar steam flow rate. The channel's inlet boundary condition for both similar velocity and similar flow rate simulation are reported in Table 5-5.

Table 5-5. Boundary condition of the channels

	Similar velocity		Similar mass flow rate	
	$v$ (m/s)	$\dot{m}$ (kg/s)	$v$ (m/s)	$\dot{m}$ (kg/s)
<b>A) Flat heat pipe channel</b>	0.35	$4.15 \times 10^{-6}$	0.35	$4.15 \times 10^{-6}$
<b>B) Cylinder of equivalent hydraulic diameter</b>	0.35	$1.90 \times 10^{-6}$	0.76	$4.15 \times 10^{-6}$
<b>C) Cylinder of equivalent perimeter</b>	0.35	$9.05 \times 10^{-6}$	0.16	$4.15 \times 10^{-6}$

#### 5.3.4.2 Results

- **Similar velocity:**

To begin with, the multi-channel flat heat pipe channel was compared to the two cylindrical channels by implementing a similar steam velocity at the channel's inlet. A constant velocity of 0.35 m/s was imposed at the inlet and the development of the flow in the channel is studied. The velocity contours of the three investigated channels are presented in Figure 5-25 once the flow is developed.

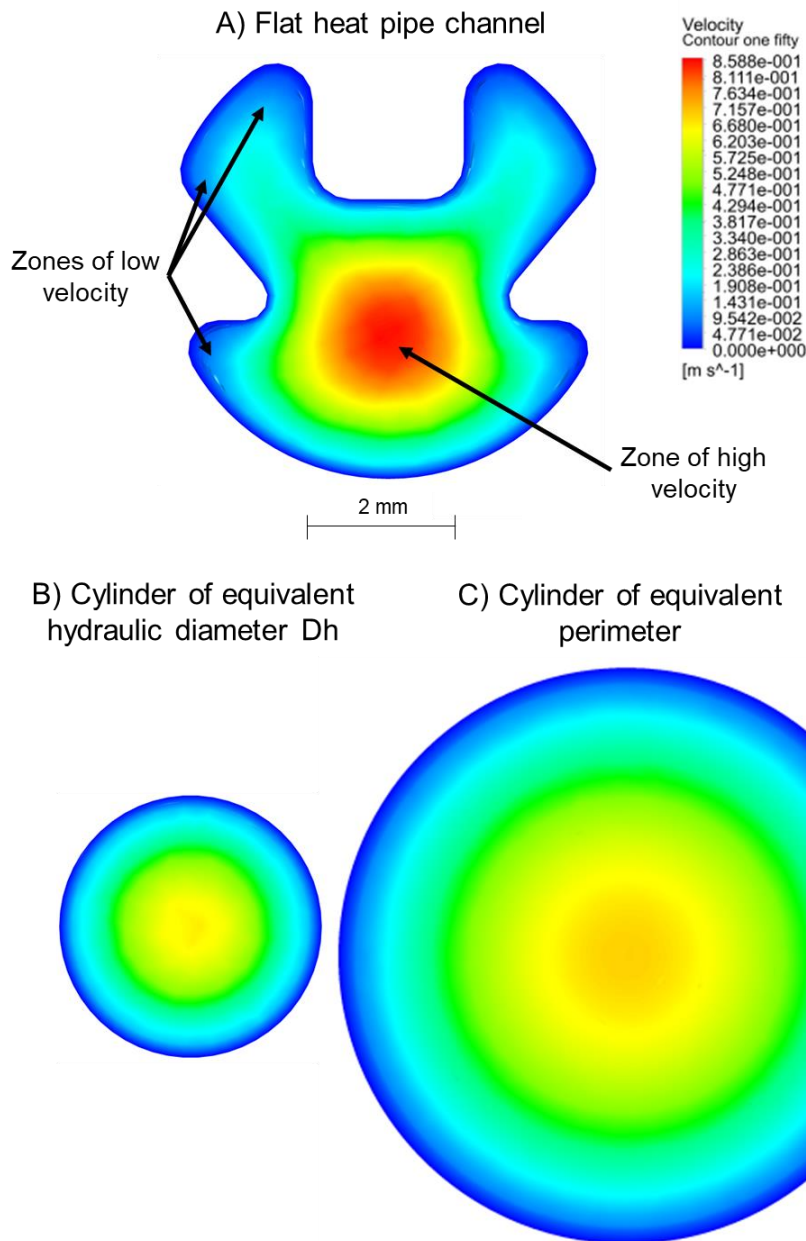


Figure 5-25. Velocity profile of the channels at similar inlet velocity

With a similar steam inlet velocity, it is observed that the velocity profiles for both cylindrical channels are very close. Indeed, with a similar inlet velocity boundary condition, the observed velocity profile only depends on the shape of the channel. For cylindrical channels, the velocity profile is axisymmetric and evenly distributed with higher vapour velocities at the centre of the channel and lower velocities near the wall. The maximum velocities at the centre of the cylinders are in the range of 0.7 m/s. The velocity profile in the channel of the multi-channel flat heat pipe is very different from that of the cylindrical heat pipe. Once the flow is developed, a zone of high vapour velocity up to 0.85 m/s is forming in the centre, away from the walls. In the corners of the channels, zones of low vapour velocity can be observed. These zones are significantly larger than in the cylindrical channel. It is therefore concluded that, under similar



inlet velocity, the shape of the channel generates higher velocity gradients in its cross-section compared to cylindrical channels. A high velocity vapour stream is generated in the core of the channel whereas, near the corners, larger zones of low velocities are formed.

- **Similar mass flow rate:**

Even if a constant velocity boundary condition permits only the impact of the channel's shape on the flow development to be studied, it seems relevant to compare the three channels with a similar mass flow rate. Indeed, in heat pipes, the mass flow rate of the rising vapour is linked to the heat transfer rate. Hence, if the heat pipe channel was replaced with another shape, the mass flow rate of the rising vapour would be similar at constant heat transfer rate. Then, depending on the cross-section of the channel, the vapour velocity changes significantly. The velocity contours of the three channels conveying a similar vapour mass flow rate are shown in Figure 5-26.

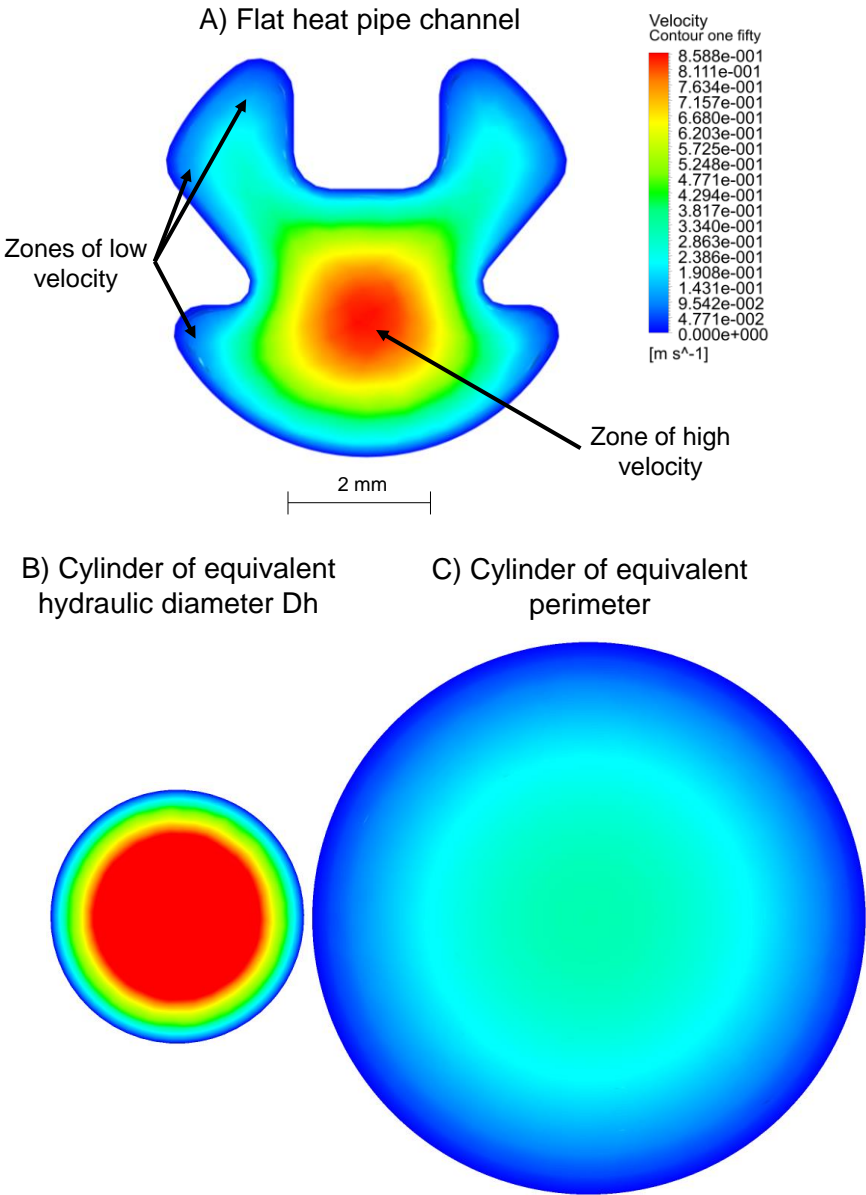


Figure 5-26. Velocity profiles of the channels at similar inlet mass flow rate

Under a similar mass transfer rate, the vapour velocity varies proportionally to the cross-sectional area of the channel. Figure 5-26 shows that, under a similar heat transfer rate (and therefore mass flow rate), the vapour velocity in the multi-channel flat heat pipe is very different from both cylindrical channels. The cylindrical channel with equivalent hydraulic diameter presents a much lower flow passage which results into high vapour velocities. On the contrary, the cylinder with an equivalent perimeter has a larger flow passage which generates low vapour velocities in the channel. In the multi-channel flat heat pipe channel, the velocity profile reveals that, in the middle of the channel, the vapour velocity is high but it remains lower than that of the channel with equivalent hydraulic diameter. In the corners of the flat heat pipe's channel, the zones of low vapour velocity are much larger than in the cylinder with equivalent hydraulic diameter. Therefore, under a similar vapour mass flow rate, using the flat heat pipe's channel shape generates vapour velocities in the middle of the channel which are much larger than that of a cylinder with an equivalent perimeter. However, in the corners, zones of vapour velocities much lower than that of a channel with an equivalent hydraulic diameter are created. In terms of heat transfer inside the multi-channel flat heat pipe, the vapour velocity near the wall has a direct impact on the convection heat transfer, two-phase flow interactions between the rising vapour and the condensate returning to the evaporator, and the filmwise condensation pattern.

### **5.3.5 Boiling flow investigation**

In this section, the influence of the multi-channel flat heat pipe's channel shape on the boiling pattern is studied. A liquid working fluid at saturation is simulated inside the heat pipe channel and the Volume of Fluid model is used to study the generation and movement of bubbles inside the liquid pool. Both R134a and water were used for these simulations.

#### *5.3.5.1 Simulation settings*

The included Lee model of ANSYS provided in the Volume of Fluid (VOF) approach is used to study the boiling pattern in the multi-channel flat heat pipe channel. To simulate the static liquid pool, a velocity of 0 m/s is implemented at the liquid inlet so that the fluid and bubble motion observed in the simulation is caused by buoyancy only. To start with, R134a was used as a working fluid as this is the working fluid used in the multi-channel flat heat pipe. A saturation temperature and initial temperature of 303.7 K was used, and the simulation was initialized at 705,793 Pa which is the saturation pressure of R134a at 303.7 K. A flat heat pipe heat transfer rate of 1000 W was chosen, which corresponds to a heat transfer rate of 23 W for a single channel. This is converted to a wall heat flux of 10 397 W/m<sup>2</sup> which was implemented on the wall of the channel. After using R134a for the simulation, it was observed that the vapour bubbles were relatively small. In this regard, water has also been implemented at a saturation temperature of 373.15 K under ambient pressure and larger bubbles were observed.

### 5.3.5.2 Results

- **R134a:**

The 3D simulation of the multi-channel flat heat pipe channel is shown in Figure 5-27 with temperature contours in the solid material and the volume fraction contours on the liquid surface.

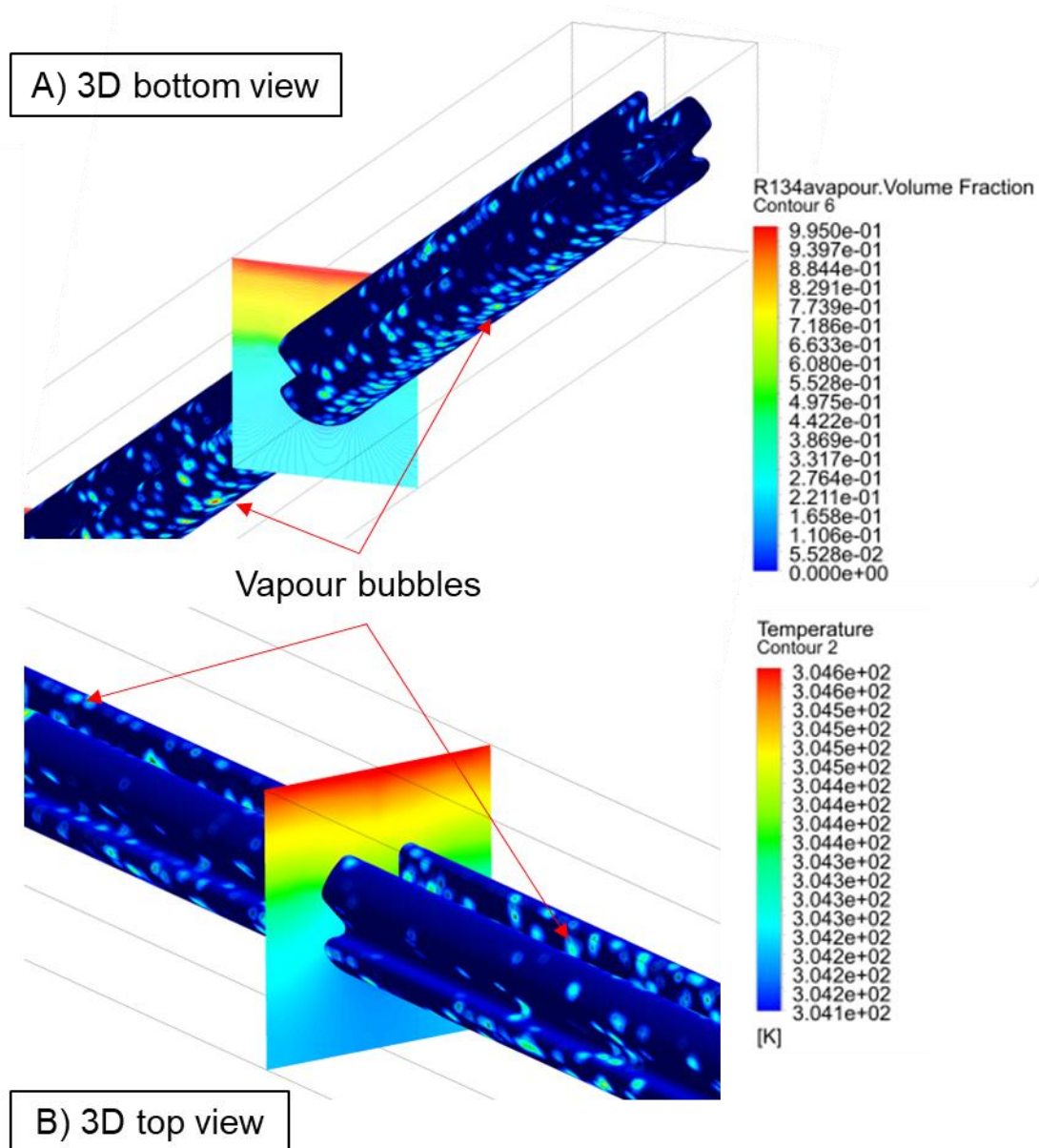


Figure 5-27. R134a boiling pattern in the multi-channel flat heat pipe channel – 3D view

From Figure 5-27 it is observed that, according to this simulation, even if the solid temperature is higher at the top of the channel, the number of vapour bubbles is not higher than at the bottom of the channel. The temperature of the solid which varies within 0.5°C does not seem to have a major impact on the bubble's location. The R134a bubbles are relatively small at such heat a flux and do not exceed 0.5mm in diameter. Surprisingly, the number of bubbles seems to be higher at the bottom of the channel near the colder part of the wall. This can be

better visualized in Figure 5-28 which shows the cross-section of the channel and the vapour volume fraction of R134a.

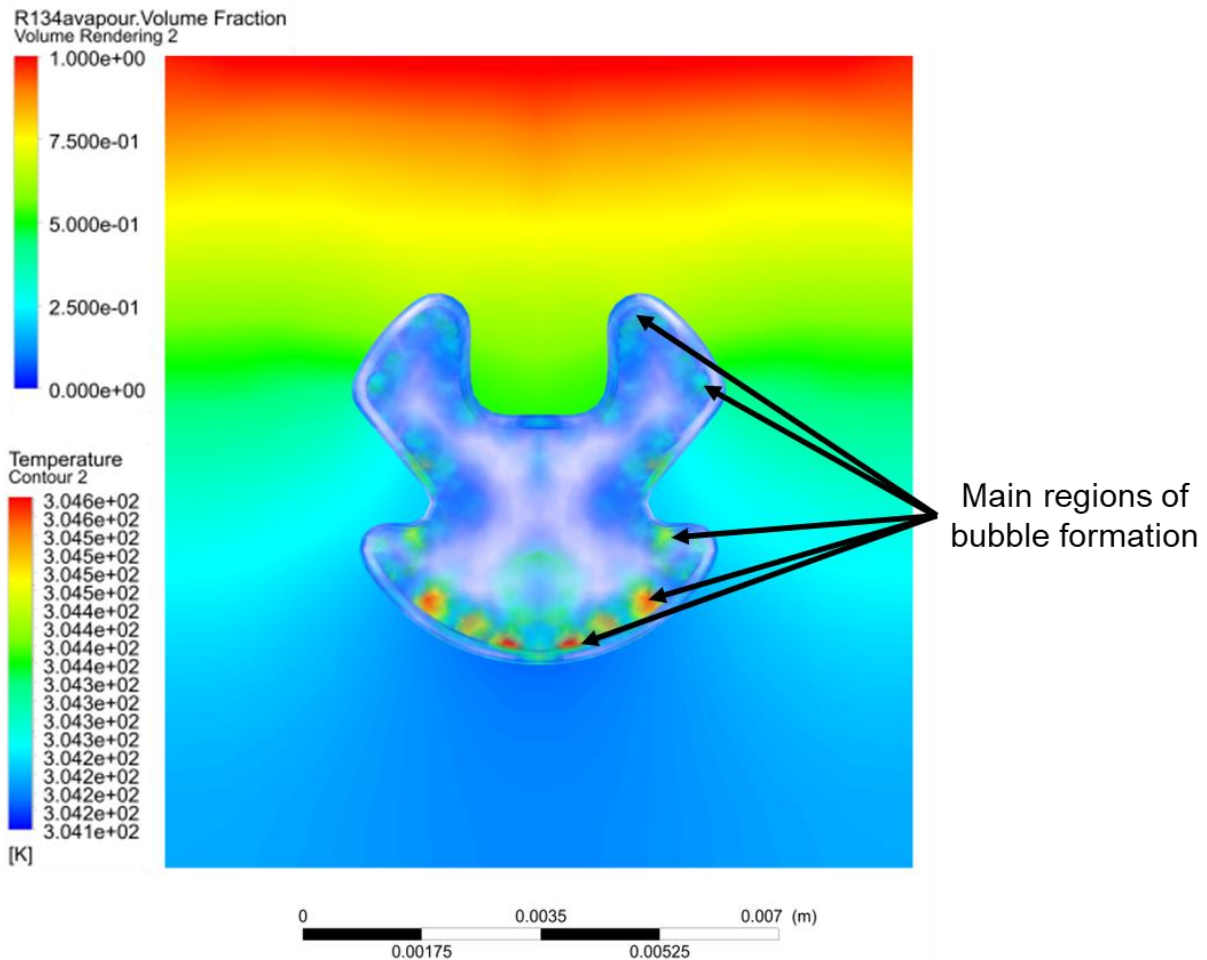


Figure 5-28. R134a boiling pattern in the multi-channel flat heat pipe channel – Cross-section view

It can be noticed in Figure 5-28 that, in the multi-channel flat heat pipe, the R134a vapour bubbles form near the wall by heterogeneous nucleation. Bubbles can be seen in the corners of the channels and at the bottom. Surprisingly, the current simulation shows a higher concentration of vapour bubbles at the bottom of the channel where red points can be seen. In the core of the channel, no bubbles form by the homogeneous nucleation process. The concentration of the bubbles in the indicated zones of the above simulation is not related to the temperature profile of the solid and fluid. Indeed, as indicated in Figure 5-29, the temperature of the liquid in the channel remains very homogeneous despite the conduction profile of the solid.

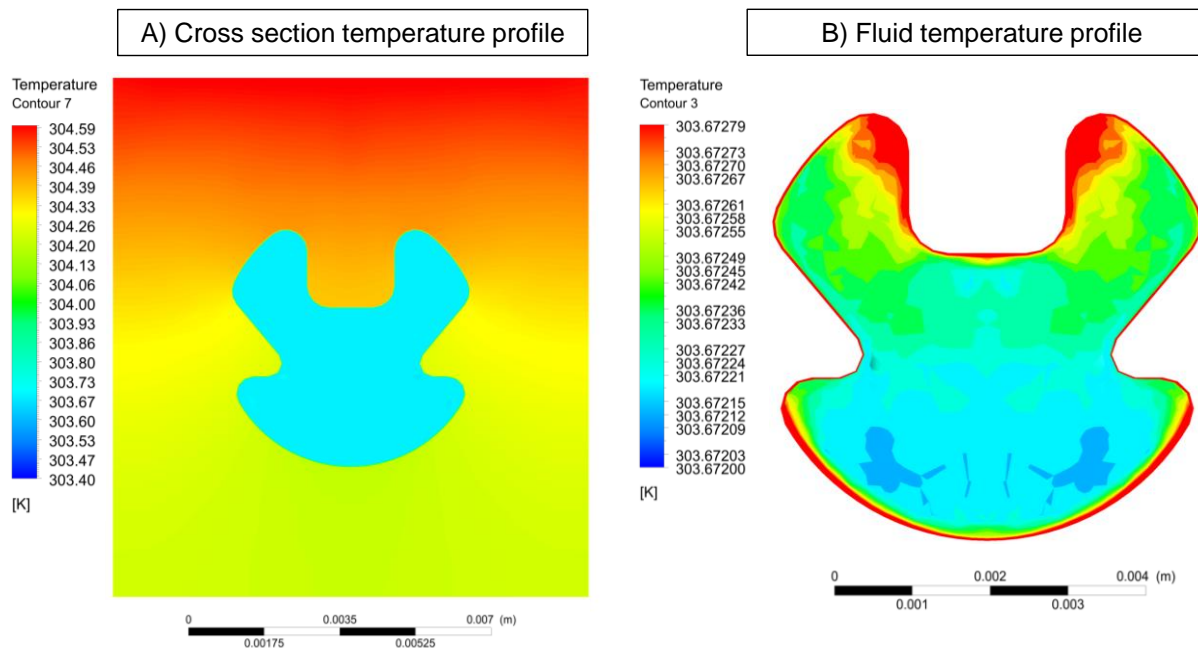


Figure 5-29. Solid and liquid temperature profile in the multi-channel flat heat pipe channel

On the left-hand side of Figure 5-29 it is observed that the temperature gradient in the solid domain is much larger than that of the liquid domain as the liquid domain shows a uniform colour. To be able to detect temperature differences in the liquid pool, fine temperature contours had to be made and these are shown on the right-hand side. According to the simulation, even if heat is transferred by conduction from the top of the channel and generates a temperature difference between the top and bottom of the solid up to 0.4 °C, the liquid temperature does not vary more than 0.0008 °C. In agreement with the conduction temperature profile, the liquid domain presents higher temperatures at the top of the profile. Overall, the temperature decreases in the bottom area of the channel. Nevertheless, it can be seen that the corners of the channels exhibit higher temperatures due to the proximity of hot walls, which is expected to favour the growth of vapour bubbles. Yet, in the simulation which uses R134a, the relation between the temperature profile of the channel and the location of vapour bubbles is not obvious. In this regard, a similar simulation was conducted with water.

- **Water.**

The vapour volume fraction in the 3D channel of the multi-channel flat heat pipe is shown in Figure 5-30 when water is used as a working fluid.

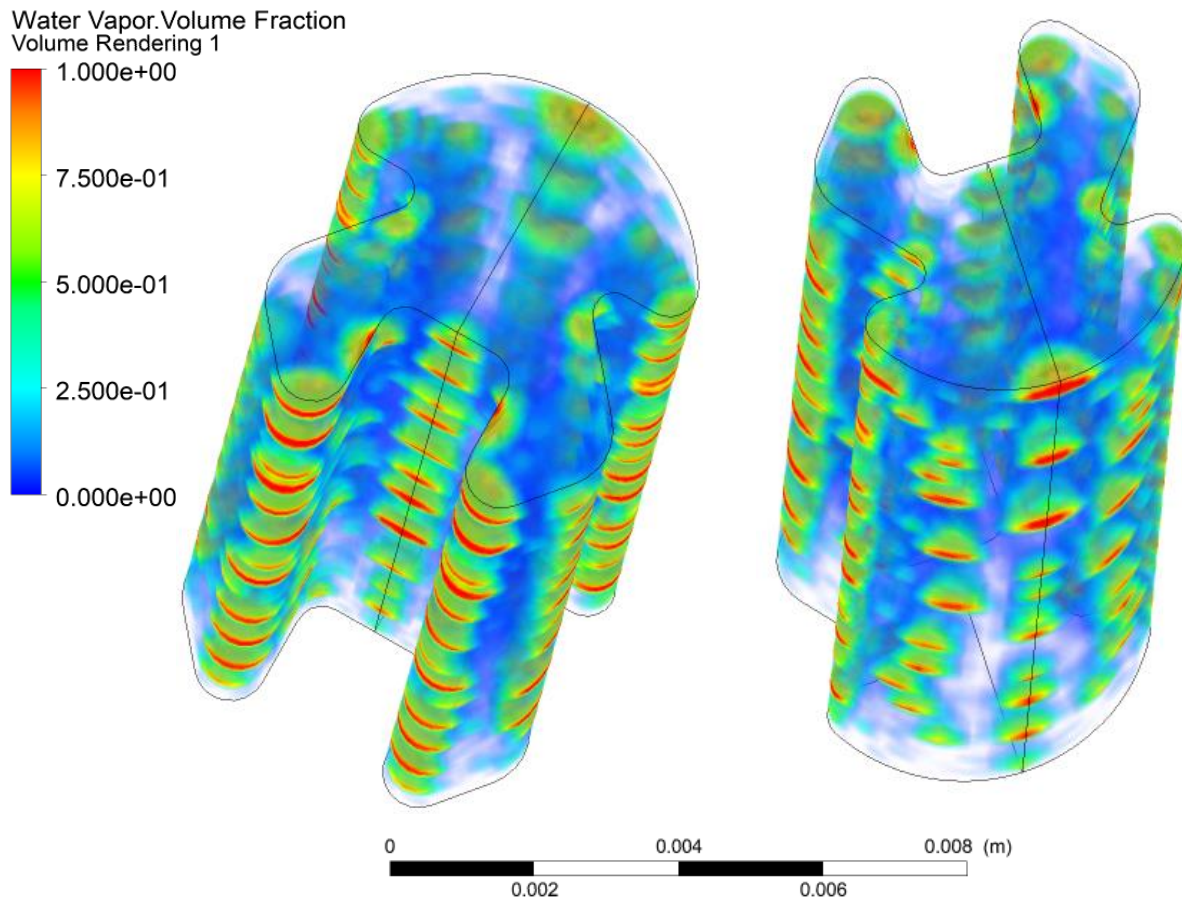


Figure 5-30. Water boiling pattern in the multi-channel flat heat pipe channel – 3D view

When using water instead of R134a, the bubbles' diameter significantly increased and the influence of the channel's shape on the boiling pattern was easier to observe. Two phenomena that were not observed in the simulation with R134a were also noted in the case of water, which are the motion of water bubbles due to the buoyancy and the coalescence of small bubbles. The location of bubbles can be clearly identified in Figure 5-30 and bubbles travelling upwards due to the buoyancy force can be seen. Those bubbles are mainly located in the two top corners of the profile, at the top and bottom of the axis of symmetry of the profile, and at the two bottom corners. Similar to R134a, an illustration of the steam volume fraction was made and permits a better identification of the main bubble locations in the profile. This is presented on the left-hand side of Figure 5-31.

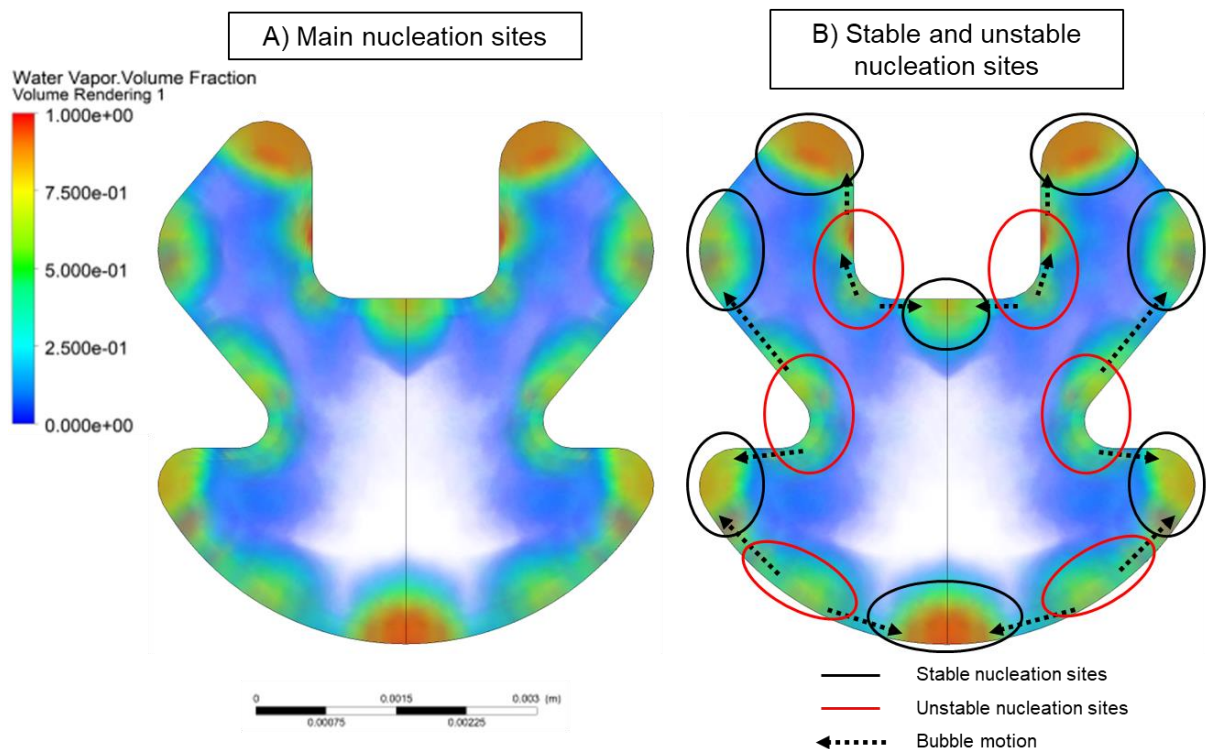


Figure 5-31. Water boiling pattern in the multi-channel flat heat pipe channel – Cross-section view

The vapour volume fraction is displayed on the left-hand side of Figure 5-31, which allows the visualisation of the vapour bubbles in the profile, whereas, on the right-hand side, the stable and unstable nucleation sites are shown. The volume fraction of steam reveals that the bubbles mainly concentrate at the top corners of the channels and at the very bottom of the lower arc. At these locations, the bubbles reach a diameter of 1mm which covers an important portion of the corner's wall. In the other corners situated on each side of the profile, bubbles are also forming and moving. Indeed, the bubbles situated in the corners tend to coalesce with other bubbles, grow, and move along the length of the profile. These locations are designated as “stable nucleation sites” on the right-hand side of Figure 5-31 and are shown in black circles. At these locations, the bubbles form, grow in diameter and remain at a similar location in the channel until the buoyancy force carries them away. In contrast, some “unstable nucleation sites” are observed and shown in red. Bubbles forming in these unstable nucleation sites are rapidly carried by the curvature of the wall to a more stable location. Once departed from the wall, these smaller bubbles coalesce with the bubbles situated in the stable nucleation sites to form larger bubbles which will then move in the stable nucleation site's locations. The observed bubble movement, which characterizes the movement of bubbles from unstable nucleation sites to stable nucleation sites, is described on the right-hand side of Figure 5-31 with black arrows. From a heat transfer point of view, the transition of bubbles from unstable to stable nucleation sites is expected to improve the local pool boiling heat transfer coefficient.

### 5.3.6 Conclusion on the single channel simulations

In this section, local CFD simulations of the multi-channel flat heat pipe channel have been conducted. The impact of the unique channel's shape on the conduction thermal resistance, velocity profile, and pool boiling pattern have been investigated. The flat heat pipe channel has been compared to cylindrical channels with equivalent hydraulic diameter and equivalent perimeter. Even if the conductive thermal resistance of the flat heat pipe channel was calculated to be 0.298 K/W from simulations, which is higher than that of a cylinder with the same hydraulic diameter, the channel's shape provides a higher heat transfer area which decreases the convective thermal resistance. To theoretically estimate the multi-channel heat pipe conduction thermal resistance, a correction factor  $F_{correction} = 0.9112$  is proposed to consider the influence of the channel's shape. From a convective point of view, the flat heat pipe channel shows significant differences in the velocity profile compared to the cylindrical profile. In the cylindrical channel, the velocity profile is more uniform whereas, in the flat heat pipe channel, low velocities are seen in the corners and high velocities in the middle of the channel. This is expected to impact the vapour rising flow at the evaporator section of the heat pipe, the two-phase flow interaction between the vapour and condensate, and the condensation heat transfer coefficient. The simulation of pool boiling in the multi-channel flat heat pipe profile reveals the presence of stable nucleation sites situated in the corners where vapour bubbles coalesce, grow, and rise due to the buoyancy force. Bubbles forming in unstable nucleation sites near the wall are carried along the profile of the channel until they reach stable nucleation sites where they coalesce to form larger bubbles. This transition of bubbles from unstable to stable nucleation sites is expected to impact the local pool boiling heat transfer coefficient.



---

## Chapter 6 - Experimental results and discussion

---

### 6.1 Three-leg multi-channel heat pipe apparatus

#### 6.1.1 Impact of the heat transfer rate on the thermal performance of the three-leg multi-channel heat pipe

To study the two-phase heat transfer taking place in a multi-channel heat pipe, the thermal performance of a three-leg heat pipe was investigated in detail. Information on the temperature distribution of a multi-channel heat pipe were collected by monitoring the temperature of each leg and collector independently. These valuable temperature measurements were used for the development of numerical (CFD) models and theoretical models for multi-channel heat pipes. The performance of the three-leg heat pipe was tested for heat transfer rates in the range 0-110 W so that the heat transfer rate in each parallel channel is similar to that of the multi-channel flat heat pipe used for PV/T application. The cooling water flow rate was fixed to 1L/min and a total of 78 experiments were done to improve the result's accuracy.

##### 6.1.1.1 *Boiling thermal resistance*

In Figure 6-1 are shown the local pool boiling and falling film boiling heat transfer coefficients measured at the evaporator of the three-leg heat pipe. The bottom collector pool boiling heat transfer coefficient was measured with the temperature difference between the bottom collector and the adiabatic section and is shown with circular markers. The legs' pool boiling heat transfer coefficient was obtained from the thermocouples at the bottom of the legs and is displayed with square markers. Finally, the falling film heat transfer coefficient was obtained from the thermocouples situated on each leg at the top of the evaporator and is shown with triangular markers. The locally measured boiling heat transfer coefficients are plotted in terms of boiling heat flux.

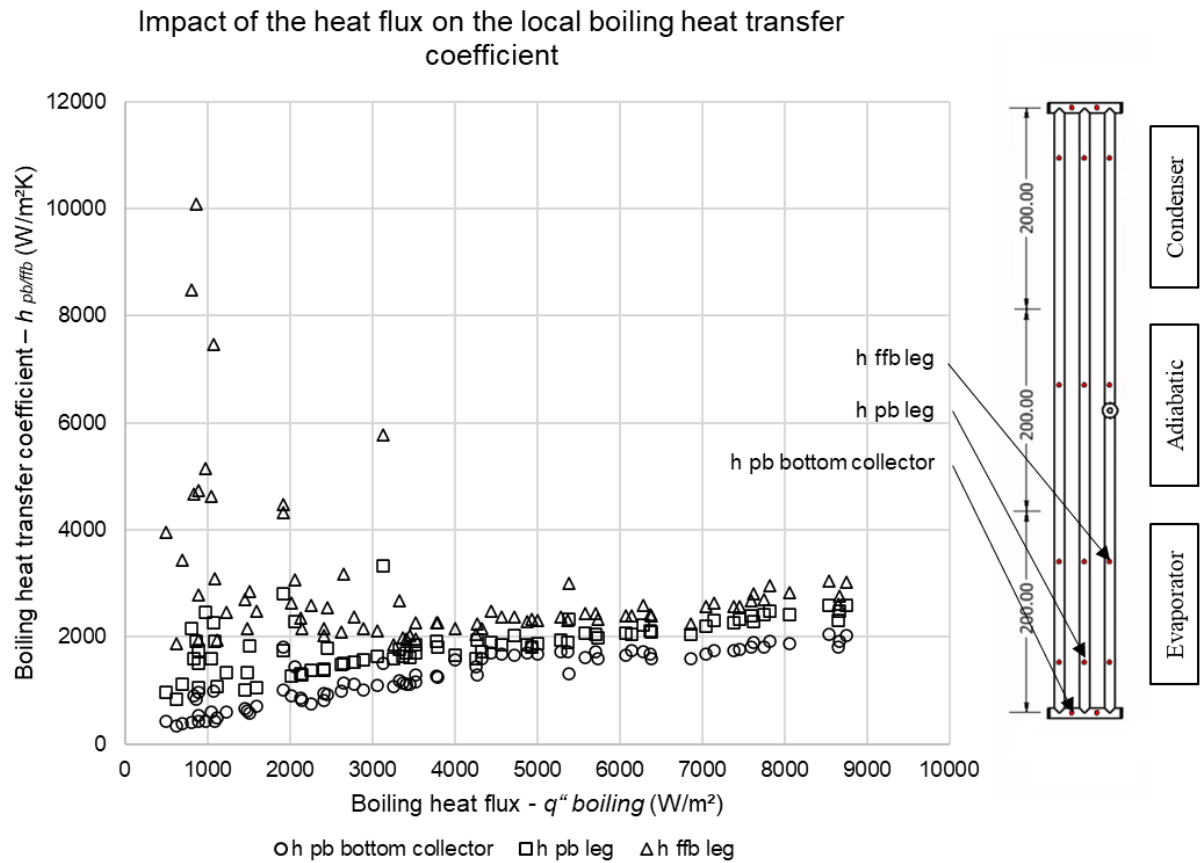


Figure 6-1. Impact of the heat flux on the local boiling heat transfer coefficients of the three-leg heat pipe

Figure 6-1 reveals that, at low heat fluxes below  $4000 W/m^2$ , significant differences can be identified in the local boiling heat transfer coefficients whereas, at higher heat flux, the three local heat transfer coefficients are close and follow a similar trend. At the evaporator of the three-leg heat pipe, the temperature is slightly higher at the bottom. Indeed, the pool boiling heat transfer coefficient of the bottom collector is slightly lower than that of the legs. At low heat flux, high falling film boiling heat transfer coefficients were measured and could reach values higher than  $6000 W/m^2K$ . Even if the scattering of the data is higher at low heat transfer rates, the falling film heat transfer coefficient measured from the top of the legs is slightly higher than the pool boiling heat transfer coefficients measured below. Yet, similar trends are observed and the slight difference between the falling film boiling and pool boiling heat transfer coefficients measured from the legs could be caused by the higher position of the thermocouples and the proximity with the adiabatic section. At higher heat flux, the similar trends may indicate that pool boiling only occurred in the three-leg heat pipe evaporator. Overall, the measured pool boiling heat transfer coefficient increases linearly from  $1000 W/m^2K$  at heat transfer rates near  $10 W$  to values around  $2500 W/m^2K$  at  $110W$ .

The corresponding local pool boiling and falling film boiling resistances measured from the three-leg heat pipe evaporator are presented in Figure 6-2.

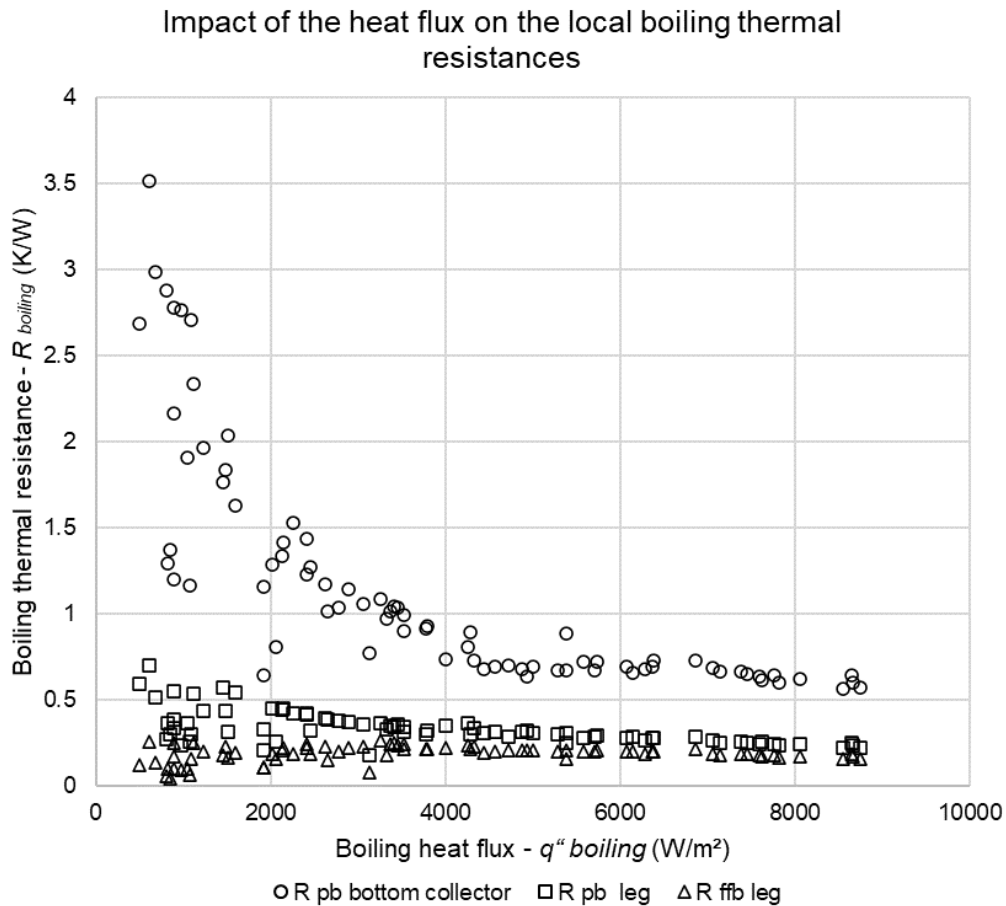


Figure 6-2. Impact of the heat flux on the local boiling thermal resistances of the three-leg heat pipe

Figure 6-2 clearly shows that the local thermal resistances measured from the legs are very close. Even if falling film boiling was expected to take place at the top of the evaporator, the experimental results seem to indicate that the heat transfer mechanism was similar along the whole length of the legs. This could be due to an inaccurate charging of the heat pipe which was tedious due to the very small amount of fluid injected. In opposition, the thermal resistance of the bottom collector is significantly higher than that of the legs. This seems to indicate that the pool boiling pattern is different in the horizontal collector than inside a vertical leg. In particular, at low heat flux, the measured pool boiling thermal resistance of the bottom collector is higher than 3 K/W whereas, for the legs, the pool boiling resistance is not higher than 0.5 K/W. With an increase of the heat transfer rate, the bubble activity increases which increases the heat transfer coefficient and decreases the pool boiling thermal resistance. As a result, the bottom collector pool boiling thermal resistance decreases sharply and is three times smaller at a heat flux of 4000  $W/m^2$  than at very small heat flux. At higher heat flux, the thermal resistance difference between the legs and bottom collector is still noticeable. At a maximum heat transfer rate of 110 W ( $\sim 9000 W/m^2$ ), the bottom collector pool boiling thermal resistance is down to 0.6 K/W whereas the leg pool boiling thermal resistance is 0.2 K/W. The total boiling thermal resistance of the three-leg heat pipe is presented in Figure 6-3.

Impact of the heat flux on the total boiling thermal resistance of the three-leg heat pipe

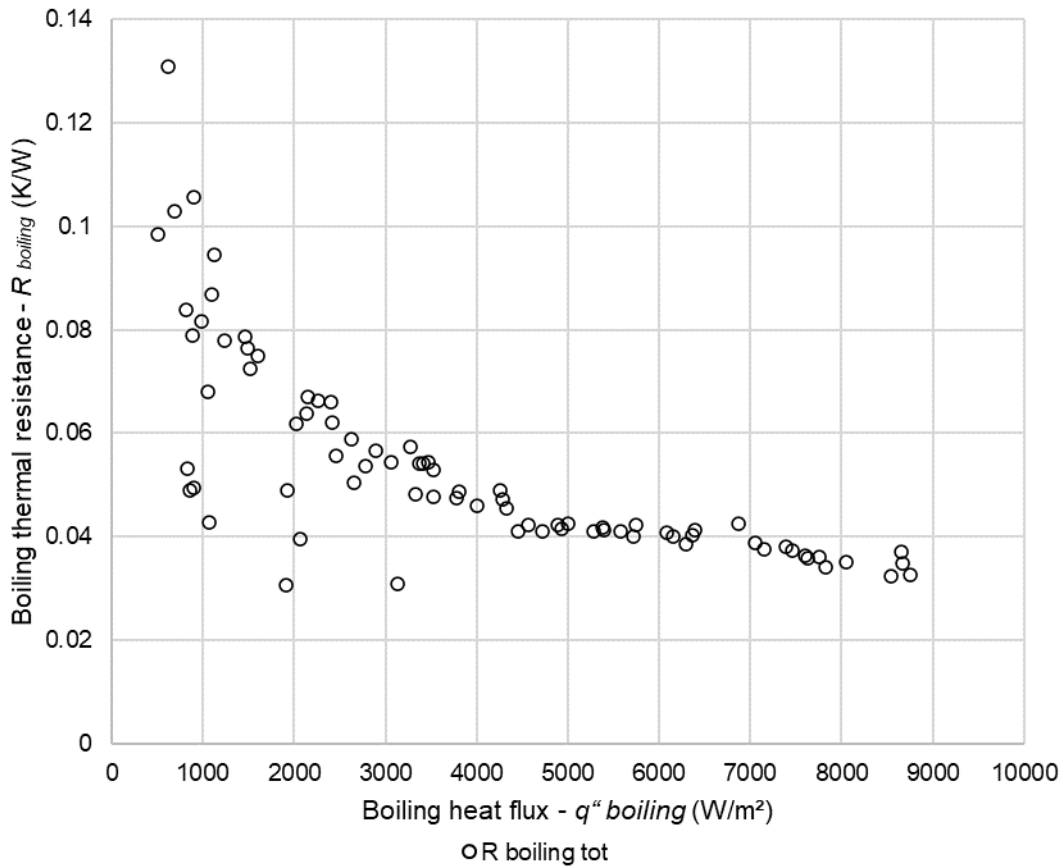


Figure 6-3. Impact of the heat flux on the total boiling thermal resistance of the three-leg heat pipe

With the simultaneous heat transfer mechanisms taking place at the bottom collector and parallel legs, the boiling thermal resistance of the three-leg heat pipe is relatively low and decreases with an increase of the heat transfer rates. At low heat flux, the three-leg heat pipe boiling thermal resistance is 0.12 K/W but decreases rapidly below 0.08 K/W at 1500 W/m<sup>2</sup>. At a heat flux of 5000 W/m<sup>2</sup> which corresponds to a heat transfer rate about 55 W, the three-leg heat pipe boiling thermal resistance reaches 0.04 K/W and, at a maximum heat flux, reaches a minimum value of 0.035 K/W.

#### 6.1.1.2 Condensation thermal resistance

In Figure 6-4 is shown the local condensation heat transfer coefficients in each leg and at the top collector for various heat flux. The condensation heat transfer coefficient for a single leg is displayed with diamond markers whereas the top collector condensation heat transfer coefficient is displayed with cross markers.

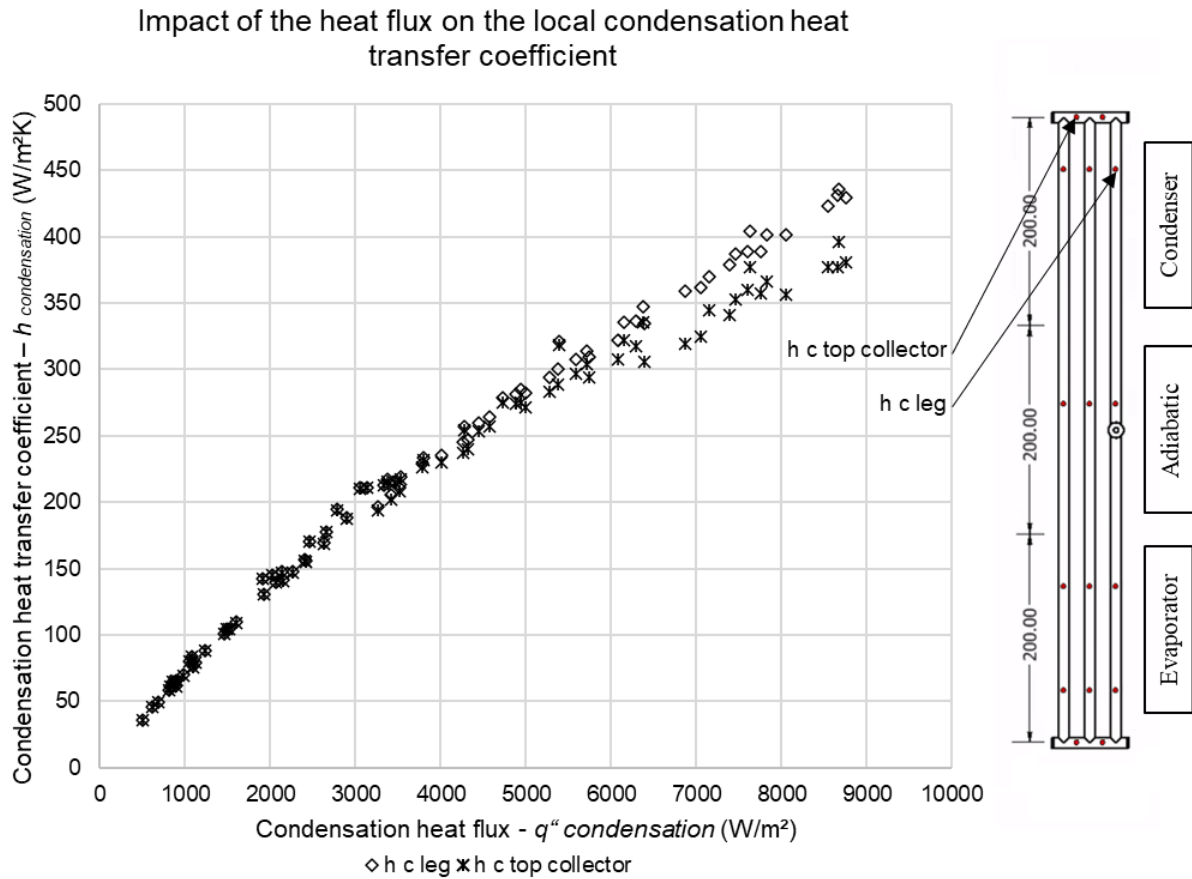


Figure 6-4. Impact of the heat flux on the local condensation heat transfer coefficients of the three-leg heat pipe

Figure 6-4 shows that the condensation heat transfer coefficients in each parallel leg and in the top collector are very similar. In the investigated range of heat fluxes up to  $9000 \text{ W/m}^2$ , the local condensation heat transfer coefficient increases with an increase of the heat transfer rate. Below a local heat flux of  $6000 \text{ W/m}^2$ , the local condensation heat transfer coefficient at the top collector and parallel legs is the same and the experimental data points merge. However, at heat fluxes higher than  $6000 \text{ W/m}^2$ , the two series can be distinguished and the condensation heat transfer coefficient in the top collector becomes slightly higher than that of the legs. Nevertheless, the difference is small. At low heat flux, the local condensation heat transfer coefficient is small and lower than  $50 \text{ W/m}^2\text{K}$ . The heat transfer coefficient increases with an increase of the heat transfer rate, and, at a heat transfer rate of  $55 \text{ W}$ , the heat transfer coefficient is close to  $300 \text{ W/m}^2\text{K}$ . At a heat transfer rate of  $110 \text{ W}$  ( $\sim 9000 \text{ W/m}^2$ ), the local condensation heat transfer coefficient is maximum and up to  $400 \text{ W/m}^2\text{K}$ .

The corresponding local condensation thermal resistances for a single leg and for the top collector are presented in Figure 6-5.

### Impact of the heat flux on the local condensation thermal resistances

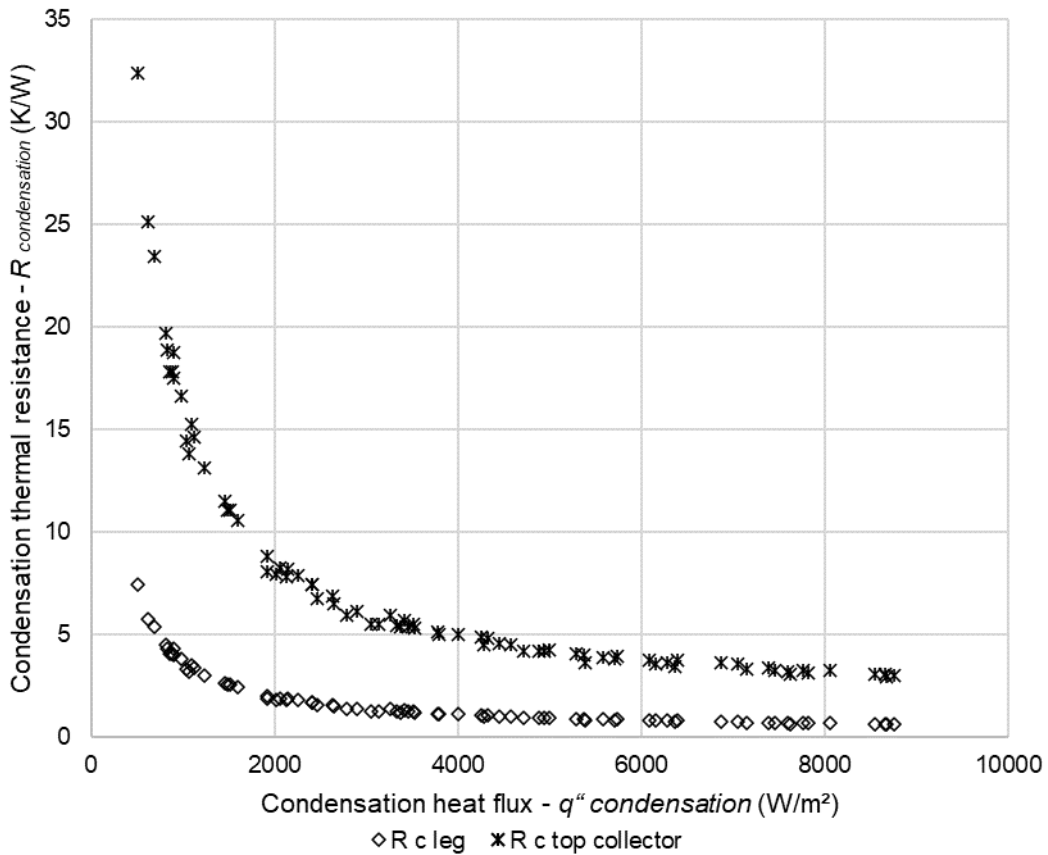


Figure 6-5. Impact of the heat flux on the local condensation thermal resistances of the three-leg heat pipe

Even if the local condensation heat transfer coefficient was shown to be similar in the parallel legs and in the top collector, with the difference of heat transfer area, the thermal resistance of a single leg logically becomes less than that of the top collector. Yet, the two thermal resistances exhibit a similar trend. The condensation thermal resistances decrease sharply with an increase of the heat flux and progressively stabilizes. At low heat flux, the leg condensation heat transfer coefficient is up to 7.4 K/W and decreases down to 1.8 K/W at 2000  $W/m^2$ . A minimum value of 0.6 K/W was reached at high heat flux for the leg condensation heat transfer coefficient. As for the top collector, the local condensation heat transfer coefficient reaches values up to 30 K/W at very low heat flux but decreases rapidly below 8 K/W at 2000  $W/m^2$ . At a maximum heat flux, the local condensation heat transfer coefficient of the top collector was 3 K/W.

The total condensation thermal resistance of the three-leg heat pipe is presented in Figure 6-6.

Impact of the heat flux on the total condensation thermal resistance of the three-leg heat pipe

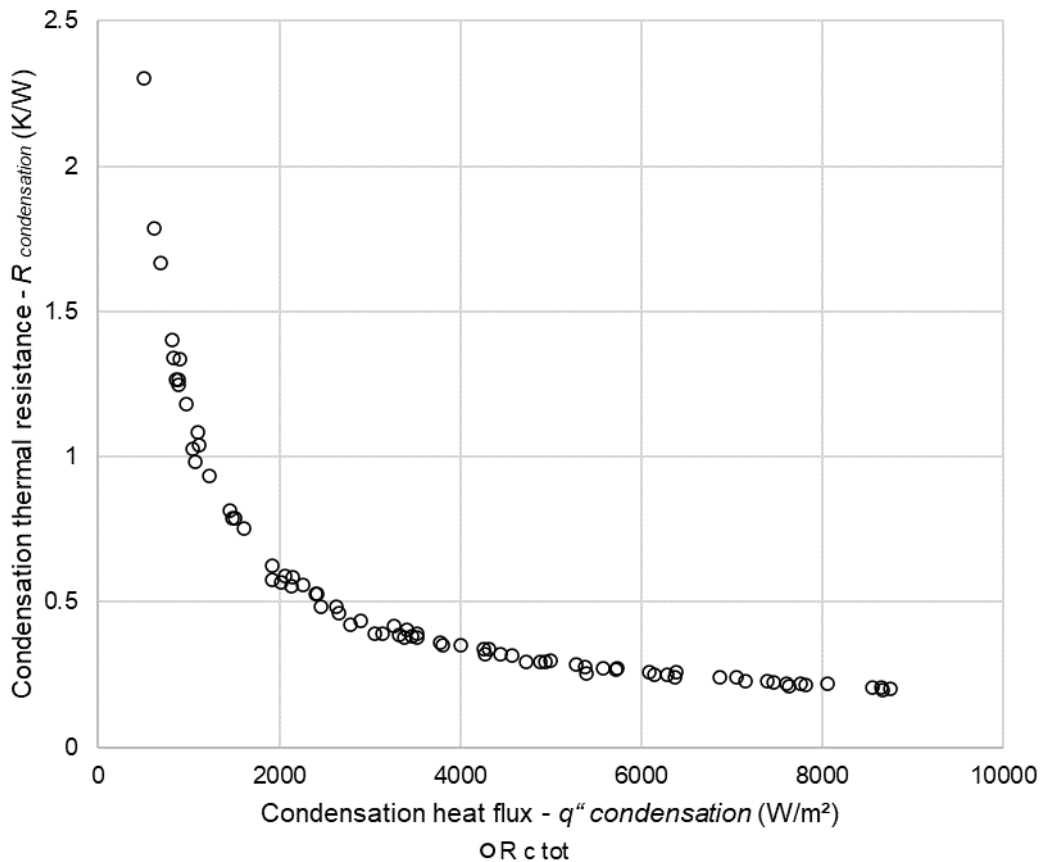


Figure 6-6. Impact of the heat flux on the total condensation thermal resistance of the three-leg heat pipe

Like the local thermal resistances, the total condensation thermal resistance of the three-leg heat pipe shows a similar trend and decreases with an increase of the heat flux. With the parallel heat transfer mechanisms taking place at the legs and top collector, the condenser thermal resistance of the three-leg heat pipe is estimated about 2 K/W at very low heat transfer rates. At a heat flux of 2400 W/m<sup>2</sup>, this thermal resistance has decreased to a value close to 0.5 K/W. Progressively, the condensation thermal resistance becomes smaller, and, at high heat flux, the three-leg heat pipe condenser thermal resistance is close to 0.2 K/W.

### 6.1.1.3 Total thermal resistance

In the previous section, it was observed that the condensation thermal resistance of the three-leg heat pipe was much higher than the boiling thermal resistance. At a maximum heat transfer rate of 110 W, the boiling thermal resistance of the three-leg heat pipe is 0.035 K/W whereas the condensation thermal resistance is 0.2 K/W. Indeed, the condensation thermal resistance is the main contributor to the total three-leg heat pipe thermal resistance, and this is shown in Figure 6-7.

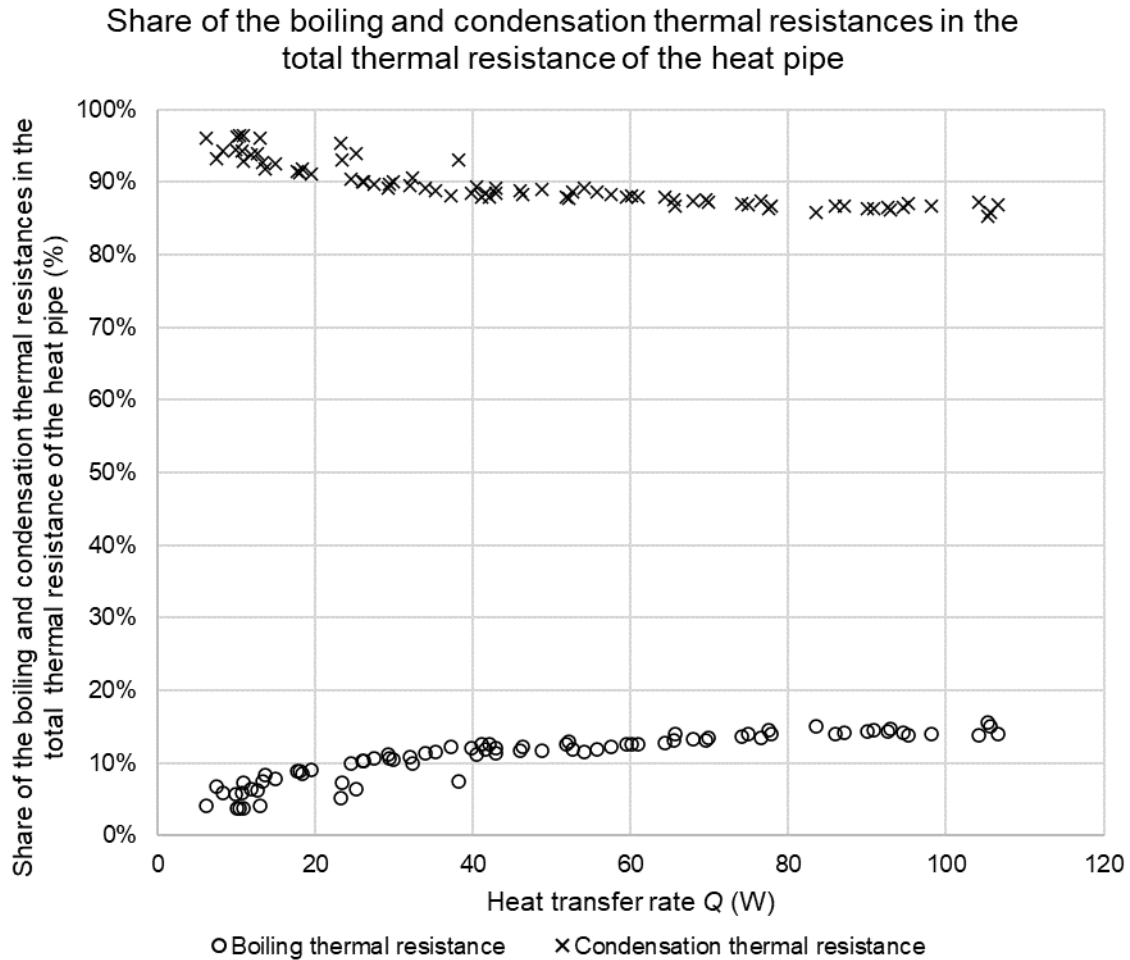


Figure 6-7. Share of the boiling and condensation thermal resistances in the total thermal resistance of the three-leg heat pipe

Despite the significant decrease of the condensation thermal resistance with an increase in the heat transfer rate, Figure 6-7 reveals that the condensation thermal resistance contributes to 85-90% of the total thermal resistance of the three-leg heat pipe. As a comparison, the boiling thermal resistance contributes to 15% maximum to the total thermal resistance of the three-leg heat pipe.

When studying the overall three-leg heat pipe thermal resistance, the conductive, boiling, and condensation thermal resistances are placed in series. In Figure 6-8 is shown the total thermal resistance of the three-leg heat pipe.



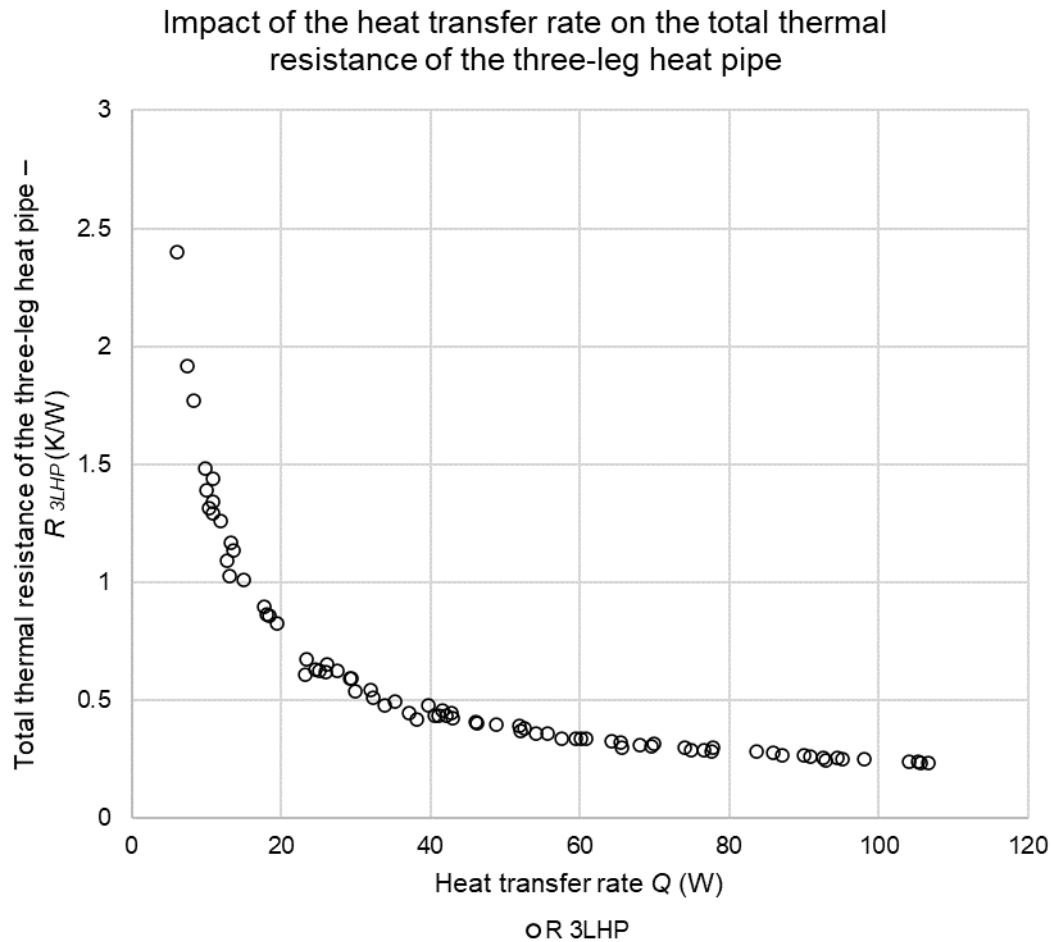


Figure 6-8. Impact of the heat transfer rate on the total thermal resistance of the three-leg heat pipe

As the condensation thermal resistance is the main contributor to the total thermal resistance of the heat pipe, the trend of the total thermal resistance of the three-leg heat pipe is similar. While increasing the heat transfer rate, the three-leg heat pipe thermal resistance decreases sharply from 10 W to 40 W. Indeed, at a heat transfer of 10 W, the total thermal resistance is as high as 2.5 K/W whereas it is five times lower and down to 0.5 K/W at a heat transfer rate of 40 W. At higher heat transfer rates, the three-leg heat pipe thermal resistance keeps decreasing and reaches a value of 0.24 K/W at 110 W.

### 6.1.2 Three-leg heat pipe temperature profile for thermal resistance model validation

In this section, the three-leg heat pipe temperature profile is analysed and compared to the proposed thermal resistance model. This aims at detecting agreements and disagreements between the proposed model and the experiments. The vertical temperature differences at different level of the three-leg heat pipe are first studied. Then, the horizontal temperature differences between the three parallel legs are investigated.

### 6.1.2.1 Temperature difference at different levels of the three-leg heat pipe – Vertical validation

In Figure 6-9 is shown the temperature of the three-leg heat pipe at different levels for various heat transfer rates.

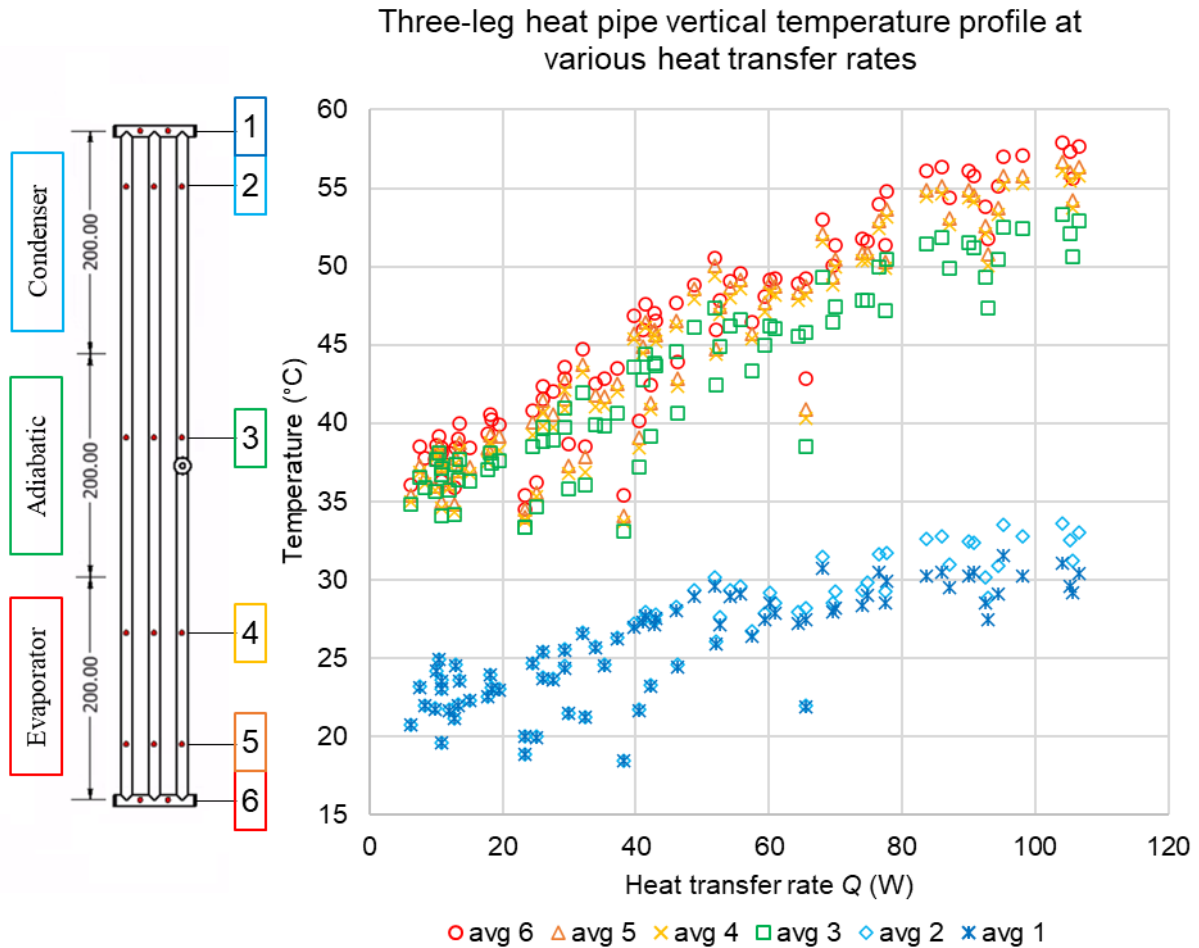


Figure 6-9. Average temperature of the three-leg heat pipe at different level for various heat transfer rates – Vertical validation

In Figure 6-9, the temperature measurement taken from the bottom collector (6) are shown with red and circular markers. The leg averaged temperature from the bottom section of the evaporator (5) is displayed with triangular orange markers whereas the leg averaged temperature from the top of the evaporator (4) is shown with yellow crosses. The temperature of the adiabatic section (3) is represented by square green markers. Finally, the leg averaged temperature of the condenser (2) is displayed with diamond blue markers whilst the temperature of the top collector (1) is shown with dark blue crosses. Obviously, the temperature of all the sections of the three-leg heat pipe increases with an increase of the heat transfer rate. More interestingly, the temperature difference between each level of the heat pipe is of interest. For instance, the temperature difference between the level 4 and 5 of the parallel legs is small and constant for all heat transfer rates. However, the temperature

difference between the legs and the top collector at the condenser (level 2 and 1) seems to increase with the heat transfer rate. To better visualise the temperature difference between each level of the three-leg heat pipe, Figure 6-10 displays the temperature difference between each consecutive level with different series.

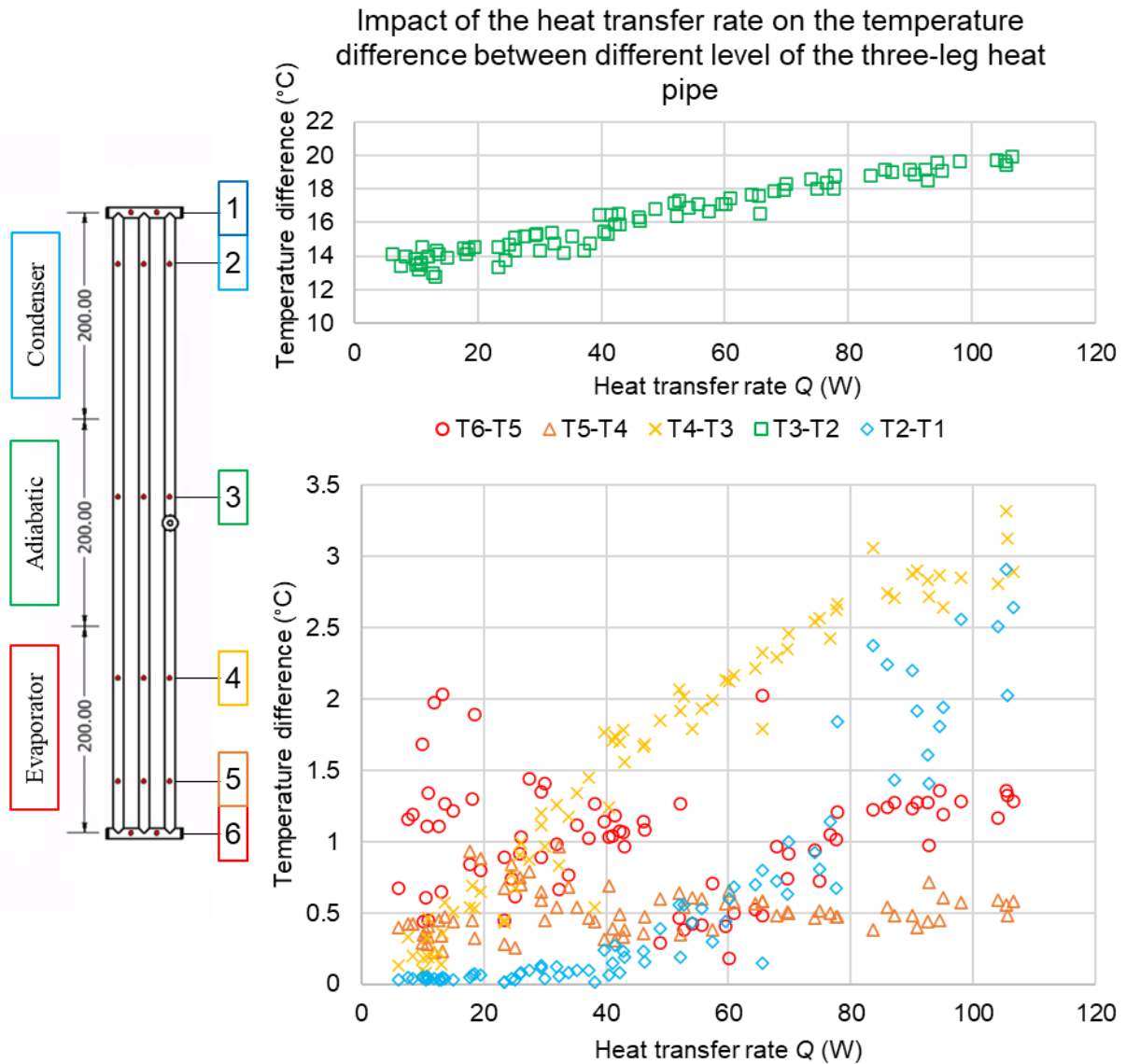


Figure 6-10. Impact of the heat transfer rate on the temperature difference between different levels of the three-leg heat pipe – Vertical validation

Starting from the evaporator section of the three-leg heat pipe, Figure 6-10 reveals that the temperature difference between the bottom collector (level 6) and the bottom of the legs (5) is relatively constant and mainly varies between 0.5°C and 1.5°C. This shows that there is no thermal resistance between the bottom collector and bottom section of the legs that varies with the heat transfer rate. The temperature difference observed is expected to be due to the difference of pool boiling heat transfer coefficient which is slightly lower for the bottom collector than in the legs. This could indicate that it is relevant to consider a different pool boiling pattern

and pool boiling heat transfer coefficient at the channels and at the bottom collector of a multi-channel heat pipe. Between the evaporator top and bottom sections of the parallel legs (level 5 and level 4), the difference of temperature is very similar for all heat transfer rates and equals  $0.5^{\circ}\text{C}$ . This is interpreted as the proof that the heat transfer mechanism taking place at the top and bottom of the legs was the same during the conducted three-leg heat pipe experiments. This constant and small temperature difference between the top and bottom of the legs is likely to be generated by the axial conduction along the heat pipe legs or by the water condensing outside of the three-leg evaporator. Regarding the validation of the three-leg model, the temperature profile of the three-leg heat pipe evaporator seems to indicate that the bottom collector should be treated differently than the parallel channels. Different pool boiling heat transfer coefficients can be expected between the channels and the bottom collector. Yet, between the top and bottom sections of the parallel legs, the temperature difference is small and can be considered uniform if the filling ratio implies that a similar boiling mechanism takes place. Finally, the evaporator temperature can be a few degrees higher ( $\sim 1.5^{\circ}\text{C}$ ) at the bottom than at the top. However, this could be due to the condensation of water vapour outside of the three-leg heat pipe legs and may be different for other experiments. To conclude, for the modelling of the evaporator, the legs temperature can be considered uniform on a vertical direction. For the bottom collector, a different pool boiling mechanism can be expected and a different correlation should be used.

The temperature difference between the evaporator section and the adiabatic section (level 4 and level 3) logically increases with an increase of the heat transfer rate. This reveals the existence of a thermal resistance between level 4 and level 3 of the three-leg heat pipe which varies with the heat transfer rate. Obviously, this thermal resistance is the pool boiling thermal resistance. A similar observation can be made between the temperature of the adiabatic section (level 3) and the temperature of the condenser (level 2) which shows the existence of a condensation thermal resistance which varies with the heat transfer rate. If those two series have lower interest, they have the merit of revealing how the temperature profile of the three-leg heat pipe can help detecting the presence of a two-phase thermal resistance which should be considered in the theoretical model.

The most interesting observation made from Figure 6-10 is the temperature difference between the parallel legs and the top collector at the condenser section. Indeed, it is clearly shown that the temperature difference between the parallel legs and the top collector increases with the heat transfer rate. This means that the measured temperature difference between the top collector and the parallel legs is caused by a two-phase phenomenon. Several assumptions explaining this temperature difference can be made. At first, inside the vertical legs, the condensate flows down to the evaporator which implies a constant removal of the condensate

near the wall. In addition, the shear stress at the interface between the condensate and rising vapour can generate Kelvin-Helmholtz instabilities which could increase the falling film turbulence and thus, improve the local condensation heat transfer coefficient. As a comparison, the vapour velocity in the top collector is expected to be lower and the condensate to accumulate due to the horizontal orientation of the collector. As such, when increasing the heat transfer rate and mass transfer rate, these phenomena would result into a higher filmwise condensation heat transfer coefficient in the parallel and vertical channels than in the top collector. As mentioned by *Rohsenow* [105] in the proposed heat pipe thermal resistance model, another assumption is the existence of a vapour rising thermal resistance between the channels and the top collector. However, *Rohsenow* [105] mentioned this thermal resistance could occur between the adiabatic and condenser section and is usually negligible. In this regard, this assumption is less likely to be verified and to explain the observed temperature difference at the condenser.

To conclude on the vertical validation of the thermal resistance model, the three-leg heat pipe vertical temperature profile indicates that both bottom and top collector should be treated separately as they usually show different temperatures than the parallel channels. Indeed, the pool boiling and condensation mechanisms are believed to vary significantly compared to the vertical legs. Along the evaporator section of the legs, the temperature profile can be considered uniform. Finally, with the axial conduction of the material, the heat pipe temperature can be slightly higher at the bottom of the heat pipe and progressively decrease on a vertical axis.

#### *6.1.2.2 Temperature difference between the three-parallel legs – Horizontal validation*

To complete the comparison between the proposed multi-channel thermal resistance network and the temperature profile of the three-leg heat pipe, a horizontal analysis is conducted. In this section, the temperature profile of each parallel leg is studied and compared. This comparison between the three parallel legs is conducted at the evaporator, adiabatic, and condenser sections. In Figure 6-11 is presented the temperature difference between each parallel leg at the evaporator section of the three-leg heat pipe. The left (L), middle (M), and right (R) legs temperatures are displayed with circular, triangle, and crosses markers, respectively.

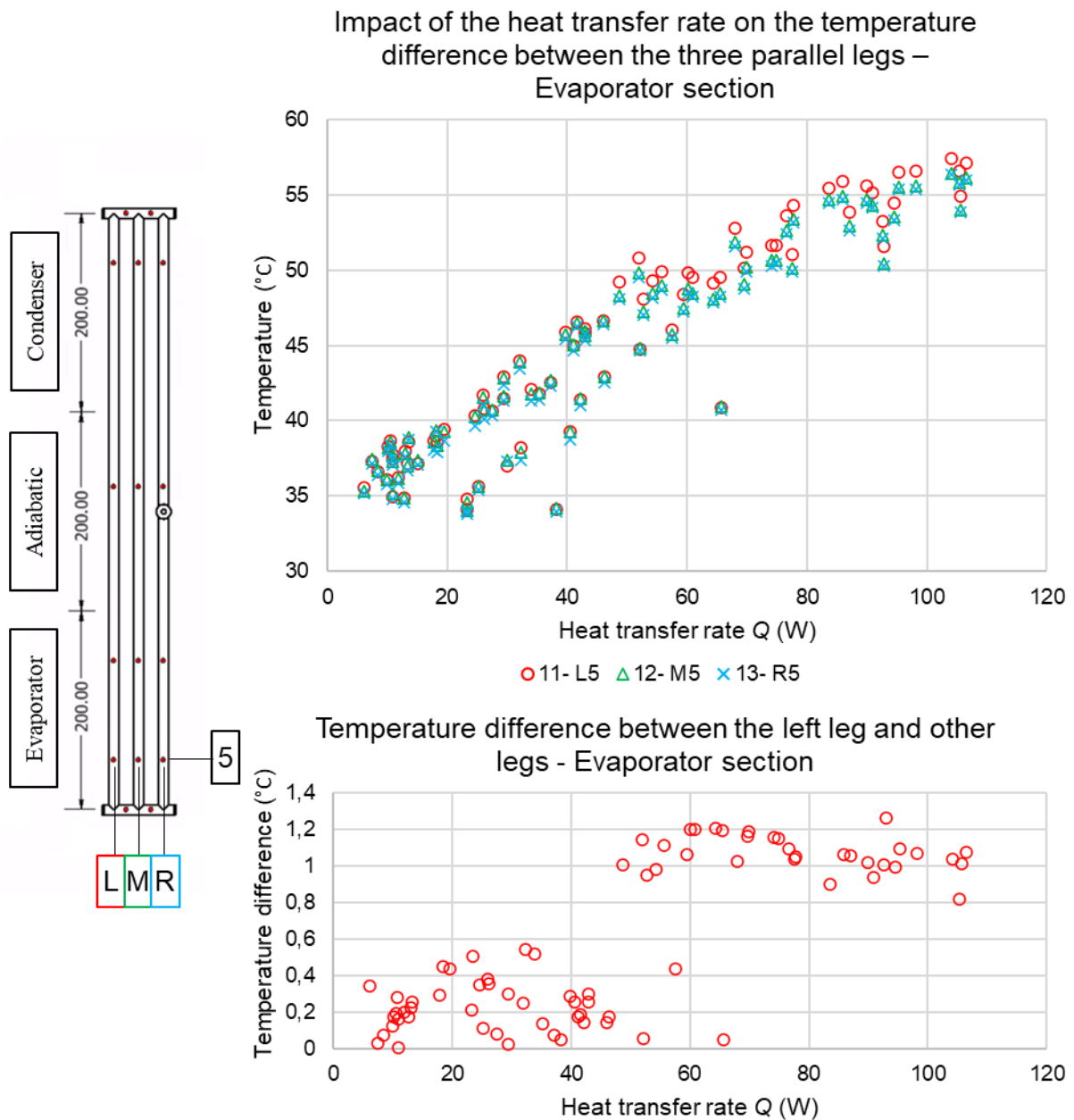


Figure 6-11. Impact of the heat transfer rate on the temperature of the three parallel legs at the evaporator section – Horizontal validation

In Figure 6-11 are analysed the legs temperature at the bottom of the evaporator (level 5). From the top graph is observed that, at heat transfer rates lower than 50 W, the temperature of the three parallel legs is the same. However, from a heat transfer rate of 50 W, the left leg presents a temperature higher than that of the two other legs. In the bottom graph of Figure 6-11 is shown that the left leg temperature is 1°C higher than the other legs. Yet, this temperature difference remains constant between a heat transfer rate of 50 W and 110 W. Therefore, it seems that the boiling activity and the pool boiling heat transfer is slightly more important in the left leg than in the middle and right legs. Interestingly, this difference of

temperature between the left leg and the other legs was not detected from the temperature measurement at the adiabatic section of the three-leg heat pipe. This is presented in Figure 6-12.

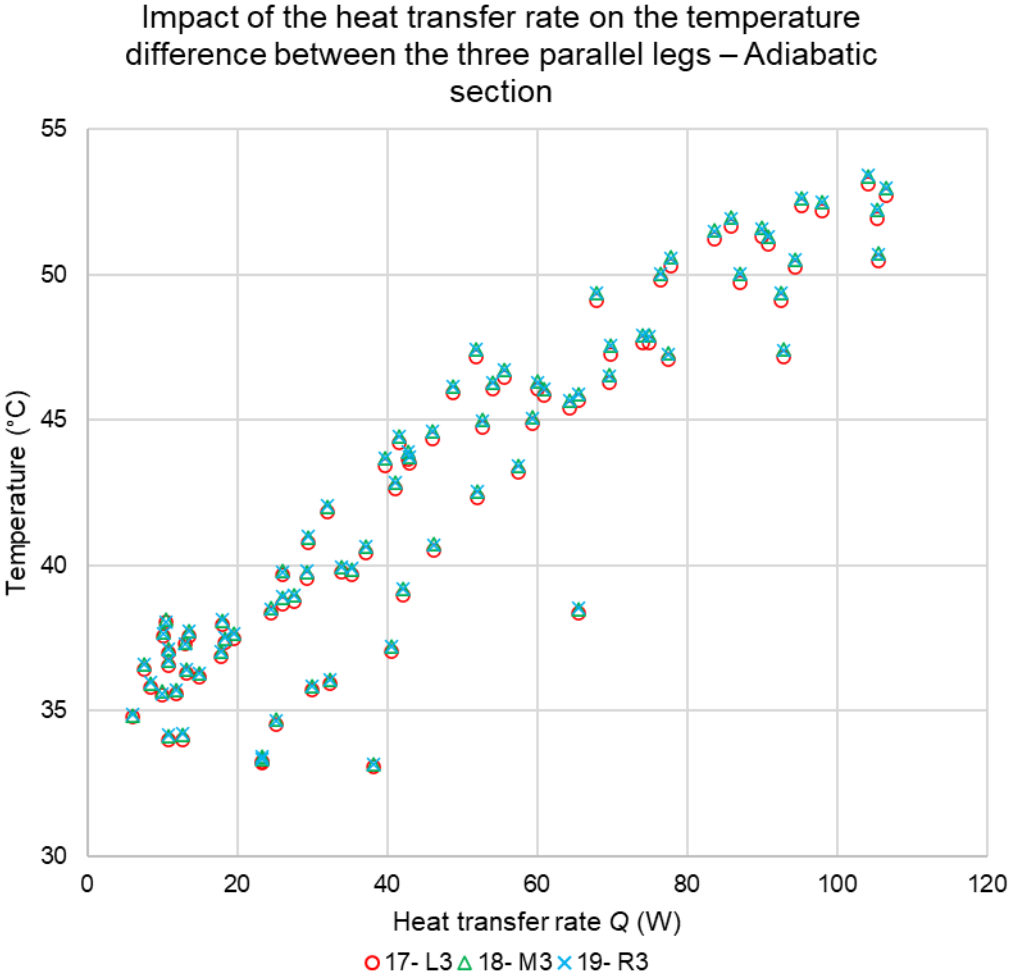
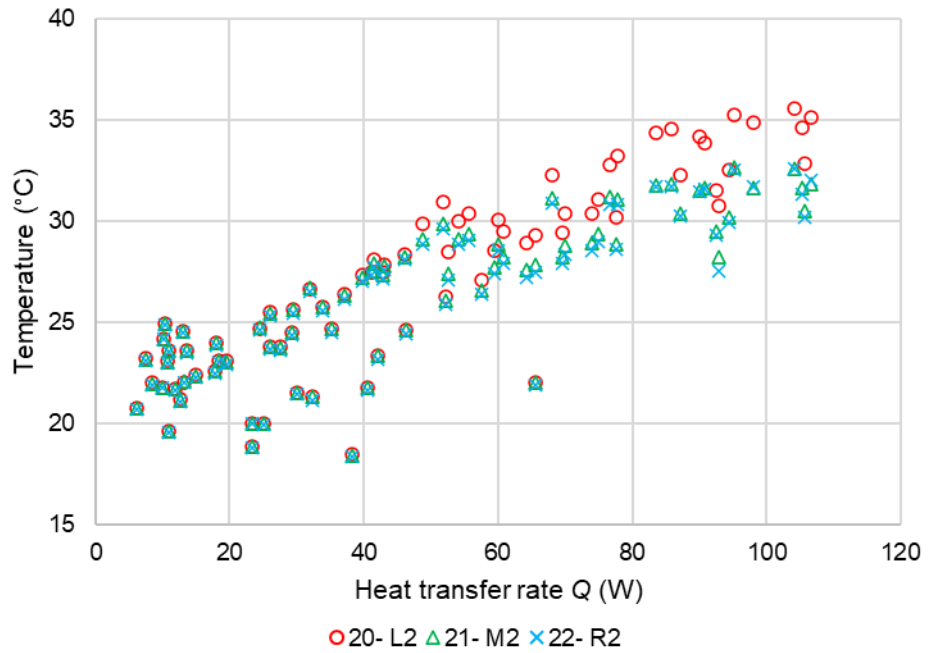
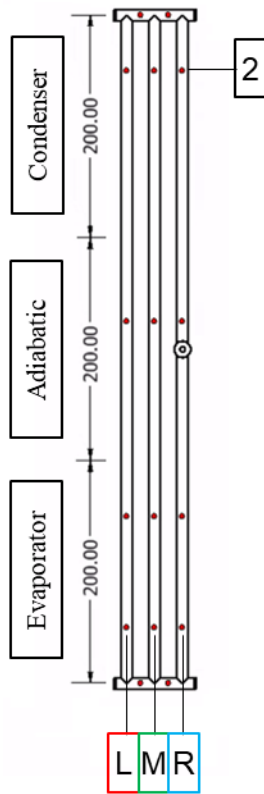


Figure 6-12. Impact of the heat transfer rate on the temperature of the three parallel legs at the adiabatic section – Horizontal validation

From Figure 6-12 is observed that the three adiabatic sections thermocouples placed on the legs measured the same temperature for all heat transfer rates in the studied range. This shows that, even if each leg can be treated separately at the evaporator and condenser, the temperature is uniform between all the parallel channels. The multi-channel heat pipe thermal resistance model should therefore link all the parallel boiling thermal resistances to a same node and consider one single temperature for the adiabatic section.

In Figure 6-13 is shown the temperature difference between the left, middle, and right legs at the condenser section.

### Impact of the heat transfer rate on the temperature difference between the three parallel legs – Condenser section



### Temperature difference between the left leg and other legs - Condenser section

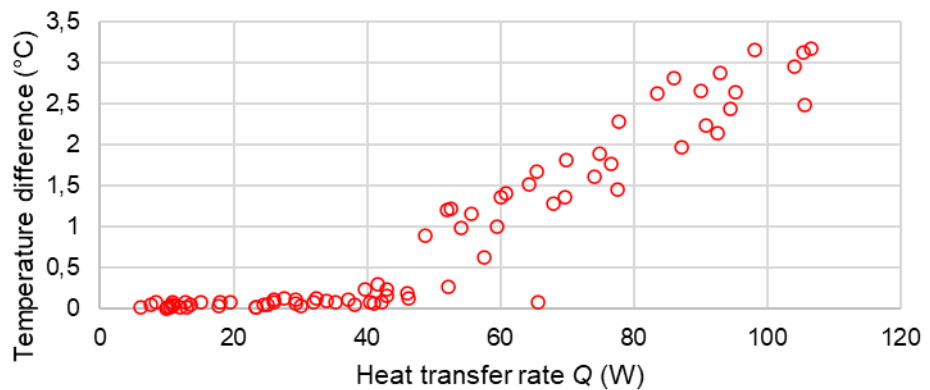


Figure 6-13. Impact of the heat transfer rate on the temperature of the three parallel legs at the condenser section – Horizontal validation

Like the pool boiling section, the condenser section also shows a difference of temperature between the left leg and the two other legs. Again, from a heat transfer rate of 50 W, the left leg temperature becomes significantly higher than that of the other two legs. Yet, unlike the observation made at the pool boiling section, at the condenser, this difference of temperature increases with an increase of the heat transfer rate. Indeed, at a heat transfer rate of 50 W, the left leg is about 1°C higher than the other legs whereas, at a heat transfer rate of 100 W, the left leg is almost 3°C higher than the middle and right legs. The fact that this temperature difference changes with the heat transfer rate indicates that this temperature difference is likely to be linked to a two-phase phenomenon. Even if the steady state thermal performance of the



three-leg heat pipe is of interest, during the transient warmup of the heat pipe, a similar temperature difference between the three parallel legs of the heat pipe was also observed. As this phenomenon is related to the observations made in Figure 6-11 and Figure 6-13, the temperature profile of the three-leg heat pipe during its transient warmup is shown in Figure 6-14 and studied.

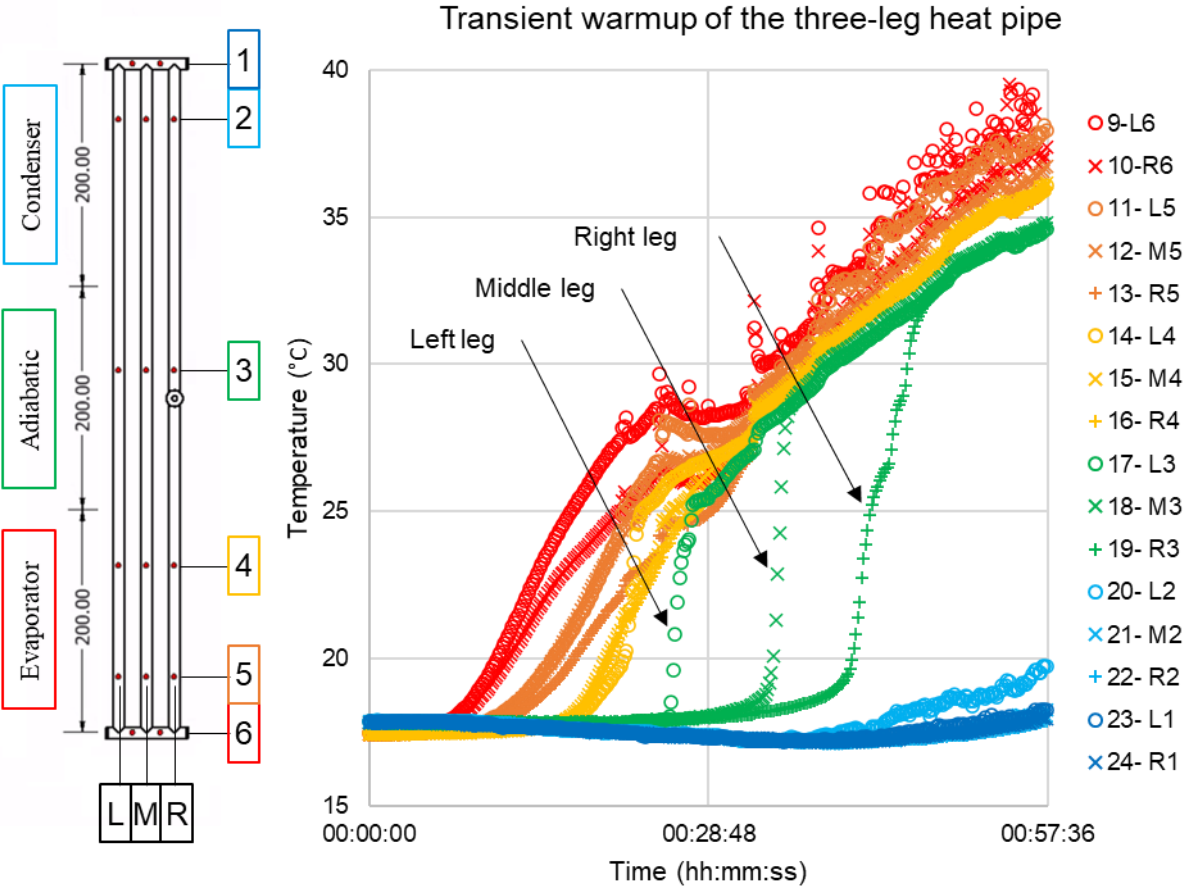


Figure 6-14. Temperature profile of the three-leg heat pipe during its transient warmup

Figure 6-14 shows the three-leg heat pipe temperature a few minutes after switching ON the electric heaters. Logically, the heat source first triggers the pool boiling heat transfer at the bottom collector which results into an increase of the bottom collector temperature followed by an increase of the legs temperature. More interestingly, in green are shown the three thermocouples placed on each leg at the adiabatic section. The transient temperature profile reveals that the adiabatic temperature of a leg increases sharply when the two-phase heat transfer is triggered. However, this sudden increase in temperature does not occur simultaneously for the three parallel legs. Instead, the left leg temperature first increases, followed by the middle leg, and finally the right leg. This agrees with the steady state observations made at the evaporator and condenser sections of the three-leg heat pipe. Yet, Figure 6-14 shows that the middle leg also warms-up before the right leg. An assumption which could explain these observations is that the three-leg heat pipe was slightly tilted on one side

which would favour the vapour rise from the left side. Yet, as the temperature of the three parallel legs is the same at the adiabatic section and that no temperature difference could be detected between the middle and right legs at the evaporator and condenser, it seems relevant for the modelling of the heat pipe to consider that the temperature is uniform between the three parallel legs. As such, for the proposed thermal resistance model, it is assumed that similar heat transfer coefficient correlations can be used for the parallel channels of a multi-channel heat pipe.

### **6.1.3 Identification of the optimized two-phase correlations**

In order to optimize the theoretical prediction of the three-leg heat pipe, the local heat transfer coefficients were compared to available pool boiling, falling film boiling, and condensation correlations. Such correlations aim at predicting the local heat transfer coefficient and are needed by the developed thermal resistance model to estimate each thermal resistance. The experimentally measured pool boiling, and condensation heat transfer coefficients are therefore used to identify the most suitable correlations for the prediction of the three-leg heat pipe performance.

#### *6.1.3.1 Optimized pool boiling correlation.*

In this section, the prediction of the pool boiling heat transfer coefficient in the three-leg heat pipe evaporator is studied. As significant differences were measured between the pool boiling heat transfer coefficient at the bottom collector and in the legs, two different correlations must be used. Hence, the pool boiling heat transfer coefficient prediction in the bottom collector and in the legs is studied separately.

- **Pool boiling in the bottom collector**

In Figure 6-15 is displayed the experimental pool boiling heat transfer coefficient at the bottom collector and is compared with 25 correlations from the literature.

Pool boiling heat transfer coefficient in the bottom collector with the boiling heat flux and heat transfer rate

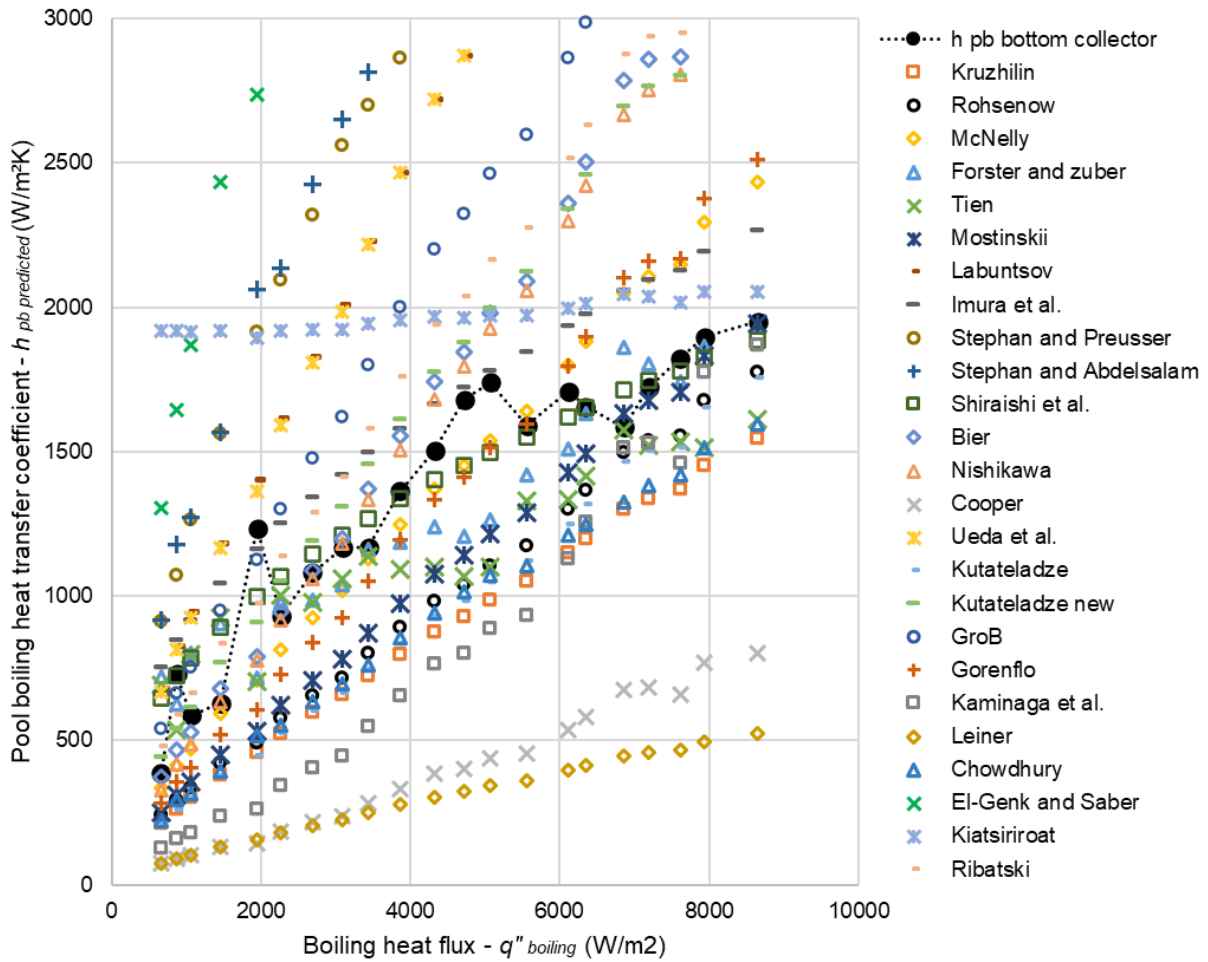


Figure 6-15. Pool boiling heat transfer coefficient with the boiling heat flux – Bottom collector

In Figure 6-15, the measured bottom collector pool boiling heat transfer coefficient is displayed with circular black markers. The correlations from the literature are shown with coloured markers. Figure 6-15 shows that, depending on the correlation used, the predicted pool boiling heat transfer coefficient varies significantly. Major discrepancies between the models can be observed as reveals the prediction by *Leiner* [157] which does not exceed 500 W/m<sup>2</sup>K whereas *El-Genk and Saber* [1] expect a pool boiling heat transfer coefficient higher than 2500 W/m<sup>2</sup>K. For clarity, the three most accurate correlations only are kept and displayed in Figure 6-16.

Pool boiling heat transfer coefficient in the bottom collector with the boiling heat flux

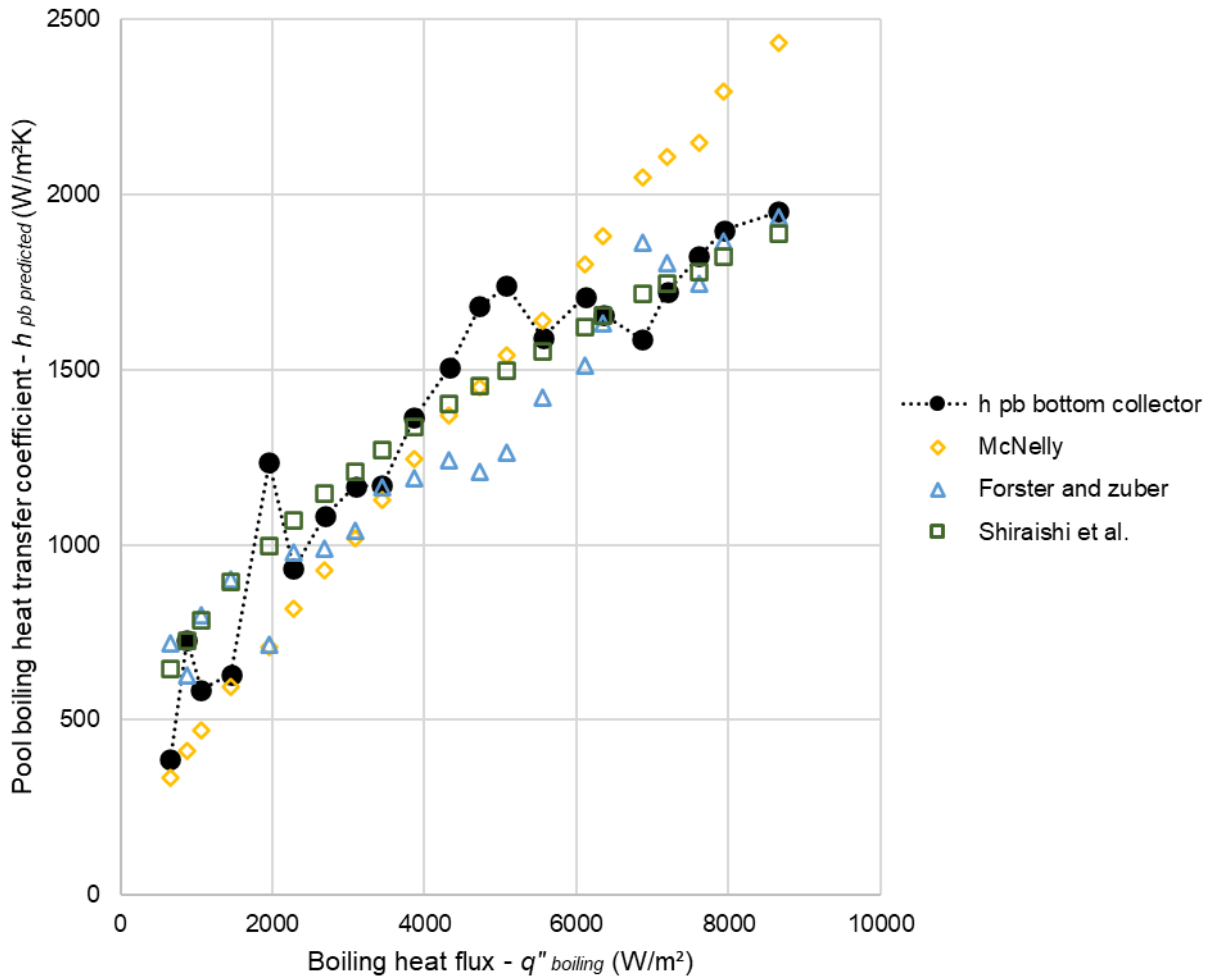


Figure 6-16. Best pool boiling heat transfer coefficient correlation with the boiling heat flux – Bottom collector

The three correlations which predictions are the closest to the measured bottom collector pool boiling heat transfer coefficient are the models from *McNelly* [138], *Forster and Zuber* [139], and *Shiraishi et al.* [148]. From Figure 6-16 is observed that the correlation by *Shiraishi et al.* [148] closely follows the evolution of the bottom collector pool boiling heat transfer coefficient with an increase of the boiling heat flux. As a comparison, the correlation by *Forster and Zuber* [139] slightly underpredicts the heat transfer coefficient, in particular at a boiling heat flux between 4000 W/m<sup>2</sup> and 6000 W/m<sup>2</sup>. Finally, the correlation by *McNelly* [138] underpredicts the pool boiling heat transfer coefficient at low heat flux but overpredicts it at high heat flux. Even if the overall accuracy of this correlation will be acceptable on the whole range of heat transfer rate, because its trend does not suit the bottom collector pool boiling heat transfer coefficient well, the use of this correlation was not recommended. To better visualize the predictive error made by each correlation, the predicted pool boiling heat transfer coefficient can be displayed in terms of experimental pool boiling heat transfer coefficient measured at the bottom collector. This is presented in Figure 6-17.

Best pool boiling correlations with the experimental bottom collector pool boiling heat transfer coefficient

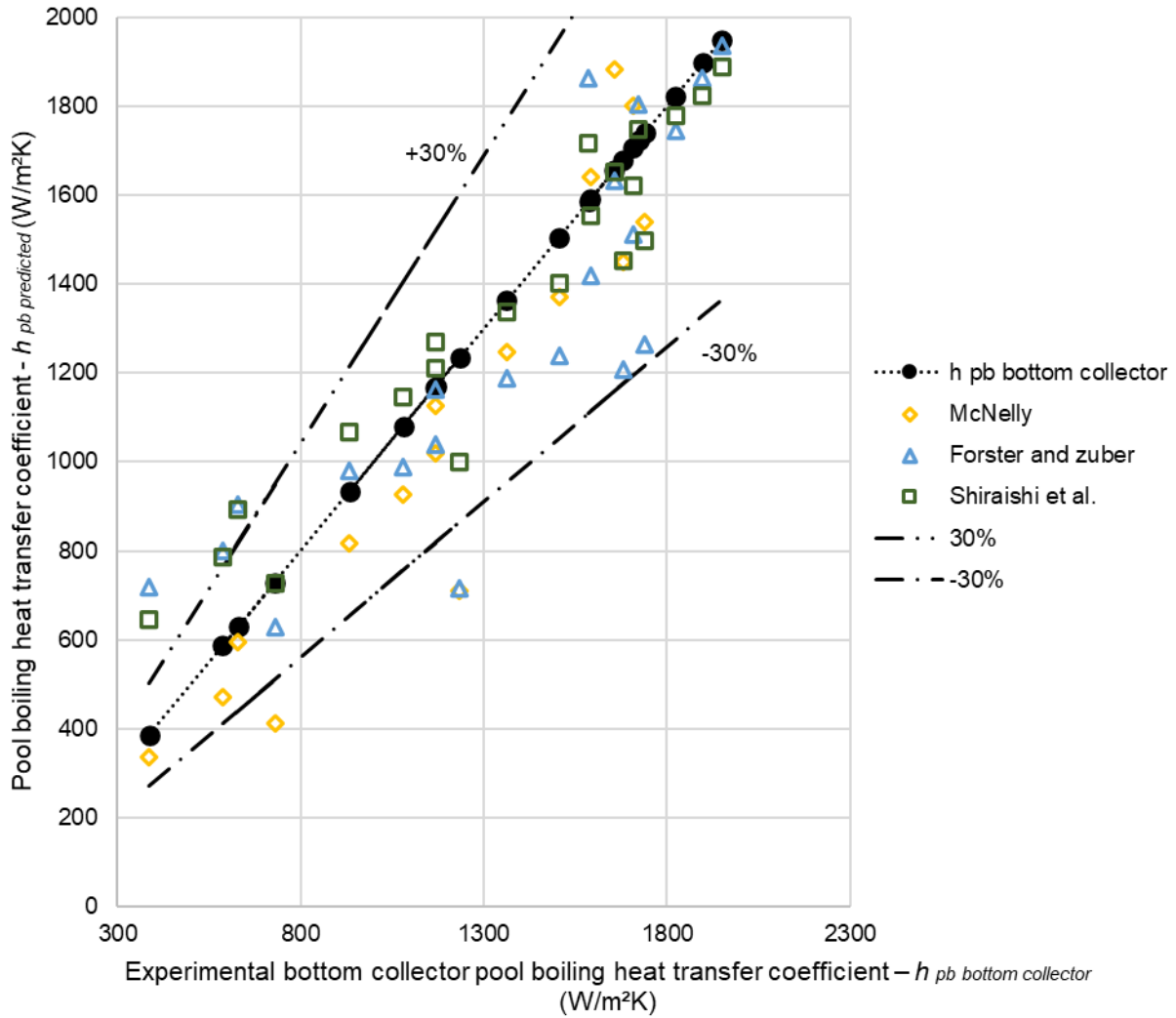


Figure 6-17. Best pool boiling correlations with the experimental pool boiling heat transfer coefficient in the bottom collector

The linear series with black markers shows the experimental pool boiling heat transfer coefficient at the bottom collector and is the target for the compared models. From Figure 6-17 can be observed that the errors made by the selected pool boiling correlations are higher at low boiling heat flux and low experimental heat transfer coefficient. Yet, with an increase of the pool boiling heat transfer coefficient, the relative error logically reduces, and the three selected correlations predict the pool boiling heat transfer coefficient with an error less than 30%. From this graph is highlighted that the prediction from *Forster and Zuber* [139] fluctuates more than the other correlations. In opposition, with an increase of the experimental heat transfer coefficient, the correlation by *Shiraishi et al.* [148] follows closely the measured bottom collector pool boiling heat transfer coefficient. This is further highlighted by Figure 6-18 which shows the accuracy of each correlation with the boiling heat flux.

Error made on the predicted bottom collector pool boiling heat transfer coefficient by the most accurate correlations

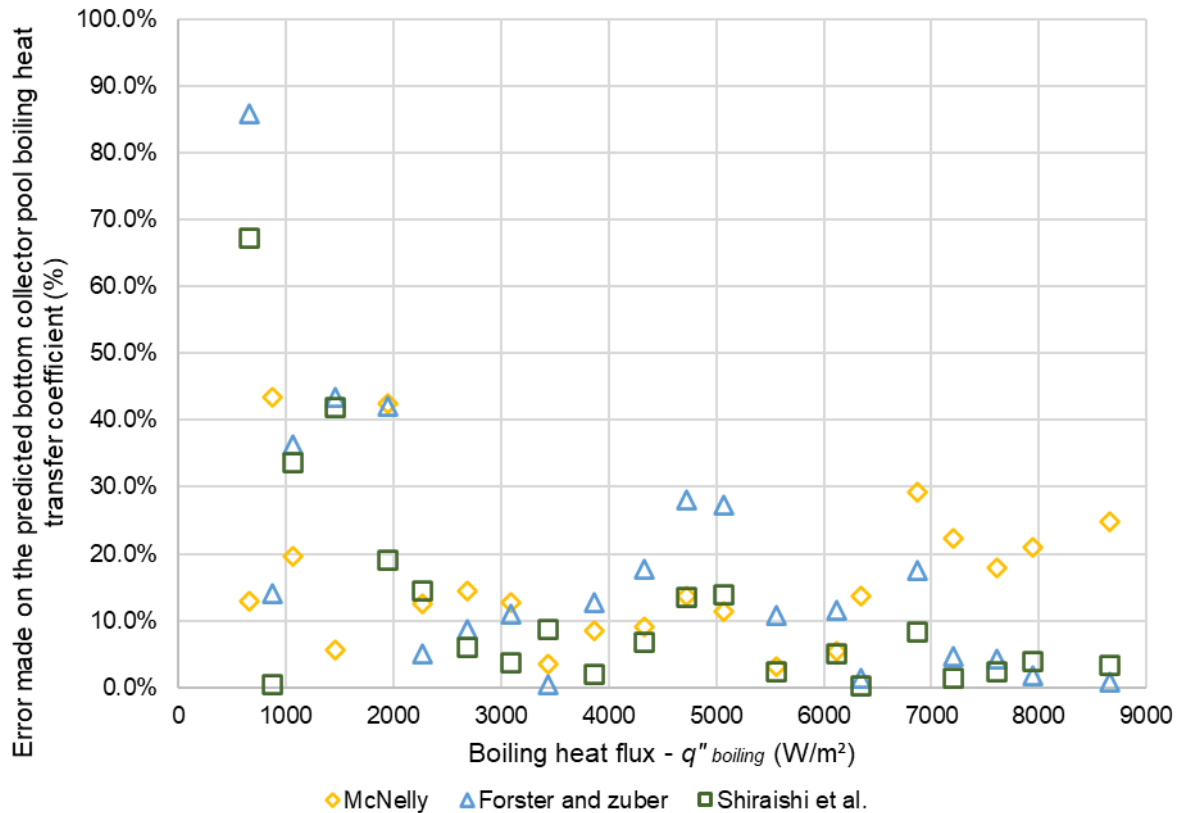


Figure 6-18. Error made on the predicted bottom collector pool boiling heat transfer coefficient by the most accurate correlations

Again, Figure 6-18 proves that the accuracy of the correlations is lower at low boiling heat flux.

The three correlations make a predictive error higher than 40% at boiling heat flux lower than 1500-2000 W/m<sup>2</sup>. Yet, at heat fluxes higher than 2000 W/m<sup>2</sup>, all the correlations can predict the bottom collector pool boiling heat transfer coefficient with an error less than 30%. As the prediction crosses the measured heat transfer coefficient, the predictive error from the correlation by *McNelly* [138] logically decreases, reaches 0%, and increases again at higher heat flux. However, as the correlation does not exhibit the same trend, the accuracy of this correlation is expected to degrade further at higher heat fluxes. Even if the prediction from the correlation by *Forster and Zuber* [139] is close to experimental data, the prediction is not as smooth and fluctuates more than other models. For instance, the error made by the correlation from *Forster and Zuber* [139] increases from 0.5% at 3400 W/m<sup>2</sup> to 28.1% at 4700 W/m<sup>2</sup>. The *Shiraishi et al.* [148] correlation performs best and, despite a higher error at heat flux below than 1500 W/m<sup>2</sup>, this correlation was able to predict the local pool boiling heat transfer coefficient in the bottom collector with an error lower than 20%. A small fluctuation can nonetheless be detected at a heat flux around 5000 W/m<sup>2</sup> where the prediction of this correlation makes an error 13.5% whereas the error falls below 10% for boiling heat flux in the range 2700 W/m<sup>2</sup> - 8700 W/m<sup>2</sup>.

The average error of the available pool boiling correlations in the prediction of the bottom collector pool boiling heat transfer coefficient over the whole range of heat transfer rate is shown in the bar graph of Figure 6-19.

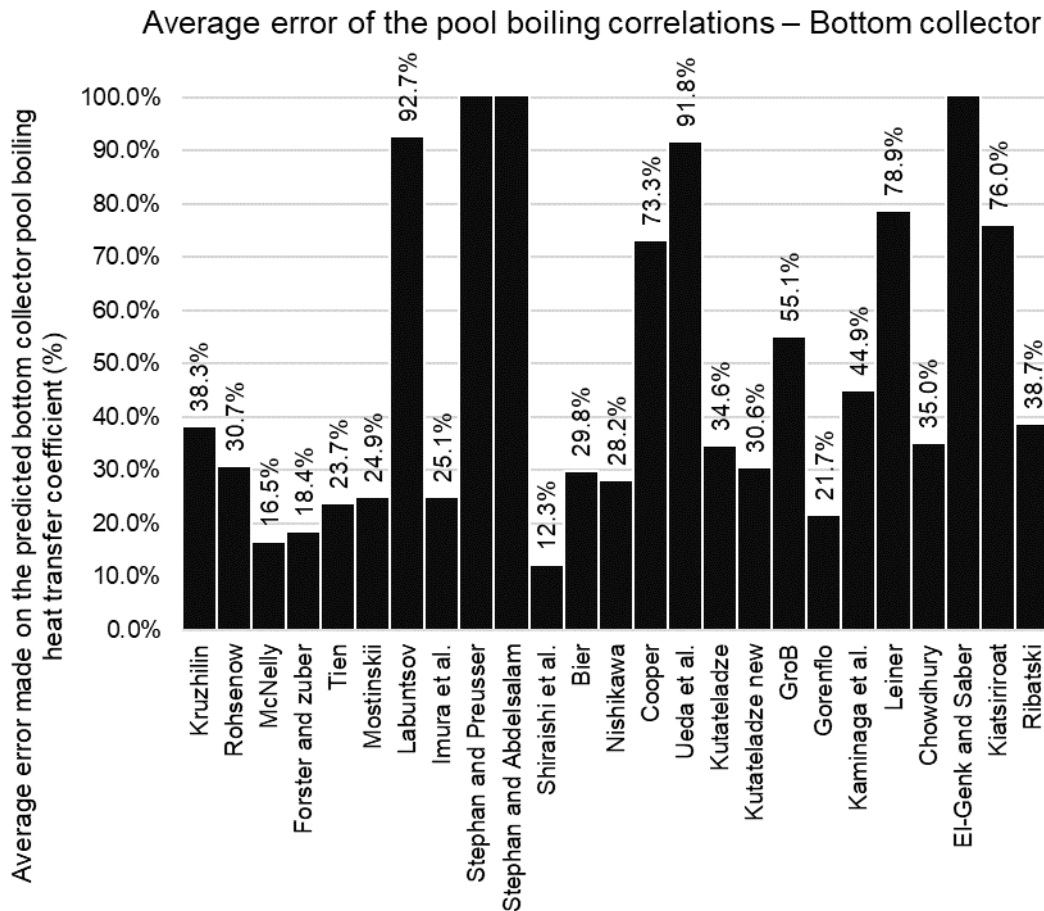


Figure 6-19. Average error of the pool boiling correlations over the whole range of heat transfer rate – Bottom collector

Over the whole range of investigated heat transfer rate, the average errors made by the *Forster and Zuber* [139] and *McNelly* [138] correlations are 18.4% and 16.5% respectively. The correlation by *Shiraishi et al.* [148] performs best with an average error of 12.3%. This correlation was therefore selected for the prediction of the local pool boiling heat transfer coefficient taking place in the bottom collector of the three-leg heat pipe.

- **Pool boiling in a leg**

A similar analysis was conducted for the pool boiling heat transfer coefficient taking place in the legs of the three-leg heat pipe. The same 25 available pool boiling correlations from the literature were compared with the local heat transfer coefficient in the legs. In Figure 6-20 are shown the measured and predicted pool boiling heat transfer coefficients at various boiling heat flux. For the pool boiling heat transfer coefficient in a single leg, the five best performing correlations are compared.

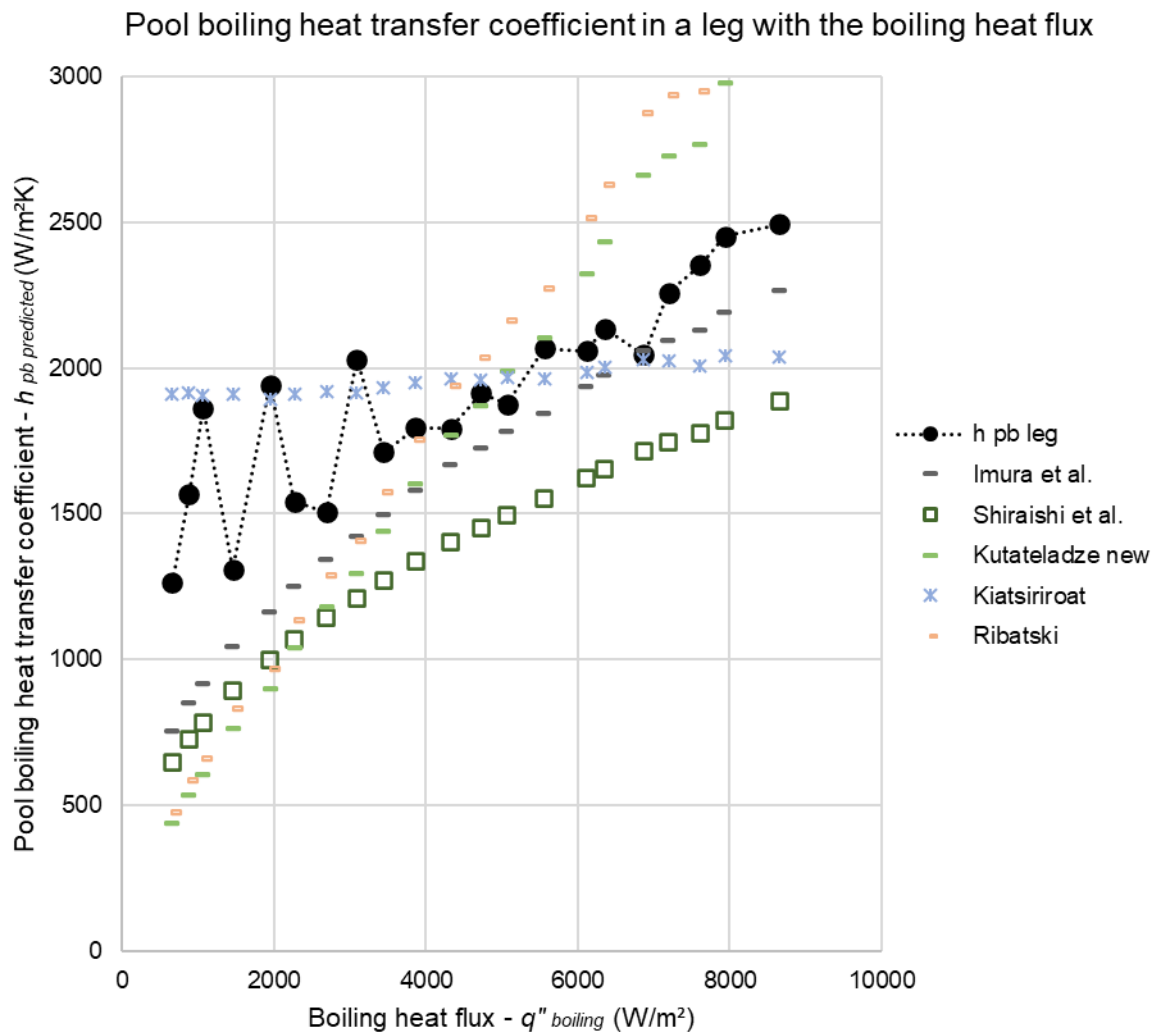


Figure 6-20. Best pool boiling heat transfer coefficient correlation with the boiling heat flux – Single leg

For the prediction of the pool boiling heat transfer coefficient in a single leg, the best performing correlation were developed by *Imura et al.* [145], *Shiraishi et al.* [148], *Kutateladze* [153], *Kiatsiriroat et al.* [160], and *Ribatski and Jabardo* [161]. In comparison with the local pool boiling heat transfer coefficient of the bottom collector, the heat transfer coefficient is higher in the legs. As a results, the correlation by *Shiraishi et al.* [148] underpredicts this heat transfer coefficient even if the trend is good. The correlation by *Kiatsiriroat et al.* [160] exhibits a very small change in its prediction with a change of the boiling heat flux and is almost constant at  $\sim 2000 \text{ W/m}^2\text{K}$  for all heat flux. Even if the overall accuracy of this correlation is acceptable because it is centred around the experimental value, it lacks physical meaning and does not seem to accurately describe a pool boiling mechanism. The two correlations from *Kutateladze* [153] and *Ribatski and Jabardo* [161] are quite similar and underpredict the leg pool boiling heat transfer coefficient below  $4000 \text{ W/m}^2$  but overpredict it at heat fluxes higher than  $5000 \text{ W/m}^2$ . The predicted increase of the pool boiling heat transfer coefficient is steeper than that measured in the leg. The correlation which is closest to the leg pool boiling heat transfer coefficient was developed by *Imura et al.* [145] and presents an acceptable trend despite a



small underprediction of the heat transfer coefficient. Figure 6-21 displays the predicted pool boiling heat transfer coefficient in terms of the local pool boiling heat transfer coefficient measured in a single leg.

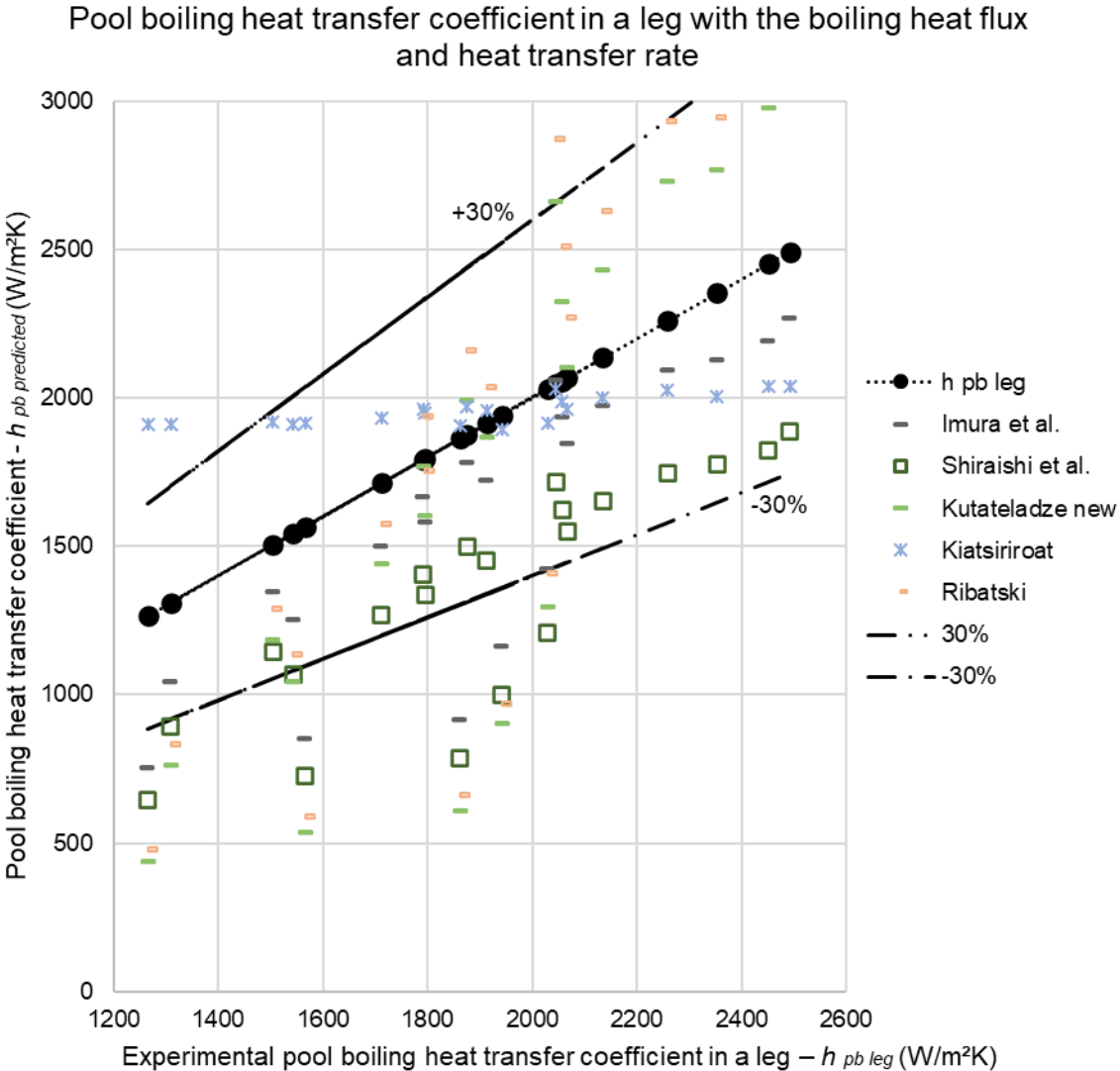


Figure 6-21. Best pool boiling correlations with the experimental pool boiling heat transfer coefficient in a leg

Similar conclusions can be made from Figure 6-21 with the correlation from *Kiatsiroat et al.* [160] being abnormally constant, and the correlations by *Kutateladze* [153] and *Ribatski and Jabardo* [161] underpredicting and then overpredicting the heat transfer coefficient. Despite several values below -30%, Figure 6-21 shows that the correlation by *Shiraishi et al.* [148] and the local pool boiling heat transfer coefficient of the leg have a similar trend as the prediction shows a linear evolution parallel to the measured data. However, the correlation by *Shiraishi et al.* [148] makes an underprediction of the pool boiling heat transfer coefficient measured from the leg and is closer to the -30% indicative line. Figure 6-21 clearly highlights that the *Imura et al.* [145] correlation outperforms the other models while predicting the leg pool boiling heat transfer coefficient. Indeed, over the whole range of heat transfer rate tested, the

predicted value remains close to the experimental value. Figure 6-21 also reveals that, at experimental heat transfer coefficient below than 2000 W/m<sup>2</sup>K, four experimental data points show strange values. Indeed, all the models largely underpredict the pool boiling heat transfer coefficient measured for these values. Those four data points are not in agreement with the rest of the measured data, and this can also be seen from Figure 6-20 at boiling heat flux lower than 4000 W/m<sup>2</sup>. Hence, it is concluded that these four data points are the results of an experimental inaccuracy. Consequently, little value is given to the correlations underprediction for these four data points in Figure 6-21. In Figure 6-22 is presented the error made by the compared correlations for various boiling heat flux.

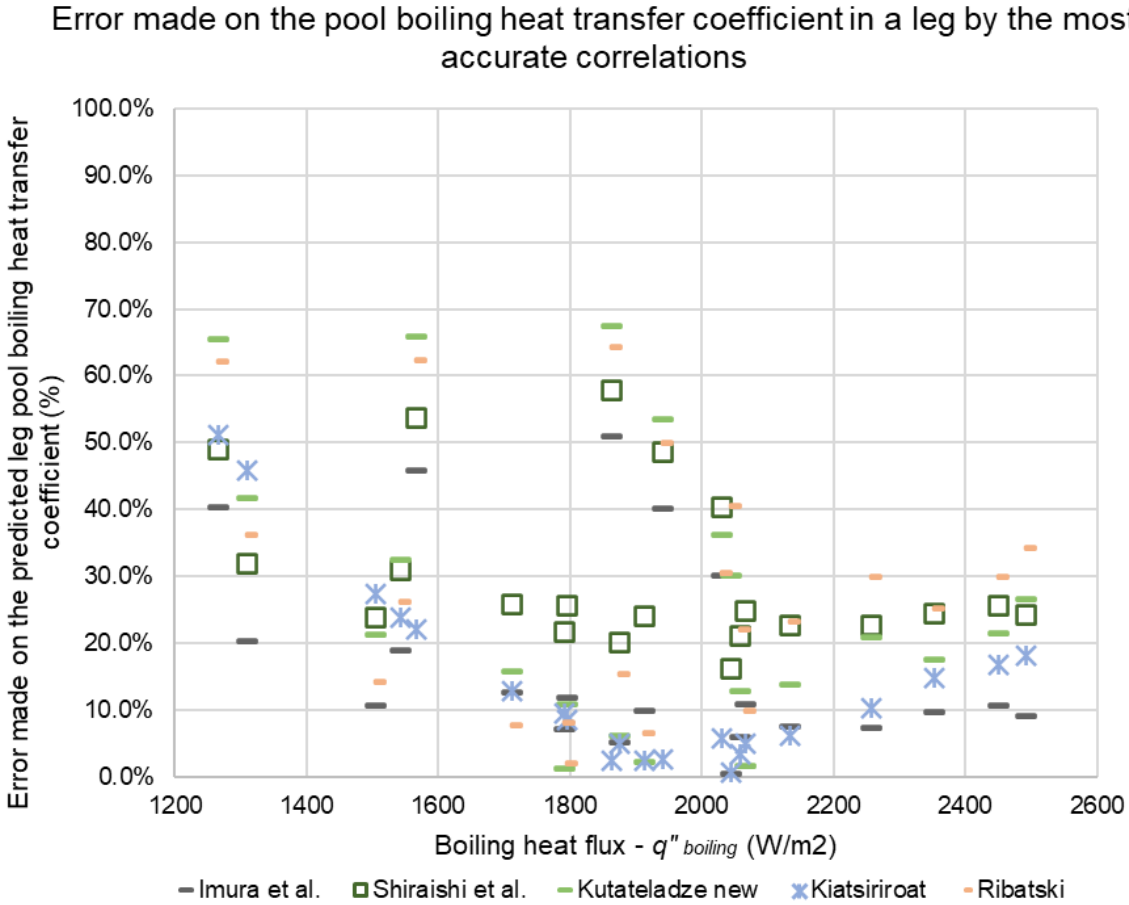


Figure 6-22. Error made on the predicted pool boiling heat transfer coefficient in a leg by the most accurate correlations

As explained earlier, the data points showing errors higher than 45% in Figure 6-22 are caused by the inaccuracy from the experimental data and not by the models themselves. Little attention is therefore given to those datapoints. Like the bottom collector, Figure 6-22 shows that the correlations' relative errors are higher at low boiling heat flux and decrease with an increase of the heat transfer coefficient. The error made by the *Shiraishi et al.* [148] correlation stabilizes around 23%. For the two correlations which cross the experimental data (*Kutateladze* [153] and *Ribatski and Jabardo* [161]), the predictive error expectedly decreases to 0% and

increases again. This is also the case for the correlation from *Kiatsiriroat et al.* [160]. Yet, as this correlation is almost constant and poorly affected by pool boiling related factors, the discrepancy of some experimental data points has no impact on the prediction which remains acceptable for all the data points. However, due to the lack of physical meaning, this correlation is not considered suitable to describe the pool boiling heat transfer. Apart from the four incorrect datapoints, the prediction from the *Imura et al.* [145] correlation decreases from 40% at low heat flux to values close to 10% at 1700 W/m<sup>2</sup>. The predictive error then remains close to 10% for higher heat flux.

In Figure 6-23 is shown the average error made by the pool boiling correlations when predicting the local pool boiling heat transfer coefficient in a leg.

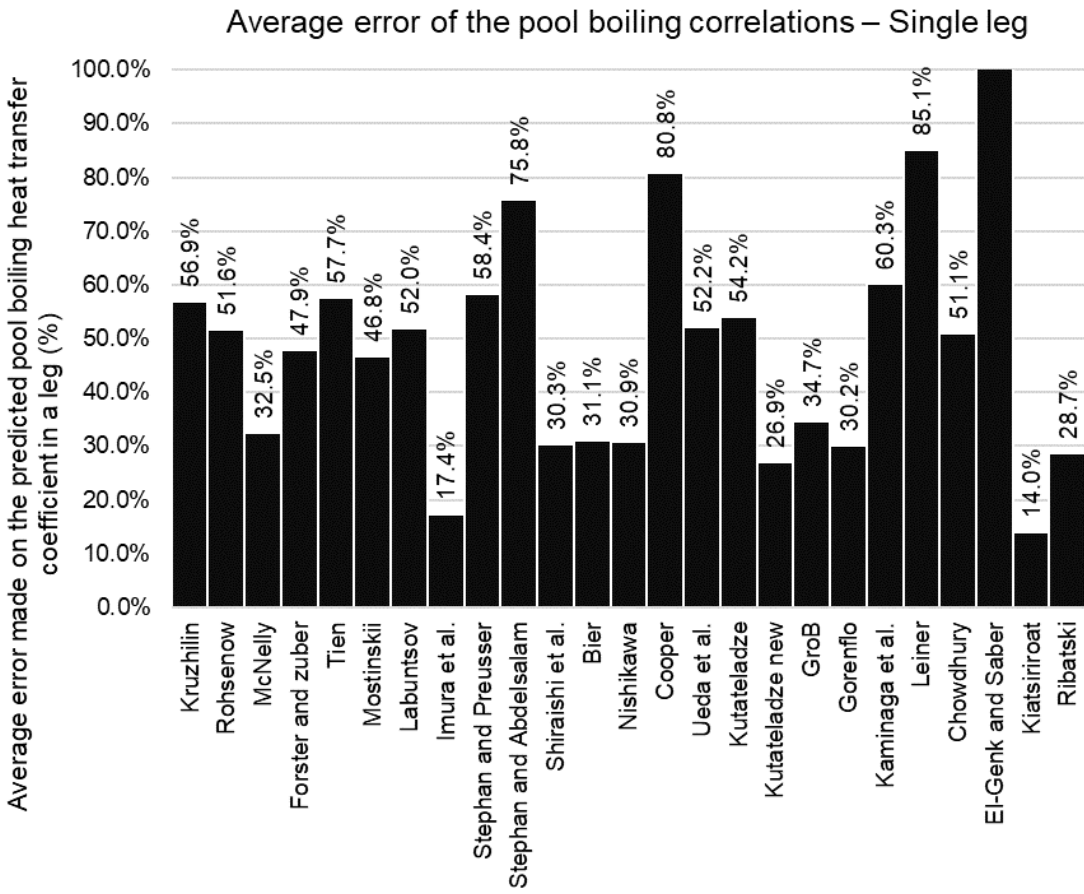


Figure 6-23. Average error of the pool boiling correlations over the whole range of heat transfer rate – Single leg

Despite a similar increase of the heat transfer coefficient with the boiling heat flux, the average error of the *Shiraishi et al.* [148] correlation is 30.3% due to its underprediction. The two correlations from *Kutateladze* [153] and *Ribatski and Jabardo* [161] reach an average error of 26.9% and 28.7%. Two correlations stand out from the other and obtain an average error lower than 20% the correlation from *Kiatsiriroat et al.* [160] and *Imura et al.* [145]. However, the accuracy of the correlation by *Kiatsiriroat et al.* [160] was improved as the correlation was not

influenced by many pool boiling related factors and predicts a similar pool boiling heat transfer coefficient for all heat flux. As such, this correlation is not considered as suitable to predict a heat transfer coefficient. The *Imura et al.* [145] correlation is therefore preferred and selected to predict the pool boiling heat transfer coefficient in a single leg as it showed an average error of 17.4%.

6.1.3.2 Absence of falling film and comparison with correlations

Originally, falling film boiling was expected to take place at the top of the evaporator’s wall. However, as explained in the previous section, the local heat transfer coefficient measured is very close to the pool boiling data from the bottom of the evaporator. As shown in Figure 6-24, when comparing falling film correlations to these experimental data, it is observed that the local heat transfer coefficient does not agree with falling film evaporation/boiling correlations.

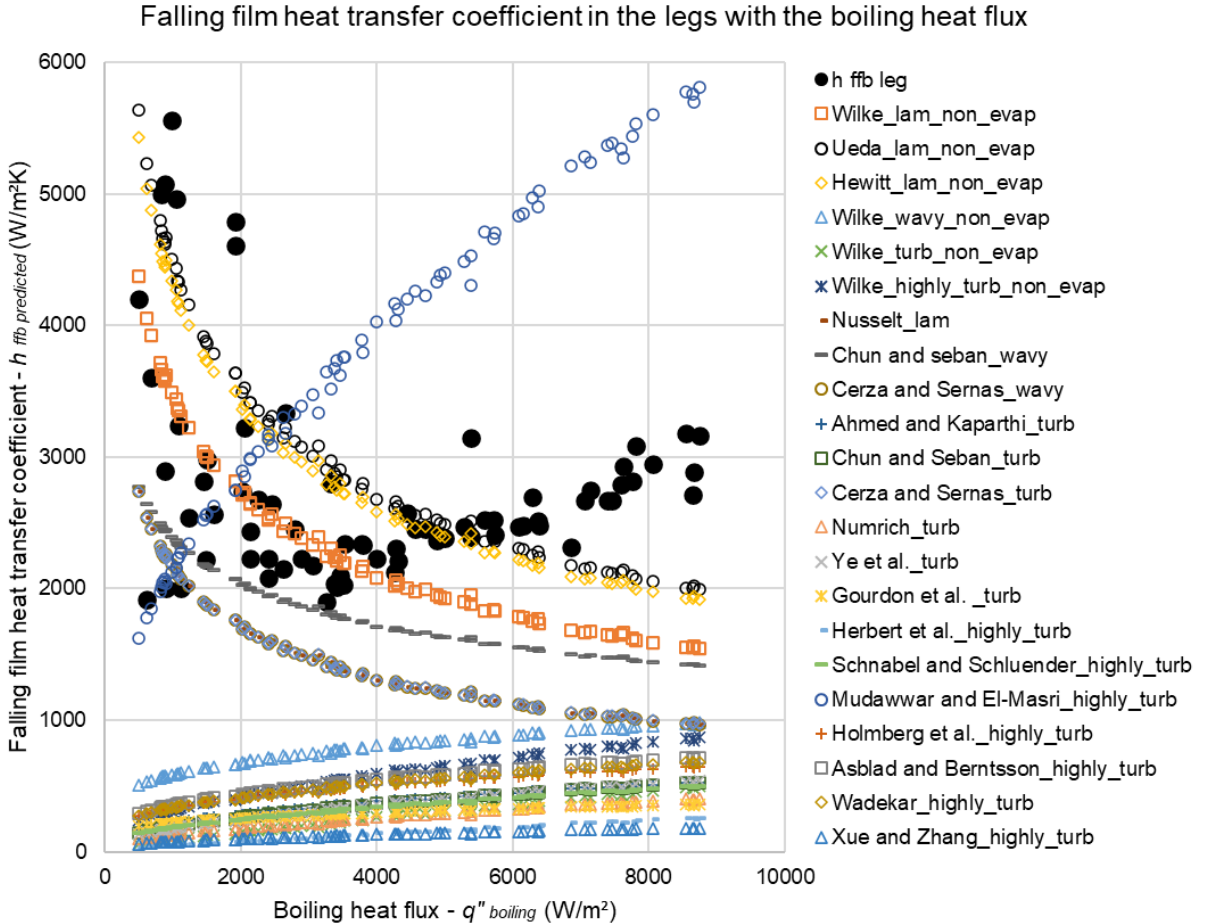


Figure 6-24. Falling film boiling heat transfer coefficient with the boiling heat flux – Single leg

This confirms the observation made from Figure 6-1 and Figure 6-2 that pool boiling only took place at the evaporator of the three-leg heat pipe. In this regard, pool boiling correlations only were used in the theoretical model to predict the heat transfer at the evaporator of the three-leg heat pipe.

### 6.1.3.3 Optimized condensation correlation.

At the condenser of the three-leg heat pipe, Figure 6-4 revealed that the local condensation heat transfer coefficients in the legs and in the top collector are very close. Differences between both can only be seen at condensation heat fluxes in the range 6000-9000 W/m<sup>2</sup>. Even at such heat flux, the two measured condensation heat transfer coefficients remain close. In this regard, the same condensation correlation will be used to predict the condensation heat transfer coefficient in the top collector and in the legs. In this section, the most suitable condensation heat transfer coefficient correlation is identified by comparing available correlations from the literature with the local condensation heat transfer coefficient measured at the top collector. This comparison is shown in Figure 6-25.

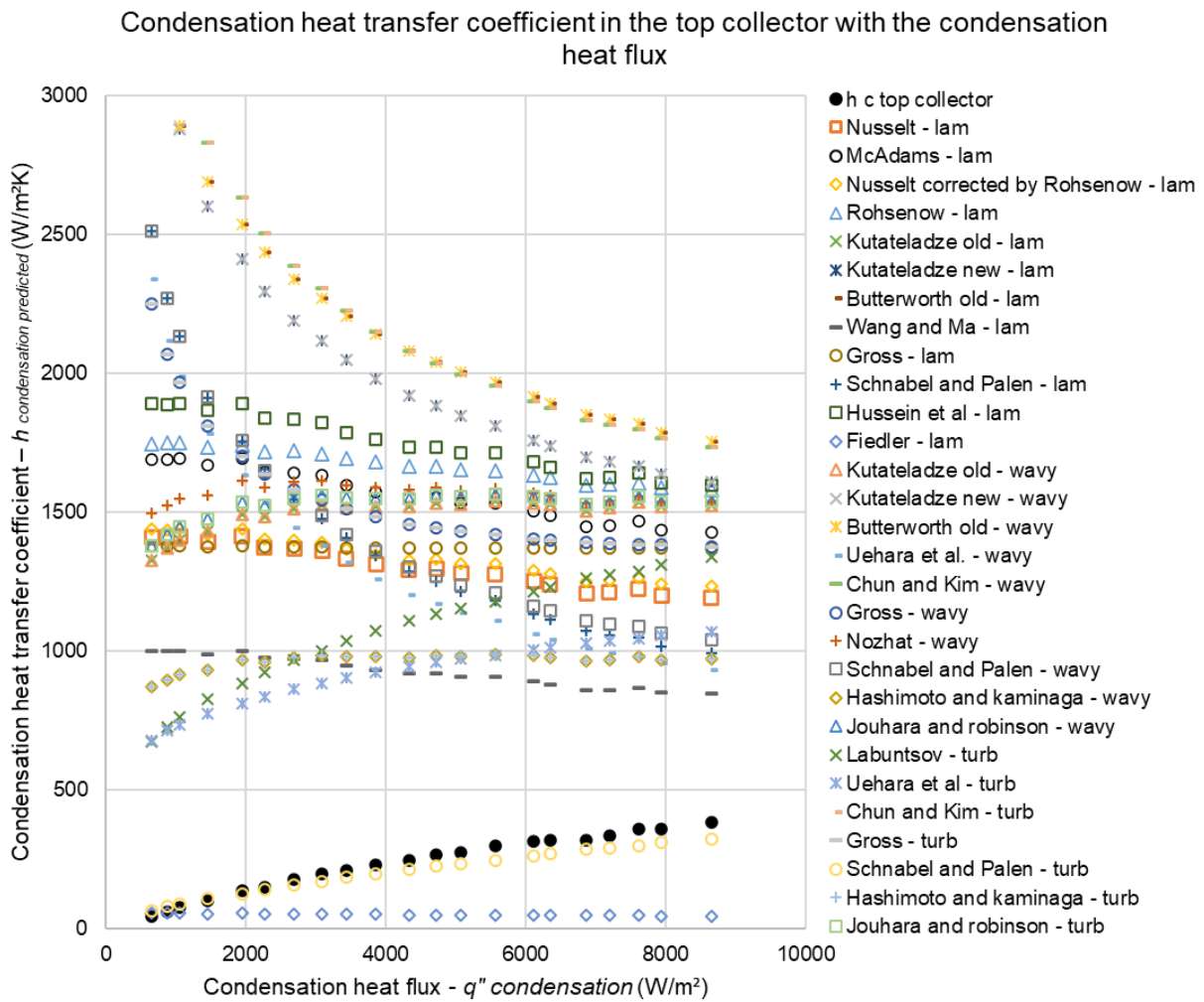


Figure 6-25. Condensation heat transfer coefficient with the condensation heat flux – top collector

In Figure 6-25, the local condensation heat transfer coefficient of the top collector is compared with 29 correlations from the literature. The measured top collector heat transfer coefficient as a function of the condensation heat flux is displayed with circular black markers. In the three-leg heat pipe experiments, it was observed that the condensation heat transfer coefficient was particularly low. Figure 6-25 reveals that most of the available correlations predicting the

condensation heat transfer coefficient expect a much higher heat transfer coefficient. To explain the low condensation heat transfer coefficient measured, assumptions are that the temperature reading at the condenser was affected by the surrounding water pool, that vapour faced some difficulty to rise in the channels, or that an important part of the condensation mass and heat transfer took place in the lower region of the condenser. In Figure 6-25 is observed that the correlation from *Schnabel and Palen* [194] only is close to the measured condensation heat transfer coefficient. This is shown better on Figure 6-26 where this correlation is displayed with the experimental condensation heat transfer coefficient of the top collector.

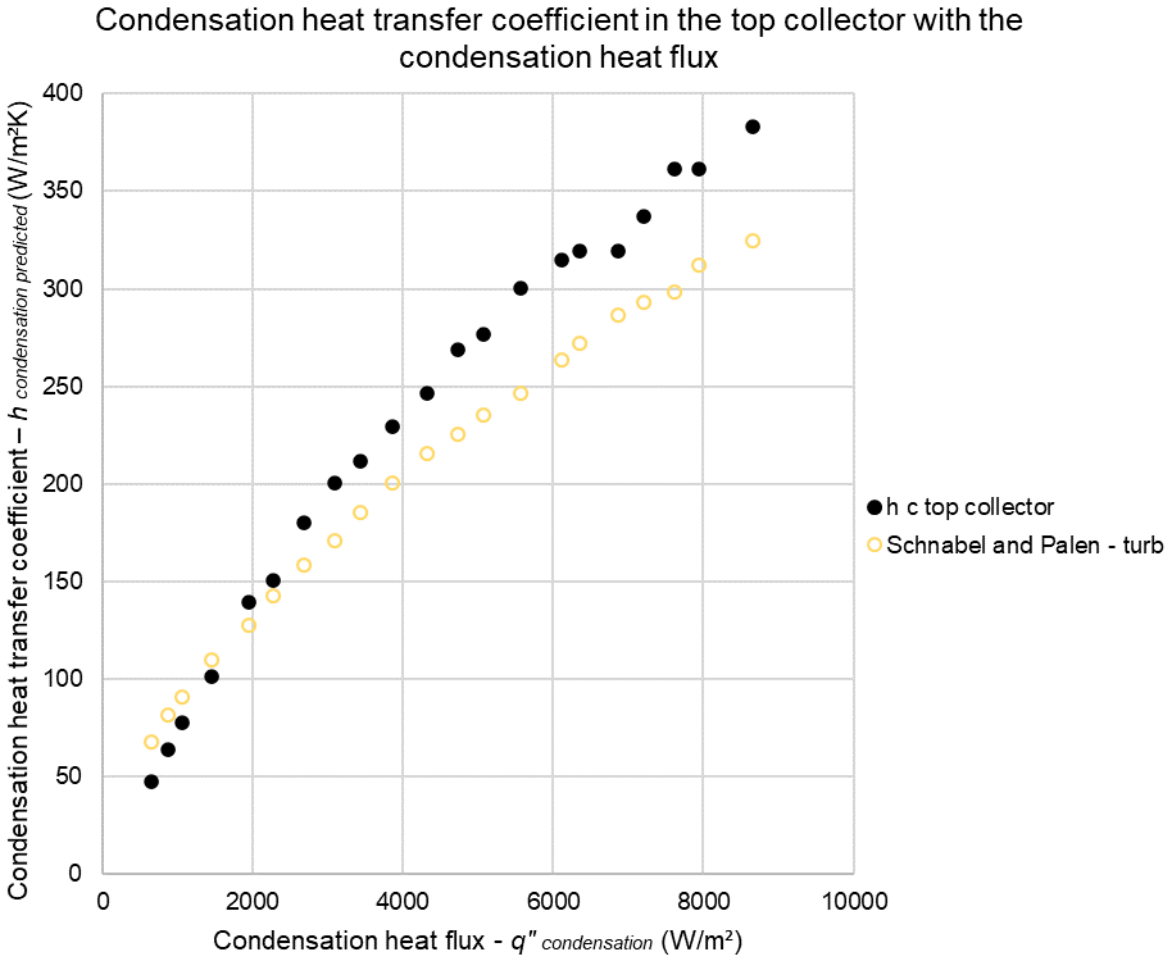


Figure 6-26. Best condensation heat transfer coefficient correlation with the condensation heat flux – top collector

In Figure 6-26, the correlation by *Schnabel and Palen* [194] is displayed with yellow circular markers. It can be noted that this correlation agrees well with the measured condensation heat transfer coefficient at heat fluxes lower than 3000 W/m<sup>2</sup>. However, the tilt of the correlation from *Schnabel and Palen* [194] is lower than that of the top collector which results into an underprediction of the condensation heat transfer coefficient at higher heat flux. Despite this underprediction, the error made by the correlation from *Schnabel and Palen* [194] remains acceptable and lower than 30% as witnesses Figure 6-27.

Condensation heat transfer coefficient in the top collector with the experimental condensation heat transfer coefficient in the top collector

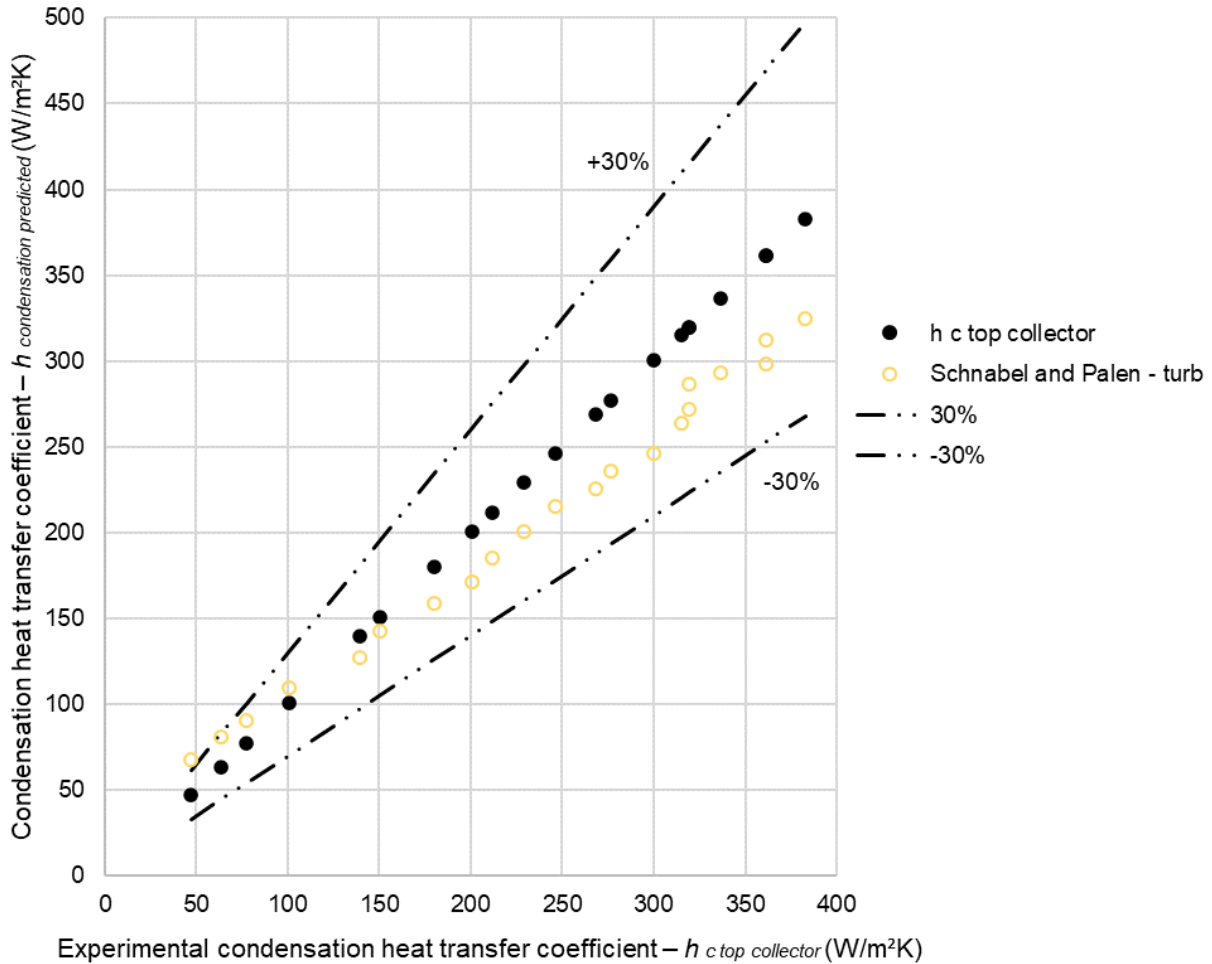


Figure 6-27. Best condensation correlations with the experimental condensation heat transfer coefficient in the top collector

In Figure 6-27 is presented the predicted condensation heat transfer coefficient as a function of the experimental condensation heat transfer coefficient measured in the top collector. It is observed that the relative error made by the *Schnabel and Palen* [194] correlation is higher than 30% when the heat transfer coefficient is lower than 50 W/m<sup>2</sup>K. Yet, this only concerns one data point and the error made by the correlation remains close to the experimental condensation heat transfer coefficient for the rest of the series. As observed in Figure 6-26, a major advantage of the correlation from *Schnabel and Palen* [194] is that, at low condensation heat flux, the prediction is close to the measured heat transfer coefficient of the top collector. This results into a low relative error when the experimental heat transfer coefficient is low. Indeed, at low heat flux, it is common to reach relative errors higher than 50%. For instance, this was observed for the prediction of the pool boiling heat transfer coefficient in the bottom collector as shown in Figure 6-18. As a result, Figure 6-28 shows that, despite its

underprediction at higher heat flux, the relative error made by the correlation from *Schnabel and Palen* [194] is mainly lower than 20%.

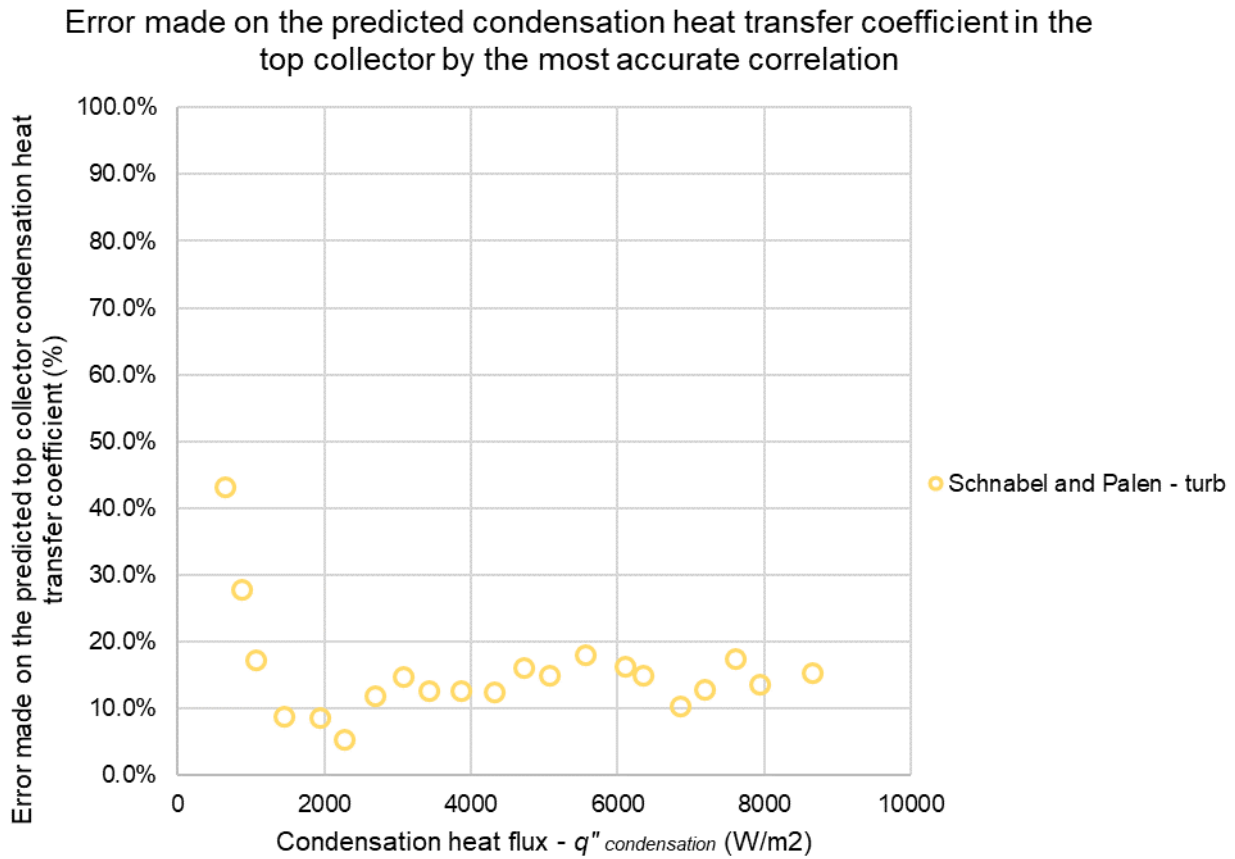


Figure 6-28. Error made on the predicted top collector condensation heat transfer coefficient by the most accurate correlation

At condensation heat flux lower than 1000 W/m<sup>2</sup>, the relative error made by the prediction from *Schnabel and Palen* [194] is contained between 50% and 20%. However, for higher heat fluxes, Figure 6-28 reveals that the relative error remains lower than 20%. Nevertheless, at higher heat flux, the underprediction made by the correlation from *Schnabel and Palen* [194] prevents the error to decrease further. Indeed, as seen in the prediction of the pool boiling heat transfer coefficient, the relative error made by the heat transfer coefficient correlations usually decreases below 10% at high heat flux. However, for the prediction of the condensation heat transfer coefficient, the error fluctuates around 15%. In the studied range of heat transfer, the average error made by the correlation from *Schnabel and Palen* [194] in the prediction of the condensation heat transfer coefficient is acceptable. This is shown in Figure 6-29.



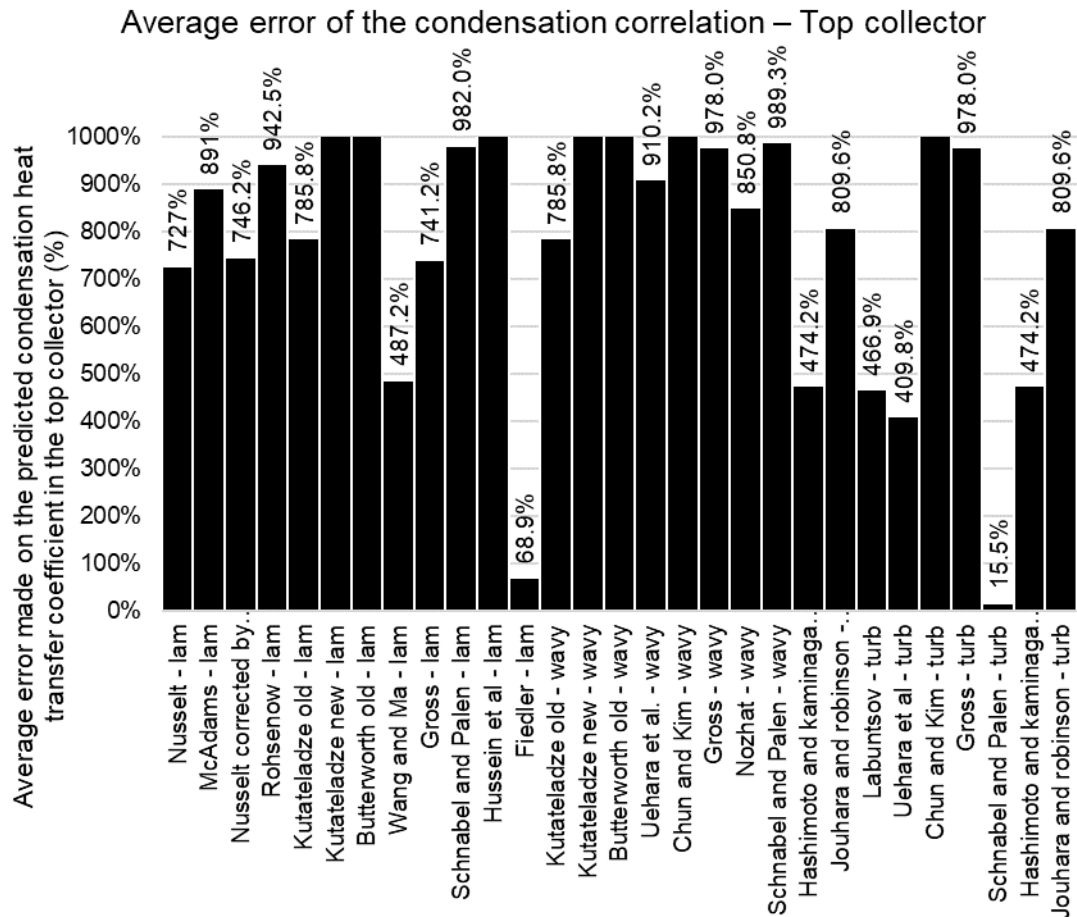


Figure 6-29. Average error of the condensation correlations over the whole range of heat transfer rate – Top collector

Again, Figure 6-29 shows the large discrepancy between the measured condensation heat transfer coefficient of the three-leg heat pipe and most of the reported condensation models. Indeed, compared to the measured condensation heat transfer coefficient, the average error made by 27 of the 29 correlations is higher than 400%. This could indicate that the measured condensation heat transfer coefficient of the three-leg heat pipe is a particular case that differs from other experiments reported in the literature. Regarding the prediction of the correlation from *Schnabel and Palen* [194], over the whole range of heat transfer rate, the average error made while predicting the condensation heat transfer coefficient is 15.5%. This is the only model that was considered suitable to estimate the condensation heat transfer coefficient of the three-leg heat pipe. This correlation was therefore selected and integrated to the developed model to estimate the local condensation heat transfer coefficient at each iteration.

#### 6.1.3.4 Conclusion on optimized correlations for the three-leg heat pipe apparatus

To conclude on the comparison between local heat transfer coefficient measured from the three-leg heat pipe experiments and the available correlations from the literature, the best performing models are listed in this section.

- **Pool boiling heat transfer coefficient:**

To predict the pool boiling heat transfer coefficient in the bottom collector, the best performing correlation are that of *Shiraishi et al.* [148] with an average error of 12.3%, *McNelly* [138], with an error of 16.5%, and *Forster and Zuber* [139] with an error of 18.4%. From the literature, the pool boiling correlation which are usually recommended for the estimation of the pool boiling heat transfer coefficient are that of *Rohsenow* [137], *Imura et al.* [145], *Stephan and Abdelsalam* [147], and *El-Genk and Saber* [1]. In comparison with the measured local pool boiling heat transfer coefficient of the bottom collector, the *Rohsenow* [137] and *Imura et al.* [145] correlations remained fairly accurate and reached average errors of 30.7% and 25.1% respectively. However, the correlations from *Stephan and Abdelsalam* [147], and *El-Genk and Saber* [1] did not perform well and showed average errors higher than 100%.

A similar comparison can be conducted regarding the prediction of the pool boiling heat transfer coefficient in the parallel legs of the three-leg heat pipe. In this case, it was observed that the most performing correlations were that of *Imura et al.* [145] with an average error of 17.4%, *Kiatsiroat et al.* [160] with an error of 14.0%, and *Kutateladze* [153] with an error of 26.9%. The usually recommended correlation from *Imura et al.* [145] clearly stands out here. In comparison, the correlation from *Rohsenow* [137] performed less and reached an average error of 51.6%. Finally, the prediction from the correlation by *Stephan and Abdelsalam* [147], and *El-Genk and Saber* [1] remained poor with errors higher than 76%.

As a conclusion, the pool boiling measurement from the three-leg heat pipe indicate that the usually recommended correlation from *Rohsenow* [137] and *Imura et al.* [145] are reliable to predict the local pool boiling heat transfer coefficient. A clear preference for the *Imura et al.* [145] is observed. Indeed, for both bottom collector and parallel legs, the correlation from *Imura et al.* [145] was able to predict the pool boiling heat transfer coefficient within 25%. However, the correlations from *Stephan and Abdelsalam* [147], and *El-Genk and Saber* [1] did not perform well.

- **Condensation heat transfer coefficient:**

In the case of the three-leg heat pipe experiment, unusual values for the local condensation heat transfer coefficient have been measured. Indeed, the experimental condensation heat transfer coefficient was much lower than the prediction from most of the correlations. The correlation from *Schnabel and Palen* [194] only suits the measured experimental data for the condensation and reaches an average error of 15.5% in its prediction. In comparison, the other available correlations made errors higher than 100%. It is therefore concluded that the condensation results obtained are very different from previously conducted experiments reported in the literature and are not relevant to conclude on the performance of the usually

recommended correlations. However, it clearly highlights how volatile condensation heat transfer coefficients can be.

### 6.1.4 Two-phase model validation – three-leg heat pipe

Based on the experimental data, a theoretical model of the three-leg heat pipe was developed. This theoretical model consists into a new thermal resistance model which can be adapted for all multi-channel heat pipe. The most suitable two-phase correlations were studied, compared to the local heat transfer coefficients, and selected to be integrated to the proposed thermal resistance model. In this section, the iterative model predictions are compared with the experimental data from the three-leg heat pipe. Conclusions are made on the capacity of the developed model to predict the thermal performance of a multi-channel heat pipe.

#### 6.1.4.1 Boiling resistance prediction

After comparing the available pool boiling correlations, the correlation from *Shiraishi et al.* [148] was selected to predict the heat transfer coefficient in the bottom collector whereas, for the parallel legs, the correlation from *Imura et al.* [145] was preferred. When integrated to the three-leg heat pipe model and tested at various heat transfer rates, the heat transfer coefficient prediction displayed in Figure 6-30 is obtained.

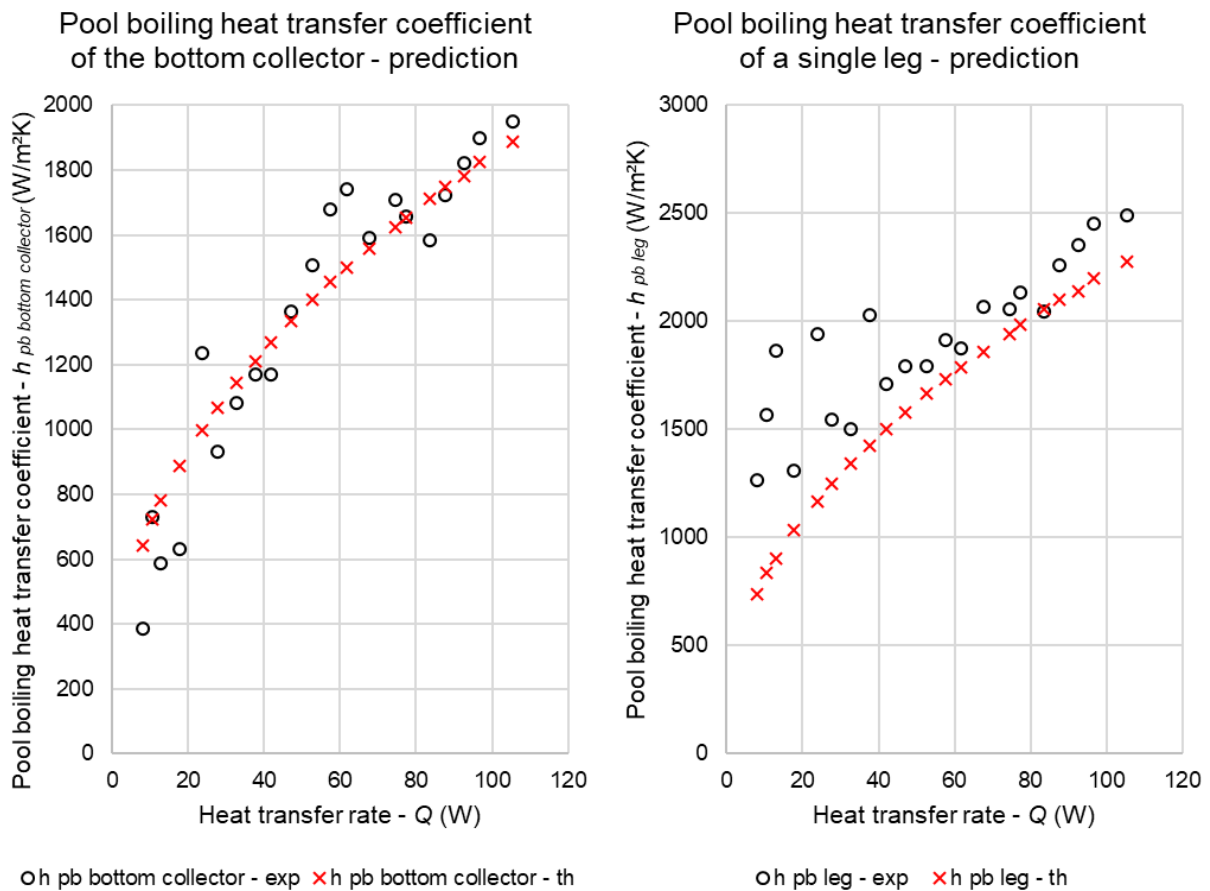


Figure 6-30. Pool boiling heat transfer coefficient prediction – Three-leg heat pipe

The heat transfer coefficient prediction presented in Figure 6-30 is directly linked to the choice of the pool boiling correlation used. For the bottom collector, the correlation from *Shiraishi et al.* [148] closely follows the experimental coefficient of the bottom collector. However, the correlation from *Imura et al.* [145] does not perform as well while predicting the pool boiling heat transfer coefficient in the legs. Indeed, an underprediction of the heat transfer coefficient can be seen at all heat transfer rates. Nevertheless, the increase of the heat transfer coefficient with the heat transfer rate is close to that of the experimental pool boiling heat transfer coefficient of the legs. At higher heat transfer rate, the prediction from *Imura et al.* [145] becomes closer to the experimental value which should result into a low relative error of the prediction. The predicted pool boiling heat transfer coefficients are used at each iteration to calculate the local thermal resistances of the bottom collector and of each parallel leg. After convergence, the predicted local thermal resistances at the three-leg heat pipe evaporator are shown in Figure 6-31.

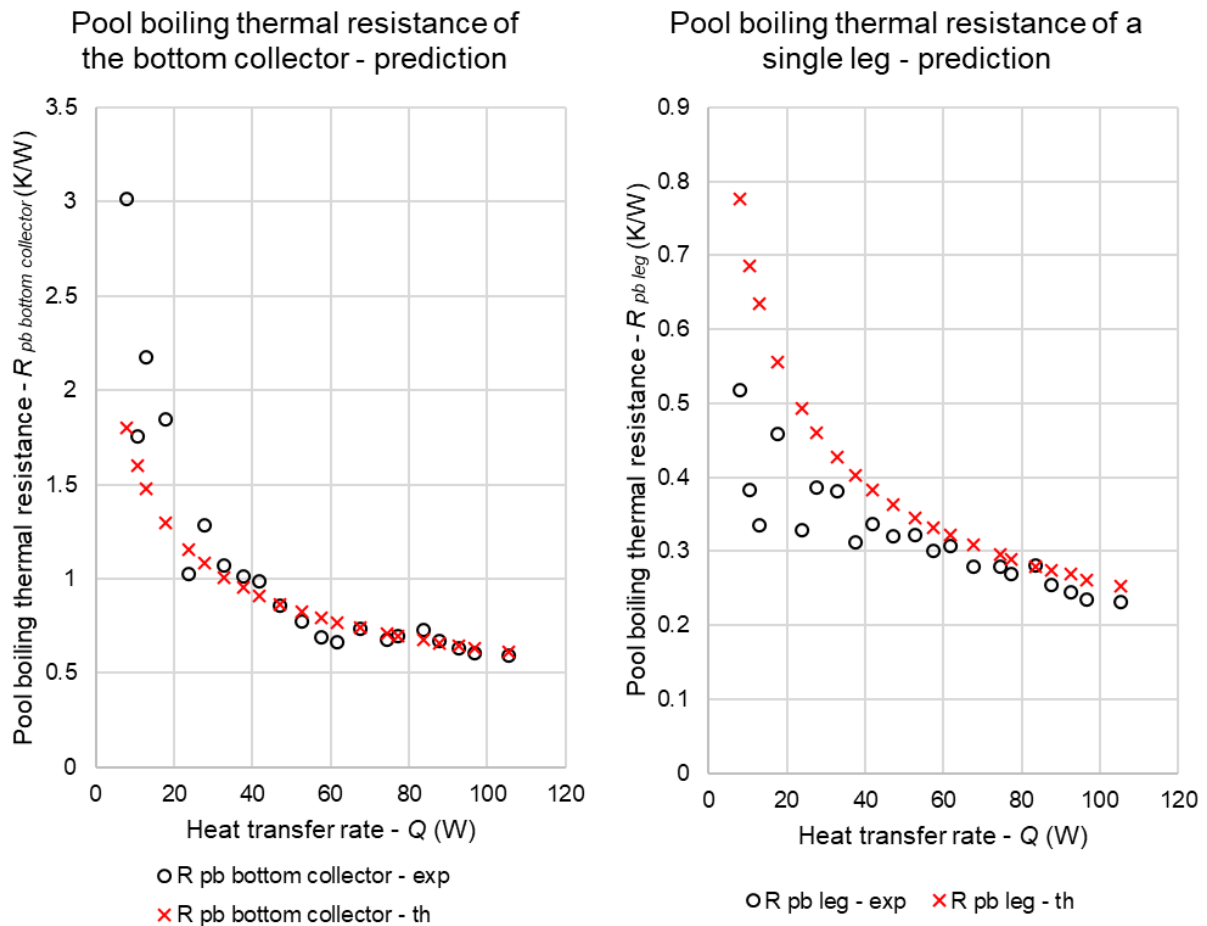


Figure 6-31. Local pool boiling thermal resistances prediction – Three-leg heat pipe

After using the pool boiling heat transfer coefficients to calculate the local thermal resistances, it is observed that the bottom collector thermal resistance is accurately predicted at heat transfer rate higher than 20 W. Below 20 W, a small underprediction of the bottom collector

thermal resistance is observed. Regarding the prediction of the thermal resistance of a single leg, the underpredicted heat transfer coefficient leads to an overprediction of the thermal resistance for almost all the heat transfer rates. If this overestimation is large at low heat transfer rates, from a heat transfer rate of 40 W, the difference with the experimental thermal resistance becomes small. This can be better visualized in Figure 6-32 which presents the error of the prediction for both bottom collector and leg thermal resistances.

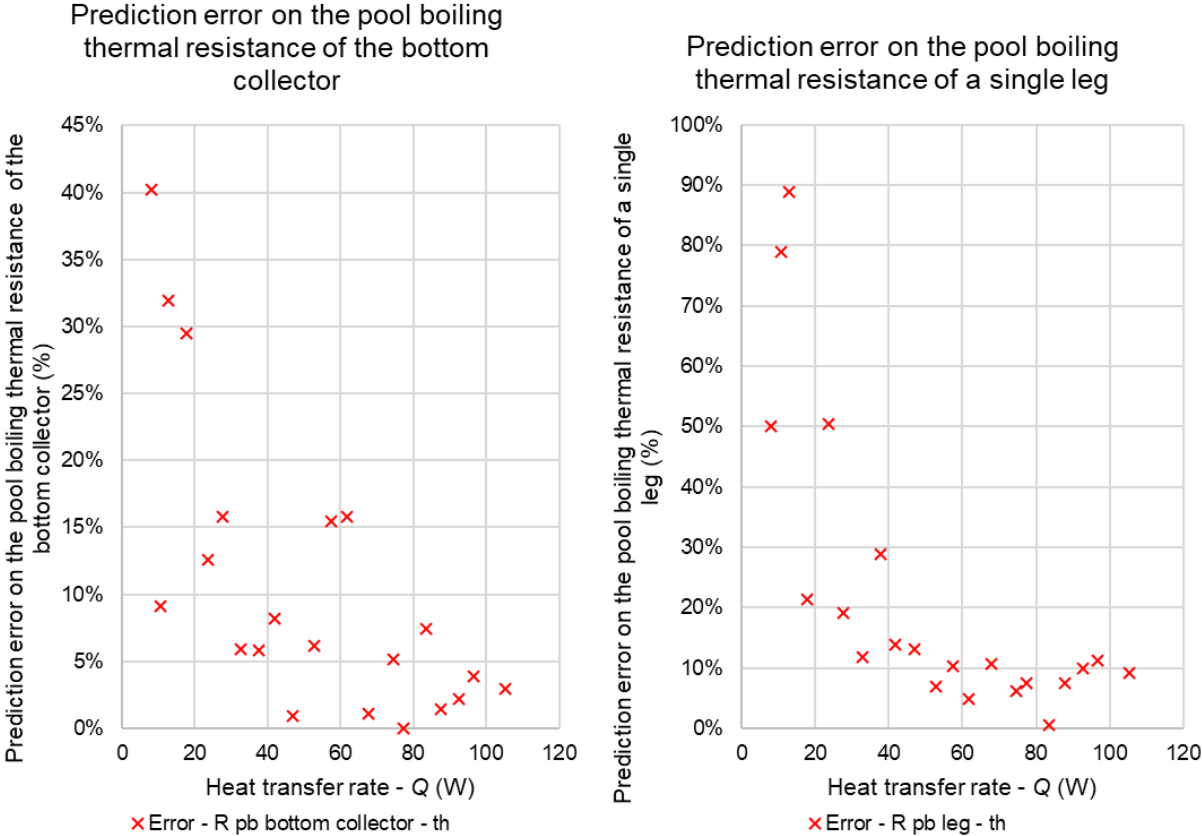


Figure 6-32. Prediction error on the local boiling thermal resistances – Three-leg heat pipe

For both local resistances, it is observed that the error made by the theoretical model is the highest at the lowest heat transfer rates. However, this error is lower in the prediction of the bottom collector thermal resistance than for the leg thermal resistance. Indeed, the bottom collector thermal resistance is predicted with a maximum error of 40% at 10 W whereas this error reaches 90% for the single leg thermal resistance. With an increase of the heat transfer rate, the predictive error decreases quickly and, for both thermal resistances, the error becomes lower than 30% at 30 W. For the prediction of the bottom collector thermal resistance, the error is lower than 16% at heat transfer rates in the range 20 W - 60 W and this error decreases to values lower than 10% at heat transfer rates higher than 70 W. For the prediction of the leg thermal resistance, the error is higher at low heat transfer rates. However, beyond a heat transfer rate of 40 W, the theoretical model error is lower than 20%. By using the proposed thermal resistance model, the local thermal resistances of the three-leg heat pipe evaporator

can be reduced to an equivalent boiling thermal resistance. This equivalent thermal resistance consists into the parallel addition of the bottom collector and parallel legs pool boiling thermal resistances as per the simplification rules of a thermal resistance network. The prediction of the equivalent boiling thermal resistance of the three-leg heat pipe is investigated in Figure 6-33.

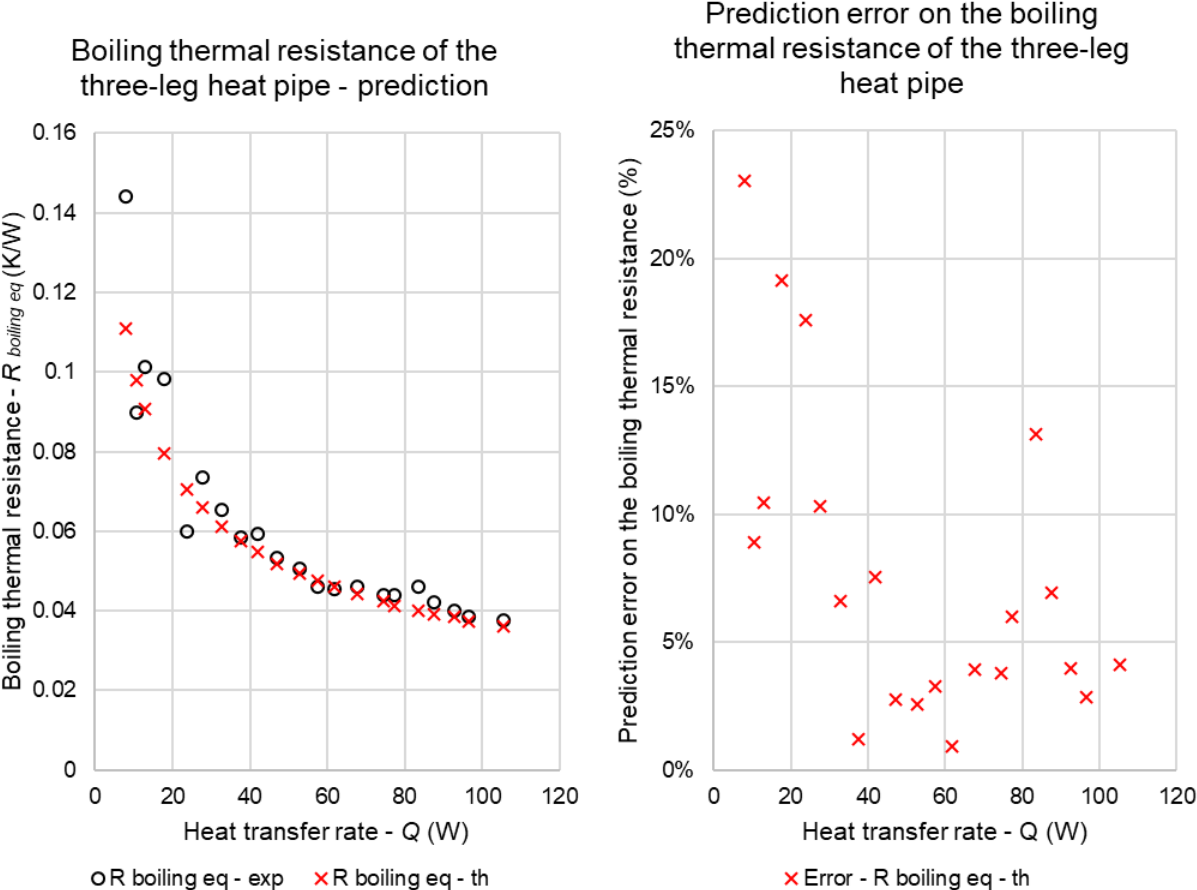


Figure 6-33. Equivalent boiling thermal resistance prediction - Three-leg heat pipe

On the left-hand side of Figure 6-33 is shown the prediction of the boiling thermal resistance of the three-leg heat pipe. By using the proposed thermal resistance model of a multi-channel heat pipe, the equivalent boiling thermal resistance of the three-leg heat pipe was predicted with an error lower than 25% for all heat transfer rates. It can be seen that the theoretical model has the tendency to slightly underpredict the boiling thermal resistance of the three-leg heat pipe. This is mainly due to the underprediction of the leg pool boiling heat transfer coefficient by the *Imura et al.* [145] correlation. The right-hand side of Figure 6-33 reveals that the prediction error is about 20% at heat transfer rates lower than 20W but this error decreases below 10% for heat transfer rates higher than 30 W. Only one data point at ~80 W presents a difference higher than 10% between the experimental data and theoretical model. However, the right-hand side of Figure 6-33 shows that this discrepancy could be due to an inaccuracy of the experiment itself. Indeed, at a heat transfer rate of 80 W, the measured boiling thermal

resistance was higher than that measured at 75 W. Over the whole range of heat transfer rate investigated, the boiling thermal resistance of the three-leg heat pipe was predicted by the theoretical model with an average error of 7.6%.

#### 6.1.4.2 Condensation resistance prediction

For the prediction of the condensation heat transfer coefficient, the correlation from *Schnabel and Palen* [194] was selected to predict both condensation heat transfer coefficient in the parallel legs and in the top collector. Indeed, except for heat transfer rates higher than 70 W, the experimentally measured heat transfer coefficients in the legs and top collector were very close. The prediction of the local condensation heat transfer coefficients is presented in Figure 6-34.

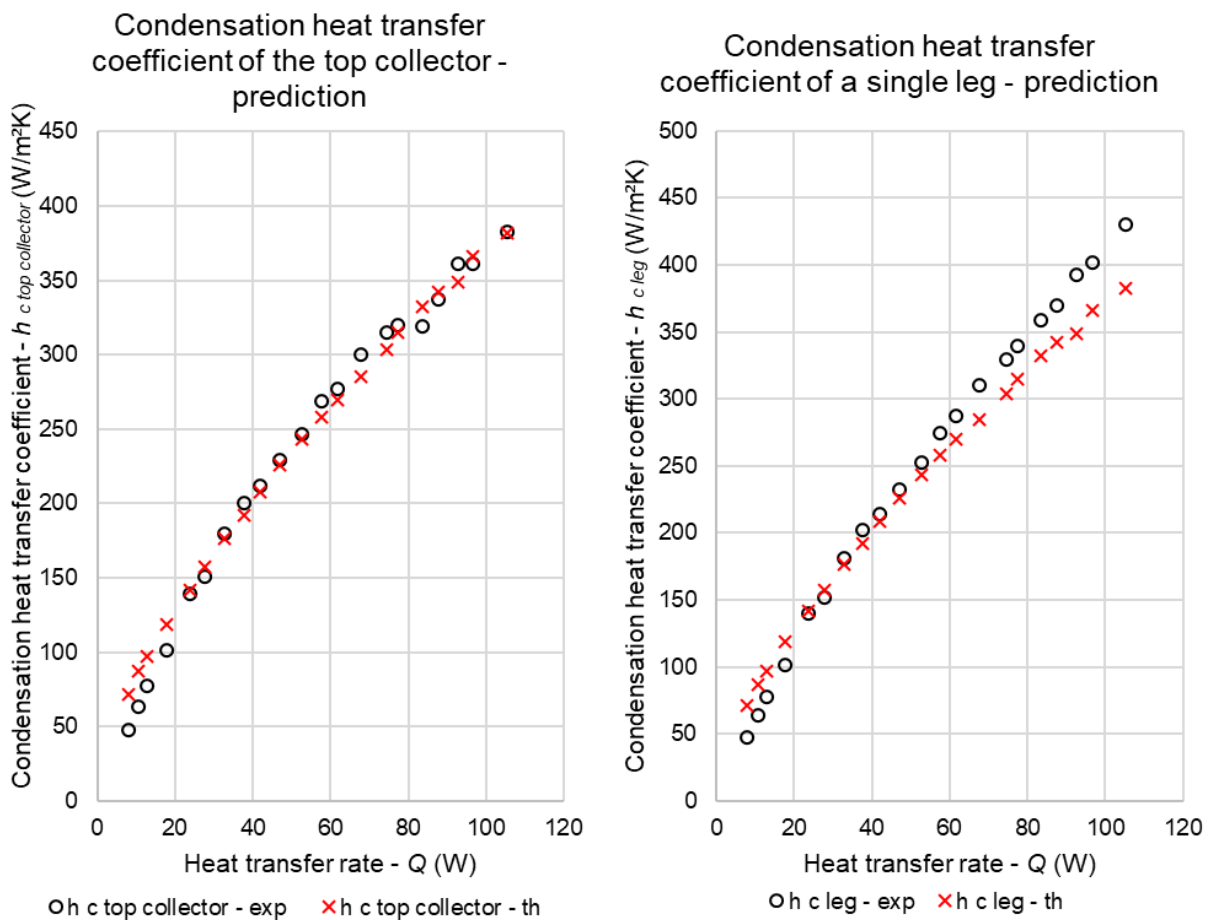


Figure 6-34. Condensation heat transfer coefficient prediction – Three-leg heat pipe

For heat transfer rates lower than 70 W, the experimental heat transfer coefficients at the top collector and in the parallel legs are similar. Hence, in this range of heat transfer rate, the prediction of the local heat transfer coefficients is the same. At heat transfer rate lower than 20 W, the correlation from *Schnabel and Palen* [194] slightly overpredicts the condensation heat transfer coefficient. For heat transfer rates from 20 W to 70 W, the predictions are very close to the measured experimental heat transfer coefficients in both top collector and in the legs.

Yet, at heat transfer rates higher than 70 W, both local heat transfer coefficients must be studied separately. Indeed, at the top collector, the increase of the condensation heat transfer coefficient closely follows the model proposed by *Schnabel and Palen* [194]. However, in the parallel legs, the local condensation heat transfer coefficient increases more than the model which leads to an underprediction of the condensation heat transfer coefficient of the parallel legs. The prediction of the local condensation heat transfer coefficients leads to the estimation of the respective thermal resistances presented in Figure 6-35.

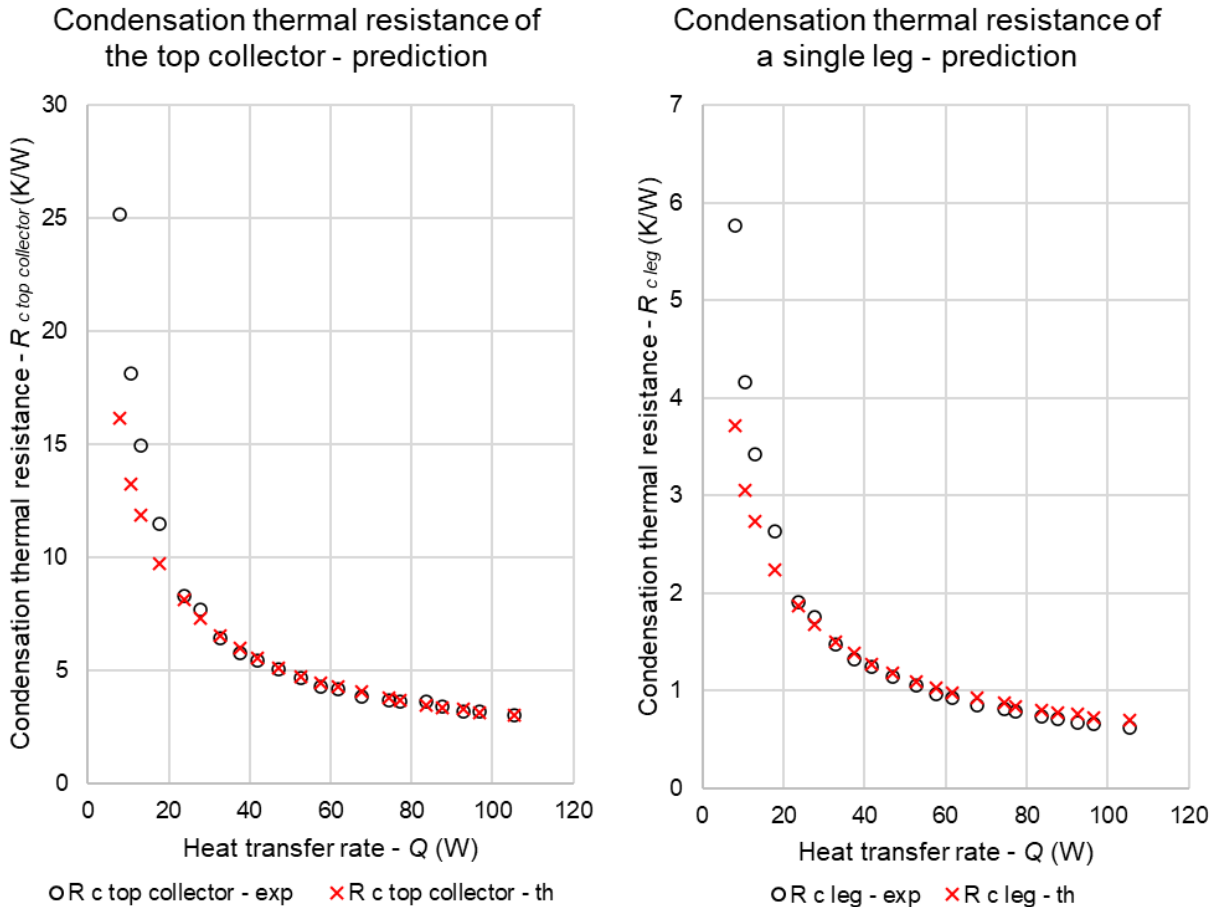


Figure 6-35. Local condensation thermal resistances prediction – Three-leg heat pipe

In agreement with the prediction of the condensation heat transfer coefficient, the prediction of both condensation thermal resistances in the parallel legs and in the top collector is the same below 70 W. The condensation thermal resistances are slightly underpredicted as heat transfer rates lower than 20 W. From 20 W to 70 W, the prediction of the condensation thermal resistances is accurate and closely follows the experimental measurement. Finally, for heat transfer rates higher than 70 W, the prediction of the top collector condensation thermal resistance remains close to the experimental value. However, for the parallel legs, the correlation from *Schnabel and Palen* [194] leads to a small overprediction of the condensation thermal resistance. Nevertheless, the relative error remains low. This is better characterized



in Figure 6-36 which presents the prediction error of the local condensation thermal resistances.

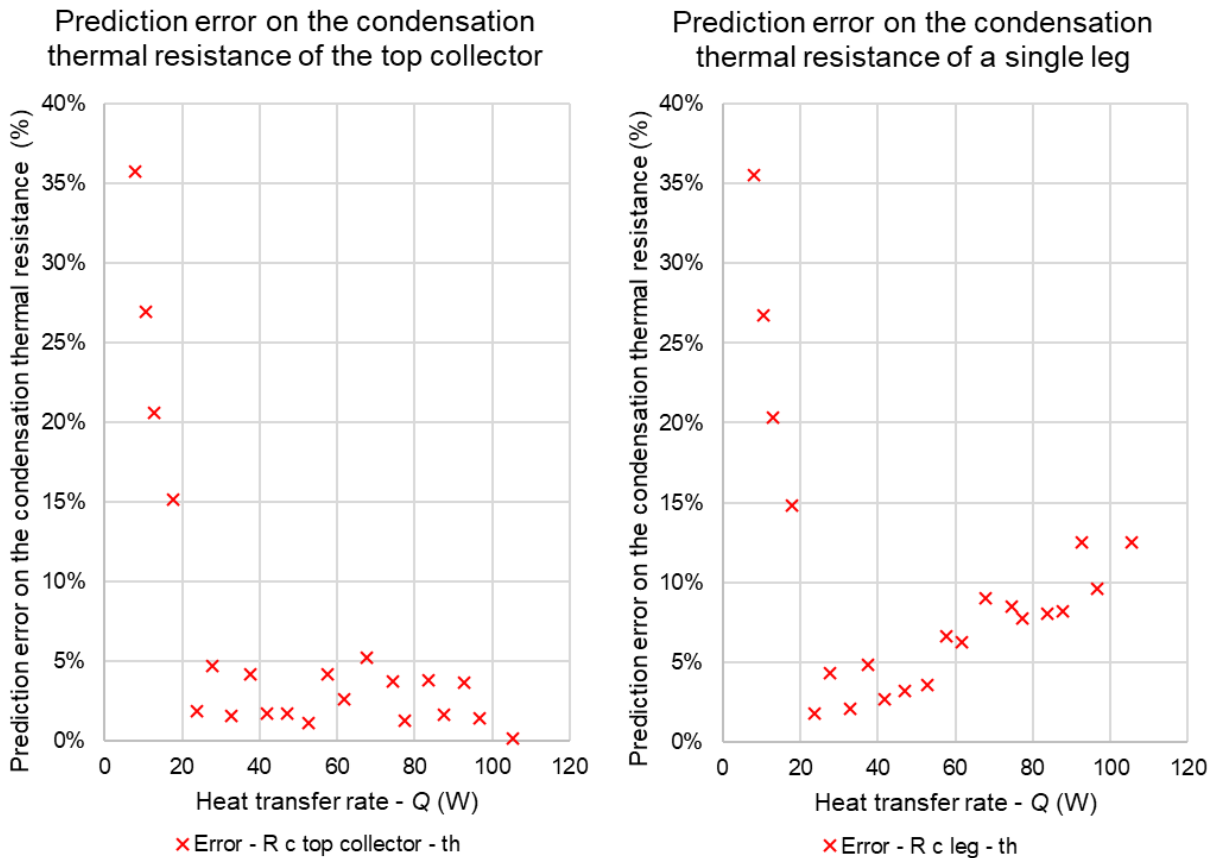


Figure 6-36. Prediction error on the local condensation thermal resistances – Three-leg heat pipe

At heat transfer rates lower than 20 W, the predictive error made by the theoretical model decreases from 35% at 7 W to 15% at 20 W for both thermal resistances. For the top collector, the error made by the theoretical model is very low and, for heat transfer rates in the range 20 W - 110 W, the local condensation thermal resistance is predicted with an error less than 5%. For the parallel legs, the predictive error is lower than 5% at 20 W but progressively increases to 13% at 110 W. This is caused by the underprediction of the condensation heat transfer coefficient by the correlation from *Schnabel and Palen* [194] at higher heat transfer rates. By using the proposed thermal resistance model, the local condensation thermal resistances of the parallel legs and top collector can be used to calculate an equivalent condensation thermal resistance of the three-leg heat pipe. The prediction of the equivalent thermal resistance of condensation in the three-leg heat pipe is presented in Figure 6-37.

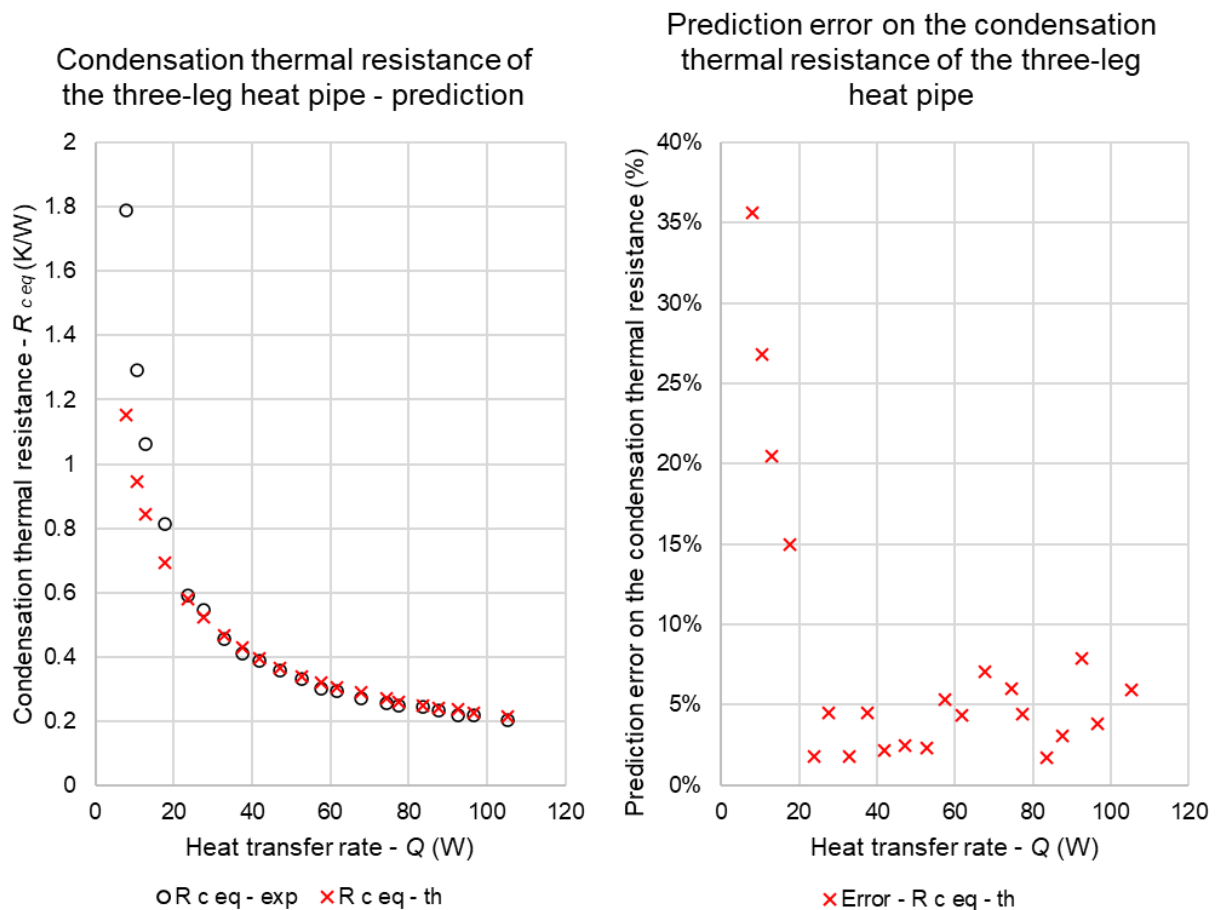


Figure 6-37. Equivalent condensation thermal resistance prediction - Three-leg heat pipe

On the left-hand side of Figure 6-37 is shown the equivalent condensation thermal resistance prediction whereas, on the right-hand side is displayed the predictive error made by the model. It is observed that the equivalent condensation thermal resistance of the three-leg heat pipe is slightly underpredicted at heat transfer rates below 20 W. This results into a predictive error up to 35% at 7 W which decreases to 15% at 20 W. From a heat transfer rate of 20 W, the theoretical model predictions are close to the experimental condensation thermal resistance of the three-leg heat pipe. Indeed, for heat transfer rates in this range, the predictive error is lower than 10%. At high heat transfer rates, a small overprediction of the thermal resistance appears. This leads to a small increase of the prediction's error from 5% at 20 W to values closer to 8% at 110 W. On average, over the whole range of heat transfer rate, the theoretical model predicted the equivalent thermal resistance of condensation with an error of 8.0%.

#### 6.1.4.3 Total three-leg multi-channel heat pipe thermal resistance prediction

To conclude on the accuracy of the proposed theoretical model, the prediction of the total thermal resistance of the three-leg multi-channel heat pipe is studied. To do so, the theoretical model used the proposed multi-channel heat pipe thermal resistance network to sum the local thermal resistances of conduction, pool boiling, and condensation obtained at the end of the

iterations. This prediction from the theoretical model is compared to the total three-leg heat pipe thermal resistance and shown in Figure 6-38.

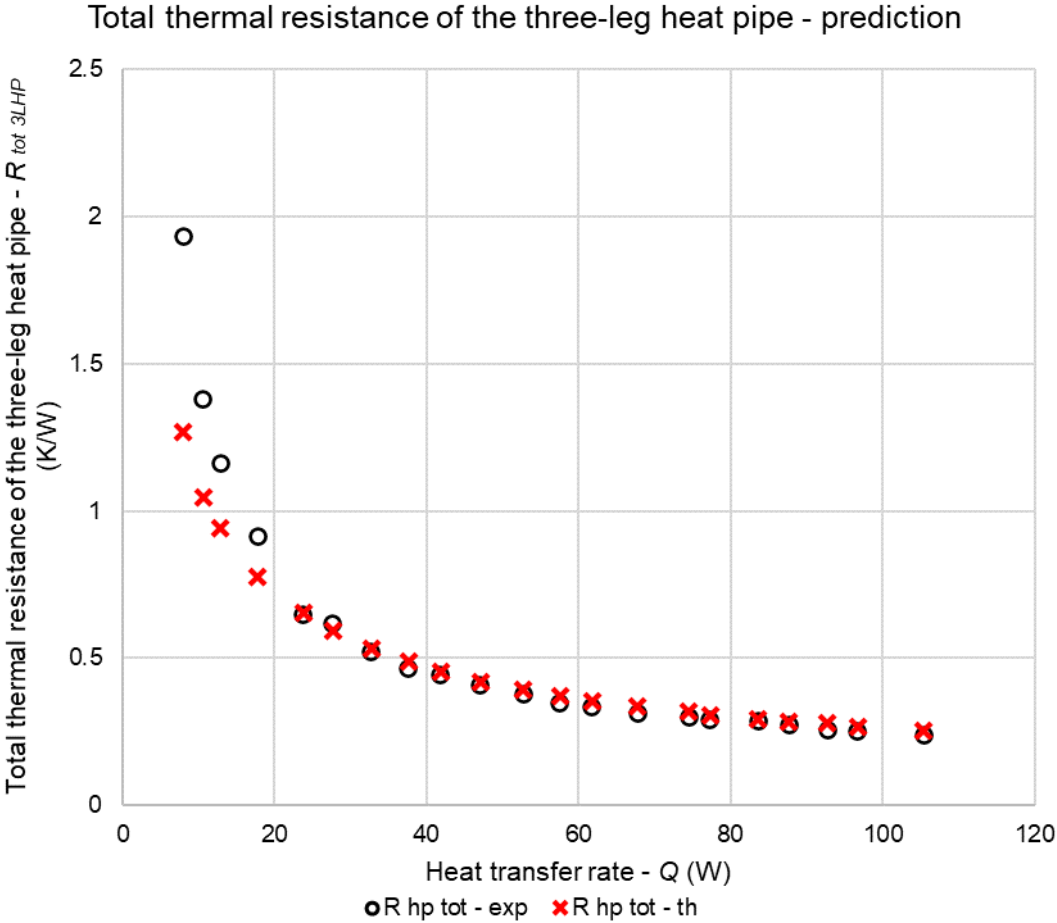


Figure 6-38. Total three-leg multi-channel heat pipe thermal resistance prediction

In Figure 6-38, the experimental three-leg heat pipe total thermal resistance is displayed with circular black markers whereas the predictions from the theoretical model are shown with red crosses. It is observed that the theoretical model prediction is close to the experimental values. However, at low heat transfer rates, the model accuracy is lower. Indeed, at a heat transfer rate of 8 W, the three-leg heat pipe total resistance is 1.93 K/W whereas the prediction is 1.27 K/W. For heat transfer rates in the range 5 W - 20 W, the model underpredicts the total three-leg heat pipe thermal resistance. This is directly linked to the underprediction of the condensation thermal resistance of the three-leg heat pipe presented in Figure 6-37. Indeed, as shown in Figure 6-7, the condensation thermal resistance represents about 85-90% of the total thermal resistance of the three-leg heat pipe. As such, the prediction of the condensation thermal resistance of the three-leg heat pipe is more significant than that of the boiling thermal resistance. This explains why the prediction of the total three-leg heat pipe thermal resistance is close to that of the condensation thermal resistance. At heat transfer rates higher than 20 W, the theoretical model predictions are close to the experimental values and the relative error

is small. The error made by the proposed theoretical model while estimating the total thermal resistance of the three-leg heat pipe is shown in Figure 6-39.

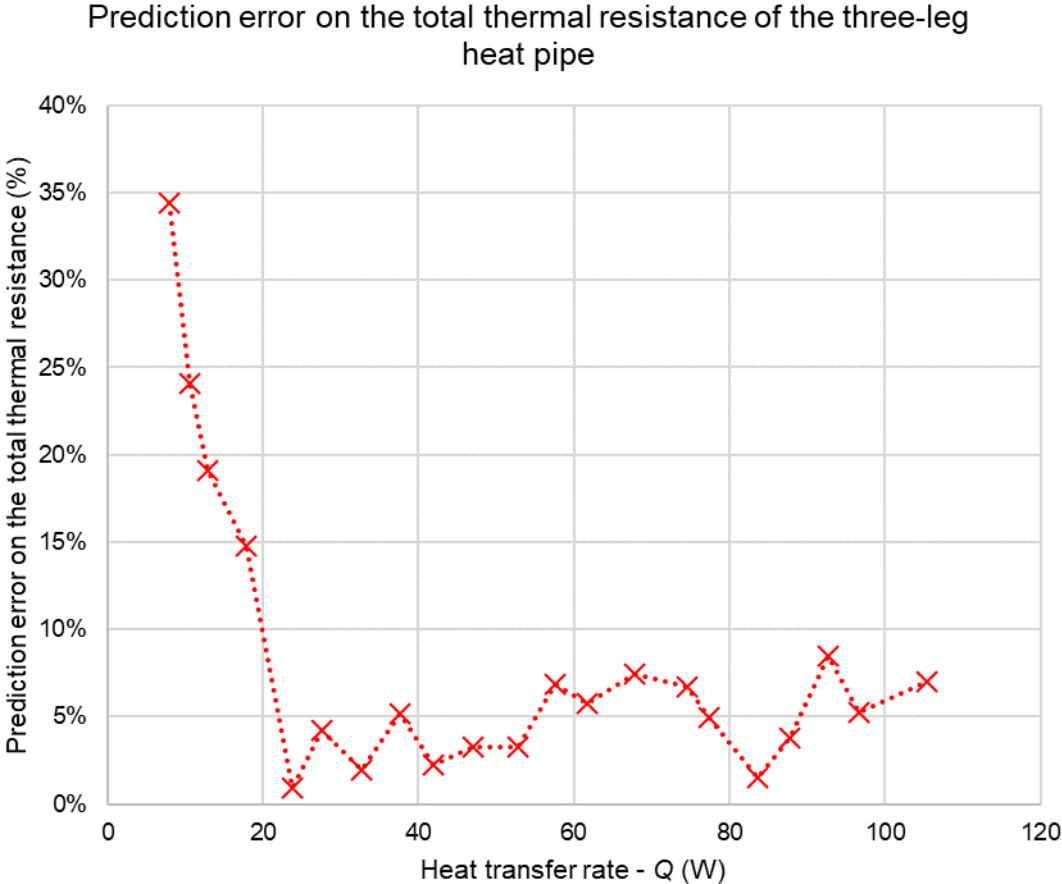


Figure 6-39. Prediction error on the total three-leg multi-channel heat pipe thermal resistance

From Figure 6-39, it can be noted that the prediction error made on the estimation of the total thermal resistance has a similar profile as the estimation of the condensation thermal resistance. From a heat transfer rate of 8 W to 18 W, the theoretical model error on the prediction of the total three-leg heat pipe decreases from 34% to 15%. Then, for heat transfer rates higher than 20 W, the relative error of the prediction remains lower than 10%. It is observed that the prediction of the three-leg heat pipe total thermal resistance is the most accurate between 20 W and 40 W, and slightly increases at higher heat transfer rates. Over the whole range of heat transfer rates investigated, the average error made by the theoretical model while predicting the total thermal resistance of the three-leg heat pipe is 8.2%. It is therefore concluded that the proposed iterative model is able to predict the thermal performance of a multi-channel heat pipe using theory. The proposed thermal resistance network of a multi-channel heat pipe will therefore be used to predict the performance of the multi-channel flat heat pipe which can be used for surface cooling application.

## 6.2 Multi-channel flat heat pipe apparatus

### 6.2.1 Impact of the heat transfer rate on the thermal performance of the multi-channel flat heat pipe

While operating under different solar irradiation, the heat transfer rate from the photovoltaic panel to the multi-channel flat heat pipe varies within a range of 0-1500 W. Due to the change in the boiling and condensation patterns observed in the case of common thermosyphons, the performance of the multi-channel flat heat pipe, i.e., its thermal resistance, is expected to change with a change of heat transfer rate. In this section, the influence of the heat transfer rate on the thermal resistances of the R134a multi-channel flat heat pipe is studied. For this investigation, the flat heat pipe was placed in a vertical position and three cooling water flow rates of 2 L/min, 4 L/min, and 6 L/min were used. A total of 180 experiments was achieved in the objective of improving the result accuracy.

#### 6.2.1.1 Boiling thermal resistance

In Figure 6-40 below is presented the impact of the heat transfer rate on the boiling resistance of the R134a multi-channel flat heat pipe.

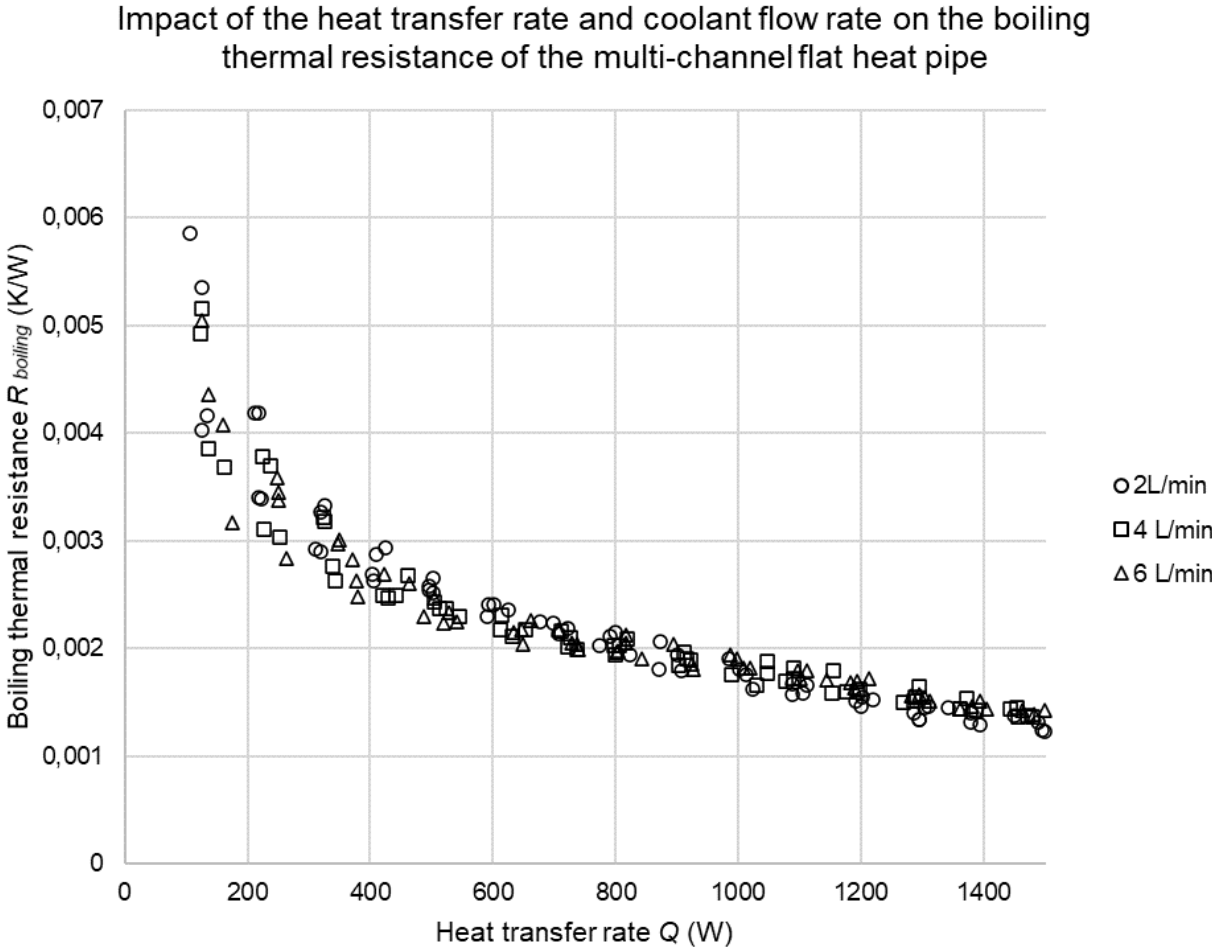


Figure 6-40. Impact of the heat transfer rate and coolant flow rate on the boiling thermal resistance of the multi-channel flat heat pipe

The experiments during which the cooling water flow rate was 2 L/min, 4 L/min, and 6 L/min are represented by circles, squares, and triangles respectively. As expected, it is observed that the coolant flow rate has no impact on the boiling thermal resistance of the multi-channel flat heat pipe. Indeed, increasing the coolant flow rate improves the forced convective heat transfer coefficient inside the cooling manifold which leads to an overall decrease of the temperature of the assembly. However, at equivalent heat transfer rate, the temperature difference between the evaporator and the adiabatic section remains unchanged. Thus, in Figure 6-40, no influence of the coolant flow rate on the boiling thermal resistance of the multi-channel flat heat pipe is detected.

Regarding the impact of the heat transfer rate on the boiling thermal resistance of the multi-channel flat heat pipe, at heat transfer rates up to 1500 W, the boiling thermal resistance keeps decreasing. Yet, at low heat transfer rates in the range 0-400 W, it is noted that the boiling thermal resistance of the multi-channel flat heat pipe is higher, with a boiling thermal resistance of 0.005 K/W at a heat transfer rate of 100 W, whereas it drops down to 0.003 K/W at 400 W. This higher boiling thermal resistance at low heat transfer rate can be explained by the nature of the pool boiling regime. At such heat transfer rates, it seems that the pool boiling regime inside the multi-channel heat pipe belongs to the natural convection boiling regime and transits towards the fully developed nucleate boiling regime, thus, increasing the pool boiling heat transfer coefficient and decreasing the respective thermal resistance. At heat transfer rates around 400 W - 500 W, a transition is observed, and the boiling thermal resistance starts decreasing slower. Beyond 500 W, it looks like the pool boiling regime inside the multi-channel heat pipe belongs to the nucleate boiling regime, with a boiling resistance progressively decreasing with an increase of the boiling activity. At a heat transfer rate of 1500 W, the boiling thermal resistance of the multi-channel flat heat pipe is 0.0014 K/W.

#### *6.2.1.2 Condensation thermal resistance*

Unlike the evaporator section where all the thermocouples showed similar readings, at the condenser section, the temperature uniformity wasn't as obvious. Indeed, the thermocouples LB1 and LB2 (designated as LB in the following) placed at the left of the condenser section showed lower temperatures than the thermocouples RB1 and RB2 (designated as RB in the following) placed on the right. In Figure 6-41 is presented the temperature difference between the thermocouples LB and RB.

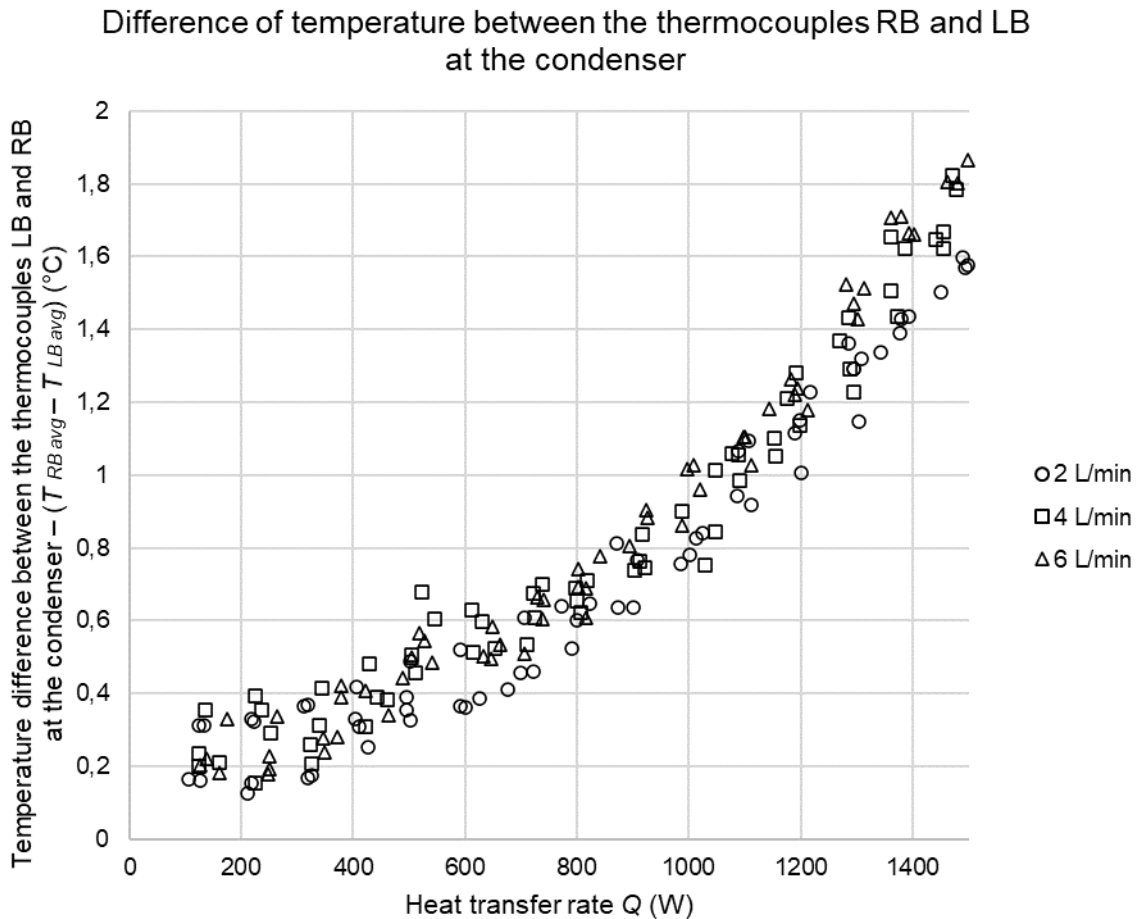


Figure 6-41. Difference of temperature between the thermocouples RB and LB at the condenser

With an increase of the heat transfer rate, it is observed that the difference of temperature between the thermocouples RB placed on the right of the condenser section and the thermocouples LB placed on the left of the condenser section increases. At first, this difference of temperature between the left and right side of the condenser section was assumed to be caused by the cooling water warming up inside the cooling manifold. Indeed, as the water absorbs thermal energy from the heat pipe, its temperature inside the cooling manifold increases and can lead to a non-uniform cooling of the condenser section. However, in the case where the warming of the cooling water inside the manifold would be responsible for the difference of temperature observed at the condenser section, this phenomenon is expected to be more significant at lower coolant flow rates where the difference of cooling water temperature between the inlet and outlet is the highest. Yet, this isn't verified in Figure 6-41 and the difference between the left and the right zones of the condenser section seems to be slightly lower at a coolant flow rate of 2 L/min.

A second factor which may be responsible of the temperature difference observed between the left and right side of the condenser section is the proximity with the cooling water inlet. As the left thermocouples are closer to the cold water inlet, their temperature measurements may

be slightly lower. In order to better understand and explain this temperature difference observed at the condenser section during those experiments, infrared imaging of this section of the flat heat pipe have been taken and are presented later in this chapter.

Due to the low value of condensation thermal resistance, the difference of temperature between the left and right sides of the condenser implies different potential values of the condensation thermal resistance of the multi-channel flat heat pipe. In Figure 6-42 are presented the condensation thermal resistances of the multi-channel flat heat pipe calculated from the left thermocouples LB, the right thermocouples RB, and the average of all the thermocouples of the condenser section.

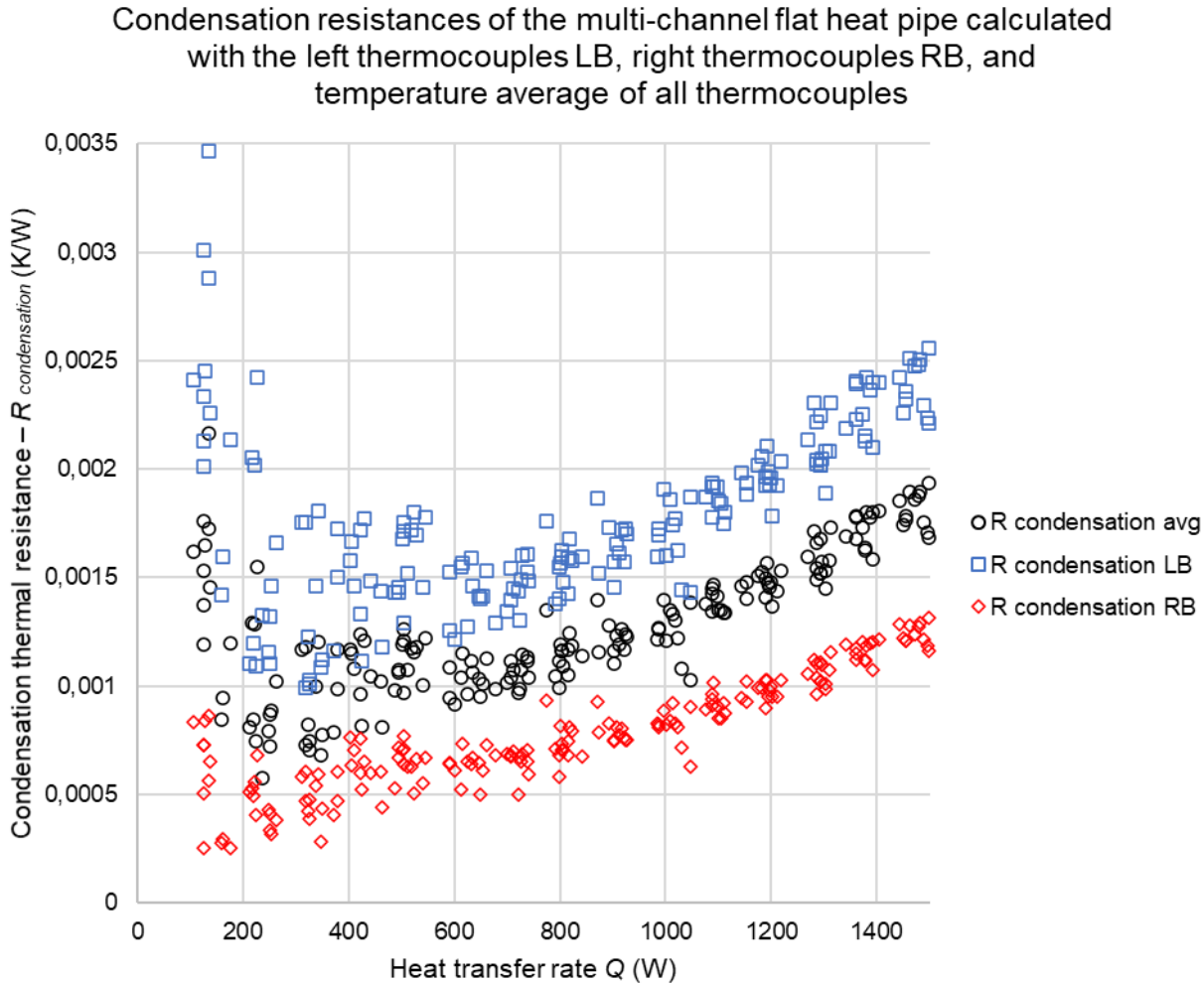


Figure 6-42. Condensation thermal resistances of the multi-channel flat heat pipe calculated with the left thermocouples LB, right thermocouples RB and temperature average of all the thermocouples

In Figure 6-42, the condensation thermal resistance calculated with the left thermocouples LB is represented by blue squares dots. The condensation thermal resistance calculated with the right thermocouples RB is represented by red diamonds dots and the condensation thermal resistance calculated with the average of both left and right thermocouples is represented by



black circular markers. Based on the temperature difference observed between the right and left side of the condenser section, the condensation thermal resistance calculated with the thermocouples on the left is twice the thermal resistance calculated with the thermocouples on the right. At low heat transfer rates, the experimental data is more scattered which is explained by a higher thermocouple's uncertainty due to the low temperature difference between the condenser and adiabatic section. Yet, it seems that the experimental results of the left thermocouples LB are more scattered than those of the right thermocouples RB. In both cases, a similar trend is observed with an increasing condensation thermal resistance with the heat transfer rate. This increase of the condensation thermal resistance is common for heat pipes and thermosyphons and can be explained by the increase of the condensate thickness at higher heat transfer rates. In the case of the condensation thermal resistance calculated with the left thermocouples, the condensation thermal resistance seems to be the highest at very low heat transfer rates, and then, decreases sharply from 0.003 K/W at 100 W to a minimum value of 0.0012 K/W at 400 W. This thermal resistance then increases progressively up to 0.0025 K/W at 1500 W. As for the condensation thermal resistance calculated with the thermocouples on the right, the condensation thermal resistance remains very low at low heat transfer rates. From 100 W to 400 W, the condensation thermal resistance seems to stagnate around a value of 0.0006 K/W. Beyond this range of heat transfer rates, and similarly to the thermocouples on the left, the condensation thermal resistance progressively increases up to 0.00125 K/W at a heat transfer rate of 1500 W.

Because no obvious reason justifies that one reading is more valid than the other, despite some noticeable differences, both left and right thermocouples have been considered to estimate the average condensation thermal resistance of the multi-channel flat heat pipe. This assumption is later validated with the infrared imaging of the multi-channel flat heat pipe condenser's section.

The impact of the cooling water flow rate on the average condensation thermal resistance was also investigated and is presented in Figure 6-43.

Impact of the heat transfer rate and coolant flow rate on the condensation thermal resistance of the multi-channel flat heat pipe

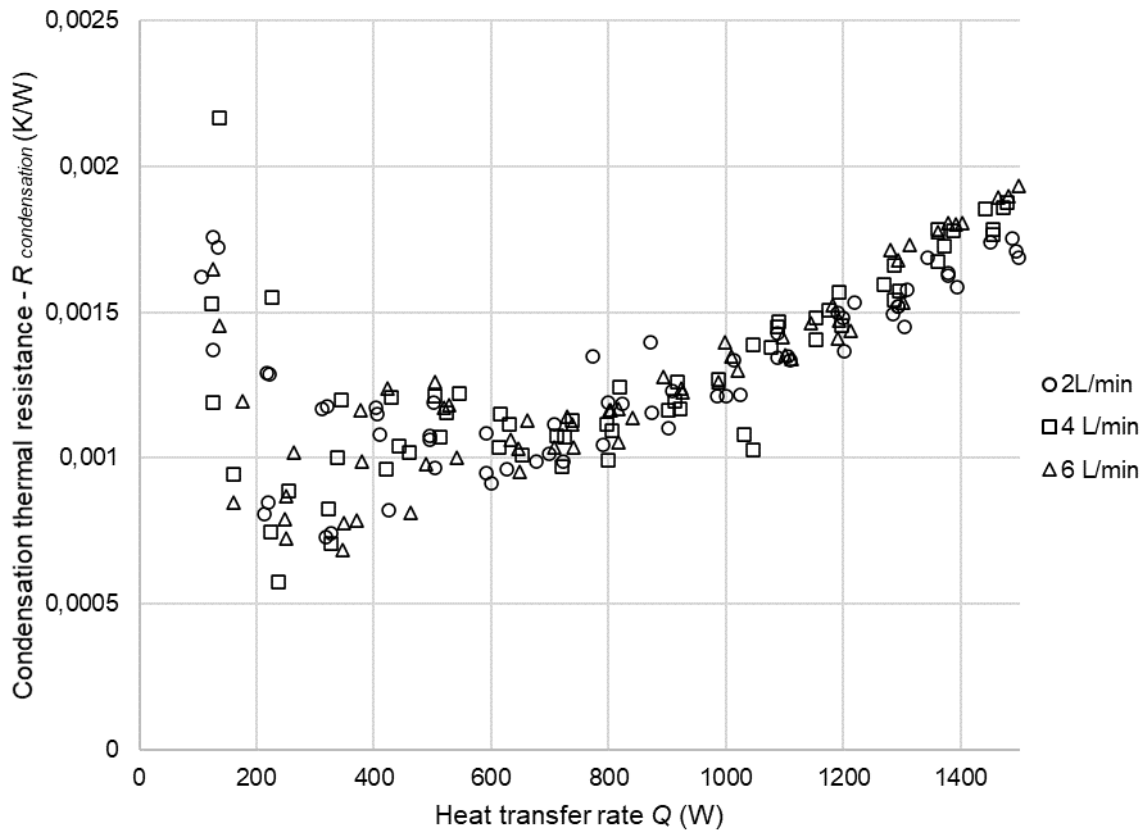


Figure 6-43. Impact of the heat transfer rate and coolant flow rate on the condensation thermal resistance of the multi-channel flat heat pipe

From Figure 6-43, one can note that the cooling water flow rate inside the manifold has no noticeable impact on the condensation thermal resistance. This is observed on the average condensation thermal resistance but was also observed on the condensation thermal resistances calculated from the right or left thermocouples. On the average condensation thermal resistance of the multi-channel flat heat pipe, the condensation thermal resistance decreases from 0.0015 K/W at a heat transfer rate of 100 W to a value slightly lower than 0.001 K/W at 200 W. Between 200 W and 600 W, the condensation thermal resistance results are scattered but seem to fluctuate around 0.001 K/W. From a heat transfer rate of 600W, the standard deviation between the different condensation thermal resistance values significantly decreases and the overall trend seems more obvious. With an increase of the heat transfer rate, the mass transfer from the vapour phase to the liquid phase at the condenser increases, and, as a result, the thickness of the condensate increases too. This results in a progressive increase of the condensation thermal resistance of the multi-channel flat heat pipe, from 0.001 K/W at 600 W, to a maximum value of 0.0019 K/W at 1500W.

### 6.2.1.3 Total thermal resistance

In the previous sections, it can be noted that the values of boiling and condensation thermal resistance can be significantly different. Thus, depending on the heat transfer rate, one resistance can be largely predominant compared to the other. For instance, at a heat transfer rate of 100 W, the boiling thermal resistance is almost 5 times that of condensation. In Figure 6-44 is presented the share of each thermal resistance in the total thermal resistance of the multi-channel flat heat pipe.

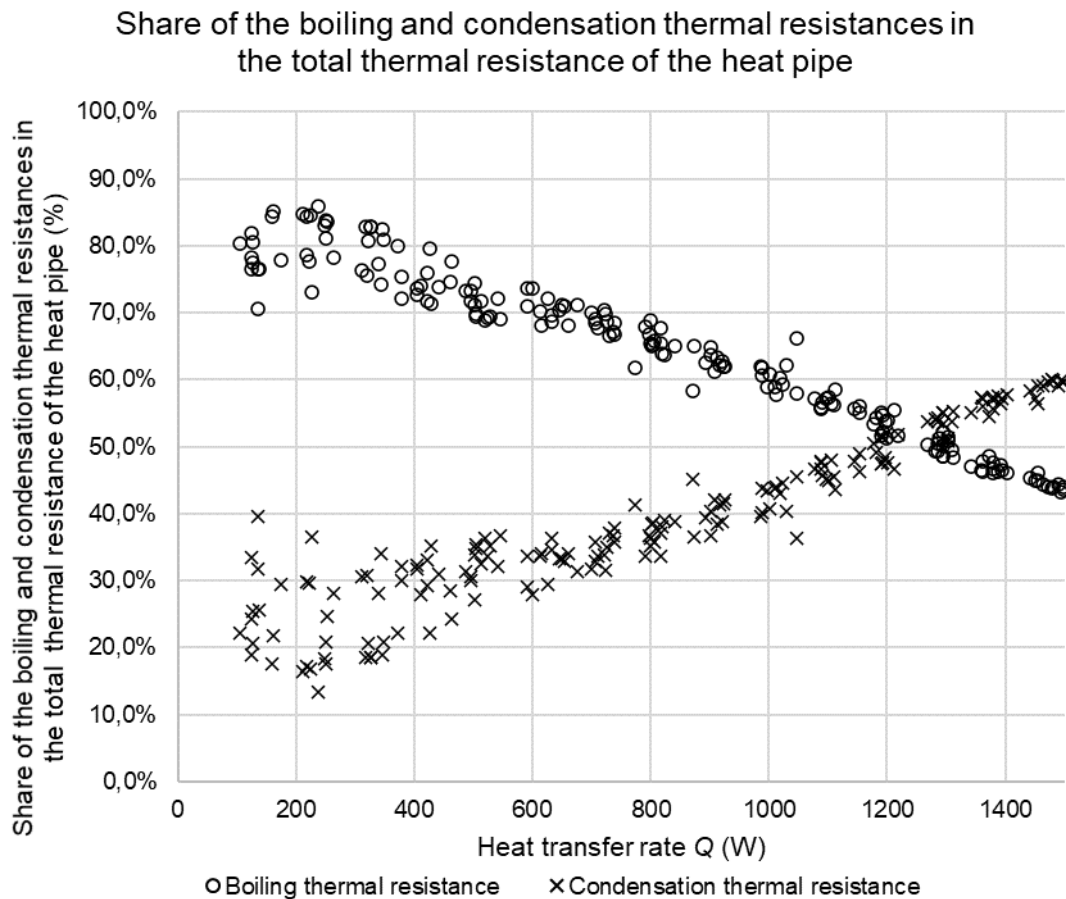


Figure 6-44. Share of the boiling and condensation thermal resistances in the total thermal resistance of the multi-channel flat heat pipe

In Figure 6-44, the circular markers represent the share of the boiling thermal resistance whereas the cross markers represent the share of the condensation thermal resistance in the total thermal resistance of the multi-channel flat heat pipe. At low heat transfer rate, the boiling thermal resistance largely predominates and represents no less than 80% of the total thermal resistance of the multi-channel flat heat pipe at a heat transfer of 200 W. With an increase of the heat transfer, the decrease of the boiling thermal resistance due to the increased boiling activity on one side, and the increase of the condensation thermal resistance due to a thicker condensate layer on the other side, progressively change this ratio. The condensation thermal resistance becomes more and more significant with an increase of the heat transfer rate, and,

at a heat transfer rate of 1200 W, the condensation thermal resistance becomes as high as the boiling thermal resistance of the multi-channel flat heat pipe. At higher heat transfer rates, the condensation thermal resistance becomes predominant and is responsible of 60% of the total thermal resistance of the multi-channel flat heat pipe at a maximum heat transfer rate of 1500 W. The total thermal resistance of the multi-channel flat heat pipe is presented in Figure 6-45.

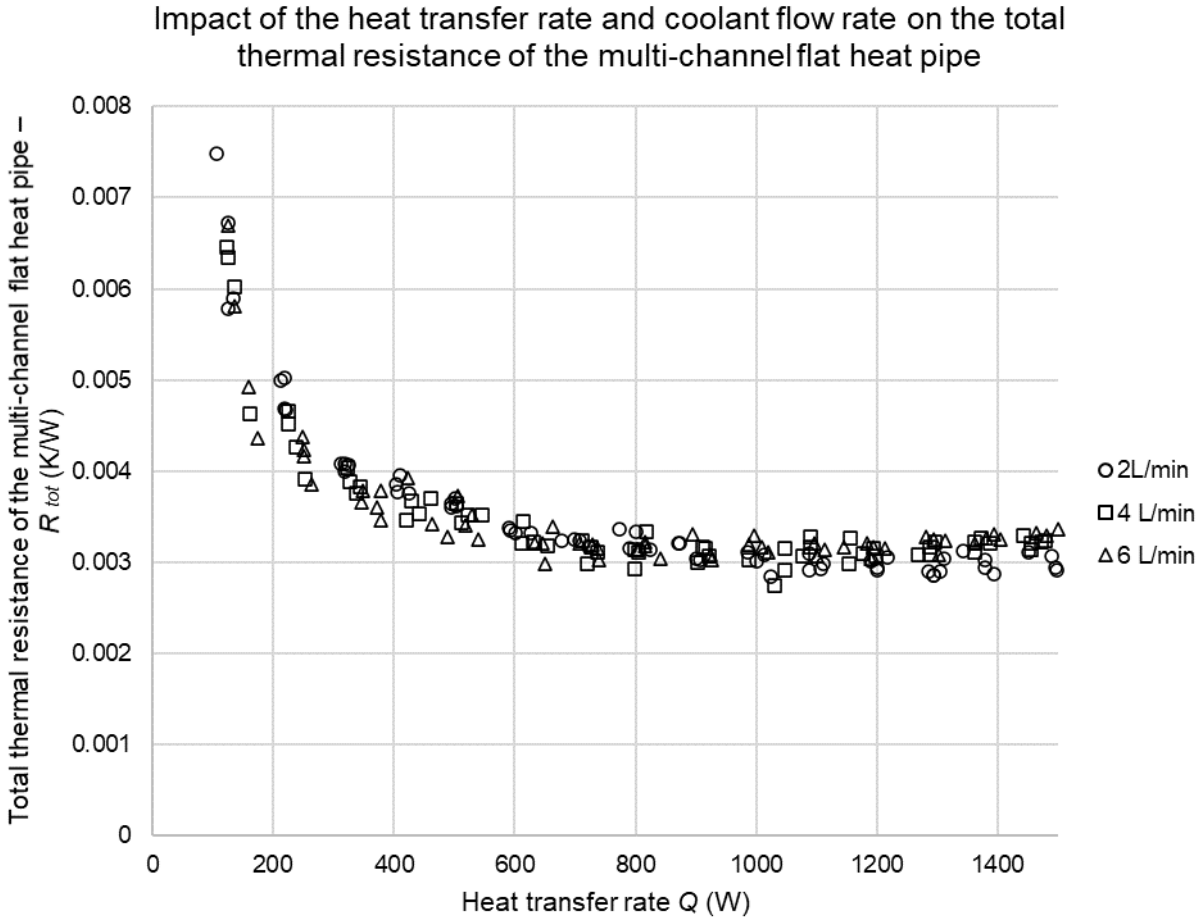


Figure 6-45. Impact of the heat transfer rate and coolant flow rate on the total thermal resistance of the multi-channel flat heat pipe

Due to the high values of boiling thermal resistance at low heat transfer rates, the total thermal resistance of the multi-channel flat heat pipe reaches its maximum value at the lowest heat transfer rate. At a heat transfer rate of 100 W, the thermal resistance of the multi-channel flat heat pipe is about 0.0065 K/W which is 80% due to the boiling thermal resistance. With the transition to the fully developed nucleate pool boiling regime, the total thermal resistance of the heat pipe sharply decreases to 0.004 K/W at a heat transfer rate of 400 W. Between 400W and 800 W, the total thermal resistance of the heat pipe slowly decreases and then stagnates from 800 W to 1200 W at its minimum value of 0.003 K/W. In this optimum region, the condensation thermal resistance progressively increases and, at 1200 W, becomes as

important as the boiling thermal resistance. Beyond a heat transfer rate of 1200 W, the total thermal resistance of the multi-channel flat heat pipe starts to increase progressively due to the increase of the condensation thermal resistance. Yet, at a maximum heat transfer rate of 1500 W, the thermal resistance of the multi-channel flat heat pipe is still relatively low and reaches a value of 0.0033 K/W. Figure 6-45 also shows that the optimum heat transfer range of the studied multi-channel flat heat pipe is 300W-1500W where the thermal resistance of the multi-channel flat heat pipe is always lower than 0.004 K/W. This is a heat transfer rate range often met during PV/T applications of the flat heat pipe.

## **6.2.2 Identification of the optimized two-phase correlations**

In the objective of improving the predictions made by the multi-channel flat heat pipe model developed, the two-phase correlations need to be optimized. Indeed, many correlations for pool boiling and condensation have been reported in the literature but show drastic differences. Hence, in this section, the available pool boiling, and condensation correlations have been compared with experimental data in order to select the most accurate ones to be included in the developed multi-channel flat heat pipe model.

### *6.2.2.1 Optimized pool boiling correlation.*

In Figure 6-46 are presented the available predictions of the pool boiling heat transfer coefficient with a change of boiling heat flux. As an indication, the equivalent heat transfer rate is also indicated on a second horizontal axis. The different correlations are compared with the experimental data displayed with black dots.

Pool boiling heat transfer coefficient with the boiling heat flux and heat transfer rate

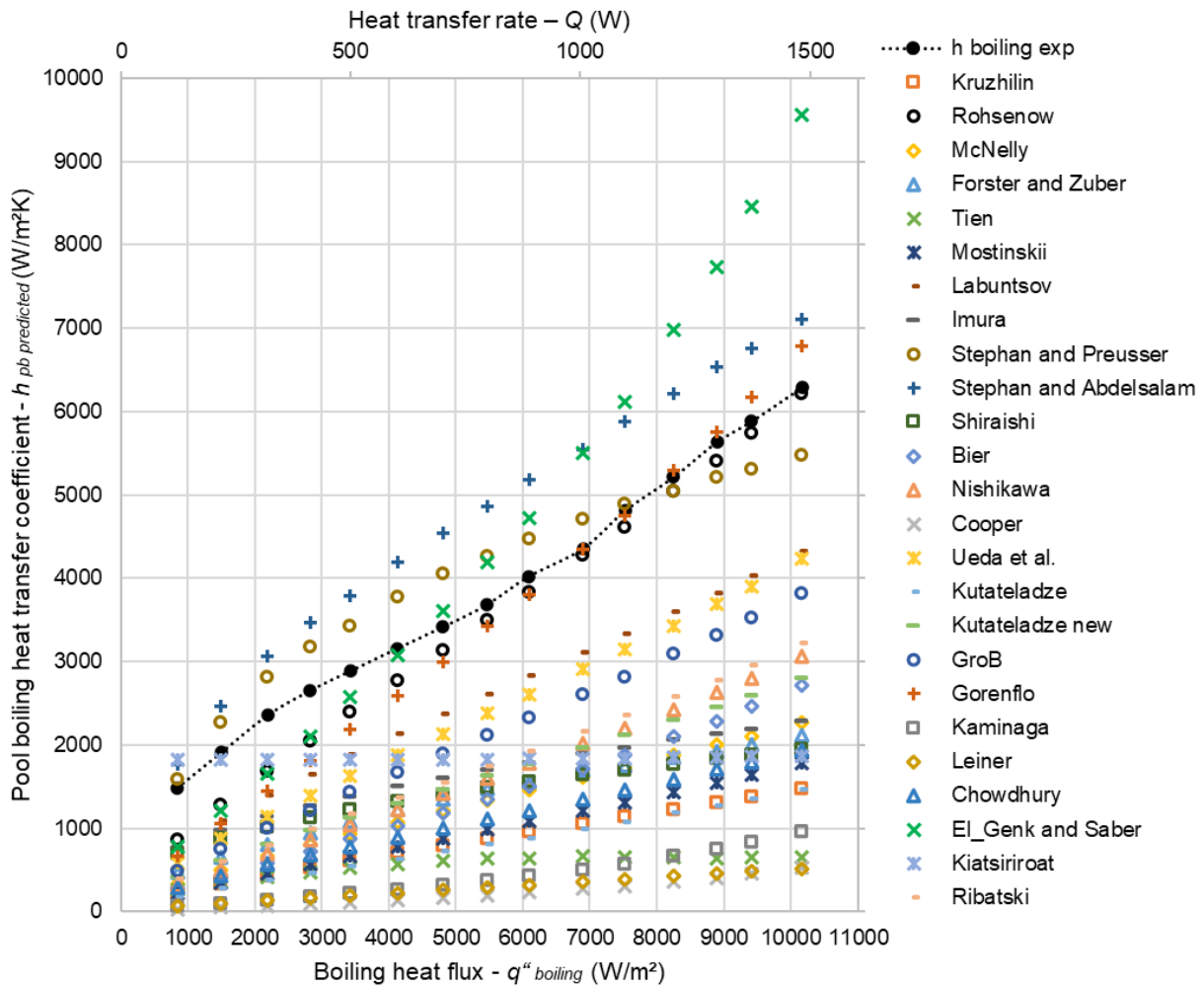


Figure 6-46. Pool boiling heat transfer coefficient with the boiling heat flux and heat transfer rate

The experimental pool boiling heat transfer coefficient is found to increase progressively with the boiling heat flux. Despite small fluctuations, the pool boiling heat transfer coefficient is closed to a linear increase with the boiling heat flux. From Figure 6-46, one can note that a high number of correlations underpredicted the experimental pool boiling heat transfer coefficient. Indeed, at a boiling heat flux of 10 000 W/m<sup>2</sup>, 18 correlations predicted the pool boiling heat transfer coefficient to be lower than 4000 W/m<sup>2</sup>K whereas the experimental heat transfer coefficient is measured at 6300 W/m<sup>2</sup>K. Even for the best performing correlations, the number of correlations with a trend similar to the experimental increase of the pool boiling heat transfer coefficient is low. To better estimate the accuracy of each correlation, the predicted pool boiling heat transfer coefficients are displayed as a function of the experimental pool boiling heat transfer coefficient in Figure 6-47.

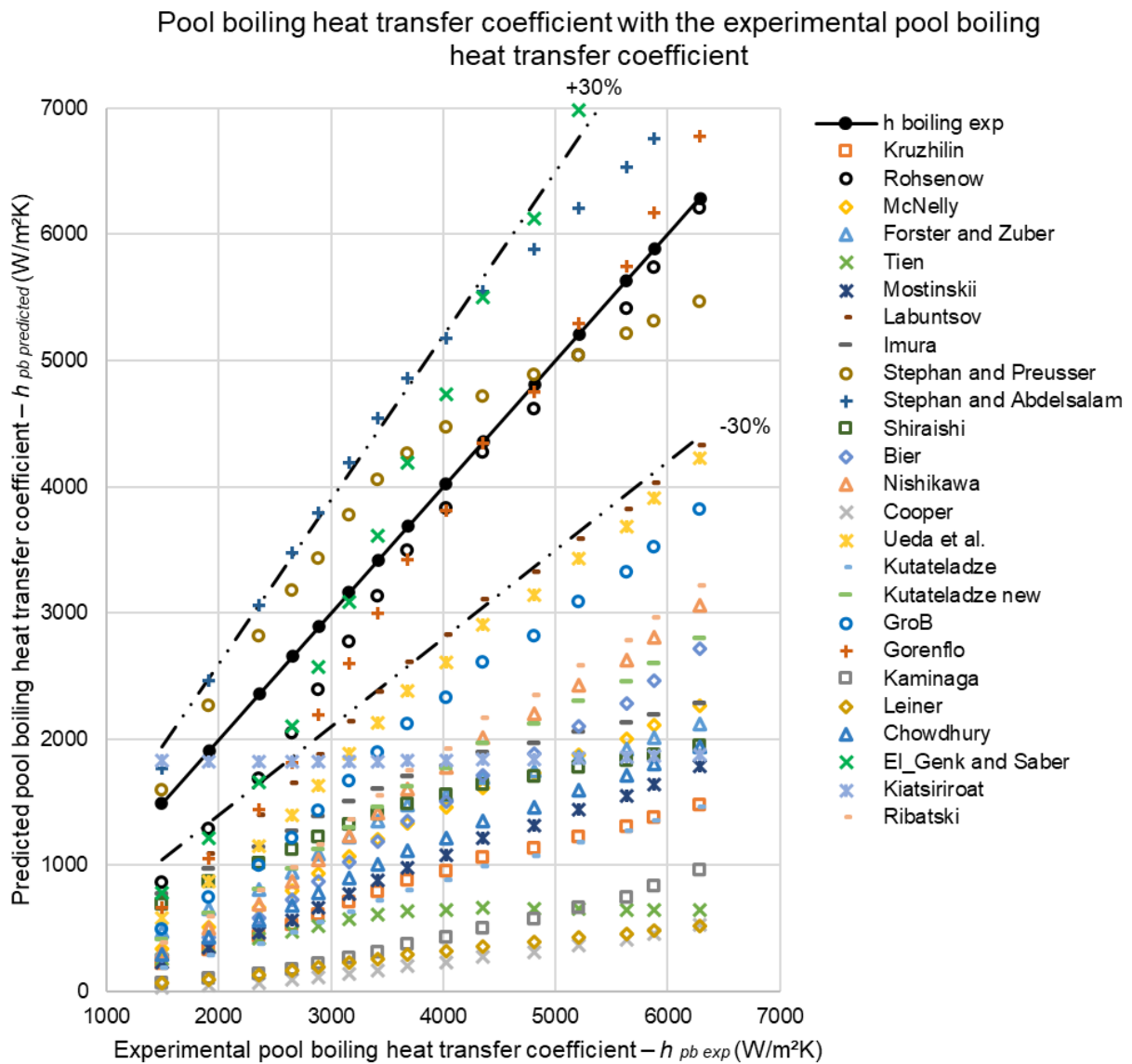


Figure 6-47. Predicted pool boiling heat transfer coefficient with the experimental pool boiling heat transfer coefficient

From Figure 6-47, it is concluded that, regardless of the pool boiling heat flux, 20 correlations made an error higher than 30% in their predictions of the pool boiling heat transfer coefficient. Beyond an inaccuracy of 30%, the correlation is considered to be unsuitable to predict the pool boiling heat transfer coefficient occurring in the multi-channel flat heat pipe. Nevertheless, five correlations, namely the correlations by *Rohsenow* [137], *El-Genk and Saber* [1], *Stephan and Preusser* [146], *Stephan and Abdelsalam* [147], and *Gorenflo et al.* [155] showed an acceptable error lower than 30%. For readability purposes and to better estimate the error made by each correlation, Figure 6-47 was simplified to show the five pool boiling correlations of interest only. This analysis is presented in Figure 6-48.

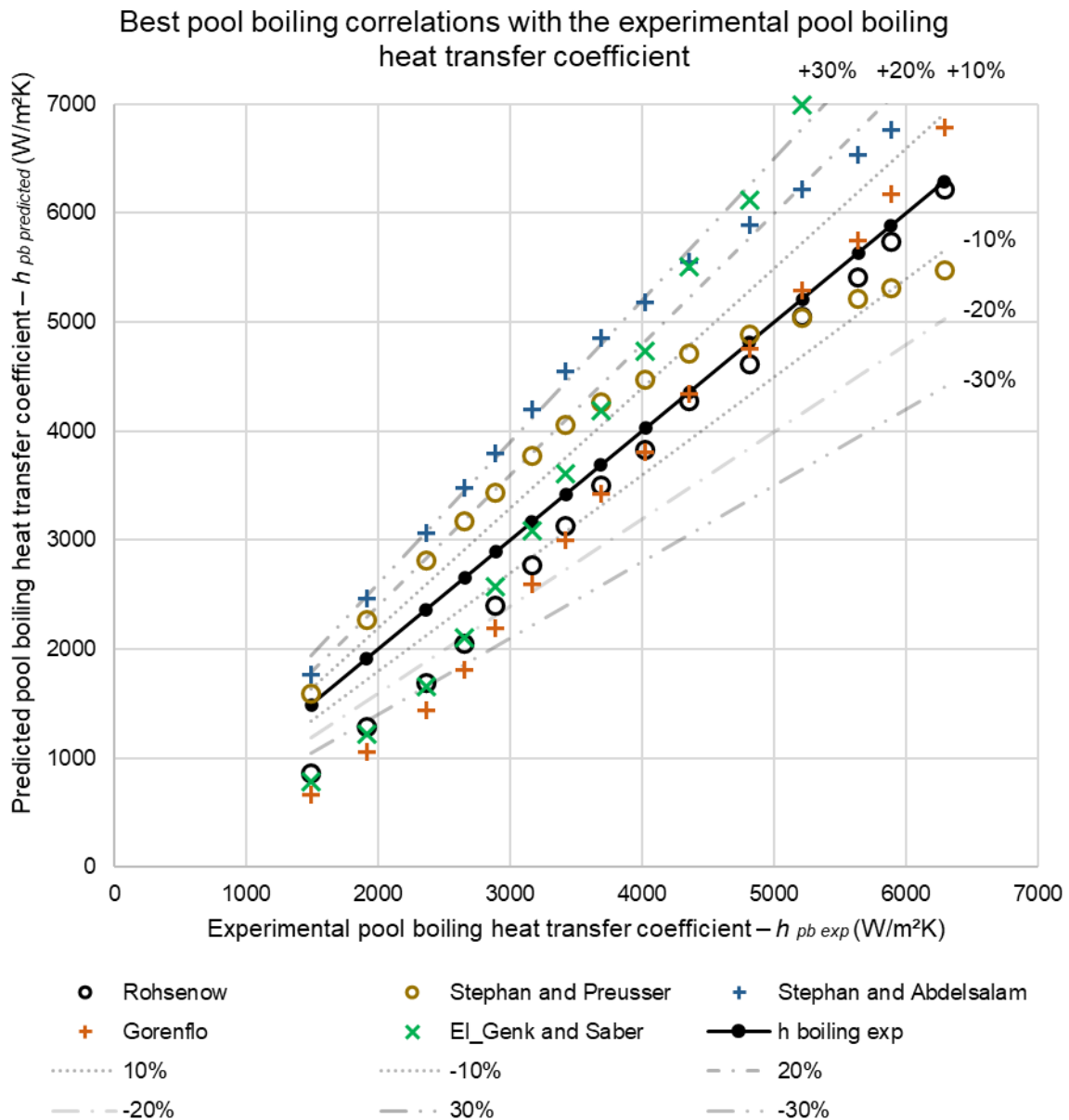


Figure 6-48. Best pool boiling correlations with the experimental pool boiling heat transfer coefficient

Among the five most accurate correlations, very different trends are observed. Based on Figure 6-46 and Figure 6-48, it is noted that the correlation from *El-Genk and Saber* [1] underestimates the pool boiling heat transfer coefficient at a boiling heat flux lower than 4000 W/m<sup>2</sup> and then overpredicts it. Indeed, the model proposed by *El-Genk and Saber* [1] expects a sharper increase of the pool boiling heat transfer coefficient than what was observed experimentally, which limits its capability to accurately estimate the pool boiling heat transfer coefficient over the whole heat transfer rate range. Despite a relatively accurate estimation of the heat transfer coefficient at 100 W, the correlation by *Stephan and Abdelsalam* [147] slightly overpredicts the pool boiling heat transfer coefficient over the whole range of heat flux. The correlation by *Stephan and Preusser* [146] first expects a more important increase of the pool boiling heat transfer coefficient until a heat flux of 4000 W/m<sup>2</sup>. However, at higher heat fluxes,



the increase is slower than what was observed experimentally. Finally, the correlations by *Rohsenow* [137] and *Gorenflo et al.* [155] have a very similar behaviour. At low heat fluxes, the correlations underpredict the pool boiling heat transfer coefficient. Yet, beyond a heat flux of 5000 W/m<sup>2</sup>, the correlations are in good agreement with the experimental data. The accuracy of the correlations of interest with the pool boiling heat flux is presented in Figure 6-49.

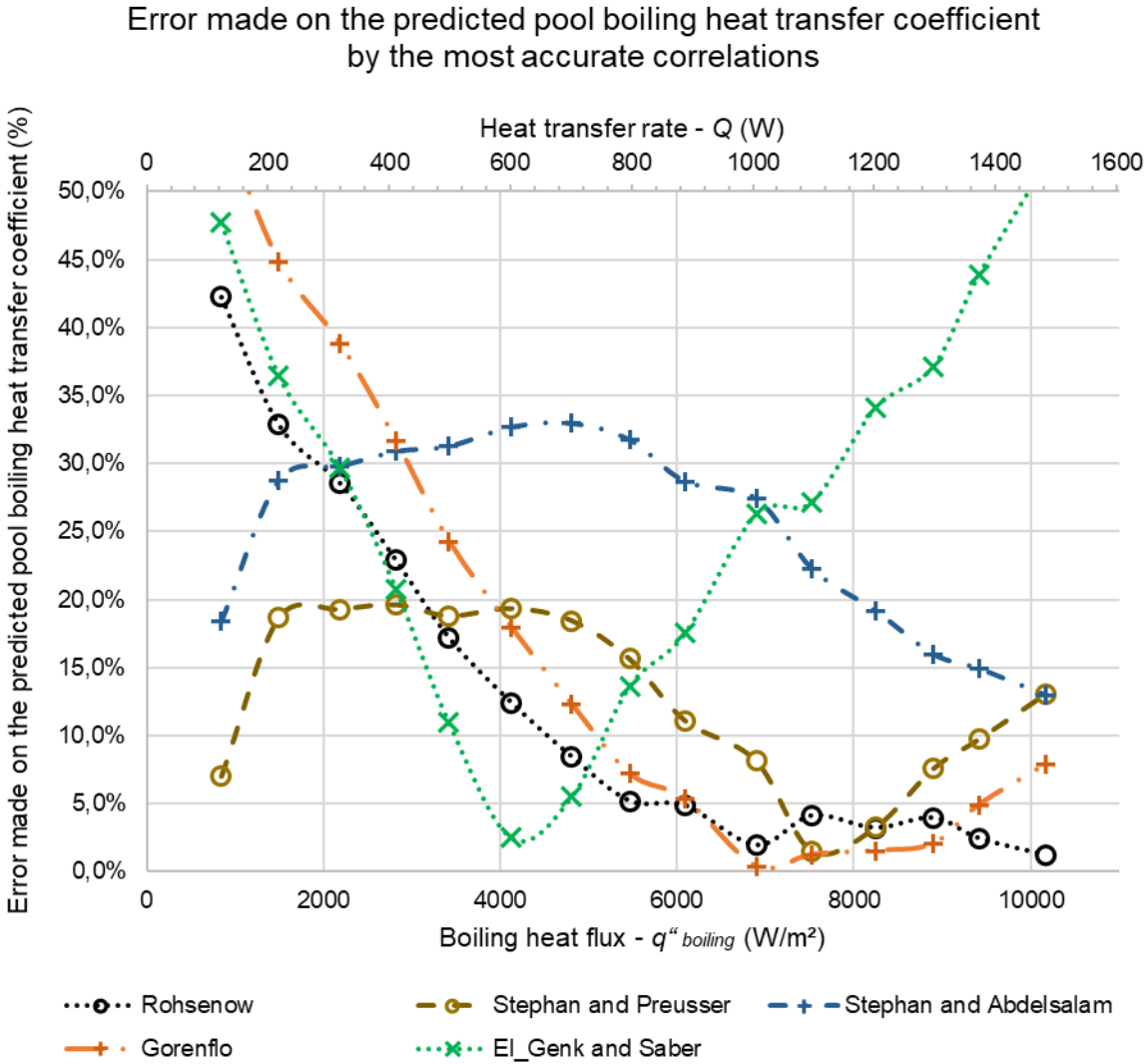


Figure 6-49. Error made on the predicted pool boiling heat transfer coefficient by the most accurate correlations

In addition to the boiling heat flux horizontal axis, a second horizontal axis with the equivalent heat transfer rate is displayed. Because of its consecutive underprediction and then overprediction of the pool boiling heat transfer coefficient, the accuracy of the correlation by *El-Genk and Saber* [1] sharply decreases and then increases again. The accuracy of this correlation is lower than 30% only at heat fluxes between 2000 W/m<sup>2</sup> and 8000 W/m<sup>2</sup> due to a significantly different trend from the experimental data. The correlation meets the experimental data at a pool boiling heat flux around 4500 W/m<sup>2</sup>. With a constant overprediction but a trend

similar to the experimental data, the accuracy of the correlation by *Stephan and Abdelsalam* [147] remains quite constant with a change of heat flux and the error mainly lies between 20-30%. At high heat flux above 8000 W/m<sup>2</sup>, it is worth noticing that this error decreases further to 13% at a maximum heat transfer rate of 1500 W. Despite the different trends observed, the correlation by *Stephan and Preusser* [146] seems to fluctuate around the experimental data but remains fairly accurate over the whole range of heat flux. This correlation is the only correlation that shows an error lower than 20% over the whole heat flux range. Finally, at low heat flux, the underprediction of the pool boiling heat transfer coefficient made by the *Rohsenow* [137] and *Gorenflo et al.* [155] correlations is translated into an error higher than 30% at heat transfer rates of 100 W and 200 W. However, at higher heat transfer rates, the accuracy of those two correlations keeps improving. Even if the trends of the two correlations are closed, the correlation by *Rohsenow* [137] performs better than that of *Gorenflo et al.* [155]. For instance, at a heat transfer rate of 300 W, the error made by the *Rohsenow* [137] correlation is already lower than 30% whereas the error made by the *Gorenflo et al.* [155] correlation is still 39%. From a heat transfer rate higher than 500 W, which corresponds to a boiling heat flux of 3420 W/m<sup>2</sup>, the correlation by *Rohsenow* [137] performs better than any other correlation. In this heat flux range, the trend from the correlation is very close to the experimentally measured pool boiling heat transfer coefficient. Within a heat transfer range of 500-1500 W, the average error made by the correlation from *Rohsenow* [137] is 5.9%. To complete the analysis on the accuracy of the available pool boiling correlations and the selection of the optimized correlation, the average error of the pool boiling correlation over the whole range of heat transfer rate of interest is shown in Figure 6-50.

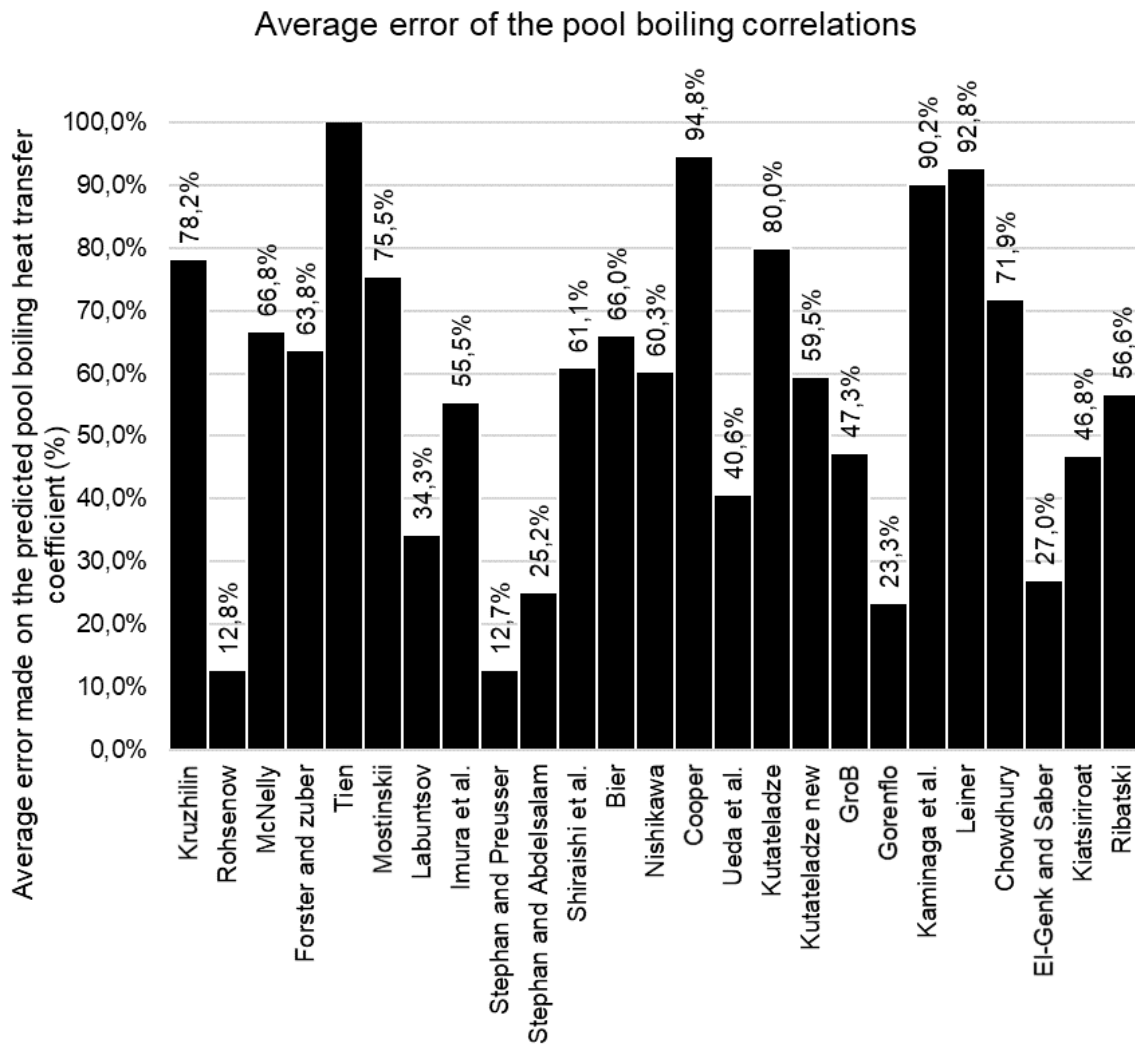


Figure 6-50. Average error of the pool boiling correlations over the whole range of heat transfer rate

On the above bar graph, it is noted that the five correlations previously discussed are the only correlations with an average error lower than 30% over the whole range of heat transfer rates. The pool boiling correlations by *El-Genk and Saber* [1], *Stephan and Abdelsalam* [147], and *Gorenflo et al.* [155] showed averages errors of 27.0%, 25.2%, and 23.3% respectively. Two correlations clearly outperformed the predictions of the pool boiling heat transfer coefficient occurring in the multi-channel flat heat pipe: the correlation by *Rohsenow* [137] with an average error of 12.8% and the correlation by *Stephan and Preusser* [146] with an average error of 12.7%. Those two correlations have been considered as the most suitable for the prediction of the multi-channel flat heat pipe performances. As both equations looked consistent, they both were integrated into the developed two-phase model of the multi-channel flat heat pipe for comparison. It was found that, despite a higher error at low heat transfer rates, the correlation from *Rohsenow* [137] showed slightly better results than the correlation by *Stephan and Preusser* [146] when combined with the condensation models described in the next section. Hence, in the final model, the correlation from *Rohsenow* [137] was used to predict the pool boiling heat transfer coefficient.

### 6.2.2.2 Optimized condensation correlation.

In this section, the available condensation correlations are compared with the experimental condensation heat transfer coefficient. Similarly to the pool boiling section, the objective is to compare and select the most suitable correlation to be integrated in the multi-channel flat heat pipe model. As the condensation correlations are divided in three categories based on the Reynolds number of the condensate, the analysis of the condensation heat transfer coefficient with the heat flux is also divided in three categories: laminar, wavy, and turbulent condensation correlations. In Figure 6-51 is presented the laminar condensation heat transfer coefficients predicted by the available correlations with a change of condensation heat flux. A second horizontal axis with the equivalent heat transfer rate is included.

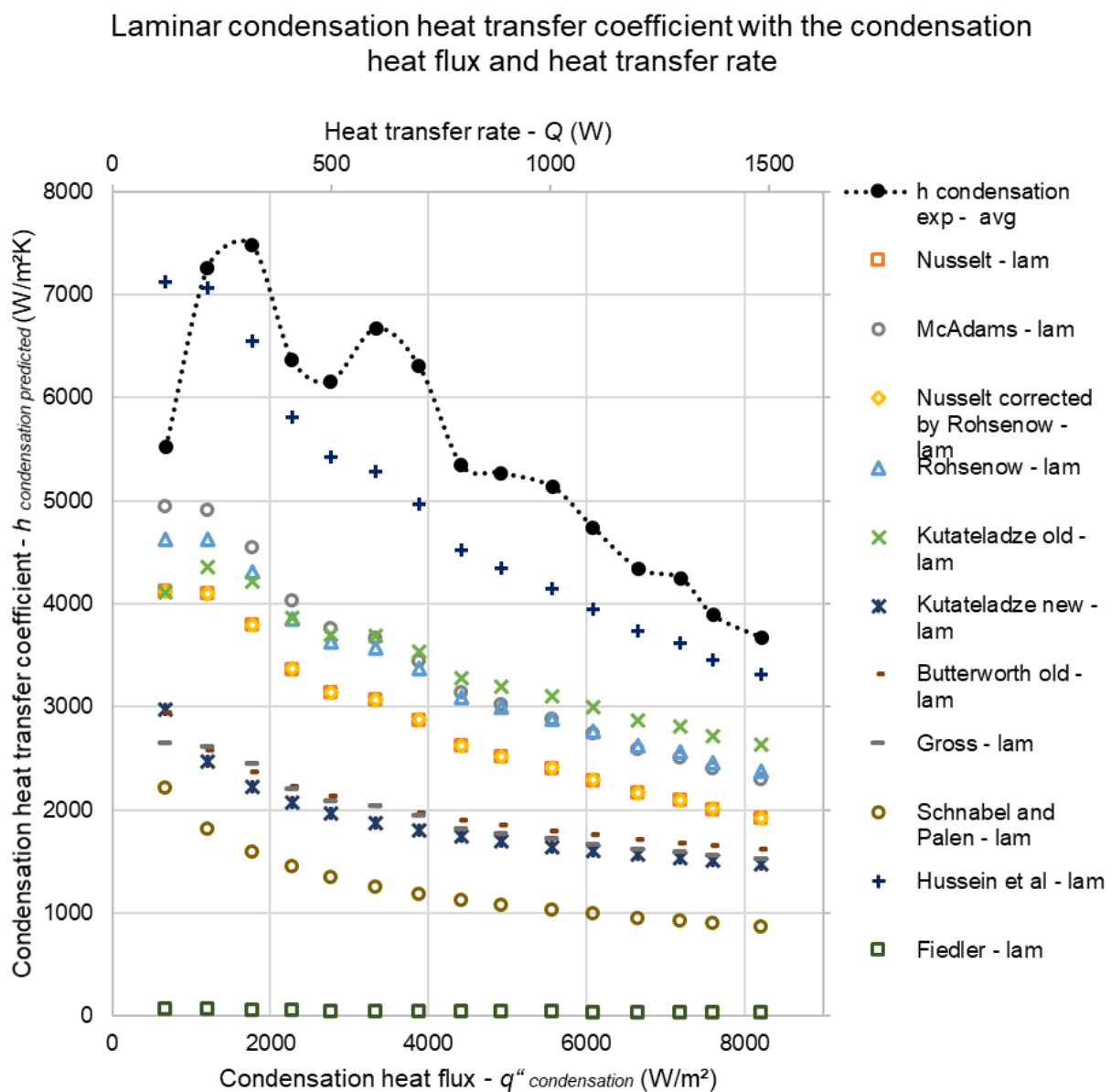


Figure 6-51. Laminar condensation heat transfer coefficient with the condensation heat flux and heat transfer rate

From Figure 6-51, it is noted that the average experimental condensation heat transfer coefficient is very high. The number of laminar correlations predicting a condensation heat transfer coefficient as high as the experimental one is very limited. Indeed, only the correlation from *Hussein et al.* [195] expects the condensation heat transfer coefficient to be as high as 7000 W/m<sup>2</sup>K at condensation heat fluxes lower than 1000 W/m<sup>2</sup>. The other laminar correlations largely underpredict the condensation heat transfer coefficient. With an increase of the condensation heat flux, the heat transfer coefficient decreases as the thickness of the condensate increases. At high heat transfer rates, the trend of the correlation fits correctly with the experimental data despite a significant offset observed. At lower heat transfer rates, the experimental condensation heat transfer coefficient is more scatter and doesn't show a clear trend. Yet, in this zone, the prediction by the correlation from *Hussein et al.* [195] is the closest to the experimental data. In Figure 6-52 and Figure 6-53 are presented the wavy and turbulent condensation correlations for the condensation heat transfer coefficient evolution with the condensation heat flux.

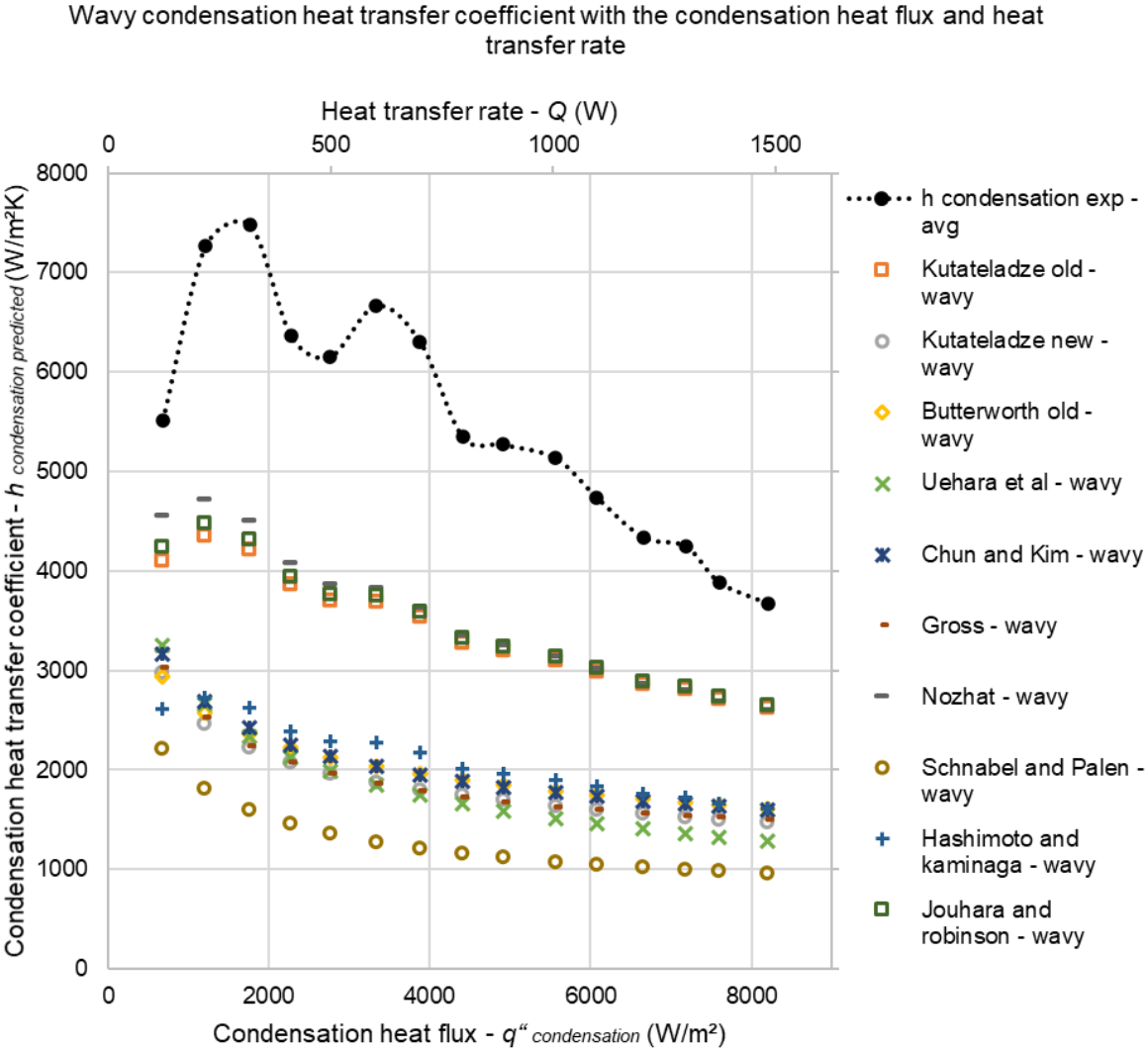


Figure 6-52. Wavy condensation heat transfer coefficient with the condensation heat flux and heat transfer rate

Turbulent condensation heat transfer coefficient with the condensation heat flux and heat transfer rate

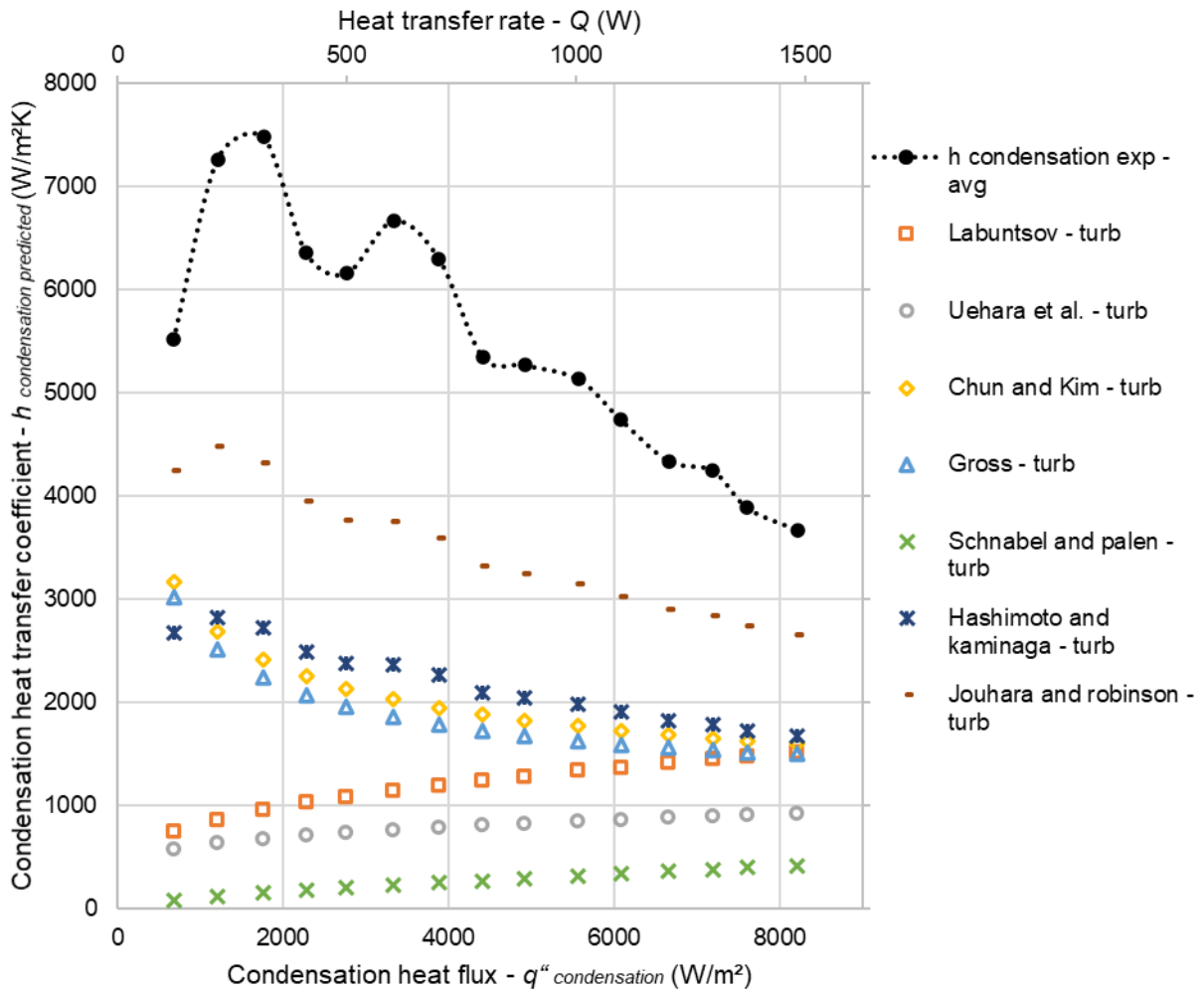


Figure 6-53. Turbulent condensation heat transfer coefficient with the condensation heat flux and heat transfer rate

From Figure 6-52 and Figure 6-53, it is found that none of the wavy and turbulent condensation correlation approach the experimentally measured condensation heat transfer coefficient. This confirms that the condensation pattern inside the multi-channel flat heat pipe at heat transfer rates in the range 0-1500 W belongs to the laminar regime. Hence, in the following, the accuracy of the laminar condensation correlations is studied only. In Figure 6-54 is presented the predicted laminar condensation heat transfer coefficient as a function of the experimental condensation heat transfer coefficient.

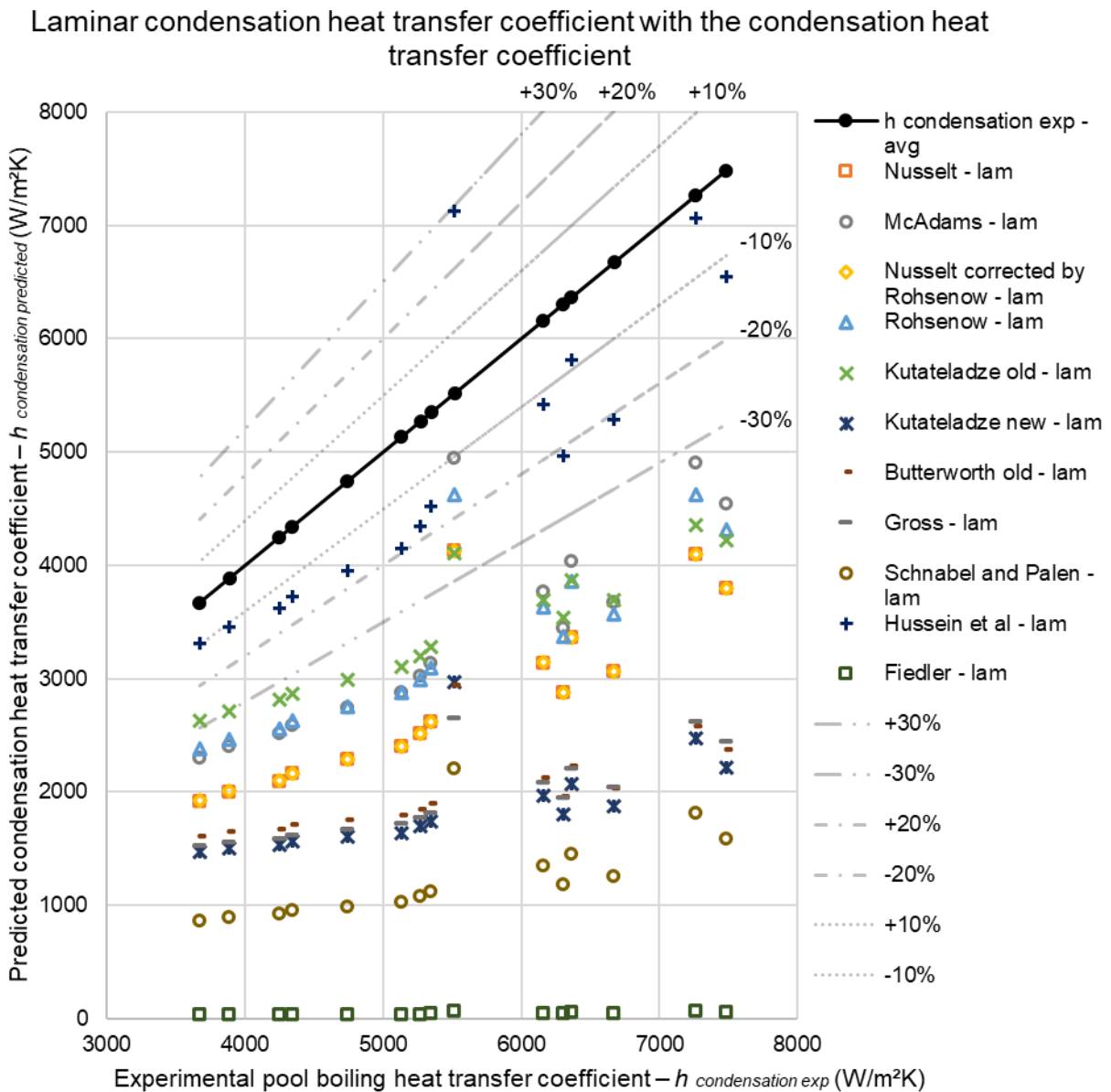


Figure 6-54. Predicted laminar condensation heat transfer coefficient with the experimental condensation heat transfer coefficient

From Figure 6-54, it is observed that the error of most of the proposed correlations is higher than 30% relative to the current experimental data. Due to the very high value of condensation heat transfer coefficient measured experimentally, most of the correlations show an underprediction. As indicated before, only the correlation by *Hussein et al.* [195] makes an error lower than 30%, which is considered as the limit to get an acceptable prediction. At low heat transfer rate which corresponds to a high experimental condensation coefficient beyond 6000 W/m<sup>2</sup>K, the error made by the correlations fluctuates more due to the fluctuation of the experimental heat transfer coefficient. At an experimental condensation heat transfer coefficient of 5500 W/m<sup>2</sup>K, it can be noted that all the correlations present an error much closer than the rest of the data point. This is due to the experimental condensation heat transfer

coefficient that was obtained at a heat transfer rate of 100 W. At such heat transfer rate, the measured experimental condensation heat transfer coefficient (5500 W/m<sup>2</sup>K) was lower whereas all the correlations predict the maximum condensation heat transfer coefficient to be reached there. As a result, at an experimental condensation heat transfer coefficient of 5500 W/m<sup>2</sup>K, several correlations such as the correlations by *McAdams* [181], *Rohsenow* [184], *Nusselt* [103], *Nusselt* [103] corrected by *Rohsenow* [184], and *Kutateladze* [190], show errors lower than 30%. However, this improved accuracy is only due to the experimental data at a heat transfer rate of 100 W. Finally, at high heat transfer rates which corresponds to an experimental condensation coefficient lower than 5400 W/m<sup>2</sup>K, the accuracy of each correlation becomes more linear. In this range of heat transfer coefficient, the correlation by *Hussein et al.* [195] shows an evolution which is close to the experimental data. The error made by the correlation by *Hussein et al.* [195] is contained between 10% and 20%. To conclude on the selection of the most suitable condensation heat transfer coefficient correlation, the average error of the correlations over the whole range of heat transfer rates is presented in Figure 6-55.

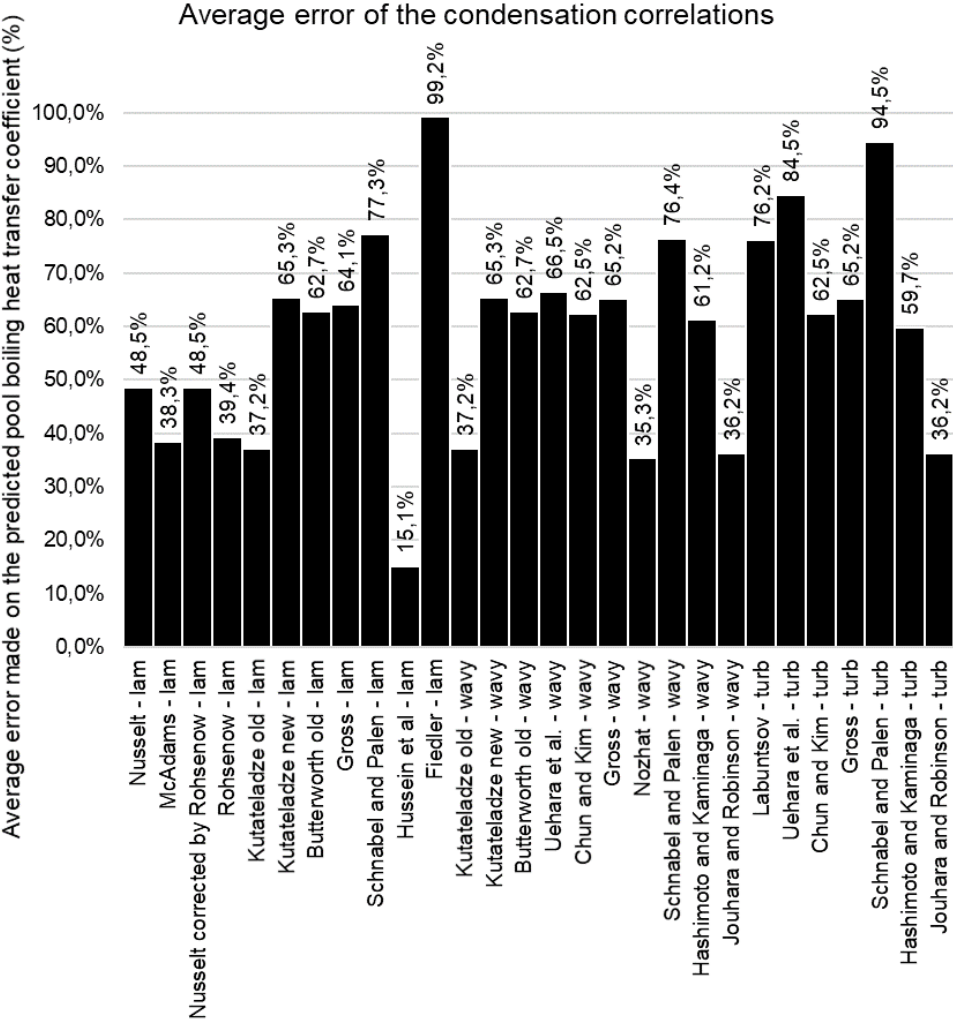


Figure 6-55. Average error of the condensation correlations over the whole range of heat transfer rate



On Figure 6-55, the correlation by *Hussein et al.* [195] clearly stands out. Over the whole range of heat transfer, the average error of this correlation is 15.1%. As a comparison, the second and third best performing correlations are found to be the correlations by *Nozhat* [199] and *Jouhara and Robinson* [169] with an average error of 35.3% and 36.2%. Yet, the experimental condensation heat transfer coefficients measured from the multi-channel flat heat pipe are found to be higher than many reported heat pipes and thermosyphons. Hence, most of the existing models are found to be unsuitable for the prediction of the condensation heat transfer in the multi-channel flat heat pipe. As a result, to predict the performance of the multi-channel flat heat pipe, the correlation by *Hussein et al.* [195] was selected and integrated into the developed model.

#### 6.2.2.3 Conclusion on optimized correlations for the multi-channel flat heat pipe apparatus

To conclude on the comparison between local heat transfer coefficient measured from the multi-channel flat heat pipe experiments and the available correlations from the literature, the best performing models are listed in this section.

- **Pool boiling heat transfer coefficient:**

To predict the local pool boiling heat transfer coefficient of the multi-channel flat heat pipe, the most performing correlation was that of *Stephan and Preusser* [146] with an average error of 12.7%, *Rohsenow* [137] with 12.8%, *Gorenflo et al.* [155] with an error of 23.3%, and *Stephan and Abdelsalam* [147] with 25.2%. It can be seen that several of the best performing correlations were recommended from the literature: *Rohsenow* [137] and *Stephan and Abdelsalam* [147]. In the case of the multi-channel flat heat pipe, the correlation from *Imura et al.* [145] performed less but reached an acceptable average error of 55.5%. The correlation from *El-Genk and Saber* [1] also performed well and obtained an average error of 27% in its predictions.

It is therefore concluded that the recommended pool boiling correlation from *Rohsenow* [137] and *Stephan and Abdelsalam* [147] are reliable to predict the pool boiling heat transfer coefficient. In the case of the multi-channel flat heat pipe, the correlation from *El-Genk and Saber* [1] also performed well.

- **Condensation heat transfer coefficient:**

In the objective of predicting the local condensation heat transfer coefficient of the multi-channel flat heat pipe, the available correlation from the literature have been compared. It was observed that most of the correlation from the literature made an error higher than 30%. However, the correlation from *Hussein et al.* [195] obtained an average error of 15.1%. The usually recommended correlation from *Nusselt* [103] corrected by *Rohsenow* [184] for strictly

laminar flow made an average error of 48.5% on its prediction. The wavy-laminar correlation from *Rohsenow* [184], *McAdams* [181], and *Kutateladze* [190] performed better with errors of 39.4%, 38.3% and 37.2% which seems to indicate that the condensate regime belonged to the wavy regime. The turbulent filmwise condensation from *Labuntsov* [201] did not perform well as its average error was measured to 76.2%.

For the condensation heat transfer coefficient prediction, it is concluded that determining the flow regime of the condensate is crucial to select a suitable correlation. In the case of the multi-channel flat heat pipe, the wavy-laminar condensations performed better than the correlations for wavy or turbulent films. The recommended correlation from *Rohsenow* [184], *McAdams* [181], and *Kutateladze* [190] performed relatively well and seem reliable to predict the condensation heat transfer coefficient.

### **6.2.3 Two-phase model validation – multi-channel flat heat pipe**

In the objective of predicting the thermal performance of the multi-channel flat heat pipe, the selected pool boiling and condensation correlations, namely the correlations by *Rohsenow* [137] and *Hussein et al.* [195], were integrated to the multi-channel flat heat pipe model developed. In this section, the theoretical predictions of the developed model are compared with the experimental data.

#### *6.2.3.1 Boiling resistance prediction*

In Figure 6-56 is presented the comparison between the theoretical and experimental pool boiling heat transfer coefficients.

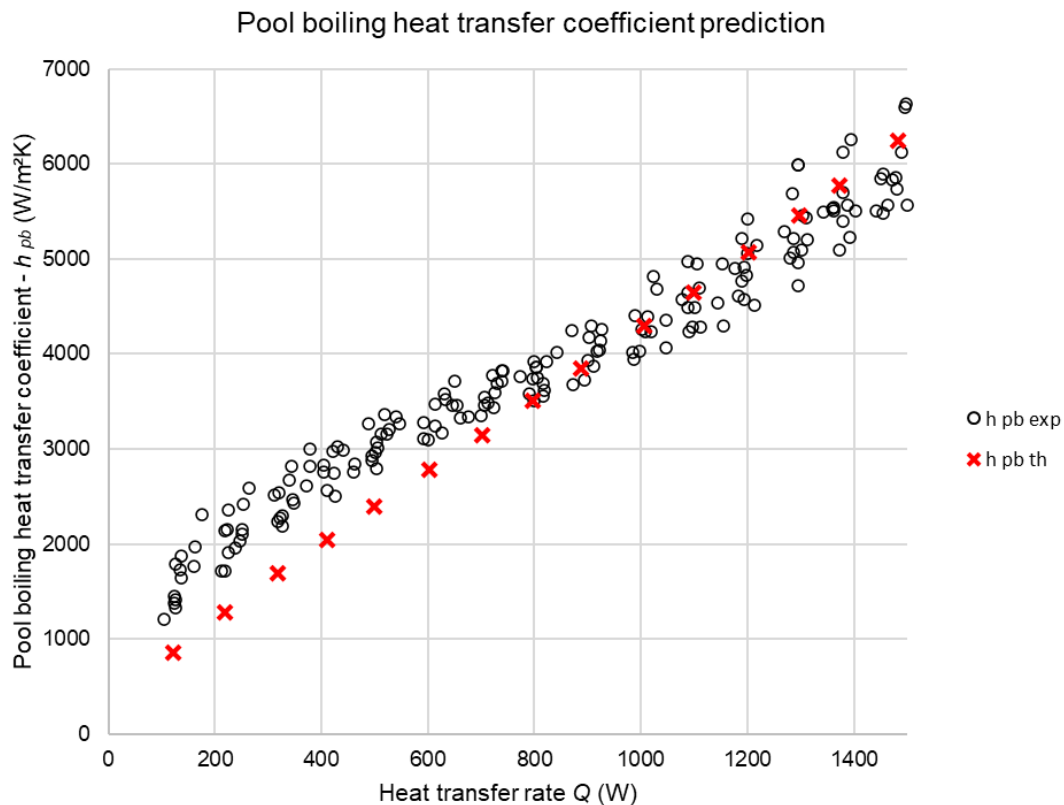


Figure 6-56. Pool boiling heat transfer coefficient prediction – Multi-channel flat heat pipe By integrating the *Rohsenow* [137] correlation to the model, the trend of the multi-channel flat heat pipe model prediction remains close to the experimental data. At low heat transfer rates, it is observed that the pool boiling heat transfer coefficient predicted by the model is slightly lower than the experimental one. At heat transfer rates lower than 700 W, the discrepancy between the experimental pool boiling heat transfer coefficient and the predicted one is the highest. At higher heat transfer rates, the agreement between the model and the experimental data improves as the heat transfer rate increases. By using the equivalent thermal resistance network developed for a multi-channel heat pipe, the overall predicted pool boiling resistance of the multi-channel flat heat pipe comprising the bottom collector and the parallel channels is presented in Figure 6-57.

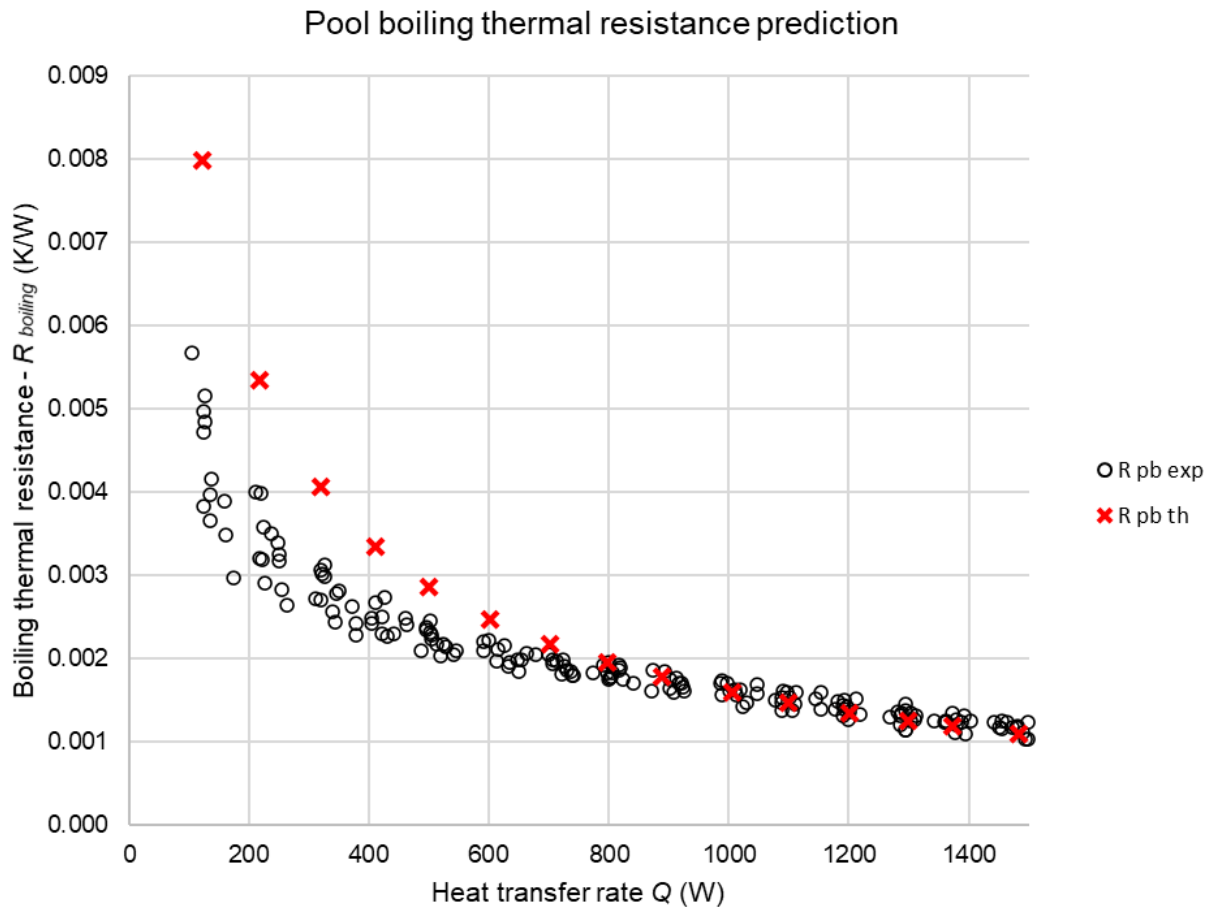


Figure 6-57. Pool boiling thermal resistance prediction – Multi-channel flat heat pipe

Like the prediction made on the pool boiling heat transfer coefficient, at low heat transfer rates, the equivalent pool boiling thermal resistance prediction is less accurate. Indeed, due to an underprediction of the pool boiling heat transfer coefficient in this region, the equivalent pool boiling resistance is thus overpredicted. With the increase of the heat transfer rate, the better prediction of the pool boiling heat transfer coefficient has a direct impact on the equivalent resistance. From a heat transfer rate of 700 W, when the pool boiling heat transfer coefficient predictions becomes more accurate, the corresponding thermal resistance fits closely with the experimental data. The prediction error made on the boiling thermal resistance at different heat transfer rates is presented in Figure 6-58.

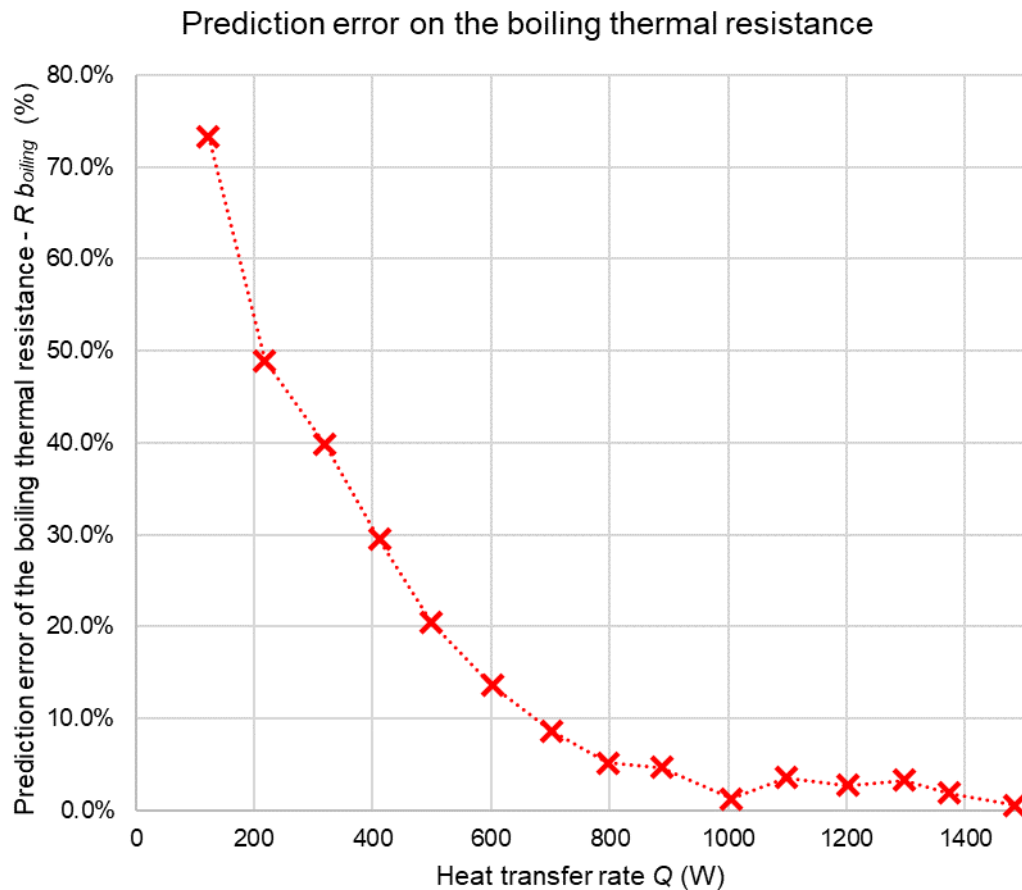


Figure 6-58. Prediction error on the boiling thermal resistance – Multi-channel flat heat pipe

Due to the under prediction of the pool boiling heat transfer coefficient at very low heat transfer rates; at 100 W, the error made on the boiling resistance prediction is maximum and reaches 73%. Yet, the error decreases rapidly with an increase of the heat transfer rate so that, at a heat transfer rate of 400 W, the boiling resistance predicting error falls below 30%. Furthermore, beyond a heat transfer rate of 700 W, the boiling resistance prediction presents an error lower than 10%. Hence, it is showed that the boiling model is less accurate at lower heat transfer rates. The average error made by the developed model to predict the boiling thermal resistance over the whole range of heat transfer rates is 17.2%. This average error is significantly degraded by the high errors at low heat transfer rates.

### 6.2.3.2 Condensation resistance prediction

To estimate the condensation thermal resistance of the multi-channel flat heat pipe, the condensation heat transfer coefficient was predicted using the correlation by *Hussein et al.* [195]. In Figure 6-59 is presented the theoretical condensation heat transfer coefficient when compared with the experimental data.

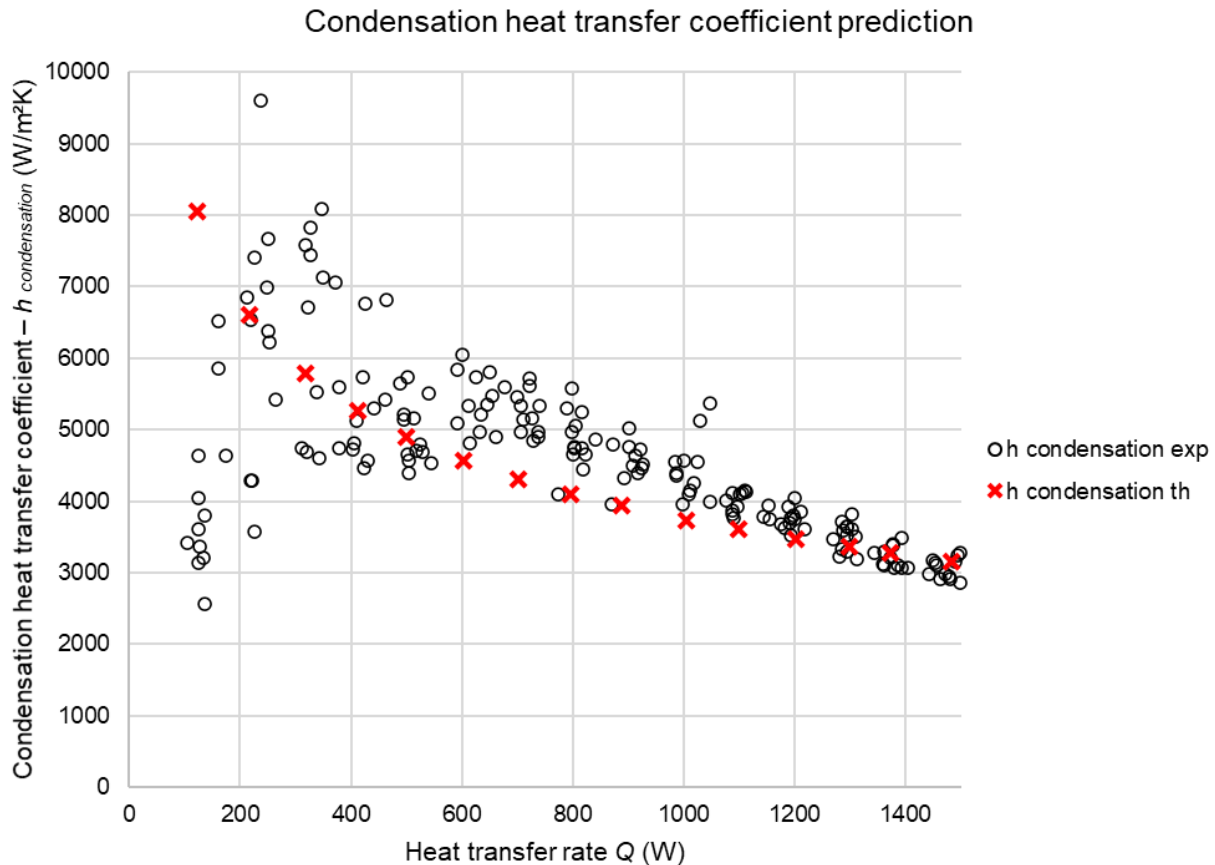


Figure 6-59. Condensation heat transfer coefficient prediction – Multi-channel flat heat pipe

By integrating the *Hussein et al.* [195] correlation to the proposed two-phase model, the theoretical condensation heat transfer coefficient shows a satisfying agreement with the experimental data at heat transfer rates higher than 100W. At heat transfer rates between 600 W and 1000 W, the experimental data trend is slightly above the prediction from the model which tends to underpredict the condensation heat transfer coefficient. At heat transfer rates lower than 500 W, the condensation experimental data are more scattered which makes the comparison with the theoretical model more difficult. Nonetheless, in this range of heat transfer rates, the theoretical condensation heat transfer coefficient is situated in the centre of the experimental point cloud which seems to attest a decent prediction from the model. When integrated to the channels and top collector condensation thermal resistance, the equivalent condensation thermal resistance obtained by the proposed multi-channel flat heat pipe model is shown in Figure 6-60.

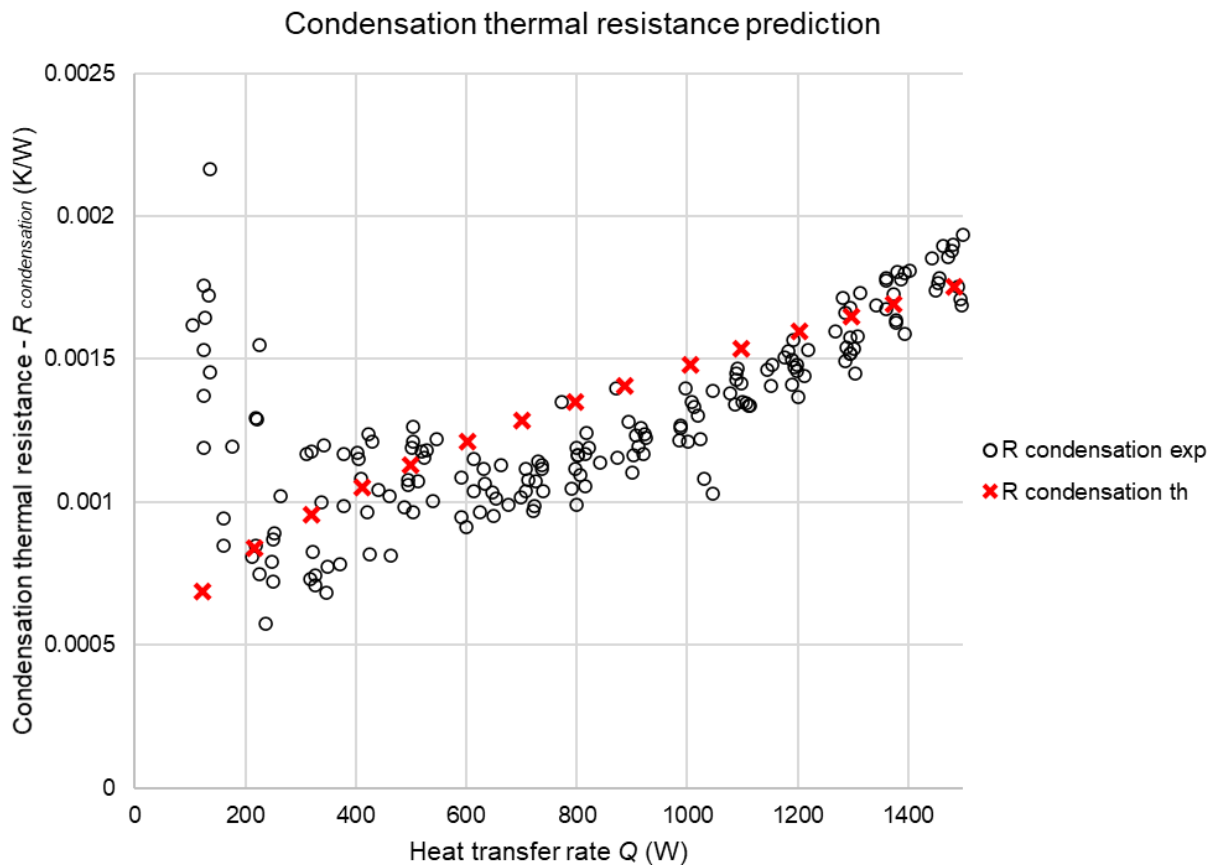


Figure 6-60. Condensation thermal resistance prediction – Multi-channel flat heat pipe

Similar to the boiling thermal resistance prediction, the condensation thermal resistance evolution is closely linked to the heat transfer coefficient's one. At a minimum heat transfer rate of 100 W, the predicted condensation thermal resistance is much lower than the experimental data. It seems that the data at 100 W are significantly influenced by the start-up of the heat pipe, and that the condensation occurring is more limited than the expectations. However, from a heat transfer rate of 200 W, the condensation experimental data and the proposed model agree. Despite the scattering of the experimental data between 200 W and 600 W, the predicted condensation thermal resistance is situated close to the middle of the data points. Yet, the trend of the theoretical condensation thermal resistance isn't totally similar to the experimentally measured thermal resistance. Indeed, at low heat transfer rates up to 800 W the theoretical condensation thermal resistance increases faster than the experimental data, and then increases slower than the measured condensation thermal resistance. As a result, between 600 W and 1000 W, the multi-channel flat heat pipe model slightly overpredicts the condensation thermal resistance. At heat transfer rates higher than 1000 W, the model and the experimental condensation data fit better as the two curves cross each other. In this region, the error made by the condensation model is reduced as presented in Figure 6-61.

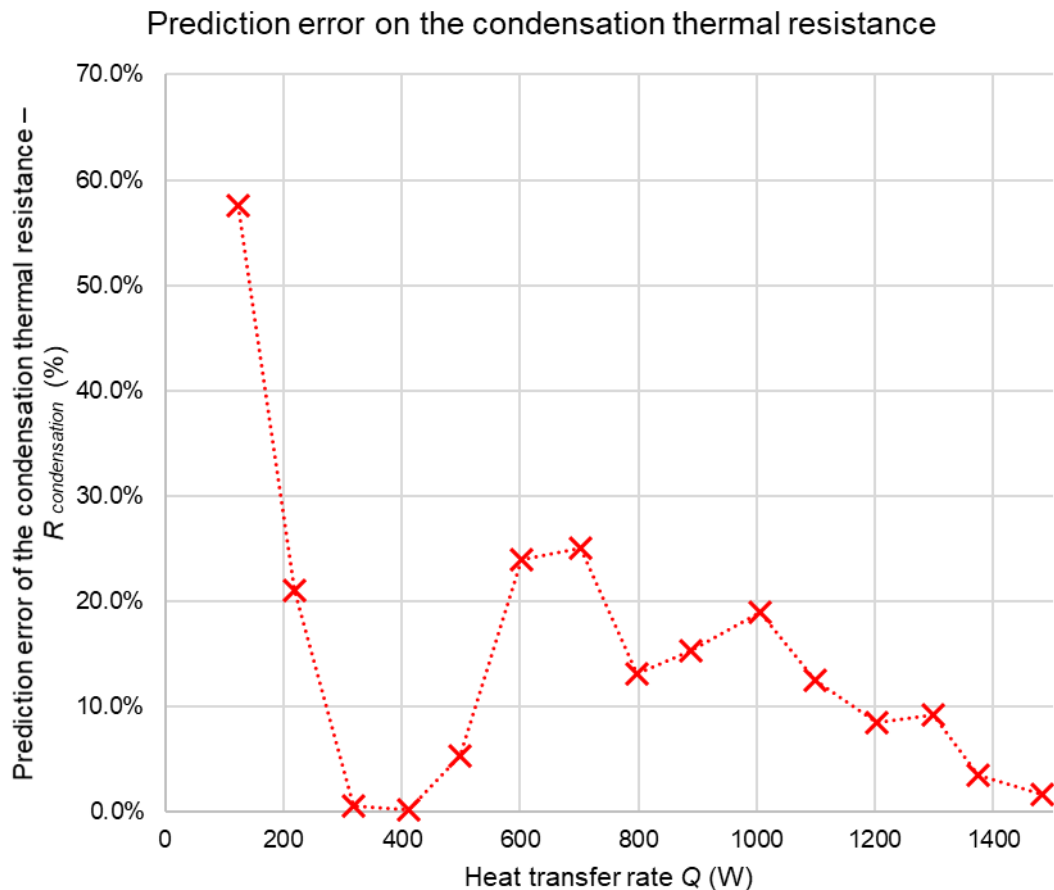


Figure 6-61. Prediction error on the condensation thermal resistance – Multi-channel flat heat pipe

With the underprediction of the condensation thermal resistance at a heat transfer rate of 100 W, the accuracy of the proposed model is the lowest at 100 W and shows an error of 58%. Yet, at a heat transfer rate of 200 W, the accuracy of the model is greatly improved, and the error is down to 21%. Indeed, it is noted that the error made by the proposed condensation model remains lower than 30% for all the heat transfer rates but 100 W. Beyond 200 W, the error made by the proposed model first increases and then decreases due to the different theoretical and experimental trends. From a heat transfer rate of 300 W to 700 W, the model error increases from 0% to 25%. The error then decreases back from 25% to 1% at heat transfer rates from 700 W to 1500 W. Over the whole range of heat transfer rates studied, the average error made by the proposed model on the condensation thermal resistance prediction is 14.4%.

### 6.2.3.3 Total multi-channel flat heat pipe thermal resistance prediction

By using the total multi-channel flat heat pipe model proposed which includes the conduction, boiling, and condensation thermal resistances, the total multi-channel flat heat pipe thermal resistance was predicted. The predicted total thermal resistance of the multi-channel flat heat pipe is compared with the experimental data in Figure 6-62.



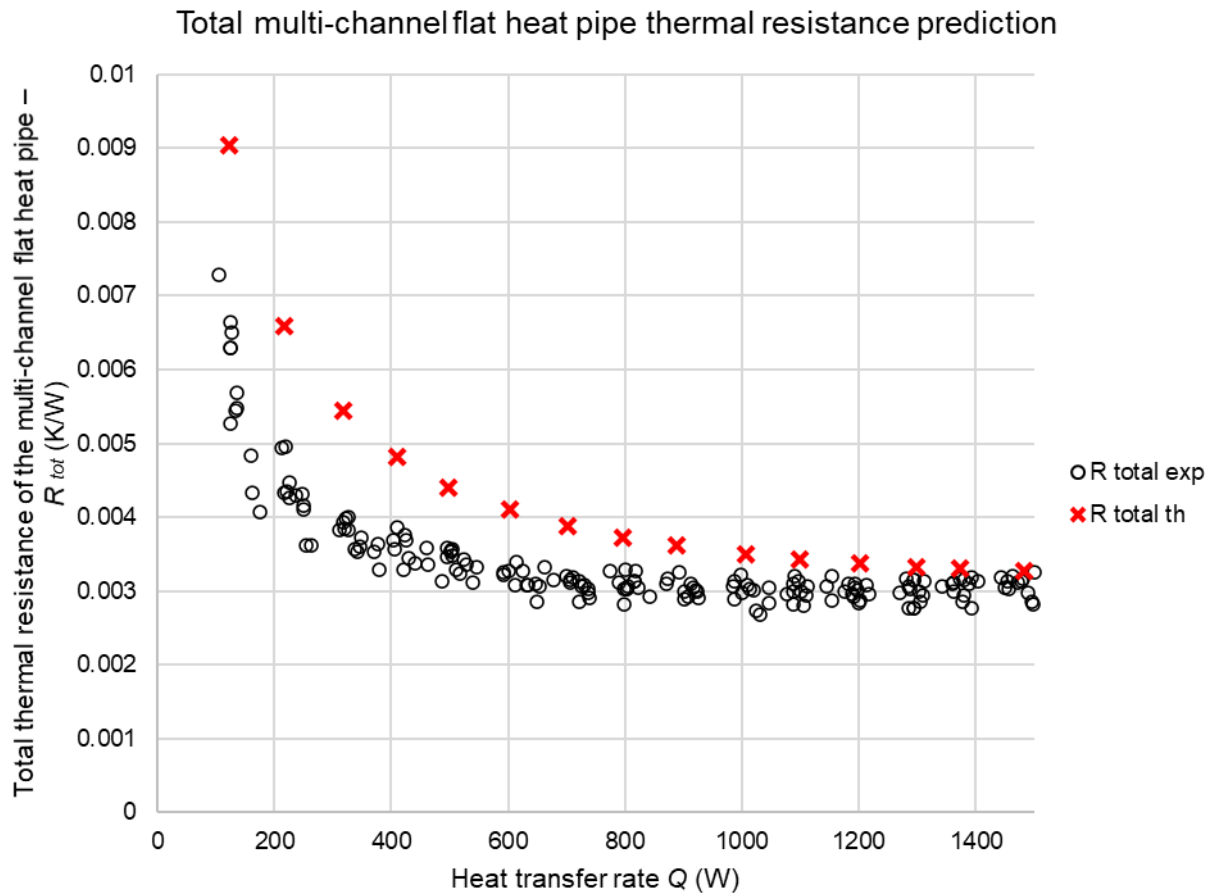


Figure 6-62. Total multi-channel flat heat pipe thermal resistance prediction

Overall, the predicted multi-channel flat heat pipe total resistance is higher than the experimental measurements. At heat transfer rates from 100 W to 600 W, this overprediction is mainly due to the over prediction of the boiling thermal resistance. With an increase of the heat transfer rate, the accuracy of the model improves, and the theoretical total resistance of the heat pipe agrees more with the experimental measurements. At heat transfer rates higher than 800 W, the prediction fits closely with the experimental thermal resistance of the multi-channel flat heat pipe. This improved accuracy can be visualized better in Figure 6-63 presenting the error made by the proposed theoretical model on the estimation of the total multi-channel flat heat pipe thermal resistance.

Prediction error on the total multi-channel flat heat pipe thermal resistance

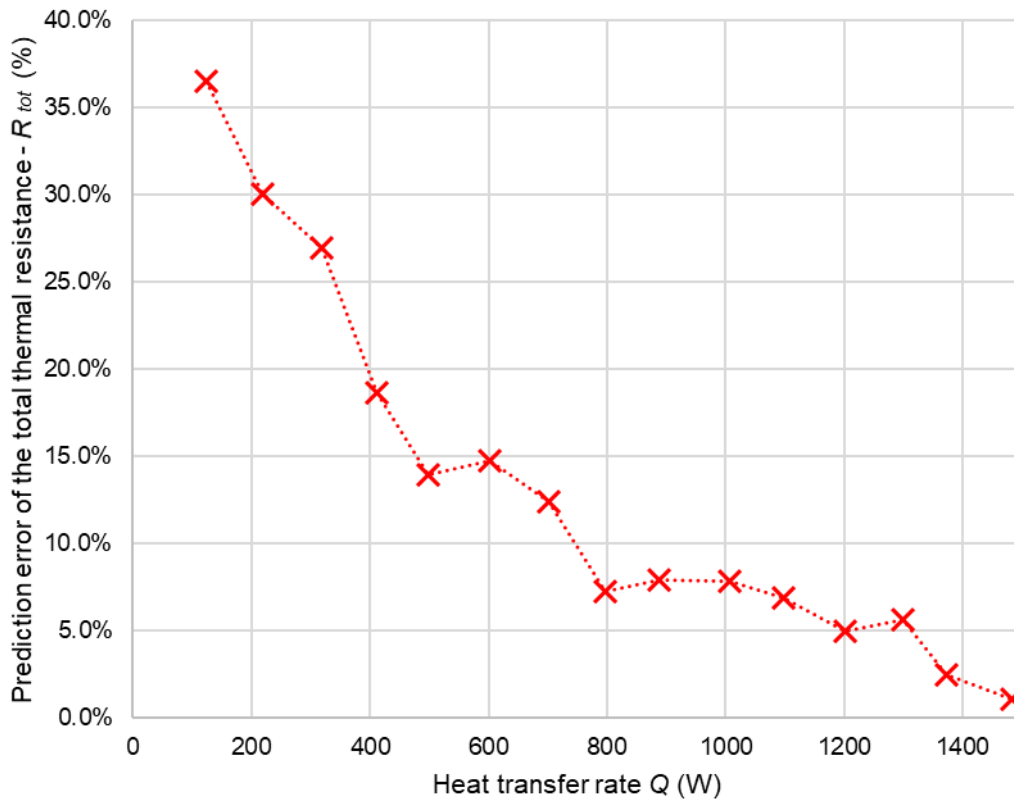


Figure 6-63. Prediction error on the total multi-channel flat heat pipe thermal resistance

From Figure 6-63, it can be noted that the error made by the proposed model is higher than the 30% limit at a heat transfer rate of 100 W only. Indeed, it seems that the theoretical model overpredicts the boiling thermal resistance at low heat transfer rates which results in a lower accuracy. Nevertheless, this accuracy improves with an increase of the heat transfer rate and the prediction error of the total thermal resistance of the multi-channel flat heat pipe becomes less than 30% from a heat transfer rate of 200 W. It is also observed that, from a heat transfer rate of 800 W, the error made by the proposed theoretical model on the estimation of the heat pipe thermal resistance remains below 10%. Overall, on the studied heat transfer rate range of 0-1500 W, the average error made by the multi-channel flat heat pipe model on the prediction of the total thermal resistance is 13.1%.

## 6.2.4 Impact of the tilt angle on the thermal resistance of the multi-channel flat heat pipe

For PV/T applications, in the case where a multi-channel flat heat pipe is used to remove the heat from photovoltaic cells, the multi-channel flat heat pipe is likely to be placed on a roof structure and, as such, to be inclined. In the case where the multi-channel flat heat pipe isn't placed vertically, its thermal performance may be impacted due to some changes in the two-phase working fluid cycle inside the heat pipe. Hence, in this section, the thermal performance of the studied multi-channel flat heat pipe is measured at different tilt angles.

### 6.2.4.1 Boiling thermal resistance

In Figure 6-64 is presented the boiling thermal resistance of the multi-channel flat heat pipe at tilt angles of 90° (vertical), 45°, 20°, 10°, 5°, and 2°. As the impact of the tilt angle on the thermal performance of the heat pipe may change with the boiling and condensation activity, different heat transfer rates from 100 W to 1500 W are investigated.

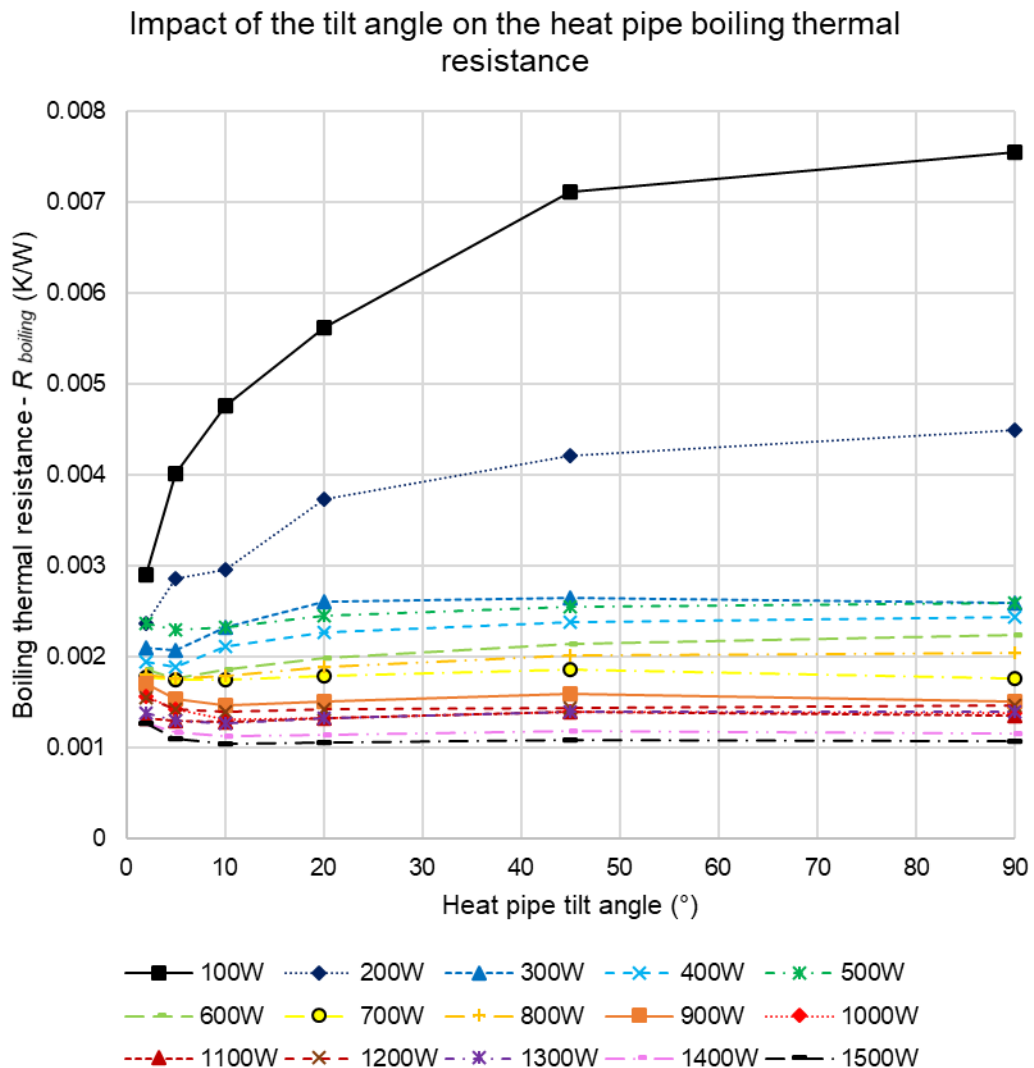


Figure 6-64. Impact of the tilt angle on the multi-channel flat heat pipe boiling thermal resistance

In Figure 6-64, each curve represents one heat transfer rate investigated. As a first observation, it is confirmed that, depending on the heat transfer rate, the impact of the tilt angle on the boiling thermal resistance of the heat pipe is significantly different. Indeed, for a heat transfer rate of 100 W, it is noted that there is a large impact of the tilt angle on the performance of the heat pipe whereas, at 1500 W, this impact is very limited. Indeed, between a tilt angle of 2° (almost horizontal) and 90° (vertical), the boiling thermal resistance varies by 0.0046 K/W at a heat transfer rate of 100 W whereas it only varies by 0.0002 K/W at 1500 W. Overall, it is first concluded that the lower the heat transfer rate, the higher the impact of the tilt angle on the boiling thermal resistance. Going further, this means that, at a lower boiling activity where the pool boiling regime belongs to the natural convection boiling, the impact of the tilt angle is more significant. As the boiling activity increases and the pool boiling regime transits to a fully developed saturated boiling regime, the impact of the tilt angle on the boiling resistance reduces drastically.

From Figure 6-64, two curves mainly stand out from the others: the 100 W and 200 W curves. Indeed, from a heat transfer rate of 300 W and onwards, the curves are much closer from each other's. At a heat transfer rate of 100 W and 200 W, the boiling thermal resistance increases as the flat heat pipe transits from a horizontal position to a vertical position. The overall increase trend is similar to a natural logarithm function, with a sharp increase of the boiling resistance at tilt angles in the range 2°-10°, and an increase that progressively flattens at higher angles. Even if the trend is similar, the variation of the boiling thermal resistance is much smaller at 200 W compared to 100 W. It is also observed that, between a tilt angle of 45°-90°, the boiling resistances at 100 W and 200 W remain similar.

At heat transfer rates in the range 300–800 W, at tilt angles between 90° and 20°, the boiling thermal resistance of the multi-channel flat heat pipe is almost constant. Then, when decreasing the tilt angle from 20° to 5°, the boiling resistance seems to decrease slightly. This variation remains limited, and the most important decrease was 0.00054 K/W at a heat transfer rate of 300 W. Only at a tilt angle of 2° close to the horizontal, is observed a very small increase of the boiling thermal resistance in the order of 0.0001 K/W.

At higher heat transfer rates in the range 900-1500 W, the boiling thermal resistance stagnates at tilt angles from 90° (vertical) to 10°. At positions closer to the horizontal, a small increase of the boiling thermal resistance is observed when the tilt angle is lower than 10°. For instance, at a heat transfer rate of 1500 W, the boiling thermal resistance of the multi-channel flat heat pipe increases from 0.001 K/W to 0.0012 K/W. Hence, it is concluded that, when the pool boiling regime belongs to the fully developed saturated boiling regime, the tilt angle of the multi-

channel flat heat pipe only has a noticeable impact on the boiling thermal resistance at tilt angles close to the horizontal.

#### 6.2.4.2 Condensation thermal resistance

Like the analysis done on the impact of the tilt angle on the boiling thermal resistance, in Figure 6-65 is presented the impact of the tilt angle of the multi-channel flat heat pipe on the condensation thermal resistance.

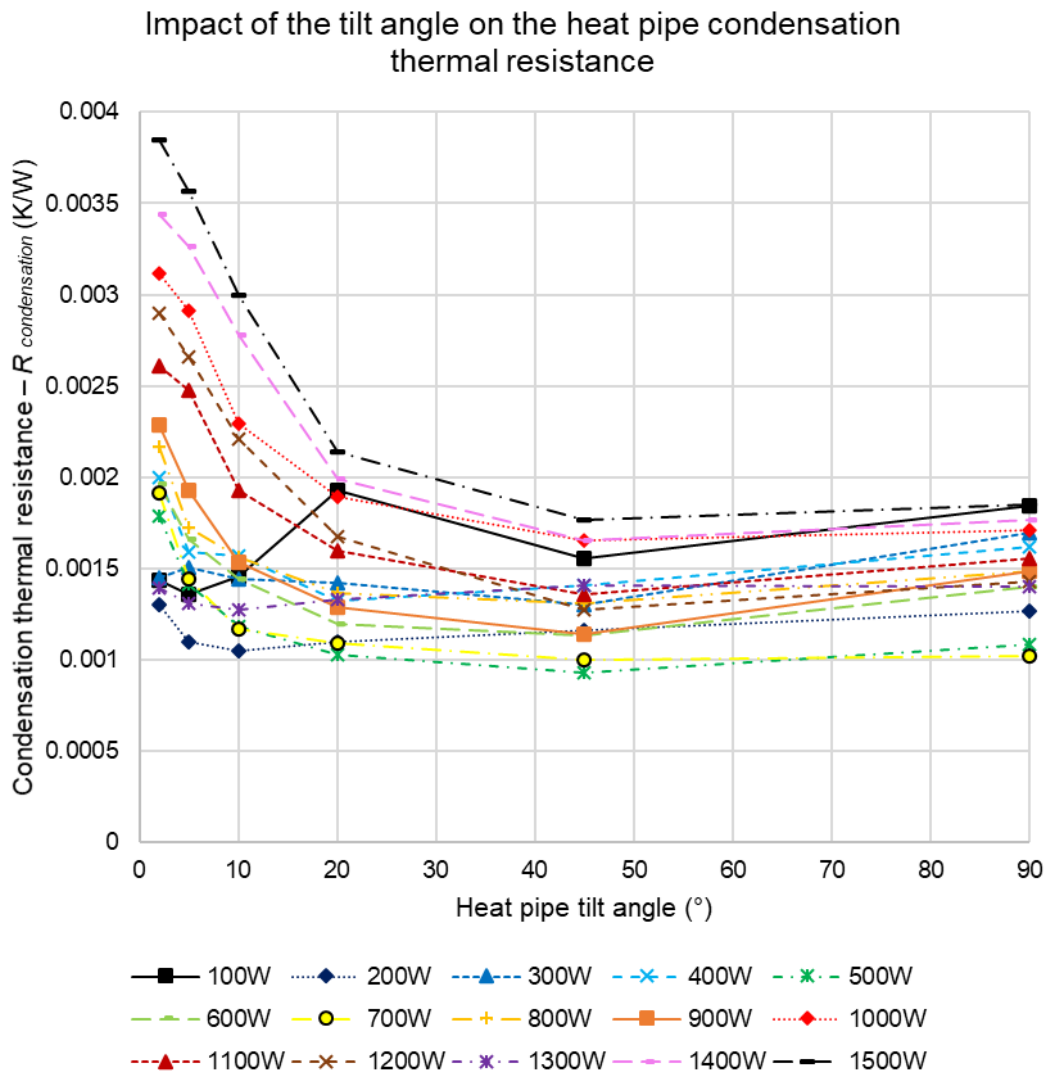


Figure 6-65. Impact of the tilt angle on the multi-channel flat heat pipe condensation thermal resistance

From Figure 6-65, it is observed that a discontinuous trend of the condensation thermal resistance at 100 W is obtained. Based on the previous study of the impact of the heat transfer rate on the condensation thermal resistance of the flat heat pipe, it is concluded that the data at 100 W for the condensation thermal resistance is inaccurate. Hence, to study the impact of the tilt angle on the condensation thermal resistance at low heat transfer rates, more attention is given to the data at 200 W.

In opposition to the impact of the tilt angle on the boiling thermal resistance, the impact of the angle on the condensation thermal resistance is minimum at low heat transfer rates and maximum at high heat transfer rates. Indeed, at 200 W, the maximum variation of the condensation thermal resistance between a horizontal and vertical position is 0.00026 K/W whereas, at 1500 W, this variation is up to 0.002 K/W.

At low heat transfer rates in the range 100-300 W, it seems that the condensation thermal resistance of the multi-channel heat pipe is mainly impacted by the tilt angle when the angle is decreased below 10°. Indeed, from a tilt angle of 10° to 90°, a slight increase of the condensation thermal resistance is observed but the variation is limited. For instance, at a heat transfer rate of 200 W, the condensation thermal resistance increases by 0.00022 K/W from a tilt angle of 10° to 90° whereas it increases by 0.00026 K/W from a tilt angle of 10° to 2°.

At heat transfer rates between 400 W and 800 W, the increase of the condensation thermal resistance no longer occurs at tilt angle lower than 10° only. Indeed, from a tilt angle of 20°, it is noted that the condensation thermal resistance is higher than at a tilt angle of 45°.

Overall, the increase of the condensation thermal resistance with a decrease of the heat pipe tilt angle is exponential. Furthermore, increasing the heat transfer rate makes the exponential increase to start at higher tilt angles, which results into more important exponential increase of the condensation thermal resistance.

Hence, at higher heat transfer rates in the range 900-1500 W, the difference of condensation thermal resistances between a tilt angle of 45° and 20° is more and more important. The variation is also maximum at the highest heat transfer rate: at 1500 W, between a tilt angle of 45° and 2°, the condensation thermal resistance increases by 0.0021 K/W. In comparison, at heat transfer rates of 1000 W and 500 W, the condensation thermal resistance increases by 0.0015 K/W and 0.0009 K/W.

To understand the reason of the increase of the condensation thermal resistance at low tilt angles, the multi-channel flat heat pipe temperature under a heat transfer rate of 1500 W at the adiabatic and condenser sections is studied in Figure 6-66.

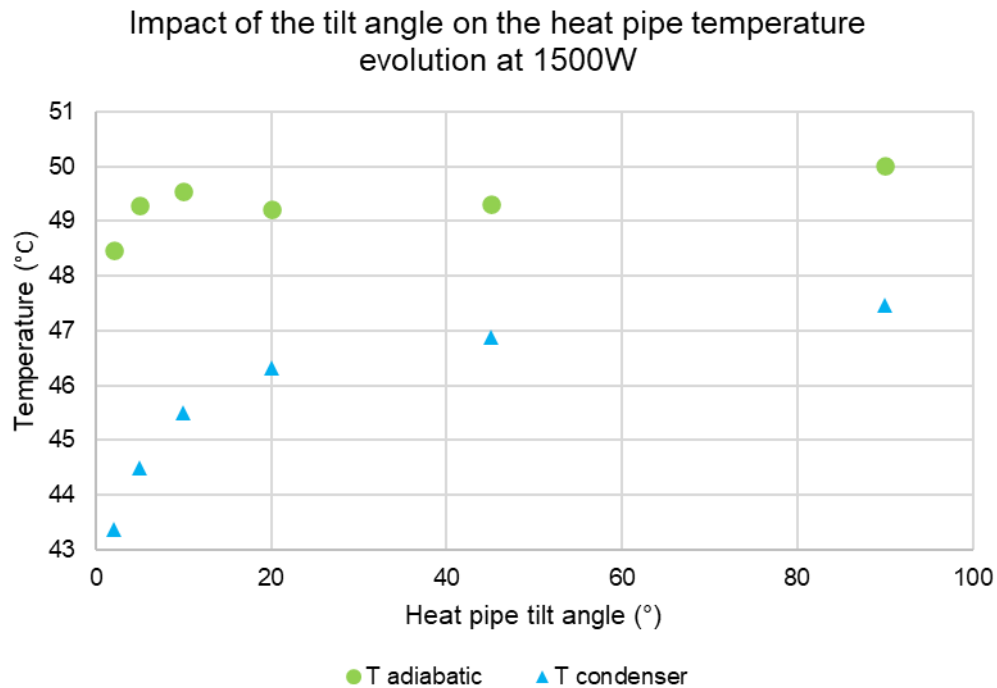


Figure 6-66. Impact of the tilt angle on the adiabatic and condenser temperature of the heat pipe at a heat transfer rate of 1500W.

From Figure 6-66, it is observed that the increase of the condensation thermal resistance at low tilt angles is mainly due to a significant decrease of the condenser temperature at tilt angles lower than 20°. At the adiabatic section, a decrease of temperature is also occurring but is more limited. Indeed, at 1500 W, between a tilt angle of 2° and 10°, the adiabatic temperature changes by 1.1°C whereas the condenser temperature varies by 2.1°C.

At this stage, the physical explanation of the increase of the condensation thermal resistance at low tilt angles can be explained by hypothesis only. Potential hypothesis can be a difficulty of the vapour to rise, the difficult formation of a condensate layer on the top wall of the channels, the condensate falling on the bottom surface of the channels and no longer wiping the newly formed condensate, or a different condensate/rising vapour interaction. Yet, to better understand the observed phenomena, further investigations are needed.

Finally, for all the heat transfer rates, it seems important to mention that the condensation thermal resistance of the multi-channel flat heat pipe is minimal at 45°. This is a valuable information as the ideal position of a PV/T installation is in a range 30°-60° (depending on the location) where the condensation thermal resistance of the flat heat pipe is minimum.

### 6.2.4.3 Total thermal resistance

In Figure 6-67 is presented the impact of the tilt angle of the multi-channel flat heat pipe on the total thermal resistance.

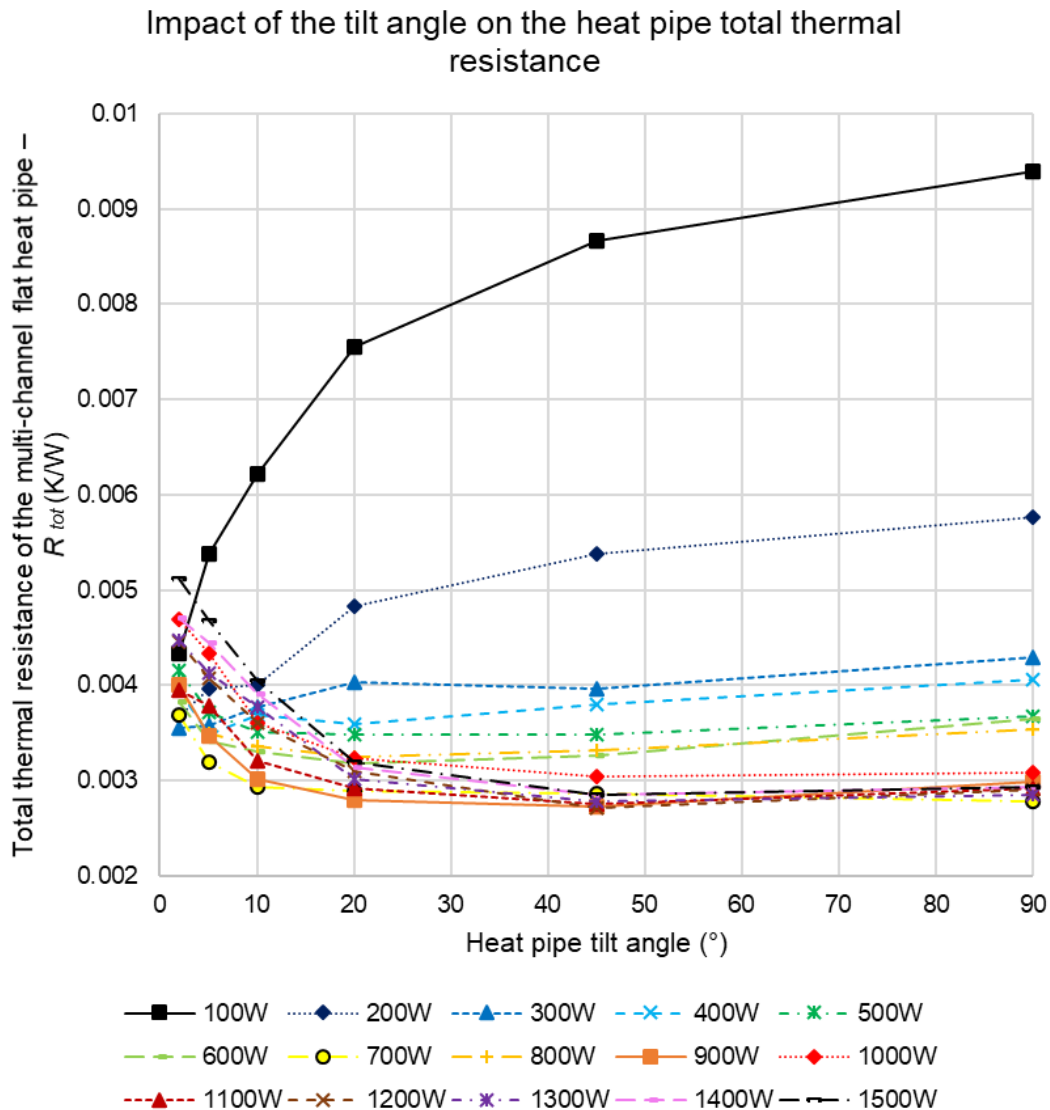


Figure 6-67. Impact of the tilt angle on the multi-channel flat heat pipe total thermal resistance

From Figure 6-67, the phenomena observed during the study of the impact of the tilt angle on the boiling and condensation thermal resistances are clearly visible. At low heat transfer rates, it is clear that the total thermal resistance of the heat pipe increases when rotating the multi-channel flat heat pipe from a horizontal position (2°) to a vertical position (90°) due to the increase of the boiling thermal resistance. With an increase of the heat transfer rate, the change in the boiling thermal resistance becomes small whereas the change of the condensation thermal resistance becomes significant at low tilt angles. As a result, at higher heat transfer rates, an increase of the multi-channel flat heat pipe thermal resistance can be seen at low tilt angles. For clarity purposes and to better analyse the different heat transfer



rates, the analysis of the impact of the tilt angle on the total thermal resistance of the flat heat pipe is divided in Figure 6-68 in three graphs: low heat transfer rates, medium heat transfer rates, and high heat transfer rates.

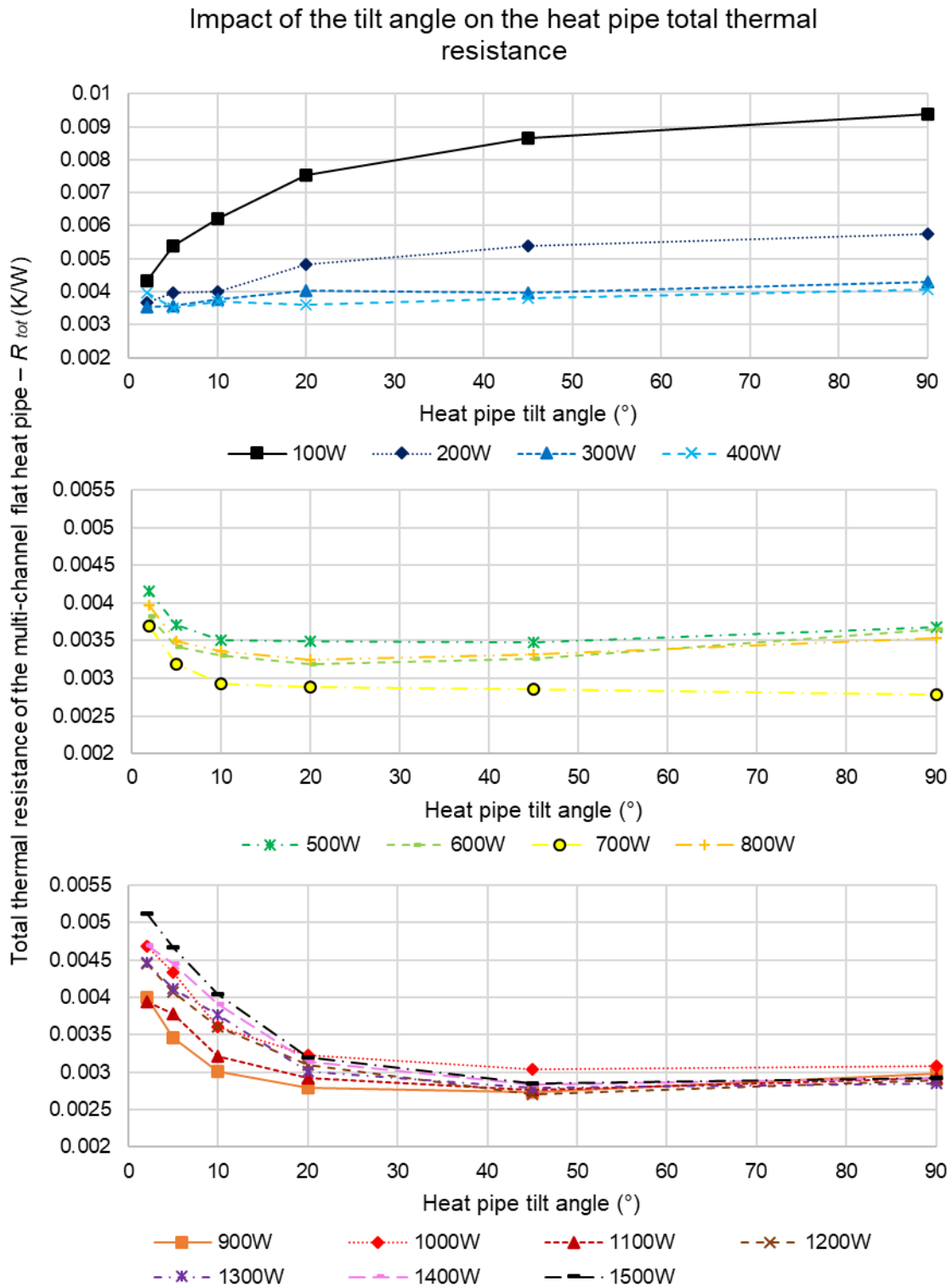


Figure 6-68. Impact of the tilt angle on the multi-channel flat heat pipe total thermal resistance for low, medium, and high heat transfer rates.

At low heat transfer rates, changing the tilt angle of the multi-channel flat heat pipe has a significant impact on the boiling thermal resistance but a small impact on the condensation thermal resistance. As a result, at heat transfer rates lower than 100 W, the total thermal resistance of the heat pipe increases with an increase of the tilt angle from 2° to 90°. Yet, this increase is less important with the increase of the boiling activity. Indeed, at heat transfer rates of 100 W, 200 W, and 300 W, between 2° (horizontal) and 90° (vertical), the total thermal resistance of the heat pipe increases by 0.0051 K/W, 0.0021 K/W, and 0.0007 K/W, respectively. At a heat transfer rate of 400 W, the total thermal resistance of the heat pipe is fairly constant at a value of 0.0037 K/W. Only a small increase of the total thermal resistance can be noted at a tilt angle of 2°.

At medium heat transfer rates, a change of the tilt angle no longer impacts the boiling thermal resistance of the multi-channel flat heat pipe. Instead, changing the tilt angle increases the condensation thermal resistance at angles lower than 10°. As a result, the total thermal resistance of the heat pipe increases exponentially at heat transfer rates in the range 500–800 W when the tilt angle is decreased from 10° to 2°. This increase of the total thermal resistance is about 0.0006 K/W. For medium heat transfer rates, at higher tilt angle from 10° to 45°, the total thermal resistance remains constant. Only a slight increase of the heat pipe thermal resistance is observed when the heat pipe is placed in a vertical position.

At high heat transfer rates, changing the tilt angle of the multi-channel flat heat pipe has a negligible impact on the boiling thermal resistance but a significant impact on the condensation thermal resistance. Hence, the same phenomenon observed on the condensation resistance is observed on the total thermal resistance of the multi-channel flat heat pipe: decreasing the tilt angle of the heat pipe lower than 20° results into a significant increase of the total thermal resistance. The higher the heat transfer rate, the more important the increase of the total thermal resistance at positions near the horizontal. Indeed, at a heat transfer rate of 1500 W, between a tilt angle of 20° and 2°, the total thermal resistance of the heat pipe increases from 0.0032 K/W to 0.0052 K/W.

Again, to better explain the observed increase of condensation thermal resistance at high heat transfer rates and low tilt angles, further investigations are needed.

Overall, at heat transfer rates higher than 200 W, the total thermal resistance of the multi-channel flat heat pipe is the lowest for a tilt angle range of 20°-60° which suits the optimum tilt angles for photovoltaic electrical production. Hence, the investigated multi-channel flat heat pipe seems adapted to such PV cooling applications.

## 6.2.5 Infrared imaging of the multi-channel flat heat pipe

In the objective of verifying the temperature uniformity characteristic of the flat heat pipe and bringing visual observations of the thermal performance of the investigated multi-channel flat heat pipe, infrared imaging of the multi-channel flat heat pipe has been conducted. In particular, to explain the measured temperature difference between the left and the right of the condenser section, infrared imaging of the cooling manifold and of the condenser section are of interest.

### 6.2.5.1 Infrared imaging of the multi-channel flat heat pipe at 1000W

In this section, infrared imaging of the multi-channel flat heat pipe is studied at a heat transfer rate of 1000 W. At such heat transfer rate, the difference of temperatures within the heat pipe sections are expected to be large enough to be observed with accuracy. Both front and back heat pipe surfaces were observed. Indeed, from the front surface, the evaporator and condenser sections of the heat pipe can't be observed due to the presence of the electrical heaters and cooling manifold. Hence, to observe the temperature distribution of the evaporator and condenser, the back surface must be observed. In this section, the multi-channel flat heat pipe was kept in a vertical position. In Figure 6-69 are shown the different heat pipe sections for the front and back heat pipe surfaces.

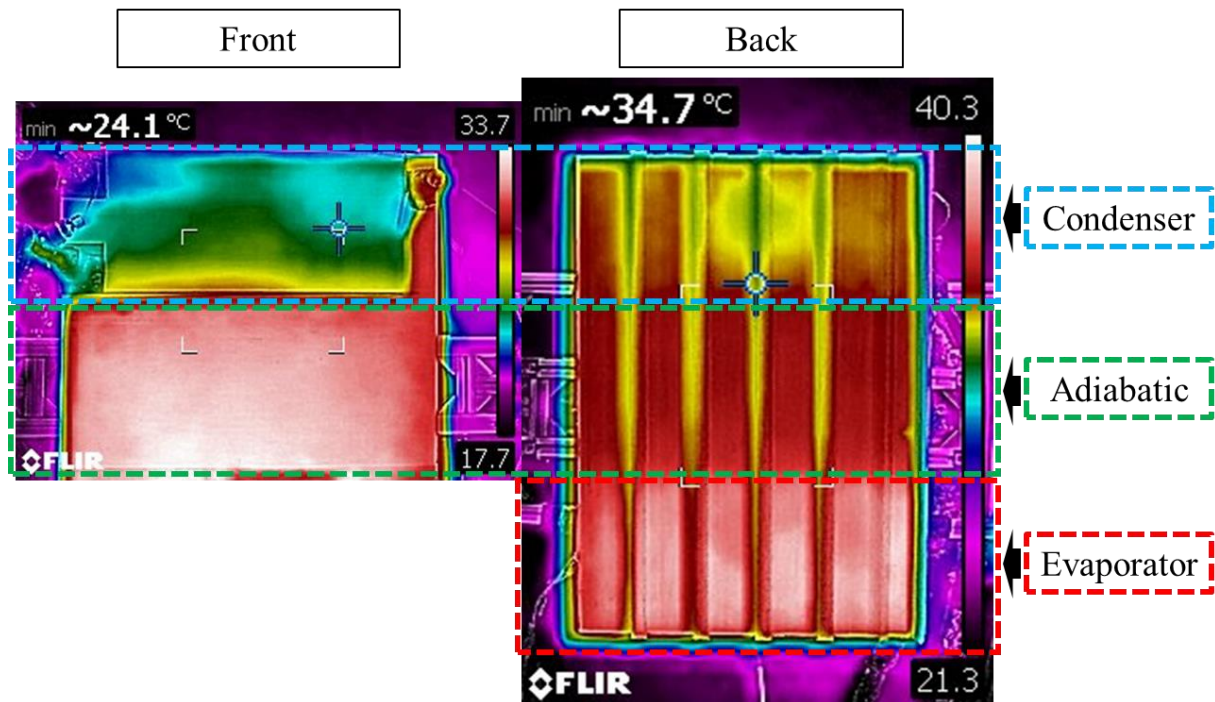


Figure 6-69. Infrared imaging of the front and back surfaces of the multi-channel flat heat pipe at a heat transfer rate of 1000W.

On the left-hand side of Figure 6-69 is shown the front surface of the multi-channel flat heat pipe whereas, on the right-hand side is shown the back surface. In the above, the evaporator, adiabatic, and condenser sections are indicated by red, green, and blue dashed lines. On the

front view of the heat pipe can be observed the adiabatic section and the cooling manifold. Below the adiabatic section were placed the electrical heaters which remained insulated to limit thermal losses and not disturb the thermal imaging of the adiabatic section. The detailed infrared imaging of the front heat pipe surface is presented in Figure 6-70.



Figure 6-70. Detailed infrared imaging of the front heat pipe surface

From Figure 6-70, it can be observed that the temperature distribution of the adiabatic section of the multi-channel flat heat pipe is very uniform. Indeed, no significant temperature gradient can be observed in the vertical or horizontal direction. On the left and right sides of the heat pipe, a red border can be seen which indicates that the temperature is slightly lower. This can be explained by the increased contact area of those zones with the ambient air which increases the thermal losses to the environment and thus slightly decreases the temperature in these zones. A similar red layer can be seen underneath the cooling manifold where the proximity of the cooling manifold slightly reduces the adiabatic surface temperature. Nevertheless, the temperature variation observed from the front adiabatic surface are small, and the temperature uniformity characteristics of the multi-channel flat heat pipe seems validated. At the top of the adiabatic section, a more important temperature gradient is observed on the cooling manifold. This is investigated closely in Figure 6-71.

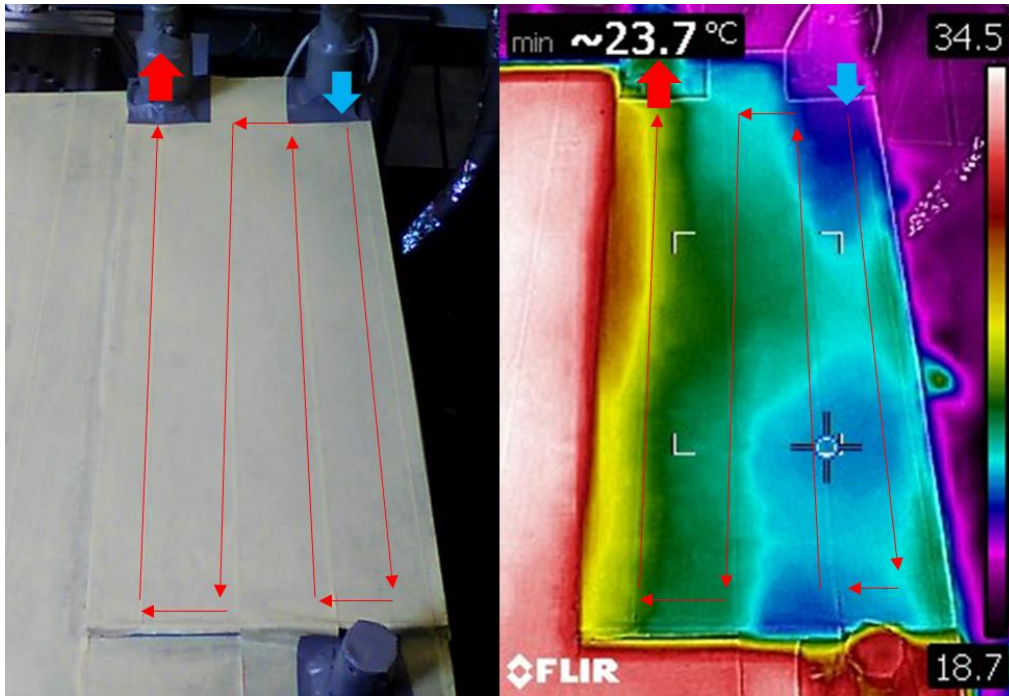


Figure 6-71. Detailed infrared imaging of the cooling manifold

On the left-hand side of Figure 6-71 is shown the picture of the cooling manifold whereas the right-hand side shows the infrared imaging of the cooling manifold. On both sides, red arrows describe the cooling water circulation through the four different passes inside the cooling manifold. The cold-water inlet is located on the right of the picture which is the top of the cooling manifold. From the infrared imaging, it is observed that the cooling manifold temperature is lower at the top, and higher at the bottom of the manifold. This is expected and explained by the increase of the water temperature inside the cooling manifold as it recovers thermal energy from the heat pipe. Even if the transient warmup of the cooling water implies a temperature gradient from top to bottom, the differences of temperatures between the right and left sides of the manifold is limited. Nevertheless, in the middle of the cooling manifold, a zone of higher temperature is observed in green in Figure 6-71. Hence, it seems that the cooling manifold absorbs more energy from the middle of the manifold. This phenomenon is confirmed by observing the condenser section at the back of the multi-channel flat heat pipe presented in Figure 6-72.

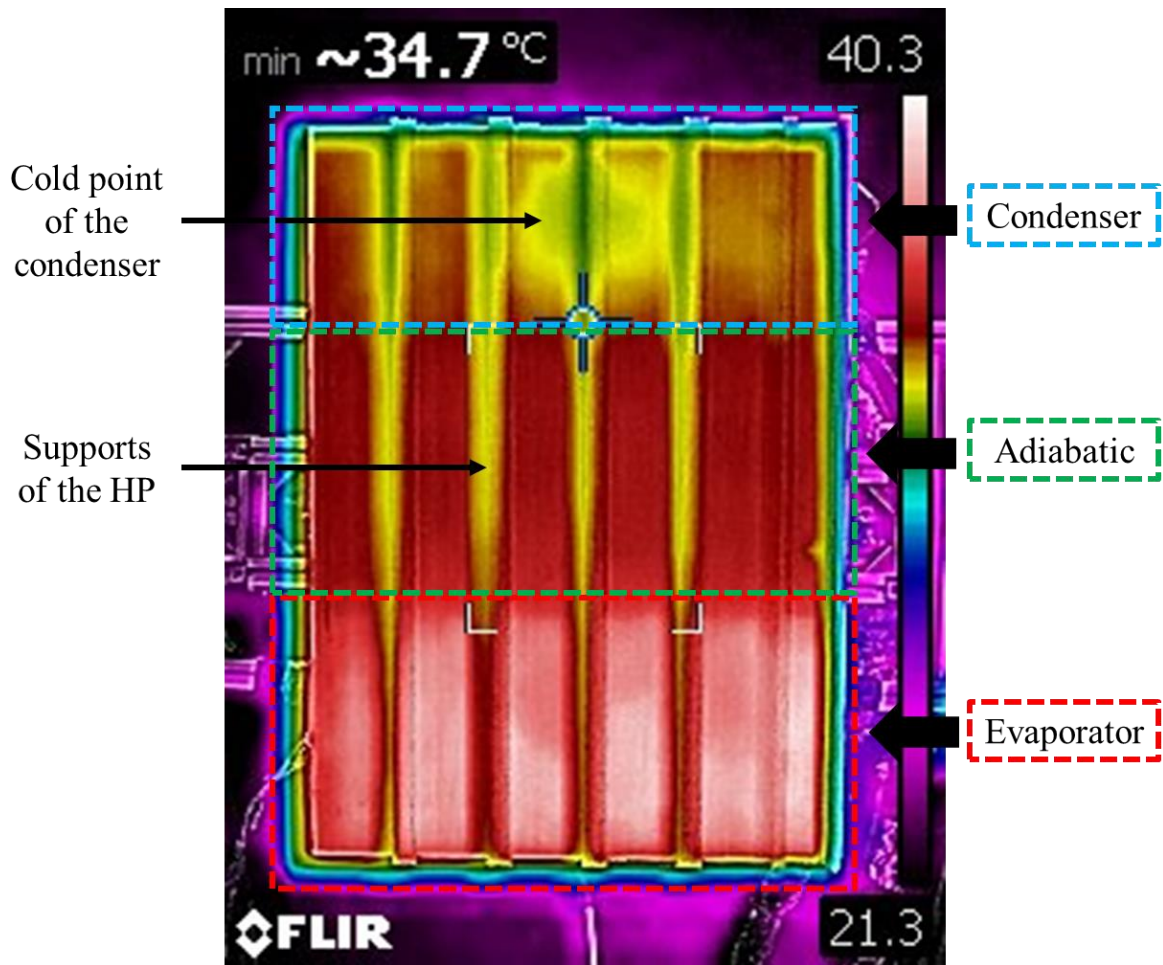


Figure 6-72. Detailed infrared imaging of the back heat pipe surface

From the infrared imaging of the back heat pipe surface, the three sections of the multi-channel flat heat pipe (namely evaporator, adiabatic, and condenser) can be observed. Four vertical lines of colder temperature can be seen and correspond to the inactive and metallic supports of the flat heat pipe. At the bottom of the multi-channel flat heat pipe, the hottest section shows the temperature uniformity of the evaporator section. No significant difference of temperatures can be seen between the top and bottom of the evaporator. Between the left and right sides of the evaporator, even if the right side of the evaporator seems slightly hotter than the left side, the difference of temperature is minimum. As for the adiabatic section, the infrared imaging confirms the constant temperature of the section. The observed temperature uniformity of the evaporator and adiabatic sections agree with the temperature measurements taken from thermocouples presented earlier. However, at the condenser, it was observed that significant differences of temperatures were detected between the right and the left of the condenser sections. From the infrared imaging of the condenser section, one can note that a cold point situated in the middle of the section is observed. In agreement with the observation of the cooling manifold, the infrared imaging reveals that more energy was absorbed from the middle of the condenser section. This cold section of the condenser sections explains the difference

of temperature measured in the study of the condensation thermal resistance of the multi-channel flat heat pipe. Indeed, the two thermocouples LB1 and LB2 were placed closer to the cold point of the condenser as shown in Figure 6-73.

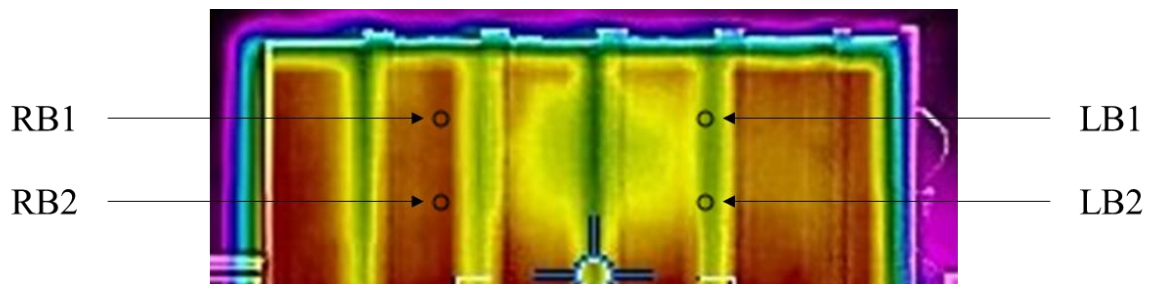


Figure 6-73. Thermocouple's location on the infrared imaging of the condenser

Hence, the measured temperature at the right of the condenser was higher than the left side of the condenser. Nevertheless, it is also observed that a significant portion of the condenser section isn't covered by the cold zone observed. Hence, in the calculation of the heat pipe thermal resistances, taking an average of the condenser temperature measurements seemed relevant and representative of the condenser temperature.

Interestingly, the cold point of the condenser isn't situated on the side near the water inlet. Indeed, the heat recovery could be expected to be higher were the temperature difference between the heat pipe and cooling water is maximum. In this scenario, the cold point would be situated on the side of the heat pipe. However, in this case, the cold point is situated in the middle of the condenser. Several factors can be responsible of this phenomenon. A first hypothesis is the quality of the contact interface between the heat pipe and the cooling manifold. Indeed, depending on the layer of thermal paste placed at the interface, the thermal contact between the cooling manifold and the heat pipe can be improved locally and generate the observed phenomenon. A second hypothesis is that the flow circulation inside the cooling manifold favours the heat absorption in this section of the cooling manifold. Finally, a less likely but potential hypothesis is that such cold point would be created due to a limited working fluid circulation of the heat pipe. However, in the design of the multi-channel flat heat pipe, the horizontal collectors at the top and bottom linking the parallel channels are expected to allow the circulation of the working fluid from each side of the heat pipe. Hence, it seems relevant to investigate the capacity of the multi-channel flat heat pipe and of its internal geometry to circulate the working fluid from one side to the other. In this regard, in the next section, the cooling manifold was placed on the right of the heat pipe and the temperature distribution is investigated with infrared imaging.

### 6.2.5.2 Infrared imaging of the flat heat pipe with the cooling manifold situated on one side

In this section, the vertical position of the heat pipe and the heat transfer rate of 1000 W remain unchanged. However, in the objective of investigating the capacity of the multi-channel heat pipe to maintain a uniform temperature distribution when the heat sink is placed on the side, in this section, the cooling manifold was placed on the left of the heat pipe. In Figure 6-74 is presented the infrared imaging of the back surface of the multi-channel flat heat pipe with the cooling manifold placed on the side.

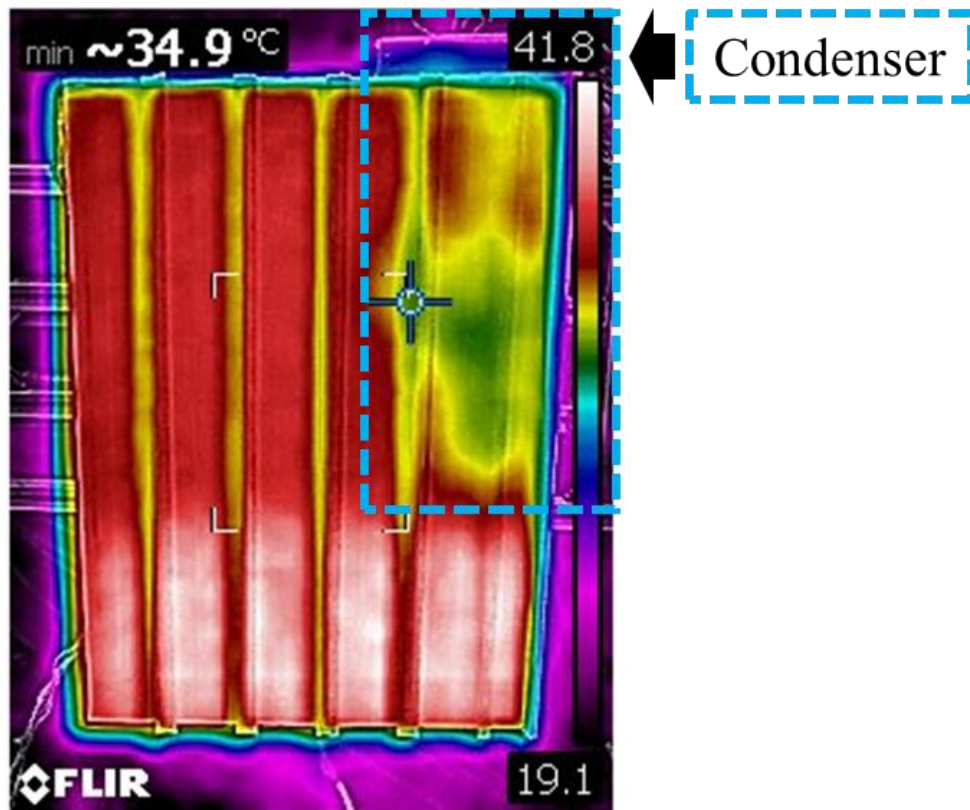


Figure 6-74. Infrared imaging of the back heat pipe surface with a cooling manifold placed on the side

In the above figure, the location of the cooling manifold is shown with blue dotted lines. It is observed that the temperature distribution of the evaporator and adiabatic sections remains very uniform despite the location of the condenser. For instance, due to the proximity of the cooling manifold, the right side of the evaporator could present lower temperatures than the rest of the evaporator section. However, experimentally, the temperature of the evaporator remains constant regardless of the position of the heat sink. Moreover, it is observed that the adiabatic section temperature is also uniform. No accumulation of heat at the top of the heat pipe can be observed which attest that the thermal energy is transmitted from the left side of the heat pipe to the right and is well extracted from the cooling manifold situated on the right side. Hence, it seems that the studied multi-channel flat heat pipe and its internal thermal geometry allows a satisfying circulation of the working fluid and an efficient heat transfer in



both vertical and horizontal direction and this, regardless of the location of the heat sink. As a conclusion, the cold point observed at the middle of the condenser section when the cooling manifold was placed at the top was not due to the working fluid circulation inside the heat pipe. Focusing on the temperature profile of the condenser, in the case where the cooling manifold was placed on one side, it is observed that a similar cold spot appears at the middle of the condenser. However, compared to the horizontal top position of the cooling manifold, the cold spot is larger and stretches down in a vertical direction. This is likely to be generated by the influence of gravity on the water flow inside the cooling manifold channels. Nevertheless, the quality of the thermal past contact interface between the cooling manifold and the heat pipe remains a significant factor that could potentially create the formation of such cold spot at the heat pipe condenser. While removing the cooling manifold from the heat pipe, the traces of thermal paste remaining on the heat pipe surface seemed to correspond well with the cold zones observed on the infrared imaging of the condenser. This is shown in Figure 6-75.

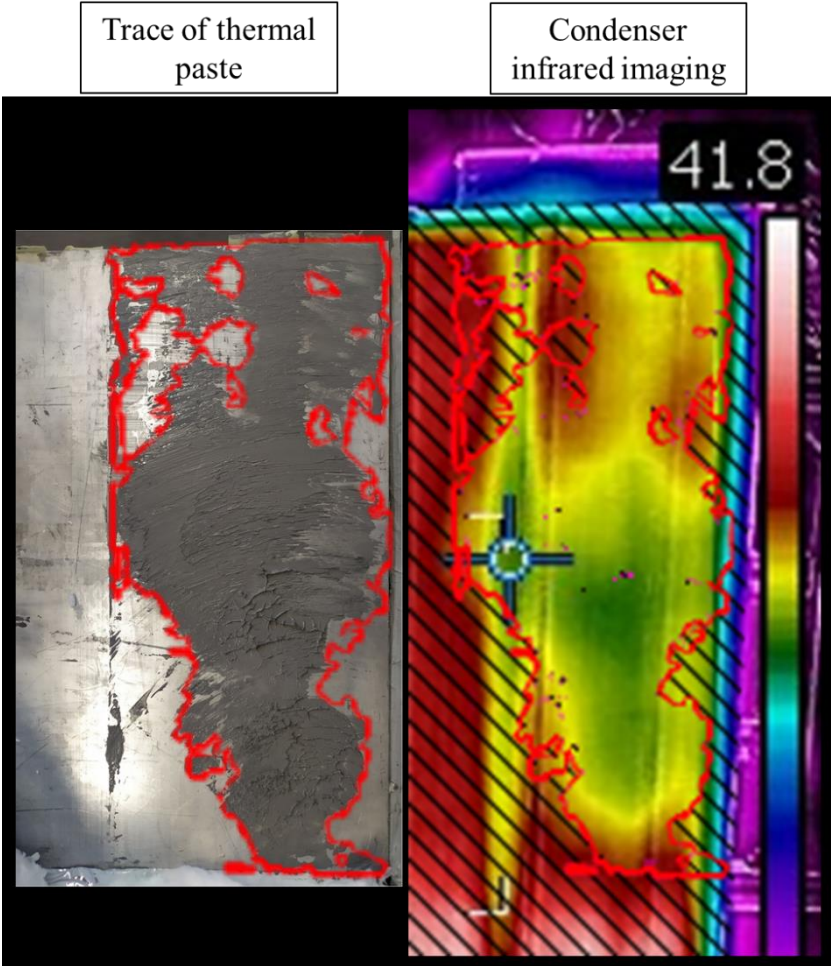


Figure 6-75. Comparison between the traces of thermal paste on the condenser and infrared imaging of the condenser.

As can be seen from Figure 6-75, it seems that the cold spots observed on the infrared imaging correspond to the zones where the amount of thermal paste was higher. Indeed, even if the

cooling manifold surface was fully covered with thermal paste, it seems that, in some zones, the thermal paste didn't adhere to the heat pipe surface. This observation also highlights how important the quality of the interface between the cooling manifold and the flat heat pipe is. If a sufficient amount of thermal paste is needed to assure a good contact, too much thermal paste also results in an increased thickness of the thermal paste which significantly increases the thermal resistance of the interface. Obviously, the thermal conductivity of the thermal paste used also plays a major role in the quality of the contact. Therefore, the cold spot observed at the condenser section is assumed to be caused by the quality of the thermal paste interface between the heat pipe and cooling manifold.

6.2.5.3 Infrared imaging of the Impact of the tilt-angle

In this section, the impact of the tilt angle on the thermal performances of the multi-channel flat heat pipe is observed using infrared imaging. To do so, a heat transfer rate of 1000 W was selected. In Figure 6-76 is shown the front heat pipe infrared imaging at various tilt angles.

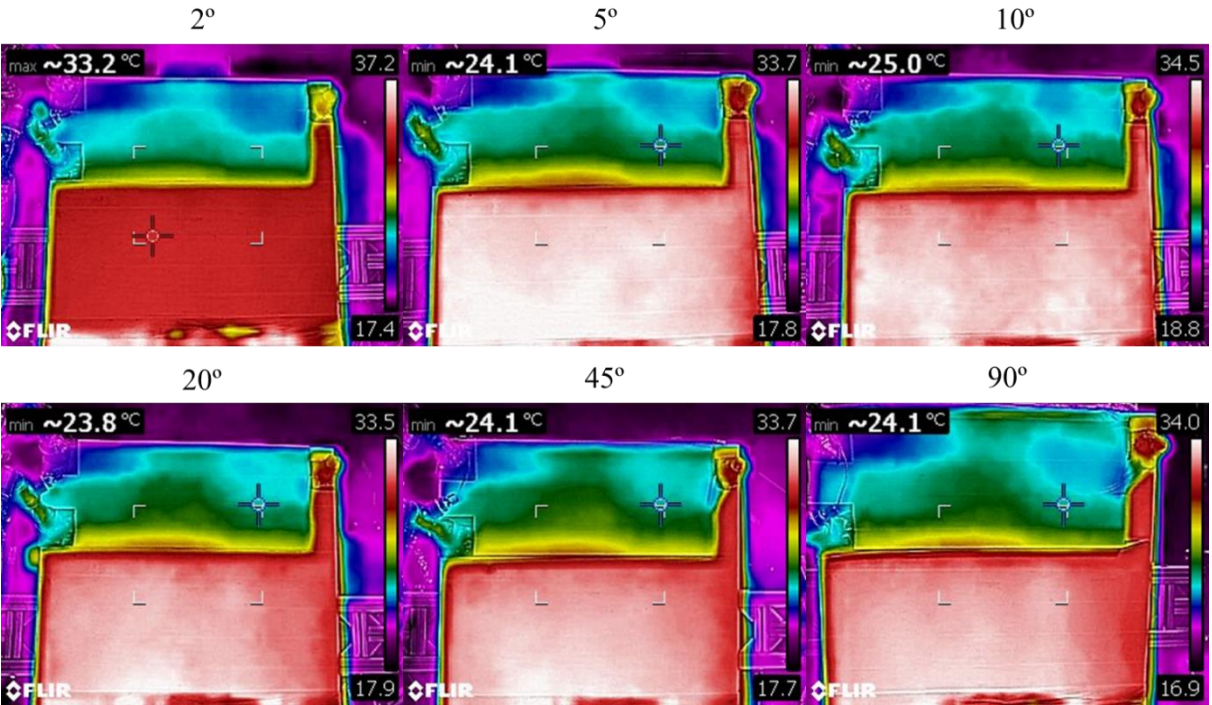


Figure 6-76. Infrared imaging of the front heat pipe surface at various tilt angles

In agreement with the investigation of the tilt angle impact on the thermal performances of the flat heat pipe, the temperature of the adiabatic section remains similar at all tilt angles. More importantly, it is observed that the temperature uniformity of the multi-channel heat pipe is maintained while changing the tilt angle. No changes of the temperature profile can be detected on the cooling manifold either. Unfortunately, due to the position of the heat pipe and of the test rig used, the back surface of the flat heat pipe could not be observed at low tilt angles. Yet, in the future, it would be interesting to visualise the evolution of the condenser temperature

profile at low tilt angles to provide more elements on the observed increase of the condenser thermal resistance close to the horizontal.

#### 6.2.5.4 Infrared imaging of the impact of the heat transfer rate

To complete the investigation of the impact of the heat transfer rate on the thermal performance of the multi-channel flat heat pipe, the back surface of the heat pipe was observed with the infrared camera at different heat transfer rates in a vertical position. This is presented in Figure 6-77.

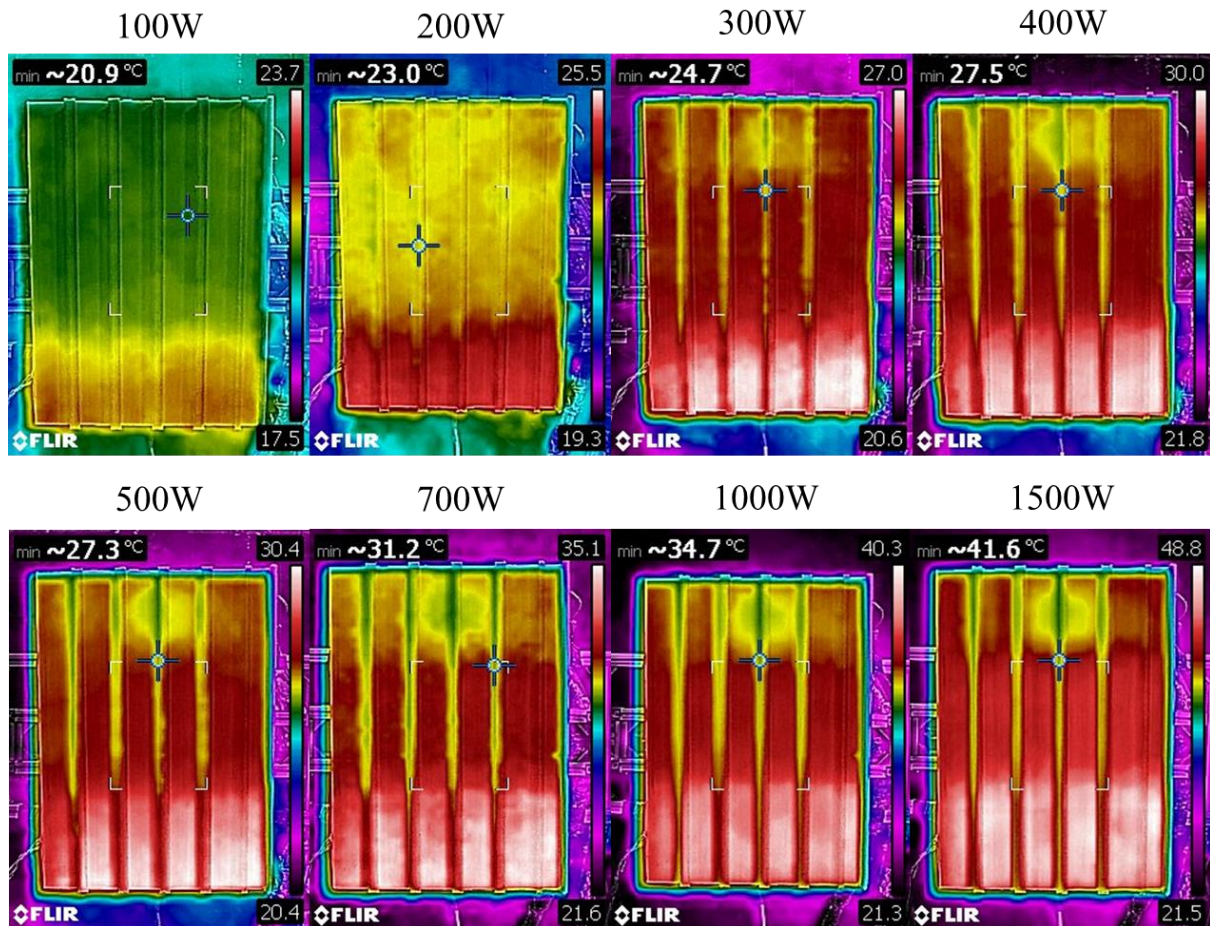


Figure 6-77. Infrared imaging of the back heat pipe surface at various heat transfer rates

At a heat transfer rate of 100 W, the evaporator section is clearly seen in orange at the bottom of the surface. However, the small temperature difference between the adiabatic and condenser sections cannot be detected by the infrared camera. Thus, the condenser section cannot be seen at heat transfer rates of 100 W and 200 W. From a heat transfer rate of 300 W, the temperature difference between the adiabatic and condenser section reaches 1°C and a colder zone at the condenser appears on the infrared imaging. The coldest point of the condenser is situated in the middle of the section where the thermal paste contact was observed to be optimum. This colder zone at the condenser becomes wider at heat transfer rates of 400 W and 500 W. At the evaporator and adiabatic sections, the temperature profile is uniform. The only potential observation that can be made is that the extreme left of the heat

pipe evaporator seems to be slightly colder at heat transfer rates in the range 300 W - 500 W. This seems to be indicated by a reddish zone on the left of the evaporator. Yet, this difference of temperature isn't obvious and cannot be observed at higher heat transfer rates. From a heat transfer rate of 700 W and beyond, the multi-channel flat heat pipe temperature profile observed from the thermal camera is similar: the evaporator and adiabatic sections show a uniform temperature symbolized by white and red surfaces respectively. At the condenser section, the previously described temperature profile is clearly seen, with colder spots observed where the layer of thermal paste was more important.

6.2.5.5 Infrared imaging of the transient warmup of the multi-channel flat heat pipe

The temperature uniformity of the multi-channel flat heat pipe was also visualized during its transient warmup. To do so, thermal imaging of the back surface of the heat pipe was taken every 5s during its warmup at a heat transfer rate of 1000 W. The heat pipe was placed in a vertical position. This is presented in Figure 6-78.

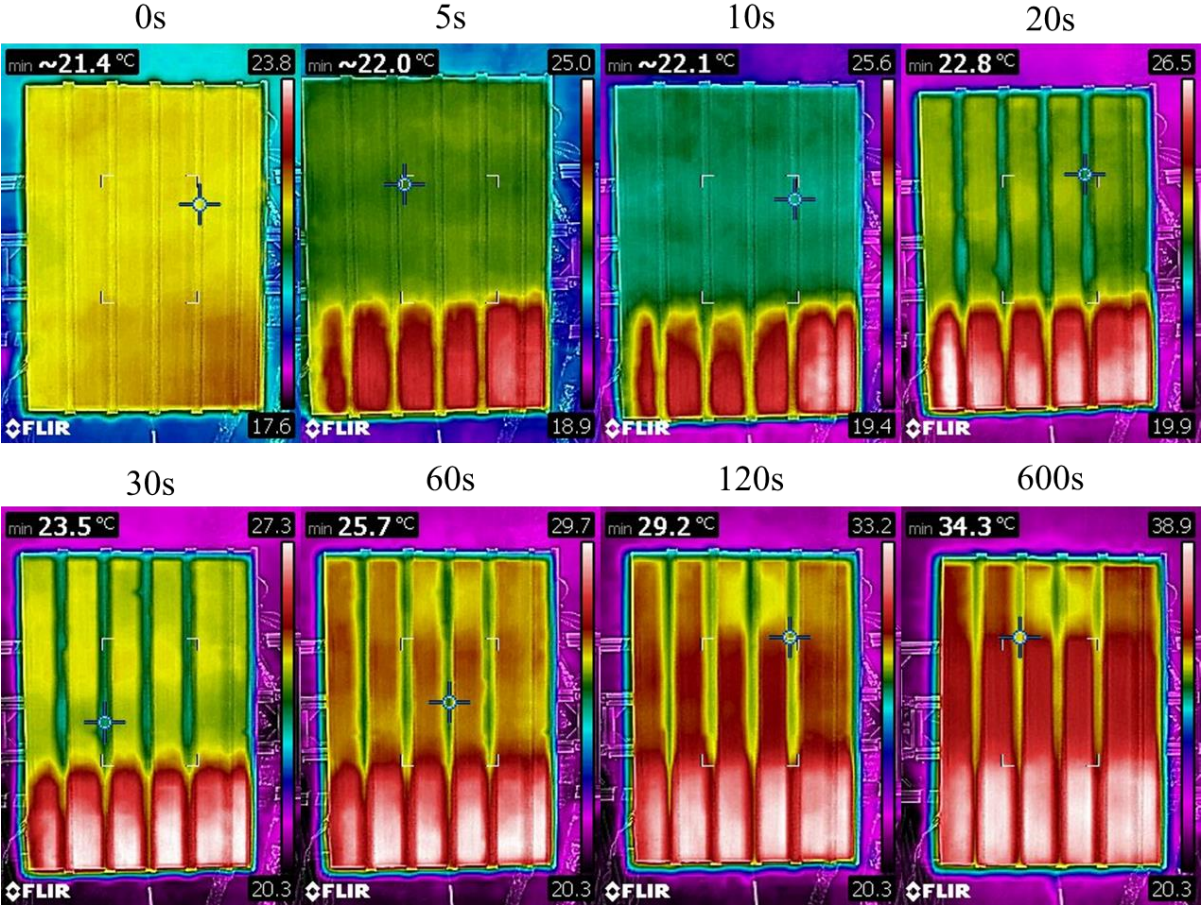


Figure 6-78. Infrared imaging of the transient warmup of the multi-channel flat heat pipe

From the transient imaging of the heat pipe, it is observed that, below 10s, the right side of the evaporator has a temperature slightly higher than that of the left side. This was explained by the heater temperature which was higher on the right than on the left. After 20s, with the increase of the boiling activity, the temperature uniformity of the evaporator section improves,

and no temperature difference can be detected between the right and left side of the evaporator anymore. At the adiabatic and condenser section, a uniform warmup of the multi-channel flat heat pipe is observed during the first 30s. Before 60s of warmup, the temperature difference between the adiabatic and condenser section cannot be visualized by the infrared camera. Yet, after 1 minute, the colder spot in the middle of the condenser section starts to appear and contrasts more and more with the increasing temperature of the adiabatic section. After 2 minutes of transient warmup of the heat pipe, the temperature profile observed is very close to the steady state profile. At 600s, no more temperature evolution can be seen from the infrared imaging and steady state is reached.

## **6.2.6 Phasing out of R134a to a low GWP refrigerant**

### *6.2.6.1 Context and objective*

In a context of global warming and with the introduction of environmental measures such as signed in the Montreal and Kyoto protocols [252], [253], the use of toxic and hazardous refrigerants must be reduced. Indeed, the working fluids used in heat pipes such as R134a which was used in this study can be harmful for the environment. In this regard, new environment-friendly refrigerants are currently investigated to replace the commonly used heat transfer fluids. In the objective of estimating the toxicity of a refrigerant for the environment, the Global Warming Potential (GWP) indicator has been introduced. The GWP of a refrigerant represents the ratio of the time-integrated radiative efficiency conveyed due to a unit increase of the refrigerant abundance in the atmosphere, to that of a reference gas. For the calculation of the GWP, the reference element is carbon dioxide (CO<sub>2</sub>). Hence, a refrigerant with a GWP of 150 means that 1kg of this refrigerant has the same global warming impact as 150kg of carbon dioxide. The GWP indicator of refrigerants including R134a which was used in this study is presented in Figure 6-79 [242], [254]–[262].

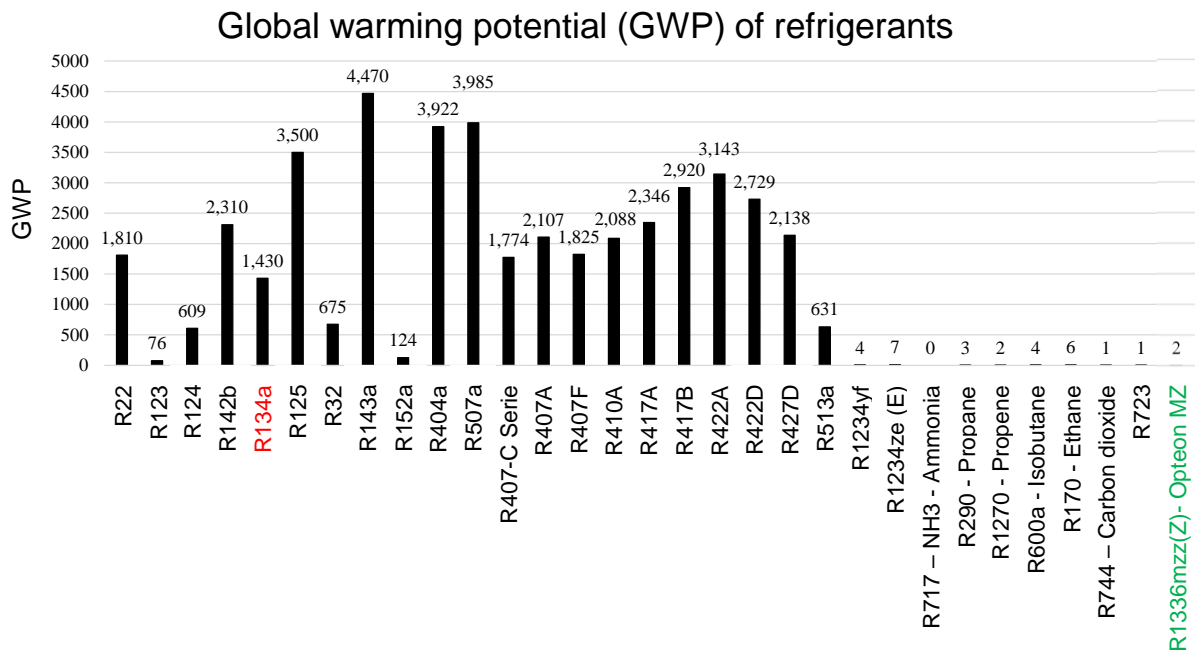


Figure 6-79. Global warming potential (GWP) of refrigerants

On Figure 6-79, a significant difference can be seen between high and medium GWP refrigerants on the left-hand side, and low GWP refrigerants on the right-hand side. R134a, which is the working fluid that was used in the investigated multi-channel heat pipes, is 1430 times more harmful for the environment than carbon dioxide. These indicators clearly highlight the impact of each refrigerant on the global warming and puts in perspective the urgent need of reducing the use of high GWP refrigerants. In this perspective, a new refrigerant called R1336mzz(Z) Opteon MZ was tested in the multi-channel flat heat pipe to investigate its suitability to replace R134a. This new refrigerant has a low GWP of 2 and its thermal performances at steady state are compared with the investigated R134a. For this test, the multi-channel flat heat pipe was maintained in a vertical position only.

#### 6.2.6.2 Thermal resistances comparison

In Figure 6-80 is presented the boiling thermal resistance of the new refrigerant and is compared with that of R134a.

### Boiling thermal resistance comparison between R134a and R1336

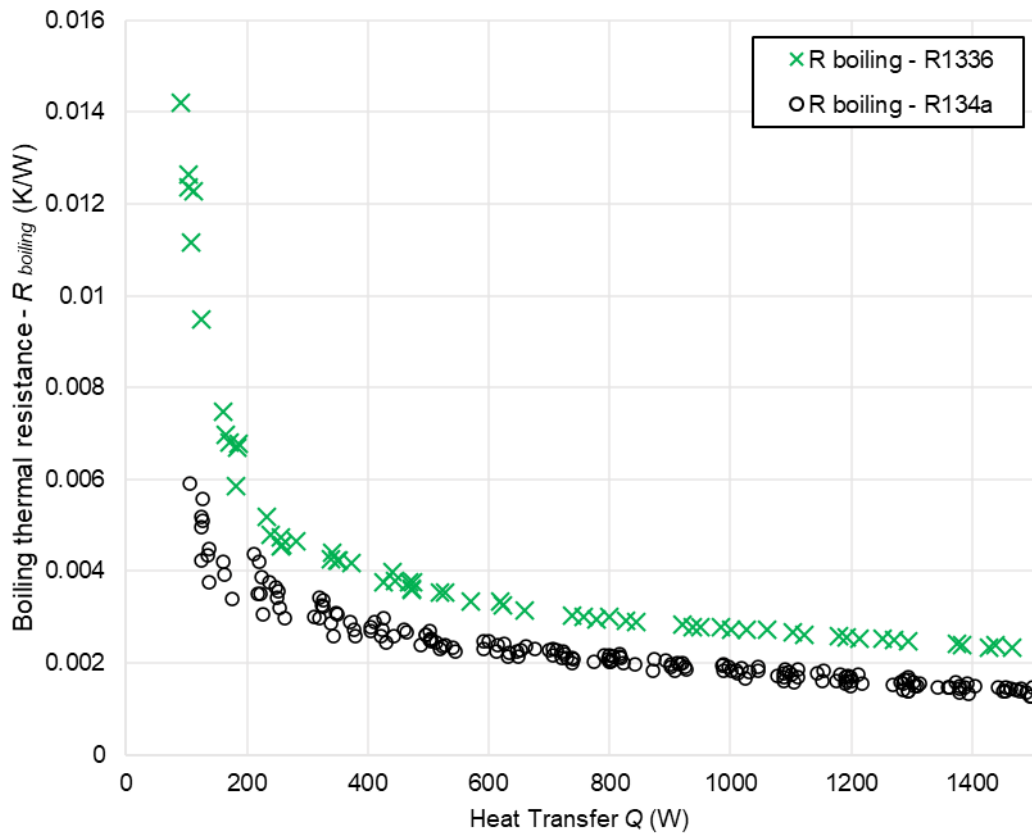


Figure 6-80. Boiling thermal resistance comparison between R134a and Opteon

In Figure 6-80, the multi-channel flat heat pipe boiling thermal resistance using R1336 is represented by green cross markers whereas the boiling thermal resistance using R134a is shown with circular black markers. From Figure 6-80 is observed that the impact of the heat transfer rate on the boiling thermal resistance of the flat heat pipe is similar with both working fluids. At low heat transfer rates, the boiling resistance is high but decreases quickly while increasing the heat transfer rate from 100 W to 400 W. At higher heat transfer rates up to 1500 W, the boiling resistance of both working fluids decreases progressively and reaches its minimum value at 1500 W. Even if the boiling behaviours of both tested fluids look similar, it is observed that, at very low heat transfer rates between 100 W – 200 W, the boiling resistance of R1336 is much higher than that of R134a. Indeed, at a heat transfer rate of 100 W, the boiling thermal resistance of R1336 can be as high as 0.014 K/W whereas it is 0.006 K/W for R134a. From a heat transfer rate of 200 W until 1500 W, the boiling thermal resistance of R1336 closely follows that of R134a with an excess of 0.001 K/W.

In Figure 6-81 is shown the condensation thermal resistance comparison between R134a and the new refrigerant.

### Condensation thermal resistance comparison between R134a and R1336

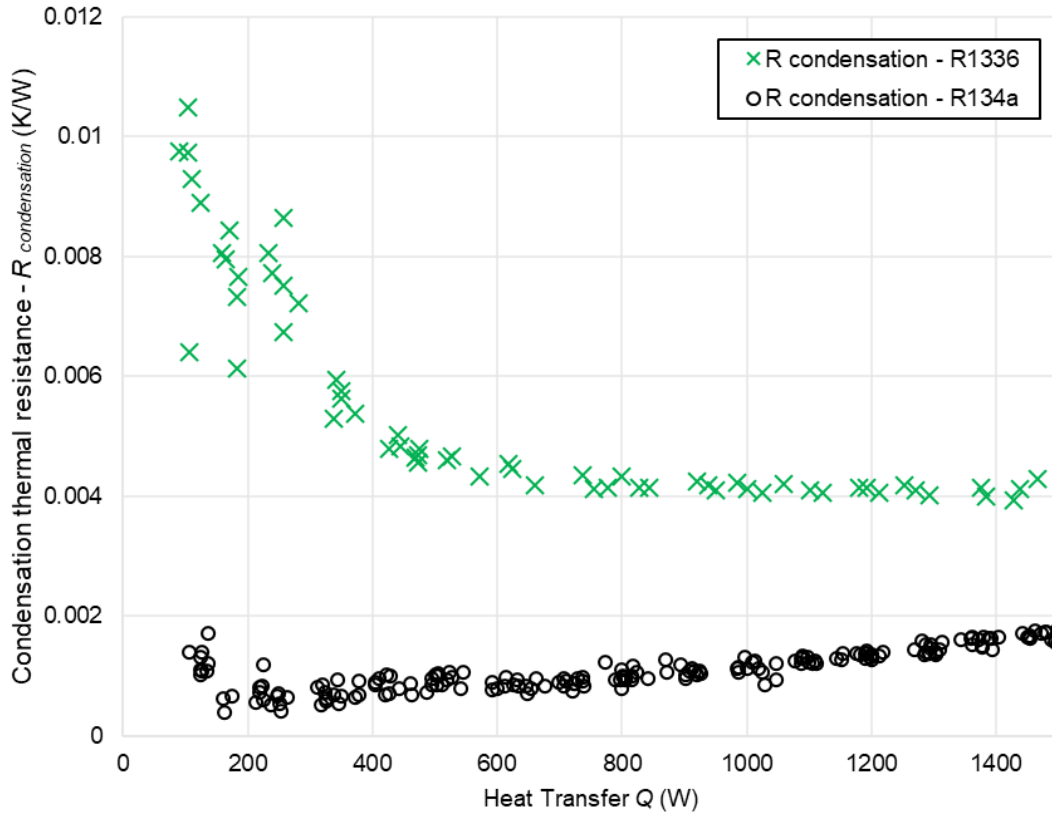


Figure 6-81. Condensation thermal resistance comparison between R134a and Opteon

If the boiling resistance of R1336 looked similar than that of R134a, for the condensation thermal resistance, different behaviours are observed. While the condensation thermal resistance of R134a mainly increases with an increase of the heat transfer rate, at heat transfer rates from 100 W to 600 W, the condensation thermal resistance of R1336 decreases from 0.01 K/W to 0.004 K/W and then stabilizes. As a comparison, the condensation thermal resistance of R134a remains below 0.002 K/W at all heat transfer rates. According to what is observed, R1336 is more difficult to be carried to the top of the multi-channel flat heat pipe and to condense. Yet, at high heat transfer rates, the thermal performance of R1336 become close to that of R134a which potentially indicates that this new refrigerant is more suitable for high temperatures and heat transfer rates.

In Figure 6-82 is shown the total multi-channel flat heat pipe thermal resistance for both R134a and R1336.



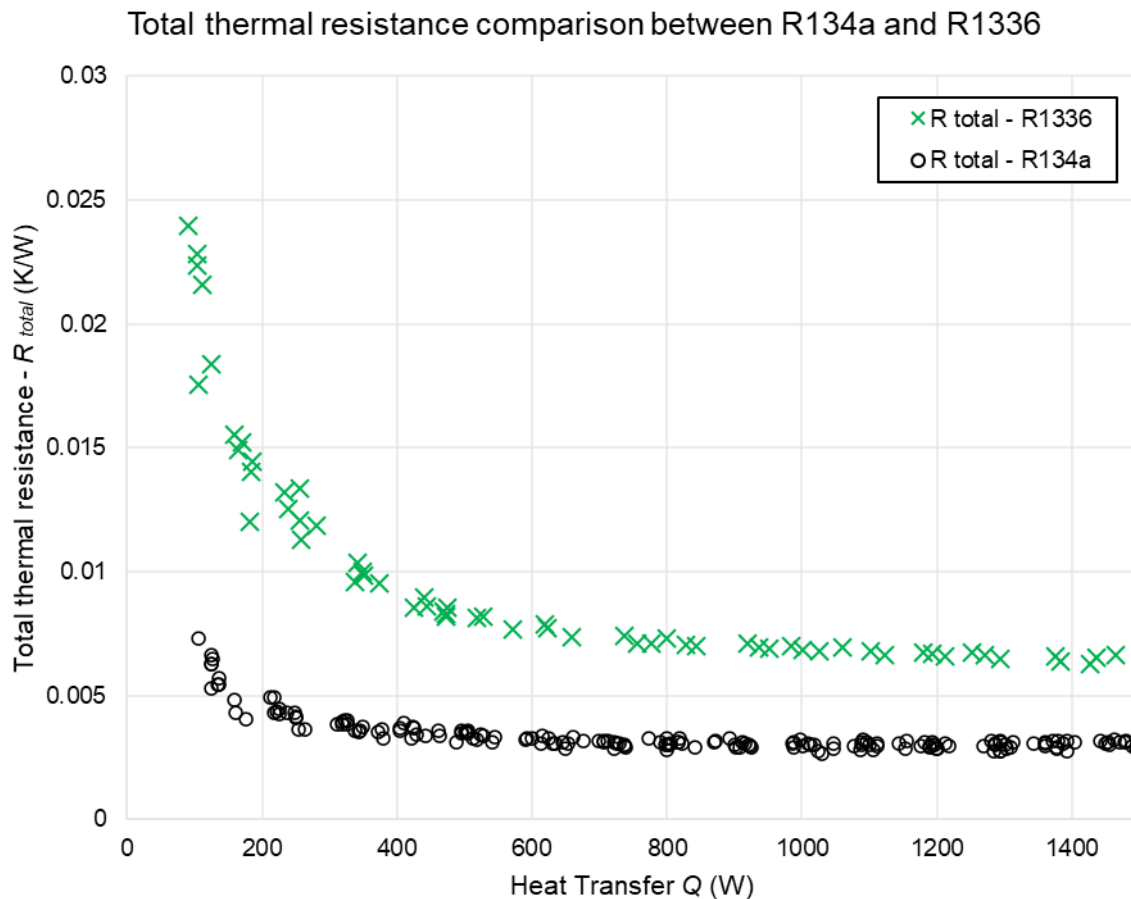


Figure 6-82. Total thermal resistance comparison between R134a and Opteon

Due to the combination of both boiling and condensation thermal resistances, the evolution of the total thermal resistance of the flat heat pipe with the heat transfer rate is similar for both working fluids. At low heat transfer rates ( $\sim 100$  W), the total thermal resistance of the heat pipe is high but decreases sharply until 400 W. Indeed, by increasing the heat transfer rate from 100 W to 400 W, the total thermal resistance of the flat heat pipe with R134a decreases from 0.007 K/W to 0.0035 K/W whereas, for R1336, this total resistance decreases from 0.024 K/W to 0.008 K/W. Beyond a heat transfer rate of 400 W, the total resistance of the flat heat pipe slightly decreases and stabilizes for both working fluids. From a heat transfer rate of 600 W, the difference between the total resistance for both working fluids is close to be constant. While using R1336, the total thermal resistance of the multi-channel flat heat pipe stabilizes around 0.0065 K/W whereas, for R134a, the total thermal resistance at 1500 W is about 0.003 K/W. As a conclusion, using R1336 as a replacement of R134a for environmental purposes implies an increase of the total thermal resistance of the multi-channel flat heat pipe by 130%. Nevertheless, the total thermal resistance of the flat heat pipe above 400 W remains small and below 0.01 K/W when R1336 is used which makes it a potential option for surface cooling application.

---

## Chapter 7 - Conclusions, impact, and suggestions for future work

---

### 7.1 Conclusions from study

In this study, the fundamentals of two-phase heat transfer taking place inside a multi-channel flat heat pipe were investigated. Such flat heat pipes have recently been introduced as thermal absorbers for surface cooling application. For instance, promising performance were observed while using flat heat pipes at the rear of photovoltaic cells (PV) as it permits to maintain a high electrical efficiency of the PV cells and simultaneously recover the excess heat. However, the complex two-phase heat transfer taking place inside such multi-channel flat heat pipe is still poorly understood and remained to be investigated. Furthermore, a review of the literature revealed that the theoretical and numerical (CFD) modelling of such heat pipe is still at an early stage.

The main conclusions from this study are listed below:

- To better understand the two-phase (boiling and condensation) mechanisms taking place inside a multi-channel flat heat pipe, a unique three-leg heat pipe prototype was designed and built. This three-leg heat pipe was developed so that local temperature measurements could be taken from each independent channel and each collector at various locations.
- Based on the theory of two-phase heat transfer, a new thermal resistance model considering the multi-channel geometry of the investigated heat pipes was developed and proposed. This multi-channel heat pipe thermal resistance network considers an independent resistance for both top and bottom collectors, and for all the parallel channels. The proposed multi-channel heat pipe thermal resistance model can be adapted to predict the performance of all multi-channel heat pipes.
- For validation, the proposed thermal resistance model was compared to experimental data from the three-leg heat pipe. The vertical temperature profile of the three-leg heat pipe revealed that different two-phase mechanisms take place in the horizontal collectors compared to the parallel legs. It is therefore relevant to consider different thermal resistances for the bottom and top collectors. Based on the developed multi-channel heat pipe thermal resistance network, a theoretical model was built. To predict the local pool boiling and condensation heat transfer coefficients, correlations from the literature were compared, selected, and integrated to the model. A high discrepancy between the available correlation was shown, and, as a result, the accuracy of the

theoretical prediction is greatly influenced by the choice of the pool boiling and condensation correlation selected.

- By integrating the suitable pool boiling and condensation correlations to the model, the equivalent boiling thermal resistance of the three-leg heat pipe was predicted with an average error of 7.6%. The equivalent condensation thermal resistance was predicted with an error of 8.0% and the total thermal resistance of the three-leg heat pipe was predicted by the theoretical model with an average error of 8.2%. It was therefore concluded that the developed iterative model with the proposed multi-channel heat pipe thermal resistance network was suitable to predict the thermal performance of a multi-channel heat pipe.
- To simulate heat pipes using Computational Fluid Dynamics (CFD), the commonly recommended *Lee* [67] model was used to describe the mass and heat transfer between the phases. This model has been integrated to simulate and numerically predict the three-leg heat pipe temperature using ANSYS\_2020 Fluent. In order to implement the source terms to the usual transport equations, user-defined functions (UDF) were coded in C language and integrated to the software. However, the investigation conducted in this study revealed that the *Lee* [67] model requires three inputs which cannot be numerically determined by the CFD software: 1) the saturation temperature  $T_{sat}$ , 2) the evaporation mass transfer coefficient  $\beta_e$ , and 3) the condensation mass transfer coefficient  $\beta_c$ . In this study, it was proved that such coefficients can be adapted to change the evaporator, adiabatic, and condenser sections' temperatures of the simulated heat pipe. The current *Lee* [67] model is therefore unable of predicting the thermal performance of a heat pipe using CFD. Moreover, manipulation of the *Lee* [67] model have shown that this model has a low physical consistency as the mass transfer and heat transfer between the vapour and liquid phases are poorly linked and can be adjusted independently. As a result, using the *Lee* [67] model for a heat pipe simulation can lead to physical nonsense such as a vapour temperature being much higher than that of the evaporative pool from which the vapour comes from. It is therefore concluded that the *Lee* [67] model is currently unable to simulate and predict the thermal performance of a heat pipe using CFD.
- Instead of simulating the overall heat pipe operation, CFD was used to conduct local simulations and study the impact of the channel's shape on the heat transfer inside the multi-channel flat heat pipe. The flat heat pipe channel has been compared to circular channels to characterise its impact on 1) the conduction profile of the channel, 2) the velocity profile of the fluid inside the channel, and 3) the boiling pattern of the working fluid. According to the conduction simulations, the radial conduction thermal resistance of the channel was found to be 0.298 K/W. Then, to estimate the conduction thermal

resistance of the channel using usual theoretical equation, a correction factor  $F_{correction} = 0.9112$  is proposed to consider the influence of the channel's shape. From a convective point of view, the channel's shape is believed to create zones of low velocity in its corners, and a zone of high velocity in the middle of the channel. Finally, the simulation of pool boiling inside the channel revealed the existence of stable nucleation sites in the corners of the channel where vapour bubbles coalesce, grow, and rise. Bubbles forming in unstable nucleation sites tend to be carried away by the profile shape toward a stable nucleation site. This transition and bubble movement is expected to have a significant impact on the pool boiling heat transfer coefficient in the multi-channel flat heat pipe.

- As the centre point of this study, a multi-channel flat heat pipe which can be used for surface cooling application was tested experimentally. Inside the flat heat pipe, the working fluid (R134a) travels through a multi-channel network which consists into 44 parallel channels linked at the bottom and top by horizontal collectors. The channels' shape is unique and was patented by *Jouhara and Lester* [110].
- During PV/T (photovoltaic/thermal) application, several factors can affect the thermal performance of the heat pipe and must be studied. Depending on the solar irradiation and temperature of the PV cell, heat transfer rates in the range 0-1500 W can take place. The impact of the heat transfer rate on the thermal performance of the multi-channel flat heat pipe was therefore investigated. It was found that an increase of the heat transfer rate decreases the boiling thermal resistance of the multi-channel flat heat pipe because the boiling activity increases and improves the pool boiling heat transfer coefficient. However, an increase of the heat transfer rate tends to increase the condensation thermal resistance of the multi-channel flat heat pipe as the condensate thickness increases. At a heat transfer rate of 100 W, the total thermal resistance of the multi-channel flat heat pipe is maximum and up to 0.0065 K/W. Yet, this thermal resistance decreases rapidly and, for heat transfer rates higher than 600 W, stabilizes around 0.003 K/W.
- The theoretical multi-channel model developed was used to predict the thermal performance of the multi-channel flat heat pipe. After convergence, the iterative model predicted the boiling and condensation thermal resistances of the multi-channel flat heat pipe with an average error of 17.2% and 14.4%, respectively. Overall, the theoretical model was able to predict the total thermal resistance of the multi-channel flat heat pipe with an average error of 13.1%.
- Another factor which can influence the multi-channel flat heat pipe performance when it is used for PV/T application on a roof is the tilt angle. The impact of the tilt angle on the thermal performance of the multi-channel flat heat pipe was therefore studied. It

was observed that the impact of the tilt angle is different depending on the heat transfer rate occurring. At low heat transfer rate (100 W – 400 W), with an increase of the tilt angle from 2° (close to horizontal) to 90°, the boiling thermal resistance of the multi-channel flat heat pipe increases. For medium heat transfer rates (500 W – 800 W), a small increase of the total thermal resistance can be detected at tilt angles close to horizontal (< 10°). At high heat transfer rates (900 W – 1500 W), when decreasing the tilt angle from 20° to 2°, a significant increase of the condensation thermal resistance can be seen. Overall, as the total thermal resistance of the multi-channel flat heat pipe is minimum for tilt angles between 20° and 70° which include optimum angles for PV/T applications.

- To explain the temperature difference detected at the condenser of the multi-channel flat heat pipe, infrared imaging of the flat heat pipe surface has been conducted. At the evaporator and adiabatic section, the infrared imaging confirms the temperature uniformity of the multi-channel flat heat pipe. Yet, at the condenser, a colder spot could be detected and was found to be generated by the quality of the interface between the flat heat pipe and its cooling manifold. The infrared imaging revealed that the temperature of the evaporator and adiabatic sections of the flat heat pipe remains uniform regardless of the heat sink location. It was concluded that the multi-channel geometry of the flat heat pipe allows an efficient heat transfer in both vertical and horizontal direction.
- Finally, for environmental purposes, an investigation to replace the working fluid of the multi-channel flat heat pipe for a low Global Warming Potential (GWP) refrigerant was done. To replace R134a which has a GWP of 1430, a replacing candidate, R1336 which has a GWP of 2 was proposed and charged into the multi-channel flat heat pipe. As a result, when R1336 is used as a working fluid, the total thermal resistance of the multi-channel flat heat pipe stabilizes around 0.0065 K/W whereas it stabilizes at 0.003 K/W for R134a. It was therefore concluded that using R1336 to replace R134a as an environmental-friendly working fluid in the multi-channel flat heat pipe implies an increase of the total thermal resistance of the multi-channel flat heat pipe by 130%.

## **7.2 Impact on the research field**

In the frame of this research, a novel three-leg heat pipe prototype was developed, built, and used to investigate the two-phase heat transfer in a multi-channel geometry. For the first time, local temperature measurements were taken at different level of the parallel channels. Furthermore, the temperature of both top and bottom collectors could also be measured. The three-leg heat pipe prototype revealed important information on the temperature profile of a multi-channel heat pipe. In particular, the three-leg heat pipe made possible the measurement

of local heat transfer coefficients in the parallel channels and in the collectors. The experimental data revealed that different pool boiling, and condensation pattern can take place in both horizontal collectors. The local heat transfer coefficient can therefore be lower than that of the parallel channels.

With the help of the three-leg heat pipe prototype, advances have been made on the theoretical modelling of multi-channel heat pipes. It was shown that different thermal resistances should be considered for the top and bottom collectors which link the parallel channels. The experimental data also indicate that the temperature of the parallel channels is usually uniformed and that a similar temperature can be considered during the theoretical modelling of multi-channel heat pipes. It was shown that the choice of the pool boiling, and condensation correlation has a major impact on the prediction as the discrepancy between existing model is important. For the prediction of the heat transfer coefficient in the collectors, different correlations than that of the parallel channels are advised. Finally, a new thermal resistance network was proposed and can be reused by any researcher who wants to predict the thermal performance of a multi-channel heat pipe. Indeed, by integrating the proposed multi-channel heat pipe thermal resistance network into an iterative tool, the three-leg heat pipe thermal resistance could be predicted with an error of 8.2%.

In the hot topic of Computational Fluid Dynamics (CFD) modelling of heat pipes, this study revealed major limits in the commonly used *Lee* [67] model. Indeed, this model requires three inputs which cannot be predicted numerically: 1) the saturation temperature  $T_{sat}$ , 2) the evaporation mass transfer coefficient  $\beta_e$ , and 3) the condensation mass transfer coefficient  $\beta_c$ . Up to date, those coefficients have usually been derived from experimental data to adjust the heat pipe simulations. However, the current *Lee* [67] model is unable to numerically predict the temperature of a heat pipe. Moreover, this model shows low physical consistency which can lead to physical nonsense in the results. In this regard, this study encourages a turning point to be taken in the simulation of heat pipes. To simulate heat pipes, other models should be considered or the *Lee* [67] model needs to be modified.

Local simulations on a single channel of the multi-channel flat heat pipe have brought new elements to understand how thermal energy is locally transferred from the top surface to the working fluid. The conduction profile revealed zones of slightly higher temperature in the top corners. A new correction factor was derived from the simulation to calculate the radial conduction thermal resistance of the multi-channel flat heat pipe using theory. The convective profile of the channel's shape indicates that the rising vapour can present lower velocities in the corner. Finally, the pool boiling simulation of the flat heat pipe channel revealed the presence of stable and non-stable nucleation sites which can significantly influence the pool

boiling heat transfer coefficient inside the flat heat pipe. Those local simulation have brought better knowledge on the influence of the shape on the two-phase heat transfer occurring inside the multi-channel flat heat pipe. Such information can later be used to develop and try new channel's shapes to improve further the thermal performance of such multi-channel flat heat pipe.

The intensive testing of the multi-channel flat heat pipe brought a full characterisation of this thermal absorber for PV/T application. The thermal performance of such multi-channel flat heat pipe at a given heat transfer rate, cooling flow rate, and tilt angle are now known and determined experimentally. This can be reused for future application of the multi-channel flat heat pipe. The conducted experiments, including the infrared imaging, demonstrated the capacity of the multi-channel flat heat pipe to transmit thermal energy in all directions while maintaining a uniform surface temperature. This demonstrates the potential of such thermal absorbers and open new opportunities for other applications of multi-channel flat heat pipe such as battery thermal management, refrigeration purposes, heat concentration apparatus for thermoelectric generators, and any other application which can benefit from the fact that the temperature of the absorber will remain the same everywhere.

The proposed theoretical model was also used to predict the thermal performance of the multi-channel flat heat pipe. By using the developed multi-channel thermal resistance model, the iterative model could predict the total thermal resistance of the flat heat pipe with an error of 13.1%. This shows that the proposed thermal resistance network is able to predict the performance of a multi-channel flat heat pipe and can therefore be reused by researchers and industrials. This tool can also help in the design and sizing of future multi-channel flat heat pipes for new industrial applications.

Finally, an attempt to replace R134a for a low GWP refrigerant has revealed that using R1336 instead of R134a implies an increase of the total thermal resistance of the multi-channel flat heat pipe by 130%. For industrial applications where an increased thermal resistance of the flat heat pipe is acceptable, this study showed that a more environment-friendly refrigerant can be used.

### **7.3 Recommendations for future work**

In the time frame of this research, new elements have been brought which provided some answers, but also raised new questions. Furthermore, some limitations have been faced and new challenges must be addressed.

- The three-leg heat pipe experimental apparatus can be further adapted to allow temperature measurements to be taken from the inner wall of a multi-channel flat heat

pipe. Pressure measurement inside the heat pipe would also be valuable to measure the variation of saturation pressure. New refrigerants can also be tested inside the three-leg heat pipe apparatus. Unfortunately, due to the inaccurate charge of the three-leg heat pipe and small volume of the legs, falling film boiling did not take place in the legs of the three-leg heat pipe. This two-phase mechanism can play a significant role in heat pipes and remain to be studied in a multi-channel geometry. To visualize the two-phase heat transfer and, in particular, the pool boiling pattern (bubbles sizes, shapes and activity), a see-through multi-channel heat pipe could bring new elements to explain the difference of heat transfer coefficients between the parallel channels and the horizontal collectors.

- In the theoretical modelling of multi-channel heat pipes, this study revealed that the accuracy of theoretical models highly depends on the correlations selected. However, a crucial question to address is how to predict which correlation suits best a given experiment. The fundamental research on boiling and condensation have shown that the heat transfer coefficient can be greatly influenced by the microscopic aspect of the surface. Yet, industrials and heat pipe designers are usually not willing to invest in cutting-edge technology to accurately describe the surface aspect of heat pipes and better choose a predicting correlation. Easiest and accessible way of characterising the surface aspect and select relevant correlations are needed.
- For the simulation of heat pipe using Computational Fluid Dynamics (CFD) technique, attention must be paid to make sure the selected multi-phase model is fully numerical and allow a prediction of the heat pipe temperature. In this regard, the Lee [67] model needs to be modified. As intended in this study with the modified Lee [67] model user-defined-function, the saturation temperature and mass transfer coefficients must be determined by the numerical solver and cannot be provided by the user. It is also encouraged to consider other multi-phase models which may be less flexible but present better physical consistency than the Lee [67] model.
- The characterisation of the multi-channel flat heat pipe carried out showed that such thermal absorber can be used for the cooling of photovoltaic cells and flat surfaces. The demonstrated uniform temperature characteristic opens new opportunities for this technology. For instance, the use of such flat heat pipe to control the temperature of batteries in electric vehicles is currently investigated. The flat heat pipe also has a great potential to be used as refrigeration shelves. A new application which could be considered is the association of heat pipes with thermoelectric generators (TEG) as heat pipes can be used for concentrating the heat transfer on a small surface and create high temperature gradient on the TEG cell.



- The multi-channel flat heat pipe can also be improved to reach better thermal performance. For instance, in the overall tested assembly, it was found that the cooling manifold thermal resistance and its interface with the heat pipe is significant. A potential improvement would be having a single apparatus with a heat pipe and cooling manifold manufactured from the same plate. Another solution could be the welding of a cooling manifold with channels open on one side to eliminate one conduction thermal resistance and the interface thermal resistance. Finally, investigation of the channel's shape has shown that the shape has an impact on the two-phase heat transfer. It seems interesting to investigate new channel's shape for multi-channel flat heat pipes to improve further the two-phase heat transfer and reduce the thermal resistance of a multi-channel flat heat pipe.
- Last but not least, the environmental transition encourages researchers and industries to use low Global Warming Potential (GWP) refrigerants for heat transfer purposes. This is particularly important when the core of the heat pipe activity is to recover waste energy. In this study, it was shown that replacing R134a by R1336 implies an increase of the multi-channel flat heat pipe thermal resistance by 130%. This remains high and, for many heat transfer applications, R134a is still likely to be preferred compared to R1336. In this regard, new refrigerants, or blends with low GWP must be investigated for two-phase heat transfer purposes to be used in multi-channel flat heat pipes.

# Annexes

## Annexe 1

### Three-leg heat pipe design calculation tool interface

The image displays the user interface of a design calculation tool for a three-leg heat pipe. The interface is organized into several main sections, each containing a table of input parameters and calculated results. The sections are:

- Heat transfer rate:** Contains a table for 'Evaporator temperature out Teo' and 'Conduction at the bottom cylinder'.
- Pool boiling at the bottom cylinder:** Includes a table for 'Temperature for evaporation calculation' and 'Pool boiling'.
- Condensation on the legs of the three leg heat pipe:** Features a table for 'Condensation on legs' and 'Condensation on wall'.
- Boiling in the three legs Heat Pipe:** Contains a table for 'Temperature for condensation calculation' and 'Boiling in the three legs'.
- Conduction in the three legs Heat Pipe evaporator:** Includes a table for 'Conduction in the three legs'.
- Boiling in the three legs Heat Pipe:** (Bottom section) Contains a table for 'Temperature for condensation calculation' and 'Conduction in the three legs Heat Pipe condenser'.

Each table lists various parameters such as mass flow rates, temperatures, and heat transfer coefficients. The interface also includes a central diagram of a three-leg heat pipe and several smaller diagrams illustrating different components and flow paths. Arrows indicate the flow of data between different sections of the tool.

Figure 0-1. Three-leg heat pipe design calculation tool interface (1)



## Annexe 2

### Heat pipe limits

Objective: Verify that the heat pipe limits are respected and that the heat pipe design is safe.

- **Entrainment limitation**

The maximum heat transfer rate achievable before entrainment limit is given by [108]:

$$\dot{Q}_{max,entrainment} = f_1 f_2 f_3 A_v i_{lv} (\rho_v)^{0.5} [\sigma g (\rho_l - \rho_v)]^{0.25} \quad (1)$$

with  $A_v$  the vapour cross-sectional area (m<sup>2</sup>),  $i_{lv}$  the latent heat of vaporization (J/kg),  $\rho_v$  the vapour density (kg/m<sup>3</sup>),  $\sigma$  the surface tension (N/m),  $g$  the gravity acceleration (m/s<sup>2</sup>), and  $\rho_l$  the liquid density (kg/m<sup>3</sup>). The factor  $f_1$  is a function of the Bond number:

$$Bo = D \left[ \frac{g(\rho_l - \rho_v)}{\sigma} \right]^{0.5} \quad (2)$$

with  $D$  the heat pipe diameter (m). The parameter  $f_1$  can be read from the following graph [108]:

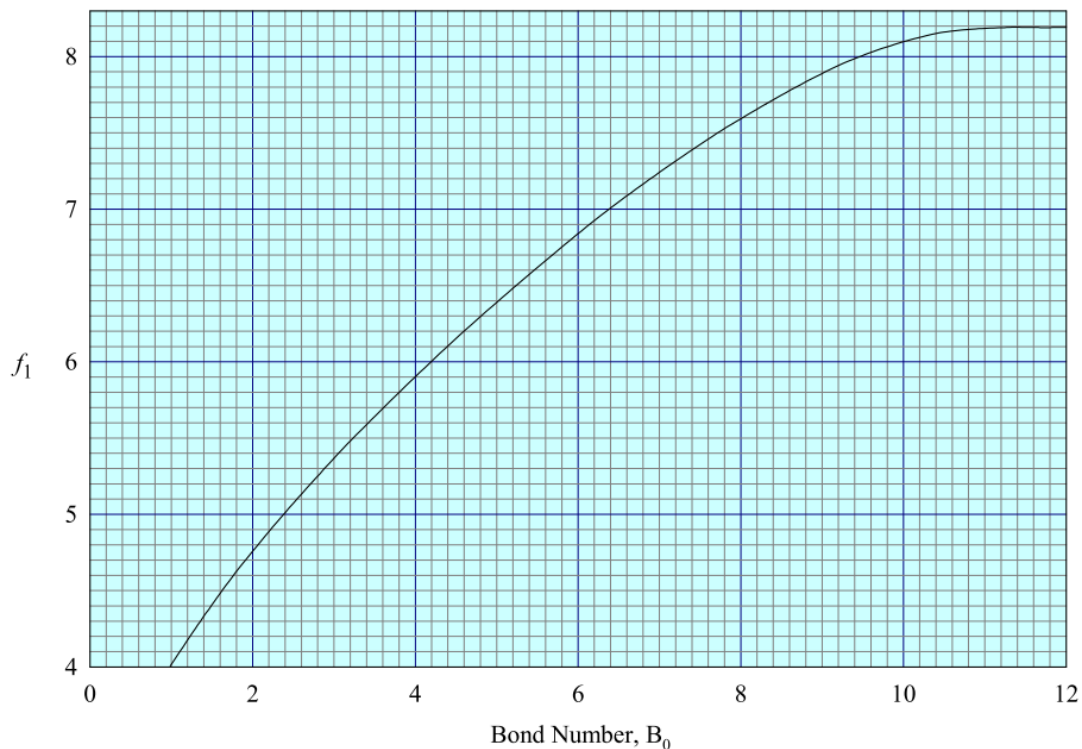


Figure 0-3. Variation of the factor  $f_1$  [108]

This graph can be translated into an equation by:

$$\begin{aligned}
 f_1 = & -0,00000006402241758963 \times Bo^6 & (3) \\
 & + 0,00005313824010303290 \times Bo^5 \\
 & - 0,00198282249555956000 \times Bo^4 \\
 & + 0,02608798707075440000 \times Bo^3 \\
 & - 0,18132463867338800000 \times Bo^2 \\
 & + 1,17340942874538000000 \times Bo \\
 & + 3,07659797113802000000
 \end{aligned}$$

For  $Bo > 11$ ,  $f_1 = 8.2$ .

The factor  $f_2$  is a function of the dimensionless parameter  $K_p$ :

$$K_p = \frac{P_v}{[\sigma g(\rho_l - \rho_v)]^{0.5}} \quad (4)$$

With  $P_v$  the vapour pressure (Pa). And,

$$\begin{cases}
 f_2 = K_p^{-0.17} & \text{if } K_p \leq 4 \times 10^4 \\
 f_2 = 0.165 & \text{if } K_p > 4 \times 10^4
 \end{cases} \quad (5)$$

For a vertical pipe,  $f_3 = 1$ .

- **Viscous limitation**

The maximum heat transfer rate by viscous limitation can be estimated by [263]:

$$\dot{Q}_{max,viscous} = \frac{\pi r_v^4 i_{lv} P_v \rho_v}{12 \mu_v L_{eff}} \quad (6)$$

with  $r_v$  the vapour core radius (m),  $i_{lv}$  the latent heat of vaporization (J/kg),  $P_v$  the vapour pressure (Pa),  $\rho_v$  the vapour density (kg/m<sup>3</sup>),  $\mu_v$  the dynamic viscosity (Pa.s),  $L_{eff}$  the effective length (m).

- **Sonic limitation**

The maximum axial vapour mass flux  $\dot{Q}_{max}/AL$  is given by [263]:

$$\dot{Q}_{max,sonic} = 0.474 A_v i_{lv} (P_v \rho_v)^{0.5} \quad \text{in } kg/(s.m^2) \quad (7)$$

with  $A_v$  the vapour cross-sectional area (m<sup>2</sup>),  $i_{lv}$  the latent heat of vaporization (J/kg),  $P_v$  the vapour pressure (Pa),  $\rho_v$  the vapour density (kg/m<sup>3</sup>). This formula applied regardless of the orientation [108].

- **Boiling limitation**

The maximum heat transfer rate by boiling limit is estimated by [108]:

$$\dot{Q}_{max,boiling} = \pi D L_e 0.12 i_{lv} (\rho_v)^{0.5} [\sigma g(\rho_l - \rho_v)]^{0.25} \quad (8)$$

with  $D$  the heat pipe diameter (m),  $L_e$  evaporator length (m),  $i_{lv}$  the latent heat of vaporization (J/kg),  $\rho_v$  the vapour density (kg/m<sup>3</sup>),  $\sigma$  the surface tension (N/m),  $g$  the gravity acceleration (m/s<sup>2</sup>), and  $\rho_l$  the liquid density (kg/m<sup>3</sup>).

- **Dryout limitation**

To prevent dryout at the evaporator, the following criterion should be verified [108]:

$$V_l \geq 0.001D(L_e + L_a + L_c) \quad (9)$$

with  $V_l$  the liquid pool volume (m<sup>3</sup>),  $D$  the internal diameter of the thermosyphon (m),  $L_e$ ,  $L_a$  and  $L_c$  the evaporator, adiabatic, and condenser length (m). The filling ratio  $FR$  of the heat pipe is defined by:

$$FR = \frac{V_l}{AL_e} \quad (10)$$

$$A = \pi D^2/4 \quad (11)$$

For thermosyphons, the liquid fill should be in the range 40%-60% [108].

- **Vapour pressure limit**

The maximum heat transfer rate by vapour pressure limit is estimated by:

$$\dot{Q}_{max,vapour\ pressure} = \frac{A_v D_{Ev}^2 i_{lv} P_v \rho_v}{64 \mu_v L_{eff}} \quad (12)$$

$$L_{eff} = L_e/2 + L_a + L_c/2 \quad (13)$$

$$D_{Ev} = \frac{4A_v}{P_v} \quad (14)$$

with  $A_v$  the vapour cross-sectional area (m<sup>2</sup>),  $D_{Ev}$  the equivalent vapour diameter (m),  $i_{lv}$  the latent heat of vaporization (J/kg),  $P_v$  the vapour pressure (Pa),  $\rho_v$  the vapour density (kg/m<sup>3</sup>),  $\mu_v$  the dynamic viscosity (Pa.s),  $L_{eff}$  the effective length (m),  $L_e$ ,  $L_a$  and  $L_c$  the evaporator, adiabatic, and condenser length (m).

## Annexe 3

### Water and R134a properties code

```
'=====Water properties====='  
Function cp_water_0_100(x)  
x = 3.43018828774945E-13 * x ^ 6 - 1.38782230499346E-10 * x ^ 5 + 2.37891895626952E-08 * x ^ 4 -  
2.18284787045775E-06 * x ^ 3 + 1.18928757274261E-04 * x ^ 2 - 3.41468909800824E-03 * x +  
4.21655956124778  
cp_water_0_100 = 1000 * x  
End Function  
  
'=====R134a properties====='  
Function Pv_R134a(t)  
Pv_R134a = 4057000 * Exp(1 / ((t + 273.15) / 374.25) * ((-7.58916) * (1 - ((t + 273.15) / 374.25)) + (1.612) * (1 -  
((t + 273.15) / 374.25)) ^ (3 / 2) + (-2.3539) * (1 - ((t + 273.15) / 374.25)) ^ (5 / 2) + (-3.095) * (1 - ((t + 273.15) /  
374.25)) ^ 5))  
End Function  
  
Function rho_liq_R134a(t)  
rho_liq_R134a = 510 * Exp(1.81027 * (1 - ((t + 273.15) / 374.25)) ^ (1 / 3) - 0.67536 * (1 - ((t + 273.15) / 374.25)) ^  
(2 / 3) + 0 * (1 - ((t + 273.15) / 374.25)) + 0.23925 * (1 - ((t + 273.15) / 374.25)) ^ (4 / 3))  
End Function  
  
Function rho_vap_R134a(t)  
rho_vap_R134a = 510 * Exp(-1.43757 * (1 / ((t + 273.15) / 374.25) - 1) ^ (1 / 3) - 4.64691 * (1 / ((t + 273.15) /  
374.25) - 1) ^ (2 / 3) + 2.78419 * (1 / ((t + 273.15) / 374.25) - 1) - 3.34676 * (1 / ((t + 273.15) / 374.25) - 1) ^ (4 / 3)  
- 1.47576 * (1 / ((t + 273.15) / 374.25) - 1) ^ (5 / 3))  
End Function  
  
Function hfg_R134a(t)  
hfg_R134a = (1000) * ((36 - 169.21 * (1 - ((t + 273.15) / 374.25)) ^ (1 / 3) + 796.685 * (1 - ((t + 273.15) / 374.25)) ^  
(2 / 3) - 1442.47 * (1 - ((t + 273.15) / 374.25)) + 594.281 * (1 - ((t + 273.15) / 374.25)) ^ (4 / 3)) - (36 - 315.796 * (1  
- ((t + 273.15) / 374.25)) ^ (1 / 3) + 208.015 * (1 - ((t + 273.15) / 374.25)) ^ (2 / 3) - 685.931 * (1 - ((t + 273.15) /  
374.25)) + 238.66 * (1 - ((t + 273.15) / 374.25)) ^ (4 / 3)))  
End Function  
  
Function cp_R134a(t)  
cp_R134a = 1000 * (1.65113 * (1 + 0.015111 * (1 - ((t + 273.15) / 374.25)) ^ (-1) - 1.31769 * (1 - ((t + 273.15) /  
374.25)) + 1.91306 * (1 - ((t + 273.15) / 374.25)) ^ (2) - 1.2325 * (1 - ((t + 273.15) / 374.25)) ^ (3)))  
End Function  
  
Function K_R134a(t)  
K_R134a = (10 ^ -3) * 43.97 * (1 + 3.4 * (1 - ((t + 273.15) / 374.25)) ^ (1 / 3) - 9.2 * (1 - ((t + 273.15) / 374.25)) ^ (2  
/ 3) + 10.2 * (1 - ((t + 273.15) / 374.25)))  
End Function
```

Function surftension\_R134a(t)

surftension\_R134a = (10 ^ -3) \* 61.02 \* (1 - ((t + 273.15) / 374.25)) ^ 1.25808 \* (1 + 0 \* (1 - ((t + 273.15) / 374.25)))

End Function

Function viscos\_liq\_R134a(t)

viscos\_liq\_R134a = -1.14072256E-12 \* t ^ 4 + 9.626379739E-11 \* t ^ 3 + 1.190813963439E-08 \* t ^ 2 - 3.18156739053548E-06 \* t + 2.65915592283245E-04

End Function

Function viscos\_vap\_R134a(t)

viscos\_vap\_R134a = 2.238424E-14 \* t ^ 5 - 4.67723104E-12 \* t ^ 4 + 3.4790210903E-10 \* t ^ 3 - 1.043817779474E-08 \* t ^ 2 + 1.4760355604069E-07 \* t + 1.05488468419507E-05

End Function



# Annexe 4

## Multi-channel flat heat pipe model interface

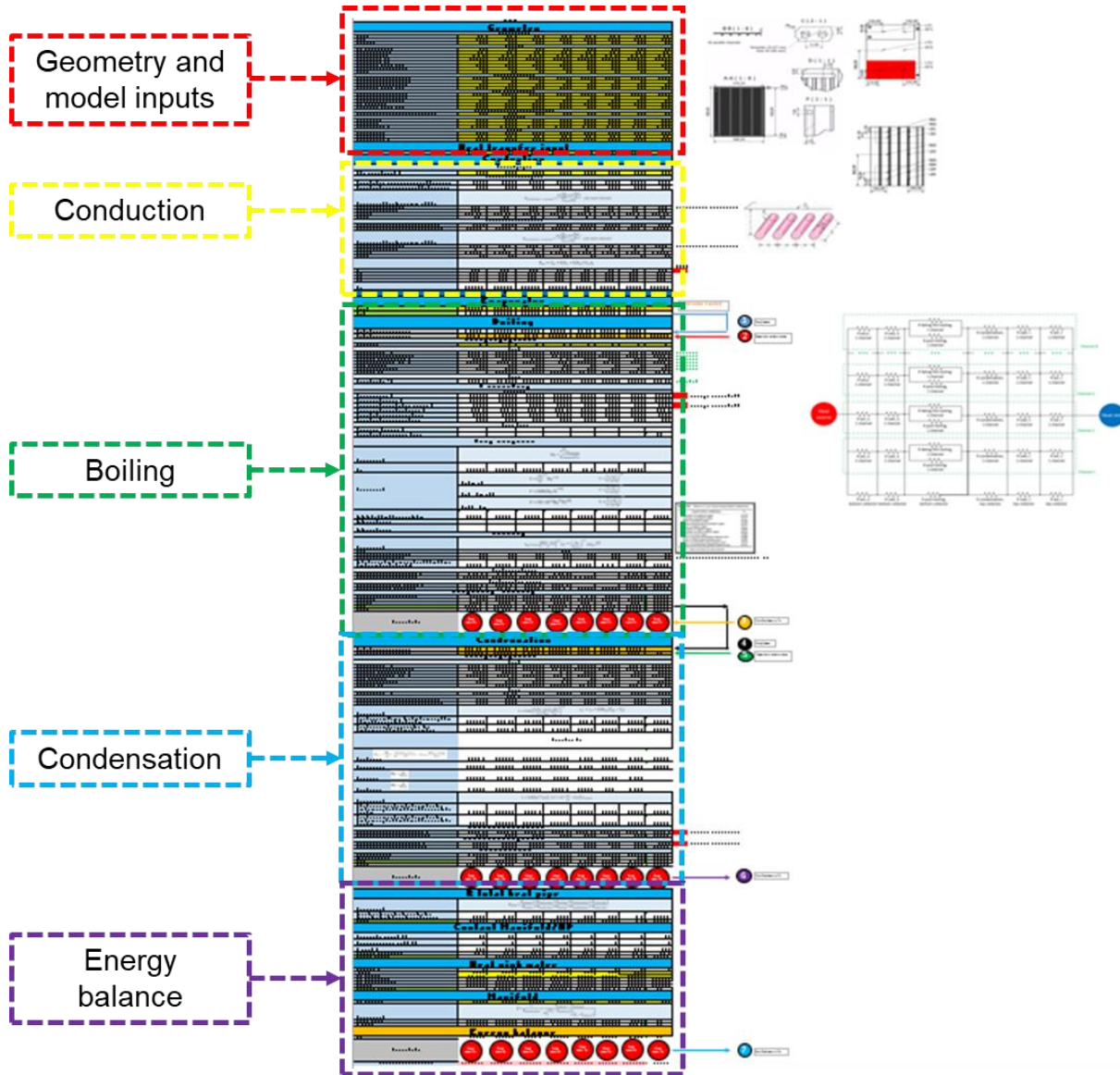


Figure 0-4. Multi-channel flat heat pipe model interface

## Annexe 5

### Transport equations

In the following, the transport equations are projected in rectangular coordinates. In rectangular coordinates, the velocity vector is given as follows:

$$\vec{V} = u\vec{e}_x + v\vec{e}_y + w\vec{e}_z$$

- **Continuity equation:**

As the mass of each control volume is constant, the sum of the internal mass variation and of the mass going in or out of the volume is null. Hence, the **continuity equation** for each cell is given by [105]:

$$\frac{\partial \rho}{\partial t} + \vec{\nabla}(\rho\vec{V}) = 0 \quad (15)$$

where  $\rho$  is the fluid density (kg/m<sup>3</sup>), and  $\vec{V}$  is the velocity vector (m/s). In the continuity equation, the following groups are represented:

<i>Mathematical group</i>	<i>Physical meaning</i>
$\frac{\partial \rho}{\partial t}$	Internal mass variation
$\vec{\nabla}(\rho\vec{V})$	Mass going in or out of the volume

For a fluid with constant density (incompressible fluid), the continuity equation can be simply written as:

$$\vec{\nabla} \cdot \vec{V} = 0$$

which gives in rectangular coordinates:

$$\frac{\partial \rho}{\partial t} + \frac{\partial}{\partial x}(\rho u) + \frac{\partial}{\partial y}(\rho v) + \frac{\partial}{\partial z}(\rho w) = 0$$

where  $u$ ,  $v$ , and  $w$  are the velocity vector components (m/s).

- **Equation of motion:**

For a Newtonian fluid, the **equation of motion** is as follows [105]:

$$\frac{\partial \rho \vec{V}}{\partial t} = -\rho(\vec{\nabla} \cdot \vec{V})\vec{V} - \vec{\nabla} P + \vec{\nabla} \cdot \vec{\tau} + \rho \vec{g} \quad (16)$$

with  $\rho$  the fluid density (kg/m<sup>3</sup>),  $\vec{V}$  the velocity vector (m/s),  $P$  the pressure (Pa),  $\vec{\tau}$  the stress tensor due to the fluid viscosity (N/m<sup>2</sup>), and  $\vec{g}$  the volumetric force vector including gravity, magnetic, electrostatic forces among others (m/s<sup>2</sup>). In the equation of motion, the following groups are represented:

<i>Mathematical group</i>	<i>Physical meaning</i>
$\frac{\partial \rho \vec{V}}{\partial t}$	Difference of momentum in the volume
$\rho(\vec{\nabla} \cdot \vec{V})\vec{V}$	Momentum gain due to convection
$\vec{\nabla} P$	Pressure force on the volume
$\vec{\nabla} \cdot \vec{\tau}$	Momentum gain due to viscous transfer
$\rho \vec{g}$	Volumetric force (gravity)

By using the continuity equation, the equation of motion can be simplified ( $m\vec{a} = \sum \vec{F}$ ):

$$\rho \frac{D\vec{V}}{Dt} = -\vec{\nabla} P + \vec{\nabla} \cdot \vec{\tau} + \rho \vec{g}$$

which can be expressed in rectangular coordinates as:

x direction	$\rho \left( \frac{\partial u}{\partial t} + u \frac{\partial u}{\partial x} + v \frac{\partial u}{\partial y} + w \frac{\partial u}{\partial z} \right) = -\frac{\partial P}{\partial x} + \left( \frac{\partial \tau_{xx}}{\partial x} + \frac{\partial \tau_{yx}}{\partial y} + \frac{\partial \tau_{zx}}{\partial z} \right) + \rho g_x$
y direction	$\rho \left( \frac{\partial v}{\partial t} + u \frac{\partial v}{\partial x} + v \frac{\partial v}{\partial y} + w \frac{\partial v}{\partial z} \right) = -\frac{\partial P}{\partial y} + \left( \frac{\partial \tau_{xy}}{\partial x} + \frac{\partial \tau_{yy}}{\partial y} + \frac{\partial \tau_{zy}}{\partial z} \right) + \rho g_y$
z direction	$\rho \left( \frac{\partial w}{\partial t} + u \frac{\partial w}{\partial x} + v \frac{\partial w}{\partial y} + w \frac{\partial w}{\partial z} \right) = -\frac{\partial P}{\partial z} + \left( \frac{\partial \tau_{xz}}{\partial x} + \frac{\partial \tau_{yz}}{\partial y} + \frac{\partial \tau_{zz}}{\partial z} \right) + \rho g_z$

- **Energy equation:**

For a stationary control volume through which a fluid is flowing, the **energy equation** is expressed by:

$$\frac{\partial}{\partial t} \rho(\bar{U} + 1/2 V^2) = -\vec{\nabla} \cdot \rho \vec{V}(\bar{U} + 1/2 V^2) - \vec{\nabla} \cdot \vec{q}'' + \rho(\vec{V} \cdot \vec{g}) - \vec{\nabla} \cdot P \vec{V} + \vec{\nabla} \cdot (\vec{\tau} \vec{V}) + q'''_g \quad (17)$$

where  $\bar{U}$  the internal energy vector (J/kg),  $\vec{V}$  the velocity vector (m/s),  $\rho$  the fluid density (kg/m<sup>3</sup>),  $\vec{q}''$  the heat flux (W/m<sup>2</sup>),  $\vec{g}$  the volumetric force vector (m/s<sup>2</sup>),  $P$  the pressure (Pa),  $\vec{\tau}$  the stress tensor (N/m<sup>2</sup>), and  $q'''_g$  the volumetric heat source (W/m<sup>3</sup>). In the energy equation, the following groups are represented:

<i>Mathematical group</i>	<i>Physical meaning</i>
$\frac{\partial}{\partial t} \rho(\bar{U} + 1/2 V^2)$	Gain of energy per unit of volume
$\vec{\nabla} \cdot \rho \vec{V}(\bar{U} + 1/2 V^2)$	Gain of energy due to convection
$\vec{\nabla} \cdot \vec{q}''$	Gain of energy due to conduction
$\rho(\vec{V} \cdot \vec{g})$	Gravitational force's work done on the fluid
$\vec{\nabla} \cdot P \vec{V}$	Pressure force's work done on the fluid
$\vec{\nabla} \cdot (\vec{\tau} \vec{V})$	Viscous force's work done on the fluid
$q'''_g$	Heat generation in the volume

By using the equation of continuity and motion, the energy equation can be rearranged as:

$$\rho \frac{D\bar{U}}{Dt} = -\vec{\nabla} \cdot \vec{q}'' - P(\vec{\nabla} \cdot \vec{V}) + \vec{\nabla} \cdot \vec{V} : \vec{\tau} + q'''_g$$

This equation can be converted in terms of temperature instead of internal energy [105]. For an ideal gas and incompressible fluid, by setting  $q'''_g = 0$  for simplicity, the energy equation becomes:

$$\rho c_p \frac{DT}{Dt} = \vec{\nabla} \cdot k \vec{\nabla} T + \mu \Phi$$

which gives in rectangular coordinates:

$$\begin{aligned} & \rho c_p \left( \frac{\partial T}{\partial t} + u \frac{\partial T}{\partial x} + v \frac{\partial T}{\partial y} + w \frac{\partial T}{\partial z} \right) \\ &= k \left( \frac{\partial^2 T}{\partial x^2} + \frac{\partial^2 T}{\partial y^2} + \frac{\partial^2 T}{\partial z^2} \right) + 2\mu \left[ \left( \frac{\partial u}{\partial x} \right)^2 + \left( \frac{\partial v}{\partial y} \right)^2 + \left( \frac{\partial w}{\partial z} \right)^2 \right] \\ &+ \mu \left[ \left( \frac{\partial u}{\partial y} + \frac{\partial v}{\partial x} \right)^2 + \left( \frac{\partial u}{\partial z} + \frac{\partial w}{\partial x} \right)^2 + \left( \frac{\partial v}{\partial z} + \frac{\partial w}{\partial y} \right)^2 \right] \end{aligned}$$

## Annexe 6

### R134a properties UDF

```
1 #include "udf.h"
2 #include "sg_mphase.h"
3 #include "para.h" /* this is needed for predicates*/
4 #include "prf.h" /*this is needed for prf commands*/
5
6 /*=====liquid properties=====*/
7 /*-----*/
8 /* UDF for liquid density */
9 DEFINE_PROPERTY(densityR134a_liquid, c, secondphasethread)

10 {
11     real RohL;
12     real temp = C_T(c, secondphasethread);
13     RohL = (-0.00000031788046906019) * temp * temp * temp * temp * temp +
            (0.00049970443464801200) * temp * temp * temp * temp +
            (-0.31375548999476700000) * temp * temp * temp +
            (98.33621645383050000000) * temp * temp + (15385.36247585570) * temp +
            (962790.773653978); /* in Kelvin*/
14     return RohL;
15 }
16
17 /*-----*/
18 /* UDF for liquid cp */
19 DEFINE_SPECIFIC_HEAT(cpR134a_liquid, T, Tref, h, yi)
20 {
21     real Cpl;

22     Cpl = (0.00000138242708694336) * T * T * T * T * T +
            (-0.00213766661179523000) * T * T * T * T + (1.32069700513460000000) * T
            * T * T + (-407.45366665628500000000) * T * T +
            (62768.564977120400000000000) * T + (-3861308.00087263000000000000);
23     *h = Cpl * (T - Tref);
24     return Cpl;
25 }
26
27 /*-----*/
28 /* UDF for liquid thermal conductivity */
29 DEFINE_PROPERTY(KR134a_liquid, c, secondphasethread)
30 {
31     real Kl;
32     real temp = C_T(c, secondphasethread);
33     Kl = (0.0000000151788486236) * temp * temp * temp +
            (-0.00000028128627899349) * temp * temp + (-0.00059411672292662700) *
            temp + 0.24509127505197400000;
34     return Kl;
35 }
36
```

```

46 /*-----*/
47 /* UDF for liquid viscosity */
48 DEFINE_PROPERTY(ViscR134a_liquid, c, secondphasethread)

49 {
50     real Viscl;
51     real temp = C_T(c, secondphasethread);
52     Viscl = (-0.00000000000114072256) * temp * temp * temp * temp +
              (0.00000000134261726358) * temp * temp * temp +
              (-0.00000057763740307236) * temp * temp + (0.00010485158998092000) *
              temp + (-0.00628857827681295000);
53     return Viscl;
54 }
55
56 /*-----*/
57 /* UDF for surface tension */
58 DEFINE_PROPERTY(surface_tension_R134a, c, t)
59 {
60     real sigma;
61     real temp = C_T(c, t);
62     sigma = (0.0000000000042197320) * temp * temp * temp * temp * temp +
              (-0.00000000065501591207) * temp * temp * temp * temp +
              (0.00000040706756476011)*temp * temp * temp + (-0.0001263293985145070) *
              temp * temp + (0.01940598385083600000) * temp +
              (-1.15476694959362000); /* in kelvin*/
63     return sigma;
64 }
65
66 /*=====vapour properties=====*/
67 /*-----*/
68 /* UDF for vapour density */
69 DEFINE_PROPERTY(densityR134a_vapour, c, firstphasethread)
70 {
71     real Rohv;
72     real temp = C_T(c, firstphasethread);
73     Rohv = (0.00000033131321821147) * temp * temp * temp * temp * temp +
              (-0.00052089065211999100) * temp * temp * temp * temp +
              (0.3270928635363000000) * temp * temp * temp + (-102.5253054761980) *
              temp * temp + (16039.012005179200) * temp + (-1001778.3268616100); /* in
              Kelvin*/
74     return Rohv;
75 }
76
77 /*-----*/
78 /* UDF for vapour cp */
79 DEFINE_SPECIFIC_HEAT(cpR134a_vapour, T, Tref, h, yi)
80 {
81     real Cpv;
82     Cpv = (0.00000018869327285918) * T * T * T * T * T * T +
              (-0.00035490587698278500) * T * T * T * T * T + (0.27773316135151000000) *
              T * T * T * T + (-115.74358820180600000000) * T * T * T +
              (27091.593167828500000000000) * T * T + (-3376824.75090733000000000000) *
              T + (175107254.987171000000000000000);
83     *h = Cpv * (T - Tref);
84     return Cpv;
85 }

```

```

87 /*-----*/
88 /* UDF for vapour K */
89 DEFINE_PROPERTY(KR134a_vapour, c, firstphasethread)
90 {
91     real Kv;
92     real temp = C_T(c, firstphasethread);
93     Kv = (0.00000000000058550527) * temp * temp * temp * temp * temp * temp +
          (-0.00000000110158701618) * temp * temp * temp * temp * temp +
          (0.00000086245258222811) * temp * temp * temp * temp +
          (-0.00035963542870563900) * temp * temp * temp +
          (0.08423702665224190000) * temp * temp + (-10.50782956396160000000) *
          temp + 545.34429275071800000000;
94     return Kv;
95 }
96
97 /*-----*/
98 /* UDF for vapour viscosity */
99 DEFINE_PROPERTY(ViscR134a_vapour, c, firstphasethread)
100 {
101     real Viscv;
102     real temp = C_T(c, firstphasethread);
103     Viscv = (0.0000000000000055729) * temp * temp * temp * temp * temp * temp
          + (-0.0000000000105814886) * temp * temp * temp * temp * temp +
          (0.00000000083564165241) * temp * temp * temp * temp +
          (-0.00000035131551866143) * temp * temp * temp +
          (0.00008292604959351290) * temp * temp + (-0.01041999400531120000) *
          temp + (0.54452319553948700000);
104     return Viscv;
105 }

```

## Annexe 7

### Complete modified Lee model UDF

```
1 #include "udf.h"
2 #include "sg_mphase.h"
3 #include "para.h" /* this is needed for predicates*/
4 #include "prf.h" /*this is needed for prf commands*/
5
6 /*=====liquid properties=====*/
7 /*-----*/
8 /* UDF for liquid density */
9 DEFINE_PROPERTY(densityR134a_liquid, c, secondphasethread)

10 {
11     real RohL;
12     real temp = C_T(c, secondphasethread);
13     RohL = (-0.00000031788046906019) * temp * temp * temp * temp * temp +
14           (0.00049970443464801200) * temp * temp * temp * temp +
15           (-0.31375548999476700000) * temp * temp * temp +
16           (98.33621645383050000000) * temp * temp + (15385.36247585570) * temp +
17           (962790.773653978); /* in Kelvin*/
18     return RohL;
19 }
20
21 /*-----*/
22 /* UDF for liquid cp */
23 DEFINE_SPECIFIC_HEAT(cpR134a_liquid, T, Tref, h, yi)
24 {
25     real Cpl;
26
27     Cpl = (0.00000138242708694336) * T * T * T * T * T +
28           (-0.00213766661179523000) * T * T * T * T + (1.32069700513460000000) * T
29           * T * T + (-407.45366665628500000000) * T * T +
30           (62768.564977120400000000000) * T + (-3861308.00087263000000000000);
31     *h = Cpl * (T - Tref);
32     return Cpl;
33 }
34
35 /*-----*/
36 /* UDF for liquid thermal conductivity */
37 DEFINE_PROPERTY(KR134a_liquid, c, secondphasethread)
38 {
39     real Kl;
40     real temp = C_T(c, secondphasethread);
41     Kl = (0.00000000151788486236) * temp * temp * temp +
42         (-0.00000028128627899349) * temp * temp + (-0.00059411672292662700) *
43         temp + 0.24509127505197400000;
44     return Kl;
45 }
46
47 /*-----*/
48 /* UDF for liquid viscosity */
49 DEFINE_PROPERTY(ViscR134a_liquid, c, secondphasethread)
50 {
51     real Viscl;
52     real temp = C_T(c, secondphasethread);
53     Viscl = (-0.00000000000114072256) * temp * temp * temp * temp +
54           (0.00000000134261726358) * temp * temp * temp +
```



```

        (-0.00000057763740307236) * temp * temp + (0.00010485158998092000) *
        temp + (-0.00628857827681295000);
44     return Viscl;
45 }
46
47 /*-----*/
48 /* UDF for surface tension */
49 DEFINE_PROPERTY(surface_tension_R134a, c, t)
50 {
51     real sigma;
52     real temp = C_T(c, t);
53     sigma = (0.0000000000042197320) * temp * temp * temp * temp * temp +
        (-0.00000000065501591207) * temp * temp * temp * temp +
        (0.00000040706756476011)*temp * temp * temp + (-0.0001263293985145070) *
        temp * temp + (0.01940598385083600000) * temp +
        (-1.15476694959362000); /* in kelvin*/
54     return sigma;
55 }
56
57 /*=====vapour properties=====*/
58 /*-----*/
59 /* UDF for vapour density */
60 DEFINE_PROPERTY(densityR134a_vapour, c, firstphasethread)
61 {
62     real Rohv;
63     real temp = C_T(c, firstphasethread);
64     Rohv = (0.00000033131321821147) * temp * temp * temp * temp * temp +
        (-0.00052089065211999100) * temp * temp * temp * temp +
        (0.3270928635363000000) * temp * temp * temp + (-102.5253054761980) *
        temp * temp + (16039.012005179200) * temp + (-1001778.3268616100); /* in
        Kelvin*/
65     return Rohv;
66 }
67
68 /*-----*/
69 /* UDF for vapour cp */
70 DEFINE_SPECIFIC_HEAT(cpR134a_vapour, T, Tref, h, yi)
71 {
72     real Cpv;
73     Cpv = (0.00000018869327285918) * T * T * T * T * T * T +
        (-0.00035490587698278500) * T * T * T * T * T + (0.27773316135151000000)
        * T * T * T * T + (-115.74358820180600000000) * T * T * T +
        (27091.59316782850000000000) * T * T + (-3376824.75090733000000000000) *
        T + (175107254.98717100000000000000);
74     *h = Cpv * (T - Tref);
75     return Cpv;
76 }
77
78 /*-----*/
79 /* UDF for vapour K */
80 DEFINE_PROPERTY(KR134a_vapour, c, firstphasethread)
81 {
82     real Kv;
83     real temp = C_T(c, firstphasethread);
84     Kv = (0.00000000000058550527) * temp * temp * temp * temp * temp * temp +
        (-0.00000000110158701618) * temp * temp * temp * temp * temp +

```

```

(0.00000086245258222811) * temp * temp * temp * temp +
(-0.00035963542870563900) * temp * temp * temp +
(0.08423702665224190000) * temp * temp + (-10.50782956396160000000) *
temp + 545.34429275071800000000;
85     return Kv;
86 }
87
88 /*-----*/
89 /* UDF for vapour viscosity */
90 DEFINE_PROPERTY(ViscR134a_vapour, c, firstphasethread)
91 {
92     real Viscv;
93     real temp = C_T(c, firstphasethread);
94     Viscv = (0.00000000000000055729) * temp * temp * temp * temp * temp * temp
+ (-0.00000000000105814886) * temp * temp * temp * temp * temp +
(0.00000000083564165241) * temp * temp * temp * temp +
(-0.00000035131551866143) * temp * temp * temp +
(0.00008292604959351290) * temp * temp + (-0.01041999400531120000) *
temp + (0.54452319553948700000);
95     return Viscv;
96 }
97
98 /*=====Two-phase Modified Lee model=====*/
99 /*-----*/
100 /* UDF for computational based Tsat with a temperature measurement*/
101
102 /* Global variable to be used between the commands*/
103 real Tsat_sensor;
104
105 DEFINE_EXECUTE_AT_END(Tsatsensor) /* UDF to hook*/
106 {
107     #if !RP_HOST
108         real thermosensor_coordinate[ND_ND];
109         real thermosensor_temperature;
110         real xmin;
111         real xmax;
112         real ymin;
113         real ymax;
114         real zmin;
115         real zmax;
116         real x, y, z;
117         real time = RP_Get_Real("flow-time");
118         int nt; /* nt is the number of temperature measurement (counting) */
119         /* Defining cells, thread and domain */
120
121         cell_t c;
122         Domain* d;
123         Thread* t;
124         d = Get_Domain(1);
125
126         /* Defining thermocouple zone where the temperature measurement is taken
from; Temperature measurement located at coordinates (x,y,z) =
(0.050,0.280,0.050) */
127         xmin = 0.002; /* Expected that meters are needed even if geometry is in
mm*/
128         xmax = 0.072;

```

```

129     ymin = 0.002;
130     ymax = 0.008;
131     zmin = -1000;
132     zmax = 1000;
133
134     /* Initializing sensor temperature and number of temperature      ↗
       measurements nt */
135
136     thermosensor_temperature = 0;
137     nt = 0;
138
139     /* Begin loop to determine the temperature at the centroid of cells near ↗
       the thermocouple */
140
141     thread_loop_c(t, d)
142     {
143         begin_c_loop(c, t)
144         {
145             C_CENTROID(thermosensor_coordinate, c, t);
146
147             x = thermosensor_coordinate[0];
148             y = thermosensor_coordinate[1];
149             z = thermosensor_coordinate[2];
150
151             /* If cell is within the thermocouple zone: */
152
153             if ((x >= xmin) && (x <= xmax))
154             {
155                 if ((y >= ymin) && (y <= ymax))
156                 {
157                     if ((z >= zmin) && (z <= zmax))
158                     {
159                         /* get thermocouple temperature */
160                         thermosensor_temperature = thermosensor_temperature + ↗
161                         C_T(c, t);
162                         /* count number */
163                         nt = nt + 1;
164                     }
165                 }
166             }
167         }
168     }
169
170     #if RP_NODE
171     thermosensor_temperature = PRF_GRHIGH1(thermosensor_temperature); /      ↗
172     /*PRF_GRHIGH will be a float in single precision and double in double ↗
       precision!! A new variable may be needed*/
173     nt = PRF_GIHIGH1(nt); /*PRF_GRHIGH will be a float in single precision and ↗
       double in double precision!! A new variable may be needed*/
174     /*Message0("This is the thermosensor temperature from the message 0 node0 ↗
       in Execute_at_end: %g \n", thermosensor_temperature);*/
175     /*Message0("This is nt: %g \n", nt);*/
176     #endif
177     /* Averaging thermocouple temperature */

```

```

178     thermosensor_temperature = thermosensor_temperature / nt;
179     /* transmitting to global variable*/
180     if(time<0.00001)
181     {
182         Tsat_sensor=290;
183     }
184     else
185     {
186         Tsat_sensor=thermosensor_temperature;
187     }
188
189     Message0("Tsat_sensor: %g \n", Tsat_sensor);
190
191 #endif /*!RP_HOST*/
192
193 }
194
195 /*-----*/
196 /* UDF for vapour mass source terms*/
197
198 DEFINE_SOURCE(vap_src, cell, pri_th, dS, eqn)
199 {
200     Thread *mix_th, *sec_th;
201     real m_dot_v;
202     real T_SATv;
203
204     mix_th = THREAD_SUPER_THREAD(pri_th);
205     sec_th = THREAD_SUB_THREAD(mix_th, 1);
206
207     if (Tsat_sensor<200)
208     {
209         T_SATv = 290;
210     }
211     else
212     {
213         T_SATv = Tsat_sensor;
214     }
215     /*#if !RP_HOST
216     Message0("T_SATv: %g \n", T_SATv);
217     #endif*/
218
219     m_dot_v=0.;
220     if(C_T(cell, mix_th)>T_SATv)
221     {
222         m_dot_v = 0.1*C_VOF(cell, sec_th)*C_R(cell, sec_th)*fabs(C_T(cell, sec_th) -
223             T_SATv)/T_SATv;
224     }
225
226     if(C_T(cell, mix_th)<T_SATv)
227     {
228         m_dot_v = -(0.1)*C_VOF(cell, pri_th)*C_R(cell, pri_th)*fabs(T_SATv-C_T
229             (cell,pri_th))/T_SATv;
230     }
231     return m_dot_v ;

```

```

232 }
233
234 /*-----*/
235 /* UDF for liquid mass source terms*/
236 DEFINE_SOURCE(liq_src, cell, sec_th, dS, eqn)
237 {
238 Thread * mix_th, *pri_th;
239 real m_dot_l;
240 real T_SATl;
241 mix_th = THREAD_SUPER_THREAD(sec_th);
242 pri_th = THREAD_SUB_THREAD(mix_th, 0);
243
244 if (Tsat_sensor<200)
245 {
246     T_SATl = 290;
247 }
248 else
249 {
250     T_SATl = Tsat_sensor;
251 }
252 /*#if !RP_HOST
253 Message0("T_SATl: %g \n", T_SATl);
254 #endif*/
255
256 m_dot_l=0.;
257 if(C_T(cell, mix_th)>T_SATl)
258 {
259 m_dot_l = -0.1*C_VOF(cell, sec_th)*C_R(cell, sec_th)*fabs(C_T(cell, sec_th) - T_SATl)/T_SATl;
260 dS[eqn] = -0.1*C_R(cell, sec_th)*fabs(C_T(cell, sec_th) - T_SATl)/T_SATl;
261 }
262 if(C_T(cell, mix_th)<T_SATl)
263 {
264 m_dot_l = (0.1)*C_VOF(cell, pri_th)*C_R(cell, pri_th)*fabs(T_SATl-C_T
265 (cell,pri_th))/T_SATl;
266 dS[eqn] =0.;
267 }
268 return m_dot_l;
269 }
270
271 /*-----*/
272 /* UDF for energy source terms*/
273 DEFINE_SOURCE(enrg_src, cell, mix_th, dS, eqn)
274 {
275 Thread *pri_th, *sec_th;
276 real m_dot;
277 real T_SATe;
278 real LAT_HT;
279
280 pri_th = THREAD_SUB_THREAD(mix_th, 0);
281 sec_th = THREAD_SUB_THREAD(mix_th, 1);
282
283 if (Tsat_sensor<200)
284 {
285     T_SATe = 290;

```

```

286 }
287 else
288 {
289     T_SATe = Tsat_sensor;
290 }
291
292 LAT_HT = (-0.00000072060861414092) * T_SATe * T_SATe * T_SATe * T_SATe *
          T_SATe * T_SATe + (0.00135239711945318000) * T_SATe * T_SATe * T_SATe *
          T_SATe * T_SATe + (-1.05642796140732000000) * T_SATe * T_SATe * T_SATe *
          T_SATe + (439.60222743474300000000) * T_SATe * T_SATe * T_SATe +
          (-102767.74246199100000000000) * T_SATe * T_SATe +
          (12795732.48001870000000000000) * T_SATe +
          (-662641866.34617000000000000000);
293
294 /*#if !RP_HOST
295 Message0("T_SATe: %g \n", T_SATe);
296 #endif*/
297
298 m_dot=0.;
299 if(C_T(cell, mix_th)>T_SATe)
300 {
301 m_dot = -0.1*C_VOF(cell, sec_th)*C_R(cell, sec_th)*fabs(C_T(cell, sec_th) -
          T_SATe)/T_SATe;
302 dS[eqn] = -0.1*C_VOF(cell, sec_th)*C_R(cell, sec_th)*LAT_HT/T_SATe;
303 }
304
305 if(C_T(cell, mix_th)<T_SATe)
306 {
307 m_dot = (0.1)*C_VOF(cell, pri_th)*C_R(cell, pri_th)*fabs(T_SATe-C_T
          (cell,pri_th))/T_SATe;
308 dS[eqn] = (0.1)*C_VOF(cell, pri_th)*C_R(cell, pri_th)*LAT_HT/T_SATe;
309 }
310 return LAT_HT*m_dot;
311 }
312
313 /*-----*/
314

```

## Annexe 8

Mesh metrics of the three-leg multi-channel heat pipe mesh

Mesh tested	Elements	Element's size (mm)	Inflation layers	Avg element quality	Avg orthogonal quality	Avg skewness	Avg aspect ratio
Very coarse	52331	0.7	3	0.77	0.97	0.11	2.12
Coarse	108056	0.5	5	0.76	0.97	0.089	2.6
Medium	145528	0.5	10	0.56	0.95	0.16	5.55
Fine	203304	0.4	10	0.62	0.96	0.13	5.05
Very fine	252805	0.4	15	0.49	0.94	0.18	10.5

## Annexe 9

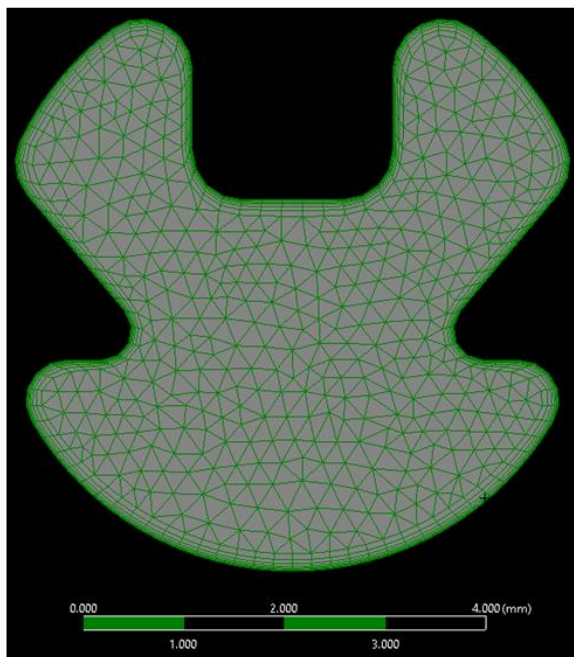
### Mesh metrics of the single channel mesh

Mesh tested	Elements	Element's size (mm)	Inflation layers	Avg element quality	Avg orthogonal quality	Avg skewness	Avg aspect ratio
Very coarse	301 357	0.5	3	0.54	0.61	0.39	4.01
Coarse	1 115 718	0.3	5	0.29	0.65	0.35	4.75
Medium	3 134 150	0.2	7	0.44	0.68	0.31	13.23
Fine	9 524 145	0.15	14	0.32	0.64	0.28	35.58

## Annexe 10

### Single channel mesh selected and equivalent cylindrical channel

A) Channel



B) Cylinder of equivalent hydraulic diameter

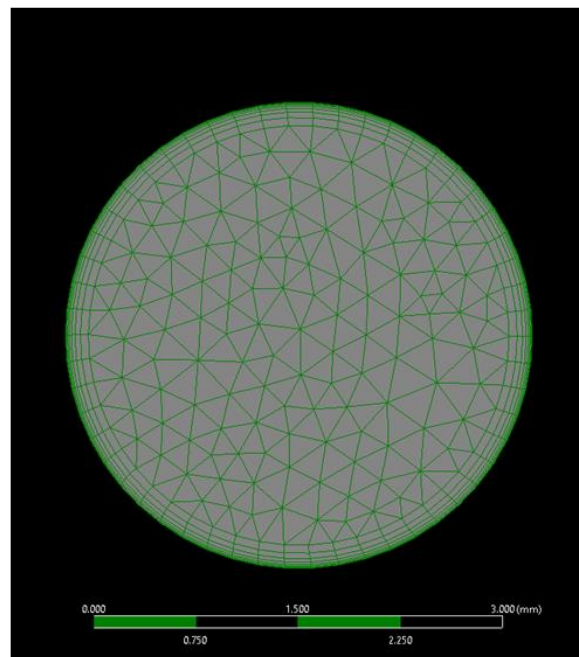


Figure 0-5. Single channel mesh selected and equivalent cylindrical channel

Mesh chosen	Elements	Element's size (mm)	Inflation layers	Avg element quality	Avg orthogonal quality	Avg skewness	Avg aspect ratio
Channel	3 134 150	0.2	7	0.44	0.68	0.31	13.23
Cylinder	1 336 122	0.2	7	0.44	0.73	0.27	12.71

---

## References

---

- [1] M. S. El-Genk and H. H. Saber, "Heat transfer correlations for small, uniformly heated liquid pools," *Int. J. Heat Mass Transf.*, vol. 41, no. 2, pp. 261–274, 1997, doi: 10.1016/S0017-9310(97)00143-9.
- [2] IEA, "World energy balances: Database Documentation (2019 Edition)," 2019.
- [3] IEA, "World Energy Outlook 2019, IEA, Paris," 2019, [Online]. Available: <https://www.iea.org/reports/world-energy-outlook-2019>.
- [4] "International Energy Agency, World energy outlook, Available at: <https://www.iea.org/weo/>," 2017. .
- [5] IEA, "Renewables 2019, IEA, Paris," 2019. [Online]. Available: <https://www.iea.org/reports/renewables-2019>.
- [6] Enerdata, "Global Energy Statistical Yearbook 2019 – Electricity production," 2019. <https://yearbook.enerdata.net/electricity/world-electricity-production-statistics.html>.
- [7] IEA, "Global Energy Review 2020, IEA, Paris," 2020, [Online]. Available: <https://www.iea.org/reports/global-energy-review-2020>.
- [8] IEA, "Installed power generation capacity by source in the Stated Policies Scenario, 2000-2040 , IEA, Paris," 2020, [Online]. Available: <https://www.iea.org/data-and-statistics/charts/installed-power-generation-capacity-by-source-in-the-stated-policies-scenario-2000-2040>.
- [9] K. A. Moharram, M. S. Abd-Elhady, H. A. Kandil, and H. El-Sherif, "Enhancing the performance of photovoltaic panels by water cooling," *Ain Shams Eng. J.*, vol. 4, no. 4, pp. 869–877, Dec. 2013, doi: 10.1016/J.ASEJ.2013.03.005.
- [10] L. Tan, A. Date, G. Fernandes, B. Singh, and S. Ganguly, "Efficiency Gains of Photovoltaic System Using Latent Heat Thermal Energy Storage," *Energy Procedia*, vol. 110, pp. 83–88, Mar. 2017, doi: 10.1016/J.EGYPRO.2017.03.110.
- [11] Y. Tripanagnostopoulos, M. Bazilian, I. Zoulia, and R. Battisti, "Hybrid PV/T system with improved air heat extraction modification," *PV Eur.*, p. 43, 2002.
- [12] A. Pradhan, S. K. S. Parashar, S. M. Ali, and P. Paikray, "Water cooling method to improve efficiency of photovoltaic module," 2016, doi: <https://doi.org/10.1109/SCOPE.2016.7955600>.



- [13] E. Radziemska, "Performance analysis of a photovoltaic-thermal integrated system," *Int. J. Photoenergy*, vol. 2009, no. ii, 2009, doi: 10.1155/2009/732093.
- [14] Y. A. Cengel, "Heat Transfer: A Practical Approach," *New York McGraw-Hill*, pp. 785–841, 2003, doi: 10.1017/CBO9781107415324.004.
- [15] S.-Y. Wu, Q.-L. Zhang, L. Xiao, and F.-H. Guo, "A heat pipe photovoltaic/thermal (PV/T) hybrid system and its performance evaluation," *Energy Build.*, vol. 43, no. 12, pp. 3558–3567, Dec. 2011, doi: 10.1016/J.ENBUILD.2011.09.017.
- [16] M. A. Imteaz and A. Ahsan, "Solar panels: Real efficiencies, potential productions and payback periods for major Australian cities," *Sustain. Energy Technol. Assessments*, vol. 25, pp. 119–125, Feb. 2018, doi: 10.1016/J.SETA.2017.12.007.
- [17] N. Khordehgah, V. Guichet, S. P. Lester, and H. Jouhara, "Computational study and experimental validation of a solar photovoltaics and thermal technology," *Renew. Energy*, vol. 143, pp. 1348–1356, Dec. 2019, doi: 10.1016/J.RENENE.2019.05.108.
- [18] H. Jouhara *et al.*, "The performance of a novel flat heat pipe based thermal and PV/T (photovoltaic and thermal systems) solar collector that can be used as an energy-active building envelope material," *Energy*, vol. 108, pp. 148–154, Aug. 2016, doi: 10.1016/J.ENERGY.2015.07.063.
- [19] S. M. Sultan and M. N. Ervina Efan, "Review on recent Photovoltaic/Thermal (PV/T) technology advances and applications," *Sol. Energy*, vol. 173, pp. 939–954, Oct. 2018, doi: 10.1016/J.SOLENER.2018.08.032.
- [20] A. Tiwari and M. S. Sodha, "Parametric study of various configurations of hybrid PV/thermal air collector: Experimental validation of theoretical model," *Sol. Energy Mater. Sol. Cells*, vol. 91, no. 1, pp. 17–28, Jan. 2007, doi: 10.1016/J.SOLMAT.2006.06.061.
- [21] K. Sopian, H. T. Liu, S. Kakac, and T. N. Veziroglu, "Performance of a double pass photovoltaic thermal solar collector suitable for solar drying systems," *Energy Convers. Manag.*, vol. 41, no. 4, pp. 353–365, Mar. 2000, doi: 10.1016/S0196-8904(99)00115-6.
- [22] M. Y. Othman, B. Yatim, K. Sopian, and M. N. Abu Bakar, "Performance studies on a finned double-pass photovoltaic-thermal (PV/T) solar collector," *Desalination*, vol. 209, no. 1-3 SPEC. ISS., pp. 43–49, Apr. 2007, doi: 10.1016/j.desal.2007.04.007.
- [23] G. L. Jin *et al.*, "Evaluation of single-pass photovoltaic-thermal air collector with rectangle tunnel absorber," *Am. J. Appl. Sci.*, vol. 7, no. 2, p. 277, 2010.

- [24] S. M. Bambrook and A. B. Sproul, "Maximising the energy output of a PVT air system," *Sol. Energy*, vol. 86, no. 6, pp. 1857–1871, Jun. 2012, doi: 10.1016/J.SOLENER.2012.02.038.
- [25] R. Kumar and M. A. Rosen, "Performance evaluation of a double pass PV/T solar air heater with and without fins," *Appl. Therm. Eng.*, vol. 31, no. 8–9, pp. 1402–1410, Jun. 2011, doi: 10.1016/J.APPLTHERMALENG.2010.12.037.
- [26] L. L. Sun, M. Li, Y. P. Yuan, X. L. Cao, B. Lei, and N. Y. Yu, "Effect of tilt angle and connection mode of PVT modules on the energy efficiency of a hot water system for high-rise residential buildings," *Renew. Energy*, vol. 93, pp. 291–301, Aug. 2016, doi: 10.1016/J.RENENE.2016.02.075.
- [27] R. Tripathi and G. N. Tiwari, "Annual performance evaluation (energy and exergy) of fully covered concentrated photovoltaic thermal (PVT) water collector: An experimental validation," *Sol. Energy*, vol. 146, pp. 180–190, Apr. 2017, doi: 10.1016/J.SOLENER.2017.02.041.
- [28] L. T. Kostić, T. M. Pavlović, and Z. T. Pavlović, "Optimal design of orientation of PV/T collector with reflectors," *Appl. Energy*, vol. 87, no. 10, pp. 3023–3029, Oct. 2010, doi: 10.1016/J.APENERGY.2010.02.015.
- [29] P. Dupeyrat, C. Ménézo, M. Rommel, and H.-M. Henning, "Efficient single glazed flat plate photovoltaic–thermal hybrid collector for domestic hot water system," *Sol. Energy*, vol. 85, no. 7, pp. 1457–1468, Jul. 2011, doi: 10.1016/J.SOLENER.2011.04.002.
- [30] B. Lalović, Z. Kiss, and H. Weakliem, "A hybrid amorphous silicon photovoltaic and thermal solar collector," *Sol. Cells*, vol. 19, no. 2, pp. 131–138, Dec. 1986, doi: 10.1016/0379-6787(86)90038-4.
- [31] J. Ji, J. P. Lu, T. T. Chow, W. He, and G. Pei, "A sensitivity study of a hybrid photovoltaic/thermal water-heating system with natural circulation," *Appl. Energy*, vol. 84, no. 2, pp. 222–237, Feb. 2007, doi: 10.1016/j.apenergy.2006.04.009.
- [32] B. Sandnes and J. Rekstad, "A photovoltaic/thermal (PV/T) collector with a polymer absorber plate. Experimental study and analytical model," *Sol. Energy*, vol. 72, no. 1, pp. 63–73, Jan. 2002, doi: 10.1016/S0038-092X(01)00091-3.
- [33] J. S. Coventry, "Performance of a concentrating photovoltaic/thermal solar collector," in *Solar Energy*, Feb. 2005, vol. 78, no. 2, pp. 211–222, doi: 10.1016/j.solener.2004.03.014.

- [34] H. A. Zondag, D. W. de Vries, W. G. J. van Helden, R. J. C. van Zolingen, and A. A. van Steenhoven, "The yield of different combined PV-thermal collector designs," *Sol. Energy*, vol. 74, no. 3, pp. 253–269, Mar. 2003, doi: 10.1016/S0038-092X(03)00121-X.
- [35] M. I. Fadhel, S. M. Sultan, and S. A. Alkaff, "Theoretical Study of New Configuration of Photovoltaic/Thermal Solar Collector (PV/T) Design," *Adv. Mater. Res.*, vol. 772, no. February 2015, pp. 681–687, 2013, doi: 10.4028/www.scientific.net/AMR.772.681.
- [36] A. Nahar, M. Hasanuzzaman, and N. A. Rahim, "Numerical and experimental investigation on the performance of a photovoltaic thermal collector with parallel plate flow channel under different operating conditions in Malaysia," *Sol. Energy*, vol. 144, pp. 517–528, Mar. 2017, doi: 10.1016/J.SOLENER.2017.01.041.
- [37] R. Nasrin, M. Hasanuzzaman, and N. A. Rahim, "Effect of high irradiation and cooling on power, energy and performance of a PVT system," *Renew. Energy*, vol. 116, pp. 552–569, Feb. 2018, doi: 10.1016/j.renene.2017.10.004.
- [38] H. Jouhara, A. Chauhan, T. Nannou, S. Almahmoud, B. Delpech, and L. C. Wrobel, "Heat pipe based systems - Advances and applications," *Energy*, vol. 128, pp. 729–754, Jun. 2017, doi: 10.1016/J.ENERGY.2017.04.028.
- [39] A. Akbarzadeh and T. Wadowski, "Heat pipe-based cooling systems for photovoltaic cells under concentrated solar radiation," *Applied Thermal Engineering*, vol. 16, no. 1. Elsevier Ltd, pp. 81–87, Jan. 01, 1996, doi: 10.1016/1359-4311(95)00012-3.
- [40] W. G. Anderson, P. M. Dussinger, D. B. Sarraf, and S. Tamanna, "Heat pipe cooling of concentrating photovoltaic cells," *Conf. Rec. IEEE Photovolt. Spec. Conf.*, 2008, doi: 10.1109/PVSC.2008.4922577.
- [41] X. Tang, Z. Quan, and Y. Zhao, "Experimental Investigation of Solar Panel Cooling by a Novel Micro Heat Pipe Array," *Energy Power Eng.*, vol. 02, no. 03, pp. 171–174, 2010, doi: 10.4236/epe.2010.23025.
- [42] Y. Deng, Z. Quan, Y. Zhao, L. Wang, and Z. Liu, "Experimental research on the performance of household-type photovoltaic–thermal system based on micro-heat-pipe array in Beijing," *Energy Convers. Manag.*, vol. 106, pp. 1039–1047, Dec. 2015, doi: 10.1016/J.ENCONMAN.2015.09.067.
- [43] L. Hou, Z. Quan, Y. Zhao, L. Wang, and G. Wang, "An experimental and simulative study on a novel photovoltaic-thermal collector with micro heat pipe array (MHPA-PV/T)," *Energy Build.*, vol. 124, pp. 60–69, Jul. 2016, doi:

- 10.1016/J.ENBUILD.2016.03.056.
- [44] P. Gang, F. Huide, Z. Tao, and J. Jie, "A numerical and experimental study on a heat pipe PV/T system," *Sol. Energy*, vol. 85, no. 5, pp. 911–921, May 2011, doi: 10.1016/J.SOLENER.2011.02.006.
- [45] T. Zhang, Z. W. Yan, L. Xiao, H. D. Fu, G. Pei, and J. Ji, "Experimental, study and design sensitivity analysis of a heat pipe photovoltaic/thermal system," *Appl. Therm. Eng.*, vol. 162, p. 114318, Nov. 2019, doi: 10.1016/j.applthermaleng.2019.114318.
- [46] M. Moradgholi, S. M. Nowee, and I. Abrishamchi, "Application of heat pipe in an experimental investigation on a novel photovoltaic/thermal (PV/T) system," *Sol. Energy*, vol. 107, pp. 82–88, Sep. 2014, doi: 10.1016/J.SOLENER.2014.05.018.
- [47] M. Hu, R. Zheng, G. Pei, Y. Wang, J. Li, and J. Ji, "Experimental study of the effect of inclination angle on the thermal performance of heat pipe photovoltaic/thermal (PV/T) systems with wickless heat pipe and wire-meshed heat pipe," *Appl. Therm. Eng.*, vol. 106, pp. 651–660, Aug. 2016, doi: 10.1016/J.APPLTHERMALENG.2016.06.003.
- [48] H. Jouhara *et al.*, "The performance of a heat pipe based solar PV/T roof collector and its potential contribution in district heating applications," *Energy*, vol. 136, pp. 117–125, Oct. 2017, doi: 10.1016/J.ENERGY.2016.04.070.
- [49] M. Modjinou, J. Ji, J. Li, W. Yuan, and F. Zhou, "A numerical and experimental study of micro-channel heat pipe solar photovoltaics thermal system," *Appl. Energy*, vol. 206, pp. 708–722, Nov. 2017, doi: 10.1016/j.apenergy.2017.08.221.
- [50] M. Yu *et al.*, "Experimental Investigation of a Novel Solar Micro-Channel Loop-Heat-Pipe Photovoltaic/Thermal (MC-LHP-PV/T) System for Heat and Power Generation," *Appl. Energy*, vol. 256, p. 113929, Dec. 2019, doi: 10.1016/j.apenergy.2019.113929.
- [51] X. Ren *et al.*, "Assessment of the cost reduction potential of a novel loop-heat-pipe solar photovoltaic/thermal system by employing the distributed parameter model," *Energy*, vol. 190, p. 116338, Jan. 2020, doi: 10.1016/j.energy.2019.116338.
- [52] S. Shittu, G. Li, X. Zhao, J. Zhou, X. Ma, and Y. G. Akhlaghi, "Experimental study and exergy analysis of photovoltaic-thermoelectric with flat plate micro-channel heat pipe," *Energy Convers. Manag.*, vol. 207, p. 112515, Mar. 2020, doi: 10.1016/j.enconman.2020.112515.
- [53] G. Li *et al.*, "Performance analysis on a solar concentrating thermoelectric generator using the micro-channel heat pipe array," *Energy Convers. Manag.*, vol. 112, pp. 191–198, Mar. 2016, doi: 10.1016/j.enconman.2016.01.025.

- [54] X. Sun, L. Ling, S. Liao, Y. Chu, S. Fan, and Y. Mo, "A thermoelectric cooler coupled with a gravity-assisted heat pipe: An analysis from heat pipe perspective," *Energy Convers. Manag.*, vol. 155, pp. 230–242, Jan. 2018, doi: 10.1016/j.enconman.2017.10.068.
- [55] Y. H. Diao, L. Liang, Y. H. Zhao, Z. Y. Wang, and F. W. Bai, "Numerical investigation of the thermal performance enhancement of latent heat thermal energy storage using longitudinal rectangular fins and flat micro-heat pipe arrays," *Appl. Energy*, vol. 233–234, pp. 894–905, Jan. 2019, doi: 10.1016/j.apenergy.2018.10.024.
- [56] R. Zhao, J. Gu, and J. Liu, "An experimental study of heat pipe thermal management system with wet cooling method for lithium ion batteries," *J. Power Sources*, vol. 273, pp. 1089–1097, Jan. 2015, doi: 10.1016/j.jpowsour.2014.10.007.
- [57] L. Zhao, Z. Zheng, B. Guo, and Z. Yang, "Experimental investigation on the thermal performance of air-cooled multi-port flat heat pipes," *Int. J. Heat Mass Transf.*, vol. 154, p. 119600, Jun. 2020, doi: 10.1016/j.ijheatmasstransfer.2020.119600.
- [58] H. Jouhara, N. Serey, N. Khordehgah, R. Bennett, S. Almahmoud, and S. P. Lester, "Investigation, development and experimental analyses of a heat pipe based battery thermal management system," *Int. J. Thermofluids*, p. 100004, Nov. 2019, doi: 10.1016/j.ijft.2019.100004.
- [59] J. S. Chen and J. H. Chou, "Cooling performance of flat plate heat pipes with different liquid filling ratios," *Int. J. Heat Mass Transf.*, vol. 77, pp. 874–882, Oct. 2014, doi: 10.1016/j.ijheatmasstransfer.2014.06.029.
- [60] E. Azad, "Assessment of three types of heat pipe solar collectors," *Renewable and Sustainable Energy Reviews*, vol. 16, no. 5. Pergamon, pp. 2833–2838, Jun. 01, 2012, doi: 10.1016/j.rser.2012.02.001.
- [61] Y. Yasuda, F. Nabeshima, K. Horiuchi, and H. Nagai, "Visualization of the working fluid in a flat-plate pulsating heat pipe by neutron radiography," *Int. J. Heat Mass Transf.*, vol. 185, p. 122336, Apr. 2022, doi: 10.1016/J.IJHEATMASSTRANSFER.2021.122336.
- [62] S. Almahmoud and H. Jouhara, "Experimental and theoretical investigation on a radiative flat heat pipe heat exchanger," *Energy*, vol. 174, pp. 972–984, May 2019, doi: 10.1016/J.ENERGY.2019.03.027.
- [63] S. Almahmoud, "Experimental and theoretical investigation on a radiative flat heat pipe heat exchanger for waste recovery in the steel industry," Brunel University London,

- 2019.
- [64] B. Delpech, B. Axcell, and H. Jouhara, "Experimental investigation of a radiative heat pipe for waste heat recovery in a ceramics kiln," *Energy*, vol. 170, pp. 636–651, Mar. 2019, doi: 10.1016/J.ENERGY.2018.12.133.
- [65] M. Knudsen, "The kinetic theory of gases, methuen & co," *Ltd., London*, 1934.
- [66] R. W. Schrage, *A theoretical study of interphase mass transfer*. Columbia University Press, 1953.
- [67] W. H. Lee, "Pressure iteration scheme for two-phase flow modeling," *IN" Multiph. Transp. Fundam. React. SAFETY, Appl.*, pp. 407–432, 1980.
- [68] S. C. K. De Schepper, G. J. Heynderickx, and G. B. Marin, "Modeling the evaporation of a hydrocarbon feedstock in the convection section of a steam cracker," *Comput. Chem. Eng.*, vol. 33, no. 1, pp. 122–132, Jan. 2009, doi: 10.1016/J.COMPCHEMENG.2008.07.013.
- [69] S. C. K. De Schepper, G. J. Heynderickx, and G. B. Marin, "CFD modeling of all gas–liquid and vapor–liquid flow regimes predicted by the Baker chart," *Chem. Eng. J.*, vol. 138, no. 1–3, pp. 349–357, May 2008, doi: 10.1016/J.CEJ.2007.06.007.
- [70] X. Wang, Y. Zhu, and Y. Wang, "Development of pressure-based phase change model for CFD modelling of heat pipes," *Int. J. Heat Mass Transf.*, vol. 145, p. 118763, Dec. 2019, doi: 10.1016/j.ijheatmasstransfer.2019.118763.
- [71] Y. Kim, J. Choi, S. Kim, and Y. Zhang, "Effects of mass transfer time relaxation parameters on condensation in a thermosyphon," *J. Mech. Sci. Technol.*, vol. 29, no. 12, pp. 5497–5505, 2015, doi: 10.1007/s12206-015-1151-5.
- [72] Z. Liu, B. Sunden, and J. Yuan, "VOF modeling and analysis of filmwise condensation between vertical parallel plates," *Heat Transf. Res.*, vol. 43.1, 2012.
- [73] V. Guichet, S. Almahmoud, and H. Jouhara, "Nucleate pool boiling heat transfer in wickless heat pipes (two-phase closed thermosyphons): A critical review of correlations," *Therm. Sci. Eng. Prog.*, vol. 13, 2019, doi: 10.1016/j.tsep.2019.100384.
- [74] B. A. Nichita and J. R. Thome, "A level set method and a heat transfer model implemented into FLUENT for modeling of microscale two phase flows," in *AVT-178 Specialists' Meeting on System Level Thermal Management for Enhanced Platform Efficiency*, 2010, no. CONF.
- [75] T. Wen, L. Lu, W. He, and Y. Min, "Fundamentals and applications of CFD technology

- on analyzing falling film heat and mass exchangers: A comprehensive review,” *Applied Energy*, vol. 261. Elsevier Ltd, p. 114473, Mar. 01, 2020, doi: 10.1016/j.apenergy.2019.114473.
- [76] C. R. Kharangate and I. Mudawar, “Review of computational studies on boiling and condensation,” *Int. J. Heat Mass Transf.*, vol. 108, pp. 1164–1196, May 2017, doi: 10.1016/J.IJHEATMASSTRANSFER.2016.12.065.
- [77] J. Legierski, B. Wie\_czek, and G. de Mey, “Measurements and simulations of transient characteristics of heat pipes,” *Microelectron. Reliab.*, vol. 46, no. 1, pp. 109–115, Jan. 2006, doi: 10.1016/J.MICROREL.2005.06.003.
- [78] M. Zhang, Z. Liu, G. Ma, and S. Cheng, “Numerical simulation and experimental verification of a flat two-phase thermosyphon,” *Energy Convers. Manag.*, vol. 50, no. 4, pp. 1095–1100, Apr. 2009, doi: 10.1016/J.ENCONMAN.2008.12.001.
- [79] M. Rahmat and P. Hubert, “Two-phase simulations of micro heat pipes,” *Comput. Fluids*, vol. 39, no. 3, pp. 451–460, Mar. 2010, doi: 10.1016/j.compfluid.2009.09.014.
- [80] A. Alizadehdakhel, M. Rahimi, and A. A. Alsairafi, “CFD modeling of flow and heat transfer in a thermosyphon,” *Int. Commun. Heat Mass Transf.*, vol. 37, no. 3, pp. 312–318, Mar. 2010, doi: 10.1016/J.ICHEATMASSTRANSFER.2009.09.002.
- [81] J. . Brackbill, D. . Kothe, and C. Zemach, “A continuum method for modeling surface tension,” *J. Comput. Phys.*, vol. 100, no. 2, pp. 335–354, Jun. 1992, doi: 10.1016/0021-9991(92)90240-Y.
- [82] A. S. Annamalai and V. Ramalingam, “Experimental investigation and computational fluid dynamics analysis of a air cooled condenser heat pipe,” *Therm. Sci.*, vol. 15, no. 3, pp. 759–772, 2011, doi: 10.2298/TSCI100331023A.
- [83] Z. Lin, S. Wang, R. Shirakashi, and L. Winston Zhang, “Simulation of a miniature oscillating heat pipe in bottom heating mode using CFD with unsteady modeling,” *Int. J. Heat Mass Transf.*, vol. 57, no. 2, pp. 642–656, Feb. 2013, doi: 10.1016/J.IJHEATMASSTRANSFER.2012.09.007.
- [84] B. Fadhl, L. C. Wrobel, and H. Jouhara, “Numerical modelling of the temperature distribution in a two-phase closed thermosyphon,” *Appl. Therm. Eng.*, vol. 60, no. 1–2, pp. 122–131, Oct. 2013, doi: 10.1016/J.APPLTHERMALENG.2013.06.044.
- [85] K. Kafeel and A. Turan, “Axi-symmetric simulation of a two phase vertical thermosyphon using Eulerian two-fluid methodology,” *Heat Mass Transf. und Stoffuebertragung*, vol. 49, no. 8, pp. 1089–1099, 2013, doi: 10.1007/s00231-013-

1155-6.

- [86] K. Kafeel and A. Turan, "Simulation of the response of a thermosyphon under pulsed heat input conditions," *Int. J. Therm. Sci.*, vol. 80, pp. 33–40, Jun. 2014, doi: 10.1016/J.IJTHERMALSCI.2014.01.020.
- [87] L. Asmaie, M. Haghshenasfard, A. Mehrabani-Zeinabad, and M. Nasr Esfahany, "Thermal performance analysis of nanofluids in a thermosyphon heat pipe using CFD modeling," *Heat Mass Transf. und Stoffuebertragung*, vol. 49, no. 5, pp. 667–678, 2013, doi: 10.1007/s00231-013-1110-6.
- [88] Z. H. Liu, Y. Y. Li, and R. Bao, "Thermal performance of inclined grooved heat pipes using nanofluids," *Int. J. Therm. Sci.*, vol. 49, no. 9, pp. 1680–1687, Sep. 2010, doi: 10.1016/j.ijthermalsci.2010.03.006.
- [89] B. Fadhl, L. C. Wrobel, and H. Jouhara, "CFD modelling of a two-phase closed thermosyphon charged with R134a and R404a," *Appl. Therm. Eng.*, vol. 78, pp. 482–490, Mar. 2015, doi: 10.1016/J.APPLTHERMALENG.2014.12.062.
- [90] B. Fadhl, "Modelling of the Thermal Behaviour of a Two-Phase Closed Thermosyphon," 2015.
- [91] H. Jouhara, B. Fadhl, and L. C. Wrobel, "Three-dimensional CFD simulation of geyser boiling in a two-phase closed thermosyphon," *Int. J. Hydrogen Energy*, vol. 41, no. 37, pp. 16463–16476, Oct. 2016, doi: 10.1016/J.IJHYDENE.2016.02.038.
- [92] Y. Wang *et al.*, "CFD simulation of an intermediate temperature, two-phase loop thermosiphon for use as a linear solar receiver," *Appl. Energy*, vol. 207, pp. 36–44, Dec. 2017, doi: 10.1016/J.APENERGY.2017.05.168.
- [93] S. ed-D. Fertahi, T. Bouhal, Y. Agrouaz, T. Kousksou, T. El Rhafiki, and Y. Zeraouli, "Performance optimization of a two-phase closed thermosyphon through CFD numerical simulations," *Appl. Therm. Eng.*, vol. 128, pp. 551–563, Jan. 2018, doi: 10.1016/J.APPLTHERMALENG.2017.09.049.
- [94] C. Yue, Q. Zhang, Z. Zhai, and L. Ling, "CFD simulation on the heat transfer and flow characteristics of a microchannel separate heat pipe under different filling ratios," *Appl. Therm. Eng.*, vol. 139, pp. 25–34, Jul. 2018, doi: 10.1016/j.applthermaleng.2018.01.011.
- [95] A. A. B. Temimy and A. A. Abdulrasool, "CFD Modelling for flow and heat transfer in a closed Thermosyphon charged with water-A new observation for the two phase interaction," *IOP Conf. Ser. Mater. Sci. Eng.*, vol. 518, no. 3, 2019, doi: 10.1088/1757-



899X/518/3/032053.

- [96] X. Wang, H. Liu, Y. Wang, and Y. Zhu, "CFD simulation of dynamic heat transfer behaviors in super-long thermosyphons for shallow geothermal application," *Appl. Therm. Eng.*, vol. 174, no. April, p. 115295, 2020, doi: 10.1016/j.applthermaleng.2020.115295.
- [97] X. Wang, Y. Wang, H. Chen, and Y. Zhu, "A combined CFD/visualization investigation of heat transfer behaviors during geyser boiling in two-phase closed thermosyphon," *Int. J. Heat Mass Transf.*, vol. 121, pp. 703–714, Jun. 2018, doi: 10.1016/J.IJHEATMASSTRANSFER.2018.01.005.
- [98] K. Hosseinzadeh, D. D. Ganji, and F. Ommi, "Effect of SiO<sub>2</sub> super-hydrophobic coating and self-rewetting fluid on two phase closed thermosyphon heat transfer characteristics: An experimental and numerical study," *J. Mol. Liq.*, vol. 315, p. 113748, Oct. 2020, doi: 10.1016/j.molliq.2020.113748.
- [99] W. M. Rohsenow, J. P. Hartnett, and E. N. Ganic, *Handbook of heat transfer fundamentals*. New York, 1985.
- [100] W. W. Wang, Y. Cai, L. Wang, C. W. Liu, F. Y. Zhao, and D. Liu, "Thermo-hydrodynamic analytical model, numerical solution and experimental validation of a radial heat pipe with internally finned condenser applied for building heat recovery units," *Energy Convers. Manag.*, vol. 219, p. 113041, Sep. 2020, doi: 10.1016/j.enconman.2020.113041.
- [101] A. Tarokh, C. Bliss, and A. Hemmati, "Performance enhancement of a two-phase closed thermosyphon with a vortex generator," *Appl. Therm. Eng.*, vol. 182, p. 116092, Jan. 2021, doi: 10.1016/j.applthermaleng.2020.116092.
- [102] A. Wei, X. Ren, S. Lin, and X. Zhang, "CFD analysis on flow and heat transfer mechanism of a microchannel  $\Omega$ -shape heat pipe under zero gravity condition," *Int. J. Heat Mass Transf.*, vol. 163, p. 120448, Dec. 2020, doi: 10.1016/J.IJHEATMASSTRANSFER.2020.120448.
- [103] W. Nusselt, "The condensation of steam on cooled surfaces," *Z. Ver. Dtsch. Ing.*, vol. 60, pp. 541–546, 1916.
- [104] B. Crain, "Forced convection heat transfer to a two-phase mixture of water and steam in a helical coil," 1973.
- [105] W. M. Rohsenow Editor *et al.*, "Handbook of heat transfer," 1998. Accessed: Nov. 14, 2018. [Online]. Available: <http://160592857366.free.fr/joe/ebooks/Mechanical>

- [106] R. L. Manlapaz and S. W. Churchill, "Fully developed laminar convection from a helical coil," *Chem. Eng. Commun.*, vol. 9, no. 1–6, pp. 185–200, 1981.
- [107] C. H. Daly, "Thick Walled Cylinders," 2003.  
[http://courses.washington.edu/me354a/Thick Walled Cylinders.pdf](http://courses.washington.edu/me354a/Thick%20Walled%20Cylinders.pdf).
- [108] E. by The institution of Chemical engineers and E. by The Institution of Mechanical Engineers, *ESDU 81038: Heat pipes - performances of two-phase closed thermosyphons*, no. November. London: ESDU international plc, 1983.
- [109] ESDU, "Heat pipes – performance of capillary-driven designs 1.," *ESDU 79012*, no. October, pp. 1–37, 1980.
- [110] H. Jouhara and S. Lester, "Heat Transfer Apparatus," WO2015193683, 2015.
- [111] V. Guichet and H. Jouhara, "Condensation, evaporation and boiling of falling films in wickless heat pipes (two-phase closed thermosyphons): A critical review of correlations," *Int. J. Thermofluids*, p. 100001, Oct. 2019, doi: 10.1016/j.ijft.2019.100001.
- [112] R. Cole, "Boiling Nucleation," *Adv. Heat Transf.*, vol. 10, pp. 85–166, Jan. 1974, doi: 10.1016/S0065-2717(08)70110-2.
- [113] V. P. Carey, "Liquid-Vapor Phase-Change Phenomena," *Hemisph. Publ. Corp. DC*, 1992.
- [114] W. Fritz, "Berechnung des maximalvolumens von dampfblasen," *Phys. Zeitschr*, vol. 36, pp. 379–384, 1935.
- [115] X. Wang, Z. Wu, J. Wei, and B. Sundén, "Correlations for prediction of the bubble departure radius on smooth flat surface during nucleate pool boiling," *Int. J. Heat Mass Transf.*, vol. 132, pp. 699–714, Apr. 2019, doi: 10.1016/J.IJHEATMASSTRANSFER.2018.12.029.
- [116] I. L. Pioro, W. Rohsenow, and S. S. Doerffer, "Nucleate pool-boiling heat transfer. I: Review of parametric effects of boiling surface," *Int. J. Heat Mass Transf.*, vol. 47, no. 23, pp. 5033–5044, 2004, doi: 10.1016/j.ijheatmasstransfer.2004.06.019.
- [117] J. Du, C. Zhao, and H. Bo, "A modified model for bubble growth rate and bubble departure diameter in nucleate pool boiling covering a wide range of pressures," *Appl. Therm. Eng.*, vol. 145, pp. 407–415, Dec. 2018, doi: 10.1016/J.APPLTHERMALENG.2018.09.063.

- [118] S. Hamzekhiani, M. Maniavi Falahieh, and A. Akbari, "Bubble departure diameter in nucleate pool boiling at saturation: Pure liquids and binary mixtures," *Int. J. Refrig.*, vol. 46, pp. 50–58, Oct. 2014, doi: 10.1016/J.IJREFRIG.2014.07.003.
- [119] J. Kim and M. H. Kim, "On the departure behaviors of bubble at nucleate pool boiling," *Int. J. Multiph. Flow*, vol. 32, no. 10–11, pp. 1269–1286, Oct. 2006, doi: 10.1016/J.IJMULTIPHASEFLOW.2006.06.010.
- [120] H. Chen, G. Chen, X. Zou, Y. Yao, and M. Gong, "Experimental investigations on bubble departure diameter and frequency of methane saturated nucleate pool boiling at four different pressures," *Int. J. Heat Mass Transf.*, vol. 112, pp. 662–675, Sep. 2017, doi: 10.1016/J.IJHEATMASSTRANSFER.2017.05.031.
- [121] V. K. Dhir, "Numerical simulations of pool-boiling heat transfer," *AIChE J.*, vol. 47, no. 4, pp. 813–834, 2001, doi: 10.1002/aic.690470407.
- [122] W. Gao, J. Qi, X. Yang, J. Zhang, and D. Wu, "Experimental investigation on bubble departure diameter in pool boiling under sub-atmospheric pressure," *Int. J. Heat Mass Transf.*, vol. 134, pp. 933–947, May 2019, doi: 10.1016/J.IJHEATMASSTRANSFER.2019.01.024.
- [123] R. Cole, "Bubble frequencies and departure volumes at subatmospheric pressures," *AIChE J.*, vol. 13, no. 4, pp. 779–783, 1967.
- [124] J. G. Collier and J. R. Thome, *Convective boiling and condensation*. Clarendon Press, 1994.
- [125] R. L. Mohanty and M. K. Das, "A critical review on bubble dynamics parameters influencing boiling heat transfer," *Renew. Sustain. Energy Rev.*, vol. 78, pp. 466–494, Oct. 2017, doi: 10.1016/J.RSER.2017.04.092.
- [126] T. Kumada, H. Sakashita, and H. Yamagishi, "Pool boiling heat transfer—I. Measurement and semi-empirical relations of detachment frequencies of coalesced bubbles," *Int. J. Heat Mass Transf.*, vol. 38, no. 6, pp. 969–977, Apr. 1995, doi: 10.1016/0017-9310(94)00224-J.
- [127] P. Goel, A. K. Nayak, P. P. Kulkarni, and J. B. Joshi, "Experimental study on bubble departure characteristics in subcooled nucleate pool boiling," *Int. J. Multiph. Flow*, vol. 89, pp. 163–176, Mar. 2017, doi: 10.1016/J.IJMULTIPHASEFLOW.2016.10.012.
- [128] R. Cole, "A photographic study of pool boiling in the region of the critical heat flux," *AIChE J.*, vol. 6, no. 4, pp. 533–538, 1960.

- [129] K. A. Zhokhov, "Number of vapour generating centers," *Aerodyn. Heat Transf. Work. Elem. Power Equipment, Leningrad, Russ.*, pp. 131–135, 1969.
- [130] C. H. Wang and V. K. Dhir, "On the prediction of active nucleation sites including the effect of surface wettability," in *Proceedings of the Engineering Foundation Conference on Pool and External Flow Boiling*, 1992, pp. 111–118.
- [131] B. B. Mikic and W. M. Rohsenow, "A New Correlation of Pool-Boiling Data Including the Effect of Heating Surface Characteristics," *J. Heat Transfer*, vol. 91, no. 2, pp. 245–250, May 1969, [Online]. Available: <http://dx.doi.org/10.1115/1.3580136>.
- [132] K. Nishikawa, Y. Fujita, S. Uchida, and H. Ohta, "Effect of surface configuration on nucleate boiling heat transfer," *Int. J. Heat Mass Transf.*, vol. 27, no. 9, pp. 1559–1571, 1984, doi: 10.1016/0017-9310(84)90268-0.
- [133] H. Merte Jr, H. S. Lee, and J. S. Ervin, "Transient nucleate pool boiling in microgravity: Some initial results," *Microgravity Sci. Technol.*, vol. 7, pp. 173–179, 1994.
- [134] R. F. Gaertner, "Photographic study of nucleate pool boiling on a horizontal surface," *J. Heat Transfer*, vol. 87, no. 1, pp. 17–27, 1965.
- [135] S. Nukiyama, "The maximum and minimum values of the heat Q transmitted from metal to boiling water under atmospheric pressure," *Int. J. Heat Mass Transf.*, vol. 9, no. 12, pp. 1419–1433, 1966.
- [136] G. N. Kruzhilin, "Free-convection transfer of heat from a horizontal plate and boiling liquid," *Dokl. AN SSSR (Reports USSR Acad. Sci.)*, vol. 58, no. 8, pp. 1657–1660, 1947.
- [137] W. M. Rohsenow, "A method of correlating heat-transfer data for surface boiling of liquids," 1952. Accessed: Jan. 26, 2019. [Online]. Available: <http://libraries.mit.edu/docs>.
- [138] M. J. McNelly, "A correlation of rates of heat transfer to nucleate boiling of liquids," *J. Imp. Coll. Chem. Eng. Soc.*, vol. 7, pp. 18–34, 1953.
- [139] H. K. Forster and N. Zuber, "Dynamics of vapor bubbles and boiling heat transfer," *AIChE J.*, vol. 1, no. 4, pp. 531–535, 1955.
- [140] C. L. Tien, "A hydrodynamic model for nucleate pool boiling," *Int. J. Heat Mass Transf.*, vol. 5, no. 6, pp. 533–540, Jun. 1962, doi: 10.1016/0017-9310(62)90164-3.
- [141] J. H. Lienhard, "A semi-rational nucleate boiling heat flux correlation," *Int. J. Heat Mass Transf.*, vol. 6, no. 3, pp. 215–219, Mar. 1963, doi: 10.1016/0017-

9310(63)90108-X.

- [142] I. L. Mostinkski, "Application of the rule of corresponding states for calculation of heat transfer and critical heat flux," *Teploenergetika*, vol. 4, no. 1963, pp. 66–71, 1963.
- [143] G. N. Danilova, "Correlation of boiling heat transfer data for Freons," *Heat Transf. Res*, vol. 2, no. 2, pp. 73–78, 1970.
- [144] D. A. Labuntsov, "Heat transfer problems with nucleate boiling of liquids," *Therm. Eng.(USSR)(Engl. Transl.)*, v. 19, no. 9, pp. 21-28, 1973.
- [145] H. Imura, H. Kusuda, J.-I. Ogata, T. Miyazaki, and N. Sakamoto, "Heat transfer in two-phase closed-type thermosyphons," *JSME Trans.*, vol. 45, pp. 712–722, 1979.
- [146] K. Stephan and P. Preusser, "Wärmeübergang und maximale wärmestromdichte beim behiterierenden binärer und ternärer flüssigkeitsgemische," *Chem Ing Tech*, 1979.
- [147] K. Stephan and M. Abdelsalam, "Heat-transfer correlations for natural convection boiling," *Int. J. Heat Mass Transf.*, vol. 23, no. 1, pp. 73–87, Jan. 1980, doi: 10.1016/0017-9310(80)90140-4.
- [148] M. Shiraishi, K. Kikuchi, and T. Yamanishi, "Investigation of heat transfer characteristics of a two-phase closed thermosyphon," *J. Heat Recover. Syst.*, vol. 1, no. 4, pp. 287–297, Jan. 1981, doi: 10.1016/0198-7593(81)90039-4.
- [149] K. Bier, J. Schmadl, and D. Gorenflo, "Influence of heat flux and saturation pressure on pool boiling heat transfer of binary mixtures.," *VT VERFAHRENSTECHNIK.*, vol. 16, no. 9, pp. 708–710, 1982.
- [150] K. Nishikawa, Y. Fujita, H. Ohta, and S. Hidaka, "Effect of the surface roughness on the nucleate boiling heat transfer over the wide range of pressure," in *Heat Transfer, Proceedings of the International Heat Transfer Conference*, 1982, pp. 61–66.
- [151] M. G. Cooper, "Saturation nucleate pool boiling - A simple correlation," *Inst. Chem. Eng. Symp. Ser.*, vol. 2.86, pp. 785–793, Jan. 1984, doi: 10.1016/B978-0-85295-175-0.50013-8.
- [152] T. Ueda, T. Miyashita, and P.-H. Chu, *Heat transport characteristics of a closed two-phase thermosyphon*, vol. 54. 1988.
- [153] S. S. Kutateladze, "Heat Transfer and Hydrodynamic Resistance: Handbook (in Russian), Chapter 12.7." Energoatomizdat Publishing House, Moscow, 1990.
- [154] U. Groß, "Pool Boiling Heat Transfer inside a Two-Phase Thermosyphon (Correlation

- of Experimental Data),” in *Proc. 9th Int. Heat Transfer Conf.*, 1990, 1990, vol. 2, pp. 57–62.
- [155] D. Gorenflo, P. Sokol, and S. Caplanis, “Pool boiling heat transfer from single plain tubes to various hydrocarbons,” *Int. J. Refrig.*, vol. 13, no. 5, pp. 286–292, Sep. 1990, doi: 10.1016/0140-7007(90)90059-6.
- [156] F. Kaminaga, Y. Okamoto, T. Suzuki, and T. Ma, “Study on boiling heat transfer correlation in a closed two-phase thermosyphon,” 1992.
- [157] W. Leiner, “Heat transfer by nucleate pool boiling—general correlation based on thermodynamic similarity,” *Int. J. Heat Mass Transf.*, vol. 37, no. 5, pp. 763–769, Mar. 1994, doi: 10.1016/0017-9310(94)90114-7.
- [158] W. Leiner and D. Gorenflo, “Methods of predicting the boiling curve and a new equation based on thermodynamic similarity,” *Pool Extern. Flow Boil.*, pp. 99–103, 1992.
- [159] F. M. Chowdhury, F. Kaminaga, K. Goto, and K. Matsumura, “Boiling heat transfer in a small diameter tube below atmospheric pressure on a natural circulation condition,” *J. Japan Assoc. Heat Pipe*, vol. 16, no. 1997, pp. 14–16, 1997.
- [160] T. Kiatsiriroat, A. Nuntaphan, and J. Tiansuwan, “Thermal performance enhancement of thermosyphon heat pipe with binary working fluids,” *Exp. Heat Transf.*, vol. 13, no. 2, pp. 137–152, 2000, doi: 10.1080/089161500269517.
- [161] G. Ribatski and J. M. S. Jabardo, “Experimental study of nucleate boiling of halocarbon refrigerants on cylindrical surfaces,” *Int. J. Heat Mass Transf.*, vol. 46, no. 23, pp. 4439–4451, Nov. 2003, doi: 10.1016/S0017-9310(03)00252-7.
- [162] Y. Kim, D. H. Shin, J. S. Kim, S. M. You, and J. Lee, “Boiling and condensation heat transfer of inclined two-phase closed thermosyphon with various filling ratios,” *Appl. Therm. Eng.*, vol. 145, pp. 328–342, Dec. 2018, doi: 10.1016/J.APPLTHERMALENG.2018.09.037.
- [163] H. Mroue, J. B. Ramos, L. C. Wrobel, and H. Jouhara, “Performance evaluation of a multi-pass air-to-water thermosyphon-based heat exchanger,” *Energy*, vol. 139, pp. 1243–1260, Nov. 2017, doi: 10.1016/J.ENERGY.2017.04.111.
- [164] J. Ramos, A. Chong, and H. Jouhara, “Experimental and numerical investigation of a cross flow air-to-water heat pipe-based heat exchanger used in waste heat recovery,” *Int. J. Heat Mass Transf.*, vol. 102, pp. 1267–1281, Nov. 2016, doi: 10.1016/J.IJHEATMASSTRANSFER.2016.06.100.

- [165] F. P. Incropera, D. P. DeWitt, T. L. Bergman, and A. S. Lavine, "Fundamentals of Heat and Mass Transfer," *Fundamentals of Heat and Mass Transfer*. p. 997, 2007, doi: 10.1016/j.applthermaleng.2011.03.022.
- [166] F. M. Chowdhury and Fumito Kaminaga, "Boiling heat transfer characteristics of R-113 in a vertical small diameter tube under natural circulation condition," *Int. J. Heat Mass Transf.*, vol. 45, no. 24, pp. 4823–4829, Nov. 2002, doi: 10.1016/S0017-9310(02)00174-6.
- [167] D. Jafari, S. Filippeschi, A. Franco, and P. Di Marco, "Unsteady experimental and numerical analysis of a two-phase closed thermosyphon at different filling ratios," *Exp. Therm. Fluid Sci.*, vol. 81, pp. 164–174, Feb. 2017, doi: 10.1016/J.EXPTHERMFLUSCI.2016.10.022.
- [168] D. Jafari, P. Di Marco, S. Filippeschi, and A. Franco, "An experimental investigation on the evaporation and condensation heat transfer of two-phase closed thermosyphons," *Exp. Therm. Fluid Sci.*, vol. 88, pp. 111–123, Nov. 2017, doi: 10.1016/J.EXPTHERMFLUSCI.2017.05.019.
- [169] H. Jouhara and A. J. Robinson, "Experimental investigation of small diameter two-phase closed thermosyphons charged with water, FC-84, FC-77 and FC-3283," *Appl. Therm. Eng.*, vol. 30, no. 2–3, pp. 201–211, Feb. 2010, doi: 10.1016/J.APPLTHERMALENG.2009.08.007.
- [170] I. L. Pioro, W. Rohsenow, and S. S. Doerffer, "Nucleate pool-boiling heat transfer. II: assessment of prediction methods," *Int. J. Heat Mass Transf.*, vol. 47, no. 23, pp. 5045–5057, Nov. 2004, doi: 10.1016/J.IJHEATMASSTRANSFER.2004.06.020.
- [171] Y. J. Park, H. K. Kang, and C. J. Kim, "Heat transfer characteristics of a two-phase closed thermosyphon to the fill charge ratio," *Int. J. Heat Mass Transf.*, vol. 45, no. 23, pp. 4655–4661, Nov. 2002, doi: 10.1016/S0017-9310(02)00169-2.
- [172] S. H. Noie, "Heat transfer characteristics of a two-phase closed thermosyphon," *Appl. Therm. Eng.*, vol. 25, no. 4, pp. 495–506, Mar. 2005, doi: 10.1016/J.APPLTHERMALENG.2004.06.019.
- [173] W. Guo and D. W. Nutter, "An experimental study of axial conduction through a thermosyphon pipe wall," *Appl. Therm. Eng.*, vol. 29, no. 17–18, pp. 3536–3541, Dec. 2009, doi: 10.1016/J.APPLTHERMALENG.2009.06.008.
- [174] D. Jafari, A. Franco, S. Filippeschi, and P. Di Marco, "Two-phase closed thermosyphons: A review of studies and solar applications," *Renew. Sustain. Energy*

- Rev., vol. 53, pp. 575–593, Jan. 2016, doi: 10.1016/J.RSER.2015.09.002.
- [175] I. Tanasawa, “Advances in Condensation Heat Transfer,” *Adv. Heat Transf.*, vol. 21, pp. 55–139, Jan. 1991, doi: 10.1016/S0065-2717(08)70334-4.
- [176] V. Guichet and H. Jouhara, “Condensation, evaporation and boiling of falling films in wickless heat pipes (two-phase closed thermosyphons): A critical review of correlations,” *Int. J. Thermofluids*, vol. 1–2, 2020, doi: 10.1016/j.ijft.2019.100001.
- [177] Y. Luo, M. Wang, H. Yang, L. Lu, and J. Peng, “Experimental study of the film thickness in the dehumidifier of a liquid desiccant air conditioning system,” *Energy*, vol. 84, pp. 239–246, May 2015, doi: 10.1016/J.ENERGY.2015.02.091.
- [178] H. Takahama and S. Kato, “Longitudinal flow characteristics of vertically falling liquid films without concurrent gas flow,” *Int. J. Multiph. Flow*, vol. 6, no. 3, pp. 203–215, Jun. 1980, doi: 10.1016/0301-9322(80)90011-7.
- [179] Y. Q. Yu, S. J. Wei, Y. H. Yang, and X. Cheng, “Experimental study of water film falling and spreading on a large vertical plate,” *Prog. Nucl. Energy*, vol. 54, no. 1, pp. 22–28, Jan. 2012, doi: 10.1016/J.PNUCENE.2011.09.007.
- [180] K. Moran, J. Inumaru, and M. Kawaji, “Instantaneous hydrodynamics of a laminar wavy liquid film,” *Int. J. Multiph. Flow*, vol. 28, no. 5, pp. 731–755, May 2002, doi: 10.1016/S0301-9322(02)00006-X.
- [181] W. H. McAdams, “Heat Transmission - Second Edition.” McGRAW, New York, 1942.
- [182] S. J. Chen, J. G. Reed, and C. L. Tien, “Reflux condensation in a two-phase closed thermosyphon,” *Int. J. Heat Mass Transf.*, vol. 27, no. 9, pp. 1587–1594, Sep. 1984, doi: 10.1016/0017-9310(84)90271-0.
- [183] S. Oh and S. T. Revankar, “Complete condensation in a vertical tube passive condenser,” *Int. Commun. Heat Mass Transf.*, vol. 32, no. 5, pp. 593–602, 2005, doi: 10.1016/j.icheatmasstransfer.2004.10.017.
- [184] W. M. Rohsenow, “Heat transfer and temperature distribution in laminar film condensation,” *Trans. Asme*, vol. 78, pp. 1645–1648, 1956.
- [185] P. L. Kapitza, “Wave flow of thin layers of viscous liquid. Part I. Free flow,” *Zhurnal Eksp. i Teor. Fiz.*, vol. 18, pp. 3–18, 1948.
- [186] R. P. Salazar and E. Marschall, “Three-dimensional surface characteristics of a falling liquid film,” *Int. J. Multiph. Flow*, vol. 4, no. 5–6, pp. 487–496, Dec. 1978, doi: 10.1016/0301-9322(78)90009-5.



- [187] I. A. Mudawwar and M. A. El-Masri, "Momentum and heat transfer across freely-falling turbulent liquid films," *Int. J. Multiph. Flow*, vol. 12, no. 5, pp. 771–790, Sep. 1986, doi: 10.1016/0301-9322(86)90051-0.
- [188] M. Cerza and V. Sernas, "Nucleate Boiling in Thermally Developing and Fully Developed Laminar Falling Water Films," *J. Heat Transfer*, vol. 110, no. 1, p. 221, 1988, doi: 10.1115/1.3250455.
- [189] T. Fujita and T. Ueda, "Heat transfer to falling liquid films and film breakdown—II: Saturated liquid films with nucleate boiling," *Int. J. Heat Mass Transf.*, vol. 21, no. 2, pp. 109–118, Feb. 1978, doi: 10.1016/0017-9310(78)90213-2.
- [190] S. S. Kutateladze, *Heat transfer theory fundamentals*. Atomizdat, Moscow./E. Arnold Publishers, London, Academic Press Inc, New York, 1963.
- [191] C. Butterworth, "Condensers: Basic heat transfer and fluid flow," *Kakaç, S.; Bergles, AE; Mayinger, F. Heat Exch. Therm. Fundam. Des. Washingt. Hemisph.*, pp. 289–313, 1981.
- [192] J. C. Y. Wang and Y. Ma, "Condensation Heat Transfer Inside Vertical and Inclined Thermosyphons," *J. Heat Transfer*, vol. 113, no. 3, pp. 777–780, Aug. 1991.
- [193] U. Gross, "Reflux condensation heat transfer inside a closed thermosyphon," *Int. J. Heat Mass Transf.*, vol. 35, no. 2, pp. 279–294, Feb. 1992, doi: 10.1016/0017-9310(92)90267-V.
- [194] G. Schnabel and J. W. Palen, "Wärmeübergang an senkrechten berieselten Flächen," *Springer-Verlag Sect. Md., Berlin*, 1998.
- [195] H. M. S. Hussein, M. A. Mohamad, and A. S. El-Asfour, "Theoretical analysis of laminar-film condensation heat transfer inside inclined wickless heat pipes flat-plate solar collector," *Renew. Energy*, vol. 23, no. 3–4, pp. 525–535, Jul. 2001, doi: 10.1016/S0960-1481(00)00149-X.
- [196] S. Fiedler and H. Auracher, "Experimental and theoretical investigation of reflux condensation in an inclined small diameter tube," *Int. J. Heat Mass Transf.*, vol. 47, no. 19–20, pp. 4031–4043, Sep. 2004, doi: 10.1016/J.IJHEATMASSTRANSFER.2004.06.005.
- [197] H. Uehara, H. Kusuda, T. NAKAORA, and M. Yamada, "Filmwise condensation for turbulent flow in a vertical plate," *Heat Transf. Japanese Res.*, vol. 12, no. 2, pp. 85–96, 1983.

- [198] M. H. Chun and K. T. Kim, "A natural convection heat transfer correlation for laminar and turbulent film condensation on a vertical surface," in *3rd ASME/JSME Thermal Engineering Joint Conference*, 1991, pp. 459–464.
- [199] W. M. Nozhat, "The effect of free surface curvature on the heat transfer coefficient of thin liquid films," in *Fourth American Society of Mechanical Engineers/Japanese Society of Mechanical Engineers Thermal Engineering Joint Conference, Maui, Hawaii*, 1995, vol. 2, pp. 171–178.
- [200] H. Hashimoto and F. Kaminaga, "Heat transfer characteristics in a condenser of closed two-phase thermosyphon: Effect of entrainment on heat transfer deterioration," *Heat Transf. Res.*, vol. 31, no. 3, pp. 212–225, May 2002, doi: 10.1002/htj.10030.
- [201] D. A. Labuntsov, "Heat transfer in film condensation of pure steam on vertical surfaces and horizontal tubes," *Teploenergetika*, vol. 4, no. 7, pp. 72–79, 1957.
- [202] R. A. Seban and A. Faghri, "Film condensation in a vertical tube with a closed top," *Int. J. Heat Mass Transf.*, vol. 27, no. 6, pp. 944–948, Jun. 1984, doi: 10.1016/0017-9310(84)90017-6.
- [203] T. Fujii and H. Uehara, "Laminar filmwise condensation on a vertical surface," *Int. J. Heat Mass Transf.*, vol. 15, no. 2, pp. 217–233, Feb. 1972, doi: 10.1016/0017-9310(72)90070-1.
- [204] M. Gourdon and E. Mura, "Performance evaluation of falling film evaporators in the dairy industry," *Food Bioprod. Process.*, vol. 101, pp. 22–31, Jan. 2017, doi: 10.1016/J.FBP.2016.10.004.
- [205] H. Jouhara, "4.3 Heat Pipes," in *Comprehensive Energy Systems*, vol. 4, no. m, Elsevier, 2018, pp. 70–97.
- [206] Q. Baojin, Z. Li, X. Hong, and S. Yan, "Heat transfer characteristics of titanium/water two-phase closed thermosyphon," *Energy Convers. Manag.*, vol. 50, no. 9, pp. 2174–2179, Sep. 2009, doi: 10.1016/J.ENCONMAN.2009.04.030.
- [207] C. R. Kharangate, H. Lee, and I. Mudawar, "Computational modeling of turbulent evaporating falling films," *Int. J. Heat Mass Transf.*, vol. 81, pp. 52–62, Feb. 2015, doi: 10.1016/J.IJHEATMASSTRANSFER.2014.09.068.
- [208] W. Wilke, "Wärmeübergang an Rieselfilme: Mitteilung d. Forschungsgruppe f. Wärme- u. Kältetechnik im Max-Planck-Inst. f. Strömungsforschung, Göttingen," VDI-Verlag, 1962.

- [209] G. F. Hewitt, G. L. Shires, and T. R. Bott, *Process heat transfer*, vol. 113. CRC press Boca Raton, FL, 1994.
- [210] G. J. Gimbutis, "Heat transfer of a turbulent vertically falling film," 1974.
- [211] J. A. Shmerler and I. Mudawwar, "Local heat transfer coefficient in wavy free-falling turbulent liquid films undergoing uniform sensible heating," *Int. J. Heat Mass Transf.*, vol. 31, no. 1, pp. 67–77, Jan. 1988, doi: 10.1016/0017-9310(88)90223-2.
- [212] N. M. Al-Najem, K. Y. Ezuddin, and M. A. Darwish, "Heat transfer analysis of preheated turbulent falling films in vertical tube evaporators," *Desalination*, vol. 115, no. 1, pp. 43–55, Mar. 1998, doi: 10.1016/S0011-9164(98)00025-3.
- [213] X. Ye, W. Yan, Z. Jiang, and C. Li, "Hydrodynamics of free-falling turbulent wavy films and implications for enhanced heat transfer," *Heat Transf. Eng.*, vol. 23, no. 1, pp. 48–60, 2002, doi: 10.1080/014576302753249606.
- [214] T. Fujita and T. Ueda, "Heat transfer to falling liquid films and film breakdown—I: Subcooled liquid films," *Int. J. Heat Mass Transf.*, vol. 21, no. 2, pp. 97–108, Feb. 1978, doi: 10.1016/0017-9310(78)90212-0.
- [215] A. A. Alhusseini, K. Tuzla, and J. C. Chen, "Falling film evaporation of single component liquids," *Int. J. Heat Mass Transf.*, vol. 41, no. 12, pp. 1623–1632, Jun. 1998, doi: 10.1016/S0017-9310(97)00308-6.
- [216] A. Åsblad and T. Berntsson, "Surface evaporation of turbulent falling films," *Int. J. Heat Mass Transf.*, vol. 34, no. 3, pp. 835–841, Mar. 1991, doi: 10.1016/0017-9310(91)90129-3.
- [217] B. Narváez-Romo, M. Chhay, E. W. Zavaleta-Aguilar, and J. R. Simões-Moreira, "A critical review of heat and mass transfer correlations for LiBr-H<sub>2</sub>O and NH<sub>3</sub>-H<sub>2</sub>O absorption refrigeration machines using falling liquid film technology," *Appl. Therm. Eng.*, vol. 123, pp. 1079–1095, Aug. 2017, doi: 10.1016/J.APPLTHERMALENG.2017.05.092.
- [218] W. Nusselt, "Die Oberfluchenkondensation des Wasserdampfes," *Z. VDI*, vol. 60, no. 28, p. 569, 1916.
- [219] S. Y. Ahmed and R. Kaparathi, "Heat transfer studies of falling film heat exchangers," *Indian J. Technol.*, vol. 1, pp. 377–381, 1963.
- [220] R. A. Seban and K. R. Chun, "Heat transfer to evaporating liquid films," *J. Heat Transf.*, vol. 93, pp. 391–396, 1971.

- [221] V. V WADEKAR, "Heat transfer to falling liquid films with high Prandtl numbers," in *European thermal sciences conference*, 2000, pp. 851–856.
- [222] W. H. Parken, L. S. Fletcher, V. Sernas, and J. C. Han, "Heat Transfer Through Falling Film Evaporation and Boiling on Horizontal Tubes," *J. Heat Transfer*, vol. 112, no. 3, pp. 744–750, Aug. 1990, [Online]. Available: <http://dx.doi.org/10.1115/1.2910449>.
- [223] R. Numrich, "Heat transfer in turbulent falling films," *Chem. Eng. Technol.*, vol. 18, no. 3, pp. 171–177, Jun. 1995, doi: 10.1002/ceat.270180305.
- [224] A. E. Dukler, "Predicting heat transfer coefficient for film flow," *Petro/Chem. Eng. Bd*, vol. 33, p. 198, 1961.
- [225] L. S. Herbert and V. J. Sterns, "An experimental investigation of heat transfer to water in film flow Part II—boiling runs with and without induced swirl," *Can. J. Chem. Eng.*, vol. 46, no. 6, pp. 408–412, 1968.
- [226] H. Struve, *Der Wärmeübergang an einem verdampfenden Rieselfilm*. VDI-Forschungsheft, 1969.
- [227] C. Elle, "Der Wärmeübergang bei der Rieselfilmverdampfung des Kältemittels R 11 und des Kältemittel-Öl-Gemisches R 11-51 KM 33," Technische Universität Dresden, 1970.
- [228] G. Schnabel and E. U. Schluender, "Wärmeübergang von senkrechten Wänden an nichtsiedende und siedende Rieselfilme. 'Heat Transfer from Vertical Walls to Falling Liquid Films with or Without Evaporation.,'" *Verfahrenstechnik*, vol. 14, no. 2, pp. 79–83, 1980, [Online]. Available: <https://www.scopus.com/inward/record.uri?eid=2-s2.0-0018982938&partnerID=40&md5=2e0fbe41c40346007b555a6e7784d0ef>.
- [229] P. Holmberg, L. Persson, and T. Berntsson, "Heat transfer in falling film lithiumbromide-water evaporator, an experimental study," 1991.
- [230] M. Gourdon, E. Karlsson, F. Innings, A. Jongsma, and L. Vamling, "Heat transfer for falling film evaporation of industrially relevant fluids up to very high Prandtl numbers," *Heat Mass Transf.*, vol. 52, no. 2, pp. 379–391, 2015, [Online]. Available: <https://link.springer.com/article/10.1007%2Fs00231-015-1556-9>.
- [231] T. Xue and S. Zhang, "Investigation on heat transfer characteristics of falling liquid film by planar laser-induced fluorescence," *Int. J. Heat Mass Transf.*, vol. 126, pp. 715–724, Nov. 2018, doi: 10.1016/J.IJHEATMASSTRANSFER.2018.05.039.
- [232] S. G. Kandlikar, *Handbook of phase change: boiling and condensation*. Routledge,

2018.

- [233] M. Cerza and V. Sernas, "A bubble growth model for nucleate boiling in thin, falling, superheated, laminar, water films," *Int. J. Heat Mass Transf.*, vol. 28, no. 7, pp. 1307–1316, Jul. 1985, doi: 10.1016/0017-9310(85)90161-9.
- [234] W. H. Parken Jr, "Heat transfer to thin water films on horizontal tubes," Rutgers University, 1975.
- [235] K. A. Stanzione and V. Sernas, "Some aspects of the heat transfer mechanism during boiling of falling water films," in *16th Thermophysics Conference*, 1981, p. 1064.
- [236] I. A. Kopchikov, G. I. Voronin, T. A. Kolach, D. A. Labuntsov, and P. D. Lebedev, "Liquid boiling in a thin film," *Int. J. Heat Mass Transf.*, vol. 12, no. 7, pp. 791–796, 1969, doi: 10.1016/0017-9310(69)90182-3.
- [237] M. S. El-Genk and H. H. Saber, "Determination of operation envelopes for closed, two-phase thermosyphons," *Int. J. Heat Mass Transf.*, vol. 42, no. 5, pp. 889–903, 1999, doi: 10.1016/S0017-9310(98)00212-9.
- [238] I. I. Gogonin, "The dependence of boiling heat transfer on the properties and geometric parameters of heat-transfer wall," *High Temp.*, vol. 44, no. 6, pp. 913–921, 2006, doi: 10.1007/s10740-006-0110-3.
- [239] A. Žukauskas, "Heat Transfer from Tubes in Crossflow," *Adv. Heat Transf.*, vol. 8, pp. 93–160, Jan. 1972, doi: 10.1016/S0065-2717(08)70038-8.
- [240] R. L. Manlapaz and S. W. Churchill, "Fully developed laminar flow in a helically coiled tube of finite pitch," *Chem. Eng. Commun.*, vol. 7, no. 1–3, pp. 57–78, 1980.
- [241] P. S. Srinivasan, S. S. Nandapurkar, and F. A. Holland, "Friction factors for coils," *Trans. Inst. Chem. Eng. Chem. Eng.*, vol. 48, no. 4–6, pp. T156–+, 1970.
- [242] P. J. Linstrom and W. G. Mallard, "The NIST Chemistry WebBook: A chemical data resource on the internet," *J. Chem. Eng. Data*, vol. 46, no. 5, pp. 1059–1063, 2001.
- [243] I. Ansys, "UDFs for Multiphase Flows - Advanced UDF modeling Coursed," 2008.
- [244] "ANSYS FLUENT 12.0/12.1 Documentation."  
<https://www.afs.enea.it/project/neptunius/docs/fluent/index.htm> (accessed Mar. 14, 2022).
- [245] C. Yue, Q. Zhang, Z. Zhai, and L. Ling, "Numerical investigation on thermal characteristics and flow distribution of a parallel micro-channel separate heat pipe in

- data center,” *Int. J. Refrig.*, vol. 98, pp. 150–160, Feb. 2019, doi: 10.1016/j.ijrefrig.2018.10.025.
- [246] X. Quan, Y. Geng, P. Yuan, Z. Huang, and C. Liu, “Experiment and simulation of the shrinkage of falling film upon direct contact with vapor,” *Chem. Eng. Sci.*, vol. 135, pp. 52–60, Dec. 2014, doi: 10.1016/j.ces.2015.06.055.
- [247] A. Ferrari, M. Magnini, and J. R. Thome, “Numerical analysis of slug flow boiling in square microchannels,” *Int. J. Heat Mass Transf.*, vol. 123, pp. 928–944, Aug. 2018, doi: 10.1016/J.IJHEATMASSTRANSFER.2018.03.012.
- [248] J. D. Anderson and J. Wendt, *Computational fluid dynamics*, vol. 206. Springer, 1995.
- [249] Fluent user services Center, “User-Defined Functions - Introductory FLUENT training,” 2006. [http://www.pmt.usp.br/academic/martoran/notasmodelosgrad/ANSYS Fluent UDF Manual.pdf](http://www.pmt.usp.br/academic/martoran/notasmodelosgrad/ANSYS%20Fluent%20UDF%20Manual.pdf).
- [250] I. Ansys, “ANSYS Fluent UDF Manual,” 2013. [Online]. Available: [http://scholar.google.co.uk/scholar?hl=en&q=ansys&btnG=&as\\_sdt=1%2C5&as\\_sdt=#7](http://scholar.google.co.uk/scholar?hl=en&q=ansys&btnG=&as_sdt=1%2C5&as_sdt=#7).
- [251] H. I. Mohammed, D. Giddings, and G. S. Walker, “CFD multiphase modelling of the acetone condensation and evaporation process in a horizontal circular tube,” *Int. J. Heat Mass Transf.*, vol. 134, pp. 1159–1170, May 2019, doi: 10.1016/j.ijheatmasstransfer.2019.02.062.
- [252] V. Ramiah, M. Gangemi, and M. Liu, “Environmental policies post the Kyoto Protocol on Climate Change: evidence from the US and Japan,” in *Handbook of Environmental and Sustainable Finance*, Elsevier, 2016, pp. 25–54.
- [253] C. United Nations Environment Programme. Solvents and Adhesives Technical Options Committee, *Montreal Protocol on Substances that Deplete the Ozone Layer: 1995 Assessment*. UNEP, 1994.
- [254] C. S. Choudhari and S. N. Sapali, “Performance Investigation of Natural Refrigerant R290 as a Substitute to R22 in Refrigeration Systems,” *Energy Procedia*, vol. 109, no. November 2016, pp. 346–352, 2017, doi: 10.1016/j.egypro.2017.03.084.
- [255] V. Apostol, G. Popescu, H. Pop, M. Feidt, and T. Popescu, “Thermodynamic Analysis of New Eco-Refrigerants Ammonia and Dimethylether,” *Termotehnica*, vol. 2, no. 1, pp. 75–80, 2008, [Online]. Available: <http://www.agir.ro/buletine/588.pdf>.
- [256] D. A. Good, J. S. Francisco, A. K. Jain, and D. J. Wuebbles, “Lifetimes and global

warming potentials for dimethyl ether and for fluorinated ethers: CH<sub>3</sub>OCHF<sub>3</sub> (E143a), CHF<sub>2</sub>OCHF<sub>2</sub> (E134), CHF<sub>2</sub>OCHF<sub>3</sub> (E125),” *J. Geophys. Res. Atmos.*, vol. 103, no. D21, pp. 28181–28186, 1998, doi: 10.1029/98JD01880.

- [257] Bitzer Refrigeration, “Refrigerant report 21 - A-501-21-EN,” 2020. [Online]. Available: [www.bitzer.de](http://www.bitzer.de).
- [258] Mexichem Refrigerants, “Klea ® 407A Data Sheet – SI Units,” 2016. [Online]. Available: <https://www.kouraglobal.com/products/refrigeration/r407a-refrigerant-klea407a/klea407a-tech-docs/index.html>.
- [259] eThermo, “eThermo Calculation Platform - Thermodynamics&Transport Properties.” <http://www.ethermo.us/default.aspx>.
- [260] Bitzer Refrigeration, “Complete refrigerant data - A-501-21 - digital.” [https://www.bitzer.de/shared\\_media/html/a-540/en-GB/369747979369749515.html](https://www.bitzer.de/shared_media/html/a-540/en-GB/369747979369749515.html).
- [261] Climalife - IDS Refrigeration Limited, “Climalife - Refrigerants.” <https://www.climalife.co.uk/refrigerants>.
- [262] Department for Environment; Food & Rural Affairs and Environment Agency, “Calculate the carbon dioxide equivalent quantity of an F gas - GOV.UK,” *United Kingdom Government*. 2014, [Online]. Available: <https://www.gov.uk/guidance/calculate-the-carbon-dioxide-equivalent-quantity-of-an-f-gas>.
- [263] P. Nemeč, A. Čaja, and M. Malcho, “Mathematical model for heat transfer limitations of heat pipe,” *Math. Comput. Model.*, vol. 57, no. 1–2, pp. 126–136, Jan. 2013, doi: 10.1016/J.MCM.2011.06.047.